

NASA Conference Publication 3147

26th Aerospace Mechanisms Symposium

CONFERENCE REPORT THE 26TH AEROSPACE
MECHANISMS SYMPOSIUM (NASA) 386 p CSCL 29K

N72-25091
--T440--
N72-25091
Unclass
0085011

H1/39

26th Aerospace Mechanisms Symposium

Proceedings of a symposium sponsored by the
National Aeronautics and Space Administration,
Washington, D.C., the California Institute of
Technology, Pasadena, California, and the
Lockheed Missiles and Space Company, Inc.,
Sunnyvale, California, and held at
NASA Goddard Space Flight Center,
Greenbelt, Maryland
May 13–15, 1992



National Aeronautics and
Space Administration
Office of Management
Scientific and Technical
Information Program

1992

PREFACE

The proceedings of the 26th Aerospace Mechanisms Symposium, which was hosted by the Goddard Space Flight Center, Greenbelt, Maryland, on May 13, 14, and 15, 1992, are reported in this NASA Conference Publication. The symposium was sponsored by the National Aeronautics and Space Administration, the California Institute of Technology, and Lockheed Missiles and Space Company, Inc.

The purpose of the symposium was to provide a forum for the interchange of information among those active in the field of mechanisms technology. To that end, 25 papers were presented on aeronautics and space flight, with special emphasis on actuators, aerospace mechanism applications for ground-support equipment, lubricants, latches, connectors, and other mechanisms for large space structures. The papers were prepared by authors from a broad aerospace background, including the U.S. aerospace industry, NASA, and European participants.

The efforts of the review committee, session chairmen, and speakers contributing to the technical excellence and professional character of the conference are especially appreciated.

The use of trade names or names of manufacturers in this publication does not constitute an official endorsement of such products or manufacturers, either expressed or implied, by the National Aeronautics and Space Administration.

CONTENTS

SYMPOSIUM SCHEDULE	ix
SYMPOSIUM COMMITTEES	xv

SESSION I

Development of a Non-Explosive Research Device for Aerospace Applications.....	1
<i>John D. Busch, William E. Purdy, and A. David Johnson</i>	
Novel Aerospace Mechanisms: A Passive Tether Damping Device for a Tethered Satellite, and a Pin/Latch Structural Interface System	17
<i>John W. Redmon, Jr.</i>	
ADELE: <u>A</u> rticulation de <u>D</u> eploiement à <u>L</u> âmes d' <u>E</u> nroulement	33
<i>Eric Blanc</i>	
Deployment and Retrieval Mechanism Redesigned for Spartan Spacecraft on the STS	45
<i>Greg Galloway</i>	

SESSION II

Manipulator Design and Development for the <i>Ranger</i> Satellite Servicing Vehicle	61
<i>Russell D. Howard and David L. Akin</i>	
Experiences in the Development of Rotary Joints for Robotic Manipulators in Space Applications	75
<i>Klaus Priesett</i>	
Spline-Locking Screw Fastening Strategy	91
<i>John M. Vranish</i>	
Modular Antenna Pointing System for the Explorer Platform Satellite	111
<i>James Andrus and Ed Korzeniowski</i>	

SESSION III

Wearing of Cryomechanisms at 4 K	127
<i>Gérard Luciano</i>	
Invacuo Tribological Evaluation of Coarse-Pitch Gears for Use on the Space Station Alpha Joint	139
<i>Scotty R. Allen</i>	
A Combined Earth Scanner and Momentum Wheel for Attitude Determination and Control of Small Spacecraft	157
<i>Bill Bialke</i>	
Stepper Motor Instabilities in an Aerospace Application	173
<i>Russell Kackley and Sean McCully</i>	

SESSION IV

SOHO MAMA Openable Cover/Vacuum Seal Mechanism	189
<i>Mitchell T. Wiens</i>	
Arm Deploy Mechanisms to Help Correct the Hubble Space Telescope's Vision	205
<i>F. Kent Copeland and Randall R. Whitaker</i>	
Development of a Resettable, Flexible Aperture Cover	221
<i>Scott Christiansen</i>	
Milstar's Flexible-Substrate Solar Array--Lessons Learned	235
<i>John Gibb</i>	

SESSION V

Mechanisms of the Space Active Vibration Isolation (SAVI)	245
<i>Frank Schmitt</i>	
A 23.2:1 Ratio, 300-Watt, 26 N-m Output Torque, Planetary Roller-Gear Robotic Transmission: Design and Evaluation	263
<i>Wyatt S. Newman, William J. Anderson, William Shipitalo, and Douglas Rohn</i>	

SESSION VI

Space Station Freedom Common Berthing Mechanism	281
---	-----

Erik Illi

A Multipurpose Model of HERMES-COLUMBUS Docking Mechanism	297
--	-----

J.J. González-Vallejo, W. Fehse, and A. Tobias

Design, Development, and Fabrication of Extravehicular Activity Tools for the Transfer Orbit Stage	315
---	-----

L.M. Albritton, J.R. Redmon, and T.R. Tyler

SESSION VII

Development of a Precision, Six-Axis Laboratory Dynamometer	331
---	-----

P.J. Champagne, S.A. Cordova, M.S. Jacoby, and K.R. Lorell

Mechanical Design of a Rotary Balance System for NASA-Langley's Vertical Spin Tunnel	349
---	-----

J.W. Allred and V.J. Fleck

12-Foot Pressure Wind Tunnel Restoration Project Model Support Systems	367
---	-----

Glen E. Sasaki

SYMPOSIUM SCHEDULE

Registration will take place at the Sheraton Hotel on Tuesday evening and on each day of the symposium at the Auditorium, Bldg. 8, NASA-Goddard.

TUESDAY, 12 MAY 1992

7:00-9:00 p.m. Early Registration and Social
(Salon A, Sheraton Hotel)

WEDNESDAY, 13 MAY 1992

8:30 a.m. Wednesday Authors' Breakfast
(Pebbles Parlor, Sheraton Hotel)

9:00 **REGISTRATION AND COFFEE**
(Auditorium, Bldg. 8, NASA Goddard Space Flight Center)

10:00 INTRODUCTORY REMARKS
Mr. Bowden W. Ward, Jr., Host Chairman
 NASA Goddard Space Flight Center
Dr. Charles W. Coale, General Chairman
 Lockheed Missiles & Space Co., Sunnyvale, CA

CENTER WELCOME
Dr. John M. Klineberg, Center Director
NASA Goddard Space Flight Center

10:30 **SESSION I**
 Mr. Earl D. Angulo, Session Chairman
 NASA Goddard Space Flight Center
 -- *Development of a Non-Explosive Release Device for
 Aerospace Applications*
 John D. Busch and A. David Johnson, TiNi Alloy Co.,
 Oakland, CA; William E. Purdy, Naval Research Labora-
 tory, Washington, DC
 -- *Novel Aerospace Mechanisms: A Passive Tether Damp-
 ing Device for a Tethered Satellite and A Pin/Latch
 Structural Interface System*
 John W. Redmon, Jr., NASA Marshall Space Flight
 Center, Huntsville, AL

- *ADELE: Articulation de Deploiement à Lâmes
d'Enroulement (Deployment Hinge Utilizing Wraparound
Bands)*
Eric Blanc, Aerospatiale, Cannes, France
- *Deployment and Retrieval Mechanism Redesigned for
Spartan Spacecraft on the STS*
Gregory M. Galloway, NASA Goddard Space Flight
Center, Greenbelt, MD

12:30 p.m. LUNCH

1:30 SESSION II

Mr. Ernest Schaeffer, Session Chairman

Schaeffer Magnetics, Inc., Chatsworth, CA

- *Manipulator Design and Development for the
Ranger Satellite Servicing Vehicle*
Russell D. Howard and David L. Akin, University of
Maryland, College Park, MD
- *Experiences in the Development of Rotary Joints for
Robotic Manipulators in Space Applications*
Klaus Priesett, Domier GmbH, Friedrichshafen, Germany
- *Spline-Locking Screw Fastening Strategy (SLSFS)*
John M. Vranish, NASA Goddard Space Flight Center,
Greenbelt, MD
- *Modular Antenna Pointing System for the Explorer Plat-
form Satellite*
James Andrus and Ed Korzeniowski, Honeywell, Inc.,
Glendale, AZ

3:30 BREAK

3:45 INVITED SPEAKER

- *Spacecraft Deployed Appendages/Lessons Learned*
Mr. R. Kenneth Hinkle, NASA Goddard Space Flight
Center, Greenbelt, MD

4:15 FACILITY TOUR

Mr. Robert Federline, Tour Chairman

NASA Goddard Space Flight Center

6:00 WELCOMING RECEPTION

Visitor Center, NASA Goddard Space Flight Center

THURSDAY, 14 MAY 1992

7:00 a.m. Thursday Authors' Breakfast
(Pebbles Parlor, Sheraton Hotel)

8:30 SESSION III
Mr. Edward J. Devine, Session Chairman
Swales & Associates, Beltsville, MD

- *Wearing of Cryo-Mechanisms at 4 °K*
Gerard Luciano, Aerospatiale, Cannes, France
- *Invacuo Tribological Evaluation of Coarse-Pitch Gears
for Use on the Space Station Alpha Joint*
Scotty R. Allen, AEC-Able Engineering Co., Goleta, CA
- *A Combined Earth Scanner and Momentum Wheel for
Attitude Determination and Control of Small Spacecraft*
Bill Bialke, ITHACO, Inc., Ithaca, NY
- *Stepper Motor Instabilities in Aerospace Applications*
Russell Kackley and Sean McCully, Lockheed Missiles
& Space Co., Sunnyvale, CA

10:20 COFFEE BREAK

10:30 SESSION IV
Mr. Ted W. Nye, Session Chairman
TRW Space & Technology Group, Redondo Beach, CA

- *SOHO MAMA Openable-Cover/Vacuum-Seal
Mechanism*
Mitchell T. Wiens, Ball Aerospace, Boulder, CO
- *Arm Deploy Mechanisms to Help Correct the Hubble
Space Telescope's Vision*
F. Kent Copeland and Randall R. Whitaker, Ball Aero-
space, Boulder, CO
- *Development of a Resettable, Flexible Aperture Cover*
Scott Christiansen, Starsys Research Corp., Boulder, CO
- *Milstar's Flexible Substrate Solar Array--Lessons
Learned*
John Gibb, Lockheed Missiles & Space Co.,
Sunnyvale, CA

12:30 p.m. LUNCH

1:30

SESSION V

Mr. Charles Hudson, Session Chairman

BEI Motion Systems Co., Maumelle, AR

-- *Mechanisms of the Space Active Vibration Isolation System (SAVI)*

Frank Schmitt, Honeywell, Inc., Glendale, AZ

-- *A 23.2:1 Ratio, 300-Watt, 26 N-m Output Torque, Planetary Roller-Gear Robotic Transmission: Design and Evaluation*

W.S. Newman, Case Western Reserve University, Cleveland, OH; W.J. Anderson and W. Shipitalo, NASTEC, Inc., Cleveland, OH; and Douglas A. Rohn, NASA Lewis Research Center, Cleveland, OH

NATIONAL AIR AND SPACE MUSEUM TOUR

Mr. Stewart C. Meyers, Tour Chairman

NASA Goddard Space Flight Center

2:45

Buses depart NASA Goddard for tour

3:30

National Air and Space Museum Tour

6:00

Buses leave museum for NASA Goddard and hotel

SYMPOSIUM BANQUET AND EVENING PROGRAM

7:00

Social Hour

8:00

Banquet

9:00

Evening Program, Featured Speaker:

Mr. Frank J. Cepollina

NASA Goddard Space Flight Center

The Repair Mission of the Hubble Space Telescope

FRIDAY, 15 MAY 1992

7:00 a.m.

Friday Authors' Breakfast
(Pebbles Parlor, Sheraton Hotel)

8:30

SESSION VI

Mr. Michael Eiden, Session Chairman

ESA/ESTeC, Noordwijk, The Netherlands

- *Space Station Freedom Common Berthing Mechanism*
Erik A. Illi, The Boeing Company, Huntsville, AL
- *A Multipurpose Model of Hermes-Columbus Docking Mechanism*
J.J. González-Vallejo, SENER, Las Arenas (Vizcaya), Spain; W. Fehse and A. Tobias, ESA/ESTeC, Noordwijk, The Netherlands
- *Design, Development and Fabrication of Extravehicular Activity Tools for the Transfer Orbit Stage*
L.M. Albritton, J.R. Redmon, and T.R. Tyler, NASA Marshall Space Flight Center, Huntsville, AL

10:00 COFFEE BREAK

10:15 SESSION VII

Mr. Sterling W. Walker, Session Chairman
NASA Kennedy Space Center, FL

- *Development of a Precision, Six-Axis Laboratory Dynamometer*
P. Champagne, S.A. Cordova, M.S. Jacoby, and K.R. Lorell, Lockheed Palo Alto Research Laboratory, Palo Alto, CA
- *Mechanical Design of a Rotary Balance System for NASA-Langley's Vertical Spin Tunnel*
Johnny W. Allred, NASA Langley Research Center, Hampton, VA
- *12-Foot Pressure Wind Tunnel Restoration Project: Model Support Systems*
Glen E. Sasaki, NASA Ames Research Center, Moffett Field, CA

11:45 GODDARD SPACE FLIGHT CENTER OVERVIEW

Mr. William P. O'Leary, VIP Protocol Officer (Ret.)
NASA Goddard Space Flight Center

12:10 p.m. HERZL AWARD

Presentation of the Dr. George Herzl Award for the best symposium paper
Mr. Frank T. Martin, Presenter
NASA Goddard Space Flight Center (Ret.)

12:20 CLOSING REMARKS
 Mr. Bowden W. Ward, Jr., Host Chairman
 NASA Goddard Space Flight Center
 Mr. Stuart H. Loewenthal, Operations Chairman
 Lockheed Missiles & Space Co., Sunnyvale, CA

12:30 LUNCH

ORGANIZING AND REVIEWING COMMITTEE

The papers presented at the symposium were selected and reviewed by the Organizing Committee. Each author is responsible for the content and the technical accuracy of their respective paper. The committee was composed of the following members:

Bowden W. Ward, Jr.	Host Chairman	NASA GSFC
Charles W. Coale	General Chairman	LMSC
Joel Burdick	Administrative Chairman	CIT
Stuart H. Loewenthal	Operations Chairman	LMSC

Edward A. Boesiger	LMSC
Obie H. Bradley	NASA LaRC
Homer S. Brown	NASA KSC
Charles S. Cornelius	NASA MSFC
Michael Eiden	ESTeC
David F. Engelbert	JPL
Harvey H. Horiuchi	JPL
Ronald E. Mancini	NASA ARC
Jerry E. McCullough	NASA JSC
Stewart C. Meyers	NASA GSFC
John W. Redmon, Sr.	NASA MSFC
John F. Rogers	NASA LaRC
Douglas A. Rohn	NASA LeRC
William C. Schneider	NASA JSC
Donald R. Sevilla	JPL
Sterling W. Walker	NASA KSC

ADVISORY COMMITTEE

Paul W. Bomke	JPL
Aleck C. Bond	NASA JSC (Ret.)
Thomas F. Bonner	Space Industries
H. Mervyn Briscoe	ESTeC (Ret.)
Kenneth C. Curry	JPL (Ret.)
Otto H. Fedor	LSOC (Ret.)
Frank T. Martin	NASA GSFC (Ret.)
James D. Phillips	NASA KSC (Ret.)
James H. Parks	NASA LaRC (Ret.)
Alfred L. Rinaldo	LMSC (Ret.)
Nathan D. Watson	NASA LaRC (Ret.)

Claef F. Hakun	Special Exhibits Coordinator	NASA GSFC
Edward A. Wegner	Publications Coordinator	LMSC (Ret.)

DEVELOPMENT OF A NON-EXPLOSIVE RELEASE DEVICE FOR AEROSPACE APPLICATIONS

John D. Busch*, William E. Purdy**, and A. David Johnson*

ABSTRACT

A simple, non-explosive, high load-capacity release mechanism using shape memory alloy is currently being developed for space flight. This device, referred to as the Frangibolt, could replace most pyrotechnic devices in applications where the need for safety, reliability, non-destructive testing, and minimal mechanical shock is more crucial than the need for rapid actuation. Prototype hardware has been designed, tested, and proven in laboratory conditions. Operation and demonstration of these devices evidenced reliable and repeatable performance, clearly indicating that extensive testing for flight qualification is warranted. This paper will discuss Frangibolt design, describe recent test results of laboratory units, and address the work that must be performed in upcoming months to qualify the device for aerospace applications.

INTRODUCTION

A. Significance

There is a confirmed need in the aerospace industry for non-explosive release mechanisms. The disadvantages and hidden expenses associated with pyrotechnic devices call for the development of safe and reliable release technologies. The Frangibolt non-explosive separation device is currently being developed to fill this need by providing aerospace engineers with an alternative choice when designing deployable systems.

The Frangibolt takes advantage of the tremendous force that can be generated by a relatively small volume of nickel-titanium (Nitinol) shape memory alloy. The device comprises a notched bolt, a pre-compressed Nitinol cylinder with an integral heater, the joint which is intended to be separated, several washers, and a securing nut (see Figure 1A). At the desired time, power is transmitted to the heater, which causes the shape memory alloy (SMA) element to heat and return to its original uncompressed shape. As it elongates, the SMA actuator generates sufficient force to fracture the bolt in tension, thereby releasing the joint (as shown in Figure 1B). Actual components are shown in Figure 2.

*TiNi Alloy Company, Oakland, CA

**Naval Research Laboratory, Washington, DC

The most undesirable feature of today's release systems is their use of explosive materials. While these devices are very reliable, they are hazardous, require expensive and frequent testing, produce high levels of pyroshock, and require heavy firing systems. Frequent and hazardous handling of ordnance generates high costs to ensure safety. The shielding necessary to prevent electromagnetic interference, and the required safing and arming systems, add significant weight and cost to a spacecraft. Any reduction in the use of ordnance on spacecraft will be beneficial to the aerospace industry.

A major advantage of the SMA operated system is that it enables non-destructive and repeated testing. Since pyrotechnic initiators are entirely consumed during operation, it is difficult to fully test explosive devices prior to launch. The SMA actuator, however, can be actuated and reloaded numerous times in order to verify proper operation of the overall system. Although bolt elements are fractured during each test, material consistency and dimensional inspection result in an accurately predicted and repeatable breaking strength. This translates into significant cost savings in that far fewer actuation devices need be purchased to achieve statistical assurance of system reliability.

Another benefit of the SMA design is that it greatly reduces the shock of release. Figure 3 shows a comparison of shock output between a Frangibolt and an equivalently sized separation nut [1]. A reduction in shock output by a factor of five was observed. Part of this improvement can be explained by the fact that the energy required to break a bolt in tension is well defined and extremely repeatable. The only shock imparted to surrounding components results from the strain energy released when the bolt breaks, regardless of the specific force and stroke capabilities of the actuator. Adding margin to the actuator's performance has no consequence of additional shock to the system. In contrast, the high internal friction of a separation nut must be overcome by explosive gas pressure to effect release. Since friction values are difficult to control to less than 25% variance, an excess of explosive power must be provided in the device which is unavoidably transmitted to the structure.

There are only two potential limitations in using the Frangibolt system. First, the response time of the Frangibolt is not immediate since it operates on the basis of converting thermal energy into mechanical work. The time required to heat an SMA actuator to its actuation temperature is typically between 10 and 20 seconds. This is not foreseen as a major problem in many spacecraft applications. Second, the transition temperature of Nitinol cannot be much higher than 120°C (248°F). This restriction places a 100°C (212°F) ceiling on the maximum ambient temperature allowable near the Frangibolt actuator, yet this is not considered a problem in light of the overall thermal design of most spacecraft (e.g., temperature limitations of electronics). The low-temperature limit on Frangibolt operation (e.g., for cryogenic applications) is limited only to the endurance of the construction materials and heat flow capability of the heater.

B. Method of Operation

Shape-memory alloys are unique materials that can be deformed substantially below their specific phase transformation temperature, but are capable of returning to their original shape when heated above that temperature. This phenomenon is caused by a change in the material's crystal structure. The low-temperature phase (martensite) possesses a low elastic modulus, low yield strength, and accommodates a large degree of plastic deformation. When heated above its phase transformation temperature, the SMA must return to its parent crystal structure (austenite) by following a thermodynamic path which requires recovery of any mechanical deformation previously imparted to its low-temperature phase. The SMA will generate large internal forces, as are necessary, to overcome any forces which oppose a return to its original shape [2].

As a non-explosive release device, the Frangibolt uses the shape recovery and force-generating capabilities of Nitinol to break in tension an otherwise secure fastener. The bolt element is notched so as to concentrate the tensile strain required to cause fracture. However, the notch is also designed to maximize bolt strength by minimizing stress concentration. Dimensions of the Nitinol actuator are then selected to provide ample force and stroke, with specified margins, to yield and elongate the bolt to failure. Figure 4 illustrates the three stages of actuator operation.

C. Spacecraft Implementation

A variety of potential release applications exist for this device in spacecraft such as securing high-strength joints, which typically use separation nuts, and fastening lightweight appendages, normally achieved using bolt cutters and pin pullers. Examples of these two applications using a Frangibolt configuration are shown in Figures 1 and 5, respectively. Another good application, which lends itself well to multiple redundancy, is releasing marmon clamps (or V-clamp bands) [3]. The specific motion of pin pulling, on the other hand, is an example of a function not easily achieved using the Frangibolt.

D. Development Program

There are three stages in this ongoing development of a flight-ready product. The first has already been completed, which included prototype design and feasibility testing. This work demonstrated the capabilities and reliability of the basic concept, enabling commencement of more detailed studies. The last two stages will be supported by the Naval Research Laboratory (NRL) as part of their Advanced Release Technologies (ARTS) program [4]. This remaining work will be achieved in two phases of development. The Phase I effort will rigorously test and optimize each component, its method of manufacture, and its performance in and out of the system. Phase II will focus on qualification testing and production of experimental flight hardware. The

initial design and testing, as well as the two phases of upcoming development, are described below in more detail.

The ARTS program has the goal of developing, qualifying for spaceflight, and flying several new release mechanism systems. It is hoped that this program will evolve several new technologies to the point of flight acceptance and subsequent application to a wide variety of production spacecraft. The objective of the ARTS supported contract described herein is to deliver flight-ready Frangibolt devices by spring 1993.

DESIGN AND FEASIBILITY TESTING

The basic Frangibolt system is composed of four major component groups: (i) notched bolt element and matched nut; (ii) SMA actuator; (iii) heater and insulation; and (iv) joint materials and other hardware. The bolt, joint, and SMA actuator designs are interdependent, thus restrictions placed on one component will have an effect on the other two. Commonly, the actuator geometry is derived from the tensile characteristics of the notched bolt, which is defined by the required load capacity and configuration of the joint. The joint materials and hardware must be designed to transmit all the force and stroke of the actuator to the bolt with minimal loss. The heater and insulation materials present a separate set of design issues. It is important to produce a heater with high output power, but one which meets aerospace standards. The selected heater configuration will determine response time of the device and degree of redundancy. Design considerations for each of the four major Frangibolt components have been briefly investigated and are discussed below in more detail.

A. Bolt Element

Selection of bolt material is perhaps the most crucial element in Frangibolt design. It is necessary to use a material with a low elongation-to-failure such that the strain recovery of the shape memory actuator is sufficient to strain the bolt element beyond its ultimate tensile limit. Strain concentration is achieved by incorporating a notch in the bolt, the design of which must not create unacceptable stress concentration. Further, the bolt element must possess good fatigue properties and corrosion resistance.

A number of different bolt materials were studied, including Grade 5 and Grade 8 steels, A286, NAS6704 (high strength A286), and NAS674 (6Al-4V titanium alloy). Both the Grade 5 and regular A286 demonstrated excessive elongations as witnessed by tensile testing. The remaining materials (Grade 8, NAS6704, and NAS674) all exhibited elongations-to-failure in the range of 10 to 15%. Such materials are considered well-suited to the elongation properties of the actuator. Testing of Grade 8 material has been discontinued since it is not considered suitable for

aerospace applications. Efforts are now focused on NAS6704, NAS674, and similar aerospace-grade bolt materials.

Of the different notch geometries possible, there are two that have been investigated. The first comprises a rectangular profile cut to the desired depth (Figure 6a). The second constitutes a two-step notch in which the bolt shank is first turned to its root diameter, or slightly less, and then the rectangular profile as above is cut in the center of the turned portion (Figure 6b). After performing tensile tests on both types, little difference between the two was discerned in regard to ultimate tensile strength and elongation-to-failure. However, preliminary finite element modeling of these notch geometries indicates there may be some benefits to the two-step notch with regard to torsion and shear loads. Notch design will be tested further in the Phase I development program.

The notch width, diameter, and material characteristics determine the yield strain required to fracture the bolt, and the degree of notch strengthening. The notch diameter is specified so as to maximize bolt strength but also to ensure that the majority of strain is concentrated in the notch. As the notch diameter approaches the original bolt diameter, the elastic strain component from the unnotched portion of the bolt increases, thus requiring a longer actuator to break the bolt. It has been found that using a notch diameter which is 65% of the bolt's major diameter provides the best compromise between bolt strength and minimal elongation-to-failure.

A beneficial property of notch geometry is that with proper design it need not produce a high degree of stress concentration. Notch strengthening occurs when boundary conditions on the notch establish triaxial stresses. Under these conditions, materials which exhibit some degree of ductility can distribute a portion of direct tensile stress to components of shear stress such that the maximum stress needed to cause yielding has greater magnitude than if the material experiences only pure tensile stress [5]. This effect is seen in bolt specimens where the notch width is much smaller than its diameter. Figure 7 presents a comparison of bolts with a) no notch, b) a narrow notch, and c) a wide notch. These plots show that a narrow notch can exhibit a higher ultimate strength than a wider notch of equal diameter.

B. Actuator Element

The actuator element is fabricated from the Nitinol shape-memory alloy. This is the preferred SMA because it produces higher forces and larger strain recoveries than other available materials, and its manufacture is sufficiently mature to meet aerospace specifications. Nitinol can generate as much as 400 MPa (60,000 psi) in internal stress to restore its original shape. The preferred strain recovery is 3%, which can enable millions of repeated cycles. As an example, the $\frac{1}{4}$ " Frangibolt unit incorporates a 25-mm (1.0-inch)-long Nitinol cylinder with a 6.6-mm (0.260-inch) inside diameter and a 12.7-mm (0.500-inch) outside diameter. This actuator will generate up to 32,000 N (8600 lbs) in axial force with

a stroke of 0.75 mm (0.030 inch). If additional force and/or stroke is needed, the cross-sectional area and length of the Nitinol cylinder can be increased respectively. This makes the Frangibolt scalable to almost any bolt size.

The actuator must provide two distinct quantities: force and elongation. As described above, the cross-sectional area of the actuator determines the amount of force which can be generated, while the length determines its stroke. In keeping with the desire to reuse these actuators many times, recovery stress and strain are designed to be 200 MPa (30,000 psi) and 3% respectively. Under these conditions, our tests indicate that the actuators do not degrade in either force generation or elongation after as many as 30 cycles. Since Nitinol can internally generate at least twice this design stress, it will have inherently a factor of two in force margin. However, the preferred strain recovery is 3% of actuator length, which represents the full stroke available from an actuator under present design criteria. Therefore, the actuator design must incorporate an appropriate stroke margin by increasing actuator length by the desired proportion.

Specific dimensions of the actuator are determined based on the selected notch diameter, the outside diameter of the bolt, required grip length, and the desired safety margin. At present, the actuator's inside diameter is chosen to be only slightly larger than the diameter of the bolt. The actuator's outside diameter is determined by a calculation of the cross-sectional area required. To calculate the length of the actuator, one must estimate and/or experimentally verify both the elastic and yield strains of the bolt, as well as the compressive strain of the system (including washers, flanges, and other intermediate materials) and the desired safety margin.

Bolt preload also benefits the operation of the actuator. By increasing preload, the actuator stroke needed to break the bolt is decreased. However, to accommodate any potential loss of preload over time, the actuator is designed to provide sufficient strain recovery to break the bolt even with minimal preload. This will translate to an additional safety margin if the initial preload is maintained.

Due to the nature of the Frangibolt system and actuator design, this device technology can be scaled to almost any bolt size and joint configuration. If a larger bolt size is needed to achieve specific load requirements, the Nitinol actuator is sized proportionally. Only in very large devices will the heating power requirements render this device impractical. One of the objectives of this development program is to identify the sizing limits for practical application. It is anticipated that needs will exist for devices as small as size 6 machine screws and as large as $\frac{1}{2}$ " bolts.

A final consideration for actuator design is the transformation temperature of the shape-memory alloy. It is possible that aerospace engineers will have a need for devices which operate at lower temperatures, as in cryogenic applications. If such uses exist, Nitinol

compositions with lower transformation temperatures are readily available. However, additional development would be required to incorporate heater materials capable of enduring the colder temperatures.

C. Heater

The heater must maximize power density in order to assure quick actuation and adequate heat transfer margins. It must also tolerate repeated 3% compression-elongation cycles. The minimum heat energy required to completely transform a Nitinol actuator (assuming a rise in temperature of 120°C) is 65 joules per gram. This translates to 1000 joules of heat energy for a $\frac{1}{4}$ " actuator assuming no thermal losses. With an 80-watt heater and typical heat loss, this actuator will transform in approximately 15 seconds. Such requirements present a challenging heater design.

The present heater consists of a single etched-foil heating element adhered to the Nitinol cylinder and encapsulated with an injection molded silicone rubber insulation jacket. The result is a very durable heater assembly capable of delivering 12 Watts/cm² (80 Watts/in²) and surviving numerous compression-elongation cycles without mechanical or electrical failure. The only potential disadvantage of this design is the degree of outgassing for the selected silicone rubber. Outgassing tests will be conducted in vacuum to determine the seriousness of this concern. Kapton heaters and commercially available heater tape, both of which are already available in space-qualified configurations, do not exhibit sufficient power densities to meet the necessary requirements. Therefore, a heater configuration must be developed which satisfies heating rate requirements, provides a redundant circuit, and meets aerospace acceptance standards.

D. Joint Materials and Hardware

The joint designs which incorporate the Frangibolt release device will vary from user to user. There is little opportunity to standardize the device in this regard. Such lack of standardization is acceptable provided an adequate set of core requirements (for most of the anticipated joint configurations) is defined. Early development testing has demonstrated how important proper joint design is to the Frangibolt system. The major requirement of the joint is that there be minimal deformation in the components during operation. This helps to ensure that a) most of the actuator's force and stroke are transmitted to the bolt without attenuation, and b) the forces transmitted to the bolt from external joint loads are minimized.

All joint hardware, such as flanges and washers, must use materials with compressive resilience. Washers are of particular importance since the actuator forces must be properly distributed into the flange materials to avoid bearing yield. For example, Frangibolt tests using soft washers have shown that a 0.1-mm (0.004-inch) permanent deformation is possible.

This is significant in comparison to a 0.75-mm (0.030-inch) actuator stroke. Therefore, it is important to evaluate each joint and hardware component in the system and clearly determine its contribution to diminution of actuator function.

DEVELOPMENT PROGRAM

The initial design, development, and proof of feasibility took the Frangibolt from conception to its present state as a reliable, but not yet space-ready, mechanism. Significant knowledge concerning the interrelationships between notch geometry, bolt stiffness, elongations-to-failure, system strength, and installation was gained. Performance characteristics and material requirements of the heater were also defined. In continuation of this work, the NRL-supported Phase I and Phase II efforts will focus on engineering optimization and qualification testing. Following is an outline of the projected development program intended to put the Frangibolt into space.

A. Phase I Tasks

The Phase I objective is to develop the Frangibolt system to the stage where its design meets or exceeds the requirements of flight spacecraft. Emphasis will be placed on gaining a thorough understanding of the overall design and each of its parameters and margins. Development will be directed towards producing a highly reliable, testable mechanism. Efforts will concentrate on design, testing, and characterization of each component, both by itself as well as in the complete Frangibolt system. The areas of investigation include:

- Optimizing notch geometry by analysis and testing.
- Verifying stress/strain/temperature characteristics of the SMA actuator.
- Determining degree of repeatability of the actuator.
- Identifying a low outgassing heater construction, optimizing performance, incorporating redundancy.
- Determining installation methods and sensitivities.
- Analyzing of joint design and hardware.
- Identifying effects of preload, applied load, and temperature on system performance.
- Thorough margin testing of design parameters; identifying performance envelope of the operational system.

Notch geometries will be analyzed using finite element modeling techniques and then experimentally tested to determine breaking strain, breaking load, and total strength under installation and external joint loading. Further, it will be important to learn how bolt performance varies as a function of deviations in the notch geometry. This will define the permissible tolerances in notch dimensions.

Actuator performance will be measured to identify exactly its force and displacement capabilities. These actuator properties will be correlated with degree of preload and number of cycles. To determine repeatability and longevity, actuators will be subjected to 100 cycles; many times the number of cycles likely to be demanded by end users.

Heater design will be iterated several times to optimize power density and reliability. Included in these iterations will be an investigation of construction and power tolerances. Questions which must be answered include: What maximum current level can be driven through the heater before failure? What minimum power level is still capable of bringing the actuator to temperature? How does current level affect repeatability and cycle lifetime of the heater element? What is the best method for providing redundant heaters?

Tests will be performed to examine load carrying capabilities of a jointed system that incorporates the Frangibolt. Understanding of the joint's internal load distribution and its reaction to external loading is critical to system reliability. The system will be tested to determine the optimum as well as the acceptable minimum and maximum preloads for the bolted joint. Preload control methods must also be tested. Such testing will enable us to develop a set of installation procedures aimed at preloading the joint in a predictable manner. Cyclical loading of the joint at varying percentages of maximum strength will be performed and the resulting joint integrity determined. These latter tests will attempt to measure the effects of bending and shear loading as well as tensile loading.

The Frangibolt must be evaluated as a system during and after the development of its individual components. An important part of this testing phase will be the determination of exact margins for each component in the system. This will be accomplished by measuring component performances using nominal configurations and then intentionally varying key parameters. It is expected that a performance envelope for this system will be defined by the completion of Phase I.

B. Phase II Tasks

Phase II will focus on production and qualification of flight hardware. This will provide the knowledge required for successful device integration by performing formal production qualification and installation of the Frangibolt on an actual flight spacecraft. Fabrication and assembly will be completed under quality-control practices to be developed from Phase I test results. The objective will be to comprehend each of the crucial parameters of the Frangibolt system, define the quantitative values for each, and use these as benchmarks in a series of appropriate inspection and/or acceptance tests. The qualification testing which follows will be equivalent to those tests performed on existing separation devices. Qualification will include thermal cycling tests, thermal vacuum, vibration, shock, and lifecycle testing at load, as well as temperature and

electrical power margin tests. The culmination of Phase II is intended to be the operation of a Frangibolt system in orbit.

C. Flight Demonstration

Spring 1993 is the target date for installation of flight hardware on a host spacecraft. As this will be the first flight operation of the Frangibolt, it will not be employed in a critical function. The flight approval process including safety, quality review, and spacecraft integration will be an important learning experience and helpful to final product development. Release of the experimental mechanism is expected to occur approximately six months after launch.

APPLICATION

A. Usage

Since the response time of the Frangibolt system is not instantaneous, it is not readily applied to simultaneous release of multiple units or for precisely timed releases. In many instances, however, simple schemes can be used to achieve balanced release of an appendage or payload. A suggested method is to use one Frangibolt which is centrally located yet not intended to carry launch loads; additional devices are attached where necessary to secure the structure for launch. Once the spacecraft is in orbit, the load-bearing devices can be released in any order and at any time. When complete separation is desired, the central device is actuated causing the structure to detach in a balanced and uniform fashion. In addition to such alternative approaches in the separation of multiple units, methods for enabling simultaneity among Frangibolts will be investigated.

B. Engineering Considerations

Many of the following design guidelines are the direct result of problems already encountered during feasibility testing. By presenting a summary of the considerations which must be addressed, it is hoped that the aerospace engineer will better understand the applications and limitations of a Frangibolt system.

1. Yielding can occur in soft washers, low-strength nuts, soft joint materials, and in locations where the actuator force is not adequately spread out. Since the actuator has a finite stroke, the compressive deformation of the joint hardware must be minimized.
2. Increasing bolt preload reduces the actuator stroke necessary to break the bolt. Conversely, loss of preload increases the stroke required. This means that the joint must be assembled with a known preload, which must then be maintained until the moment of

operation. It is best to minimize the stroke required as this will minimize actuator length and reduce power requirements. Further, the shorter the bolt required to pass through the joint, the shorter the actuator needs to be.

3. Because the force generated by the actuator must be transmitted as efficiently as possible to the bolt, the axial force lines must pass through solid material at all points. Therefore, the actuator inside diameter must be equal to, or greater than, the through-hole diameters in both the joint and washers. Otherwise, generated forces will be lost in the unsupported areas.
4. Another consideration is thermal conduction from actuator to joint. To minimize power requirements, such thermal losses must be limited. Kapton insulating washers in conjunction with titanium washers have provided the best results thus far.
5. It cannot be over-emphasized that implementation of this technology, as simple as it may appear, must be a team effort between the user and supplier.

C. Redundancy Considerations

An issue which has not yet been explored in detail, but must be addressed in the Phase II program, is that of redundancy. Electrical redundancy implies two heaters on one actuator. This is relatively easy to accomplish and will undoubtedly be part of any flight system. Pyrotechnic release devices use a similar approach to redundancy by incorporating two initiators on one mechanism.

Mechanical redundancy, however, is more complicated and implies having two actuators each on its own completely separate bolt element. Incorporating two actuators onto one bolt element does not provide complete redundancy. For example, two concentric actuators or two collinear actuators only provide redundancy in force or stroke respectively, not both. Complete mechanical redundancy requires the use of several separate Frangibolt systems. This is exemplified by the marmon clamp configuration mentioned earlier.

In some applications, mechanical redundancy will be impractical. The end user must therefore rely on performance margins to ensure reliability. Increasing the cross-sectional area of the actuator, or its length, will, by the same proportion, increase the safety margin of the system. This can accommodate unexpected variations in bolt properties, joint materials, and installation flaws. The only drawback to providing additional margins will be an increase in power consumption.

CONCLUSIONS

It is very important for the spacecraft designer to understand where and how to best utilize the Frangibolt system. The Frangibolt system offers many advantages to spacecraft systems including reduction of safety costs, reduced shock output, and simple, lightweight control electronics. There are many different ways to use the Frangibolt concept to release spacecraft components. The delay before release makes the Frangibolt poorly suited for some release operations, but its safety and inherent simplicity make it well suited for many others. To begin the integration of such a device, it is extremely important for the spacecraft and Frangibolt designers to work together as a team to produce a reliable release system. Both parties must recognize that the Frangibolt and the joint which it secures represent an integrated release system. By encouraging aerospace engineers, each of whom will have a different application in mind, to begin integrating and testing the Frangibolt in their systems, the extent of its benefit to the aerospace industry will be realized.

REFERENCES

1. Shock tests comparing the Frangibolt with a standard separation nut were performed by Mr. Howard Eller at TRW in Redondo Beach, CA.
2. T.W. Duerig, K.N. Melton, D. Stoeckel, and C.M. Wayman, Engineering Aspects of Shape Memory Alloys, Butterworth-Heinemann, London, 1990.
3. "Flight Separation Mechanisms," NASA Document SP8056, October 1970.
4. Inquiries regarding the Advanced Release Technologies program at the Naval Research Laboratory should be addressed to Mr. William Purdy at (202) 767-0529.
5. A.J. Durelli, E.A. Philips, and C.H. Tsao, Introduction to the Theoretical and Experimental Analysis of Stress and Strain, McGraw-Hill, New York, 1958.

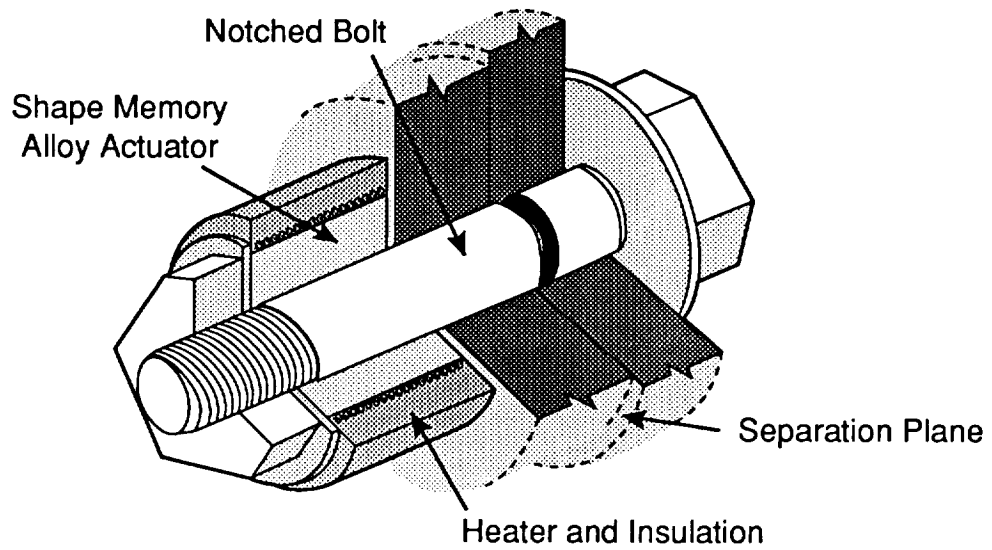


Figure 1A. Secure Frangibolt Assembly

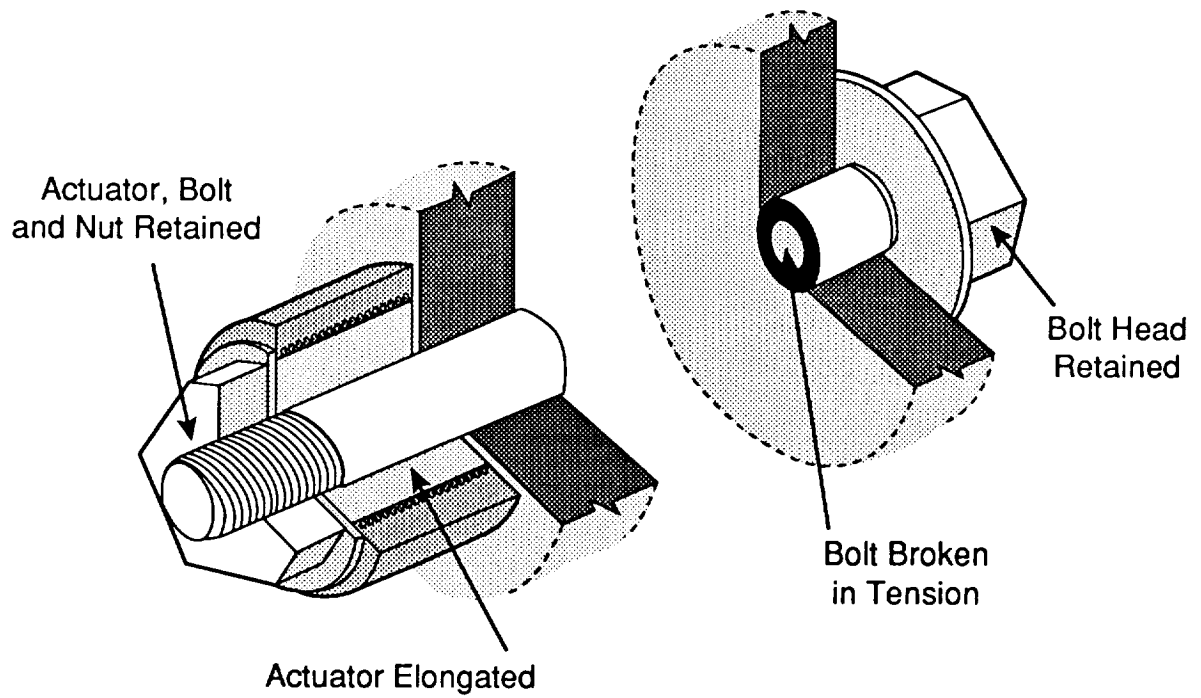


Figure 1B. Separated Frangibolt Assembly

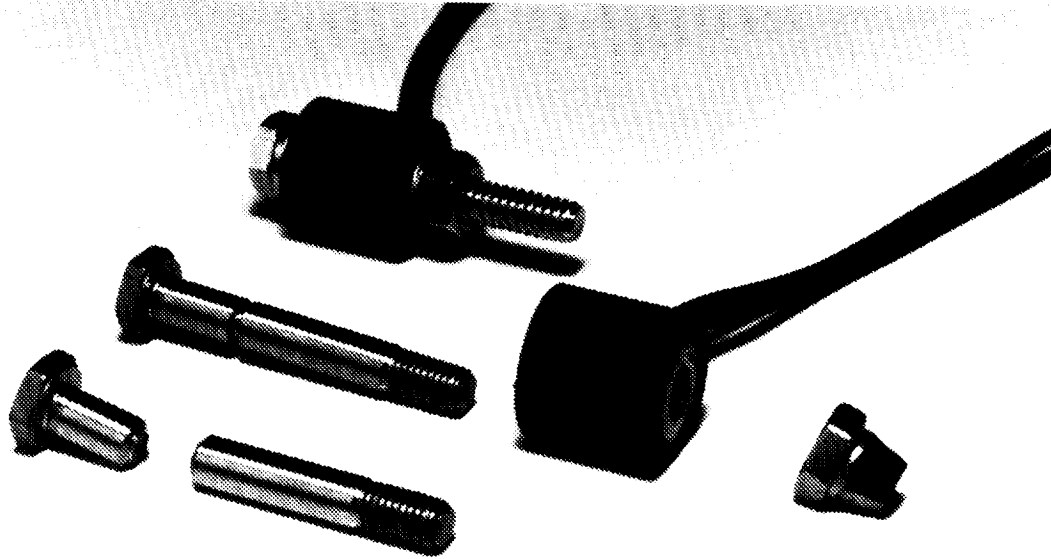


Figure 2. Photograph Showing Frangibolt Components

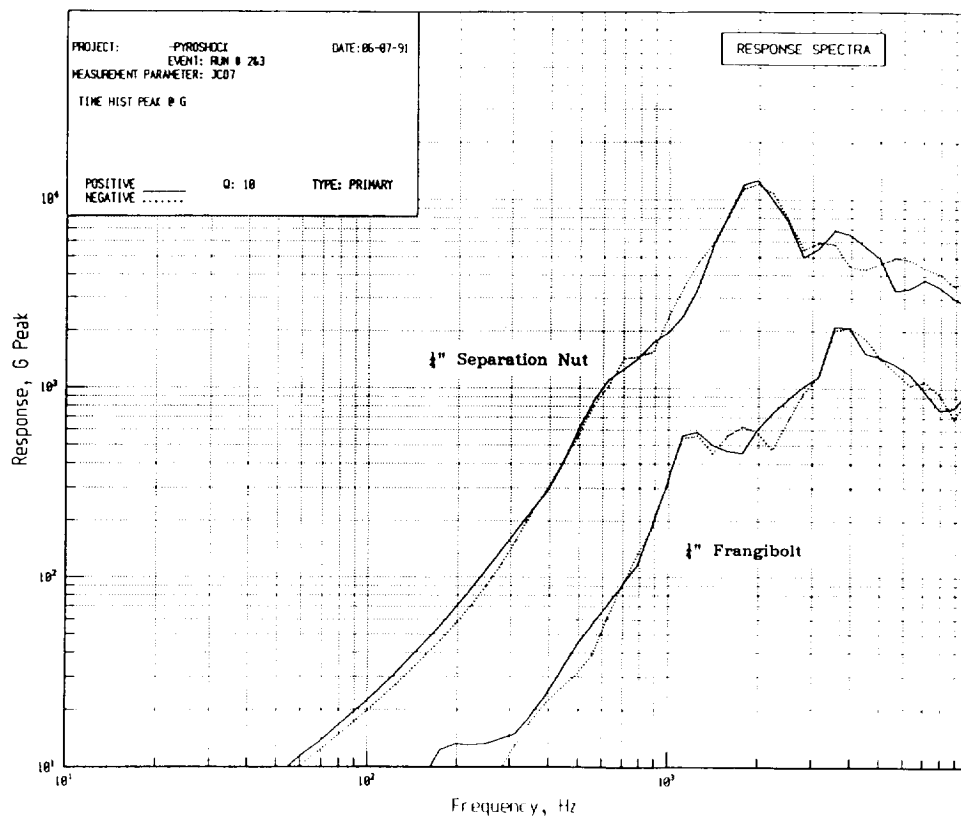


Figure 3. Comparison of Shock Output Between Frangibolt and Separation Nut

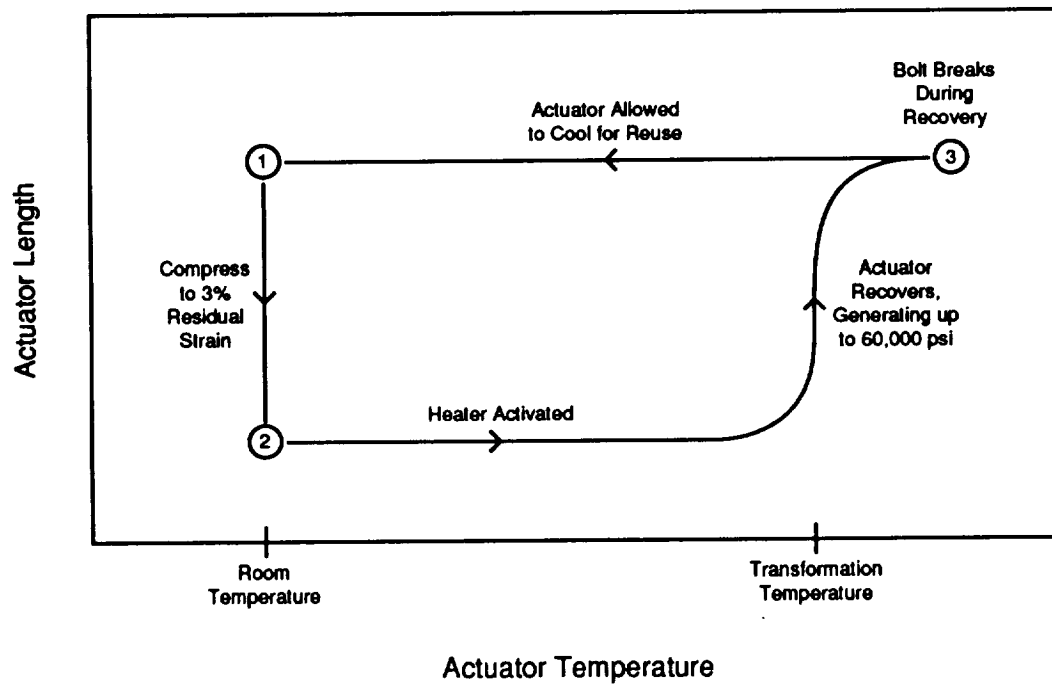


Figure 4. Nitinol Actuator Operation

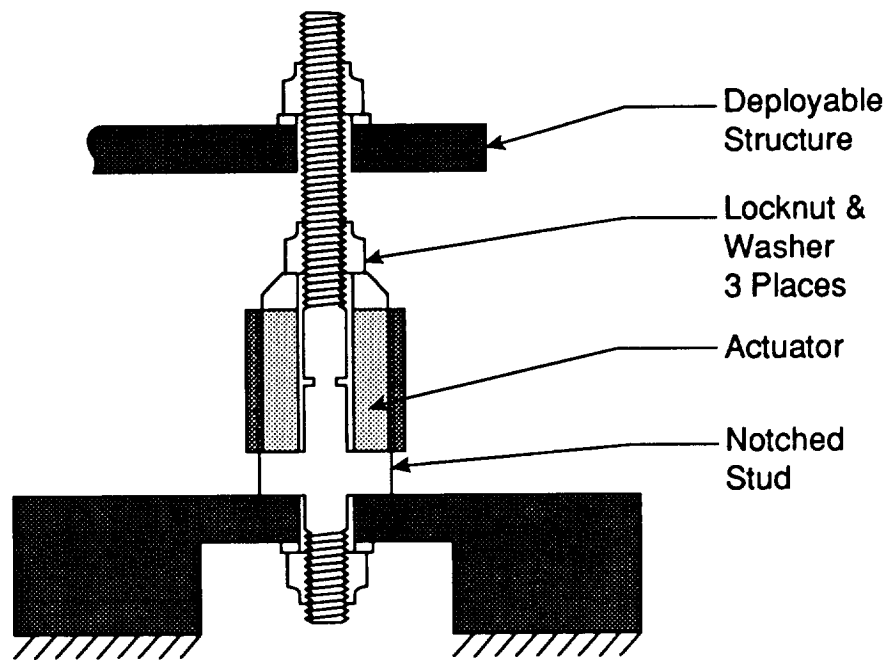


Figure 5. Frangibolt Embodiment for Appendage Release

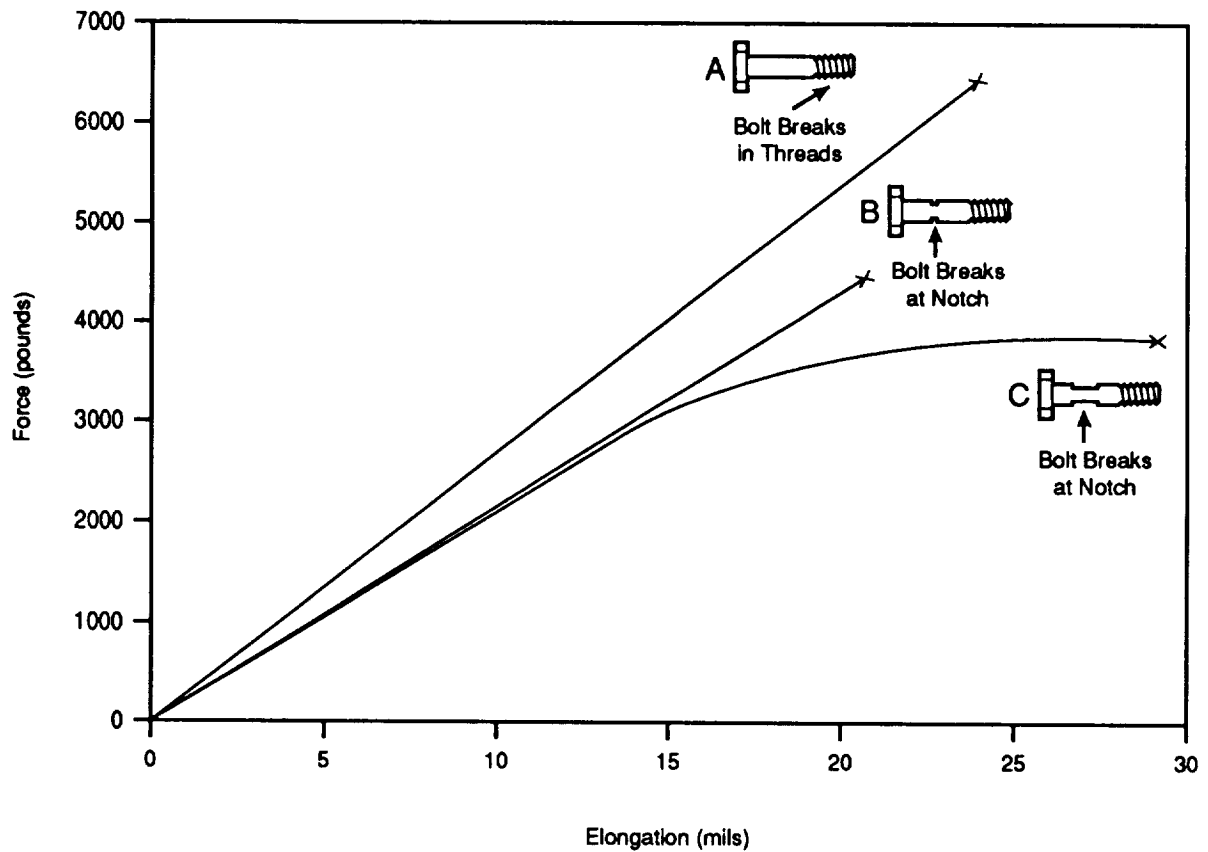
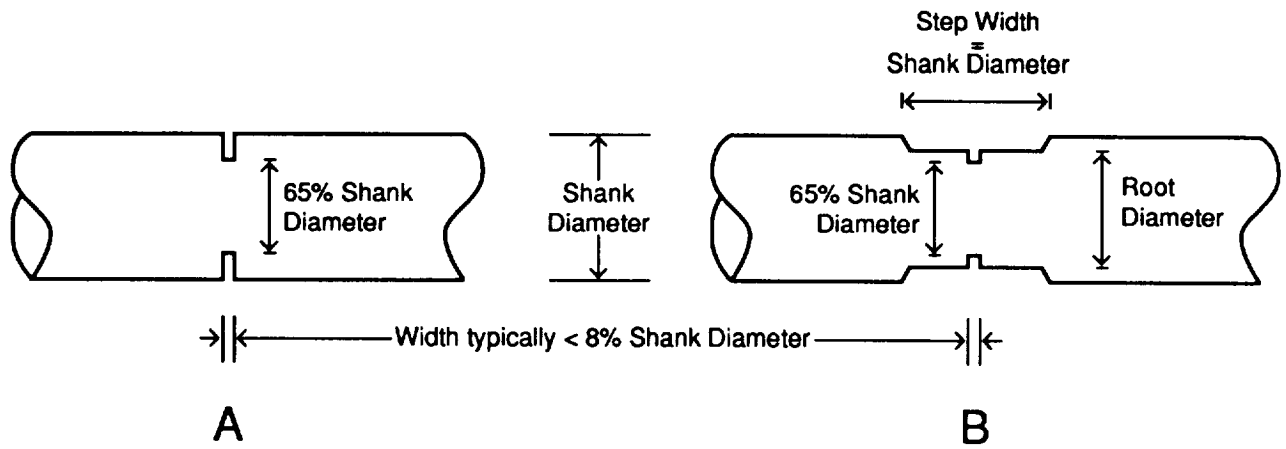


Figure 7. Comparison of Mechanical Properties Between Bolts with a) no notch, b) a narrow notch, and c) a wide notch

NOVEL AEROSPACE MECHANISMS: A PASSIVE TETHER DAMPING
DEVICE FOR TETHERED SATELLITE, AND A PIN/LATCH
STRUCTURAL INTERFACE SYSTEM

John W. Redmon, Jr.*

ABSTRACT

This paper is a collection of development tasks that have been accomplished over the past year at Marshall Space Flight Center's Structures and Dynamics Laboratory. Dissemination of task findings are reported for the following reasons: (1) the task involves new or evolving technology (as is the case with tethered satellite); and (2) the task depicts a technique that could have application to extravehicular activity (EVA) or robotic assembly of space structures (the pin/latch system).

A PASSIVE TETHER DAMPING DEVICE

The Tethered Satellite System (Figure 1) is a space shuttle-mounted system by which to deploy and retrieve 500-kg science gathering satellites on a Nomex/Kevlar/copper tether. Distances up to 20 km from the orbiter's cargo bay are achieved. During retrieval of the satellite, a dangerous "skip rope" mode vibration can occur in the tether due to the EMF generated by the tether's core conductor being accelerated through the Earth's magnetosphere. Allowed to continue, this vibration could cause loss of control of the satellite and thus endanger the mission. Damage to the orbiter vehicle could occur if loss of control occurs in close proximity. Probably one of the more challenging problems to arise in developing the Tethered Satellite System has been to rectify the "skip rope" problem. The following is a brief account of that development.

Once the problem was acknowledged, a team of NASA and Martin Marietta personnel were assembled with a rather unprecedented goal: design and test an ultra-low frequency/ultra-low stiffness passive mechanism by which to damp the tether's oscillation. A depiction of the vibration is shown in Figure 1. A schematic representation and requirements are shown in Figure 2. What soon became apparent was just how difficult it is to appreciably affect tether "skip rope" motions at a position on the deployer 50 to 100 m away (as shown). For example, if the damping mechanism had too much stiffness, a "hard-point" would occur and motion of the lightly loaded tether would not be damped. Damping forces were so slight that they were referred to with terms like "goose feathers." Frequencies of oscillation were around 0.10 Hz. Also, physical simulation of the problem was confounding due to the enormity of 1-g effects and air resistance.

A basic design with several variations followed. The basic design consisted of three constant force spring motors situated as shown in the deployer. The constant-force spring motors served to deploy a damping device some distance (L1) out along the tether, as well as provide some damping due to hysteresis and friction. There were two damping devices under consideration for the deployment: (1) a frictional-type device, and

* NASA, Marshall Space Flight Center, Huntsville, Alabama.

(2) a more elaborate vernier damping mechanism. Figure 3 shows the deployed damper configuration. Figure 4 shows the candidate passive damping devices. Early tests with the constant-force motors proved to be a disappointment. Although the motors performed exceptionally for deployment, they proved too stiff to offer appreciable damping. Emphasis was placed on development of the so-called vernier damping mechanism.

The vernier mechanism is shown in Figure 5. The device may be described as a two-bar planar linkage with free end excursions limited by the circular opening (the tether can travel anywhere within the circle). The theory behind the device was to achieve the absolute lowest friction (damping) with the idea that an adjustable amount of drag could be added (it was desired that the device operate down to zero "skip rope" amplitude at which point the required force is zero). To attain "frictionless" motion of the device, a specially mounted miniature ABEC 5 deep-groove ball bearing was fitted at each pivot. No lubrication was used on the ball bearings since temperature excursions and viscous effects would contribute to unwanted (temperature-dependent) drag. Since loads were miniscule, there was not a tribology problem. To achieve an adjustable drag (damping force) with a myriad of design variables, a spring/VESPEL roller/cam arrangement was fitted at each pivot. Types of these devices are shown in Figure 6. Testing of the device proved its operation flawless. The device truly damped the tether's "skip rope" down to zero amplitude.

Successful demonstration of the vernier mechanism proved that the low end of the damping envelope was achievable. Based on this, lubrication-free bearings were fitted to the spring motors to further reduce friction and provide greater damping at the larger amplitudes. This modification enabled the spring motors to damp 0.1-m amplitudes at a deployed distance of 10 m (which was deemed sufficient for docking). Characteristic test results are shown in Figure 7. A NASA Technical Memorandum (to be published) will cover the detailed design, analysis, and test of tether damping schemes. The first tethered satellite mission is scheduled to occur in 1992. The mission will tether an Italian satellite for study of the magnetosphere.

A PIN/LATCH STRUCTURAL INTERFACE SYSTEM

The design of a pin/monobearing structural latch mechanism for restraint of large orbital replaceable units (ORU's) is described herein. The application described is destined for restraint of the 400- to 700-kg space station rack units designed by Boeing Defense and Space Group. The device is made for hand operation but is easily converted for EVA or robotic use. The device exhibits many desirable qualities which make its application to other structural interface systems attractive. Desirable qualities are: low input torque, large capture envelope, high load capability, quick-acting (short throw), tactile behavior, positive load stability, good tribology factors, and simplicity. Further, the device is convertible to many constraint schemes (i.e., quantity of latch points, degree of constraint, preloading, spring mounting, take-up, etc.), and utilizes a relatively common and accepted interface (the monoball or spherical bearing).

The design of high-integrity latches has always been a difficult task. The design of latches is not without dilemma and this latch is no different. A particularly emotional issue with regard to latch design is the use of "over-center" locking means (which this device

uses). Admittedly, "over-center" locking is somewhat frowned upon for space hardware. It is claimed, however, that this design steers clear of the pitfalls of typical over-center locking with the help of a special compliant element. The compliant element allows the device to be parked over-center without the inherently high loads and high torques of typical over-center latches. Spring element stiffness is selected to be high relative to the applied load, but low compared to the mechanism elements. Use of this compliant element allows the desirable qualities (tactile behavior, short throw, low torque, etc.) to be achieved and lends itself to EVA or robotic methods. Figure 8 portrays the crank position versus load relationship for the device using a constant input moment.

The location of the latch is shown in Figure 9. As can be seen, no moments are allowed to cross the interface. The lower/back interfaces require special attention as to the capture and mating. As anyone who has ever attempted to insert a 0.2500-in-diameter dowel pin into a 0.2505-in-diameter hole knows, this type of mating is very difficult. The latch location "A" is especially difficult in that axial X play must be removed. It is further complicated by monoball mounting, the necessity of a "large" capture envelope, and blind/remote actuation. The design selected is shown in Figures 10 through 14; features and operation are evident. The mechanism may be described as a hand-actuated, slider-crank-driven, progressive mating, compound pin latch with compliant preloading/over-center locking. Geometry of the device has been optimized with regard to force amplification. As mentioned previously, compliance for locking/loading of the device is provided by a 2,000-lb belleville spring; higher rates are easily attainable. Physical characteristics and performance data are given in Figure 15. Alternative latch schemes are portrayed in Figure 17. Note that latch points can be "sprung" relative to each other for dimensional take-up.

Prior to fabrication of the first metal prototype, a stereolithography model (Figure 16) was constructed. This model was used to ascertain the clearance and volume relationships of the capture feature. Once the correct geometries were obtained, the drawings were modified and the metal prototype was fabricated. Thus far, development and testing of the device has gone exceptionally well. Capture of the monoball is flawless and smooth. Since most of the load is generated when the device's components are nearly static, galling has not been a problem. The device remains smooth and frictionless after many cycles. Further testing to ascertain the stability under vibrating loads is underway, and a secondary (redundant) lock scheme is under study. Other work will include a lightened housing and optimization of tribological parameters for cold case/vacuum use.

REFERENCES

1. Medlar, Dennis K., "Stereolithography: A Primer." *Aerospace Engineering*, December 1990.
2. "Preliminary Test Results, Concentric Ring Damper and Vernier Damper," Martin Marietta presentation to MSFC, February 7, 1991.
3. Redmon, J. W., Reed, D. K., and Brewster, S. R.: "The Design, Analysis, and Testing of Tethered Satellite Damping Devices." (A NASA Technical Memorandum to be published).

4. Dahlgren, J. B., and Kan, E. P.: "Flight Telerobot Mechanism Design: Problems and Challenges." 23rd Aerospace Mechanisms Symposium. NASA conference publication 3032, May 1989.

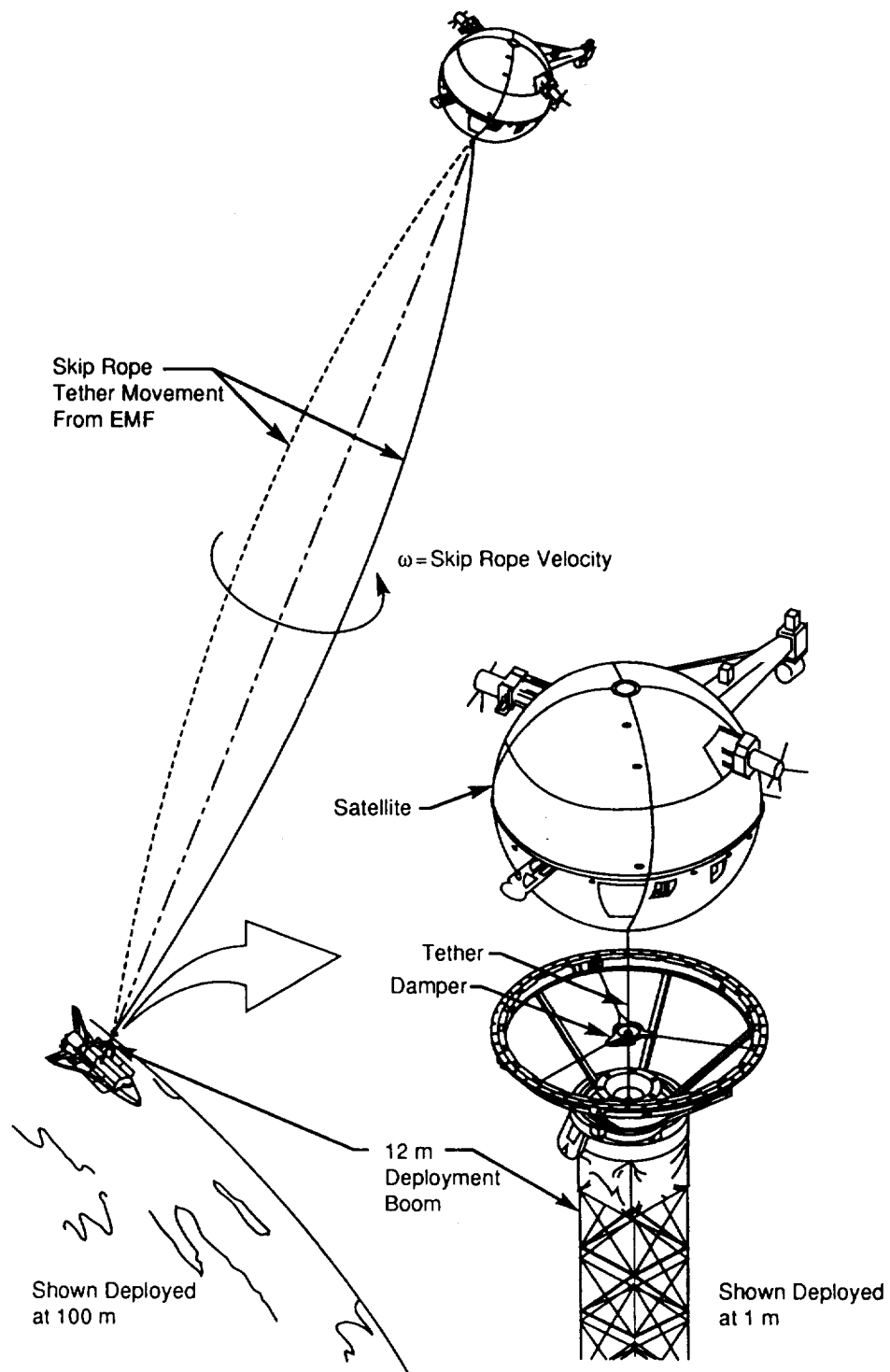
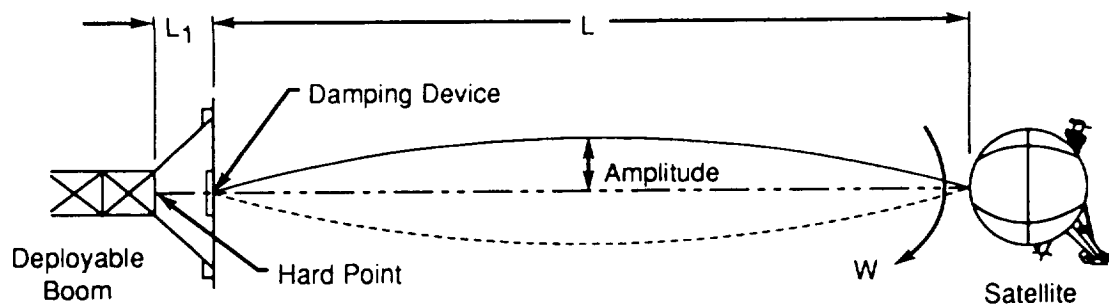


Figure 1. The Tethered Satellite System.



- Passive deploy/passive stow
- Device weight less than 185 g
- Tether tension is 0.45 lbs
- Period = 10.0 s*
- Angular velocity of tether = 0.628 rad/s*
- Damping device shall constrain midnode amplitude to less than $L/20$ m for a deployed distance between 10 and 80 m
- Damping device shall constrain midnode amplitude to less than 0.50 m for a deployed distance less than 10 m (docking criteria).

* Values given at $L = 80$ m

Figure 2. Low-Amplitude/Low-Force Damper Requirements.

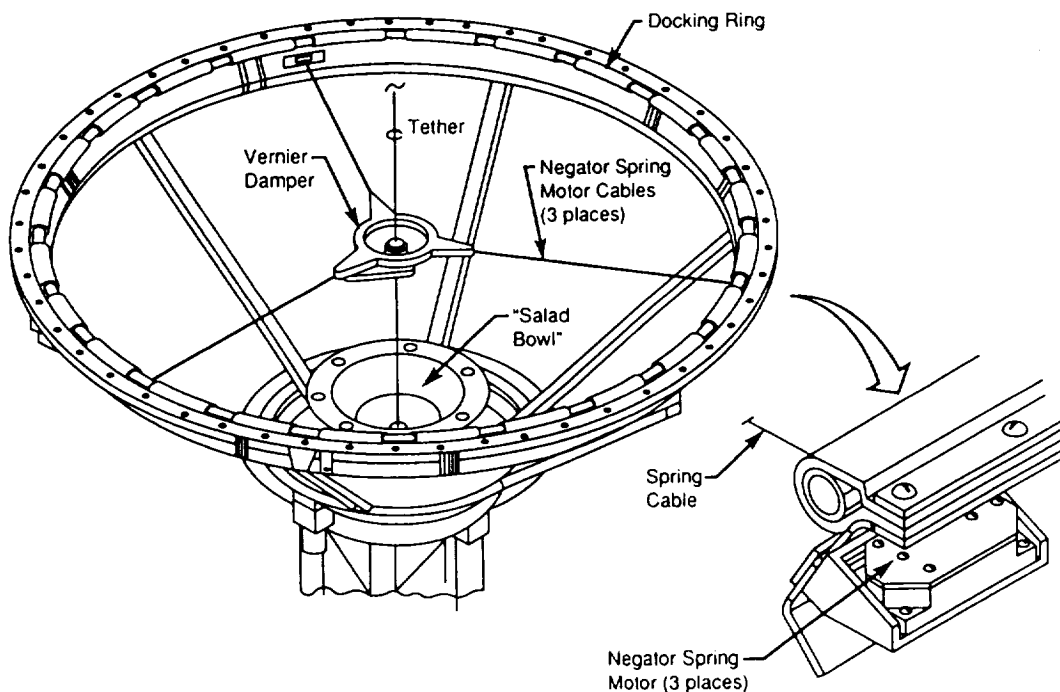
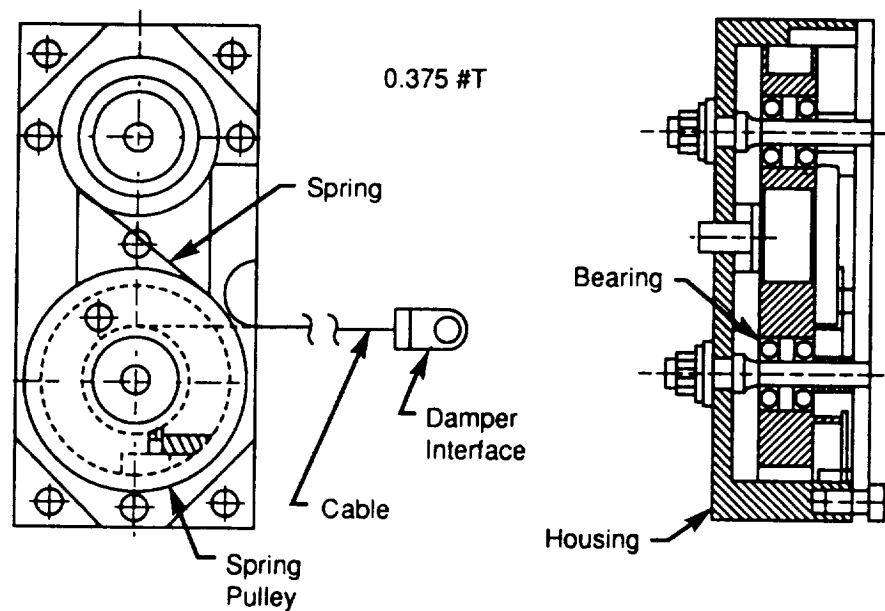
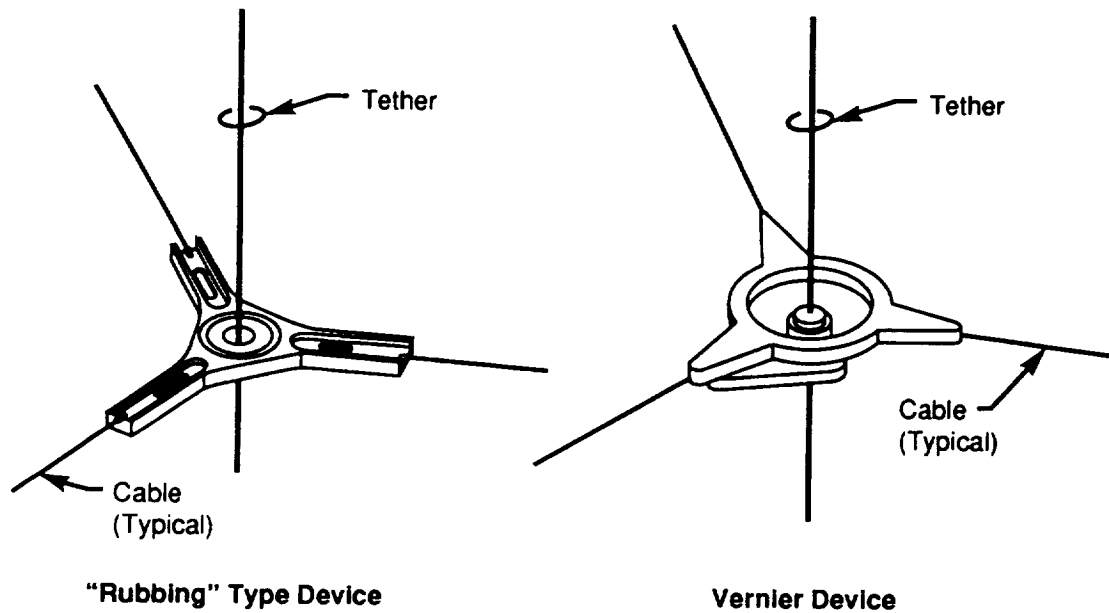


Figure 3. Deployed Satellite Configuration Showing Damping Device and Constant-Force Spring Motors. In the stowed configuration, the damping device rests in a receptacle against the satellite.



Spring Motor Assembly (3 places)

Figure 4. Tether Damping Devices.

ORIGINAL PAGE
BLACK AND WHITE PHOTOGRAPH



Figure 5. Vernier Damping Mechanism.



Figure 6. Vernier Damping Mechanism Disassembled. Cams at each pivoting joint are slightly roller-spring loaded for an adjustable drag force.

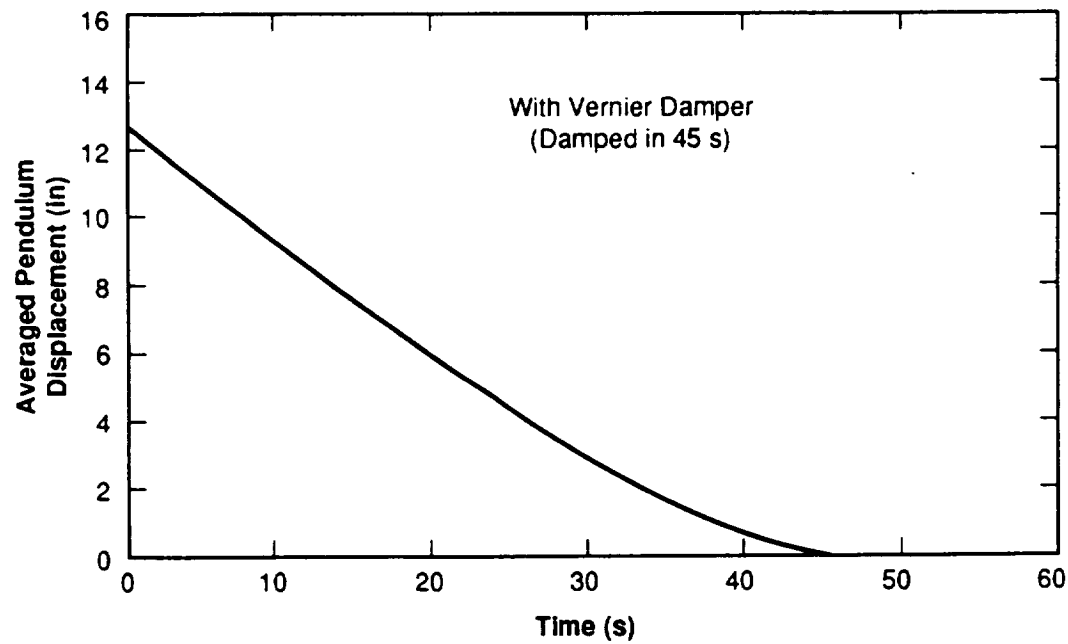
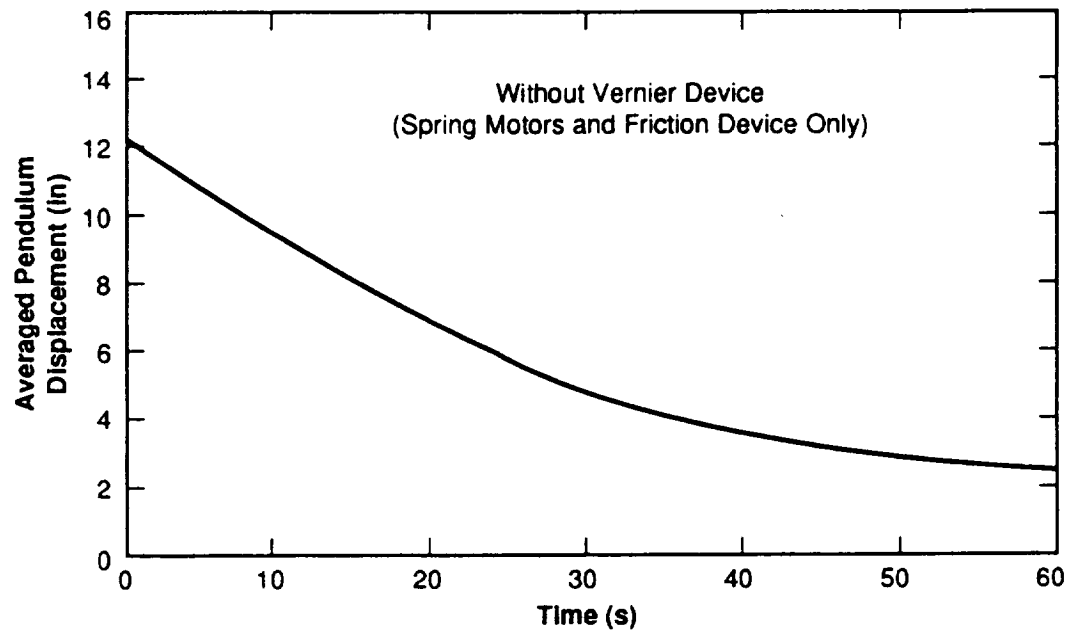


Figure 7. Damping Test Results Showing the Effectiveness of the Vernier Device.

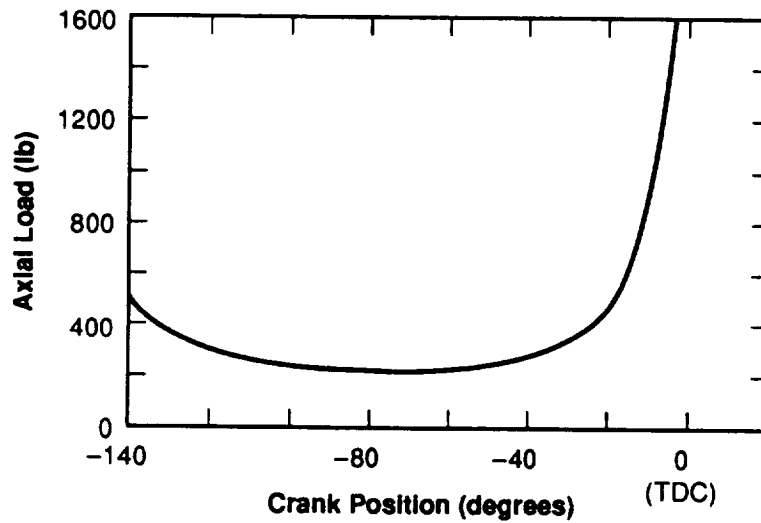


Figure 8. Input Crank Position Versus Axial (Mating) Force of Latch for a Given Input Moment of 200 in-lb. Note that the force goes to infinity at TDC.

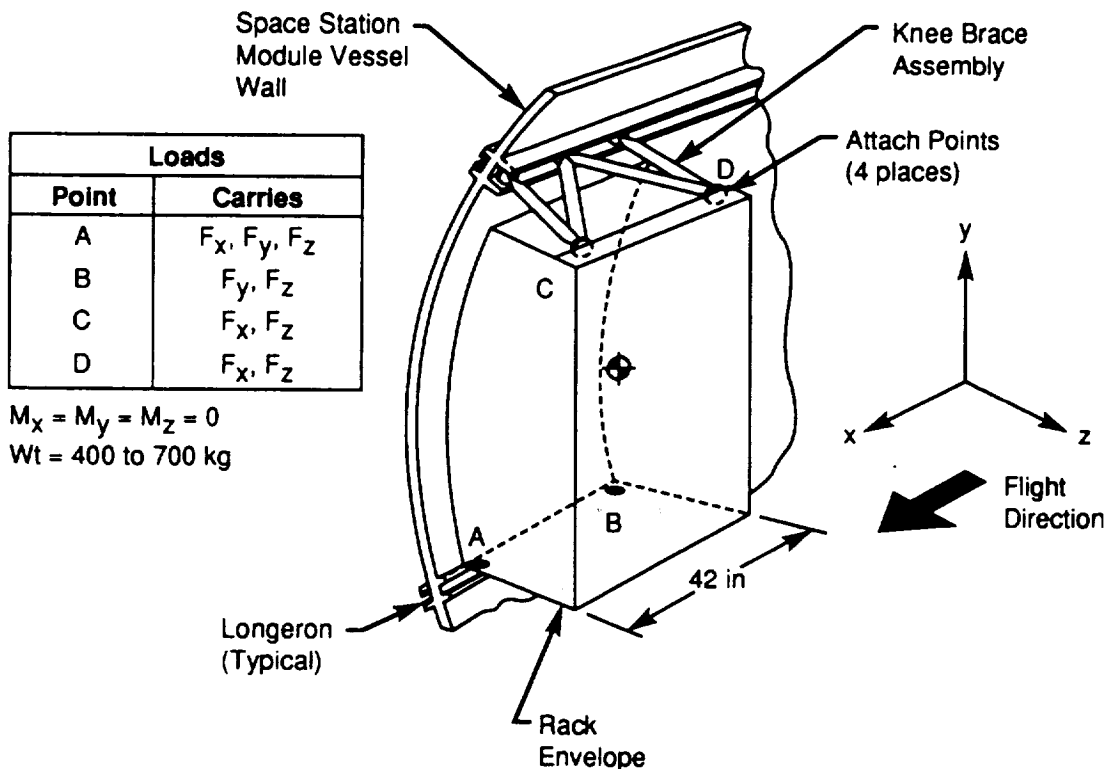
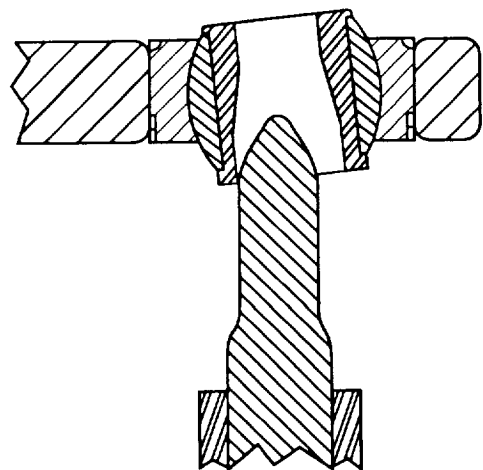
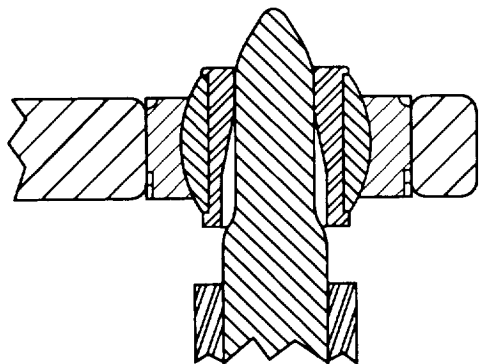


Figure 9. Latch Scheme for the Space Station Racks.

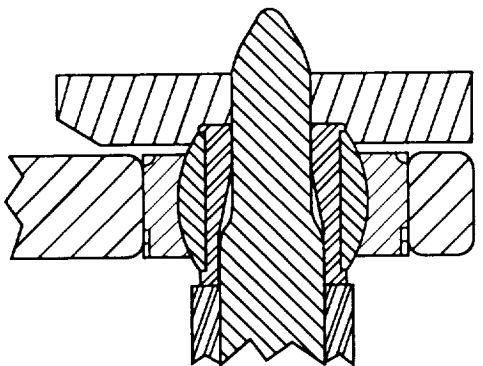
The upper interfaces are simple pin joints and are easily accessible by a crewmember. The lower latch points are difficult due to remote/blind actuation. Latch point "A" was further complicated by the need to carry X-loads.



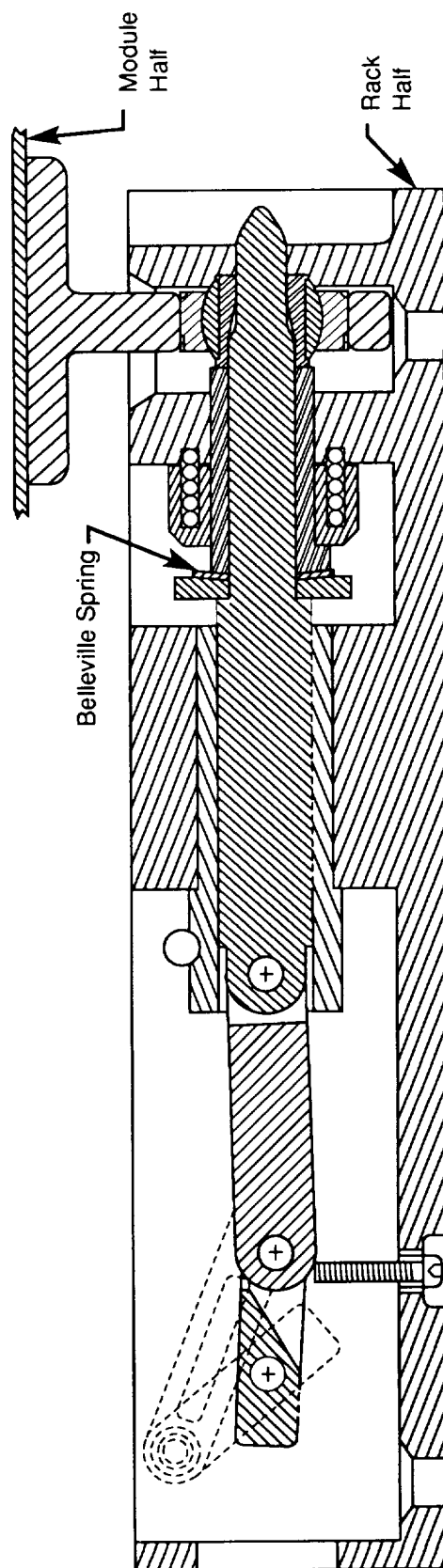
Stage 1
(Capture)



Stage 2
(Align)



Stage 3
(Rigidize)



Closed (Latched)

Figure 10. Latch Assembly Sectional Views. Note the large capture range. Diametrical clearance of the pin in the ball is 0.0005 to 0.001 in. High axial force and the ramping surface make possible smooth and flawless mating.

Figure 11. A Disassembled View.

ORIGINAL PAGE
BLACK AND WHITE PHOTOGRAPH

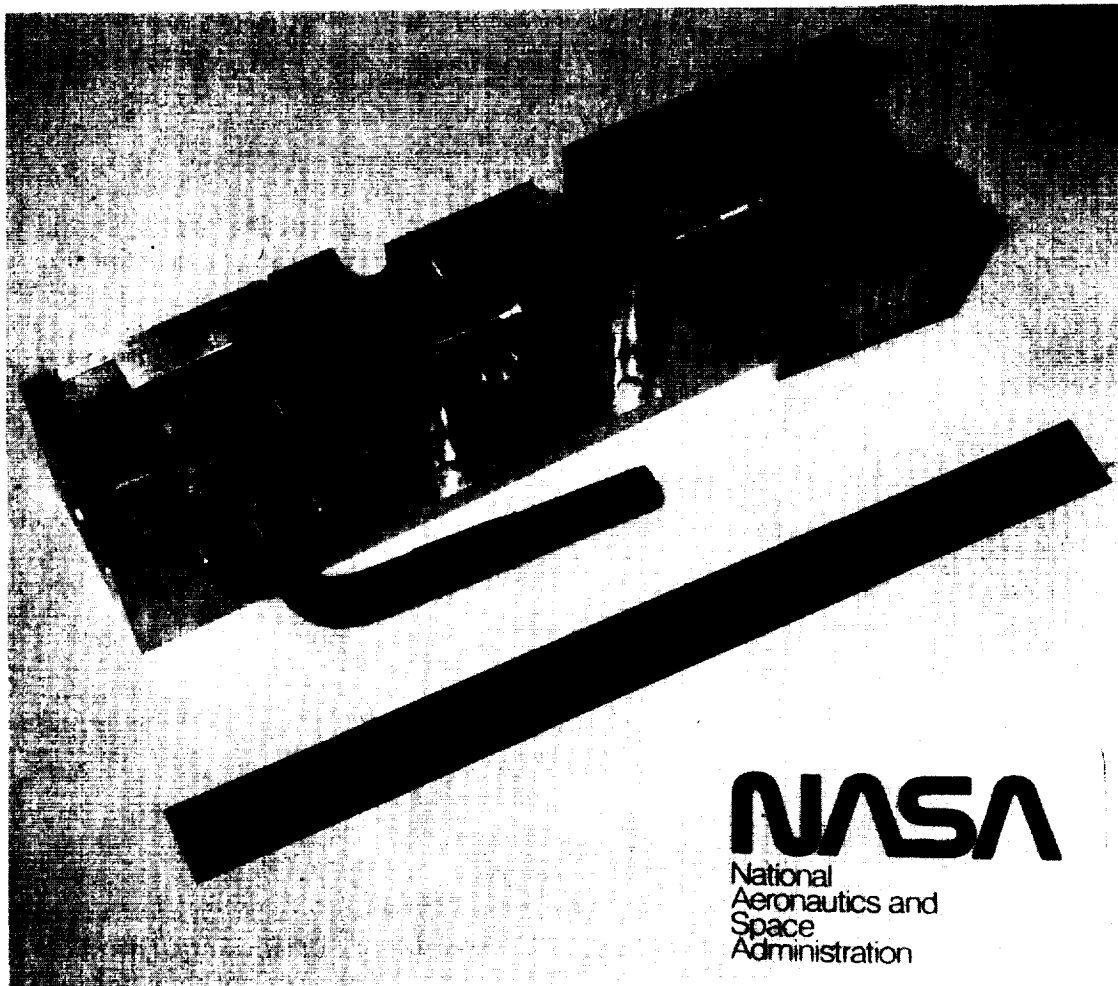
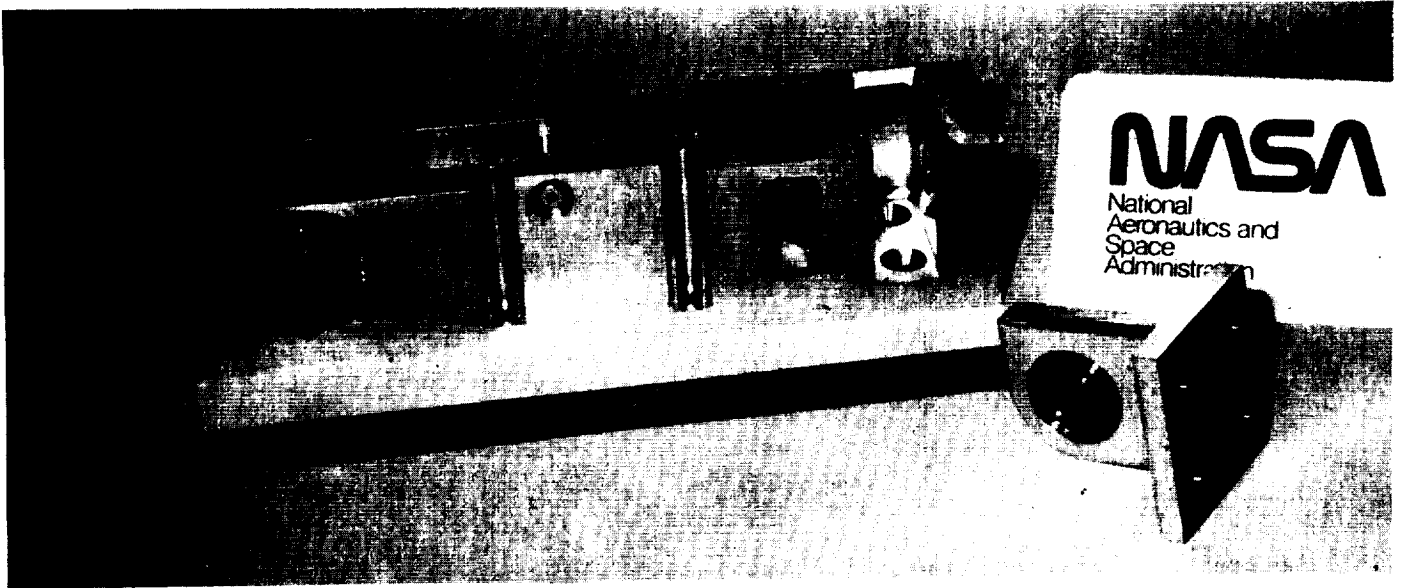


Figure 12. Photographs Showing the Open and Mated Configurations.
Travel of crankpin is 135° . This number was selected to maximize capturing forces.

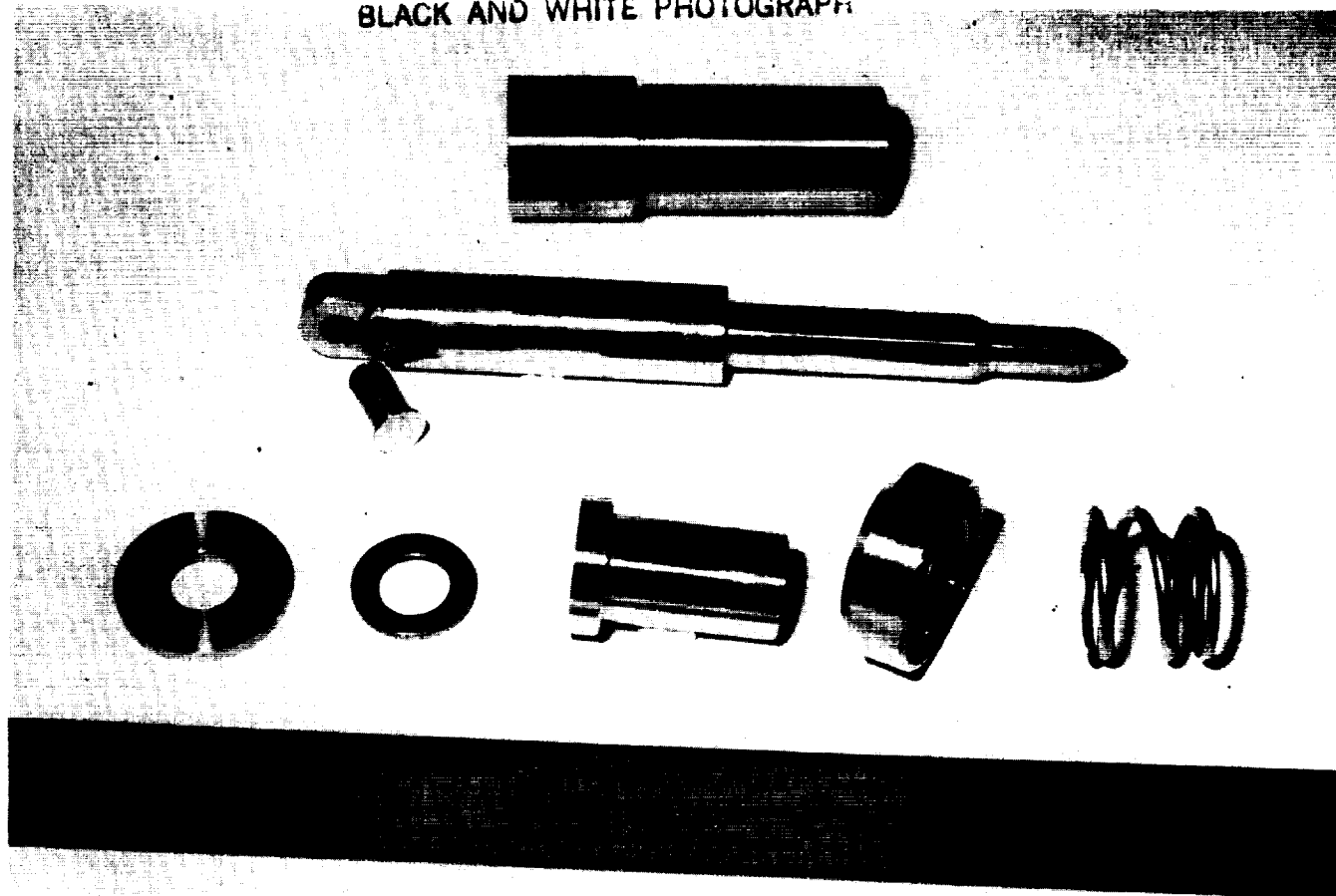


Figure 13. Photographs showing a more close-up view of the pin, belleville seat, belleville spring, "rigidizing" bushing, coil spring seat, and coil spring. The coil spring is for retraction only.

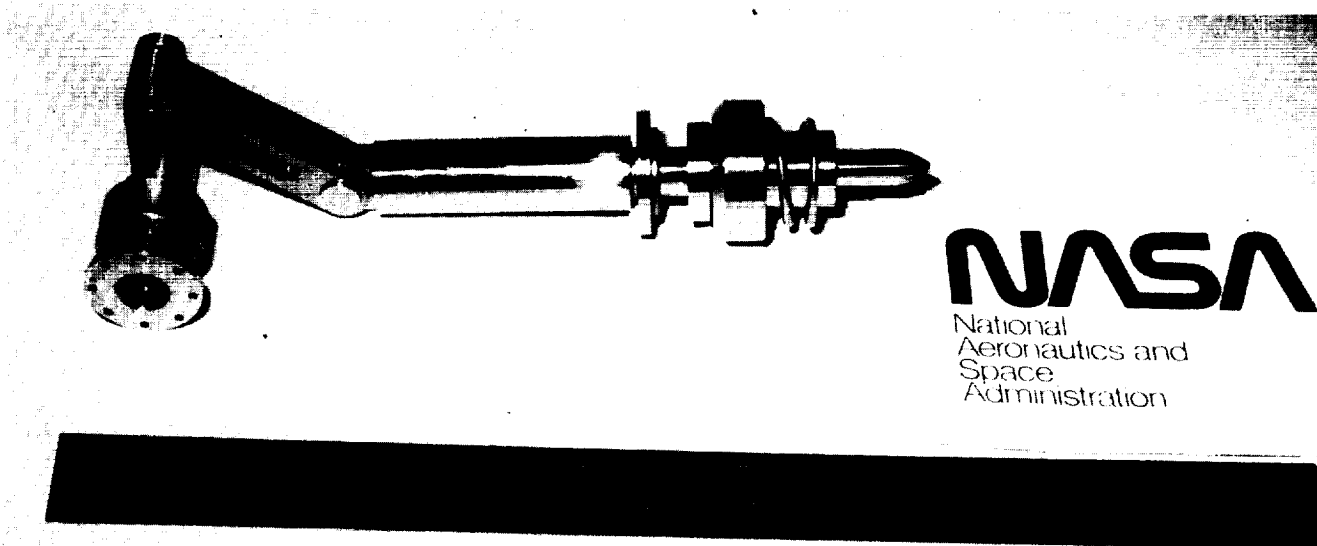


Figure 14. Subassembly Photograph of Components Less Housing. The slider-crank linkage was selected for the drive element because of its short-throw, low torque/high force characteristics, and "tactile feel." Any number of drive devices can be used.

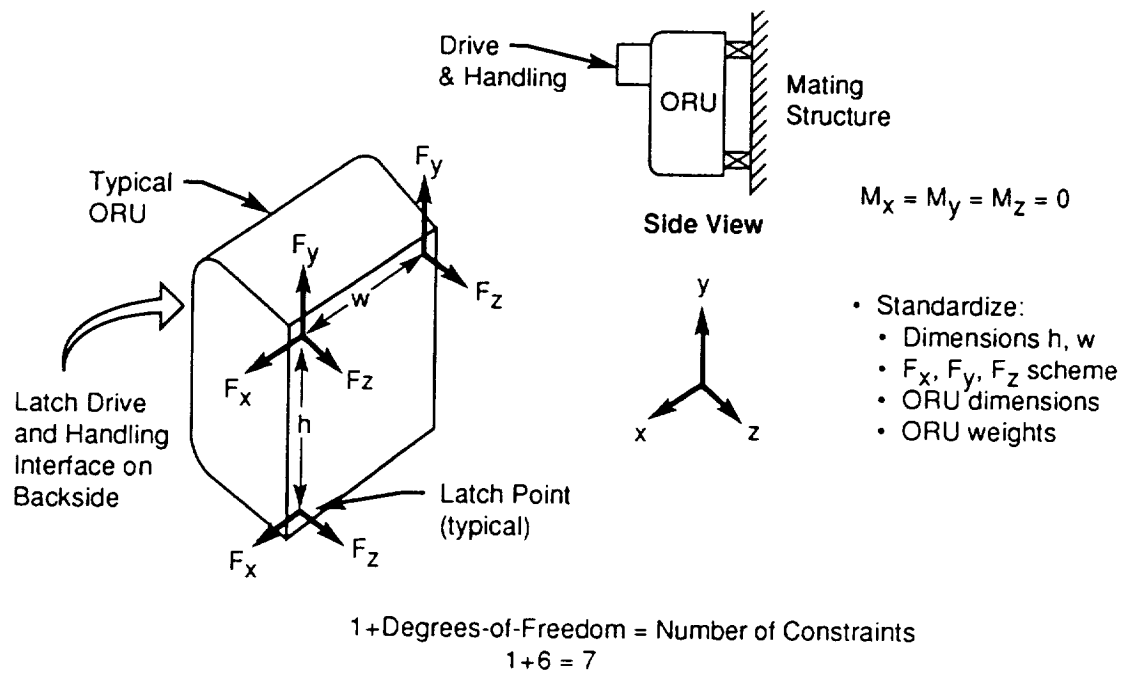
Load Capability	4000 lbs (x, y, and z)*
Max Input Torque	45.0 in-pounds**
Actuation Angle	135 deg
Pin Stroke	1.63 in
Capture Range	0.25 in diameter (y-z plane) 0.19 in (x axis) 20 degrees angular
Materials	17-4 PH (H900), 17-7 PH, MP35N, 6061-T6, Nitronic 60, 440-C
Belleville Spring	2000 lbs @ solid height 0.005 in nominal travel to S.L. (spring is solid at TDC)***
Overall Dimensions	11.0 x 2.50 x 2.50 in

- Conservative estimate
- ** At nominal conditions
- *** Higher spring loads are easily achieved

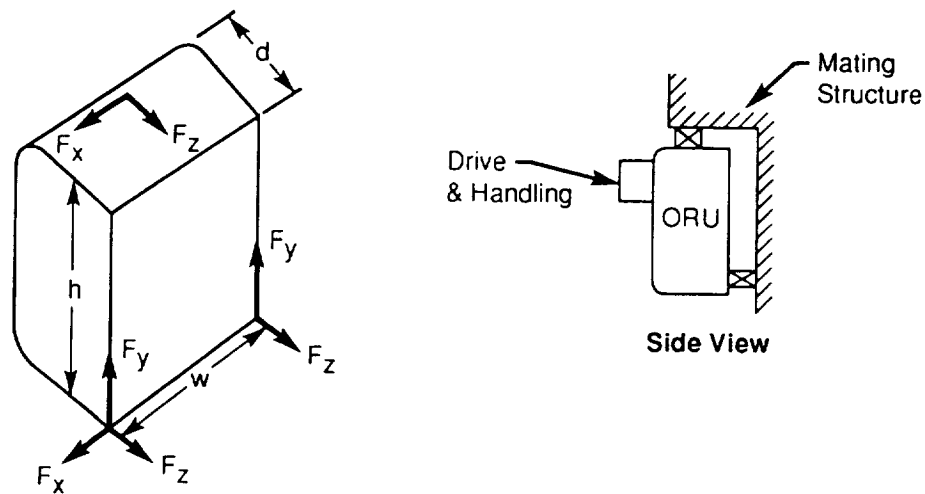
Figure 15. Latch Specifications.



Figure 16. Stereolithography Model of Latch. This model helped to visualize capture and mating. Fidelity and accuracy of model is poor. Cost of such models is probably higher than a machined metal model.



Standard 3-Point Planar Interface



3-Point Diagonal Interface

Figure 17. Alternative Latch Schemes. Specification of latch points, schemes, spacings, etc., is the start of standard interfaces (robotic, IVA, or EVA). These latches would be used where high loads are encountered such as the transferral of massive items to and from Earth.

ADELE

Articulation de DEploiement à Lames d'Enroulement⁽¹⁾

Eric BLANC*

ABSTRACT

AEROSPATIALE has developed a new appendage deployment concept called AMEDE⁽²⁾ with a view toward increased simplicity and functional reliability.

This new concept--applicable to the deployment of any type of spaceborne appendage, in particular to solar arrays--enables deployment without synchronization or speed regulation devices. On the other hand, it requires the use of hinges with low driving or resistive torques.

The ADELE hinge is the first compliant industrial product built on that principle.

This paper comprises 3 parts :

- Part 1 outlines the AMEDE concept as compared to the conventional deployment concept.
- The conceptual and functional principles for the ADELE hinge are presented in part 2, along with the hinge's main characteristics.
- The paper closes with part 3, which addresses development status of both the AMEDE concept (AMADEUS⁽³⁾ experiment) and the ADELE hinge.

ABBREVIATIONS

- (1) **ADELE** : Articulation de DEploiement à Lames d'Enroulement
 (Deployment hinge using wraparound strips)
- (2) **AMEDE** : Amélioration des MEcanismes de DEploiement
 (Improvement of deployment mechanisms)
- (3) **AMADEUS** : Adaptation de Mécanismes pour Appendices DEployables
 à Usage Spatial
 *(Adaptation of mechanisms for spaceborne deployable
 appendages)*

* AEROSPATIALE/Space and Strategic Systems Division, Cannes Center, FRANCE

1. INTRODUCTION

1.1 CONVENTIONAL DEPLOYMENT MECHANISMS

Deployment of most current rigid solar arrays involves three types of mechanisms:

- **Inter-panel hinges (Fig. 1)**
These hinges ensure rotation, motorization and end-of-deployment locking/latching of the solar array panels.
- **One-speed regulation device (Fig. 2)**
This mechanism regulates the panels' deployment speed so as to minimize end-of-deployment shocks.
It dissipates energy through regulation devices based on dry-friction centrifuge, hydraulic, or eddy current principles.
- **One synchronization device (Fig. 3)**
The synchronization device provides control over the deployment kinematics.
It ensures a quasi-constant aperture angle between the panels.

This deployment concept has now completed final validation. However, it appears as a complex assembly whose qualification—particularly the demonstration of its reliability—requires a considerable development effort.

Hence AEROSPATIALE's commitment to simplify this product.

1.2 THE AMEDE CONCEPT (Fig. 4)

AEROSPATIALE has developed a new deployment concept called AMEDE, in order to increase simplicity and reliability of deployment mechanisms for spaceborne appendages.

This concept is based on the finding that--among the mechanisms mentioned above--only the motorized hinge is strictly essential to deployment.

Therefore, the complementary synchronization and speed regulation devices are now deleted, at the cost of additional requirements being specified for the hinges.

These requirements are provided in section 2 hereafter, along with a presentation of that hinge concept that successfully meets such requirements.

The AMEDE concept is supported by a deployment kinematics prediction software which provides for :

- no interference from spacecraft's main body during deployment of the appendage
- deployment time.

2. ADELE (Articulation de DEploiement à Lames d'Enroulement)

2.1 GENERAL

The essential, basically novel requirements entailed by the AMEDE concept are expressed as follows :

- low driving and resistive torques
- very high reproducibility of these two parameters.

Moreover, the objective of significantly improving these products' reliability led us to take into account two additional requirements:

- eliminate the friction effects, resulting in :
 - no binding hazards
 - compliance with motorization margins
- minimize the number of moving parts.

Comparative analysis of the different technological solutions led us to adoption of an original hinge concept offering a quasi-zero resistive torque. This hinge's operating principle is based on two fittings' cylindrical surfaces rolling over each other, with rotational guiding ensured by so-called wraparound strips.

Motorization is provided by an elastic device, which is also frictionless.

2.2 MECHANISM DESCRIPTION

2.2.1 Mechanical Architecture

Architecture of the ADELE hinge is illustrated in Figure 5.

2.2.2 Functions

The ADELE hinge ensures four major functions:

- rotation
- motorization
- locking in deployed position
- stiffness

2.2.2.1 Rotation

The fittings' rotation is provided by the motion of two cylindrical fittings rolling over each other (*see Fig. 6*).

These fittings are rotationally guided by the wraparound strips.

The tension applied through these strips imparts a motion of the "slippage-free rolling" type, thus precluding any spurious friction effects.

2.2.2.2 Motorization

Hinge motorization is provided by the Carpentier's joints (*Fig. 7*).

Each joint consists of two convex spring-action blades.

The motorization imparted by the joints is not a constant value. It is dependent on the hinge's deployment angle. (*Fig. 8*).

The minimum torque is obtained at 30-deg aperture, as against the maximal value at the end of deployment.

Motorization is modulated by the number of joints utilized.

2.2.2.3 Locking in deployed position

The hinge must lock into deployed position and remain so at loads induced by the spacecraft's attitude and orbit control system (AOCS).

This function is fulfilled by the Carpentier's joints.

The hinge's withstanding of orbital torques is a function of the number of Carpentier's joints.

2.2.2.4 Stiffness in deployed position

The hinge's stiffness in deployed position is a fundamental parameter, as it is a major contributor to the solar wing's deployed frequency.

We distinguish between:

- **Stiffness about own rotation axis :**

This hinge's concept offers high, perfectly linear stiffness over a broad range of torques (*see Table 1*).

This type of stiffness is ensured by the fittings, the Carpentier's joints and the wraparound guide strips.

- **Stiffness about X and Y axes (*see sketch in Table 1*)**

Stiffness about these two axes is ensured by the Carpentier's joints and the guide strips.

Its value is high, as shown in Table 1.

2.3 HINGE PERFORMANCE (2 - joint version)

The main characteristics of ADELE performance are given in Table 1.

3. DEVELOPMENT STATUS

3.1 VALIDATION OF THE AMEDE CONCEPT : THE AMADEUS EXPERIMENT (*Fig. 9*)

The French-Soviet experiment AMADEUS, conducted on board the MIR Station in 1988, was a crucial step in the development of the AMEDE concept.

Tests, which were performed in 10 different configurations by varying

- the type of deployment (*2 D or 3 D*)
- the amount of motorization
- inertia,

resulted in validation of :

- the prediction software for the deployment kinematics
- the ADELE hinge's functional principle, as well as its adaptability to 2D and 3D deployments.

3.2 QUALIFICATION OF THE ADELE HINGE

After a successful development test campaign, the ADELE hinge is now undergoing qualification as part of the SPOT 4 Solar Array program (*see figure 10*).

This qualification, which is to be completed in late 1991, comprises five categories of tests :

- vibration (*sine, random*)
- motorization (*environmental, thermal conditions*)
- stiffness (*in deployed and stowed configurations*)
- resistance to quasi-static loads in deployed configuration
- endurance.

Note : A lighter weight version of the ADELE hinge is currently under study at AEROSPATIALE.

Such a hinge is slated to equip the upcoming generation of the SPACEBUS family of telecommunications satellites.

4. CONCLUSION

The ADELE hinge is a simple, reliable and high-performance product.

Associated with the AMEDE concept, ADELE significantly enhances simplicity and reliability of spaceborne appendage deployment

A perfectly fit solution for solar arrays, ADELE holds promise for yet another deployment applications currently under development; i.e., to antennas, radiators, baffles, etc.

Furthermore, from its versatile design, ADELE is readily customized to a broad variety of deployment configurations.

ORIGINAL PAGE
BLACK AND WHITE PHOTOGRAPH

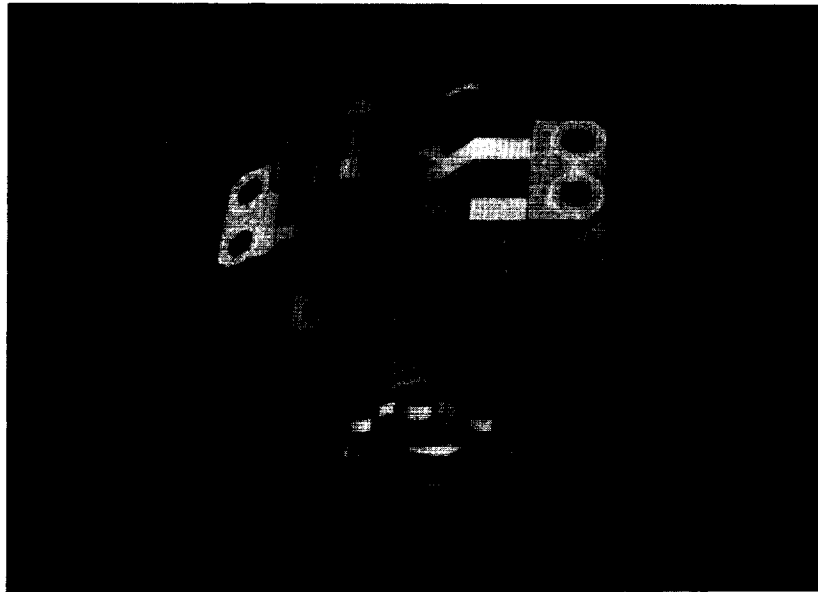


Figure 1. TDF-type hinge

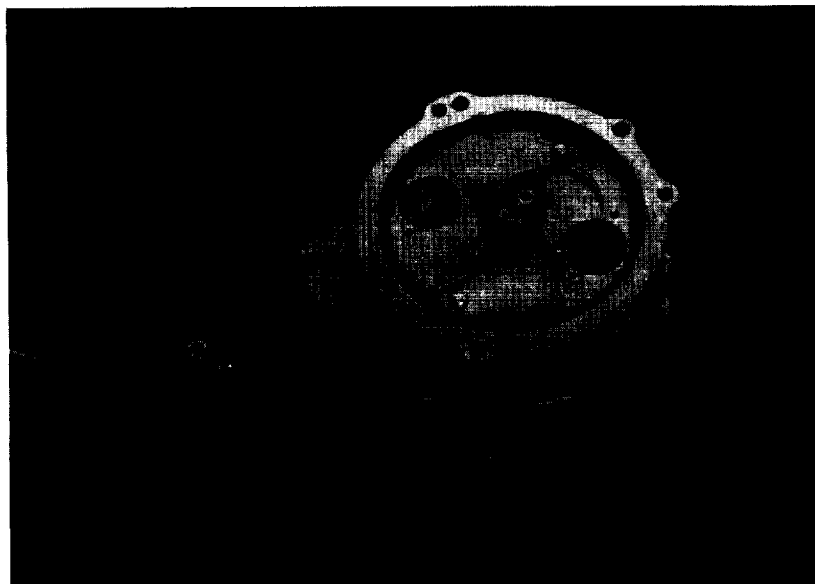


Figure 2. Centrifugal regulator

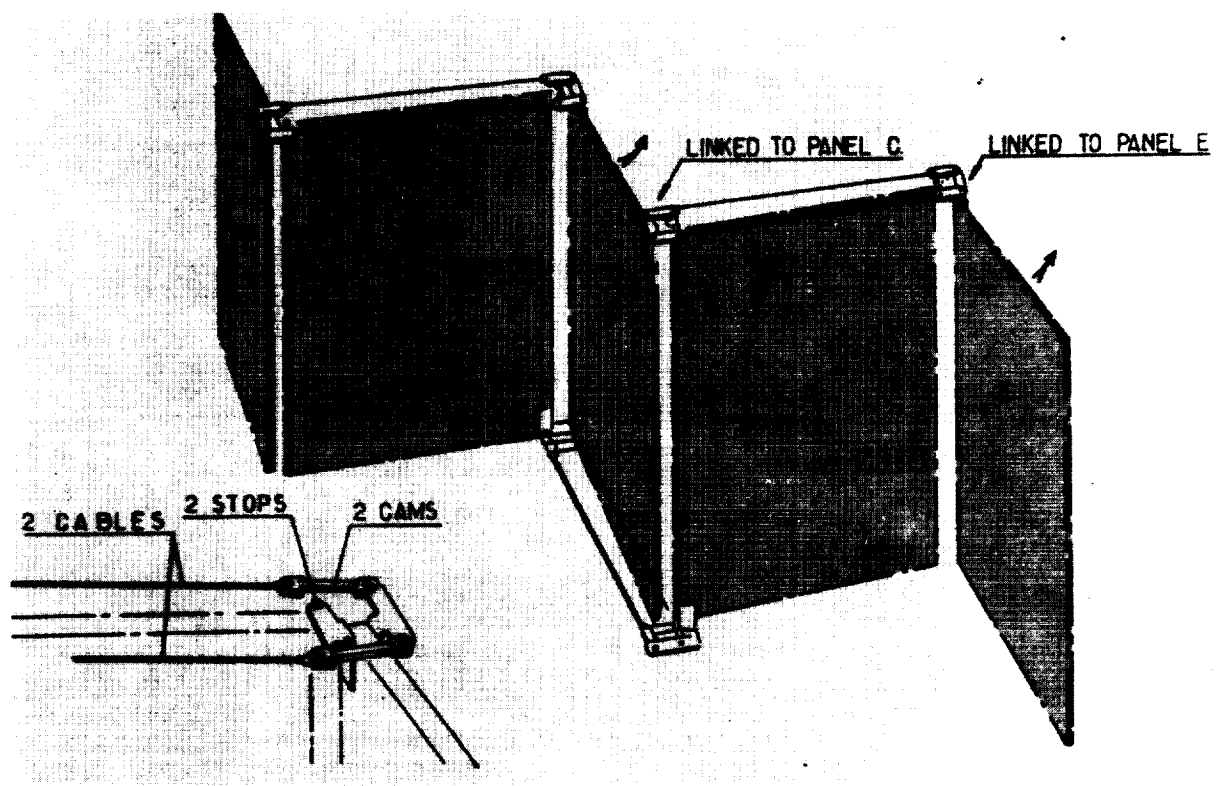


Figure 3. Synchronization device

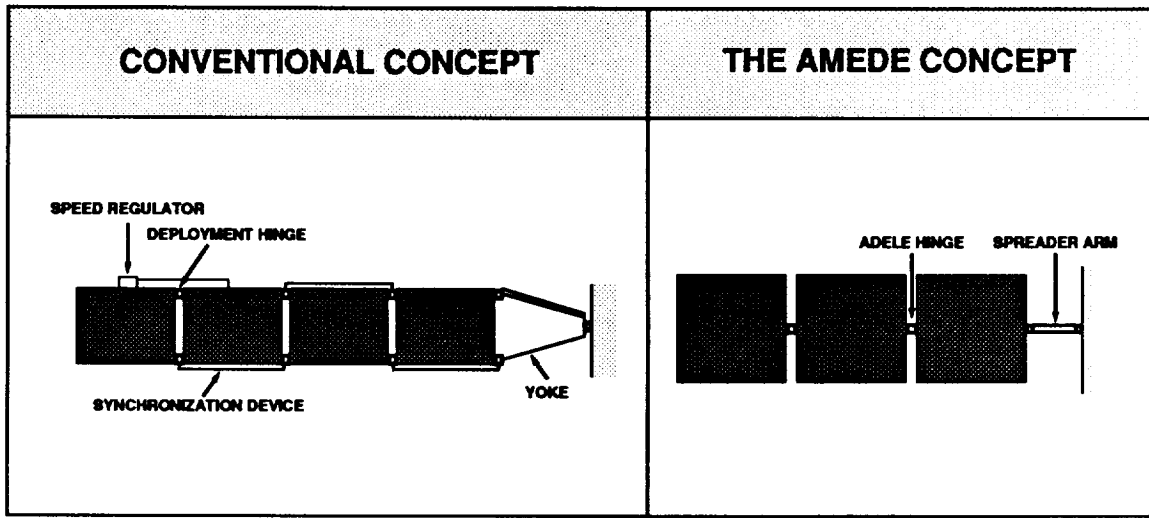


Figure 4. The AMEDE concept

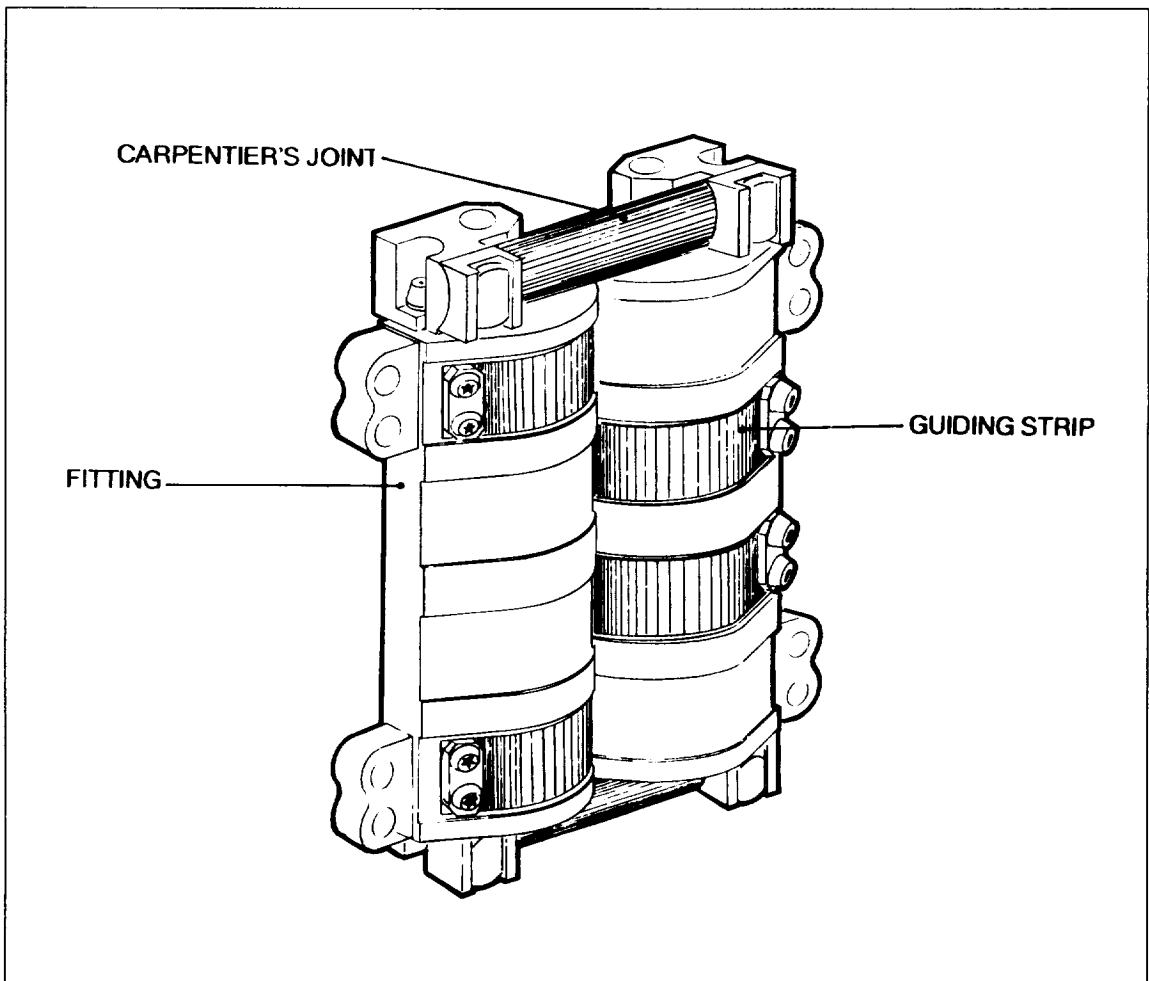


Figure 5. The ADELE hinge

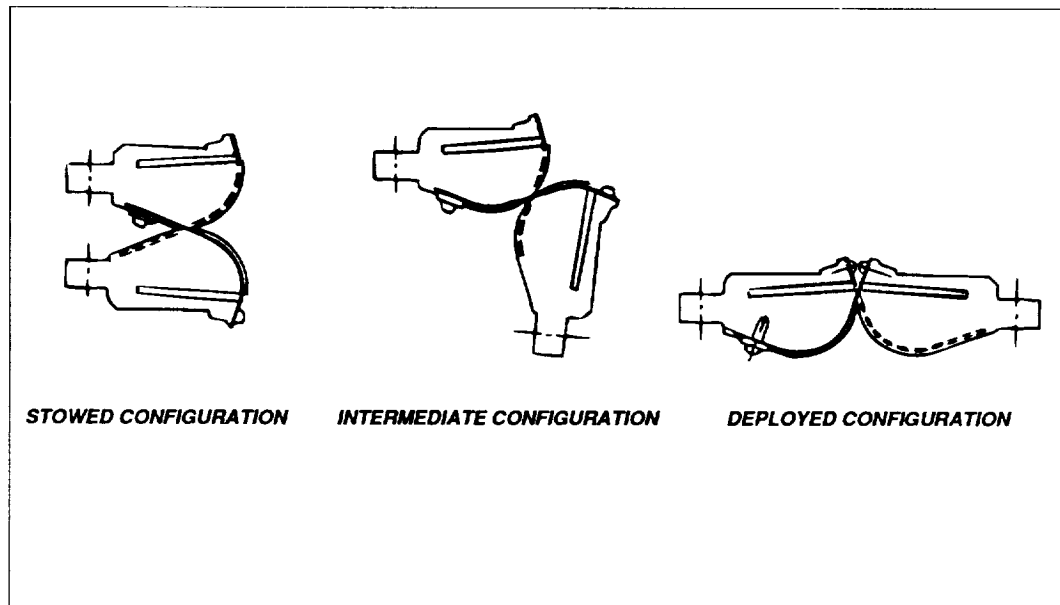


Figure 6. Rotation

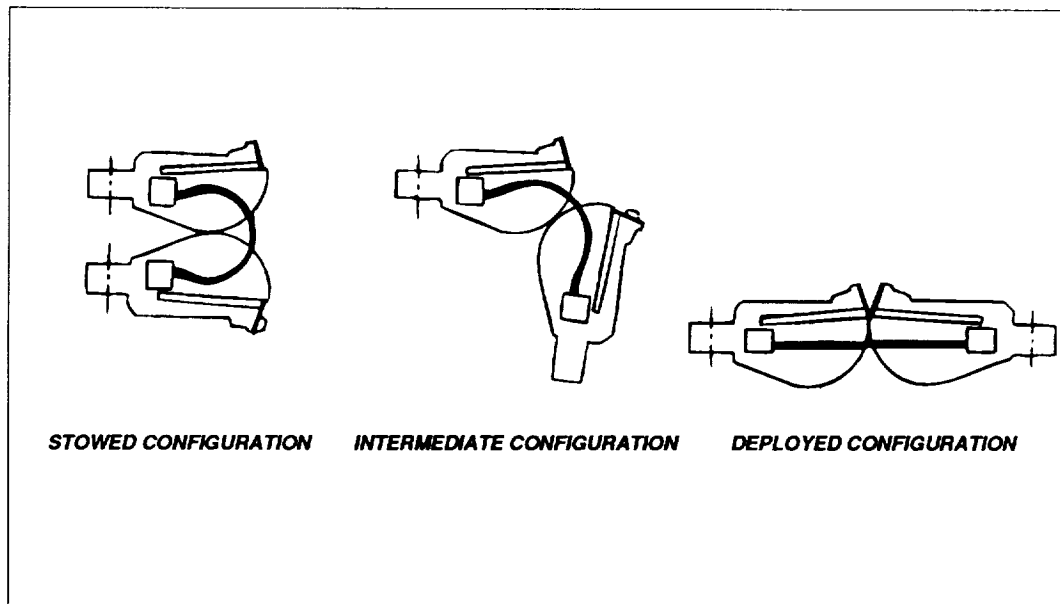


Figure 7. Motorization

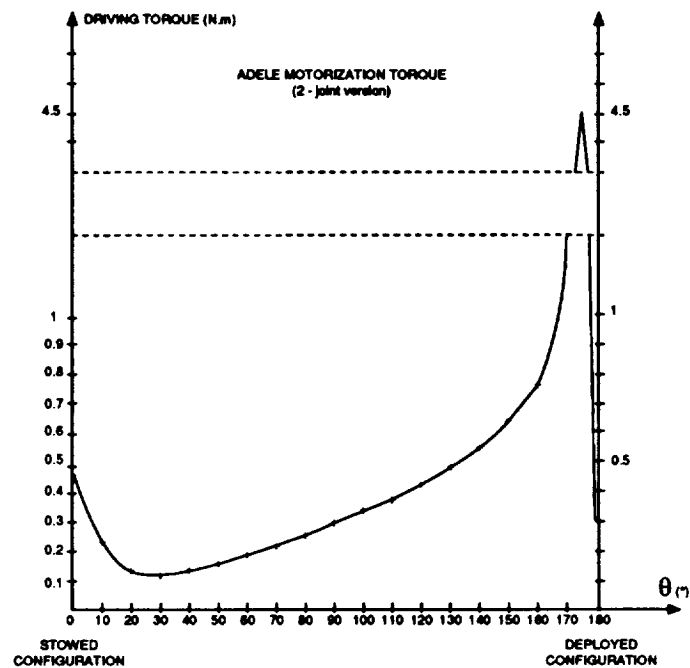


Figure 8. Motorization curve

Table 1. ADELE performance (2 - joint version)

FUNCTION	PERFORMANCE
ROTATION	0 to 180°
MOTORIZATION	see Fig. 8
STIFFNESS	<ul style="list-style-type: none"> TORSIONAL $K\theta_x = 20,000 \text{ N.m/rd}$ (within $\pm 9 \text{ N.m}$) BENDING $K\theta_z = 2,800 \text{ N.m/rd}$ (within $\pm 9 \text{ N.m}$)
RESISTANCE TO QUASI-STATIC LOADS IN DEPLOYED CONFIGURATION	$M_x = 150 \text{ N.m}$ $M_y = 150 \text{ N.m}$ $M_z = 220 \text{ N.m}$

ORIGINAL PAGE
BLACK AND WHITE PHOTOGRAPH

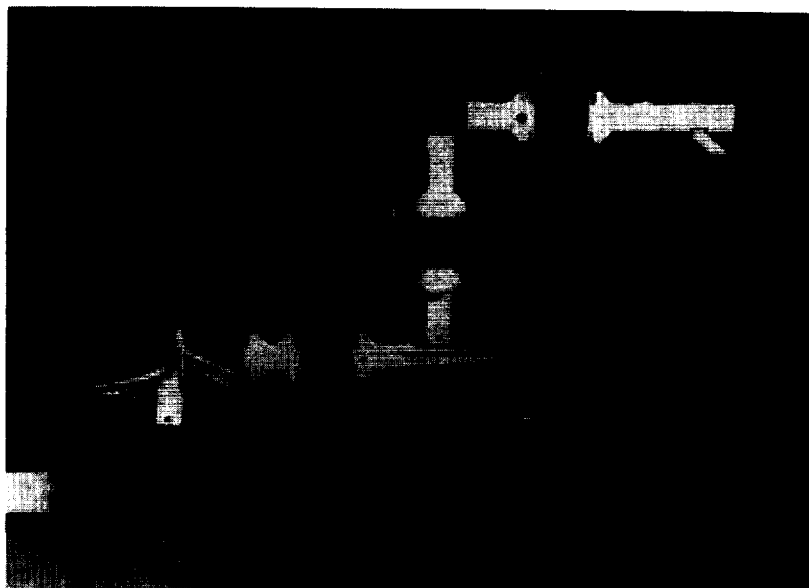


Figure 9. The AMADEUS experiment

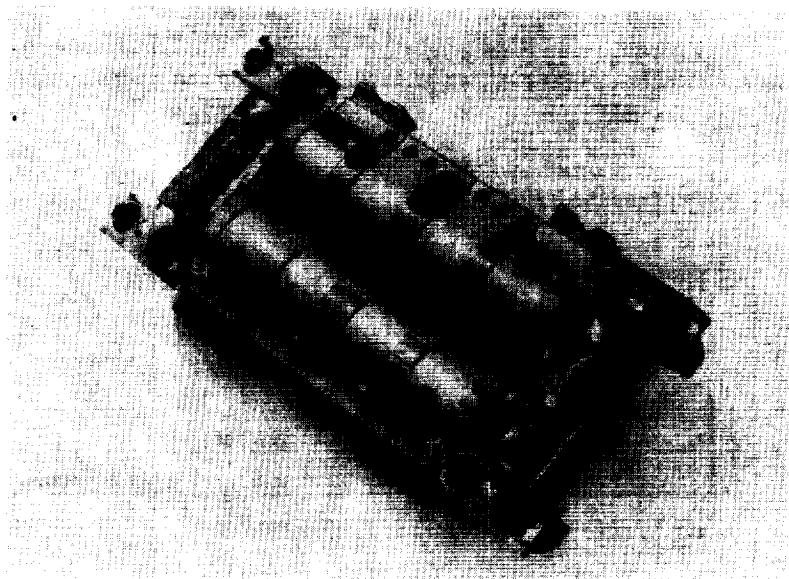


Figure 10. The ADELE qualification model (*SPOT 4* program)

DEPLOYMENT AND RETRIEVAL MECHANISM
REDESIGNED FOR SPARTAN SPACECRAFT ON THE STS
Greg Galloway*

ABSTRACT

The Spartan Release Engage Mechanism (REM) is a system designed to restrain the Spartan spacecraft during Space Transportation System (STS) launch and landing. The mechanism is designed to allow deployment and retrieval of the Spartan free flyer spacecraft from the shuttle payload bay. The Goddard Space Flight Center (GSFC) Special Payloads Division adapted the REM concept from the original Marshall Space Flight Center (MSFC) design. Because current Spartan spacecraft are much heavier than payloads intended for the original REM, an extensive redesign, analysis, and test program was necessary. Also, increased emphasis on safety in the post Challenger era prompted a reevaluation of possible failures. Much of the design effort focused on improving the latch mechanism gearbox. Key concerns were effective gear lubrication, thermal gradients at the gearbox mounts, operation at thermal extremes, and gear-train failure contingencies. Increased concern for reliability led to the design of an Extra Vehicular Activity (EVA) backup latch system.

INTRODUCTION

Figure 1 illustrates how the GSFC REM is used as part of the Spartan Flight Support Structure (SFSS). Figure 2 illustrates the REM primary and backup latching systems that allow the spacecraft to be deployed and retrieved by the STS/Remote Manipulating System (RMS) on orbit. Figure 9 shows how the REM adapter mates with the REM. This adapter is an integral part of a Spartan spacecraft. The original REM was designed, built and flown in November 1981 by MSFC for the Induced Environmental Contamination Monitor (IECM) payload, which weighed 816 pounds. The Special Payloads Division at GSFC used this REM design to fly the Spartan 101 spacecraft in June 1985. It weighed approximately 2000 pounds. This was pushing the capacity of that REM design. Post-flight inspection revealed severe galling of the worm drive and some bent bolts mounting the gearbox. The same REM design was slightly reworked in the gearbox and subsequently lost on the Challenger. After this, STS safety requirements were reevaluated and more strictly enforced. Planned Spartan 200 series spacecraft would weigh as much as 3000 pounds. It was therefore decided to redesign the REM for higher load capacity, more safety, and more redundancy. This was achieved by eliminating certain single-point failure modes and adding a backup latch mechanism.

REM functional description

The REM primary latch mechanism operation is illustrated in figure 3. An AC motor-driven gearbox rotates a bellcrank clockwise which rotates the latch links via the turnbuckles. Once the shuttle RMS has positioned the

*NASA Goddard Space Flight Center, Greenbelt, MD

spacecraft for latching, latch link rotation translates the spacecraft in the +Y direction, and engages the four adapter pins into the REM receiver plates. After the pins are engaged all the way, the bellcrank continues to rotate and compress belleville washers in the turnbuckles to apply a clamping preload. Rotation continues until the bellcrank has reached a position 3 degrees over center where it is stopped by contacting a limit switch. Braked motors, plus the resistance to back driving by the worm, hold the bellcrank at 3 degrees and react -Y flight loads through the mechanism. X,+Y,and Z loads are reacted by the REM base.

The REM backup latching mechanism operation is illustrated in figure 4. This mechanism is operated manually by astronauts during an EVA. Astronauts will first disable the primary latch mechanism by use of a de-clutch device. This device mechanically uncouples the gearbox from the primary latching linkages. The primary latch linkages now move freely and allow operation of the EVA backup mechanism. The astronaut rotates a shaft that runs the width of the REM. This shaft drives the two independent sides of the backup system. Both sides of the mechanism are identical. Each side utilizes a four-bar linkage/toggle device to convert the applied torque to a translating motion of a piston. The pistons slide axially on cam follower guides and push directly on the spacecraft adapter to engage the adapter pins in the REM base. These pistons use the same arrangement of belleville washers as the turnbuckles to develop a latching preload. After the pins move all the way into the receiver holes, the linkage continues to apply load to the piston. Here again, the concept of driving the mechanism "over center" is employed. The pistons are compressed to a maximum where they are in line with the toggle linkage arms. Then the toggle snaps past this point to a hard stop at 3 degrees over center. With the primary mechanism de-clutched the backup mechanism must also be able to unlatch the spacecraft. This is accomplished by latch hooks located on the ends of each piston. The latch hook locks onto a catch latch on the underside of the spacecraft adapter when the backup system is engaged. Figure 4 shows a catch latch on the spacecraft adapter. If the backup system is then unlatched the latch hooks will pull the spacecraft back. At the end of mechanism travel, the latch hooks unlock from the catch latches. The spacecraft is then free from the REM.

Should both the primary and backup latch systems fail, there is a bolt removal device installed at each of the four bolted interfaces between the REM and the support bridge to allow the REM to be unbolted by the astronaut and jettisoned overboard with the spacecraft.

REM system components

The primary system gearbox is illustrated in figure 5 with a top cover cutaway view. Important features include the kinematic mounting feet, the double-envelopment steel worm/ bronze gear combination, the Common Drive Unit (CDU), the splined drive shaft, and the use of heating elements on the gearbox housing to allow operation at cold temperature extremes. The double-envelopment worm utilized makes contact with the gear on four teeth, as opposed to one tooth for a straight worm. The worm/gear teeth are coated with grease. Dissimilar materials are used on the worm and the gear to greatly

reduce the possibility of gear galling. The CDU was purchased from Honeywell. This unit is currently used in several other space-flight applications and has proven its reliability. The unit consists of two 400-Hz AC motors, equipped with brakes, coupled to one shaft by a differential gear with planetary gear reduction. Torque is transferred from the CDU to the worm by a flex coupling.

The next level of primary system assembly is illustrated in figure 6. Here the bellcrank and de-clutch mechanism are shown assembled to the gearbox. This is a cutaway view of the de-clutch mechanism and the bellcrank. The bellcrank is composed of inner and outer sections. The inner section has a spline pattern that mates with the splined shaft from the gearbox. The outer section connects with the primary system turnbuckles. Between these sections are bearings to allow free rotation of the outer section when not clutched to the inner section. The clutch plate has raised surfaces that fit into a corresponding female pattern shared by the inner and outer bellcrank sections. When clutched together, torque is transmitted from the gearbox to the inner section through the clutch plate to the outer section and then to the turnbuckles. The de-clutch mechanism is operated by manually turning a crank and ballscrew which pulls the de-clutch lever. Moving this lever causes a cam follower ring to move away from the bellcrank taking the clutch plate with it. Once the system is de-clutched it cannot be re-clutched. At this point, an astronaut would manually engage the backup latch mechanism.

A cutaway view of a primary system turnbuckle is shown in figure 7. The assembly includes a plunger that fits into one end of a housing. Captured between these are 15 belleville washer springs arranged as five parallel sets three in series. Self-aligning tie rod bearings are located at each end of the turnbuckle. These tie rods allow pin connections to the latch links and the bellcrank. The pins at the linkage connection points are stainless-steel coated with an impregnated dry lubricant.

A mechanical flag device was developed as a backup primary system latch indicator to the aft flight-deck instrument panel indicators. The device is illustrated in figure 8. The bellcrank makes contact with a lever on the flag unit at zero degrees over center. As the bellcrank continues to rotate over center the flag indicator rises. The flag is completely up at 3 degrees over center. A dwell is designed into the flag unit to allow the bellcrank to continue past 3 degrees in the event of a limit switch failure or de-clutch.

The pistons used in the backup system employ the same combination of belleville washer springs as the turnbuckles to develop a compressive latching preload. For economy of space, none of the connections in the four bar/ toggle linkage use bearings. Simple lugs and pins coated with a dry lubricant are used quite successfully.

Base components are illustrated in figure 2. The REM base is a one-piece structure machined from 7075-T73 aluminum alloy. Forward spacecraft adapter pins enter the forward REM base receiver plates and stop when contact is made between the spacecraft adapter and the REM base front rail.

The rear adapter pins enter their respective receiver plates but stop, leaving a gap between the spacecraft adapter back rail and the REM base back rail. The square receiver plates allow travel of the square pins in the X direction. The sliding clearance in the square receiver plates and the back rail gap allow thermal expansion and contraction of the spacecraft relative to the REM base in the X-Y plane. The spacecraft is therefore attached to the REM base in a "semi-kinematic" manner. Spacecraft inertial load is transferred through the steel spacecraft adapter pins into steel receiver plates which are bolted and pinned to the REM base structure. Directly below each of the four receiver plates, the REM base is bolted to the Spartan bridge structure. Proximity of the receiver plates to the REM/SFSS interface minimizes the load path. Spacecraft X- and Z-direction inertial load is reacted by the round-hole receiver plates. Square hole receiver plates react Z direction load. +Y direction loads are reacted by the forward base rail. -Y direction loads are reacted by the employed latching mechanism. The pins and receiver plate holes are coated with a dry-film lubricant to ease latch operation and relative growth.

Ready for latch limit switches are mounted on the REM base at three widely separated locations. These switches activate three indicators on the shuttle aft flight deck and define the plane for the RMS operator to align the spacecraft pins with the REM base receiver plates. "Y" guides are used as a rough alignment for the RMS arm. An important feature of this system is that the RMS is only required to move the spacecraft down into the Y guides until the three "ready for latch" indicators are on. After this, the REM latching mechanism takes over. No complicated maneuvers are required of the RMS.

Improvements over previous REM design

The new REM is designed for higher load capacity and increased reliability to accommodate the Spartan 200 series spacecraft. The most obvious difference between the current GSFC REM and the previous MSFC design is the existence of a backup latching system and a REM bolt removal system. After the January 1986 Challenger flight the Johnson Space Center (JSC) "two fault tolerant" safety requirement was reevaluated for the new REM design. Any system failure that could cause a safety problem had to have two backup systems. Current failure contingencies are as follows. Following a primary system failure the backup system would be employed. If the backup system failed to function then the REM could be unbolted from the Spartan bridge by the bolt removal system. The most important aspect of the backup latch system is that it is entirely independent of the primary system. There is no shared hardware between the two.

The earlier design gearbox was a rectangular shape with a mounting flange about its perimeter. The box was bolted to the base with an insulating gasket in between. This insulating gasket was used to prevent heat loss from the gearbox to the base. One problem with this was the gearbox/base relative thermal growth. It was discovered after the Spartan 101 flight that the gearbox bolts had bent. Therefore, the new design gearbox is kinematically mounted. There are two principal benefits obtained by doing this. First, the gearbox is free to expand and contract relative

to the base under varying thermal conditions. Second, this type of gearbox mounting allows a large degree of load sharing between the right and left sides of the latching mechanism when unequal flight loads are imposed. The minimal structural restraint on the gearbox allows it to flex along with the splined shaft thus transferring load from the highly loaded side of the mechanism. Because the REM base is a large heat sink it is desirable to thermally isolate the gearbox. Unfortunately, it was considered too difficult for thermal insulation to be included in the kinematic load path. Consequently, more heaters are used on the new gearbox to keep the worm gear lubrication effective.

Another change from the previous design was the placement of the heaters. Rather than placing the heaters on the gears, they were placed on the gearbox housing. Heating the gears is clearly the most direct way of keeping the lubricant warm. But warm gears and a cold gearbox housing could cause the gears to expand more and bind up. Also, the new gearbox was being designed to put out higher torque. A double envelopment worm gear was used to increase strength. Now four teeth shared the load rather than just one, as on a straight worm. These new gears require a tight tolerance on center distance. Because of this it was decided that heating the gears would probably cause them to bind. Heating the gearbox housing would, at worst, cause an increase in gear clearance.

Continuing the effort to reevaluate safety requirements, the redesigned REM incorporated features that eliminated some credible single-point failures. A single-point failure is a failure that has no backup contingency. It is rarely practical to build a completely redundant mechanical/structural system. The following describe the failure contingencies that were designed into the new REM for increased safety and reliability.

A single-point failure identified in the old latch mechanism was that it did not rotate to an over-center position. It was relying only on the worm resistance to back driving and motor brakes to stay latched. A failure of the worm and the motor brake or any of the gears in between could cause the mechanism to unlatch. To tolerate any of these failures the new system bellcrank rotates to 3 degrees over center. In this position, flight acceleration loads can only push the bellcrank further over center. The entire gear train can fail at once and the bellcrank would be stopped at 5 degrees over center by a hard stop with minimal loss of latching preload. Without this backup feature, any of the above failures would be unacceptable.

Another type of failure scenario is as follows. Should the worm gear drive seize up part way through the required rotation, or if an electrical failure occurs, the latch mechanism could neither be fully latched or unlatched. The very first MSFC REM gears used a stainless-steel worm and a bronze gear. The use of a softer material on one of the gears greatly reduces the possibility of seizing or galling. Galling is basically a type of friction welding that occurs most notoriously between stainless-steel parts. Anticipated higher flight loads required stronger gear teeth in the MSFC design. The solution was to replace the bronze gear with a stainless

gear and hope that galling would not be a problem. Spartan 101 flew with this REM design and showed evidence of galling. During thermal vacuum testing of the same REM design for a second Spartan, the gearbox seized up. This was attributed to galling of the stainless gears after repeated use. A new stainless gear was installed and this Spartan flew on the STS. The current REM primary mechanism utilizes the original concept of dissimilar materials on each gear. Because the same problem of higher loading on the gear teeth still exists, the new design also uses larger gears and a double envelopment worm which distributes the load over four teeth rather than just one.

The possibility of the gear system getting stuck half way, when latched, was still considered important enough to design a backup contingency. Should this happen, the de-clutch mechanism breaks the mechanical load path from gearbox to bellcrank. Once the bellcrank is free from the failed gearbox it can coast with the backup latch mechanism and will not hinder spacecraft deployment.

Another concern was verification of a latched payload. The principal indicators for a properly latched Spartan spacecraft are on the aft flight deck. An independent mechanical indicator was developed for the primary latch system to serve as a second indication of a latched payload or possibly as a backup indicator, should there be an electrical problem. It is a matter of operational policy, as to whether to rely only on this backup indicator alone. But, it is clear that the mechanical indicator is at least as reliable as the electrical system.

Gearbox lubrication

The successful operation of a worm gear system in space presents some challenging engineering problems. Worm gearing offers large gear reduction with an uncomplicated apparatus and the benefit of little or no back driving. One significant drawback is the friction developed between wiping gear teeth surfaces. This makes the consideration of lubrication very important. The problem of lubrication becomes more critical for high load applications. Also, cold temperatures can limit the ability of the lubrication to flow between gear teeth. Low-rpm applications do not have the benefit of a hydrodynamic boundary layer in the lubricant. Finally, the space environment does not allow a practical design in which the gear lubricant is continually replenished. Lubrication must be kept at a minimum because of outgassing, which can contaminate flight instruments. All of these worst-case scenarios combine in the REM gearbox. The REM application involves high torque, low rpm, low temperatures and, of course, a vacuum.

It was decided early on that dissimilar metals of steel and bronze were to be used on the worm and gear. But, considering the extreme operating conditions, an extensive series of tests was performed to evaluate the most effective lubricant system. Several bronze surface treatments combined with different greases were tried. Testing was performed using a Falex LFW-1 ring and block machine. For these tests the machine was used to hold a bronze specimen against a spinning steel ring at a load and speed appropriate for the application. The tangential friction

force developed on the bronze block was sensed by a load cell. Automatic shutoff occurred when this friction force reached a specified level. Number of cycles to shutoff was the criteria for test comparison. Bronze surface treatments included nickel/Teflon, titanium-nitride/lead, Hi-T Lube, shot peening to produce reservoirs for grease on the gear tooth surfaces, and finally, no treatment. Six types of aerospace-quality lubricants were tested. These were Braycote 601, 802-EP, and 815-Z and Tribolube 14-C, 17-C, and 17-CSB. In addition to LFW-1 friction testing the lubricants were evaluated for outgassing properties.

Initial LFW-1 tests were done with bronze surface treatments of Hi-T Lube, nickel/Teflon, titanium-nitride/lead and no treatment combined with either Braycote 601 or Braycote 802 EP greases. The Hi-T Lube and the TiNitride/lead treatments with either grease showed improvement over the use of grease only. The nickel/Teflon with either grease performed worse than with grease only. Later, a diluted mixture of 50% Braycote 802-EP and 50% Braycote 815-Z oil was tested on bronze with no surface treatment and performed significantly better than all previous tests. The Tribolube greases were also tested but did not perform as well as the Braycote mixture. The Braycote mixture and Tribolube 17-CSB had acceptable outgassing levels. The other two Tribolube greases did not pass. Finally, with the other bronze surface treatments eliminated, four types of shot-peened bronze were tested with the Braycote grease mixture and the Tribolube 17-CSB grease. The performance of the Tribolube increased significantly. The Braycote mixture performance was about the same as with no shot peening but was still better than the Tribolube. To summarize, the final solution was not to surface treat the bronze gear at all and to use a non-replenishable coating of the Braycote 802-EP/815-Z mixture.

ANALYSIS & TESTING

The REM system has undergone a comprehensive program of analysis and testing in order to qualify it to carry Spartan spacecraft on the Space Shuttle. A summary of the qualified capability is given at the end of this section.

Structural:

The finite element method and classical closed-form analysis were both employed in the structural analysis of the REM system. A NASTRAN Finite Element Model⁴ (FEM) was developed for prediction of load paths and areas of high stress. The FEM was also required for inclusion in the reduced payload mathematical model used for flight loads analysis. Closed-form stress analysis methods were used to predict the capacity of the mechanism and calculate margins of safety.

The FEM was validated by random vibration and static compliance testing². A low-level vibration test confirmed agreement between analytical and actual normal-mode frequencies. A series of compliance tests was performed in which the REM latching mechanisms were gradually loaded up to flight levels while system component loads and deflections were measured. This allowed direct determination of the load sharing behavior in the

preloaded mechanism and the actual system stiffness. The compliance test data was used to refine and verify the REM FEM. The compliance test data along with the validated REM FEM allowed accurate prediction of the loads in the system and the point at which the latch system would "gap" and transfer all load into the mechanism.

The REM FEM was then coupled to a simplified FEM representation of the heaviest Spartan spacecraft. Static analysis was performed using the Spartan design limit loads. The results were used to specify and carry out a qualification-level static load pull test⁶ of the REM system. The REM system also has undergone qualification-level random vibration testing.

Thermal:

A finite difference thermal model⁵ of the REM was developed and used to predict on-orbit temperature extremes. The results of the thermal analysis were used to perform the initial resistive gearbox heater sizing and to develop a thermal-vacuum environmental test plan.

Thermal-vacuum environmental tests were performed using both the REM Engineering Test Unit (ETU) and the flight REM. The REM and the lower half of the Spartan spacecraft were placed in a thermal-vacuum chamber using a fixture that allowed latch/unlatch operations with gravity negated.

One of the initial design objectives for the REM was operation at the cold temperature extreme without heaters. Testing revealed that this was not feasible. Heaters were required to meet the goal of operation at a steady state REM base structure temperature of -75 °C. Another test objective was to determine the loss of latch preload at the hot extreme temperature. Further thermal-vacuum testing after the addition of heaters to the gearbox qualified the REM system for operation on any Spartan/STS mission without constraints on orbiter attitude. The thermal-vacuum testing also provided data used to refine and validate the thermal model.

Mechanism Preload Determination:

Determination of preload is based on minimizing possible gapping while maintaining acceptable motor latching torque margin. The initial preload requirement is calculated using the relation:

$$\text{PRELOAD REQUIRED} = (0.5)(\text{S/C weight})(\ddot{Y})(\text{T.F.})$$

\ddot{Y} = expected Y direction acceleration
T.F. = thermal factor for hot case

The system has been tested beyond gapping and is certified to fly as such.

Qualified GSFC REM Capabilities:

Static load capacity: For a 2850-lb spacecraft (Spartan 201), the REM has been qualified for the following limit load accelerations.

X: ± 5.3 g, Y: ± 4.2 g, Z: ± 7.8 g

Thermal operating limits: It was determined that the REM can operate in any thermal environment predicted for the shuttle orbiter. Thermal-vacuum testing established the operating limits of +75 °C to -75 °C, steady state.

Useful Missions: Fracture analysis shows the REM system able to safely withstand 20 Spartan 201 STS missions under predicted coupled loads analysis limit loads (static limit loads divided by 1.5).

Summary and Conclusions

GSFC took a successful shuttle payload restraint system and redesigned it to carry heavier loads. The new primary latch mechanism was designed with additional safety features. An independent backup latching mechanism was added for increased reliability.

Most of the lessons learned in this redesign effort concern the primary latch system, particularly the gearbox. The mechanism was made stronger for increased loads. Kinematic mounts allow the gearbox to tolerate large temperature gradients with the base. These mounts also allow more load sharing between the left- and right-side linkages to reduce the net bending load on the gearbox. The over-center bellcrank feature makes the system tolerant of gear failure. The use of dissimilar metals in the gears reduces the possibility of galling. The double envelopment worm distributes load over several teeth. The de-clutch mechanism offers a way out if the gears should still bind up.

An extensive investigation was made to determine the best lubrication for the primary mechanism gears. Several types of bronze gear surface treatments were tried with different lubricants. The best lubricating system is a diluted form of Braycote 802 EP with no bronze gear surface treatment.

Finally, the new REM system was qualified for flight by a static load test, vibration testing, and a thermal-vacuum test. Results show that the system is ready for use with Spartan 200 series spacecraft.

REFERENCES

1. Calvert, John: "The evolution of a Release-Engage Mechanism for use on the orbiter NASA 17th Aerospace Mechanisms Symposium, Jet Propulsion Laboratory, Pasadena, CA, May 5-6, 1983.
2. Galloway, Greg: "Spartan REM Primary System Compliance Test," SPTN-TEV-005, NASA/GSFC, Greenbelt, MD, August 23, 1991.
3. Dankewitz, Cathy: "Spartan 200 series REM Finite Element Structural Analysis," SPTN-REM01-003, NASA/GSFC, Greenbelt, MD, May 1990.
4. Francis-Wheeler, Debra: "Spartan REM FEM Stress Analysis Report," SPTN-TEV-004, NASA/GSFC, date TBD.
5. Neuberger, Dave: "REM Thermal Vacuum Test," SPTN-TEV-006, Swales & Assoc. for NASA/GSFC, date TBD.
6. Francis-Wheeler, Debra: "Spartan Release/Engage Mechanism (REM) Structural Qualification Test II (REV. A)," SPTN-TEV-007, NASA/GSFC, date TBD.

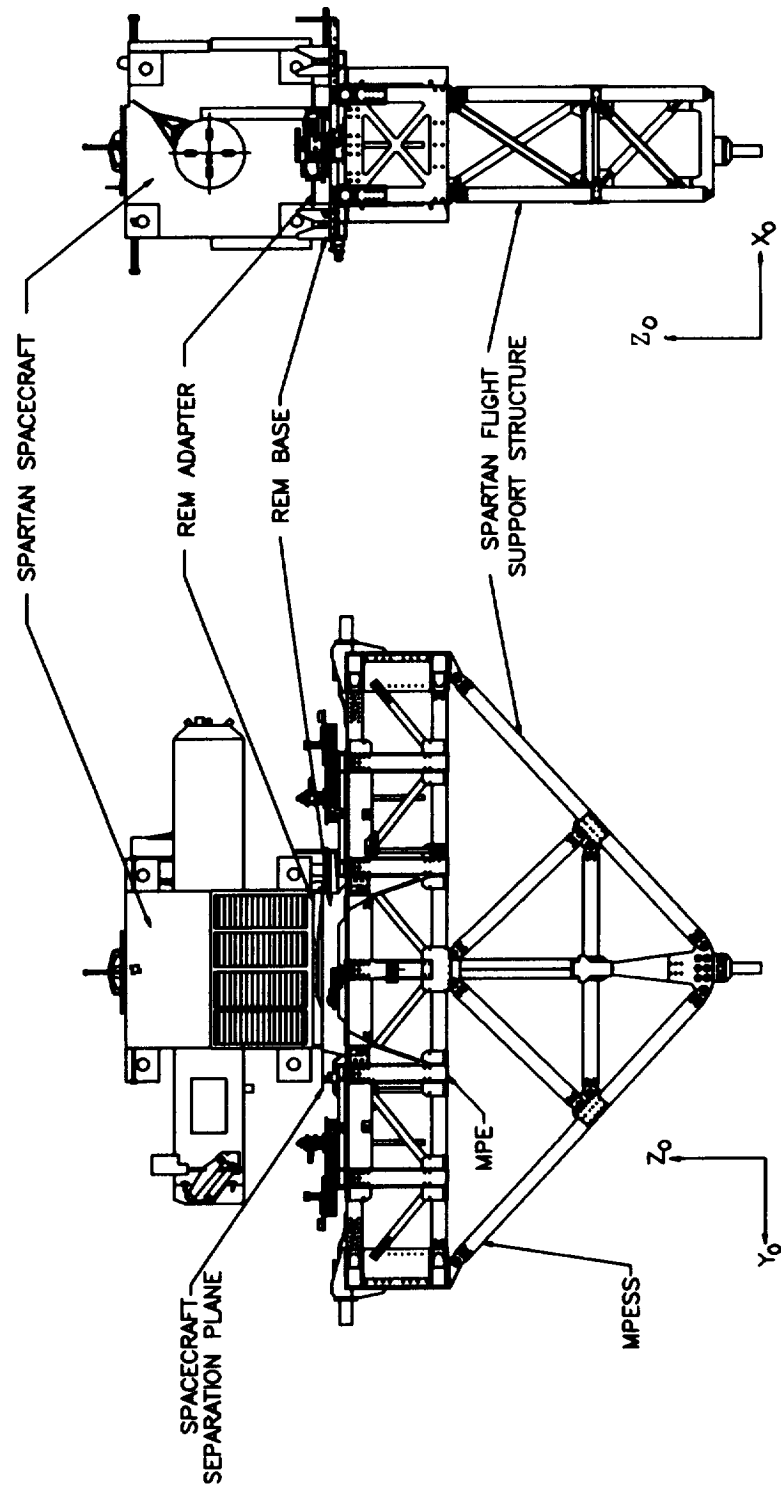


Figure 1. Spartan Spacecraft System All-Up Configuration.

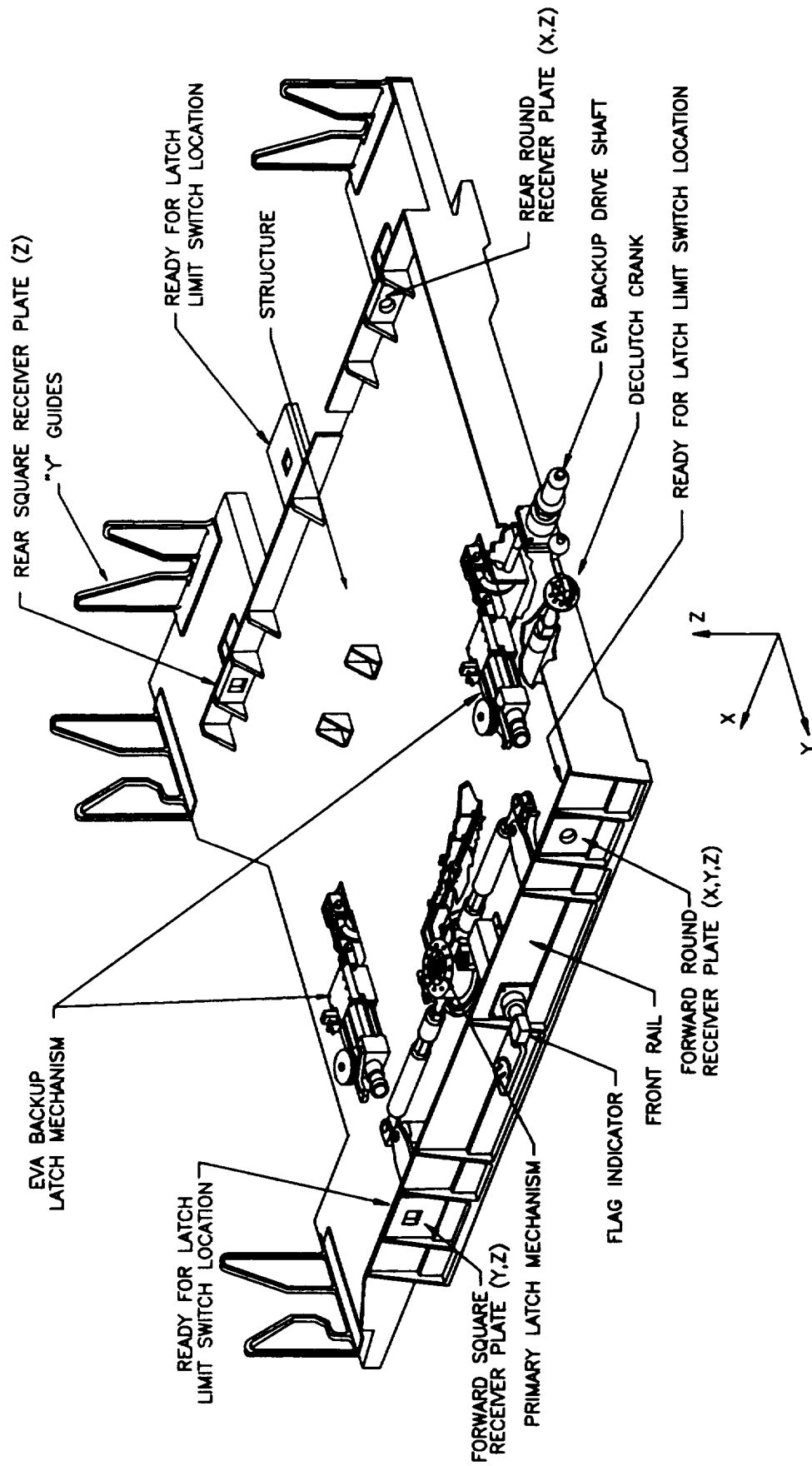


Figure 2. Release and Engage Mechanism.

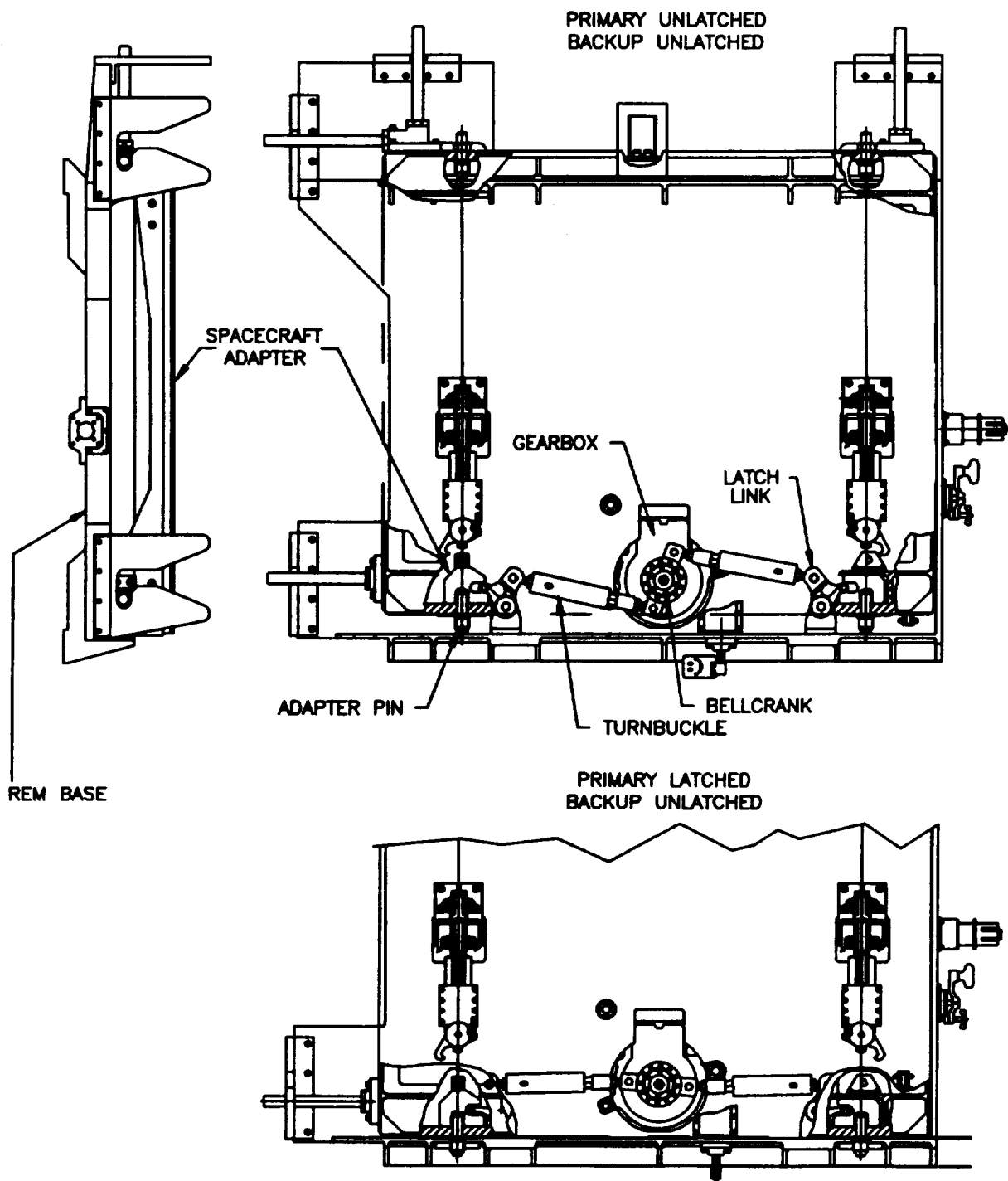


Figure 3. REM Primary Latch Mechanism Operation.

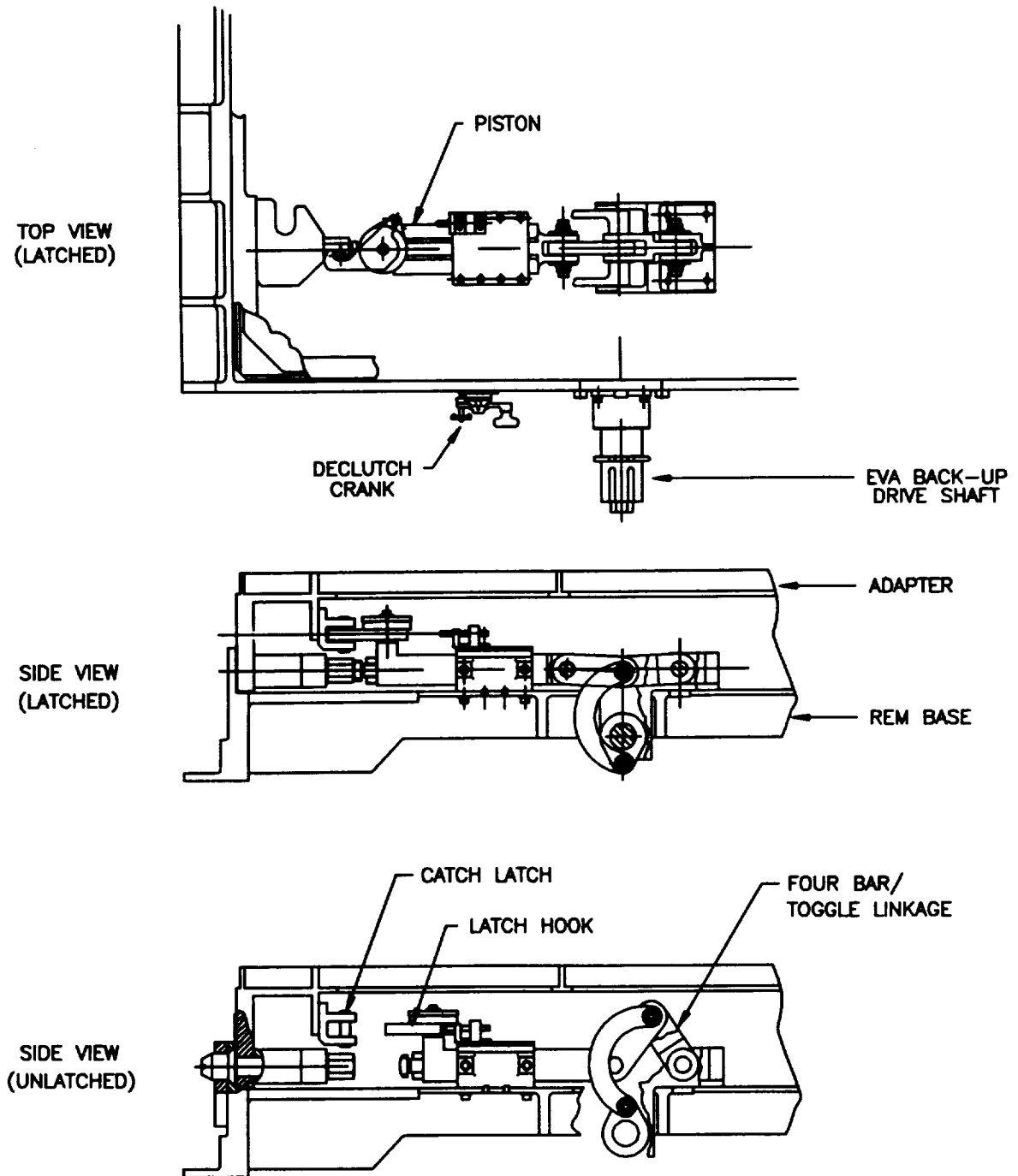


Figure 4. Backup Latch Mechanism Operation.

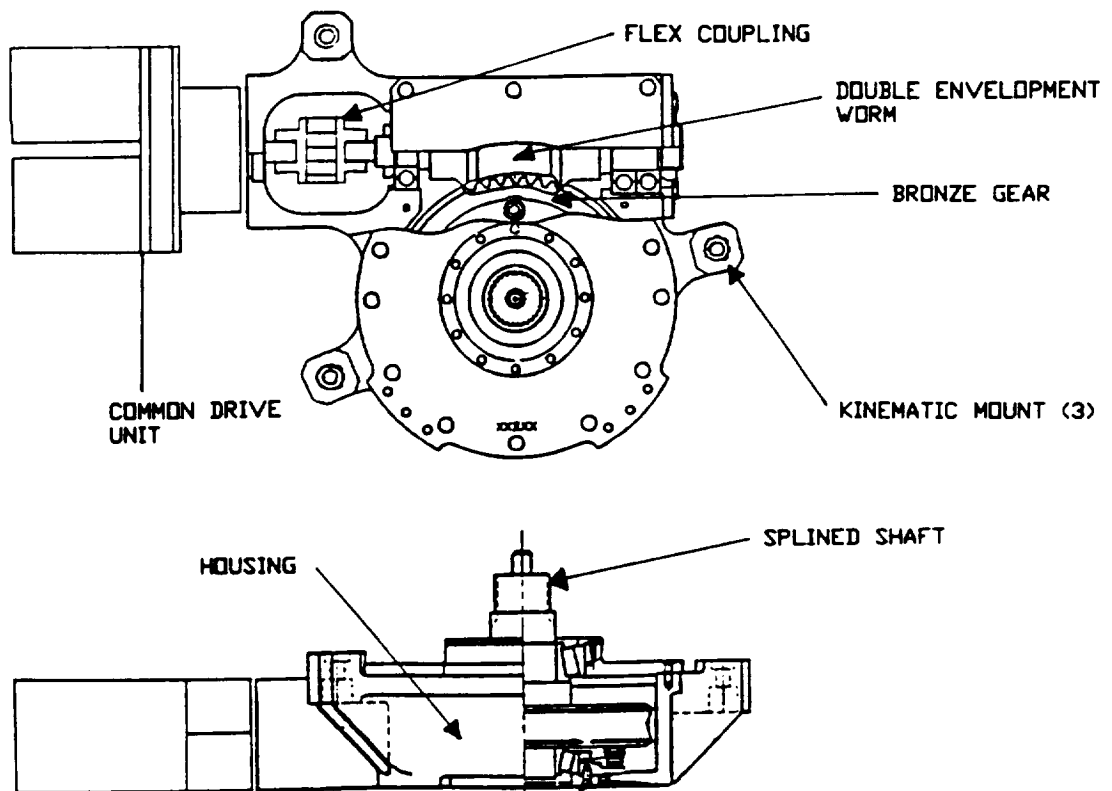


Figure 5. Primary System Gearbox.

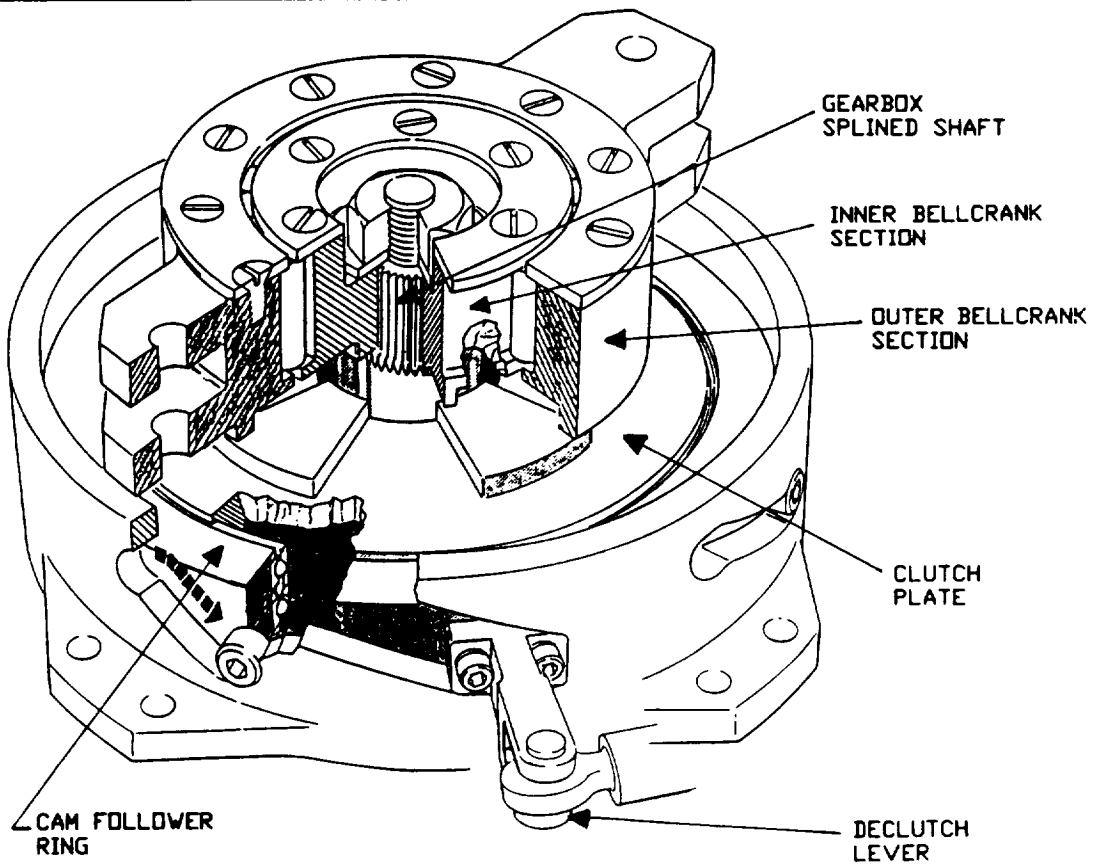


Figure 6. De-clutch Mechanism.

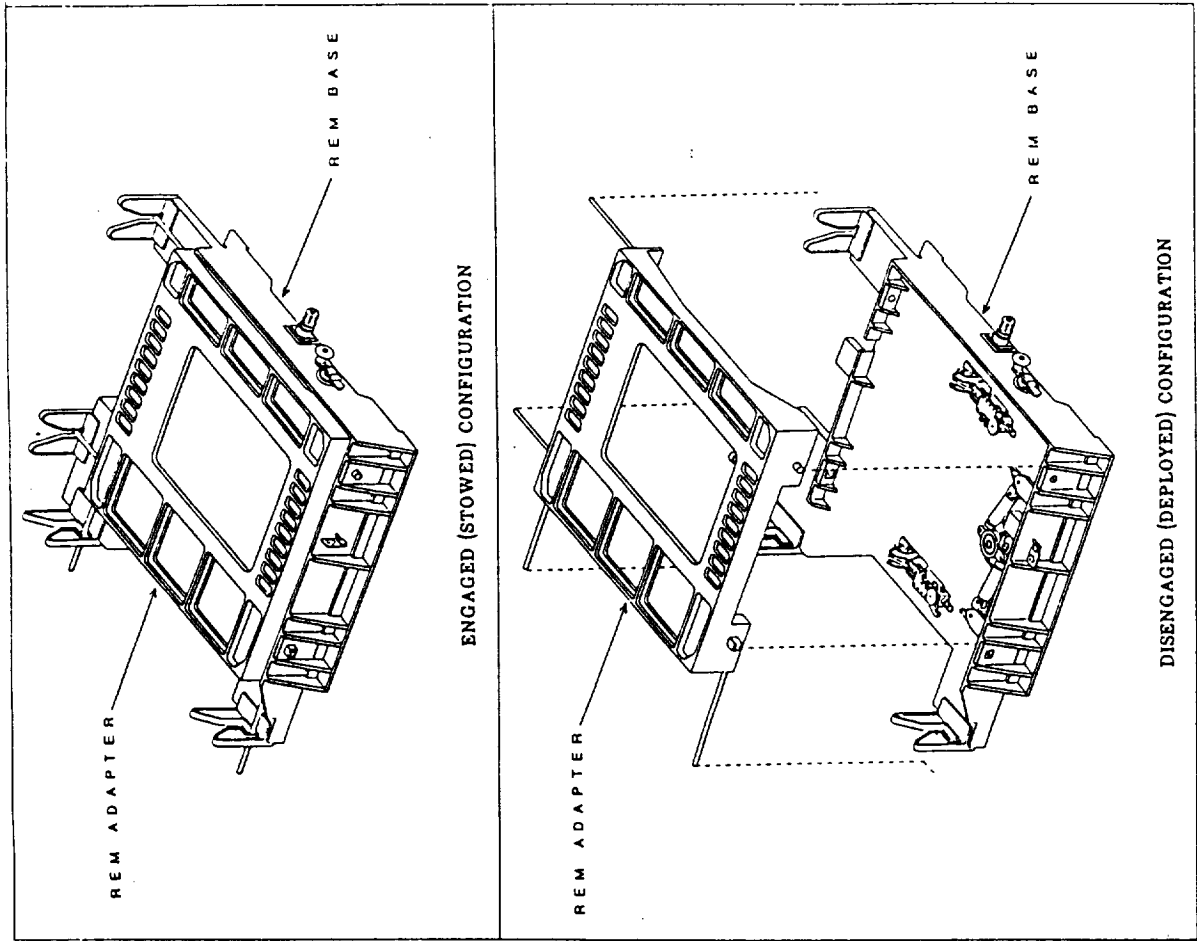


Figure 9. Spartan Release Engage Mechanism (REM).

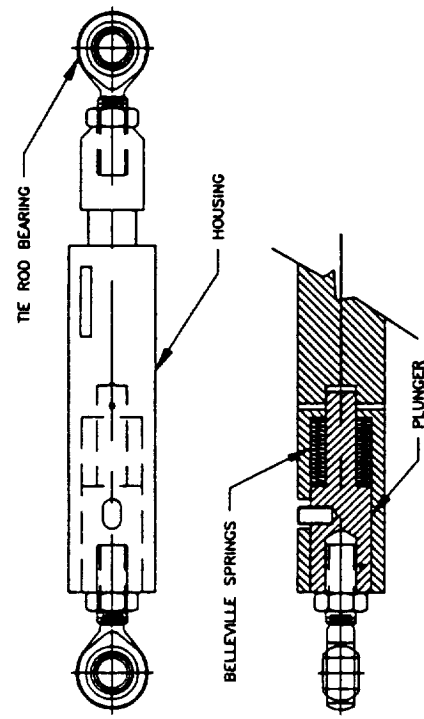


Figure 7. Turnbuckle.

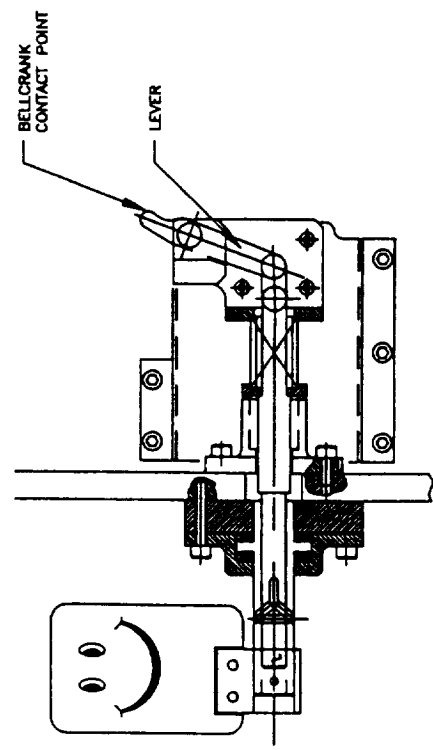


Figure 8. Flag Latch Indicator.

Manipulator Design and Development for the *Ranger* Satellite Servicing Vehicle

Russell D. Howard*
David L. Akin**

Space Systems Laboratory
Department of Aerospace Engineering
University of Maryland
College Park, MD 20742

Abstract

The *Ranger* program is a planned series of low-cost telerobotics flight experiments, based on the use of Pegasus launch vehicles. As the first step towards this goal, the Space Systems Laboratory has been developing a neutral buoyancy version of *Ranger* for use in design verification and operations testing. This paper relates the design approach and results of the *Ranger* manipulator development program.

Ranger is designed to incorporate four appendages: a pair of dexterous, seven degree-of-freedom manipulators for general manipulation; a six-DOF grapple arm for securing the vehicle to the local work site; and a five-DOF positioning manipulator for the stereo camera pair that provides feedback to the remote operator. Each of these manipulators incorporate unique approaches to satisfying design requirements. The 7-DOF dexterous arms allow anthropomorphic motions for master-slave teleoperation, as well as provide sufficient internal sensing for programmed autonomy. These arms also include a permanently installed actuator motor and six-axis wrist force-torque sensor for operating with a variety of interchangeable end effectors. The grapple manipulator uses a series of common actuators, incorporating both drive motor and active brakes for firmly fixing vehicle position to the work site. The camera manipulator is based on non-backdriveable gear configurations to provide stable camera views without active expenditure of energy. All of the *Ranger* manipulators incorporate servo-level controllers within the arm links, thus reducing the data bandwidth and number of wires required to be strung along the manipulator.

This paper will start with the numerical and operational requirements for *Ranger* manipulators, and will discuss the evolution of the differing design approaches based on similarities and differences in the requirements. Testing results for individual joints and manipulator assemblies will be presented, followed by initial results of operational testing on satellite servicing tasks with the integrated *Ranger* neutral buoyancy vehicle.

* Assistant Research Scientist

** Associate Professor and Laboratory Director

Background

In June of 1990, the Space Systems Laboratory began the design process for a new space telerobotic system. Like prior systems developed in the SSL, this would be an integrated vehicle designed for neutral buoyancy simulation of space operations. Design goals for this system included generic capability to perform a wide range of current and planned satellite servicing tasks, and the possibility of growth versions being built for actual space flight on low-cost expendable boosters. The design concept was named Ranger.

The design of the Ranger telerobot is based on 15 years of laboratory experience on space operations, 8 of them specifically focused on telerobotic systems. The prior vehicle most applicable to Ranger was the Beam Assembly Teleoperator, or BAT. As shown in Figure 1, BAT incorporates a single, five degree-of-freedom (5 DOF) dexterous manipulator on a free-flying mobility base, which also mounts video systems, a non-articulated grappling arm, and a special-purpose pick-and-place manipulator designed specifically for structural assembly tasks. This vehicle was designed specifically to assemble the same structure used in the Experimental Assembly of Structures in EVA (EASE), an experiment developed by the SSL and flown on Space Shuttle *Atlantis* in late 1985 (Figure 2).

The primary incentive for the development of Ranger was a series of experiments performed in 1989, in which BAT was used for telerobotic servicing tests on the Hubble Space Telescope. Using the high-fidelity crew training article and the NASA Marshall Space Flight Center Neutral Buoyancy Simulator, these tests examined

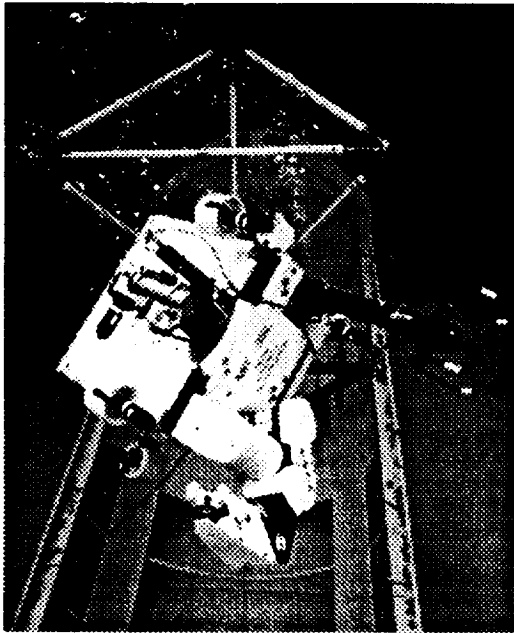


Figure 1.
Beam Assembly Teleoperator

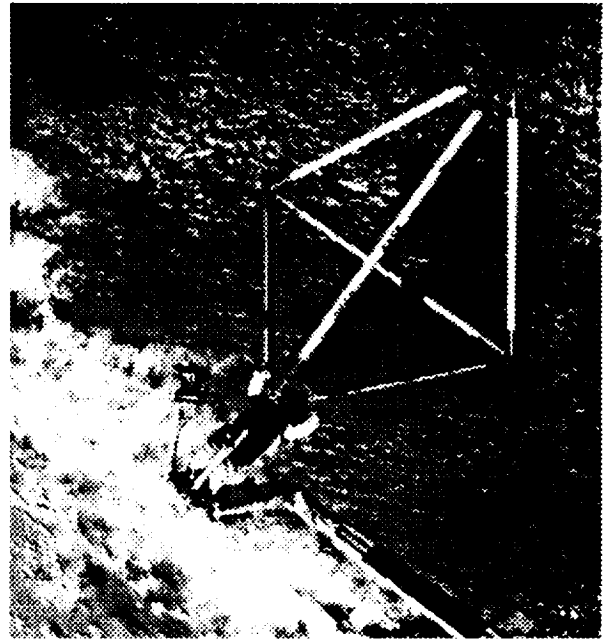


Figure 2.
EASE Structure from STS 61-B

both pure telerobotic and mixed EVA/telerobotic scenarios, and focused primarily on battery change-out operations (Figure 3). While some significant roles were found for BAT in assisting an EVA subject, its limitations arising from the limited design goals of structural assembly led to significant restrictions on its capability for independent servicing operations. Design guidelines for Ranger based on this experience include:

- bilateral dexterous manipulators – Satellites designed for EVA systems are generally designed for one-handed operation, to facilitate astronaut operations. It was felt that this would make the single dexterous arm generally capable of performing the same tasks. However, it was found that there were many supporting activities (tool hand-offs, exchanging orbital replacement units, etc.) that implicitly require the use of two (or more) hands and arms.

- higher degrees of freedom – The design of the BAT dexterous manipulator did not include a wrist pitch joint, as the EASE structural assembly task did not require one. This was severely limiting in servicing operations; for example, in many positions it was not possible to accurately position a socket tool over a bolt head due to reaching an arm singularity (Figure 4). At least six degrees of freedom are required to allow generic servicing activities. Due to the space restrictions in HST, it was decided to go to a redundant arm configuration with seven DOF to allow adjusting the arm pose (particularly the elbow orientation) within limited work volumes.

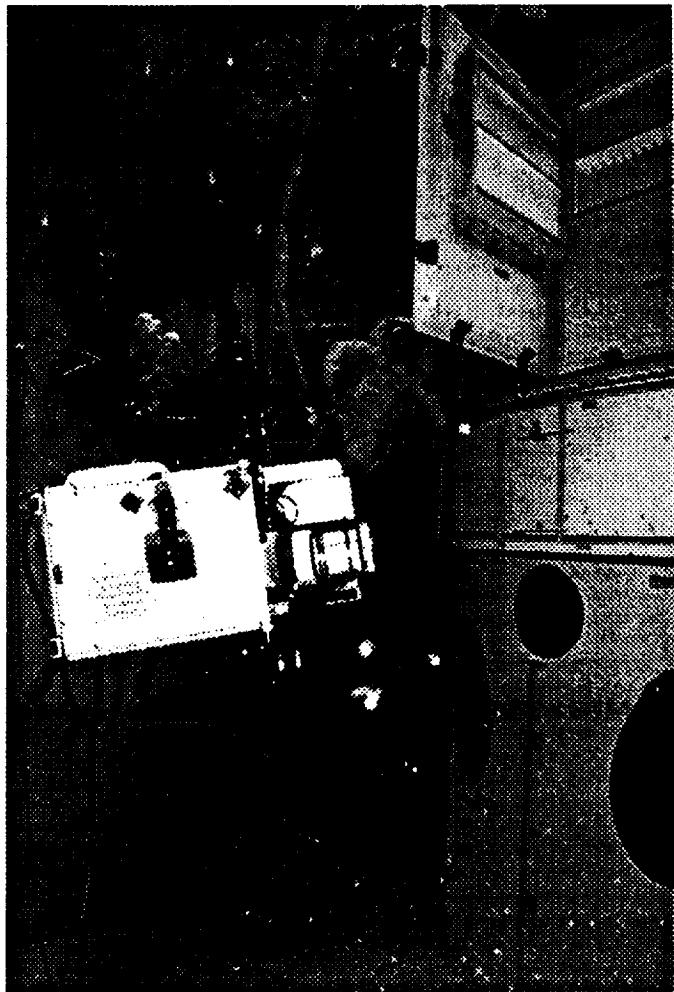


Figure 3.
BAT and EVA Subject at Start of
Battery Change-out Task

- localized manipulator mounting configuration – Many servicing designs incorporate required task operations in restricted work volumes. As shown in Figure 5, some HST tasks involved severely constricted operations at the back of a bay-type structure. BAT proved incapable of reaching many of these positions, due to the wide front end of the mobility unit and the mounting of manipulators across the width. By restricting the width of Ranger across the front and mounting the manipulators close together, the minimum work volume requirements could be dramatically reduced.
- dexterous rigid grappling manipulator – Complex manipulations require fixing the servicing vehicle with respect to the work site. BAT incorporates a fixed grappling arm, which is all that is required for structural servicing, since the tasks to be done are of limited types and locations. The fixed grappling position did not allow moving an HST work site into the optimum work envelope of the BAT dexterous manipulator. To make up for this, the BAT mobility base was mounted to the NASA Marshall remote manipulator sys-

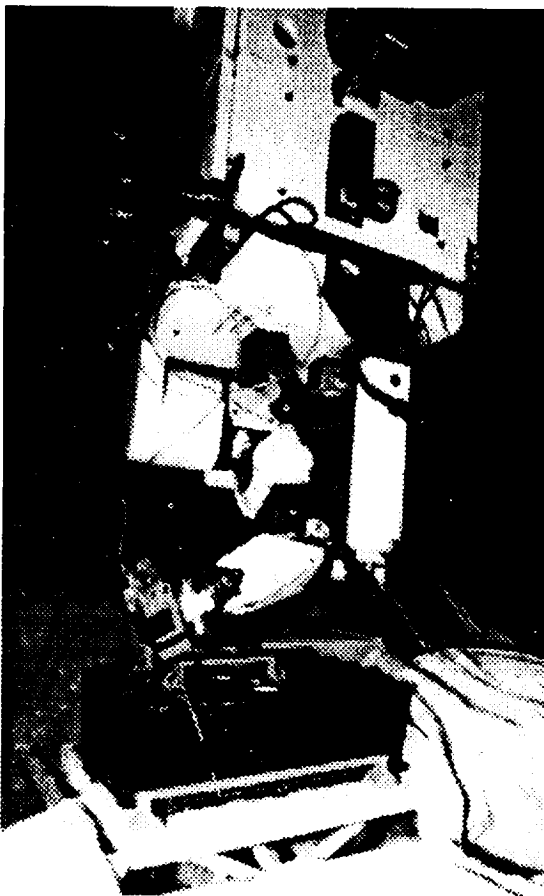


Figure 4.
Limited Tool Access due to
Manipulator Singularities

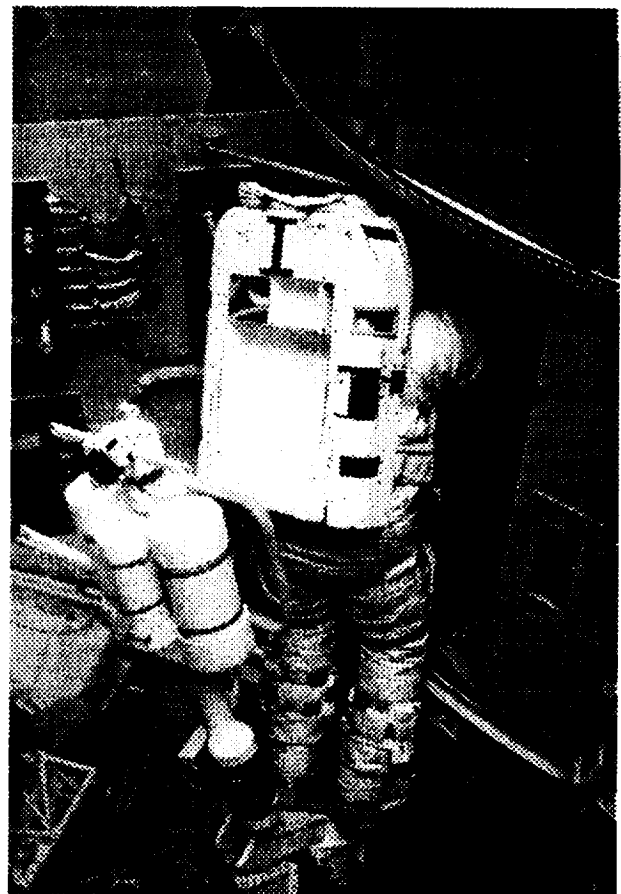


Figure 5.
Limited Access to Orbital Replacement
Units on Hubble Space Telescope

tem in the neutral buoyancy tests, but this system (both in neutral buoyancy and flight versions) is much too flexible to allow extended operations without local bracing to the work site. A dexterous grappling manipulator with at least 6 DOF will allow adjustment of the Ranger base to bring the dexterous arms into functional locations with respect to servicing tasks.

- **repositionable camera platform** – During many of the BAT operations, severe viewing limitations of the on-board video system limited the utility of BAT operations. The manipulation cameras, fixed with respect to base location and limited to pan and tilt control, frequently did not provide sufficient information to the operator. Since the camera system is designed to provide the required close view of the manipulation envelope and dexterous end effector, it does not provide information on overall manipulator pose, which is occasionally required in many tasks. Mounting the cameras on their own manipulator would allow the use of a limited camera set for a wide variety of required views.
- **interchangeable end effectors** – The wide range of satellite servicing tasks requires the use of a number of specialized tools. BAT tests showed that many of these tool operations are restricted by the strength and rigidity of the tool grip in the end effector, and result in much lower applied torques to the work site. Difficulties in the use of power tools also lead to the desire to incorporate a generic tool drive mechanism permanently in the end of the dexterous arm, allowing each interchangeable end effector to use the drive actuation for its own design purpose.
- **free-flying motion base** – All Space Systems Laboratory telerobotic systems have incorporated free-flight capability. Much of the design effort for neutral buoyancy free-flight is involved with ensuring that the center of mass of the vehicle is coincident with its center of buoyancy, such that it will have no preferred orientation and will behave as much as possible like a vehicle in microgravity. Including such a capability allows a much wider range of potential activities, and does not degrade the utility of the vehicle in alternative positioning modes, such as being attached to the Remote Manipulator System. For this reason, free-flight capability was included as a design requirement.

In addition to the design guidelines based on prior telerobotic experience, it was decided to attempt to press towards a flight-certifiable design. Although a number of proposals have been made to fly telerobotic experiments on the space shuttle, it was felt that a truly low-cost telerobotic experiment would mandate a low-cost and non-man-rated launch vehicle. For this reason, a design goal was added to make Ranger fit within the payload mass and volume restrictions of the Pegasus launch vehicle.

Configuration Development

The design approach taken was to design a space-flight version of Ranger based around the Pegasus payload limitations, then modify that design to the minimum extent possible to arrive at a neutral buoyancy vehicle. This was felt to provide the most capable neutral buoyancy vehicle possible, while providing operational experience on many flight systems. In addition, the goal of the planned eventual flight experiment would be to validate the neutral buoyancy simulation experience of Ranger, and maximizing commonality between systems is important for this task.

The initial design concept for Ranger is shown in stowed configuration in Figure 6. The design requirements described above lead to the incorporation of four manipulators: two dexterous manipulators for general servicing activity, a single grapple arm with sufficient rigidity and joint stiffness to resist resultant forces and torques from servicing tasks, and a camera manipulator capable of placing a stereo camera package within a wide envelope of positions and pointing vectors. All four of these

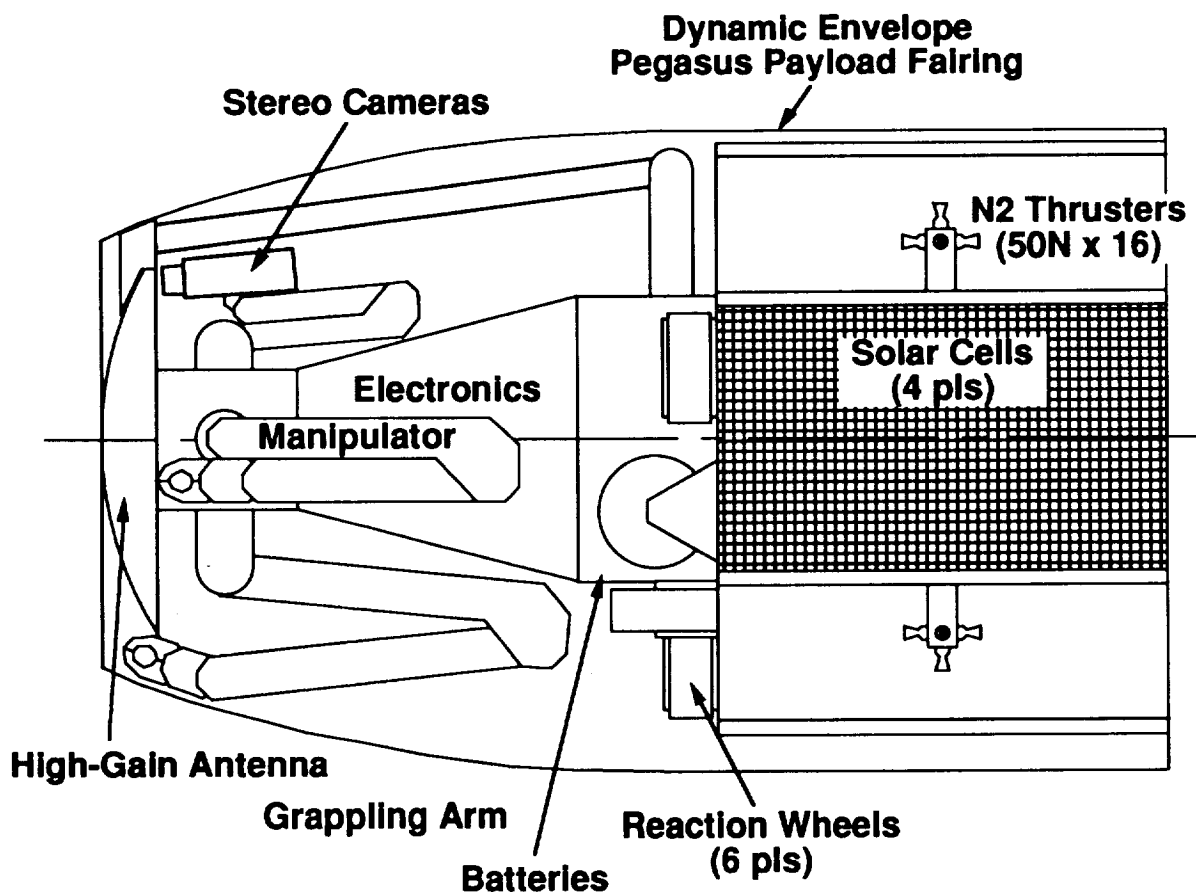


Figure 6.
Ranger Layout in Stowed Configuration

arms are mounted on a small manipulator module in the forward end of the vehicle, to meet the minimum volume requirements to allow manipulation in restricted areas. The opposite end of the vehicle is the propulsion module, and is sized around the requirements for a cold-gas maneuvering system, which is restricted primarily by allowable payload diameter at the base of the shroud. In between these two sections is a pressurized vehicle structure which tapers between the two sizes, and is used to house the control electronics for the vehicle.

An artist's concept of the Ranger vehicle in space is shown in Figure 7. The lower grapple arm allows attachment of the vehicle to the local work site, here the stabilized third stage of Pegasus shown in the foreground of the sketch. The dexterous arm pair would be used to perform basic tasks on a task board mounted on the Pegasus third stage, and the propulsion module permits a free-flight approach to grapple. The camera manipulator positions the camera system at the optimum locations for each specific task phase of the mission.

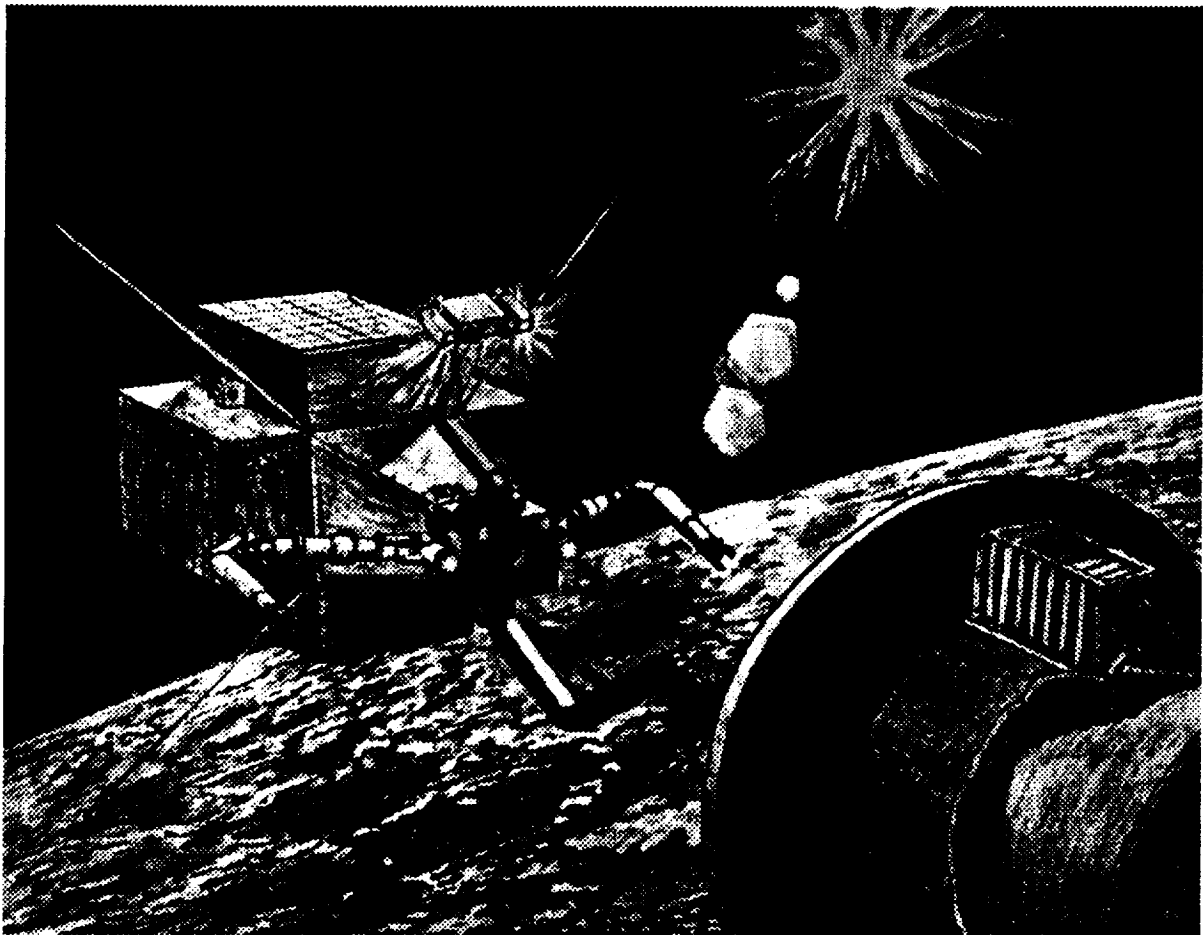


Figure 7.
Artist's Concept of Ranger Vehicle in Space

With the completion of the preliminary design of the flight vehicle, a neutral buoyancy version of Ranger was designed in detail. The largest modification was to completely redesign the propulsion module to accept eight ducted propellor units for underwater maneuvering, along with larger battery boxes to accommodate the electrical power needs of these units. All systems forward of the propulsion module are essentially the same as those planned for flight. In neutral buoyancy, all electronics, actuators, sensors, and other sophisticated components are sealed in air-filled housings to protect them from the water environment. It is planned to incorporate this same feature in the flight unit with nitrogen-filled housing, both to ease the cooling problem and eliminate the need to go to vacuum-rated components and lubricants.

Manipulator Design

A goal of this paper is to focus in some detail on the design of the manipulators of Ranger, as representative of some of the most interesting mechanism design challenges of this project. Each of the manipulator types will be covered in the following sections. However some aspects of the designs are common across all of the manipulator designs.

Past experience indicated the difficulty of wiring a manipulator arm for remote control electronics. This is especially aggravated by having to carry multiple actuator and sensor wires across actuator axes, resulting in externally hung wire loops, bulky cable runs, etc. For this reason, a goal throughout was to collocate as much of the electronics as possible within the arm sections, and near the actuators under control.

A New Micros 68HC11 card was chosen for the inner control computer, and the actual control loops are being closed by LM629 microcontrollers running PID loops on the motors. To facilitate this, all motors were constrained to be DC servo and torque motors, rather than the DC brushless more typical of past space flight. This is in accordance with past SSL design and operational experience, and these motors have worked well in prior applications.

All 68HC11 computers within a single manipulator are on a single token-passing local area network developed within the SSL. The microcomputer-microcontroller communications system (MiMiCS) is based on a simple hardware system regulating the passing of a token denoting permission to write on the network, and a software system recognizing individual controller commands coming down a shared communications line. The top-level controller (initially an Intel 80386, with development underway on a second-generation system based on a hierarchy of 80960 processors) sends joint commands to the 68HC11 controllers, and can request feedback information back on arm status, as well as engineering data (joint temperatures, voltages, etc.) Each 68HC11 is responsible for up to three actuators, and there are separate MiMiCS lines for each manipulator, as well as for the wrist force-torque

sensors in both the dexterous and the grappling manipulators. The control computer communicates to the surface using the Pilot-Vehicle Communications Software (PiVeCS) message-based protocol developed by the SSL for its earlier telerobotic vehicles.

Dexterous Manipulators

The basic configuration of the dexterous manipulator design is shown in Figure 8. This design is based on sequential revolute joints, with seven total degrees of freedom and an eighth actuator used to drive the interchangeable end effector. These manipulators are designed to be generically capable of a variety of satellite servicing tasks. As a design guideline, all joints were designed to provide a 40-lb tip force at full extension. In order to keep the arm as simple and compact as possible, no joint brakes were incorporated into these manipulators.

These manipulators are based on pairs of azimuth and elevation drives at the shoulder and elbow, as well as three wrist axes (roll, pitch, and yaw) driven about a common actuation center. Redundancy issues are addressed in the control system by incorporating all redundancy into controlling the wrist actuation center position; the wrist degrees of freedom are nominally used to control end effector orientation. This split control scheme is implemented internally within the control system, and the operator control of the manipulator may be selected from among the classic modes, such as master-slave, resolved rate, etc.

As an example, a cut-away view of the shoulder azimuth actuator is shown in Figure 9. This joint incorporates an Inland Motors T2955 DC torque motor, with speed

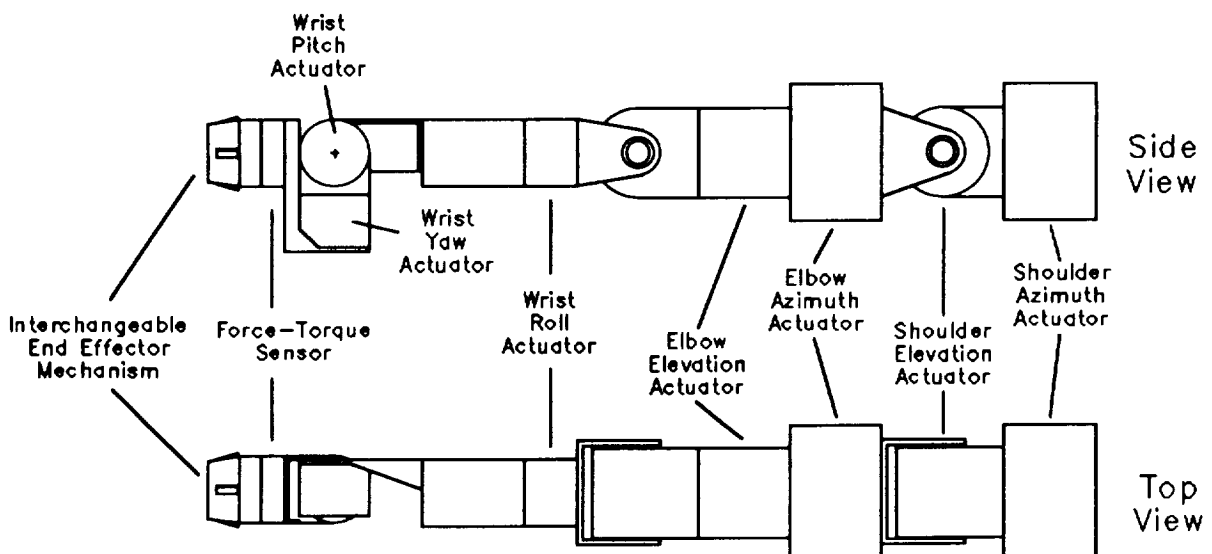


Figure 8
Dexterous Manipulator Configuration

reduction provided by an HDC 2M200 cup-type harmonic drive. The large size of this harmonic drive was set by the requirements for overall arm stiffness, and led to the use of a significantly larger unit than would otherwise be required. To save volume, the actuator was designed to incorporate the motor internally within the harmonic drive. To avoid the requirement for an inner torque loop, the joint position sensor (a Renco RM23 incremental optical encoder) was mounted to the motor side of the actuator, to prevent backlash and joint flexibility from degrading the closed-loop servo control.

The design parameters for each of the joints of the dexterous arm are summarized in Table 1. Primary design goals for the upper arm joints (shoulder and elbow) have been stiffness and torque requirements. Greater attention was paid in the wrist actuators to compact mechanical packaging and to keeping a minimum arm diameter to maintain commonality with EVA interfaces. For this reason, the wrist joints use pancake-type harmonic drives, since the reduced distance to the arm tip reduces the actuator stiffness requirements. The wrist pitch and yaw joints are the only two in the dexterous arm that use identical actuator designs. Due to the aggressive de-

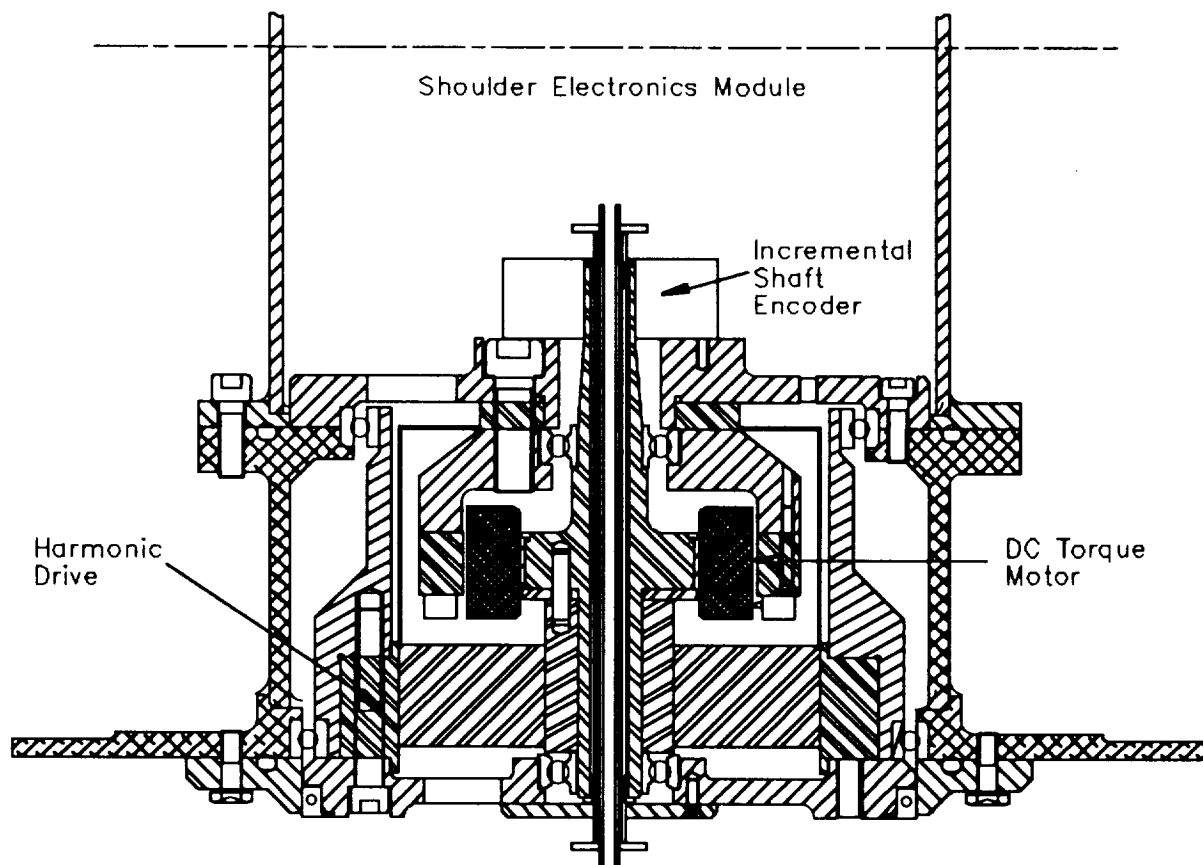


Figure 9.
Shoulder Azimuth Design Detail

sign goals for these arms, all other actuators were specifically designed for each application. There is some commonality in motor and harmonic drive types, allowing reduced stocks for spares.

In order to allow impedance control of the dexterous manipulators, it is necessary to have end-point force and torque sensing. This is accomplished by a standard configuration four-arm flexure mounted distal to the wrist actuators, with local analog amplification and analog-digital conversion, and with an independent high-speed serial line carrying the flexure strains back to the top-level control computer. There, the data may either be stored, relayed to the control station through the command data link for either visual display or real-time force reflection, and/or used locally for force and impedance control modes for arm constrained motion.

Operational experience with telerobotic satellite servicing revealed the need for extensive tool operation in completing the required tasks. It should be emphasized that the design goal for Ranger is to make it capable of performing EVA servicing tasks, rather than limiting it to tasks designed for limited robotic servicing. It had been found earlier that tool grips limited applicable torques. In addition, the dexterity required for changing power tool interfaces is difficult, as well as the fact that

Table 1
Dexterous Manipulator Actuator Characteristics

Dexterous Manipulator Joint	Motor (Inland Motors)	Speed Reduction (Harmonic Drive)	Maximum Torque (ft-lbs)	Maximum Velocity (deg/sec)	Actuator Stall Power (W)	Maximum Encoder Resolution (deg/pulse)
Shoulder Azimuth	T2955	HDC 2M200	144	48	77	.00176
Shoulder Elevation	T2955	HDC 2M200	144	48	77	.00176
Elbow Azimuth	T2215	HDC 1M160	76.5	48	41	.00220
Elbow Elevation	T2215	HDC 1M160	76.5	48	41	.00220
Wrist Roll	T1915	HDC 1M160	17	75	36	.00220
Wrist Pitch	T1915	HDR 20-160	17	75	36	.00220
Wrist Yaw	T1915	HDR 20-160	17	75	36	.00220

interfaces to a powered tool could not be made or broken in the underwater environment. For all these reasons, it was decided to design the dexterous arms around the use of interchangeable end effectors, driven by a motor which is permanently attached to the manipulator and operated through its control system. This eliminated the need for making or breaking electrical and fluid contacts underwater, and allowed for lower cost tool sets. The interchangeable end effector mechanism (IEEM) is based on wedge-shaped latches extending from a conical interface adapter. A soft-dock is accomplished by inserting the IEEM into a tool, carried on the front surface of the Ranger power module. Hard latching is accomplished by a small screw-drive mechanism, which both fully engages the drive spline in the end effector and releases the end effector latches from the stowage rack. Separation from the end effector takes place in the opposite order, with the end effector restraint latches engaging the holding fixture prior to release and retraction of the IEEM docking latches. End effectors currently under development include space station-standard two-jaw parallel grippers, a three-finger reconfigurable gripper, socket wrenches, and motorized scissors for cutting spacecraft thermal blankets.

Grappling Manipulator

The grappling manipulator is used for attaching the Ranger vehicle to the local worksite, and for stabilizing the interface between the dexterous arms and their task. It also has to transmit the torque of power tools and dexterous arm motion back into the work-site structure. A number of configurations were considered for this manipulator, including the use of two or three smaller arms to minimize the torque requirements on the actuators. However, volume and energy requirements lead to the selection of a single six-DOF revolute arm, as shown in Figure 10. It should be noted that this configuration is uniquely that of the neutral buoyancy version of Ranger: joint angle limitations of this configuration prevent stowing the manipulator within the payload shroud volume, and a seventh joint will be added to the upper arm to allow the elbow assembly to swing up against the lower surface of the elec-

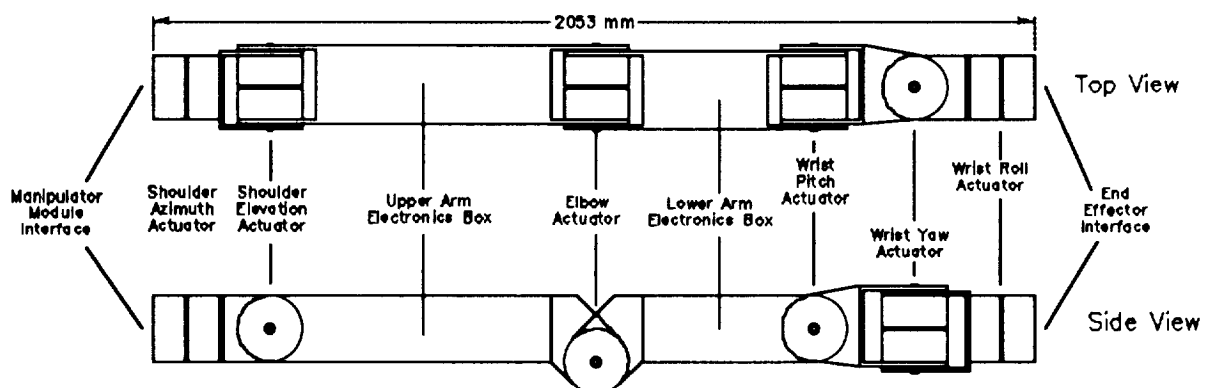


Figure 10.
Grappling Manipulator Configuration

tronics module for launch. This joint will not initially be modelled in the neutral buoyancy version to save development costs.

The concept of the grappling arm revolves around the use of a single actuator, incorporating passive brakes (brakes on when electrical power is off) to react forces through the manipulator. This actuator, apart from the electrically actuated brake, is quite similar to the dexterous arm actuator shown in Figure 9. Again, Inland Motors DC torque motors are used with harmonic drives for speed reduction. The electrical brake is mounted on the motor shaft, so that the torque is taken by backdriving the harmonic drive, reducing the required size of the brake at the expense of some potential wear of the harmonic drive spline teeth in the event of repeated over-torque conditions. By adopting a common actuator design throughout the grappling manipulator, the design process is streamlined and spares management is considerably simplified. The "price" paid for this simplification is in the reduced overall manipulator performance and increased mass, acceptable due to the limited active role of the grappling arm.

Camera Manipulator

The design goal for the camera manipulator was to maximize the potential envelope of camera locations, to provide the maximum flexibility to the Ranger operator in choosing views. As it was felt desirable to hold the camera platform to a constant roll attitude, five degrees of freedom were felt to be sufficient for this manipulator. It was also important in the design process to have a non-backdriveable arm to passively hold position during dexterous arm or grappling tasks, and to provide simple and robust operations throughout an extended vehicle lifetime. For these reasons, a modular design was chosen, with pitch and roll axes at each end, and a single elbow flexion joint.

As shown in Figure 11, the camera manipulator is designed around the use of differential to provide collocated pitch and roll motion at the ends. These differentials, based on conventional bevel gears, are driven by worm gear assemblies, to provide the non-backdriveable configuration preferred for this design. The worms themselves are driven by TRW/Globe gearhead DC motors, which are inexpensive and reliable in this type of application. The DC motors, along with control electronics and power circuitry, are sealed in the arm cavities of the camera manipulator itself. Thus, the interface to both the vehicle and camera housing are simplified to mounting plates and electrical connections, while providing the required performance in camera pointing. At a total length of 1.83m, this manipulator provides a great deal of flexibility in the use of the stereo camera pair mounted in the camera housing.

Vehicle Status

Development work is currently underway on the Ranger vehicle and its suite of manipulators. Shoulder actuators are currently being integrated for testing, and most components have been designed and released for fabrication. The complete

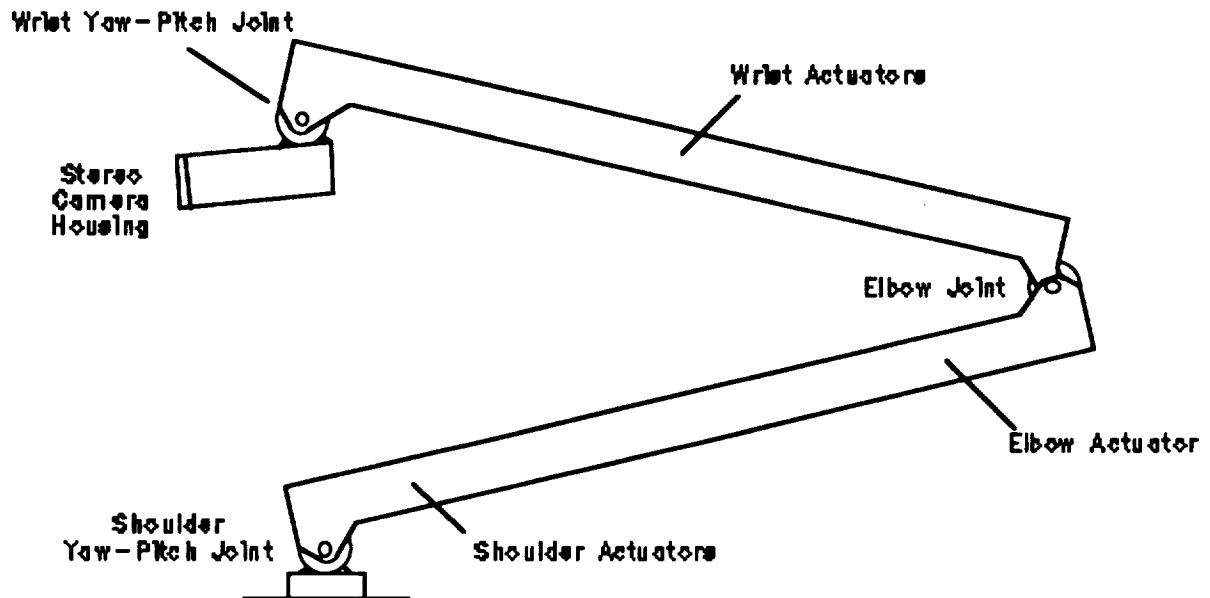


Figure 11
Camera Manipulator Configuration

vehicle is slated for initial tests in the University of Maryland Neutral Buoyancy Research Facility in June of 1992. It is anticipated that individual systems tests of the manipulators will precede the integrated tests, and results of the manipulator design tests will be included in the oral presentation of this paper in May of 1992.

Acknowledgements

The authors would like to thank the students of the Space Systems Laboratory who have devoted so much effort to Ranger manipulator design and development, particularly the lead graduate students: Jennifer Smith, Joseph Graves, and Gardell Gefke. This work is supported by grant NAGW-2245, Office of Aeronautics and Space Technology. The support and enthusiasm of grant monitors David Lavery and Dr. Mel Montemerlo are most gratefully acknowledged.

EXPERIENCES IN THE DEVELOPMENT OF ROTARY JOINTS FOR ROBOTIC MANIPULATORS IN SPACE APPLICATIONS

Klaus Priesett *

ABSTRACT

European developments in robotics for space applications have resulted in human arm-like manipulators with six or more rotational degrees of freedom. The rotary joints including their own electromechanical actuator and feedback sensors must be very compact units. This paper presents the specific joint concept as evolved so far, covering also the problems encountered during first hardware-development phases on both component and joint level.

INTRODUCTION

In view of the in-orbit infrastructures planned to be established within the next 10 to 15 years there is a growing need for automation and robotics in space. In Europe two general applications have been identified:

- Internal Robots, for the support of experiments inside laboratory modules
- External Robots, for exchange of Orbital Replacement Units, support of EVA, and inspection tasks.

As a precursor for Internal Robots a Robotics Technology Experiment (ROTEX) will be part of the next German Spacelab mission D-2, funded by the German Ministry for Research and Development and planned to be flown in 1993. ROTEX includes a small, six-joint manipulator arm located inside a Spacelab rack (Figure 1).

The development of External Robots initiated by the European Space Agency (ESA) has focussed on the Hermes Robot Arm (HERA), supported by the technology project Service Manipulator System (SMS). HERA is a relocatable, symmetric seven-joint arm with 9.09 m in length (useful range) as shown in Figure 2. HERA comprises two identical end effectors, wrist assemblies, limbs, and a single elbow assembly in the middle of the arm. Each wrist consists of three rotary joints: roll, yaw, and pitch. During operation, the wrist that is located at the base will serve as the shoulder with the yaw joint kept in a fixed position.

HERA is launched by the Hermes Spaceplane, steps over to the Columbus Man-Tended Free Flyer (MTFF) after docking, and stays there for its 10-year lifetime. It will be operated approximately twice per year when Hermes is visiting the MTFF for servicing.

* Dornier GmbH, Friedrichshafen, Germany

While the HERA project still is in its definition phase, first development hardware has been built and tested within the technology program SMS. This paper presents the HERA/SMS joints, addressing the following topics.

- joint design drivers
- joint design description
- component trade-offs
- development problems

The ROTEX joints, being smaller derivatives of the HERA/SMS joints, are covered only in the case of specifically related features or problems.

JOINT DESIGN DRIVERS

HERA must provide a high force capability as well as high positioning accuracy at the level of the end effector. This results in very stringent joint requirements like high torque capability, very low backlash, high stiffness, low friction, and high-resolution angle and speed measurements. Further design drivers are low backdrive torque, very constant braking torque, and the long stay time in orbit, with hibernation phases of more than half a year. Other significant aspects are compactness and low mass. Due to the symmetric configuration the performance requirements are the same for all joints, with exception of the angular range. The most important performance data are listed in Table 1. As indicated, several requirements still are subject to review or confirmation pending ongoing system analysis. The ROTEX joint performance requirements are given for comparison.

JOINT DESIGN DESCRIPTION

SMS JOINT DESIGN

The joints built within the technology project SMS will provide the basis for the description of the design. The SMS pitch/yaw-type joint shown in Figure 3 includes the following components/features:

- brushless DC torque motor;
- optical sensor on motor shaft, for motor commutation and speed sensing;
- electromagnetic friction brake with manual lifting device;
- backdriveable gear, consisting of Harmonic Drive with a planetary gear prestage;
- optical, absolute encoder (17-bit resolution), for joint angle measurement;
- thin-section ring ball bearings;
- titanium structure;
- endswitches and endstops at the limits of the operational range.

The pancake-type brushless DC motor is driving a hollow shaft which is supported by two preloaded angular-contact ball bearings. On the same shaft there are the (metal) code disk of the motor sensor and the brake disk. The motor sensor generates the feedback signals for motor commutation and speed control. The motor shaft is coupled to the input ele-

ment of the gear, the pinion of the planetary gearstage. This planetary gear is integrated into the main gear, a Harmonic Drive of type HIUC size 40. The flexspline of the Harmonic Drive is connected to the joint housing, and the dynamic spline is the output element and fixed to the joint output flange. The total gear ratio is 260.6.

The housed optical, absolute encoder of type MIL- 238- 17BU2F, supplied by BEI Motion Systems Company, is placed inside the motor section and coupled to the joint output flange via a long shaft running through the gear. The external mounting interfaces of the joint are at the side, perpendicular to the rotation axis, leading to a yoke-type construction of the rotating output element. Support of this output member is provided by two pairs of angular-contact ball bearings, with each pair in face-to-face arrangement and preloaded against each other. The angular rotation range of the joint is ± 120 degrees with respect to the upright position.

HERA JOINT DESIGN

The actual HERA joint design is different in a number of aspects based on the evolution of requirements and the experiences gained during the SMS development (Figure 4):

- motor and motor sensor combined on common sleeves
- no manual brake lifting
- astronaut override provision
- different Harmonic Drive configuration (HIUR), to be investigated
- resolver for joint angle readout
- same size for both output bearing pairs.

In view of the critical HERA mass situation, a change in the main structural parts material from titanium to, e.g., beryllium will have to be considered. Redundancy is required for the following items:

- windings of motor, brake, and resolver
- readout station of motor sensor
- endswitches.

The redundant motor must be accommodated within the same volume; i.e., its torque capability is reduced when only one winding is powered. Therefore, the gear ratio must be increased to about 400 in order to obtain the same output torque.

ROTEX JOINT DESIGN

The ROTEX joints are smaller versions of the SMS concept with some different features:

- no brake
- Harmonic Drive gear only
- no endswitches
- aluminum structure.

TRADE-OFFS AND DEVELOPMENT PROBLEMS

The selection of the individual techniques and components is a result of various trade-offs. The alternative solutions considered and the main conclusions are summarized in Table 2. It is evident that the current choice must be of preliminary nature, since the development still is in an early phase.

MOTOR

The selection of the drive motor is well consolidated by extensive development activities at the component level. These have resulted in an advanced design with an improved winding/lamination technique to increase the motor constant, and an improved lamination profile to reduce the detent (cogging) torque. The actual motor configuration is that included in the HERA joint design (Figure 4).

SENSORS

The investigation of different technologies have not resulted in a single, common choice for the two sensors of the HERA joint actuator. The optical devices employed within the SMS and ROTEX joints provide the required performance at lowest mass and size, however, their suitability for HERA is questioned because of reliability reasons. More detailed studies are necessary to be able to select a final, satisfactory solution.

LUBRICATION

The lubrication of ball bearings and gears is one of the major problems in the HERA joint development. While for ball bearings, relatively good experiences exist with long-life mechanisms, no space application is known to the author that employs gears within a heavy-duty mechanism for up to 10 years in orbit.

Lubrication in spacecraft mechanisms can be accomplished by either dry or liquid lubricants, or by combinations of both. For HERA, the choice is not self-evident, as for example in the case of bearings and gears in optical devices or adjacent to sliding electrical contacts, where dry lubricants are to be employed. The relative merits of dry and liquid lubricants and their influence on space mechanism design are summarized in Table 3. Liquid lubricants are less problematic insofar as their properties are unchanged between air and vacuum so that no special precautions are necessary for ground testing. Degradation can be reduced by surface protection using, e.g., TiC-coated balls and gold films on the Harmonic Drive teeth. A major concern is fluid loss by evaporation and creepage, which is time dependent and thus not testable with reasonable effort. While a replenishment can be provided for the bearing, this is normally not possible for the gears. The life of a dry lubricant is determined by wear; i.e., by the number of operational cycles, so that accelerated life testing can be performed with comparatively low effort. There are three main types: thin solid metallic films, lamellar solids, and polymeric films. The lamellar solid of MoS₂ is considered to be the only promising solution for a purely dry lubrication of the gearbox. A drawback of its use would be the need to apply nitrogen purging during ground operations, in order to avoid rapid degradation due to air.

As a conclusion from the above discussion, the following lubrication methods will be considered for the HERA joints:

- Ball Bearings
 - perfluorinated oil (e.g., Fomblin Z25 or Brayco 815Z), TiC coating of balls
 - sputtered MoS₂
 - ion-plated lead
- Gearbox
 - grease (e.g., Braycote 601), possibly gold-coated Harmonic Drive teeth
 - MoS₂ (sputtered or spray-bonded).

It is expected that a common lubrication method can be applied for both ball bearings and gears, with the gearbox being the determining factor.

GEAR

The selection of the main gear out of different solutions was governed by performance, mass and size aspects. The lubrication problem could not be adequately assessed because of the lack of reliable data. It has been decided to take the Harmonic Drive as a baseline and to try to establish a suitable lubrication method through testing of the most promising candidates.

Tests were conducted at the European Space Tribology Laboratory (ESTL) on a Harmonic Drive gearset HDUC 50-100 with both Braycote 601 grease and MoS₂ lubrication[2]. For the tests with grease performed first, about 2 ml of Braycote was applied. The dry lubrication was accomplished in different ways: on the circular spline by sputtering according to ESTL procedure (ESTL/QP/061), on the flexspline and on the wave generator by spray-bonding. The efficiency was measured at different speeds, loads, and temperatures, in forward and backdriving mode. Figure 5 shows a plot of test results in the forward mode. A significant influence of the temperature is apparent with the Braycote lubrication only. An input speed dependency is not detectable within the tested HERA range. The influence of the load is obvious at lower torques, but becomes almost negligible above 150 Nm. An inspection of the cleaned gearset after testing with grease showed a visible wear and deformation zone on both the circular spline and the flexspline in the area of highest contact pressure. Similar wear and deformation patterns were observed following the tests whilst dry-lubricated, which were run in the opposite direction. A statement concerning lubricant lifetime is not possible, since the test duration was kept short. It was concluded from the tests that the MoS₂ lubrication provides the best overall efficiency performance, and that a life test will be conducted to prove the long-term durability of this lubricant in the space environment.

The same series of tests was run on a Cycloid Drive type FA 15-59, showing rather similar results. The Harmonic Drive performs marginally better when comparing efficiency, however, the Cycloid Drive appears to be less susceptible to temperature effects. Furthermore, it has not suffered any wear damage, only light burnishing.

Within the SMS project, two basically identical joints were built, differing only by the lubrication method of the gear. One was oil-lubricated using Fomblin Z25. For the other, the

above-described MoS₂ dry-lubrication method was employed. During a planned disassembly, after a relatively short operational time of about 1 hour, the dry lubricant was found almost completely removed from the Harmonic Drive parts. The suspected cause of this rapid degradation is the operation in normal air, which reduces MoS₂ film life considerably due to high humidity content. The gear was cleaned and subsequently lubricated with Fomblin Y140/13 oil and Braycote 601 grease (Harmonic Drive teeth) in order to have a second working joint for the development of control software. The above-described lubricant failure emphasizes the need for a dry environment when using MoS₂, which means a lot of inconvenience during ground testing, handling, and storing.

Another problem associated with the Harmonic Drive is the torque ripple in excess of the required 2% measured in both SMS joints (see Figure 6), with a ripple frequency of twice that of the rotation frequency of the wave generator. If the requirement would be confirmed and compensation could not be performed, the gear trade-off would have to be revised even if the lubricant tests were successful.

During stiffness testing of the SMS joints, an excessive hysteresis was observed in both units as shown in Figure 7. The cause was an improper fixation of the Harmonic Drive wave generator due to wrong tolerancing of a bearing clamp ring inside the gear.

BRAKE

According to Table 1 the braking torque referred to the joint output level shall be between 500 and 650 Nm under all environmental conditions; i.e., it shall be kept constant at an average value with tolerable variations of up to $\pm 15\%$. The lower limit is determined by the allowed stopping distance (at end effector level) in an emergency case. Above the maximum specified torque, the brake shall slip in order to protect the joint from being overloaded. Since the brake is acting on the motor shaft, variations in gearbox efficiency due to environmental effects must be taken into account, so that the allowed torque variations become very small; i.e., less than $\pm 10\%$. The brake, as designed for the SMS technology development model joints (see Figure 8), is a fail-safe electromechanically actuated friction device, including

- a rotor (or disk) fixed to the motor shaft, carrying a friction layer, and
- a stator assembly, comprising housing, coil, diaphragm, and armature with the other friction layer.

The brake is 'ON' when the diaphragm is pressing the armature against the disk with a defined preload. Lifting is performed by powering the coil winding so that the armature is moved by electromechanical force. The electromechanical force must be high enough to overcome the diaphragm preload plus the increase in spring force due to further deflection during lifting. Since the electromechanical force is increasing quadratically with the decreasing air gap between armature and winding stator, it will be possible to keep the brake open with low power.

The attachment of the ring-type armature to a diaphragm provides the advantage of having no backlash in the brake. However, clamping of the diaphragm at its inner and outer

diameter by closed rings will create high axial-spring-force changes due to differential thermal expansions between diaphragm and rings, being made of different materials. A modification of the design is necessary in this respect, either a change in the diaphragm configuration or the use of another spring concept. In any case, a rather soft spring characteristic should be provided so that the axial force becomes less sensitive to manufacturing tolerances; e.g., axial runout of the brake disk.

The achievement of a good constancy in friction by selection of a suitable friction material combination is the more difficult task in the brake development. From the brakes of the Space Shuttle Remote Manipulator System, which use a phenolic/asbestos brake pad material, it is known that a torque anomaly occurred at certain thermal vacuum conditions [3]. As a consequence, the use of other materials has been considered as reported in [4]. For HERA, a Dornier company internal research work was started with particular emphasis on brake pad materials. The following materials have been investigated:

- metals
- polymers
- ceramics
- carbon.

After a comprehensive literature study, it was concluded that only ceramic-based materials could provide the required constancy in friction. Three materials were preselected for evaluation by test using a representative brake configuration:

- $\text{Al}_2\text{O}_3/\text{ZrO}_2$
- $\text{Al}_2\text{O}_3/\text{TiO}_2$
- WC/Co.

The established friction test set-up allowed the measurement of the axial contact force, the friction torque, and the rotation speed of the brake disk. The friction coefficient has been evaluated from continuous sliding tests at different speeds, and from braking tests; i.e., stopping an inertial load from its maximum rotation speed to zero. Tests were conducted in both ambient and thermal vacuum conditions.

The following conclusions were drawn from the tests.

- There is a substantial decrease in friction coefficient when changing from vacuum to ambient environment, obviously due to the lubrication effect of air.
- The influence of temperature is very small.
- The friction constancy of WC/Co is excellent, however, abrasive wear occurs under load, since the tungsten carbide (WC) is embedded into a relatively soft cobalt matrix. The amount of wear is small and not important for the function of the brake itself. However, it must be ensured by appropriate sealing that the function of other components is not degraded by wear particles from the brake.

As a summary, it may be concluded that WC/Co has turned out to be a viable solution for the brake pad material provided that the wear debris can be contained.

ROTEX JOINTS

Two problems were encountered:

- insufficient accuracy in motor speed measurement due to axial runout of the sensor disk;
- improper coupling of joint-angle encoder to output shaft.

The 0.1-mm-thick slotted metal disk of the motor sensor has a coarse track for identification of the motor commutation points, and a fine track with 1024 increments for generation of a velocity feedback signal for motor speed control. The sensor head includes LEDs and phototransistors, which in case of the fine track, deliver a quasi-sinusoidal voltage signal to the external electronics. This signal is modulated when the axial distance between the disk and the sensor head is not constant due to axial runout of the motor shaft and the disk itself. The latter error was too high in some cases, so that screening out of a greater number of disks became necessary in order to keep the signal modulation within acceptable limits. For further applications it was recommended to include signal preconditioning electronics directly at the sensor to simplify the interface with the joint electronics.

In one of the six joints the signal of the absolute, optical joint position encoder showed irregularities due to excessive loading of the encoder shaft, caused by the coupling to the joint output shaft. This failure could be corrected by an appropriate adjustment procedure.

CONCLUSIONS

During initial design and development work performed on rotary joints for space manipulator arms a unique configuration has been elaborated providing compactness, high stiffness and strength. For the HERA application, very stringent requirements have to be fulfilled, which make the selection of individual actuator techniques and components difficult. This specifically applies for the gear and its lubrication method, the sensor technology, and the brake. The problems have been highlighted within this paper, and possible solutions have been presented based on first development test results.

ACKNOWLEDGMENTS

The author wishes to thank the companies Fokker Space and Systems (HERA prime contractor), ETEL (motor development), and Stork Product Engineering (gear development) for having contributed to this paper by their involvement in the HERA/SMS projects.

REFERENCES

1. European Space Tribology Laboratory (ESTL), "Tribology of Spacecraft," Proceedings on a Course Held on 16-17 May 1990.
2. Foster, D.J., Gill, S., Rowntree, R.A., "Thermal Vacuum Testing of Cycloid and Harmonic Gearboxes," ESTL Technical Memorandum ESTL/TM/102, August 1991.

3. Trenouth, J.M. and MacKenzie, C.W., " Investigation of an Anomalous Canadarm Brake Behaviour," Canadian Aeronautics and Space Journal, No.32, 205-213, 1986.
4. Hawthorne, H.M., " Tribomaterial Factors in Space Mechanism Brake Performance," Proceedings of 24. Aerospace Mechanisms Symposium, Kennedy Space Center, NASA CP-3062, 231-241,1990.

Table 1: Joint Performance Requirements

PARAMETER	UNIT	HERA	ROTEX
Angular Range • Wrist Pitch/Yaw • Wrist Roll • Elbow Pitch	deg deg deg	+/-120 +/-185 +30/-180	+/-125 Pitch +/-185 Roll
Angular Speed • Max • Min	rad/sec rad/sec	0.05 4.5 E-05	0.15
Output Torque T • At Min Speed • At Max Speed	Nm Nm	≥ 450 ≥ 50	≥ 15 -
Torque Ripple • T > 25 Nm • T ≤ 25 Nm	% Nm	≤ 2 (TBR) ≤ 0.5 (TBR)	- -
Backdrive Threshold Torque	Nm	≤ 40	≤ 10
Brake Torque Referred To Output Level	Nm	500-650	-
Rotational Stiffness • T ≤ 13.5 Nm • T > 13.5 Nm	Nm/rad Nm/rad	≥ 1.1 E+05 (TBC) ≥ 1.3 E+05 (TBC)	≥ 0.5 E04 -
Joint Position Measurement • Resolution • Accuracy	arcsec arcsec	9.9 (17 Bit) ≤ 27	9,9(17 Bit) ≤ 24
Motor Speed Measurement • Resolution • Accuracy	% %	0.5 ≤ 1	- -
Power Consumption	W	≤ 30	≤ 3
Mass • Wrist (3Joints + Electronics) • Elbow (1Joint + Electronics)	kg kg	≤ 45 (TBR) ≤ 19 (TBR)	4.4 (1 Pitch J.) 4.0 (1 Roll J.)
Lifetime		10 Years, periodic Operations (20 Hours total)	1 Spacelab Mission
Temperature Range (Qual.)	deg C	-40 to +80	+6 to +65

TBC= To Be Confirmed
TBR= To Be Reviewed

Table 2. Summary of Trade-Offs

ALTERNATIVE SOLUTIONS *SELECTED BASELINE	MAIN ARGUMENTS FOR SELECTION OF BASELINE
<u>Motor</u> - Brushless Torque Motor * - Brushless, Toothless Torque Motor - Reluctant Motor	- Reluctant motor has non-linear torque/current behaviour - Baseline provides higher motor constant than toothless motor for given mass and size
<u>Sensors</u> - Resolver * - Optical Encoder * - Inductosyn	- Optical devices provide best performance - Resolver is more robust and reliable - Trade-off will continue to arrive at a common technology for both sensors
<u>Lubrication Method</u> (Treated separately)	
<u>Main Gear System</u> - Cycloid Drive - Harmonic Drive * - Planetary Gear	- Provides lowest mass and dimensions for the required performance - Is available with space-compatible materials
<u>Brake Pad Material</u> (Treated separately)	

Table 3. Relative Merits of Dry and Liquid Lubricants

DRY LUBRICANTS	LIQUID LUBRICANTS
Negligible Vapour Pressure	Finite Vapour Pressure
Wide Operating Temperature Range	Viscosity, Creep & Vapour Pressure Are Temperature Dependant
Negligible Surface Migration (Debris Can Float Free)	Creep Barriers And Seals Required
Valid Accelerated Testing	Invalid Accelerated Testing
Short Life In Laboratory Air	Insensitive To Air Or Vacuum
Debris Cause Frictional Noise	Low Frictional Noise
Friction Speed Independant	Friction Speed Dependant
Life Determined By Lubricant Wear	Life Determined By Lubric. Degradation
Poor Thermal Characteristics	Good Thermal Conductance
Electrically Conductive	Electrically Insulating

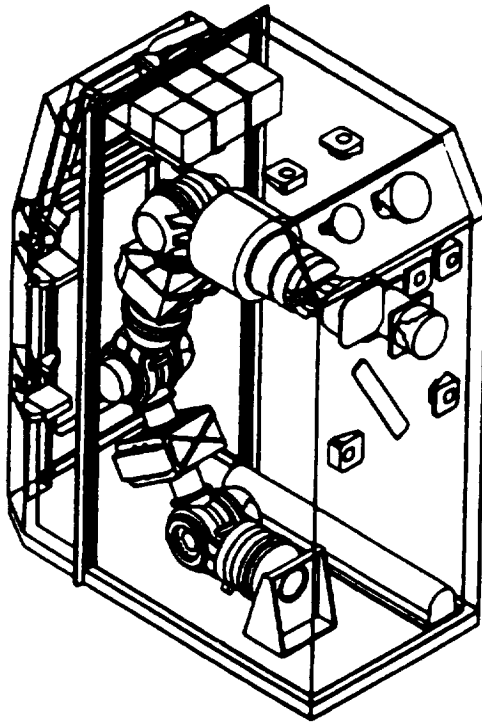


Figure 1. Rotex Arm Inside Spacelab Rack

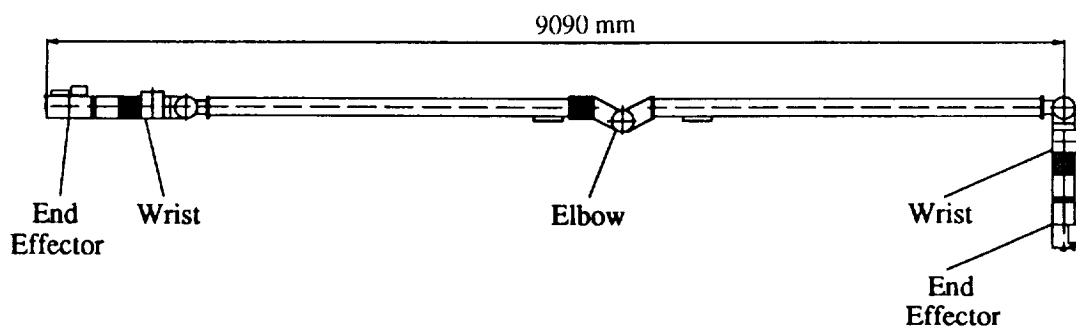


Figure 2. HERA Configuration

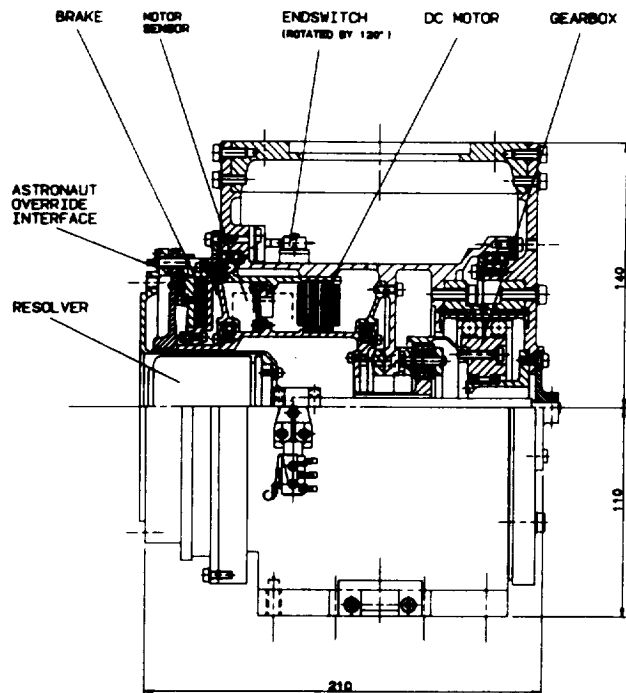


Figure 4. HERA Joint Design

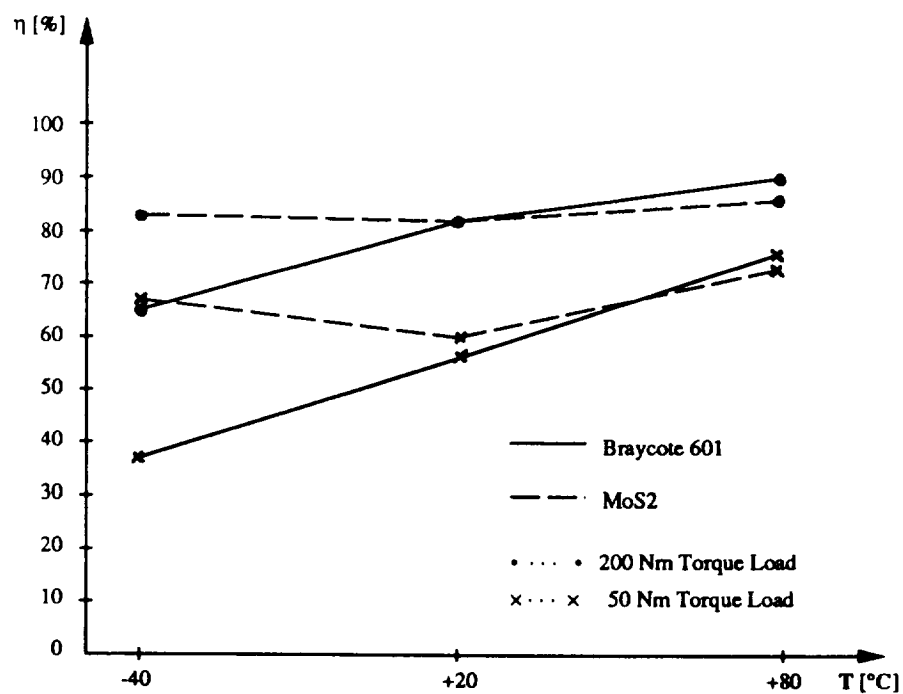


Figure 5. Harmonic Drive Efficiency η vs. Temperature T at 100 RPM Input Speed

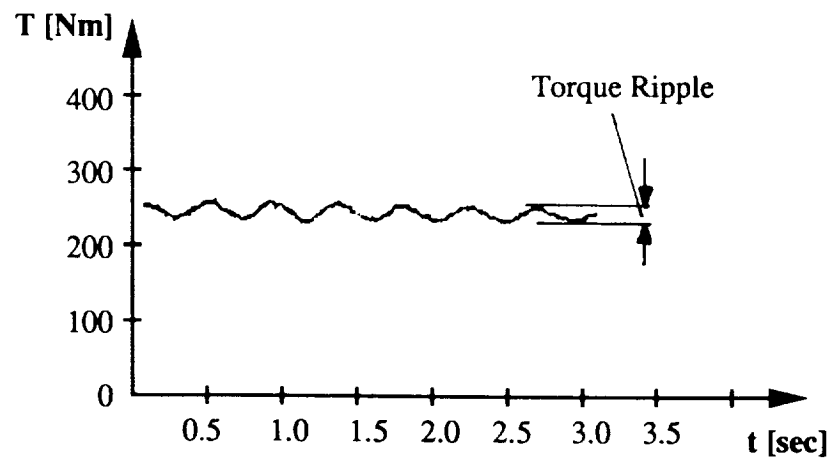


Figure 6. Torque Ripple of SMS Joint

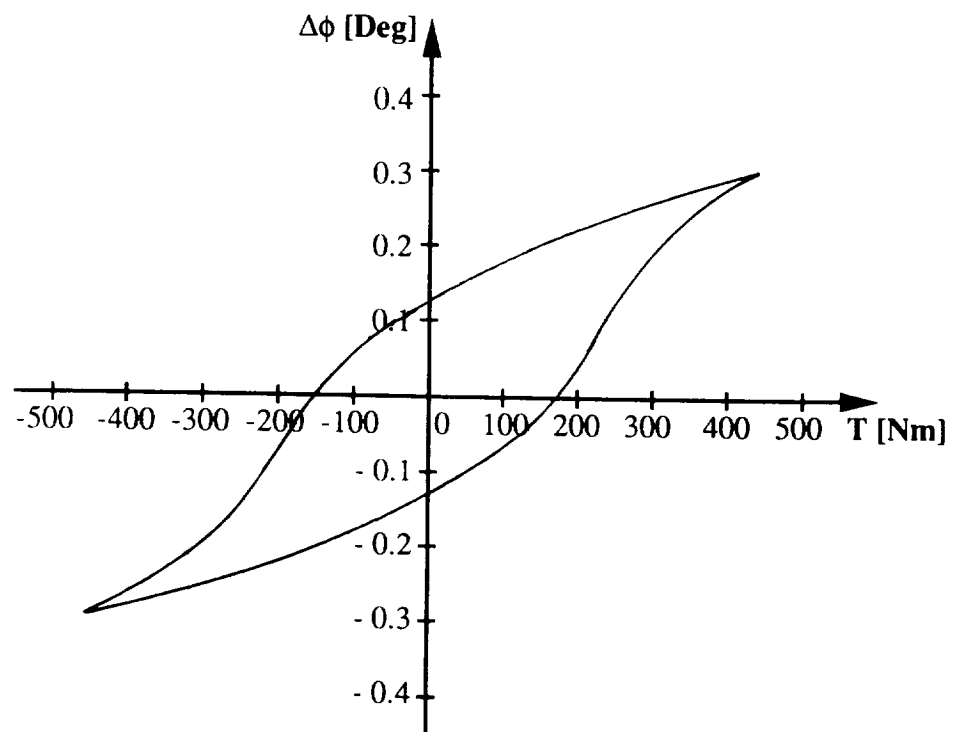


Figure 7. Anomalous Hysteresis of SMS Joints

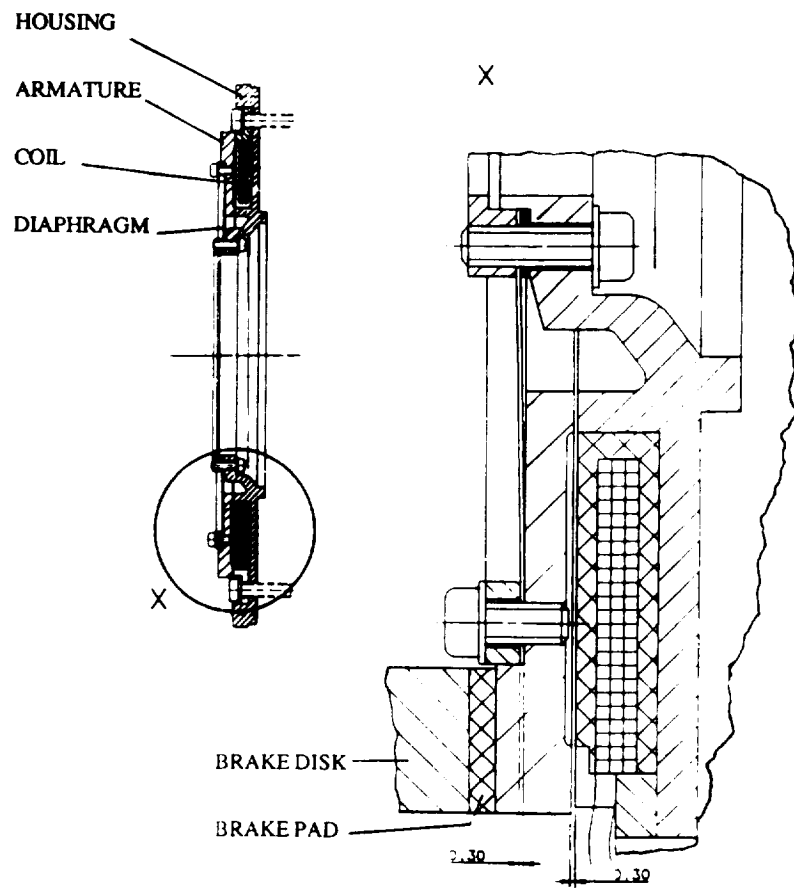


Figure 8. SMS Brake Design

N 9 2 - 2 5 0 7 4

SPLINE-LOCKING SCREW FASTENING STRATEGY

John M. Vranish

NASA/Goddard Space Flight Center
Greenbelt, Maryland 20771

ABSTRACT

A fastener has been developed by NASA/GSFC for efficiently performing assembly, maintenance, and equipment replacement functions in space using either robotic or astronaut means. This fastener, the "Spline-Locking Screw," also would have significant commercial value in advanced manufacturing. Commercial (or Department of Defense) products could be manufactured in such a way that their prime subassemblies would be assembled using Spline-Locking Screw fasteners. This would permit machines and robots to disconnect and replace these modules/parts with ease, greatly reducing life-cycle costs of the products, and greatly enhancing the quality, timeliness, and consistency of repairs, upgrades, and remanufacturing.

The operation of the basic Spline Locking Screw fastener will be detailed, including hardware and test results. Its extension into a comprehensive fastening strategy for NASA use in space also will be outlined. Following this, the discussion will turn toward potential commercial and Government applications and the potential market significance of the fastener.

PRECEDING PAGE BLANK NOT FILMED

I. INTRODUCTION

In space operations, fastening problems are unusually important. Common machine screws simply cannot be applied with the same ease as on Earth; they cross-thread easily because the astronauts must wear gloves and space suits, and therefore lose dexterity and fine motor manipulative skill when performing maintenance. Robots have cross-threading problems and more. At the same time, the violent vibrational and loads environment generated by launching payloads into orbit mandate a requirement for strong, simple, lightweight, and reliable fasteners that must be met. The Spline-Locking Screw described in this paper directly addresses this problem. But, in developing what amounts to a screw that cannot be cross-threaded, it soon became apparent that more was involved. One could make slight modifications to the basic Spline-Locking Screw by adding alignment and torque reaction pins and accomplish precise and reliable electrical connections in addition to the fastening capability. A few modifications more and a Standard Robot End Effector and related Astronaut Hand Power Tool emerged. This Standard Robot End Effector (or Astronaut Hand Power Tool) could acquire and operate other power tools, or store them in holsters for use as required. It thus became clear that by using this approach, any number of complex (or simple) tasks could be accomplished in sequence by progressively modifying a basic Spline-Locking Screw system. The purpose of this paper is to provide an introduction to the Spline-Locking Screw concept and its derivative devices, as well as to give an indication of its potential for a comprehensive fastening strategy--for both space and commercial applications.

A "proof-of-principle" prototype based on the Spline-Locking Screw concept already has been built and tested (Figure 1). It consisted of a foot to fasten the Flight Telerobotic Servicer (FTS) robot to the Space Station structure. The results of this effort immediately showed success and the device was adopted by the prime contractor and NASA as the foot that would be employed on the FTS robot, if and when it is developed for flight. (The FTS Project was not funded by NASA for FY93.) This particular device, known in NASA as the Workpiece Attachment Mechanism/Workpiece Attachment Fixture (WAM/WAF) (see Figure 1), performs electrical connections in addition to basic fastening. It will also, of course, permit a robot to walk on a space structure.

II. THE SPLINE-LOCKING SCREW

In this section, the evolution of NASA's previous fastener that was used when repairs in space were anticipated will be outlined, along with the problems this evolution caused. This will set the stage for the development of the basic Spline-Locking Screw concept.

The evolution of this NASA fastener [1] is shown in Figure 2. Many of these lessons were learned as part of the Solar Max satellite repair mission of 1982. Screws with low-pitch machine threads had been used successfully many times in space launch operations. However, these would cross-thread when the astronauts tried to fasten them while wearing gloves and space suits. A guide was added to the screw and this

helped, but did not solve the problem. Next, the low-pitch machine thread was changed to a more high-pitch acme thread. This worked, but the screw would back out during vibrational tests simulating launch conditions. To overcome this, a taper interface at the top of the screw was added. At this point, everything worked. However, these modifications added a great deal of friction to the system and this meant that large torques on the order of more than 135 N·m would be required to free up the bolts used in the Solar Max mission. This, in turn, meant that very large and clumsy hand tools had to be used and the astronauts (or robots) could be subjected to dangerously large torques and forces. For a robot, the situation was nearly impossible. Using the large tools would severely limit robot dexterity. On the other hand, the existing robot end effectors could only produce 27 N·m of torque [2].

The Spline-Locking Screw was developed by returning to the common machine screw and taking a fresh approach [3, 4]. It was decided to cut the bolt in two and to leave the bottom half of it threaded (Figure 3a). A new interface was created in the shaft of the bolt. Thus, we have the bolt head (or driver) and the object that is normally pinched by the screw system on one side of the interface, with the bolt and the threaded fixture it screws into, on the other side. The problem then was to create an interface that would complete the system. A spline-locking-type interface (Figure 3b) was chosen because it was simple, direct, and effective. There is an increase in size, but it is minimal. The operational concept of the system is shown in Figure 4. The driver is inserted into the bolt such that the male splines of the driver fit into matching female splines of the bolt. The driver is then turned clockwise to tighten the screw system. During this process, the male driver spline engages in the female bolt spline; it cannot be pulled out and the bolt and driver turn together as a single, complete machine screw. To unfasten the system, the driver is turned counterclockwise; the screw loosens and the driver splines relocate in the bolt (disengage) such that the driver can easily be pulled out of the bolt. The splines are very coarse, so they can be designed to seat and fit together such that cross-threading is virtually impossible. Because the bolt is never unthreaded, we have, in effect, a machine screw that cannot cross-thread. At the same time, it is now possible to use low-pitch machine threads so that large preload forces can be generated from minimum input torques (on the order of 11 N·m to generate 4450-N preload). Therefore, these bolts would not shake loose during launch because of their low pitch. Also, Robot End Effectors and Astronaut Hand Power Tools could now be made more modest in size and power, enhancing safety for the astronaut, and safety and dexterity for the robot.

As a practical matter, the spline-locking design requires careful and detailed treatment. This is to make certain that the splines engage and disengage properly and that the payload remains attached either to the Robot End Effector (or Astronaut Hand Power Tool) or to the fixture at all times to prevent it from drifting off into space. We will begin by examining these details as we follow the tightening sequence of steps shown in Figure 5a. When the driver encounters the bolt, it normally comes to rest initially on

top of the bolt. As the driver is rotated clockwise, it rotates with respect to the bolt until the driver and the bolt splines line up; the driver bias spring pushes the driver into the bolt (driver spline insertion, Figure 5a) and the driver is seated in the bolt. This raises a question as to how we can be certain that the bolt will not turn with the driver and prevent the relative motion of the male and female splines essential to insertion and seating. This is accomplished by adding a preload spring to the bolt (Figure 3b) to ensure that the bolt will not turn until the driver spline drops into the bolt spline, seats, and the splines engage (Figures 4b and 5a). At this point, the driver torque will simply overcome the friction from the preload spring and the driver and bolt will turn together. With the driver and bolt turning clockwise together, the bolt will translate downward and apply a large locking force between driver and bolt splines. A subtle distinction is involved between the terms "spline engagement" and "spline locking," which can be seen by comparing Figures 4 and 5 and noting that an underhook region has been added to the female bolt splines. The reason for the underhook region will be clarified below.

The details of loosening will now be discussed (Figure 5b). The sequence starts with the splines locked together and the object preloaded to the fixture (Figure 3). As the driver is turned counterclockwise, the bolt spline is held in the driver spline by the underhook (Figure 5b). Thus, the bolt and driver must turn together to break the bolt thread loose and to release the preload force. As the counterclockwise rotation continues, the driver remains in its downward position because of its preload spring, but the bolt translates upward (Figure 5b). This causes the splines to unlock and reposition for spline disengagement and removal. As the bolt translates upward, it is capable of generating a large force to "push" the object away from the fixture. This condition is termed "push-off" and it prevents cold welding or jamming of the object to the fixture. At this point, the driver and bolt turn together until the bolt threads hit a stop. The driver splines and the bolt splines remain aligned throughout for easy removal of the object from the fixture. Rationale for the underhook region now begins to emerge. This addition makes certain that during the unfastening process, the bolt is located in the fixture in the same position each time before the driver and the object can be removed. This also makes certain that the bolt and driver are properly positioned to begin the insertion and fastening process shown in Figure 5a.

III. ELECTRICAL CONNECTOR CAPABILITY

In this section, it will be shown that an electrical connection capability can be added to the fastening capability by adding minor modifications to the basic Spline-Locking Screw [4]. Further, it will be shown that this leads to an entirely new set of devices to include Robot End Effectors with tool storage and tool autochanger capabilities, the WAM/WAF, and an Astronaut Hand Power Tool.

An electrical connector capability can be incorporated in the Spline-Locking Screw concept, as shown in Figure 6. The Spline-Locking Screw bolt would be threaded on a nut, rather than into the fixture. The bolt is coupled to the fixture by means of a preload spring F_s (nominally 445 N) forcing the bolt down toward the fixture. Contact between the bottom stop on the nut and the fixture prevents the downward translation of the bolt. Thus, the bolt and nut are preloaded against the fixture with a force equal and opposite to that of the preload spring (labelled F_{RS1} in Figure 6). Also, the interface between the nut and the fixture is splined so that the nut cannot rotate, but it can translate between the fixture top and bottom stops. Electrical pins can be added to the nut, and pin receptors can be added to the fixture. In this section, both the tightening and loosening sequences will be examined.

As the driver turns, it first seats in the bolt and then follows all the steps associated with the tightening process through spline locking, as described above. At this point, the F_{RS1} force transfers from the fixture/nut interface to lock the driver and bolt splines together (shown as F_D in Figure 6). The F_D force, in turn, is reacted by the equal and opposite force (labelled F_{RS2} in Figure 6), forcing the fixture against the object. All the above forces (F_s , F_{RS1} , F_D , and F_{RS2}) are equal to each other. They are given different subscripts because they exist at different times and at different locations in the fastening sequence. As the driver continues to turn clockwise, the bolt turns with it and, since the bolt cannot translate downward--being held in place by the locked splines of the driver and the bolt--the nut cannot rotate and the nut translates upward. Throughout this process, the force sustaining the spline locking remains constant and equal to that of the preload spring, and the object and fixture are forced against each other with the same force. We thus have a new condition which will be termed "hard dock." With the proper alignment guides on the fixture and the object (not shown in Figure 6), proper preconditions have been achieved for the electrical connection. As the driver continues to turn clockwise, the nut translates upward until a precision electrical connection is made. Shortly afterwards, the nut hits its top stop on the fixture. With nut translation stopped, the bolt once again attempts to translate downward. This forces the object and fixture together with preload forces. This condition is termed "preload." Once again, it should be noted that spline locking can be done in either a hard dock or preload condition, depending on the circumstances. Both conditions are useful in ensuring that the object is properly secured to the fixture throughout the fastening process. It is also perhaps appropriate to note that the object is secured (or docked) to the fixture as soon as the splines are engaged (Figure 5a), prior to hard dock. However, there is rattle between the object and the fixture during this condition so we will describe it with the term "soft dock."

Turning the driver counterclockwise reverses the steps described above and disengages the object and the fixture as well as the driver and the bolt. As previously described, under hard dock and preload conditions, the driver spline is seated in a groove in the bolt spline (Figure 5). As described above, during counterclockwise rotation, the bolt spline underhook provides an interference obstacle preventing the two spline sets from slipping out of engagement. It should be noted that during the disengagement of the electrical connectors, the bolt preload spring provides the disengagement force, and the force holding the splines in lock (and hard dock) is the difference between the bolt preload spring force and that used in pulling the electrical connectors apart. This hard dock condition remains until the nut bottoms and the bolt translate upward, taking the system out of hard dock, unlocking the splines, then transferring into soft dock. Again, during this transition from hard dock to soft dock, the bolt translates upward and pushes the fixture and the object slightly apart (say, 1.5 mm). This condition is termed "push-off." The bolt spline is now free of the underhook and so the driver spline rotates with respect to the bolt spline until it hits a stop and both driver and bolt are stopped. This forces the two splines to be lined up such that they can easily and reliably be pulled apart.

IV. DERIVATIVE DEVICES

It now would be possible to make further minor modifications to the Spline-Locking Screw and produce a range of useful devices. One such device would be a combination special tool interface and autochanger (Figure 7) [5]. This is a straightforward extension of the arrangement shown in Figure 6. The object in Figure 6 can be fastened to a robot wrist and a motor can be splined to the driver. This coupling between motor and driver would include a compliant spring to permit the driver to be pushed up out of the way. This arrangement of object, electrical pin receptacles, and compliant driver with motor would constitute a Standard End Effector. Alignment pins would be added to the fixture (which would also serve as the special tool interface) and mating receptacles would be incorporated in the standard end effector. Any special tool could be fastened to the interface and the robot. Thus, the robot could use the Standard End Effector to mate with and fasten to a common special tool interface. Further, since any tool could be attached to the special tool interface, and power and signal could be provided, the robot could acquire and use any of a wide variety of tools. It should be noted that the mating procedure by which the robot acquires a special tool would use standard practice. That is, alignment is standard "peg-in-the-hole" using alignment pins and mating receptacles. The driver would be pushed out of the way during this process. Once this step was complete, the driver and bolt would be aligned and the spinning driver would drop into the bolt and would seat, then would go into soft dock, and soon thereafter, would go into hard dock, to be followed by establishment of electrical connections and finally, the locking together with preload forces. The WAM/WAF (Figure 1) [4] is essentially a large version of this device that has the strength to withstand torques and forces on the robot leg. The pins and receptacles are replaced by wheels and grooves to provide a kine-

matic clamp. Examining Figure 7 again, it can be seen that the bottom of the nut can be used to pinch tabs of a tool storage holster and thereby, to store special tools [5]. This system would be equally effective on Earth or in zero-g or micro-g. Thus, the system would become its own autochanger. Although not discussed in this paper, a similar approach could be taken in permitting a robot to use spline-screw techniques to release and fasten payload boxes known throughout NASA as Orbital Replacement Units [6].

V. CALCULATIONS AND TEST RESULTS

A WAM/WAF prototype (Figure 1) was constructed and tested as a first prototype. The prototype has been tested and demonstrated on a robot and was able to dock, and to go through its proper fastening sequence of soft dock, hard dock, electrical connection (to include actuating dust covers on both WAM and WAF), and to provide preload forces sufficient to allow the robot to wave a large steel table around with impunity. Without question, it has great holding strength with minimal motor torque required. More detailed testing is being conducted in the Goddard Space Flight Center robotics lab. Calculations indicate that the WAF/WAF can produce excellent preload forces with modest actuation torques.

$$dW_{in} = dW_{out} + dW_{losses} \quad (1)$$

dW_{losses} = friction losses in bolt and in reaction thrust bearing

$$T(\theta) d\theta = F(\theta) \left\{ \frac{d\theta}{2\pi L} + u_{s1} R_1 d\theta + u_{s2} R_2 d\theta \right\} \quad (2)$$

$$T(\theta) d\theta = F(\theta) \left\{ \frac{1}{2\pi L} + u_{s1} R_1 + u_{s2} R_2 \right\} \quad (3)$$

Where:

dW_{in}	= differential work done by the driver on the bolt.
dW_{out}	= differential work done by the bolt as it translates.
dW_{losses}	= friction losses in bolt and in reaction thrust bearing during differential work.
$d(\theta)$	= input torque.
$F(\theta)$	= bolt preload.
u_{s1}	= nut - bolt friction coefficient = 0.15.
u_{s2}	= coefficient of rolling friction = 0.008.
R_1	= bolt radius.
R_2	= radius of thrust bearing.
$d\theta$	= differential twist angle.
L	= bolt thread lead.

Thus, a 1.9-cm UNF 16 bolt producing 4450 N preload requires < 8.8 N·m input torque, which is a very modest value.

We will now examine the efficiency of the system.

$$E = \frac{dW_{out}}{dW_{in}} \quad (4)$$

$$E = \frac{F(\theta)}{2\pi LT(\theta)} \quad (5)$$

For the bolt, preload, and coefficient of friction listed above, we obtain an efficiency of 12.8 percent, which is more than satisfactory.

The WAM/WAF will not back-drive, hence, a brake is not required.

$$\tan(Y) = \frac{1}{2\pi LR_1} \quad (6)$$

Where Y = bolt lead angle.

When $\tan(Y) < u_{s1}$, the system will not back-drive.

$$u_{s1} 2\pi LR_1 = \text{safety factor} \quad (7)$$

For our WAM/WAF, we get a safety factor > 5, so a brake is clearly not required.

VI. COMPLEX ELECTROMECHANICAL SYSTEMS

An example of how a few more simple modifications can be added to the Spline-Locking Screw to produce a multirotational output [7] that can be monitored by electronic signals throughout the process is shown in Figure 8. This capability will, in turn, form the basis for using spline-locking screw techniques to operate complex electromechanical systems. Once again, some events must be done serially. During the process in which the robot acquires the object, the sequence is: mating; soft dock; hard dock; electrical connections; multirotational output until a stop is reached and the object is released to the custody of the robot; then finally, preload. During the process in which the robot fastens an object to some fixture, the sequence is: release of preload; hard dock; multirotational output until a stop is reached and the object is fastened to a fixture; release of the electrical connectors; soft dock; push-off of the robot Standard End Effector from the object; and separation of the robot Standard End Effector from the object. It is apparent that with multiple rotations available from an output shaft that will turn until reaching a stop, many different types of electromechanical systems can be driven by the shaft, including items as complex as clocks. We would then have what amounts to a portable motor, controller, power supply, system software and electronics, and mechanical interfaces. Most particular applications would only require an embedded

mechanical system and sensors. This would vastly simplify many tasks. And in those instances where an embedded motor is still required, the robot could supply power and controls.

VII. SMALL OBJECTS

The examples above have shown that there is virtually no limit to the complexity of tasks that can be performed by the Spline-Locking Screw system. It will now be shown that this system could also handle extremely small objects (Figure 9) [6]. Handling small objects in space would be more formidable than is commonly realized. The main problem is that the micro-g environment requires that every object be fastened to something or it will float away (or worse--accelerate to missile-like speeds). This requires that control be fastidiously maintained during each step of the hand-off process, despite the small size of the object and the required simplicity of the fastening scheme. Adding to the difficulty is the requirement that the small object be grasped by the Spline-Locking Screw Standard End Effector. As is shown in Figure 9, the problem can be solved by piercing the small object with a bolt, one end of which is a driver interface, and one end of which is the bolt spline (female) interface which mates with the driver of the Standard End Effector. A rotating socket with a compliant spring would be embedded into the fixture. Alignment tabs would be placed in the object, the Robot End Effector, and the fixture to permit the small object to be properly aligned in rotation at all times. The bolt would be threaded into the small object so that as the robot driver turned, the small object bolt would turn and translate up or down as required. During the process of fastening the small object to a fixture and releasing it from the Robot End Effector, the bolt would translate upward, locking it to the splines of the rotating socket and going through the steps of preload, hard dock, soft dock, and push-off to separation of the Robot End Effector from the object. During the process of fastening the small object to the Robot End Effector and releasing it from its storage fixture, the bolt would translate downward, locking in hard dock into the splines of the Robot End Effector, escaping from the splines of the rotating socket, pushing off from the rotating socket, attaching in preload to the Robot End Effector, and finally, separating from the rotating socket. The small object would be in proper control at all times.

VIII. FASTENING STRATEGY FOR SPACE OPERATIONS

The discussion above identifies the unusual capabilities of the Spline-Locking Screw approach. Further, it is clear that this fastener could form the basis for performing a host of operations ranging from attaching small, simple objects to acting as a transportable motor/control system/power supply and systems interface for complex electro-mechanical system, to permitting a robot to walk on a space structure or to handle tools with the same appendages as the case may be. Moreover, all of these devices could be actuated by the same rotary driver (identified as the Robot End Effector when used with robots, or the Power Hand Tool when used by astronauts). It would seem that a proper framework has been laid for a comprehensive fastening strategy in which Spline-Locking Screw mechanical and electrical interfaces can be standardized into a few size ranges (like industrial machine screws) and any number of applications, techniques,

and innovative designs could be implemented consistent with those interfaces. Parts counts on spacecraft would be drastically reduced, modularity would be enhanced, and maintenance and repair, greatly facilitated. Robotics could now be employed more extensively in assembly and maintenance operations, and astronauts would also find things simplified and safer.

IX. COMMERCIAL APPLICATIONS

Humans using their bare hands do not normally cross-thread bolts. Thus, from an industrial standpoint, the Spline-Locking Screw would be another of many available fasteners serving a small-but-important market niche typically involving bolts of 1.3 cm diameter or larger, in which the object being fastened must be periodically removed or replaced using power tools. With these larger bolts, threads are coarse, the torque involved in installing them is large and, because of their size, locking splines can easily and cost effectively be employed. Because fine machine threads could be used with the Spline-Locking Screw, required torque would be reduced and with it, the size of the power tools. Also, because the Spline-Locking Screw bolt is prethreaded, attachment is very quick; just a few turns. In the airline industry, for example, aircraft engines could be quickly dropped, overhauled and remounted. Similarly, the avionics could be installed using the Spline-Locking Screw with electrical connectors. This, in turn, suggests that the computer industry could make extensive use of Spline-Locking Screws with electrical connectors. Earth-moving and materials-handling equipment could profitably use such fasteners, as could the automotive industry (wheel lug nuts and engine and transmission mountings immediately come to mind). Military applications are particularly attractive. Military aviation has all of the problems associated with civilian aviation, but on a more pressing schedule and with field maintenance requirements. Tank and military automotive needs would also be significant.

X. SUMMARY AND CONCLUSIONS

The Spline-Locking Screw presents a unique and fundamental building block to facilitate assembly and maintenance in space (micro-g). Screw fastening, so pervasive on Earth, could now be employed in micro-g without danger of cross-threading by astronauts in space suits or by robots. This would advance the capability of assembly, maintenance and materials handling in a fundamental sense. Further, by allowing standardization and modular construction on a heretofore unprecedented scale, Spline-Locking Screws would simplify logistics; a consideration which is of special import in space.

The concept, while new, is straightforward. Indeed, Goddard Space Flight Center has already successfully constructed and demonstrated a WAM/WAF for the FTS, and End Effector Spline-Locking Screw prototypes for fastening payload boxes are in construction.

Commercial possibilities for this concept fall into an impressive market niche, particularly for bolts of 1.3 cm diameter or larger. These include civilian aviation maintenance and overhaul, mechanical systems and avionics; the computer industry; earth-moving and materials-handling systems; the automotive industry; and military applications in general, with aviation, avionics and tank and automotive support in particular.

REFERENCES

1. Rockwell International Corporation Space Division, portion of shop drawing #GL 1087209, dated 9/7/76, showing the operation of an ACME Screw Payload Fastener for the Solar Max Repair Mission of 1982, courtesy of Robert Davis, NASA/GSFC.
2. *FTS End Effector End Item Specification*, 1990, courtesy of Paul W. Richards, NASA/GSFC.
3. Vranish, John M., Invention Disclosure: *Spline-Locking Payload Fastener*, Case no. GSC 13,378-1, filed 6/5/91, dated 8/10/90, Goddard Space Flight Center.
4. Vranish, John M., Invention Disclosure: *Work Attachment Mechanism/Work Attachment Fixture (WAM/WAF)*, Case no. GSC 13,430-1, dated 2/25/91, Goddard Space Flight Center.
5. Vranish, John M., Invention Disclosure: *Spline Screw Autochanger*, Case no. GSC 13,435-1, dated 3/26/91, Goddard Space Flight Center.
6. Vranish, John M., Invention Disclosure: *Spline-Locking Payload Fastening System*, Case no. GSC 13,454-1, dated 8/10/90, Goddard Space Flight Center.
7. Vranish, John M., Invention Disclosure: *Spline Screw Multiple Rotations Mechanism*, Case no. 13,452-1, dated 6/3/91, Goddard Space Flight Center.



Figure 1. The Workpiece Attachment Mechanism/Workpiece Attachment Fixture (WAM/WAF).

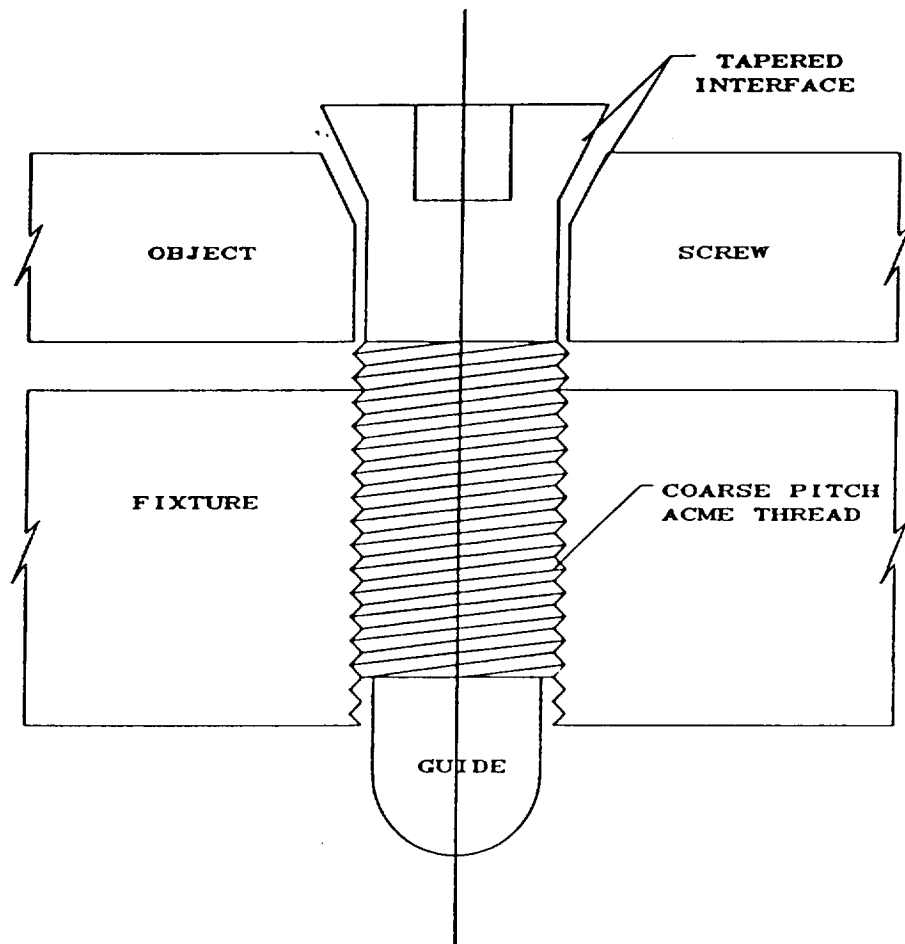
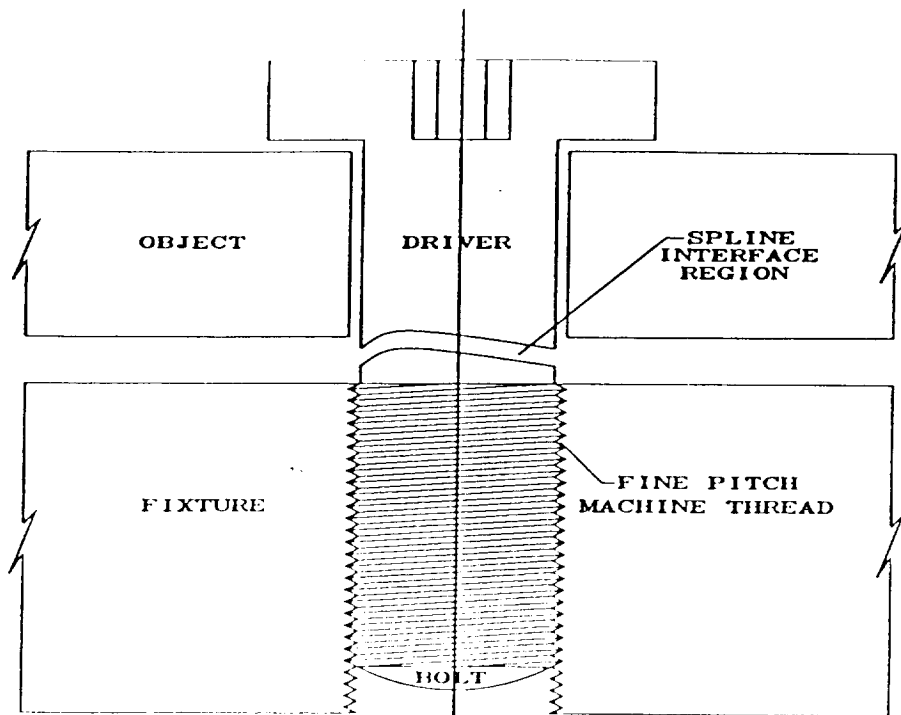
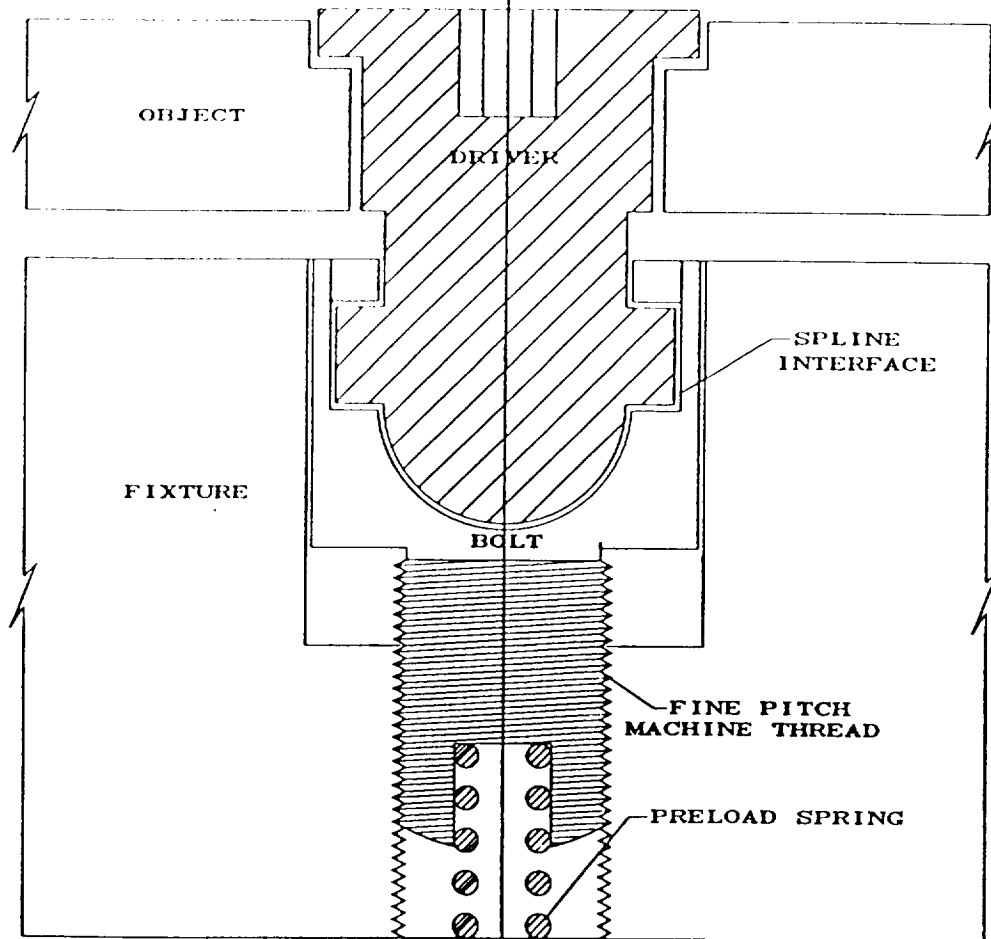


Figure 2. Present NASA Payload Fastener.



a. LOCATION OF SPLINE INTERFACE



b. SPLINE-LOCKING SCREW

Figure 3. Evolution of the Spline-Locking Screw.

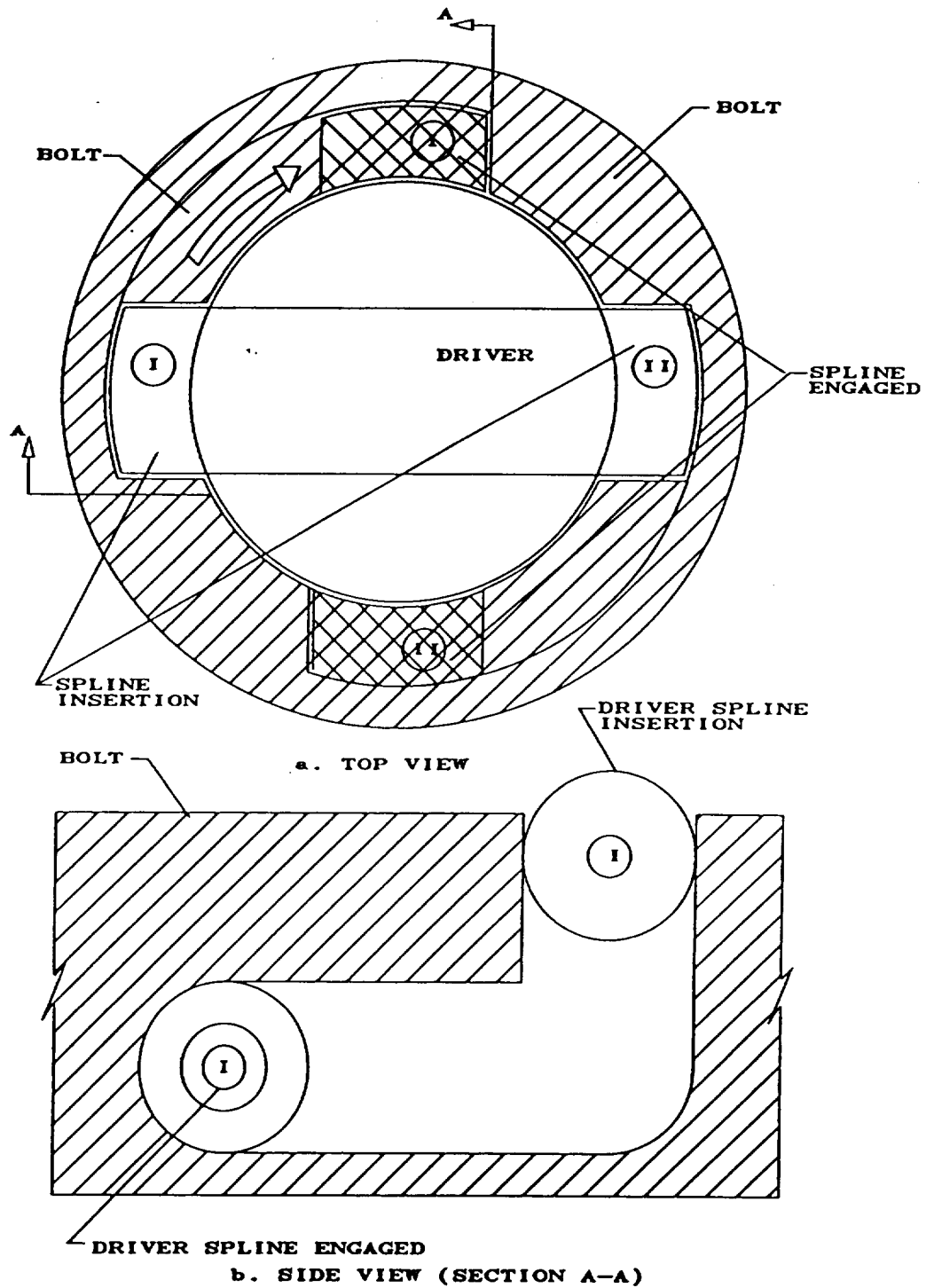


Figure 4. Spline-Locking Principle.

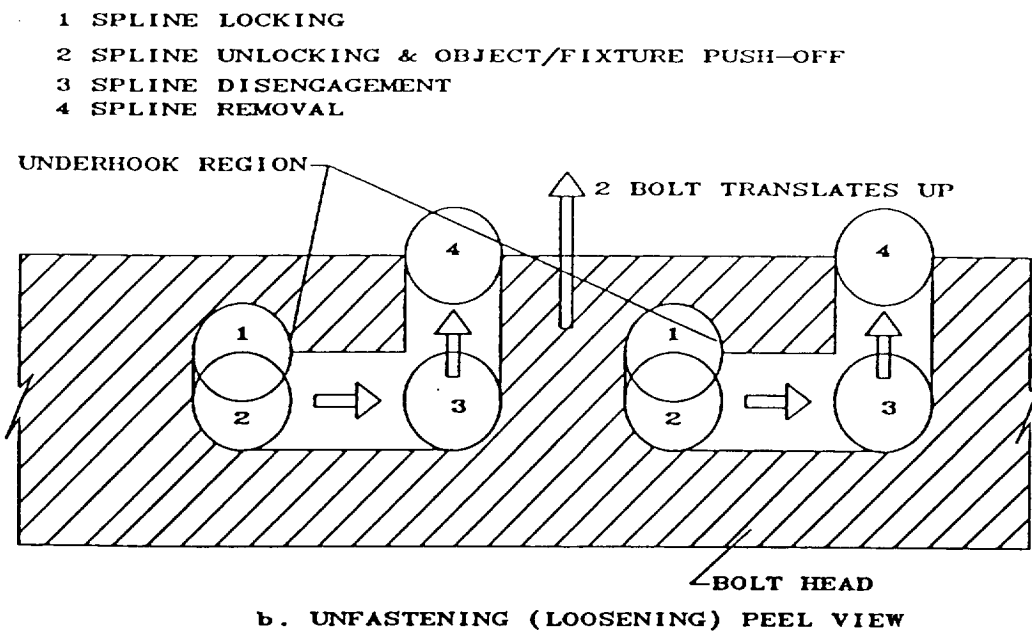
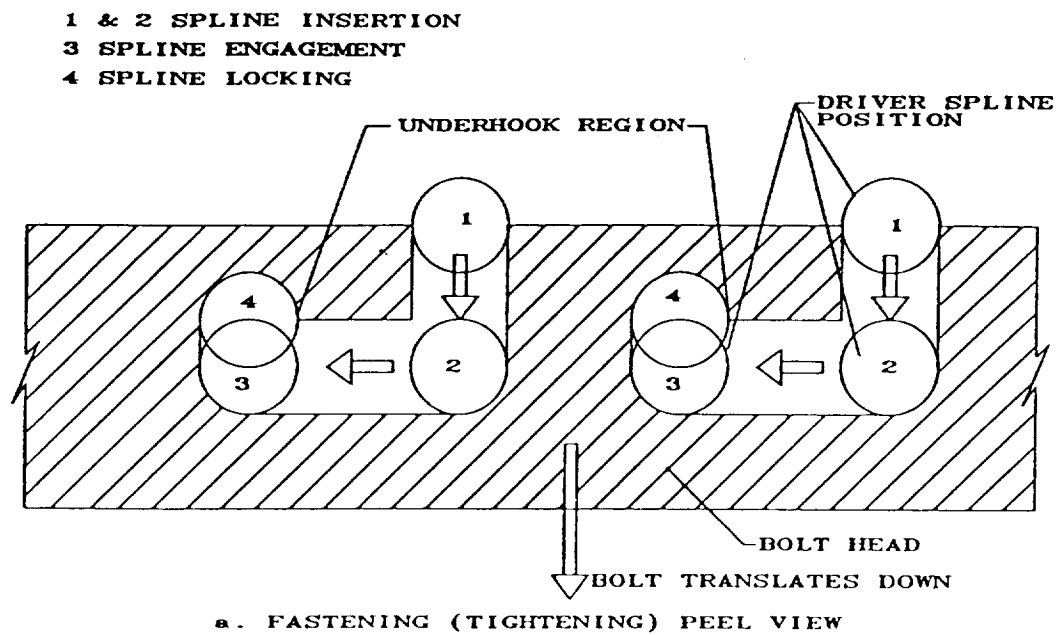


Figure 5. Relative Motions Between Driver and Bolt Splines.

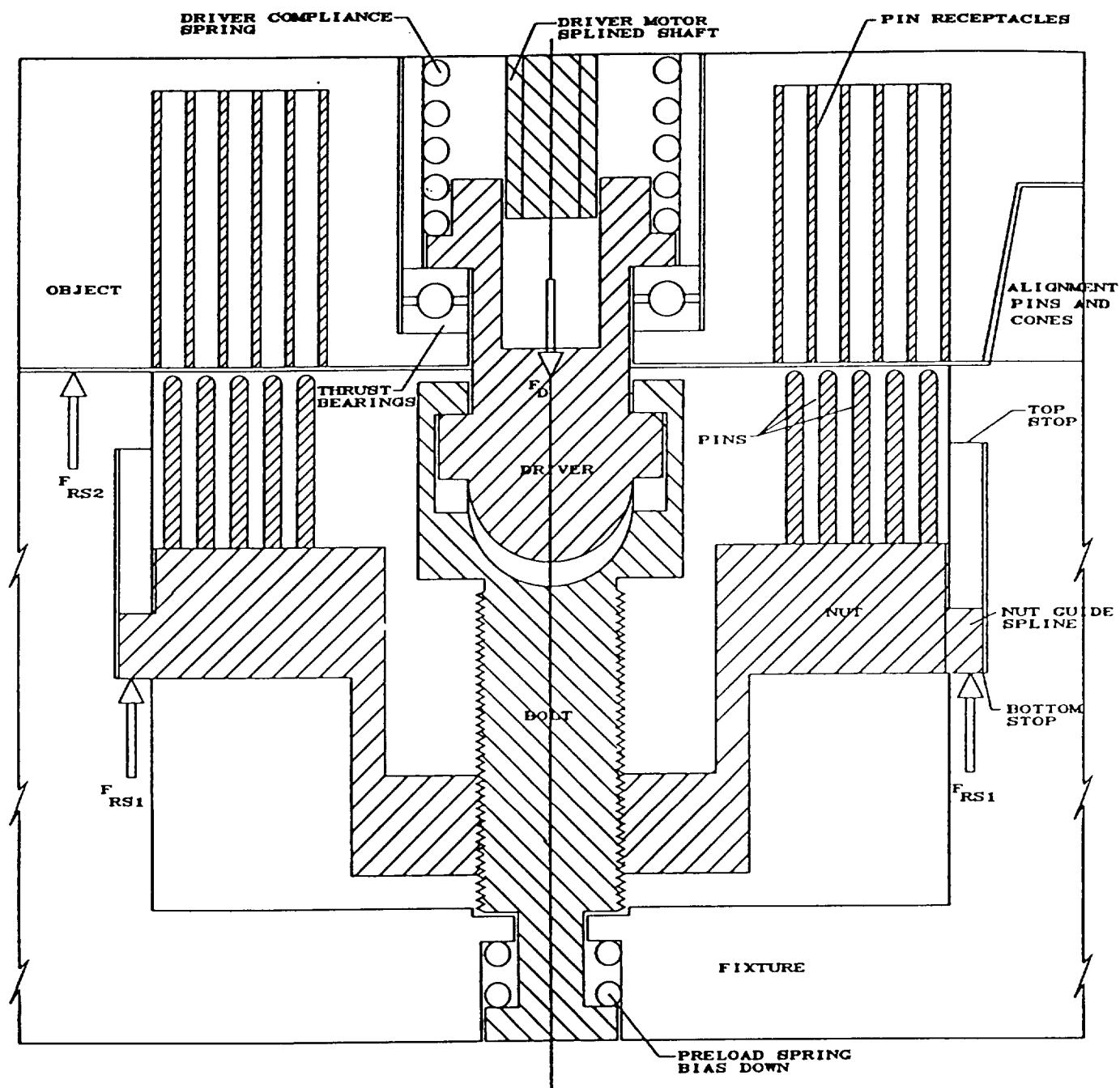


Figure 6. Spline-Locking Screw with Electrical Connectors.

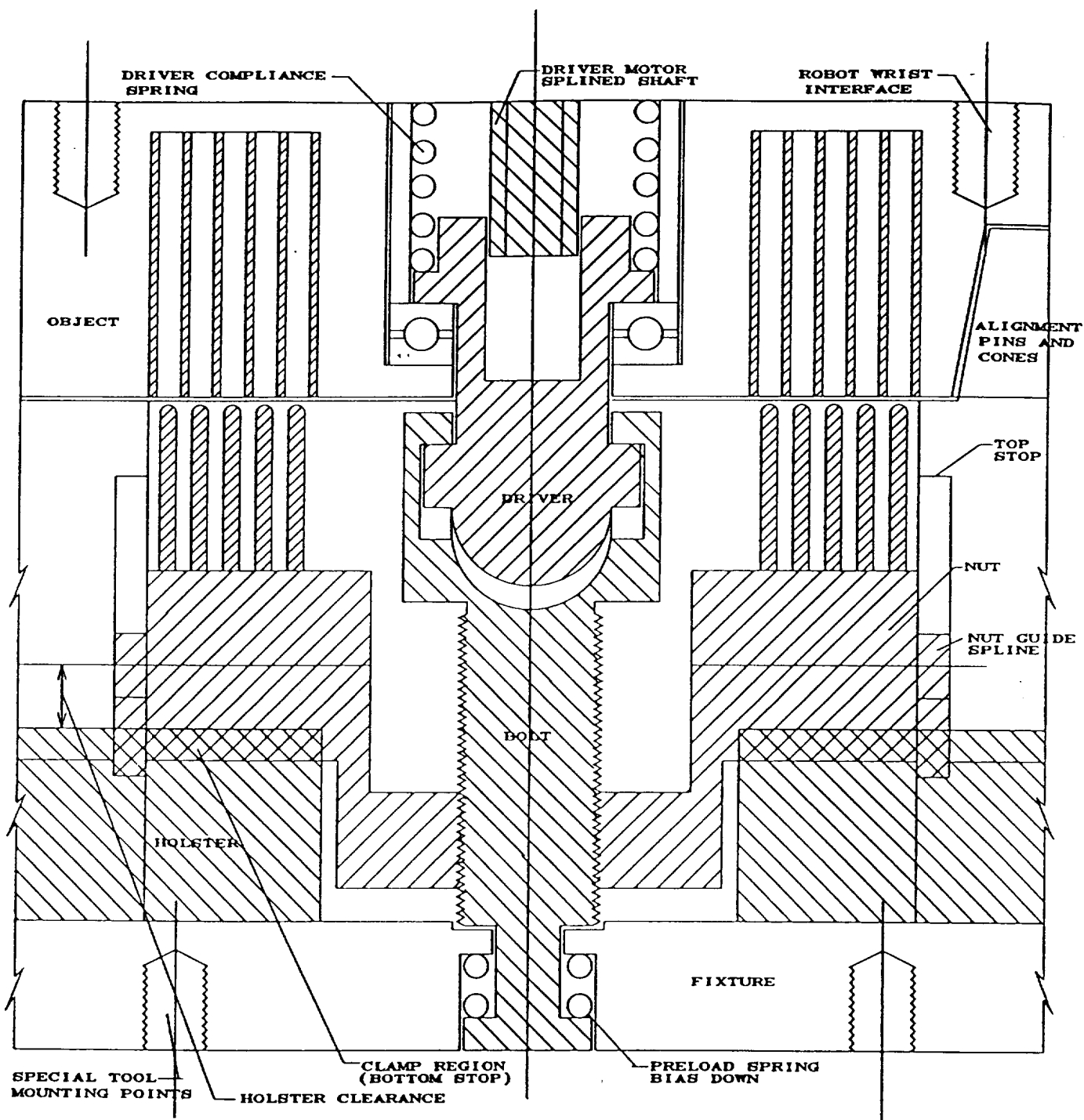


Figure 7. Special Tool Interface and Autochanger.

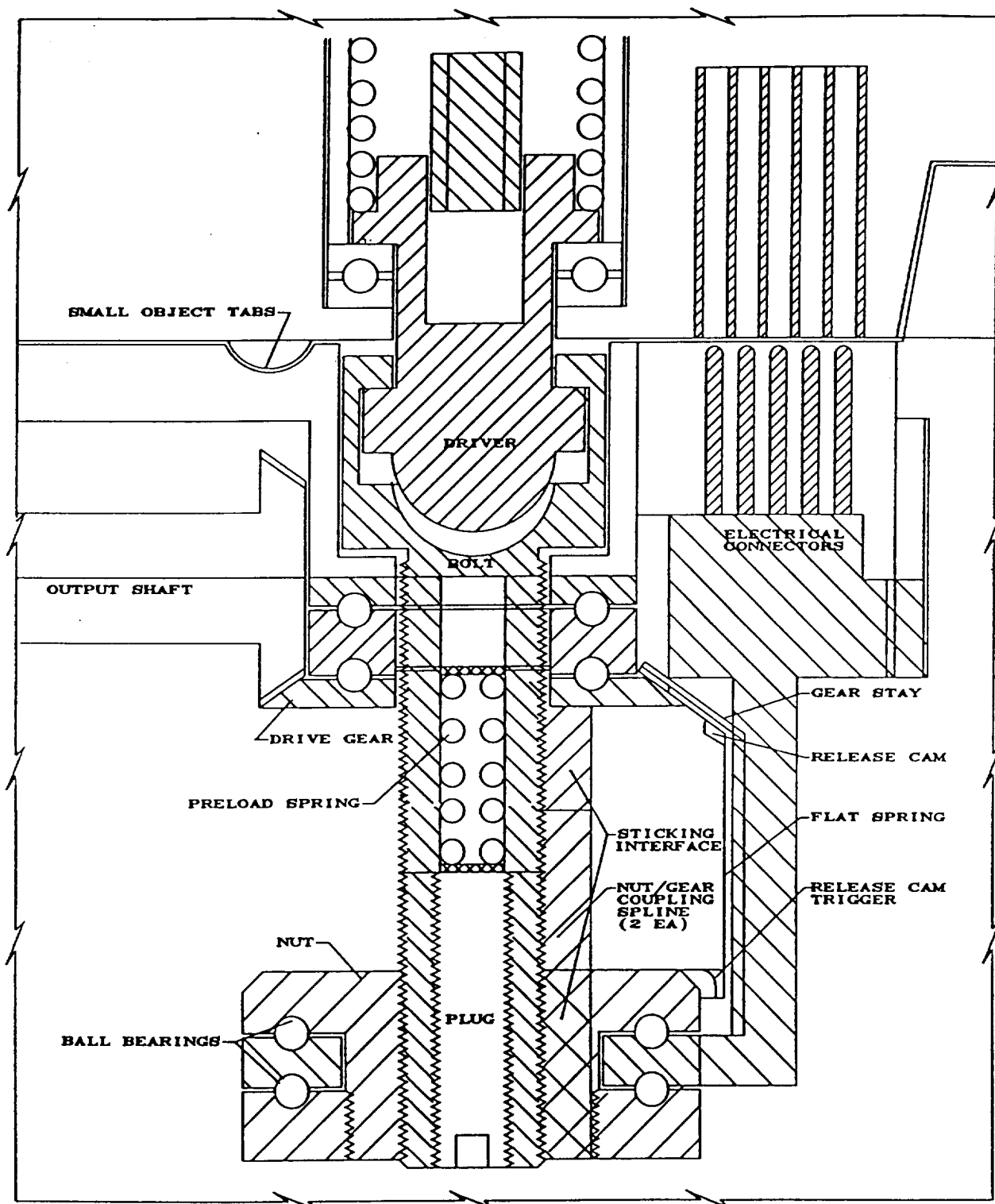


Figure 8. Spline Screw Continuous Drive with Connectors.

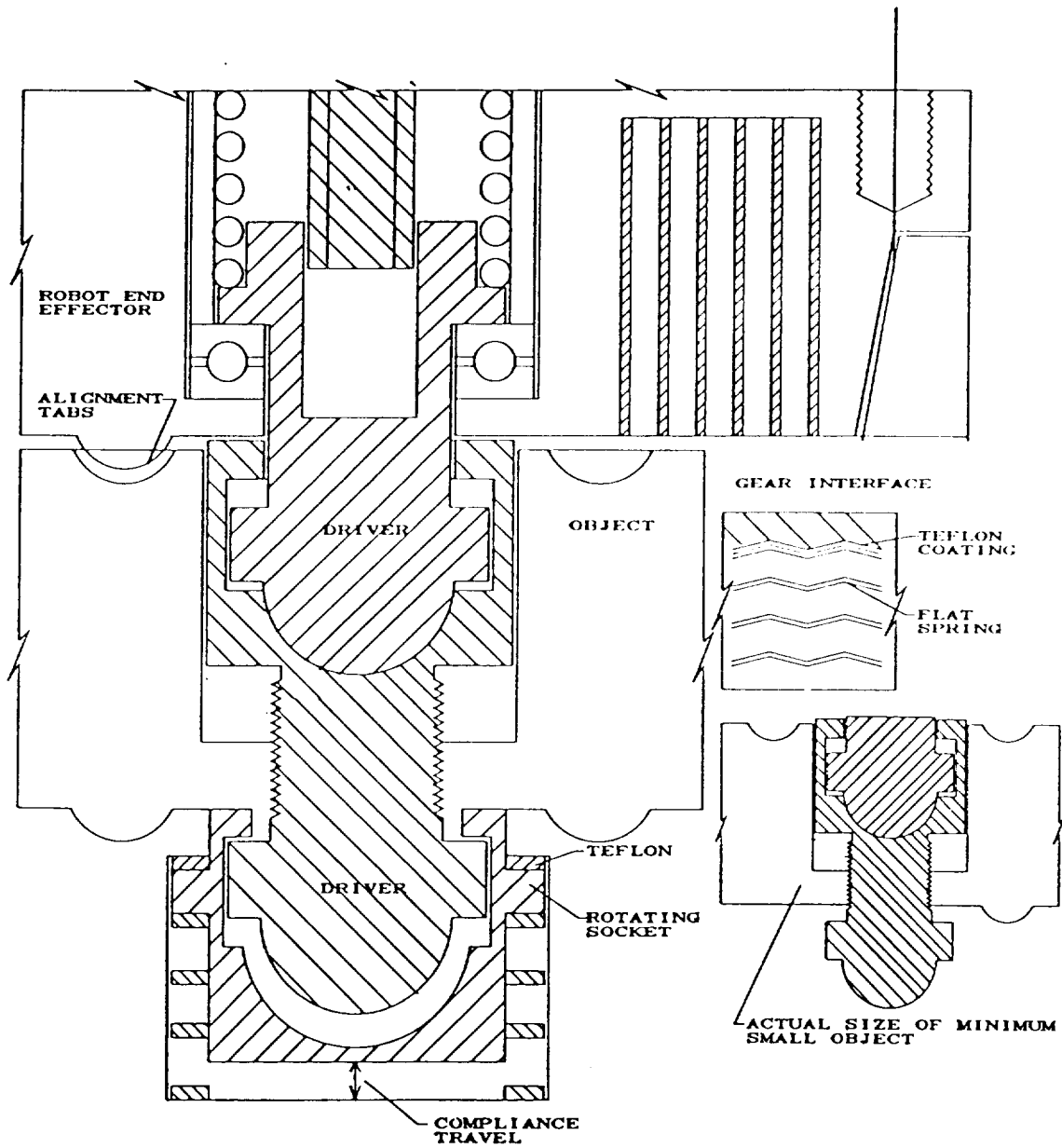


Figure 9. Small Object Fastening.

**Modular Antenna Pointing System
for the
Explorer Platform Satellite**

James Andrus* and Ed Korzeniowski*

ABSTRACT

This paper describes a Modular Antenna Pointing System (MAPS), designed for on-orbit servicing and on-orbit exchange. The MAPS provides a data link between the Explorer Platform (EP) satellite and the Tracking and Data Relay Satellite (TDRS). The MAPS consists of a two-axis gimbal set used to position a High Gain Antenna (HGA) toward TDRS, system control electronics, and an extendable mast. The system has been qualified and integrated with the EP satellite for an April 1992 launch.

INTRODUCTION

The MAPS was developed under contract with the EP systems contractor, Fairchild Space Company, who is under contract to NASA's Goddard Space Flight Center. Figure 1 shows the MAPS and the EP satellite. Mission life is 10 years and the EP is one of the first satellites designed for on-orbit servicing and on-orbit payload exchange using the Shuttle. The first EP science mission is the Extreme Ultraviolet Experiment (EUVE), which is being developed by the University of California at Berkeley. The EUVE experiment will study hot white dwarfs, coronas, binary stars, quasars, and pulsars. Additional proposals for follow-on missions are currently being evaluated by NASA. Experimental data from the EUVE will be stored in a spacecraft buffer and relayed to Earth via the MAPS high-gain antenna. Launch is scheduled for April 1992 from Kennedy Space Center on a Delta launch vehicle.

*Honeywell Inc., Satellite Systems Operation; Glendale, Arizona

MAPS DESIGN DESCRIPTION

System Design

The MAPS, shown in Figure 1, provides for deployment and steering of an HGA used for communication between the EP satellite and Earth via the TDRS satellite. The system consists of a spacecraft interface, Mast Deployment and Retraction Assembly (MDRA), Two Axis Gimbal (TAG) assembly, interface and control electronics, and the antenna. Figure 2 lists the major components of these subassemblies.

Prior to launch, the antenna mast is fully retracted into the canister and locked to protect the antenna and to conserve spacecraft volume during launch. The antenna mast is deployed approximately 1 m away from the spacecraft for operation in space. Once deployed, the gimbals are actuated to point the antenna toward TDRS as required. The MAPS requirements and measured performance are summarized in Table 1.

The functional diagram of Figure 3 includes the major components of the MAPS and their interconnection. Redundant Remote Interface Units (RIUs), designed by Fairchild Space Company, provide the command/telemetry interface between the spacecraft and the MAPS. The RIUs communicate with Honeywell's Steering Control Electronics (SCE). Each SCE box controls gimbal positions and heaters. The MAPS design is derived from the Honeywell High Gain Antenna System (HGAS) design used for the Solar Maximum Mission (SMM). The SMM, launched in 1980, was inoperable from the start because of a failed fuse in the attitude control module. After on-orbit Shuttle refurbishment in 1984, the HGAS was deployed and worked perfectly. This heritage configuration was selected to reduce development costs by using flight-proven designs.

For satellite communications, RF signals are transmitted and received through the antenna. In order to effectively perform this task, the gimbals are controlled to correctly point the antenna. Figure 4 illustrates a simplified block diagram of the gimbal control system. The two-axis gimbal set consists of Y and Z gimbals (Y gimbal closest to antenna), in accordance with the MAPS coordinate frame. The control system for each gimbal includes a command generator and a position control loop.

The command generator directs the gimbals to steer within their $\pm 110^\circ$ range, at either 1.18 or 44.8°/s, with a position command resolution of 0.215°. Both the desired slew rate and position command are selected by the user and are reflected back as telemetry.

The position loop is designed for a 0.8-Hz bandwidth. To meet the 0.7° system pointing accuracy at either steering rate, the bandwidth must be greater than 0.5 Hz. To meet the required stability margins, the maximum bandwidth is 1 Hz, based on the mast's first-mode frequency of 6.25 Hz and 2% damping. The difference between the position command and position feedback passes through the position loop compensation network to create a current command. Since current is proportional to torque, the position compensation determines the torque required to move the gimbals to their commanded location in a controlled manner. Two compensation paths lead from the position feedback signal to derive the current command. The first is the position compensation path, which is used under normal gimbaling operation. The second path is a rate dampening path, which limits the gimbal rates to approximately 3°/s. Since the rotational inertia seen by the Z gimbal is a function of the Y gimbal angle, feedback from the Y-axis resolver also feeds the Z axis inertia compensation network. Position feedback is derived from one-speed resolvers located within each gimbal assembly. The resolvers also provide position information required for torque motor commutation.

The current command, generated through the position compensation network, is scaled by commutation electronics to ensure that the current is correctly distributed through the sine and cosine torque motor windings for a given electrical angle. Each torque motor winding has its own commutation network and current loop. The output of the commutation electronics is the input to the current loop. The current loop bandwidths are approximately 100 Hz to linearize the torque motors for the position-loop compensation. Eight-kHz Pulse Width Modulated (PWM) drivers efficiently deliver current through the torque motor windings. The current loop is scaled for a minimum full-scale torque output of 0.14 N-m (20 oz-in).

The MDRA deploy and retract sequences are initiated by a command sequence generated through an active SCE box. Under normal operation, a deploy/retract sequence continues until the SCE automatically shuts off the selected MDRA motor upon receiving full deploy-

ment or retraction status. If required, the deploy/retract sequence may be halted by commanding a deploy/retract disable through the SCE.

The MAPS contains redundant heaters to maintain component temperatures within operational range for cold extremes in the SCEs, on the MDRA gear-train housing, and in each of the gimbal assemblies. Thermostats, in series with the heater drive circuits, are normally active only when closed. Thermostat closure is set at approximately 10°C for the SCEs and MDRA elements, and at -4°C for the gimbal elements. Heater bypass commands are available to drive the heating elements independent of the thermostat state.

Mechanical Design

The MAPS mechanical system, Figure 1, is composed of an extendable mast, a canister, electronics mounting plate, and spacecraft interface plate for structure, and two antenna drive assemblies (gimbals). The extendable mast, supplied by AEC-Able Engineering, is 47 cm (18.5 in.) OD and deploys to 1.52 m (5 ft) long. When retracted, the mast is 8.9 cm (3.5 in.) high, and is stowed in the canister for launch and for Shuttle servicing and payload exchange. The gimbals and the antenna are supported by three-point launch elastomeric Antenna Support Assemblies (ASA) that are preloaded by the mast during stowage. The mast and deploy/retract mechanism are described in reference 1.

The canister is constructed of a corrugated 7075 aluminum sandwich plate and the electronics mounting plate is made from aluminum honeycomb to save weight. The spacecraft interface plate is made from hogged-out aluminum, and provides both the structural and electrical interface to the spacecraft. The structural interface is via three Extravehicular Activity (EVA) 3/8-in. external hex bolts that provide a cup/cone installation alignment feature and, when torqued to 40.7 N-m (30 ft-lb), provide the necessary structural path for launch and on-orbit stiffness. The electrical interface is provided by two Module Interface Connectors (MIC), supplied by G&H Technologies, which float on the spacecraft side to allow for misalignment. Electrical connection is made when the EVA bolts are torqued. Both the MICs and the EVA bolts were supplied by Fairchild.

Gimbal Mechanism Description

The gimbals are based on the SMM and Space Telescope gimbal flight designs. The most critical design consideration is drag torque, since torque motor capability is 0.14 N-m (20 in.-oz) max. Contributors to drag torque are the magnetics, flex capsule, bearing preload, lubrication of the bearings and sliding interfaces, loads induced by temperature change, and thermal gradients across the bearings. Measured drag torque due to all of these effects was less than 0.08 N-m (12 in.-oz) at worst-case cold conditions. Each gimbal provides $\pm 110^\circ$ range of motion with an overall system pointing accuracy $\leq 0.7^\circ$. The gimbals are optimized for low power, weight (10.1 kg), drag torque (≈ 0.014 N-m nominal), and torque ripple. Figure 5 is a cutaway cross-section of a single gimbal and Figure 6 is a view of the two-axis flight gimbal pair installed on the mast during system functional testing. Each gimbal contains redundant brushless DC permanent magnet torque motors and redundant single-speed resolvers. The torque motor is a two-phase, continuously commutated, four-pole type with completely enclosed samarium-cobalt magnet material; motor weight: 0.59 kg per motor (two required per assembly); torque ripple: $<5\%$, 0 to peak. This approach was selected to reduce vibrations caused by the MAPS to the spacecraft. The resolvers are single-speed, sine-cosine and are used for commutation and position feedback; resolver weight: <0.81 kg; accuracy: ± 4 arcmin; zero stability: ± 1 arcmin. Both the motors and resolvers were supplied by Honeywell Electrocomponents in Durham, North Carolina.

The gimbal housing is aluminum and the shaft is titanium, supported by Barden (2.7-cm ID, 3.8-cm OD) duplex angular contact, DF-mounted bearing pairs with Teflon® toroid ball separators. Bearing material was selected as 52100 steel with 52100 balls based on volume and load requirements, since this material combination has the highest load capacity with minimum size. The bearing pairs are both preloaded to 6.8 kg (15 lb); one pair is fixed, while the other is allowed to float along the rotational axis to compensate for temperature changes. Bearing cartridge material is titanium with the floating-side bearing housing made of 52100 to match the bearing thermal coefficients. The sliding interface consists of silver plating the 52100, with Apiezone H grease applied on the interface. This surface treatment and lubrication was selected to preclude galling and stiction, which could load the bearing pairs and increase drag torque. The bearings are lubricated with KG-80 oil; Micro-well reservoirs and labyrinth seals are used to

meet the life requirement. Lubricant selection was based on space-proven heritage on both the Solar Maximum Mission and Space Telescope programs. Power and telemetry are passed through a wire-wrap flex capsule, and RF is passed through a noncontacting rotary joint. The gimbals also contain redundant heaters, thermistors, and thermostats (set at -4°C), which maintain gimbal temperature above -38°C .

The gimbals were subjected to both acceptance and protoflight testing, including alignment, RF, weight and center of gravity, drag torque, random vibration, and Thermal Vacuum (TV) testing. System-level testing with the electronics included a repeat of functional, random vibration, and TV testing.

Electrical Design

The major electrical subassemblies of the MAPS include SCEs, RIUs, and Mast Deploy/Retract Assembly (MDRA) electronics. Redundant SCEs are the central control modules for the MAPS. An active SCE box provides control for the two-axis gimbal assembly, system heaters, and the mast deploy/retract mechanism. The selected SCE communicates with the spacecraft computer via either of the MAPS RIU modules. The MDRA electronics work in conjunction with the active SCE, providing MDRA telemetry and deploy-motor direction control.

Each SCE contains ten functional modules, as shown in Figure 7, each consisting of two Circuit Card Assemblies (CCAs) mounted to a common module frame. The module frame provides structural support and thermal heat-sinking for the CCAs. These modules also provide structural support for the SCE chassis frame when installed. An internal SCE harness provides electrical connections between modules and to six external interface connectors.

Figure 8 shows the electronic CCA functional partitioning for each SCE. The CCA functions are separated into power conditioning electronics, interface and data distribution electronics, and MAPS control electronics. Power conditioning modules consist of turn-on/off electronics, EMI electronics, and a switch-mode secondary power supply that provides the SCE with ± 15 VDC, 5 VDC, ± 6 VDC, and 28 VDC for relays. Interface and data distribution electronics interface with the RIUs, and condition the command and telemetry signals to and from the MAPS control electronics. The MAPS control electronics implement

position and current control laws to control the gimbals, condition feedback and telemetry sensor signals, and drive the MAPS heaters and MDRA motors, as required, for thermal control and mast deploy/retract. Gimbal overcurrent protection is included to prevent full current from being driven into the gimbal motors for more than 65 s.

SYSTEM PERFORMANCE

The MAPS has been flight qualified and performs as outlined in Table 1. The flight qualification program included in-process testing, SCE/gimbal testing, and integrated MAPS testing.

Honeywell performed component-level tests for each SCE and gimbal assembly; Fairchild performed RIU testing; AEC-Able Engineering did the MDRA testing; and General Electric completed the antenna testing. In-process tests included CCA testing, ambient functional testing, vibration (workmanship levels) testing, and thermal or TV testing.

Flight SCEs and gimbals were mated for the first time during SCE/gimbal testing. Their combined performance was tested under ambient and TV conditions. The specified temperatures for TV testing were +45 and -5°C. The SCE/gimbal pointing calibrations were established and verified over temperature. Telemetry from the SCE is accurate to within 0.3° over the 110° gimbal range, and gimbal pointing accuracy (command angle versus actual mechanical angle) is within 0.49°. Pointing performance was tested by calibrating each resolver relative to a precision angular-indexing device using an Angle Position Indicator (API), accurate to 0.005°, to read the incremental angles. The same API was used throughout testing to verify pointing accuracy.

Integrated MAPS testing included ambient functional tests at Honeywell and NASA-Goddard, vibration testing at Wyle Laboratories and NASA-Goddard, and system TV and EMI/EMC testing at NASA-Goddard. Integrated functional testing included verification of deploy/retract operation, gimbal pointing performance, heater/thermostat operation, and override functions. Figures 6 and 9 are photographs of the MAPS during integrated testing at Honeywell.

The MAPS has been integrated into the EP spacecraft. Ambient functional, TV, vibration, and acoustic testing were performed at the spacecraft level.

PROBLEMS RESOLVED

Minimizing drag torque at the worst-case cold temperature proved to be a difficult challenge, since the temperature range was beyond those of the existing design. Torque spikes were discovered each time the gimbals were exposed to hot qualification temperatures. The torque spikes looked like a characteristic Brinelling, in this case an outer race, but the problem disappeared with time. Although these torque spikes did not affect system performance, disassembly was necessary to determine if permanent damage had occurred or if the exposure affected life. After complete gimbal disassembly, no evidence of Brinelling could be found. The cause of the problem was never determined, but it is speculated that the Teflon® toroids somehow took a set during the exposure and returned to their original geometry with time.

A ball-blocking phenomenon had been discovered on the Space Telescope program and was corrected by changing the ball curvature ratio and changing from phenolic retainers to Teflon® toroid ball separators. A similar-looking problem was detected soon after initial gimbal build. The problem was traced to the flex capsule after meticulous piece-by-piece disassembly. A critical internal radius, although specified on the drawing, was in reality not referenced correctly to the right locations and therefore allowed the part to pass 100% inspection with a larger radius. The larger radius allowed the flex capsule to cock, causing the drag torque to increase when the gimbal was rotated toward the end-of-travel stops. This problem had not been experienced until a new vendor was selected to supply the flex capsule housing. The lesson learned was that all critical tolerances and callouts on old drawings should be reviewed at the start of any new program. The lack of problems with purchased parts on past programs does not preclude problems on a new program, even when the parts are purchased based on the same drawing.

Another problem was in the thermal isolation interface. Thermal isolation washers made from G-11 are used to thermally isolate the gimbals from antenna and mast. Washers also establish alignment, and are bonded to the yoke during machining and are precision machined to the shaft bore diameter. One of the washers was accidentally knocked off during TV testing and alignment was lost. The washer was rebonded

onto the gimbal and a method to reestablish alignment was developed. Future designs will include better support for the washers.

The RF cable is the most critical component, in that the system's main function is to transmit and receive data. The Voltage Standing Wave Ratio (VSWR) and insertion-loss requirements are tight; small changes due to nicks in the cable have a significant effect. Damage to the cable was caused by bending the cable out of the way during assembly and test. In one instance, the MIC connector backshell crushed the cable. The lesson learned is to have the cable supplier involved in the design from the beginning and to ensure that everyone working on the program understands how sensitive the cable is to handling, minimum bend radius, and routing adjacent to sharp edges. Armor coverings were also added to protect the cable and an additional connector was added to facilitate assembly.

Development of the MAPS was more difficult and costly than original estimates, with lack of engineering development hardware the most dominant reason. When engineering hardware was available as a development tool, its flight equivalent was integrated and tested with few or no errors. Modifications required for the MAPS usually occurred where an engineering development equivalent was not available. The schedule and cost penalties associated with troubleshooting flight hardware, relative to engineering hardware, were high. Engineering hardware, closely replicating flight hardware, is recommended for all new development.

RECOMMENDATIONS FOR FUTURE SYSTEMS

The MAPS was conceived by NASA-Goddard and Honeywell as a heritage development from the SMM HGAS program to contain cost, which gave little opportunity for improving system performance. However, newer technology might have improved performance and reduced cost. Although this is a difficult trade-off to make, a trade study of technologies will be completed early in future programs. One such study and design is completed, as described in the next paragraph.

Future Design

The next-generation gimbal set, the Antenna Control Gimbal (ACG), was designed and built for NASA-Goddard. The two-gimbal set, Figure 10, weighs less than 9 kg, including electronics, versus

approximately 23 kg for the MAPS equivalent hardware. This design incorporates lessons learned and features a closed-loop pointing control with integrated electronics, a high-data-rate fiber-optic communications link, and both S- and K-band data links. Electronics piece parts are reduced 10 to 1 over the analog design by using hybrids and processor-based digital control. Also, the design was optimized to facilitate assembly and test. Major subassemblies were identified and designed as separate modules that can be assembled and tested at the module level before system assembly. This allows flexibility, in that any module can be repaired or replaced with another completed and tested module, thereby speeding up the assembly process. Figure 11 shows a photograph of the shaft module.

ACKNOWLEDGEMENTS

The design presented in this paper was performed under contract to NASA-Goddard Space Flight Center, Greenbelt, Maryland, and Fairchild Space Company, Germantown, Maryland. The authors wish to thank both Fairchild Space Company and NASA-Goddard for their permission to publish this paper and to the many engineers, technicians, assemblers, and designers at Honeywell who contributed to program success.

Reference 1: "Relatchable Launch Restraint Mechanism For Deployable Booms," by Robert M. Warden, AEC-Able Engineering, presented in the 24th Aerospace Mechanisms Symposium.

Table 1. System Requirements Versus Measured Performance

Parameter	Specification	Performance
Pointing		
• Range	$\pm 110^\circ$	$\pm 112 \pm 0.5^\circ$ to stops
• Accuracy	$\pm 0.71^\circ$	$\pm 0.69^\circ$ (worst case)
Peak Rates		
• Steering	1.2°/min	1.18°/min
• Slewing	45°/min	44.8°/min
Weight	<84.3 kg (185.5 lb)	84.0 kg
Power	<33 W average	21.4 W average
Voltage Range	21-35 VDC	21-35 VDC
Life	>3 yr	
Structural modes		
• Deployed	>7 Hz	6.25 Hz
• Stowed	>50 Hz, goal	80 Hz
RF Performance		
• Frequency	2106.4 \pm 20 MHz 2287.5 \pm 20 MHz	Band 1 Band 2
• VSWR	<1.5:1; <1.8:1	Band 1 (1.4:1); Band 2 (1.53:1)
• Return Loss		Band 1 (1.98) Band 2 (2.2)
Deployment/Retraction Time	<5.0 min	<7.8 min (worst case)
Temperature		
• Operating	-37° to 52°C (-35 to 125°F)	Tested
• Nonoperating	-40° to 71°C (-40 to 160°F)	
Launch Environments	Delta Launch Vehicle	Tested per vibration spectrum
Alignment	0.2°	S/C to Ant 0.102°

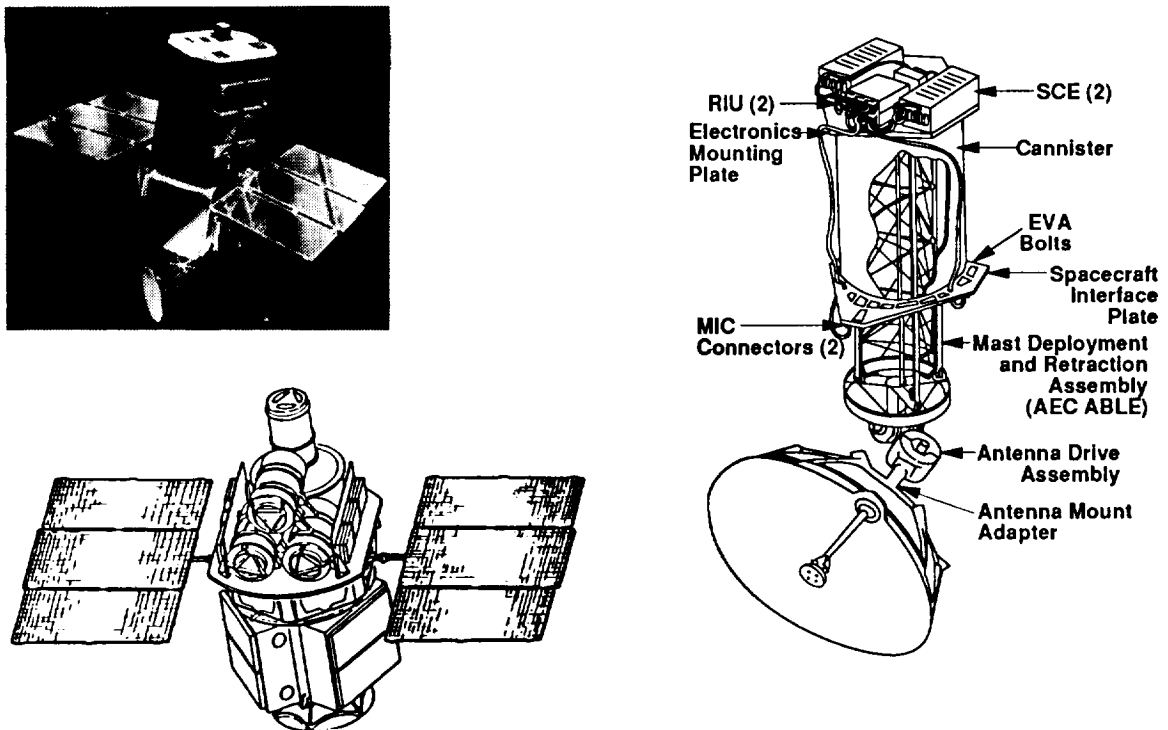


Figure 1. EP MAPS Antenna Pointing System

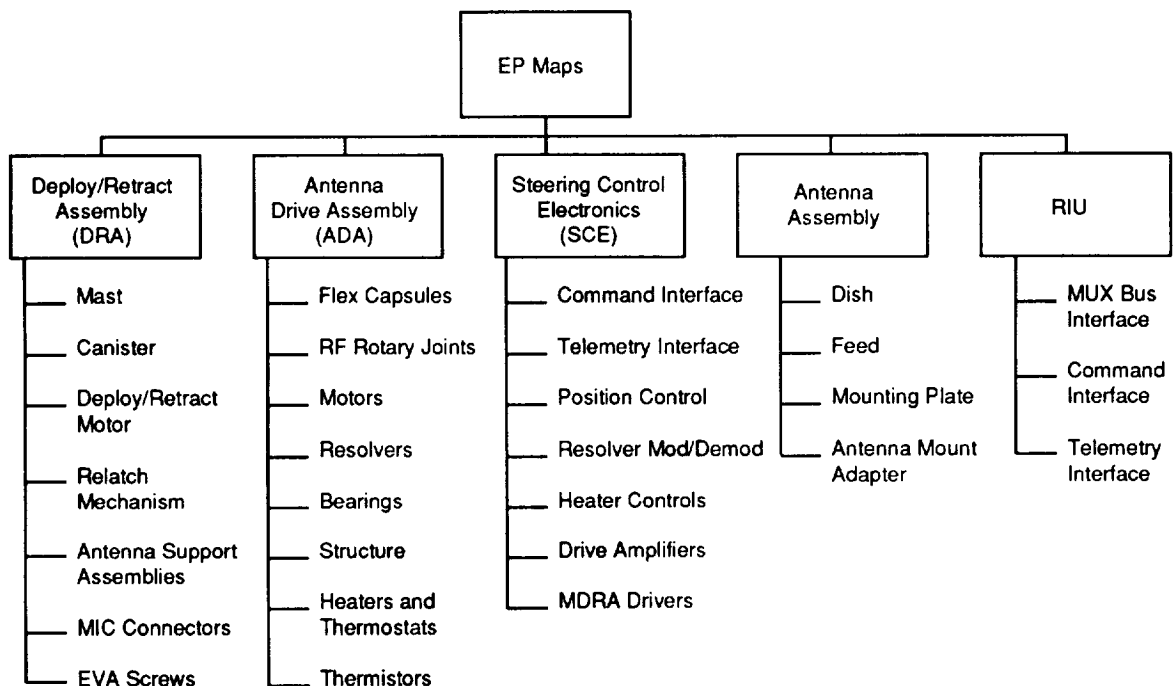


Figure 2. EP MAPS System Breakdown

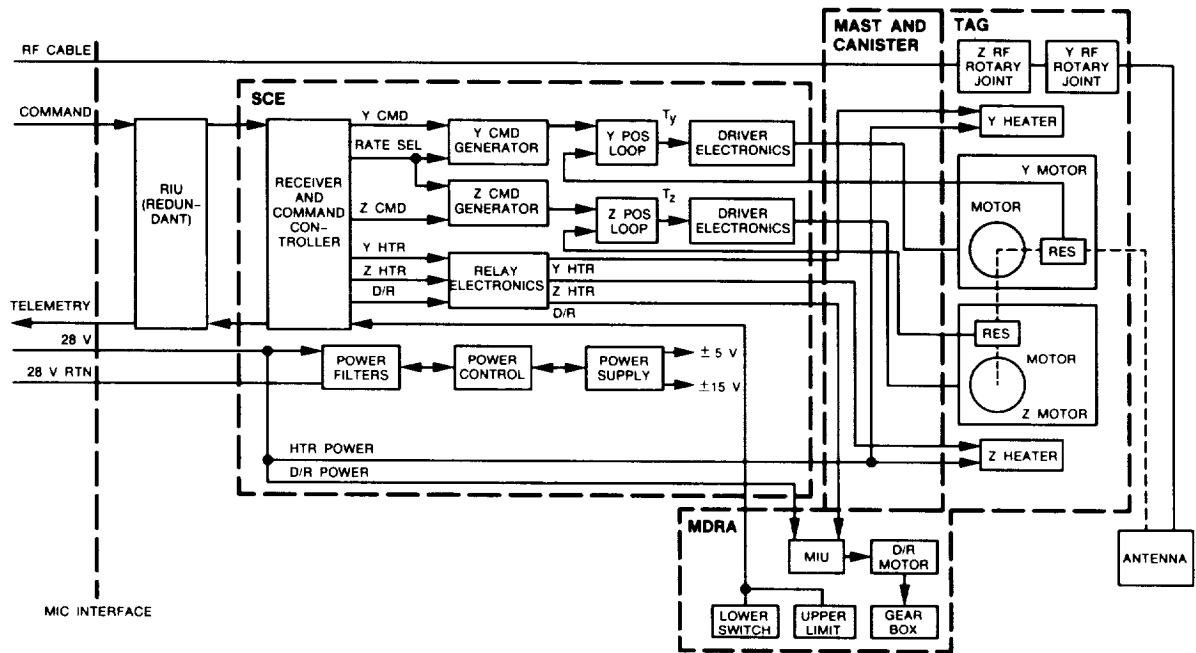


Figure 3. EP MAPS System Functional Block Diagram

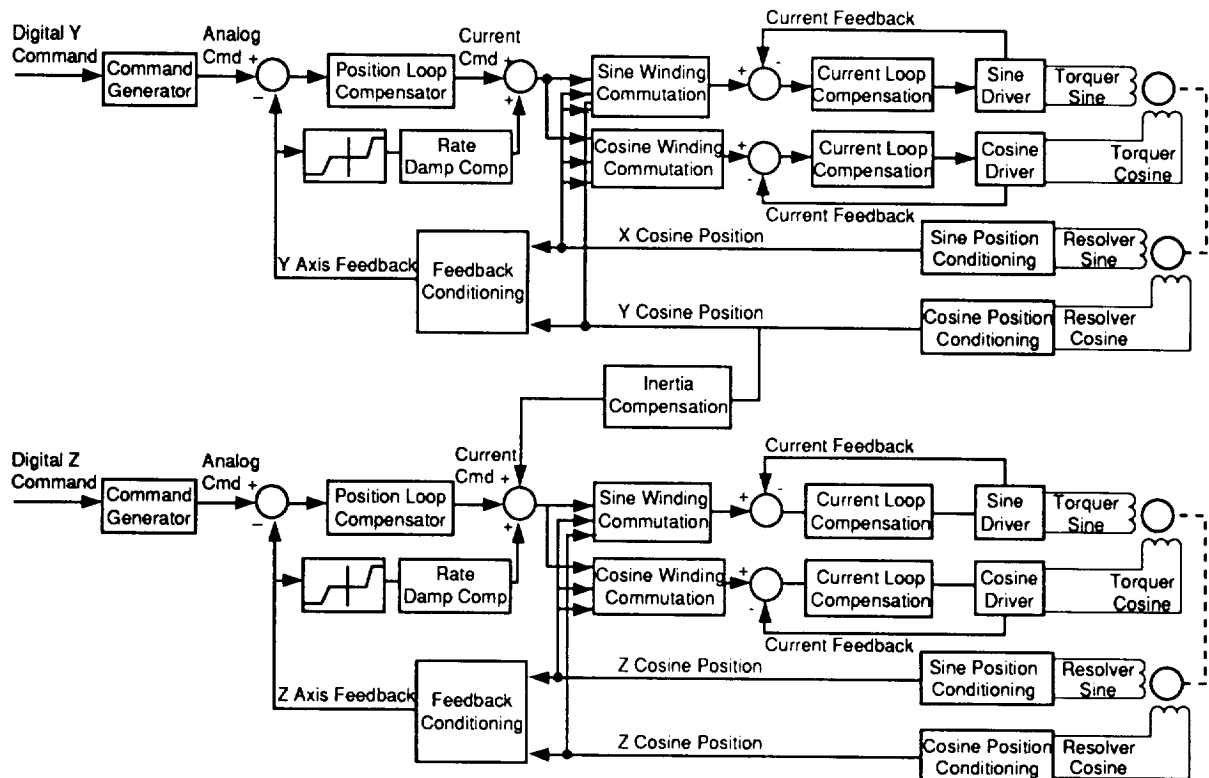


Figure 4. EP MAPS Gimbal Control System Block Diagram

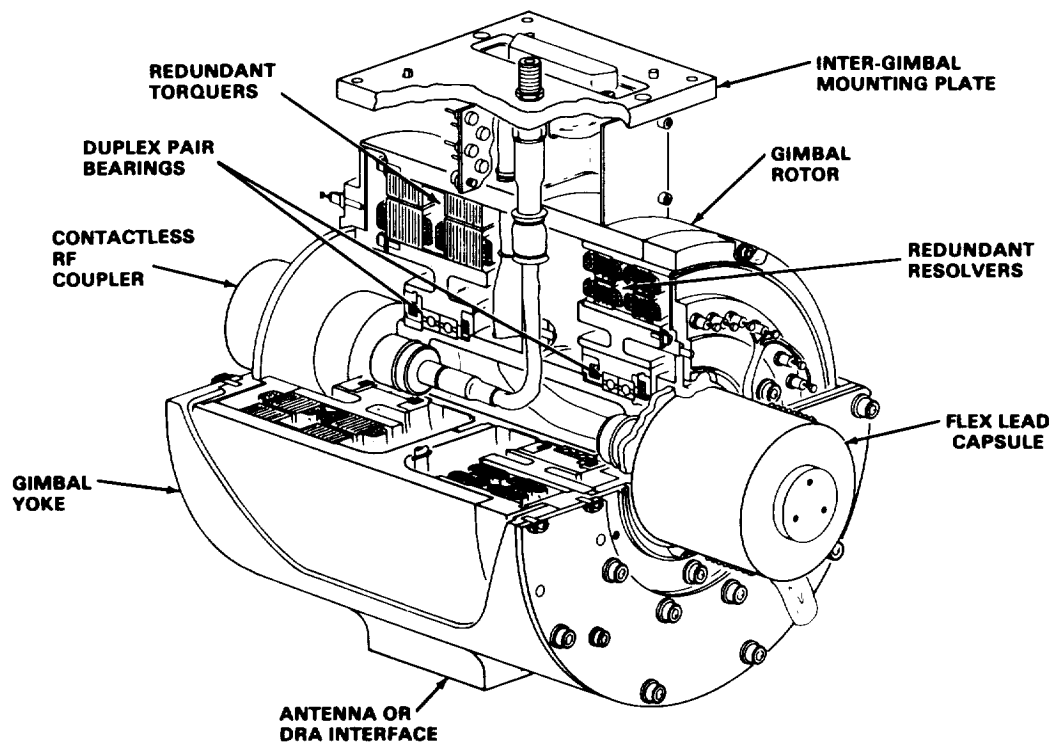


Figure 5. Gimbal Cross Section

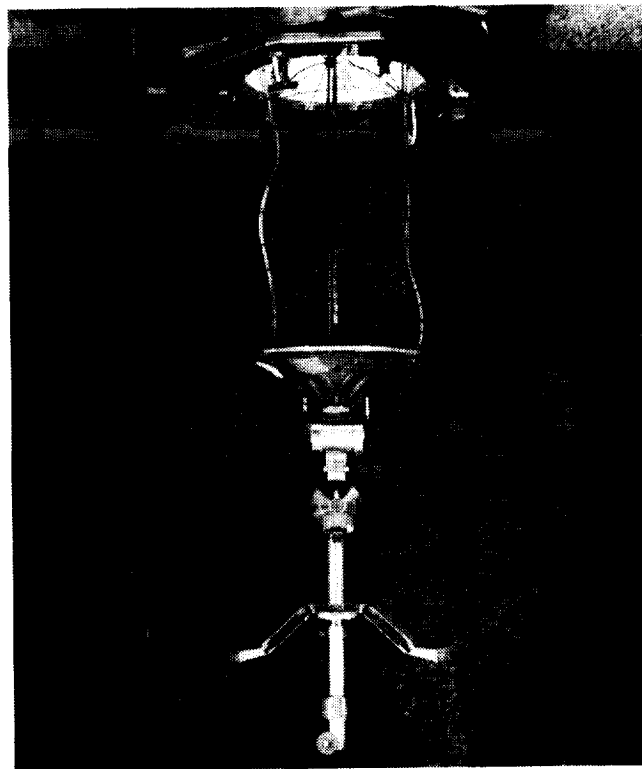


Figure 6. EP MAPS Mast and Gimbals During System Performance Test

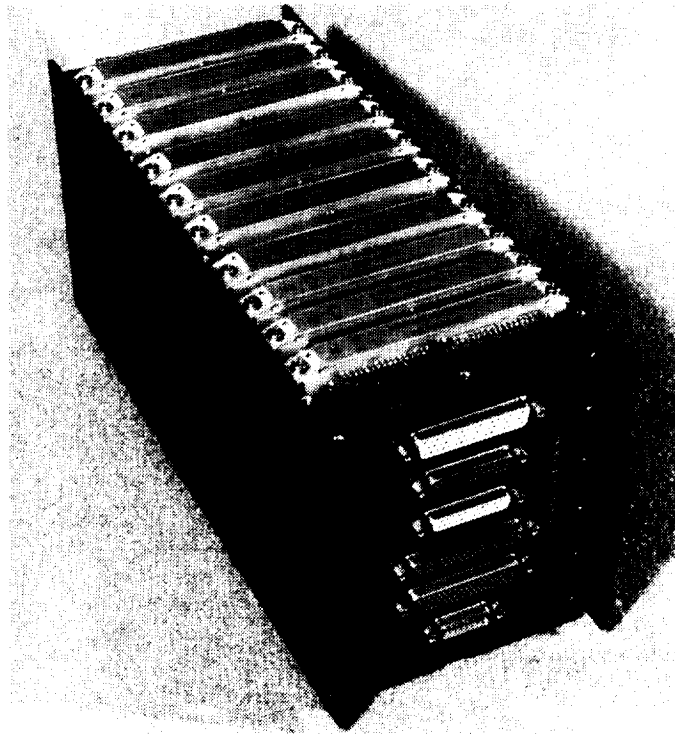


Figure 7. Steering Control Electronics Box

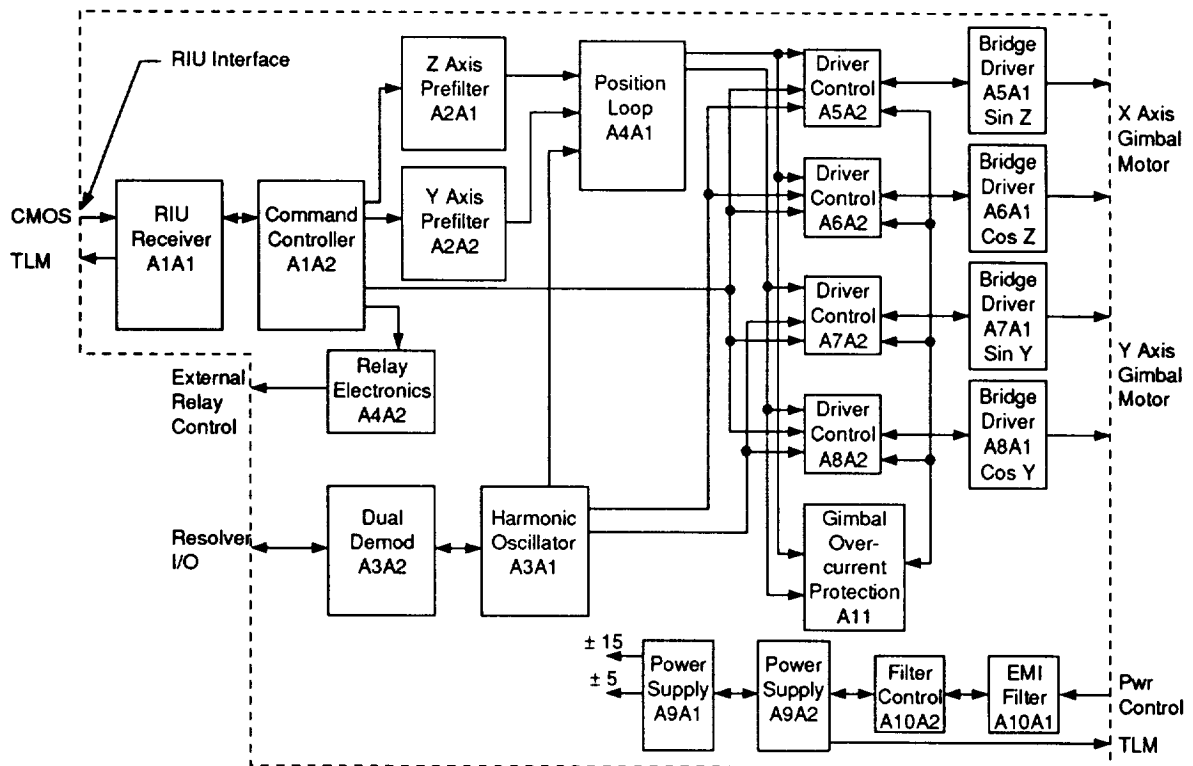


Figure 8. EP MAPS SCE Block Diagram

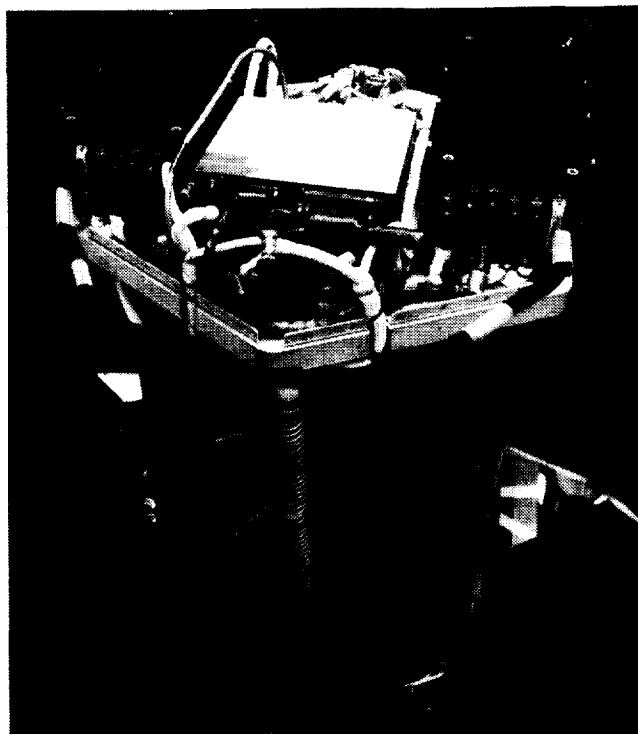


Figure 9. EP MAPS Electronics Mounting Plate

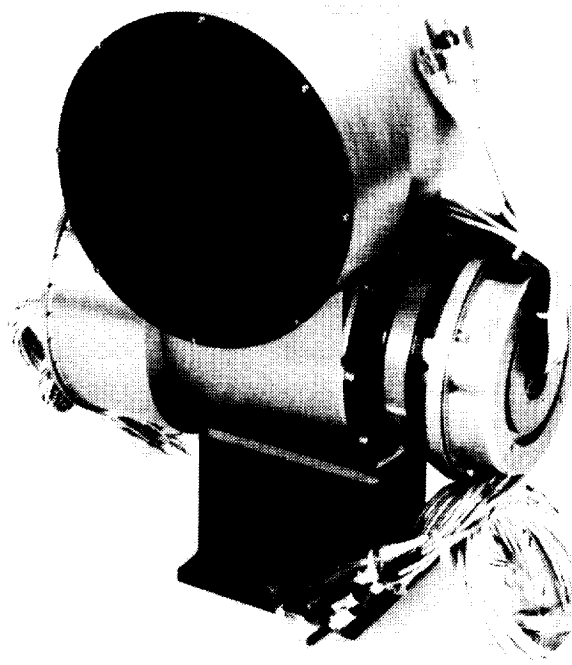


Figure 10. ACG Completed Assembly

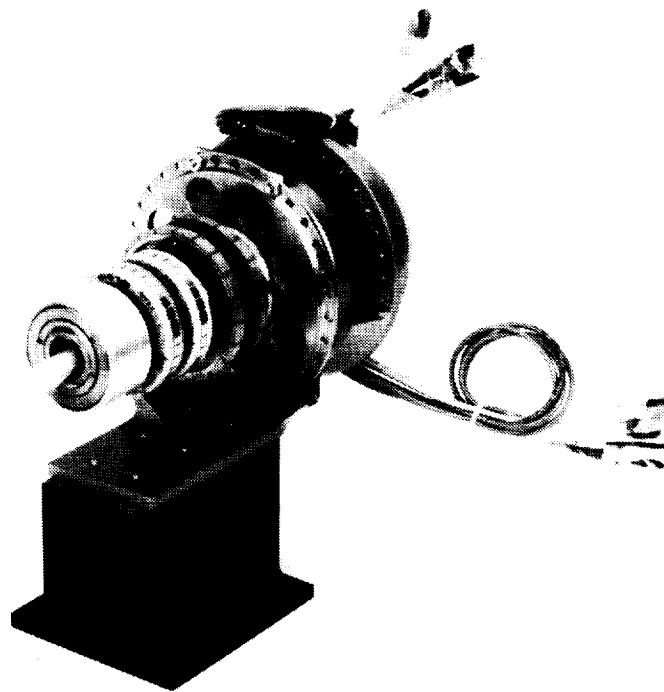


Figure 11. ACG Shaft Module

WEARING OF CRYOMECHANISMS AT 4K

Gérard LUCIANO*

ABSTRACT

Certain spaceborne optics include components that are designed to improve the instrument's performance. Where such mechanisms cannot be decoupled from the optical devices, pollution from the wear of those mechanisms must be minimized due to impossibility of in-flight, or even sometimes on-ground cleaning of optical devices.

AEROSPATIALE, who is responsible for the Optical Bench of the Infrared Camera to be flown on board the ISO spacecraft, have therefore been led to develop non-polluting mechanisms. Comparative tests were performed on several material couples, resulting in the choice of a satisfactory solution.

1. FOREWORD

Spaceborne observation in the infrared necessitates the design of cryogenic mechanisms governed by stringent operating requirements. One of the most exacting among those requirements is cleanliness, since image quality primarily depends on how clean the imaging instrument's optical components are. In some cases, it proves very difficult to tightly insulate the instrument's mechanism from its optical part.

In the optical bench of the infrared camera, currently developed for the ISO spacecraft, the optical components (lenses, filters, mirrors, polarisers) are mounted in the mechanisms' close vicinity (see figure 1). Pollution from the mechanisms must therefore be minimized.

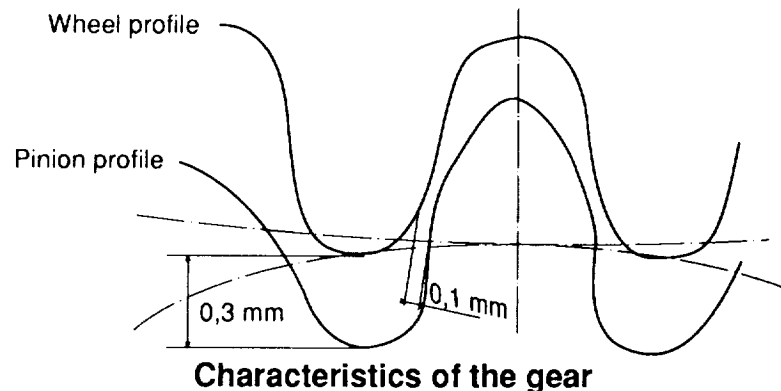
* AEROSPATIALE/Space and Strategic Systems Division, Cannes Center, France

2. DESCRIPTION OF MECHANISMS

As a primary function, these cryomechanisms must ensure accurate positioning of parts in front of the optical beam from the telescope. The overall architecture shows the mechanical assembly, consisting of a bearing-supported wheel carrying the optical devices. (see Figure 2).

The wheel is driven by a stepping motor via reduction gears, with angular positions of the wheel registered by three magnetoresistor sensors. One of the sensors provides the wheel's zero setting, while the other two, distributed around the cogged wheel integral with the motor's axis, count and subtract the motor's steps.

The reduction gear's teeth are specifically designed to allow ± 0.3 mm center-to-center distance, while assuring functional play less than 0.1 mm at the nominal center-to-center distance.



This requirement was specified to prevent the wheel from inflicting shock to the gear at the launch-induced vibrations, as these generate ± 0.3 -mm radial deflections of the wheel.

3. OPERATIONAL CONDITIONS

- The operating temperature for the cryomechanisms is 4 Kelvin (i.e.- 269°C). This is also the mechanisms' temperature at launch time.
- In-orbit lifetime is 18 months, which amounts to approx. 800,000 revolutions of the motor.
- The following requirements apply to cleanliness:
 - 0.17×10^{-7} g/cm² for molecular contamination

- 1×10^{-4} for the obscuration factor due to particulate contamination.

These are highly stringent requirements, the more since most of the optical components are not cleanable. Therefore, the qualification procedure for the mechanisms did provide for sine and random vibration sequences at 4 Kelvin, to be followed by an endurance test at 4 Kelvin, complete with cleanliness inspection.

4. ENDURANCE TEST RESULTS

4.1 TEST CONDITIONS

The endurance test was conducted in vacuo, at a temperature of 4 K, and involved 800,000 revolutions of the motor.

The control loop parameters were:

Frequency	:	60 steps/sec
Current	:	90 mA

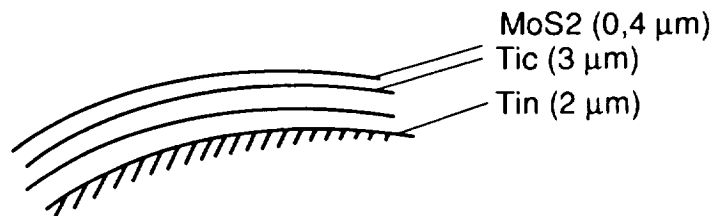
4.2 TEST RESULTS

On completion on the endurance test, a particulate deposit was found in line with the dentures' mutual contact zone of the gear teeth.

4.3 TEST SPECIMEN

The gear under test consisted of:

- One stainless-steel pinion coated with a layer of titanium nitride (TiN) a layer of titanium carbide (TiC) and lubricated with PVD- deposited molybdenum disulphide (MoS_2).



Stainless-steel pinion's coating

- One titanium wheel treated with sulphuric anodization, and lubricated by PVD- MoS_2 just like the pinion.

Quite a number of selection criteria were applied to the two metals above; i.e., differential expansion, cryogenic behavior, thermal conductivity, etc.

4.4 POST-TEST DEFECT INVESTIGATION

a. Dust check

Dust composition is fourfold :
Ti; Mo; Si; Fe.

Debris sizes are up to 100 micrometers in size. The particles observed are quite numerous.

b. Wheel examination

- Examination of the wheel at several points reveal its immunity to the endurance test.
- While no peeling of the material is found, some MoS₂ removal is observed over the contact area.
- The wheel's teeth do not contact all over their length (due to faulty pinion axes/wheel parallelism).

c. Pinion examination

Pinion wear consisted in both crazing/cracking and peeling of the TiC layer, and therefore that of the MoS₂ layer. Wear of the TiC, TiN and MoS₂ layers was quite visible, and the ground-base metal was stripped out at some places.

The observed dust particles essentially emanated from the pinion. Thus, although the mechanism's functional performance was unchanged, pinion wear was nevertheless unacceptable, as it amounted to high contamination risk for the nearby optical components.

5. PINION DEFECT ANALYSIS

The pinion is controlled by a stepping motor (24 steps per revolution) at a 60 steps/sec frequency. Thus, the motor delivers successive pulses to the pinion, and the driving torque is not constant.

The wheel's comparatively high inertia with respect to the pinion causes shocks between the gear's teeth during operation.

Those shocks, which are detectable by the unaided ear, were clearly identified from motion pictures shot with a high-speed movie camera. Thus, the crazing/cracking of the TiC layer results from the dual action of friction and shocks. The calculations performed on the teeth identified the location of the maximal shearing stress at a depth ranging between 2 and 6 μm . This is the zone in which the TiC/TiN/ stainless steel interface is situated. The numerous shocks can also cause destruction of the TiC-TiN. Where the substrate is too soft and deforms under shocks, flexural fatigue affects the TiC film, which then peels off into platelets that are found in the debris.

6. SUBSTITUTE MATERIALS AND LUBRICANTS

Following the failure of the first selected tribological approach, a two-pronged research effort was initiated towards other ground-base metal, or, alternatively, another lubricant. This led to the following findings.

- a. Use of annealed, quenched 440-C steel, whose hardness, greater than Z2 CN 18.09 steel's, precludes substrate penetration and assures good TiC behavior.

This candidate material does not solve the problem of MoS_2 wear, nor does it match shearing depth with the TiC/TiN/440-C steel interface, and it is therefore discarded.

- b. Use of a softer material, with shock-absorbing properties.

As an acetal resin, the candidate material Delrin 100NC10 offers the dual advantage of low friction and wear coefficients. On this basis, it was selected for use in comparative tests. The cryogenic behavior of the Delrin 100NC10 material has been examined through tension tests at a temperature of 4K.

- c. Use of softer, self-lubricating materials for shock-absorbing purposes.

The candidate material is Vespel SP-3 (15% MoS_2). A polyimide resin, Vespel, comes in five different grades. Mechanical and thermal characteristics differ from one resin to the other, although the properties are similar, since the same matrix is used. On account of its very low in-vacuo friction coefficient (0.03) Vespel SP-3 best meets our requirements.

- d. Use of another lubrication mode : a self-lubricating coating.

This method had already proved successful as evidenced by the constancy of friction torque on the gears, with hardly any significant change in the appearance of the contacting surfaces observed after running-in.

The candidate coating is a PTFE material, NUFLON N.

One of the properties of NUFLON N is a maximum friction coefficient of 0.02. Moreover, the parts thus coated are not functionally influenced by operating temperature, which is quite an asset at cryogenic temperatures or in absolute vacuum.

Based on all above accounts, the three solutions tabulated below were selected as suitable candidates.

SOLUTIONS	PINION	WHEEL
VESPEL	VESPEL SP3	TA 5E + SULPHURIC ANODIZING
NUFLON	Z2 CN 18-09 + NUFLON - N	TA 5E + NUFLON - N
DELFIN	DELFIN 100 NC 10	TA 5E + SULPHURIC ANODIZING

Candidate solutions

The characteristics of the gear are:

Reduction ratio : 20
Center-to-center distance (mm) : 72.450
Module : 0.575

	WHEEL	PINION
Number of teeth	240	12
Diameter (mm)	138.000	6.900

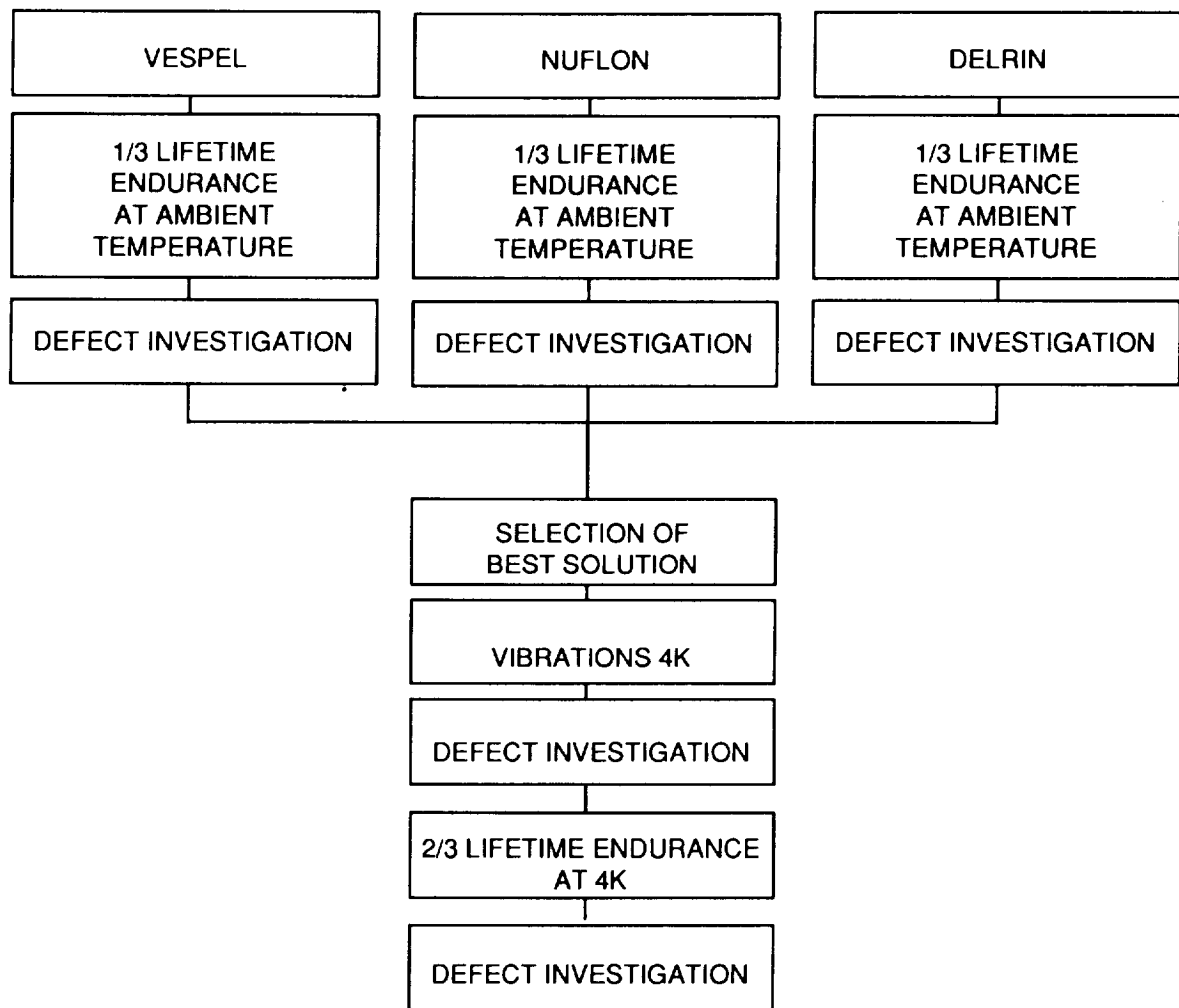
The three candidate solutions were subjected to a comparative tests in order to determine which offers the best performance.

7. COMPARATIVE TESTS

7.1 TEST PROGRAM

To minimize costly, time-consuming cryogenic tests, a first selection was made from the three candidate solutions after partial endurance tests at ambient temperature. The tests were run in vacuo in order to avoid airflow motions, as these may scatter debris, if any. The tests involved 1/3 the total lifetime, approximately 260,000 motor rotations.

On completion of those tests, the solution with the best results was vibration tested at 4 Kelvin, followed by an endurance sequence amounting to 2/3 lifetime at 4K.



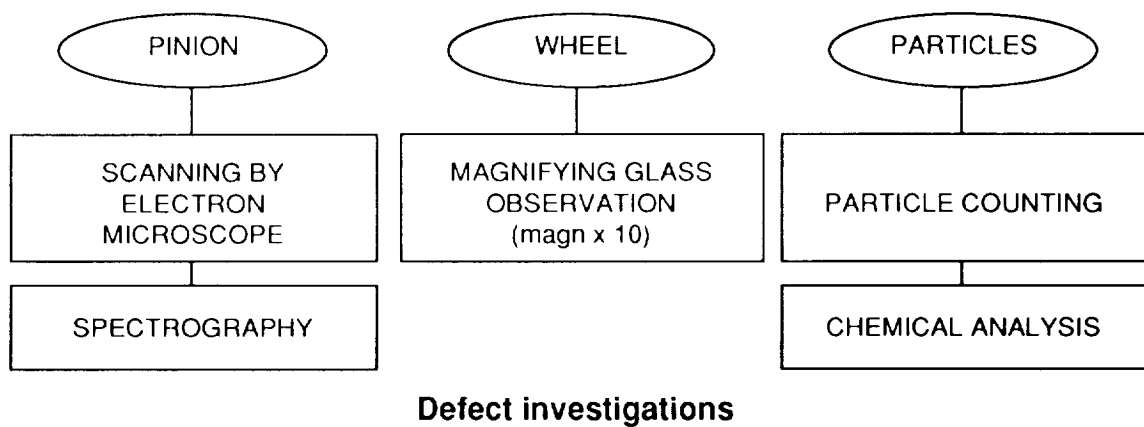
Test program

7.2 TEST-SET-UP

Since the purpose of the test is to compare the contamination levels produced by any of the solutions, a system is provided to collect the wear-generated particulate debris (see Figure 3).

7.3 DEFECT INVESTIGATIONS

The pinion, the wheel and whatever generated wear debris was subjected to a post-test defect investigation in accordance with the procedure diagrammed below:



8. TEST RESULTS

8.1. RESULTS FROM AMBIENT TEMPERATURE COMPARATIVE TESTS

The findings from defect investigations are tabulated below for the ambient temperature comparative tests:

Based on the results from the ambient temperature comparative tests, the Vespel solution has been selected for the follow-on cryogenic temperature tests.

8.2 RESULTS FROM 4 K VIBRATION TESTS

- PINION : The Vespel pinion was free from any cracks.
- WHEEL : Free from any damage.
- WEAR-GENERATED PARTICLES : These could not be collected in the vibration tests.

SOLUTIONS	VOLUME OF WEAR	ALTERATIONS ON PARTS	
		WHEEL	PINION
VESPEL	LOST IN BACKGROUND NOISE	- DEPOSITS CEMENTED OVER TEETH SIDES	- PEENING OF TEETH SIDES - DUST PARTICLES CEMENTED
NUFLON	DUST PARTICLES VISIBLE BY UNAIDED EYE	- FLOW OF THE DEPOSIT OUT OF CONTACT AREA - LINT, FIBRE DEBRIS, CHIPS	- PEENING OF STAINLESS-STEEL MATERIAL
DELTRIN	LOST IN BACKGROUND NOISE	- DEPOSITS CEMENTED OVER TEETH SIDES	- PEENING OF TEETH SIDES - BLACK TRACKS OVER TEETH SIDES

Results from ambient temperature comparative tests

8.3 RESULTS FROM 4 K ENDURANCE TESTS

- PINION : Normal wear. Slight flow out of the contacting zones.

Presence of dust particles cemented to the teeth.

- WHEEL : Deposits cemented to the teeth. Good surface condition.
- WEAR DEBRIS: Some 10 x particles, sizes 30 and 100 micrometers were found.

The insufficient quantity of particles precluded chemical analysis.

9. CONCLUSIONS

The contamination rates after the vibration and endurance tests on the Vespel pinion are found to be low and compatible with the cleanliness requirements.

Examination of the pinion and wheel showed no incipient degradation.
The Vespel material's self-lubricating character indicates good gear efficiency.

Due to the step motor's operation, the Vespel pinion's relative flexibility enables it to absorb inter-tooth shocks.

Thus, we may conclude that this type of material is quite fit for extended-life use at cryogenic temperature, while meeting stringent cleanliness requirements.

ORIGINAL PAGE
BLACK AND WHITE PHOTOGRAPH

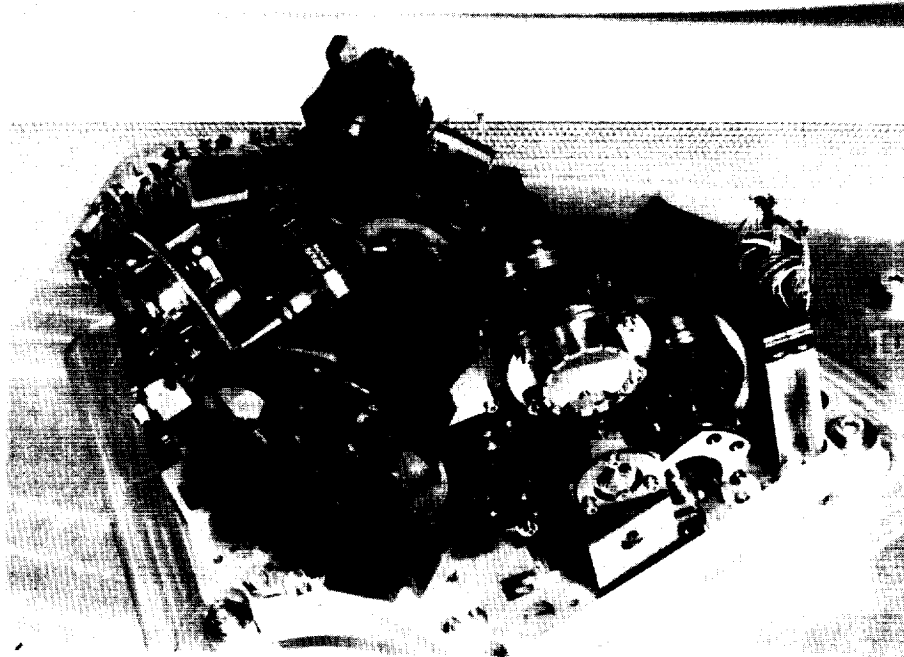


Figure 1. Optical bench of the ISO CAMERA

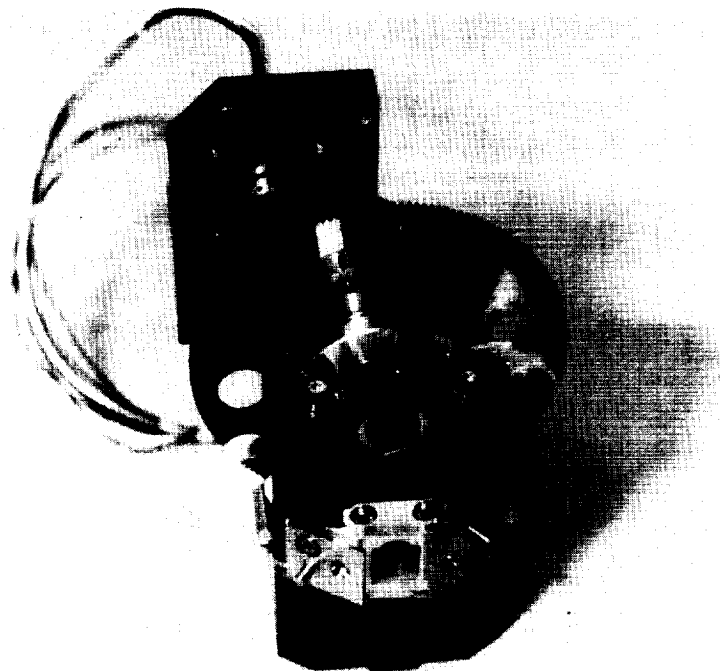


Figure 2 . Detail of the wheel supporting mirrors

ORIGINAL PAGE
BLACK AND WHITE PHOTOGRAPH



Figure 3 . Debris collection layout

INVACUO TRIBOLOGICAL EVALUATION OF COARSE-PITCH GEARS FOR USE ON THE SPACE STATION ALPHA JOINT

Scotty R. Allen*

ABSTRACT

Existing invacuo or ambient test data of slow-speed (<30 meters per minute pitch line velocity), coarse-pitch gears could not be found suitable for use in evaluating gear materials and surface treatments for the gear-driven bearing race of the Solar Alpha Rotary Joint (SARJ) for Space Station Freedom (SSF). Gear testing was conducted by AEC-Able Engineering Company, Inc. to obtain design data for this critical SSF component.

Some bull gear/pinion/lubrication combinations endured over 600,000 cycles (100 SSF years) without measurable wear, while other combinations experienced surface treatment degradation after only 40,000 cycles (seven SSF years). No catastrophic failures, such as seizing or tooth breakage, occurred during any test--all of which were run at least 201,000 cycles (34.5 SSF years). Specific results such as debris characteristics, mechanical efficiencies, effectiveness and degradation of lubrication, and wear data for the various gear combinations tested are described within the body of the report.

INTRODUCTION

AEC-Able Engineering Company, Inc. (ABLE) is presently tasked with the design and manufacture of the gear-driven bearing races for the Solar Alpha Rotary Joint (SARJ) for Space Station Freedom (SSF). The heart of the SARJ is the race ring: a 3.23-meter (127-inch)-diameter ring which functions as a structural bearing race and has a spur gear machined on the outside diameter for purposes of positioning the outboard truss structure of SSF in one of the two rotational degrees of freedom needed to keep the solar panels facing the Sun. The speed of rotation of the SARJ is one revolution every 90 minutes which is equivalent to a gear pitch line velocity of 11.5 centimeters (4.5 inches) per minute. ABLE designed a unique gear test fixture and conducted a

*AEC-Able Engineering Company, Inc.
93 Castilian Drive, Goleta, California 93117

series of invacuo gear tests in order to generate design data for the SARJ race ring.

The gears used for this testing had a 10-diametral-pitch (DP) tooth size. The gear testing was accomplished in a series of four test matrices. The pinions were all made from Nitalloy 135 Modified which was gas nitrided. The pinion tooth surfaces were either left bare, or further treated in some test configurations with either ion-plated gold, or thin-dense-chromium (TDC) plating. The mating bull gears were made either from 15-5PH corrosion-resistant steel (CRES), or titanium-6Al-4V alloys. The 15-5PH CRES gears were treated by either gas nitriding, TDC plating, or gas nitriding followed by TDC plating. The titanium alloy gears were surface-hardened by gas nitriding. These bull gears were run in mesh with the pinions in various combinations, either dry or lubricated with a perflourinated polyether grease. The load on each gear mesh was applied by spring preloading each pair of bull gears against a common pinion to achieve a constant force on the teeth of each gear mesh. The pitch line velocity during testing ranged from 6.8 to 10.3 meters (22.5 to 33.8 feet) per minute.

TEST APPARATUS DESCRIPTION

The bull gears and pinion were mounted in a gearbox wholly contained within a vacuum chamber. The pinion was driven by an electric motor mounted externally to the vacuum chamber and connected to the pinion shaft via a ferro-fluidic feed-through. The axial width of the pinion was sufficient to allow dual top and bottom tracks for the mating bull gears. A delrin skirt was placed on the pinion to prevent wear debris from the upper gear track from contaminating the lower gear track. Four bull gears could be run against the pinion under spring preload such that each bull gear contacted a unique portion of the pinion tooth. Figure 1, Gearbox With Top Cover Removed, shows two pairs of bull gears in mesh with the pinion. The four bull gear stations are identified alphabetically as follows: Station A, lower right; Station B, upper right; Station C, upper left; Station D, lower left. The top bull gear of the right-hand pair is spring preloaded in a counter-clockwise direction against the pinion by the coil compression springs visible in the milled pockets of the top gear. The lower bull gear is reacting the force of the springs such that it is preloaded against the pinion in the clockwise direction. The top bull gear of the left-hand pair is spring preloaded in the clockwise

direction (opposite to the top bull gear of the right-hand pair) while the lower bull gear is reacting the spring preload in the counter-clockwise direction. Thus with the right and left pairs preloaded in opposite directions, the two co-planar bull gears in the top track contact the same pinion tooth on opposite sides. The same holds true for the lower co-planar bull gears.

Once the gearbox is assembled, the preload force is set by turning an adjustment screw which changes the relative clocking of each bull gear pair, thus varying the compression of the coil preload springs. The preload force on the teeth of each bull gear was set to 467 newtons (105 pounds force) \pm 5 percent. Therefore, the pinion must react 30.25 newton-meters of torque from each bull gear. This load generates nominal gear contact stresses for a steel versus nitrided steel gear interface of 489 megapascals (71,000 pounds per square inch).

The vacuum chamber illustrated in Figure 2, Gear Test Vacuum Chamber consisted of a 1-meter-diameter cylinder 0.3 meter deep with stiffened end plates, all constructed of aluminum. View ports located on the side and top of the chamber permitted visual observations of the gear operations. The vacuum was provided by a rotary vacuum pump in combination with a diffusion stack. The chamber pressure was maintained below 0.00001 torr during all vacuum tests.

Instrumentation consisted of a load cell/lever arm arrangement to measure drive motor reaction torque; a tachometer calibrated to measure bull gear speed; and temperature sensors to measure pinion temperature, gearbox temperature, and ambient air temperature. These parameters were digitized and stored by a computerized data collection system. Pinion drive torque was also measured manually with a torque wrench periodically during testing. Only pinion drive torque could be measured. Therefore, the contribution of each bull gear/pinion mesh to the overall pinion drive torque could not be determined by either drive torque measurement method.

TEST ARTICLE DESCRIPTION

All gears were by hobbed, shaved, and honed to American Gear Manufacturers Association (AGMA) quality number 10 requirements. However, the application of TDC plating can reduce the quality of the involute profile form to AGMA quality number 9. The parameters described below are common to all of the pinions and bull gears used in each of the test matrices.

PINION (P):

Material: Nitralloy 135 Mod. per AMS 6470

Heat treatment: Rc36 core hardness, gas nitrided 0.38-0.50
millimeter (0.015-0.020 inch) deep

Pitch diameter = 12.954 centimeters (5.10 inches)

Number of teeth = 51

Face width = 3.81 centimeters (1.50 inches)

Tooth size = 10 DP, 3.429 mm (0.135 inch) addendum

BULL GEAR (BG):

Pitch diameter = 21.844 centimeters (8.60 inches)

Number of teeth = 86

Face width = 0.940 centimeter (0.37 inch)

Tooth size = 10 DP, 1.651 millimeter (0.065 inch) addendum

Three different pinion surface treatments were tested and are designated P1, P2, and P3, respectively. Only one pinion of each type of surface treatment was manufactured. These different surface treatments used the nitrided surface as the substrate and are described below:

P1: ion-plated gold 1500-2000 Angstroms (7 microinches) thick

P2: bare nitrided surface

P3: TDC plating 0.005 millimeter (0.0002 inch) thick maximum

The ion-plated gold was selected because it had flight history on nitrided gears to provide corrosion protection and dry lubrication. The TDC plating was selected as a more durable corrosion protection and wear enhancement to the nitrided surface.

Four different bull gear material and surface treatment configurations were tested and are designated BG1, BG2, BG3, and BG4, respectively. The materials and surface treatments are described below:

- BG1: 15-5PH CRES per AMS 5659, condition H1075, gas nitrided 0.127-0.178 millimeter (0.005-0.007 inch) deep;
- BG2: 15-5PH CRES per AMS 5659, condition H1075, TDC plated 0.0025-0.0178 millimeter (0.0001-0.0007 inch) thick;
- BG3: 15-5PH CRES per AMS 5659, condition H1075, gas nitrided 0.127-0.178 millimeter (0.005-0.007 inch) deep, and TDC plated 0.0050 millimeter (0.0002 inch) thick maximum;
- BG4: Titanium 6Al-4V per MIL-T-9047, annealed condition, gas nitrided 0.127-0.178 millimeter (0.005-0.007 inch) deep (etched case).

The TDC plating on the BG2 bull gear was for the specific purpose of providing wear resistance and prevention of galling of the CRES base metal. The TDC plating on the BG3 bull gear was also, like P3, for durable corrosion protection and wear enhancement of the nitrided surface. The nitrided titanium BG4 was selected for the potential 40-percent weight savings of a race ring made from titanium instead of steel.

A description of the pinion and gear configurations used during each of four test runs is contained in Table 1, Gear Test Matrix Description.

TEST RESULTS AND DISCUSSION

A summary of the total number of cycles each gear experienced during the course of testing is provided in Table 2, Gear Cycle Summary.

TEST MATRIX 1

This test matrix was run without any lubrication on any gears. The ion-plated gold on the pinion wore off by flaking after less than 100 tooth contacts on each of the gear interfaces. Each pinion tooth experienced 340,000 cycles, and each bull gear tooth, 201,700 cycles.

BG1-A1 and BG2-C2 both completed the test with the surface coatings intact without measurable wear. Base metal from both BG2-B1 and BG4-D1 began galling to the pinion after 40,000 cycles, but were tested to completion without seizing or tooth breaking.

The total reaction torque at the pinion was 121.00 newton-meters (1071 inch-pounds). The drive torque at the pinion (less 0.4 newton-meter of unloaded bearing drag torque) ranged from 2.2 to 3.2 newton-meters. Thus the gear efficiency was 97-98 percent. During a 2400-cycle period at the onset of galling, the drive torque did exceed the previously described torque range and peaked at 4.1 newton-meters before trending down within the nominal range again. Drive torque was insensitive to bull gear speed between 0.5 and 15 revolutions per minute.

Prior to galling, small amounts of black, powdery debris were generated at all gear/pinion meshes. The volume of debris occupied less than 10 percent of the clearance existing between the tip and root of mating gear teeth. The debris tended to accumulate in lines around the edges of tooth contact areas on both the pinion and gear teeth. Most of the debris was observed to accumulate in the roots of the pinion teeth. Some debris did fall onto the debris shield and onto the bottom of the gearbox. Portions of the faces of the gear and pinion teeth were also colored black by the debris.

BG1-A1, BG2-C2, and the corresponding pinion meshes experienced negligible wear. There was a slight degradation in the surface finish of the pinion teeth from a polished, honed finish to a dull, slightly rougher appearance. The honed finish of BG1-A1 was nearly unchanged. The TDC plating on BG2-C2 was burnished and intact.

BG2-B1 completed the test with a combination of pitting and galling of the 15-5PH CRES gear material. The TDC plating initially wore through on the dedendum at the lower edge of the teeth. From there the galling began and spread up the remainder of the dedendum and outward on to the addendum of the teeth. The TDC appears to have come off in flakes 50-200 microns in size with a thickness corresponding to that of the original plating. The stainless-steel gear material removed from pits on the dedendum was deposited onto the addendum of the pinion teeth, and at the pitch line of the bull gear teeth, but did not form detectable amounts of loose debris. This transfer of material actually resulted in a build-up of the tooth profile

on both gears in this mesh. There was between 0.023 and 0.048 millimeter of build-up on the bull gear teeth within 0.89 millimeter (0.035 inch) of the pitch line.

BG4-D1 completed the test with substantial debris generation and moderate galling of titanium to the pinion teeth. The addendum of the bull gear teeth experienced 0.127-0.152 millimeter (0.005-0.006 inch) of wear; the dedendum had 0.102-0.127 millimeter of wear. The bull gear teeth were scored with pitting at the pitch line. Several tooth tips of the pinion were chipped during the latter half of the test as a ridge developed at the line of deepest tooth contact on the dedendum of the bull gear. The debris particles were 40-200 microns in size and generally accumulated in a pile on the gearbox bottom beneath the gear mesh. However, some particles were ejected at velocities calculated (based upon trajectories) to be in excess of 16 kilometers per hour.

TEST MATRIX 2

This test matrix was initially run with grease on only the P3/BG4-D3 gear interface; the other gears were initially dry. Bull gears BG3-C3 and BG4-D3 were only tested for 200 cycles in atmosphere before being removed from the test because the TDC plating from the pinion began to transfer to the TDC plating on BG3-C3, and the drive torque had increased by 50 percent. For the remaining two gear interfaces, each pinion tooth experienced 343,000 cycles, and each bull gear tooth, 203,400 cycles. BG1-A3 completed the test with the surface coating intact without measurable wear. 15-5PH CRES base metal from BG2-B2 began galling to the pinion at some point between 30,000 and 40,000 cycles. No significant change in drive torque attributable to this phenomenon was discernible. Approximately one cubic centimeter of grease was then applied five times to BG2-B2 during the remainder of the test.

With only one pair of preloaded bull gears driven by the pinion, total reaction torque at the pinion was 60.5 newton-meters. The drive torque at the pinion (less 0.1 newton-meters of unloaded bearing drag torque) ranged from 0.6 to 1.2 newton-meters both before and after grease was applied to BG2-B2. Thus the gear efficiency was 98-99 percent. The drive torque was insensitive to bull gear speeds between 0.5-15 revolutions per minute.

BG1-A3 performed very similarly to BG1-A1 in the first test matrix. The pinion interface with BG1-A3 did generate a thin line of black debris which accumulated near the pitch line of both gears. In addition, a rust-colored powder collected at the root of the pinion and on the tip chamfer of the bull gear. The amount of debris generated was approximately less than half that formed in the first test matrix.

The TDC plating began to wear through on BG2-B2 very much like it did in the first test matrix. When the grease was applied, the galled stainless steel adhering to the pinion teeth was removed. Some metallic particles of what appeared to be TDC plating and possibly some stainless steel from BG2-B2 were also trapped by the grease. The TDC plating remained intact of the addendum of the gear teeth, but was completely worn off of the dedendum.

The TDC plating on the pinion became burnished at the interface with all of the mating gears, but did not flake off. A spot of TDC plating roughly 1.5 millimeters in diameter located at the top edge of the tooth contact area and also on the inner half of the addendum nearest the pitch line was transferred to BG3-C3 from each of the pinion teeth. The TDC plating on the pinion did wear through on the BG2-B2 gear path on the inner half of the addendum nearest to the pitch line.

Lubrication of the gears was accomplished by applying the grease to each bull gear tooth with a syringe. Between 0.5 and 1.0 cubic centimeter of grease was applied to the gear each time it was relubricated. Most of the grease was pushed to the edges of the tooth contact where it collected in berms, but was not consumed. No migration of the grease was observed. The lubrication intervals for BG2-B2 were at 41; 55; 132; 146; and 173 kilocycles. The bull gear teeth began to dry out between 118 to 132 kilocycles (63 to 77 kilocycles since the previous relubrication) and galling again occurred. However, once grease was reapplied, the galling was healed and a smooth pinion tooth surface was restored. A relubrication interval of 40,000 cycles was sufficient to keep the gear surfaces wetted, although over 63,000 cycles were accomplished without galling reoccurring.

The grease that was applied to the nitrided titanium bull gear and later to the TDC plated 15-5PH CRES bull gear turned a dark gray--almost black color after only 200-300 cycles (30 minutes) of operation. The grease eventually turned black and pasty in consistency

on the BG2-B2 interface as the test progressed. The perflourinated polyether in the grease was apparently breaking down while operating in the boundary lubrication regime under the gear contact stresses.

TEST MATRIX 3

This test matrix was run with lubrication on all gear interfaces. Each pinion tooth experienced 343,000 cycles, and each bull gear tooth, an additional 203,000 cycles. All four gear interfaces completed the test without measurable wear. The surface finish on the pinion teeth remained smooth and appeared slightly more polished. BG1-A3 had been used in the previous test matrix and continued to perform without any indication of measurable wear. No further wear occurred on BG2-B2, which had also been tested in the previous matrix, other than a slight burnishing of the TDC plating remaining on the addendum of the teeth. BG4-D3 (nitrided titanium) did have the gold surface color removed on the lower 20-30 percent of the dedendum during the first 94,000 cycles when this interface had not been properly relubricated, but did not exhibit any further indications of wear during the remainder of the test. There was no visible evidence of metallic debris or galling from any of the four gear interfaces. The drive torque was lower, and the operation of the gear train was smoother than the previous test matrices which did not have lubrication on all gear interfaces.

Each gear interface was initially lubricated and subsequently relubricated at the specified intervals with 0.5 cubic centimeter of grease applied directly to the bull gear teeth. BG1-A3 and BG2-B2 were relubricated at 40 and 85 kilocycles, but gears BG2-C2 and BG4-D3 were not properly relubricated until 94,000 cycles. Then all gear interfaces were properly relubricated at 125 and 176 kilocycles. The grease turned a dark gray to black color at each of the gear interfaces within a few thousand cycles, and continued to degrade as described in the previous test matrix as the test progressed.

The drive torque was normally between 0.8 to 1.4 newton-meters (less 0.1 newton-meter of unloaded bearing drag), except for the first several hundred cycles after relubrication when the drive torque dropped as low as 0.3 newton-meter. The gear efficiency was 99 percent.

TEST MATRIX 4

This test matrix was run with lubrication on all gear interfaces. Each pinion tooth experienced an additional 351,000 cycles (702,000 total), and each bull gear tooth, 213,000 cycles. Again, all four gear interfaces completed the test without measurable wear. The surface finish on the pinion teeth continued to remain smooth and appeared slightly more polished. BG1-A3 had been used in the previous two test matrices and continued to perform without any indication of measurable wear. No further wear occurred on BG2-B2, which had also been tested in the previous two matrices, other than continued burnishing of the TDC plating remaining on the addendum of the teeth. The TDC plating on BG3-C3 adhered perfectly during the entire test, was burnished on the dedendum portion of the gear teeth, and did wear through to the nitrided substrate only on the deepest 1 millimeter of the contact area on the tooth dedendum. BG4-D3 (nitrided titanium) had been used in the previous test matrix and did not exhibit any indications of further wear. There was no visible evidence of metallic debris or galling from any of the four gear interfaces.

Each gear interface was initially lubricated and subsequently relubricated at the specified intervals with 0.5 cubic centimeter of grease applied directly to each gear contact path on the pinion teeth. All gears were relubricated at 28, 60, 103, 135 and 169 kilocycles. As in the previous tests, the grease turned a dark gray to black color at each of the gear interfaces within a few thousand cycles, and continued to degrade as the test progressed.

The drive torque was normally between 1.1 to 1.8 newton-meters (less 0.1 newton-meter of unloaded bearing drag). After relubrication, the drive torque would drop as low as 0.5 newton-meter and then rapidly increase during the first several hundred cycles back to the normal range. The gear efficiency varied between 98.5 and 99 percent.

During the course of testing, the direction of pinion rotation was reversed for several revolutions in order to clear debris from the drive motor brushes which began squeaking occasionally. It was observed

that the drive torque would immediately drop for a few hundred cycles as if the gears had been relubricated. However, instead of the torque returning to the previous level, the drive torque would climb higher than before for approximately 2000 cycles, and then settle down to the nominal level. On one such occasion the drive torque briefly increased to 2.3 newton-meters. This phenomenon became more exaggerated as the test progressed. The best explanation of this effect appears to be that the action of the gear mesh changes slightly when the direction of rotation is reversed; thus some of the grease accumulating around the area of the gear mesh is redistributed onto the active face of the gear teeth contact. This effectively relubricates the gears. However, as the grease degrades, the pasty by-products of the grease degradation also are drawn into the gear mesh. The good grease is pushed aside faster than the by products of the grease degradation, thus the drive torque increases to a level higher than before the reversal.

CONCLUSIONS

The nitrided 15-5PH CRES (BG1) bull gears in mesh with any of the nitrided Nitralloy 135 Modified pinions proved to be the best combination tested when no lubrication was used on the gear interface. The BG1 gear type had no significant indications of wear, and was the only wear surface treatment that consistently remained intact throughout each unlubricated test.

The worst gear combination tested was the nitrided and TDC plated 15-5PH CRES (BG3) bull gear in unlubricated mesh with the TDC plated (P3) pinion. The TDC plating from the pinion transferred to the TDC plating on the bull gear with an increase in drive torque of 50 percent after only 200 cycles. This performance was unacceptable and the BG3 bull gear was removed from that test. This phenomenon did not occur in any other bull gear/pinion combination involving TDC plating.

The performance of two other unlubricated bull gears in mesh with the gold plated pinion (P1) were also considered unacceptable: nitrided titanium (BG4), and TDC plated 15-5PH CRES (BG2). Although the BG2 gears did not generate a significant amount of debris (one of the three BG2 gears did successfully complete the required life cycle unlubricated), the galled CRES material caused a build-up on both the bull gear and pinion teeth. Given the actual gear ratio of pinion to race ring and slow pitch line velocity of the SARJ, the material build-up on the gear teeth of both mating gears may have been sufficient to cause a

tight mesh condition resulting in failure of the SARJ by seizing, excessive drive torque, or tooth breakage. The quantity of debris generated by BG4 posed an unacceptable hazard to other SSF systems.

Periodic lubrication of the gear mesh every 30,000 to 50,000 cycles with a perflourinated polyether grease enabled every type of bull gear/pinion combination tested to perform without significant indications of wear through at least one 200,000-cycle lifetime. BG1, BG2, and BG4 bull gears in mesh with the P2 pinion exceeded two life cycles without significant wear.

The perflourinated polyether grease did experience degradation during testing at all gear interfaces. Degradation of the grease did not appear to be influenced by the gear materials. This degradation did not seem to be a result of contamination by wear debris from the gears, but was a result of chemical breakdown of the grease as it operated in boundary-condition lubrication under nominal gear contact stresses of 489 mega-pascals (71,000 pounds per square inch).

ACKNOWLEDGEMENTS

The author wishes to express his appreciation to Robert Haake, also of Able Engineering Company, Inc., for his ingenuity in designing the gear test fixture, and support during the gear testing. Photo-micrographic and elemental analyses of debris particles from the first test matrix were provided by Lockheed Missiles and Space Company, Inc., Sunnyvale, California.

TABLE 1. GEAR TEST MATRIX DESCRIPTION

BULL GEAR TYPE-STATION PINION and S/N LUBE			BULL GEAR TYPE-STATION PINION and S/N LUBE		
TEST #1 (a)			TEST #3 (a,b,d)		
P 1	BG1-A1	None	P 2	BG1-A3	Grease
P 1	BG2-B1	None	P 2	BG2-B2	Grease
P 1	BG2-C2	None	P 2	BG2-C2	Grease
P 1	BG4-D1	None	P 2	BG4-D3	Grease
TEST #2 (b,d)			TEST #4 (b,d)		
P 3	BG1-A3	None	P 2	BG1-A3	Grease
P 3	BG2-B2	(c)	P 2	BG2-B2	Grease
P 3	BG3-C3	None	P 2	BG3-C3	Grease
P 3	BG4-D3	Grease	P 2	BG4-D3	Grease

NOTES:

- (a) The same gear, BG2-C2, was used in tests 1 and 3. No refurbishment other than cleaning was done between tests.
- (b) The same gears, BG1-A3 and BG2-B2, were used in tests 2,3 and 4. No refurbishment other than cleaning was done between tests.
- (c) No lubrication was initially used. When localized wearing through of the TDC on the bull gear occurred after 40,000 cycles, grease was periodically applied for the remainder of the test.
- (d) The grease was Braycote 600 micronic, a perflourinated polyether oil thickened with polytetrafluoroethylene.

TABLE 2. GEAR CYCLE SUMMARY

GEAR	NUMBER OF CYCLES		
	Dry	W/GREASE	TOTAL
P1	340,000	NA	340,000
P2	N/A	702,000	702,000
P3	343,000	275,000	343,000
BG1-A1	202,000	NA	202,000
BG1-A3	203,000	417,000	620,000
BG2-B1	202,000	NA	202,000
BG2-B2	41,000	579,000	620,000
BG2-C2	202,000	203,000	405,000
BG3-C3	200	213,000	213,000
BG4-D1	202,000	NA	202,000
BG4-D3	NA	417,000	417,000

ORIGINAL PAGE
BLACK AND WHITE PHOTOGRAPH

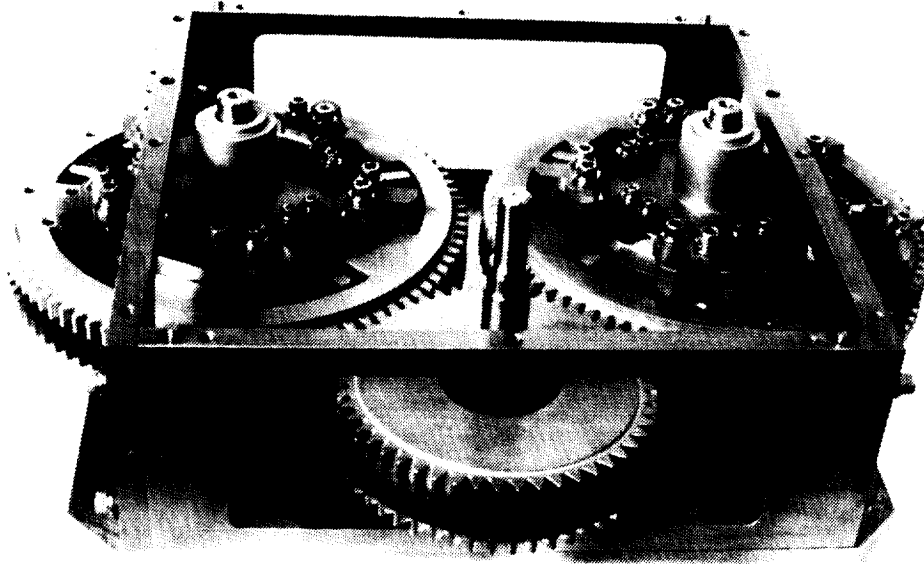


FIGURE 1. GEARBOX WITH TOP COVER REMOVED

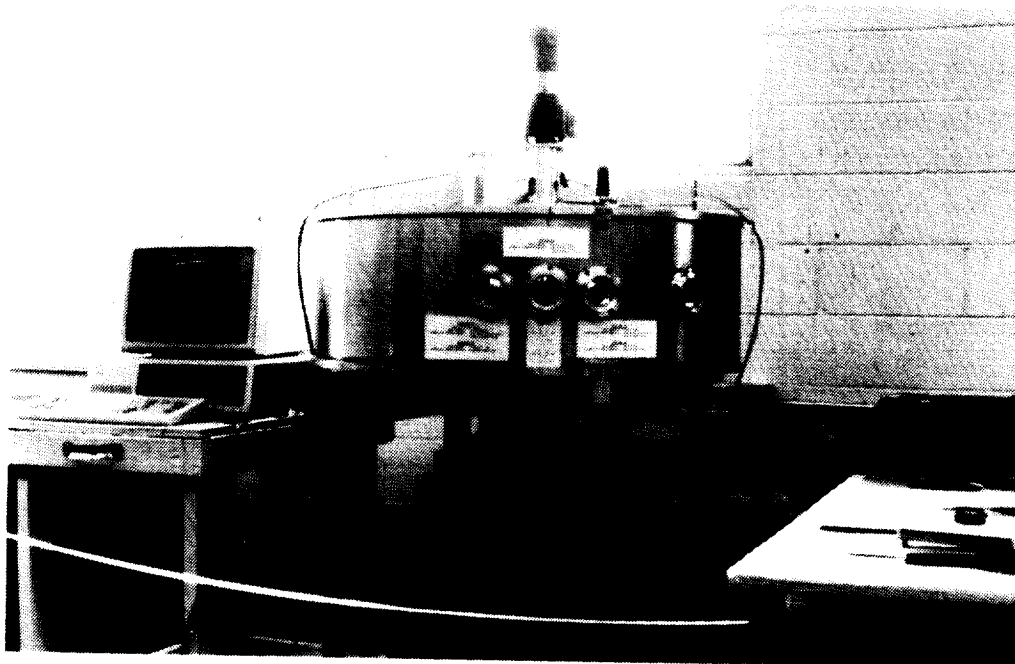


FIGURE 2. GEAR TEST VACUUM CHAMBER

TABLE 1. GEAR TEST MATRIX DESCRIPTION

BULL GEAR TYPE-STATION PINION and S/N LUBE			BULL GEAR TYPE-STATION PINION and S/N LUBE		
TEST #1 (a)			TEST #3 (a,b,d)		
P 1	BG1-A1	None	P 2	BG1-A3	Grease
P 1	BG2-B1	None	P 2	BG2-B2	Grease
P 1	BG2-C2	None	P 2	BG2-C2	Grease
P 1	BG4-D1	None	P 2	BG4-D3	Grease
TEST #2 (b,d)			TEST #4 (b,d)		
P 3	BG1-A3	None	P 2	BG1-A3	Grease
P 3	BG2-B2	(c)	P 2	BG2-B2	Grease
P 3	BG3-C3	None	P 2	BG3-C3	Grease
P 3	BG4-D3	Grease	P 2	BG4-D3	Grease

NOTES:

- (a) The same gear, BG2-C2, was used in tests 1 and 3. No refurbishment other than cleaning was done between tests.
- (b) The same gears, BG1-A3 and BG2-B2, were used in tests 2,3 and 4. No refurbishment other than cleaning was done between tests.
- (c) No lubrication was initially used. When localized wearing through of the TDC on the bull gear occurred after 40,000 cycles, grease was periodically applied for the remainder of the test.
- (d) The grease was Braycote 600 micronic, a perflourinated polyether oil thickened with polytetraflouroethylene.

TABLE 2. GEAR CYCLE SUMMARY

GEAR	NUMBER OF CYCLES		
	Dry	W/GREASE	TOTAL
P1	340,000	NA	340,000
P2	N/A	702,000	702,000
P3	343,000	275,000	343,000
BG1-A1	202,000	NA	202,000
BG1-A3	203,000	417,000	620,000
BG2-B1	202,000	NA	202,000
BG2-B2	41,000	579,000	620,000
BG2-C2	202,000	203,000	405,000
BG3-C3	200	213,000	213,000
BG4-D1	202,000	NA	202,000
BG4-D3	NA	417,000	417,000

**A COMBINED EARTH SCANNER AND MOMENTUM WHEEL
FOR ATTITUDE DETERMINATION AND CONTROL
OF SMALL SPACECRAFT**

Bill Bialke*

ABSTRACT

In order to satisfy the stringent cost and power requirements of small satellites, an advanced SCANWHEEL® has been designed, built and qualified by ITHACO, Inc. The T-SCANWHEEL is a modular momentum/reaction wheel with an integral conical Earth scanner. The momentum wheel provides momentum bias and control torques about the pitch axis of a spacecraft. An angled scan mirror coupled to the rotating shaft of the momentum wheel provides a conical scan of the field-of-view of an infrared sensor to provide pitch-and-roll attitude information. By using the same motor and bearings for the momentum wheel and Earth scanner, the overall power consumption is reduced and the system reliability is enhanced. The evolution of the T-SCANWHEEL is presented, including design ground rules, tradeoff analyses, and performance results.

BACKGROUND

The concept for a SCANWHEEL evolved from recognition of the fact that many attitude control systems for Earth-pointing spacecraft employ both conical Earth sensors and momentum wheels. A SCANWHEEL was developed during the 1960s for Nimbus D, E and F, and subsequently was flown successfully on 18 spacecraft. The on-orbit geometry of a typical attitude control system configuration using a pair of SCANWHEELs for attitude determination and control is shown in Figure 1. A single SCANWHEEL can be used for circular orbits.

In 1987, a low-cost, low-power solution was sought to provide attitude determination and control of small spacecraft, specifically for a NASA standard small satellite. This 150-pound Exceptional Satellite (XSAT) was designed to be ejected from a Get-Away-Special (GAS) Canister aboard the space shuttle. The previous SCANWHEEL design had proven to be too power-hungry and too expensive for the application, so a development effort was initiated to redesign the SCANWHEEL to specifically meet the small satellite requirements. A photograph of the newly developed hardware is shown in Figure 2.

A cross section of the original ITHACO SCANWHEEL is shown in Figure 3. This design featured a hollow shaft motor, a flywheel with an integral rotating prism/lens, an immersed thermistor bolometer for infrared detection, magnetic pickups for speed and scan phasing information, and an induction motor contained within a hermetically sealed housing. This design was not compatible with small, low-cost, low-power spacecraft since the hollow shaft motor required to feed the bolometer leads from the on-axis optical path required large-diameter bearings with a correspondingly high drag torque. This high drag torque coupled with the low efficiency of the AC induction motor resulted in unacceptable steady-state power consumption for a small spacecraft. In addition, the fabrication costs were out of the range of small spacecraft financial budgets.

*ITHACO, Inc., Ithaca, New York

GROUND RULES

A set of ground rules was established early in the design phase of the improved SCANWHEEL in order to ensure that the design tradeoff decisions made during the hardware development were compatible with the ultimate development program goals. The basic approach to achieve low cost was to maintain simplicity by taking advantage of standard components and common materials. At the same time, a rigid ground rule was established to maintain the ability to upgrade any feature in the design to Class S spacecraft hardware. A ranking of the critical tradeoff parameters was established to be used in the tradeoff analyses during the design process. These basic parameters were power consumption, cost, reliability, weight, and accuracy.

The highest ranked tradeoff parameter was deemed to be power consumption. Small spacecraft typically have body-mounted solar arrays and a minimum amount of surface area for solar cells; thus, power is at a premium. As an example, the XSAT satellite has a total power generation capability of 7.8 watts. The power consumption of the basic bus is 2.5 watts average, so the power budget for the attitude control system was less than 3 watts, to leave just over 2 watts for the experiment. Low power consumption was therefore imperative to enable the SCANWHEEL to be practical, given this type of power budget. The second-ranked tradeoff parameter was cost, for if the costs were too high, the small satellite experimenters could not afford an attitude control system. The third-ranked tradeoff parameter was reliability. The long-term reliability and lifetime were not of major importance in the low-cost/high-value spacecraft for which the hardware was targeted. The approach was to design the hardware for a 1-year mission as a minimum, with a goal of 3 to 5 years. Typical spaceflight hardware is designed with 5- to 10-year missions in mind. The lowest ranked tradeoff parameter was weight.

Accuracy of the Earth sensor was a nebulous tradeoff parameter, since it was deemed that small, low-cost spacecraft may not require an extremely accurate attitude sensor. An accuracy of $\pm 0.5^\circ$ was established in the early phases of development. However, the ground rule of upgradability conflicted with this coarse specification, since a typical electro-optical system requires redesign from the ground up to improve accuracy. As a result, it was determined that the accuracy of the system would not be compromised during the development in order to satisfy the highest number of potential users. A target accuracy of $\pm 0.1^\circ$ was established, since it covers a broad range of attitude determination requirements, and is achievable with an Earth-scanning sensor.

DESIGN SPECIFICATIONS

A summary of the relevant design specifications is presented in Table 1. For the sake of modularity, the design of the momentum wheel subassembly required that it be able to be used as an independent momentum wheel or reaction wheel. The size was established as that required for a small satellite on the order of XSAT. The 6-Volt bus was chosen because that is the bus voltage on XSAT. The typical bus voltage for spacecraft is 28 Volts, but smaller spacecraft have fewer solar cells to string together, so the available bus voltage may be lower. One design goal was to make it useable with either a 28-Volt bus or a 6-Volt bus. The final design met all of the minimum requirements, and met every goal with the exception of steady-state power consumption. The goal of <0.5 watt at 1000 rpm was impossible to attain within the program constraints.

DESIGN TRADEOFFS

STRUCTURE

Structural support of the flywheel is provided by a pair of spoked flexures separated by a cylindrical ring. This can be seen in the cutaway portion of Figure 4. The spokes allow visual and mechanical access to the flywheel when it is completely assembled into the housing. This eliminates a blind assembly which would occur if the enclosure and support structure were combined into a single part. With open flexures on both sides of the housing, inspection can be performed prior to close-up to detect the presence of contamination and to verify correct direction of rotation polarity.

The infrared scanning mirror prohibits sealing of the unit without a large, complex and expensive infrared window. In order to eliminate the costs associated with both hermetically sealing the housing and incorporating this impractical window, a vented housing was used. A quasi-sealed environment was achieved by using thin aluminum sheet stock to fabricate covers which are placed over the spoked support structure.

The scheme devised for supporting the off-axis optics housing above the rotating scan mirror includes a bridge that spans two of the mounting tabs on the reaction wheel, as shown in Figure 5. A pedestal supports an optics housing that contains the detector, objective mirror, and the preamplifier. The shaft angle position sensor and the connector are contained in the bridge portion of the assembly. The entire subassembly consisting of the detector, optics housing, objective mirror, detector, filter lens, pedestal, bridge, connector, position sensor, and pre-amplifier is referred to as the Infrared Sensor Assembly (IRSA).

BEARINGS

Various standard ball-bearing designs were considered in the bearing selection tradeoff. Deep-groove bearings have full shoulders on both sides of the raceways of the inner and outer rings. They can accept radial loads, thrust loads in either direction, or combinations of loads. In order to allow assembly with the full shoulders, these bearings require a two-piece steel ribbon-type retainer. Angular-contact bearings have one ring shoulder partially or totally removed. They can support thrust loads in one direction or combinations of radial and thrust loads, but not radial loading alone. Load capacities are higher than for deep-groove bearings, since the removed shoulder on one race allows a higher ball complement. The removed shoulder also allows the use of a phenolic retainer. This is desirable for low retainer wear, and for the ability to vacuum impregnate the retainer with a small supply of lubricant. Both deep-groove and angular-contact ball bearings can be combined to form a duplex pair for increased capacity and rigidity.

Figure 6 shows several alternative methods of combining both types of bearings, in duplex pairs and separately. Two axially separated deep-groove bearings have the advantage that they could be used without preloading, resulting in low drag torque, but this would result in non-repetitive runout. Two duplex pairs have the advantage of high capacity and low runout, but would be more costly and consume more power due to the higher bearing count. A set of duplex pairs on one end and a deep-groove bearing on the other end has the advantage of high capacity, but requires two types of bearings. A set of two angular-contact bearings has all of the advantages of low runout due to the required preload, low cost and low drag torque due to

the low bearing count, and high capacity from the angular-contact bearings. The disadvantage of this configuration is being unable to accept bidirectional thrust loading during operation. This is not an issue in the momentum wheel design, since the application does not require thrust loading during operation. The set of angular contact bearings was therefore selected, requiring a preload scheme.

Preloading is desirable for a precision device such as the momentum wheel in order to remove radial and axial play for more precise shaft positioning. By maintaining ball-race contact, noise is reduced by preventing ball skidding, and load sharing is improved between bearings. The only disadvantages with preloading are that increased wear and higher drag torque result when compared to a bearing with zero load. However, the precision and stability required for the optical scanning system dictate that a preloaded scheme be incorporated. The simplest method of preloading is with a spring. This turns out to be the preferred method for the momentum wheel due to its simplicity, and the fact that it easily accommodates differential thermal expansion between the shaft and the housing. Spring preloading also accommodates minor misalignment better than alternative methods. A stainless-steel wavy washer spring was selected to preload the bearing pair. The final bearing suspension layout is shown in Figure 7.

The final bearing selection was based on capacity and availability. A high-capacity R4 bearing was selected from The Barden Corporation. This bearing is a hybrid of a conventional R4 bearing which has a high load rating. Thin section bearing tolerances, larger balls and a low conformity ratio were designed into the bearing to lower the contact stresses and increase the capacity. The negative tradeoff of this configuration is higher drag torque. However, these same parameters also increase the lubricant elasto-hydro-dynamic (EHD) film thickness, resulting in less asperity contact and less wear. The Barden Corporation does not have the required size of TiC-coated balls available off-the-shelf, but a standard R4 bearing is available from Miniature Precision Bearing Corporation (MPB) with TiC-coated balls. A comparison of the parameters of the MPB bearing and the Barden bearing is shown in Table 2. The capacity of the Barden bearing allows it to be used with nearly any current launch vehicle random vibration spectrum. The capacity of the TiC-coated MPB bearing is only compatible with very low random vibration environments.

LUBRICATION

The most common types of lubrication systems in spaceflight mechanisms are dry films and liquid lubricants such as oil and grease. Dry film lubricants such as MoS_2 have the advantage of vacuum stability and no viscous drag and are used in some low duty-cycle applications, but do not have the endurance for a continuously operating system such as a momentum wheel. Liquid lubrication systems using grease and/or oil have been used successfully in many spaceflight mechanisms. An oil lubrication system was eventually selected over grease in order to avoid the unpredictable drag torque behavior of greases over temperature ranges and lifespans. Since the suspension system is vented to space vacuum, a low-vapor-pressure oil was desirable to minimize lubricant depletion due to evaporation, which eliminated the majority of natural hydrocarbons.

Bray 815Z, a synthetic fluorocarbon perfluoropolyalkylether (PFPE) oil, was originally selected based on its extremely low vapor pressure and high viscosity index. Many experiences with synthetic fluorocarbons such as Bray 815Z have shown that they do not perform well under boundary lubrication conditions (Ref. 1,2). Typically, performance in the boundary region can be enhanced by using antiwear additives. However, since the PFPE fluids are unable to dissolve additives, significant wear can be expected when operating in the boundary region. In addition, the Bray 815Z has demonstrated polymerization when used in high-wear applications. Knowledge of this potentially catastrophic failure mode started a search for an alternative lubricant.

A newly synthesized hydrocarbon is available from Pennzoil which has a vapor pressure as low as the Bray 815Z. This lubricant, known as Pennzane™ X2000, has flight experience and has been tested in boundary lubrication tests at Aerospace Corp (Ref. 3). The tests demonstrated successful performance operating in the boundary region under vacuum conditions.

The properties of the Bray 815Z and the Pennzane™ X2000 are listed in Table 3 for comparison. The relevant properties include the viscosity, the viscosity index, and the vapor pressure. It can be seen from the table that the viscosity of the two oils at room temperature is similar. The high viscosity index of the Bray is preferred to reduce the performance variations over temperature excursions and to sustain EHD liftoff as temperatures are increased. The vapor pressures of the two oils are nearly identical.

The lubricant is used in the vicinity of a rotating scan mirror which reflects infrared radiation into a narrow bandpass optical system to detect the Earth's horizon. After long-term exposure in space vacuum, there is a potential for lubricant to condense on the mirror surface and reduce the effective transmission of the optical system. Infrared absorption scans for the two lubricants were compared, and it was revealed that the Pennzane™ has a much higher transmission in the region of the horizon sensor's infrared bandpass from 14.2 to 15.6 μm . An absorption spike occurs at 13.8 μm (wavenumber 721) in the Pennzane™, but it is very narrowband and not in the horizon sensor's optical passband. The Bray 815Z demonstrates some broadband absorbance at 14.5 μm (wavenumber 690) which is in the optical passband, so the Pennzane™ has preferable optical properties. Both lubricants are virtually transparent in the visible portion of the spectrum.

With the exception of its lower viscosity index, the Pennzane™ X2000 appeared superior to the Bray 815Z for the application. Both oils should perform satisfactory in a biased speed operation in the EHD regime, but the Bray is highly suspect for a reaction wheel application required to operate throughout the entire speed range, and through zero. The Pennzane™ does exhibit a power consumption penalty at low temperatures, but the alternative of using the Bray, which may polymerize in such a boundary lubrication application, is unacceptable. Therefore, the Pennzane™ X2000 with 5% Lead Napthanate as an antiwear additive was selected for use in the application.

MOTOR

An integral direct-drive motor was required to spin up the flywheel, maintain speed, and provide instantaneous reaction torque to the spacecraft. The two candidate motor types that do not require life-limiting brushes were AC induction motors and brushless DC motors.

The AC induction motor had the advantage that it can be driven open loop by a simple circuit consisting of two square-wave current sources 90° out of phase. There is no cogging or low-frequency torque ripple, and the speed is conveniently limited by the synchronous frequency of the driver. The disadvantages of the induction motor are that the torque is not linear with respect to rotation speed, and the efficiency is quite low. The linearity is desirable, but not necessarily critical, since it has been successfully dealt with in numerous attitude control systems. However, the high priority placed on power consumption in the tradeoff considerations dealt the induction motor a severe blow. An alternative was to employ a brushless DC motor due to its higher efficiency and linear torque. This type of motor is more power efficient than the induction motor, resulting also in a lower stator mass required to conduct waste heat away from the windings. One disadvantage is a slightly more complex motor driver requiring rotor position feedback information for commutation. The fact that this type of information is required for tachometer feedback from the wheel for the attitude control system turns this into an advantage. The brushless DC motor does have significant torque ripple, at a frequency corresponding to the commutation rate. For a two-phase, six-pole motor operating at 500 rpm, this corresponds to a torque ripple frequency of 100 Hz, which could be low enough to cause undesirable torque disturbances on some spacecraft. The presence of rotating permanent magnets in the brushless DC motor design also produces cogging and eddy-current drag torque.

A cross section of an ironless armature brushless DC motor is shown in Figure 8. It consists of a thin armature that supports the windings, with a set of magnets on one side and a flux return path on the other side. The result is a motor that exhibits no cogging or eddy current drag, since there is no relative movement between the magnets and the iron flux return ring. Because of this, the iron components need not be laminated, which reduces the cost of these parts. The efficiency of an ironless armature motor is maximized by utilizing the largest possible diameter, since a high number of poles are used and torque radius is increased. By increasing the number of poles, the resolution of the tachometer signal from the commutation signal is also increased. Hence, the ironless armature motor is ideal for the momentum wheel drive, by being both power and weight efficient. In typical applications, the ironless armature motor is more massive than a comparable conventional brushless DC motor, because the magnet gap is extremely large to accommodate a thin-section armature inserted into the gap with clearance on both sides. This enlarged gap requires large magnets and heavier low-reluctance iron components to compensate for the increase in magnetic gap. In the momentum wheel application, however, the added weight contributes to fulfilling the flywheel inertia requirements. This unique combination of lowest power consumption and lowest weight occurs only once in a lifetime in tradeoff analyses, which makes the ironless armature motor the obvious choice.

POSITION SENSOR AND TACHOMETER

A shaft angle position sensor was required to establish the phasing of the Earth scan relative to the fixed portion of the sensor. This is commonly referred to as the Top Dead Center (TDC) or Bottom Dead Center (BDC) pulse, and typically determines the pitch orientation of the spacecraft. In addition, a tachometer is required for speed and direction of rotation feedback from the momentum wheel. This discrete signal is also used to commutate the brushless DC motor. Digital position indicators and tachometer signals are commonly generated by eddy current probes, optical switches, magnetic pickups, and hall generators.

Signals derived from eddy-current probes are insensitive to the speed of the flywheel, but require a complex, unreliable oscillator circuit to stimulate the eddy-current effect. The accuracy of the eddy-current systems is low and the power consumption is high relative to other devices. Optical switches are also used for tachometers and position sensors, especially where high resolution and high accuracy is desired. Light from an LED is directed towards a phototransistor and interrupted by a shutter or an alternately reflecting/absorbing surface. The simplicity of this design ranks it very high, but the power required to illuminate the LED is too high for an ultra-low power consumption design.

Magnetic pickups are rugged, reliable, passive devices, used commonly in applications operating at a biased speed. However, the amplitude of the signal generated from these devices is proportional to speed, so the signal disappears as the speed approaches zero. This is not compatible with a tachometer in a reaction wheel application requiring bidirectional operation through zero speed, but is adequate for a position sensor in a biased momentum wheel or SCANWHEEL. This type of position sensor is passive, so it consumes no power, and is extremely reliable due to its simplicity.

Hall-effect generators are commonly employed for commutation of brushless DC motors. The Hall generators can be stimulated directly from the permanent magnets in the motor, so a separate gear or code wheel is not required. The phasing of the Hall sensor's signals when stimulated by the actual motor magnets is exactly correct for commutation, eliminating any alignment procedure required to clock a separate gear to the motor. The circuitry to bias the Hall sensors is very simple, requiring only a constant current source. The sinusoidal output of the Hall sensors when excited by the motor magnets can be easily processed into discrete commutation and digital tachometer signals with a simple comparator circuit.

The Hall generators were selected for the momentum wheel tachometer because their simplicity eliminated the need for many additional parts. They can be integrated directly into the armature assembly to minimize the packaging requirements for the commutation and tachometer components. The Hall sensors provide a digital tachometer signal, but do not provide any once-per-revolution clocking indication to establish the phasing of the scan. In order to maintain the modularity of the momentum wheel, this position sensor was incorporated in the Infrared Sensor Assembly (IRSA) which is attached to the momentum wheel. Based on its heritage, simplicity, reliability and ultra-low power consumption, the magnetic pickup was selected to derive the once-per-revolution index pulse. An iron slug is attached to the scan mirror and a rugged magnetic pickup is threaded into a port in the lower part of the IRSA.

OPTICAL SYSTEM

The optical system of ITHACO's previously manufactured SCANWHEEL is shown in Figure 3. A rotating germanium prism and lens scans through a germanium spectral filter window to stimulate an immersed bolometer. This optical design has been flown on a large number of spacecraft. In spite of this extensive heritage, it is not compatible with a system optimized for low power consumption due to the hollow shaft motor required to access the infrared detector.

An off-axis optical scan geometry is necessary in the absence of the access provided by a hollow shaft motor, so the scan mechanism of choice is a planar, diamond-machined, first-surface mirror coupled directly to the momentum wheel shaft. Refractive scan elements do not readily lend themselves to the off-axis system topology, and thus were not considered further. The high optical efficiency of the reflective elements contributes favorably to their selection. The configuration selected for the design includes a diamond-machined off-axis parabolic mirror suspended by a pedestal in one section of the scan path. This requires blanking a 90° sector of the scan perimeter. Most spacecraft require a blanked region to avoid optical interference with solar panels or antenna booms, so this is not a serious consequence. In addition, the configuration allows modification to the scan cone angle from 45° to 85° for higher altitude applications by merely changing the angle on the scan mirror. The remainder of the optical system consists of a germanium meniscus filter lens, and a pyroelectric infrared detector. The scan mirror reflects light by 45°, causing the field of view to sweep a 45° half-apex angle cone in space. When the field of view alternately crosses cold Space and the hot Earth, the infrared signal produced by the Earth is detected, amplified, and sent to a separate electronics box for processing into pitch-and-roll attitude information.

MATERIALS

Aluminum was selected as the primary structural material due to its relative low cost, low weight, and high thermal conductivity. The one drawback of the aluminum is its relatively high coefficient of thermal expansion (CTE). In optical systems, materials with a low CTE are frequently used to minimize focal length changes which can defocus the system. The relatively long focal length and large detector area in the optical design result in small effects from focal length changes. More critical than the CTE, then, was the ratio between the CTE and the thermal conductivity. This ratio will influence the tendency of the structure to thermally distort when it is placed in an ambient environment where it is heated on one side from direct sunlight exposure, and cooled on the other side due to radiation to cold space. Assessing the candidate materials of aluminum, magnesium, titanium, steel, copper and beryllium, aluminum is found to be superior to titanium, steel and magnesium, but slightly inferior to copper and beryllium. For structural and cost reasons, the aluminum was selected. Aluminum alloy 6061-T6 was chosen for the SCANWHEEL structure for its low cost, its demonstrated dimensional stability, high resistance to stress corrosion cracking, and extremely high fracture toughness.

A stainless-steel bearing mount was selected due to its close CTE match with the bearing material. The sleeve within the mount in which the outer race of the bearing is installed is coated with Titanium Nitride to prevent the fretting corrosion which would be inevitable at the bearing and mount interface due to the relative microscopic movements of the race during operation. The spring preload scheme selected requires one bearing to be fixed, and one bearing to be able to float axially during relative changes in the shaft and housing dimensions due to thermal expansion and transient pressure differentials on the housing. The Titanium Nitride coating ensures that this floating action of the second bearing is preserved.

PERFORMANCE MEASUREMENTS

Power consumption tests on the unit included steady-state power consumption measurements in vacuum. Figure 9 shows the measured steady-state power consumption as a function of speed with the MPB bearings and the Barden high-capacity bearings. The overall power consumption is the combined power from the bus and the secondary power supplies. The power consumption specification of less than 1 watt total for the momentum wheel and motor driver was met with the MPB bearings, and nearly met with the Barden bearings. The overall efficiency increases with load and speed, typical of a low-torque motor, as the quiescent power consumption of 0.5 watt becomes a smaller percentage of the total load. The overall efficiency of the momentum wheel motor and drive electronics approaches a phenomenal 90% at 6000 rpm. At lower speeds, the efficiency is more on the order of 60% to 70%.

CONCLUSION

The development effort succeeded in producing a low-cost, low-power consumption SCANWHEEL as an elegant solution for small satellite attitude determination and control with a minimum amount of hardware. Simplistic and reliable techniques were employed to result in a rugged, yet efficient, design. The versatile T-SCANWHEEL has since been commissioned for several small satellite programs, including the Air Force's Space Test Experiment Platform (STEP) mission series, and NASA's Total Ozone Mapping Spectrometer (TOMS) spacecraft. These spacecraft typically use a pair of T-SCANWHEELs and an independent reaction wheel in their reconfigurable attitude control systems. In addition, an independent momentum wheel has been built for BREMSAT. This GAS Canister launched satellite is being built for the University of Bremen in Germany to perform microgravity experiments.

ACKNOWLEDGEMENTS

The majority of the work presented in this paper was done under two separate Small Business Innovation Research (SBIR) contracts from Goddard Space Flight Center. The original SCANWHEEL concept was conceived jointly by Bob Fowler of ITHACO and Seymour Kant of GSFC in 1963. ITHACO would like to thank Mr. Kant for his technical advisement and continued support during the SBIR development.

REFERENCES

- (1) Peter Conley and John J. Bohner, *Experience With Synthetic Fluorinated Fluid Lubricants*, Hughes Aircraft Company, Space & Communications Group, El Segundo, CA.
- (2) Bryan H. Baxter and Barry P. Hall, *The Use of Perfluoroether Lubricants in Unprotected Space Environments*, European Space Tribology Laboratory, Risley England.
- (3) David J. Carre', *The Performance of Perfluoropolyalkylether Oils under Boundary Lubrication Conditions*, The Aerospace Corporation, El Segundo, CA.

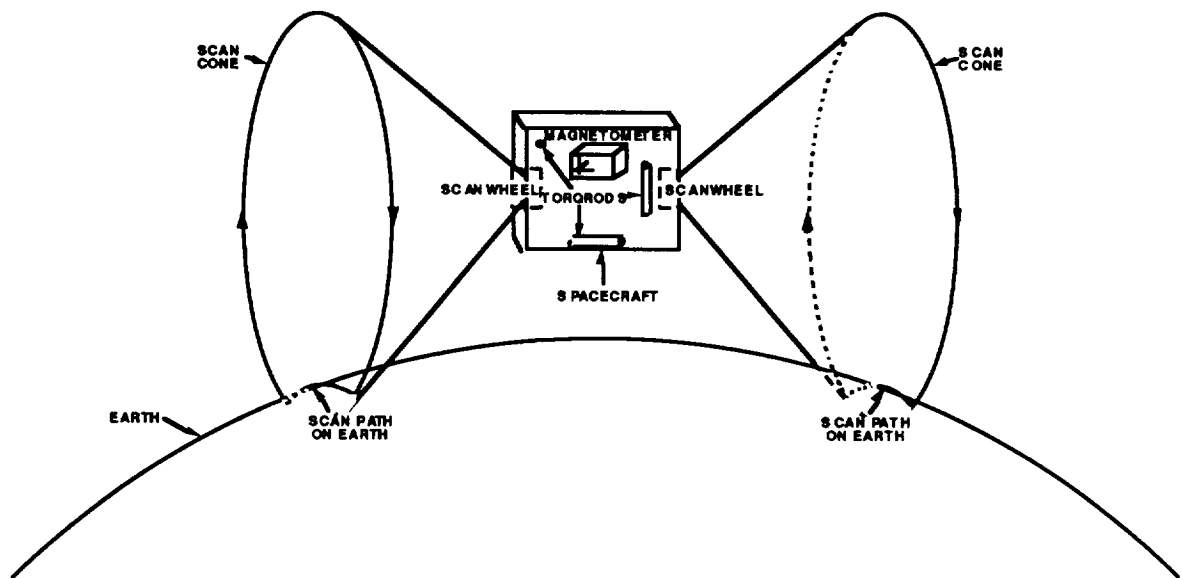


Figure 1. This on-orbit geometry of a typical attitude control system utilizing two SCANWHEELs is augmented with a magnetometer and three TORQRODs.

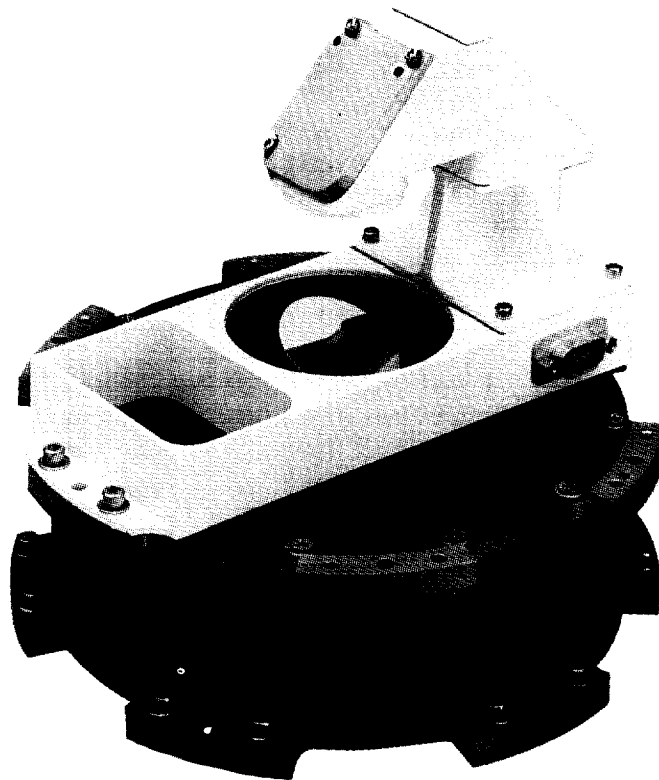


Figure 2. The T-SCANWHEEL combines the functions of a biased momentum wheel and a scanning Earth sensor into a single unit.

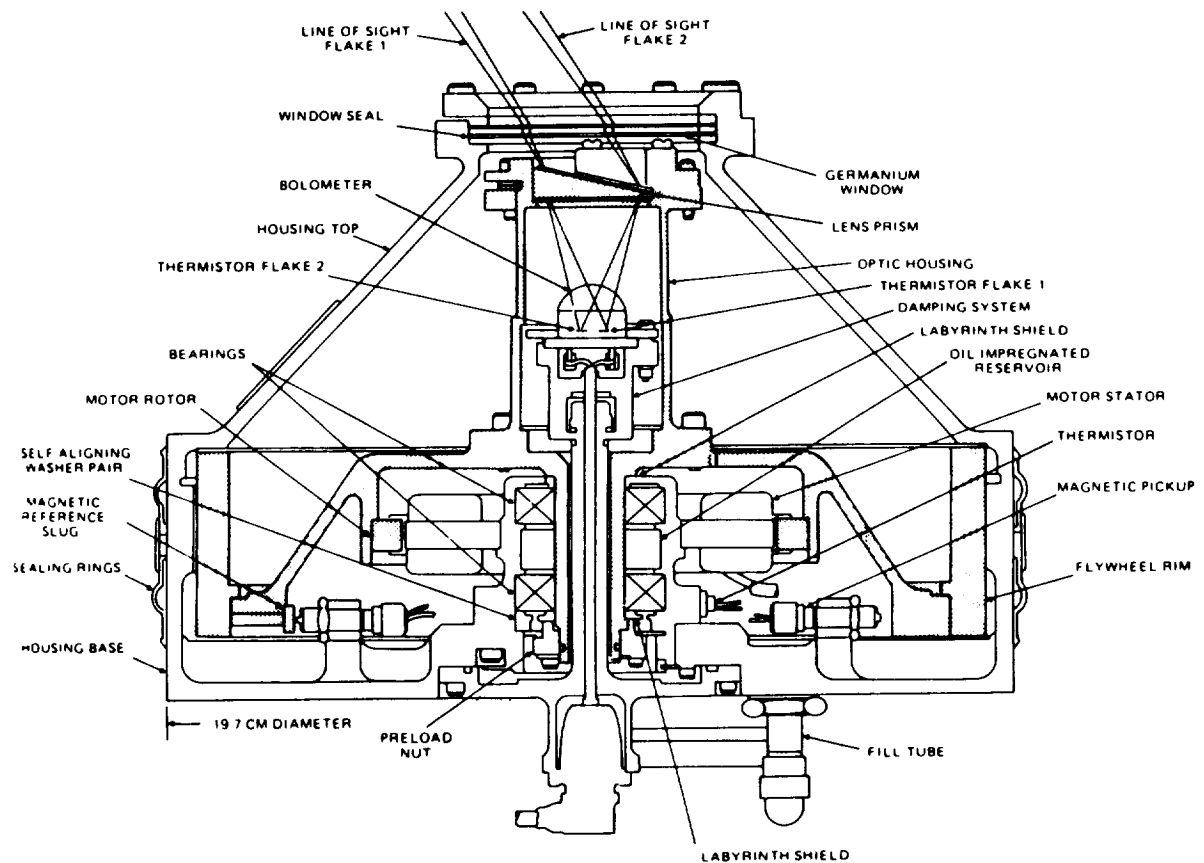


Figure 3. The original ITHACO SCANWHEEL featured a hollow shaft rotor in order to accommodate the on-axis refractive optical system. Shading indicates rotating components consisting of flywheel and prism assembly.

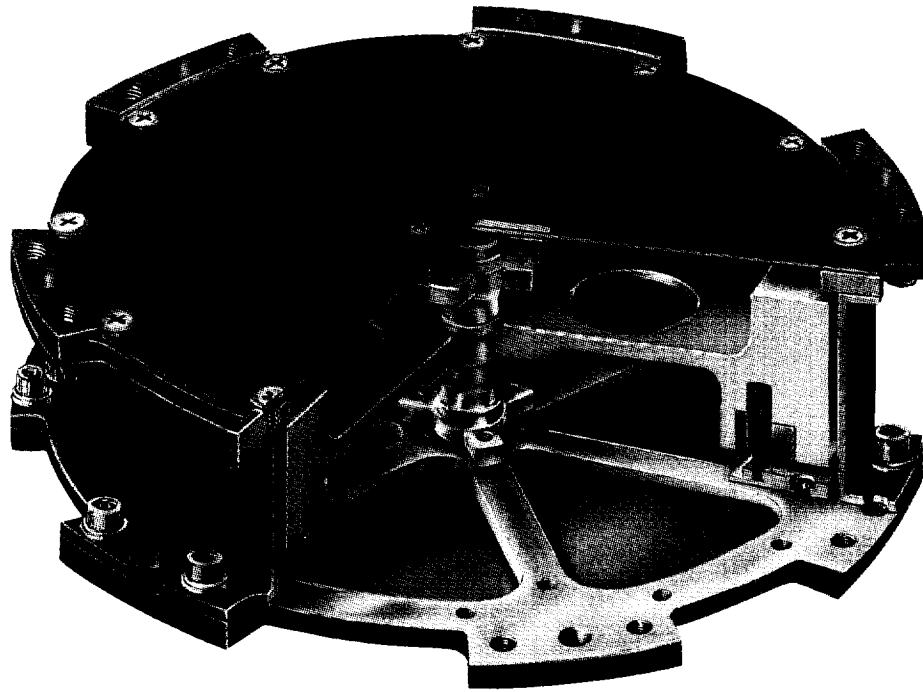


Figure 4. The modularity of the momentum wheel subassembly of the new design allows it to be used as an independent momentum wheel or reaction wheel.

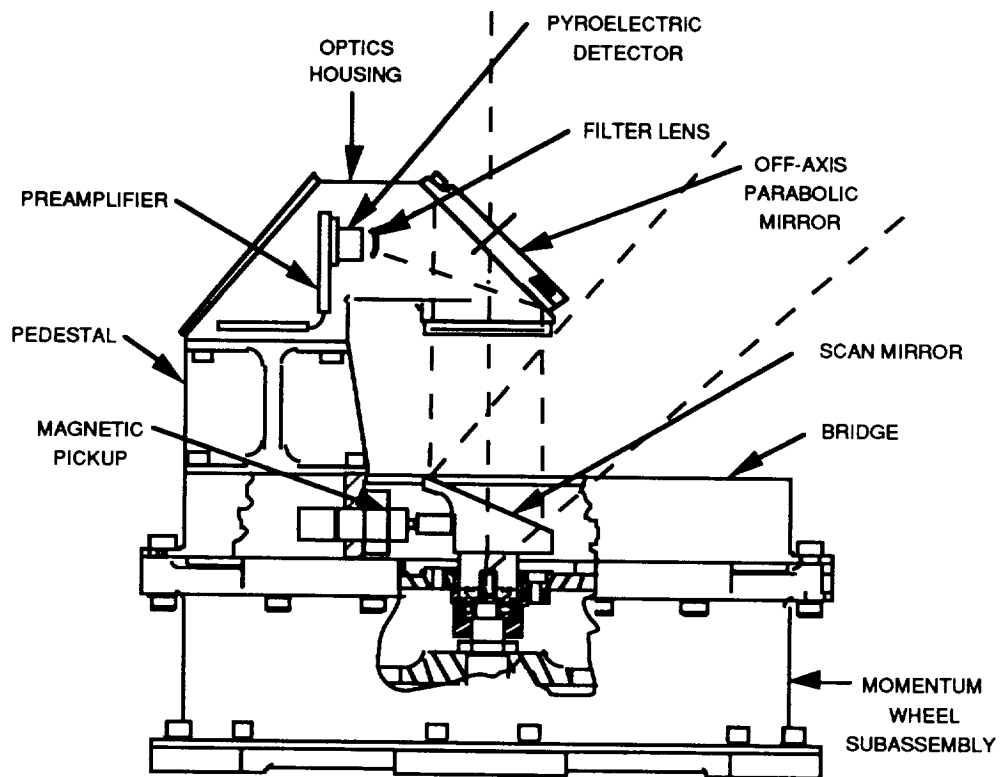


Figure 5. The new T-SCANWHEEL design utilizes a reflective off-axis optical system.


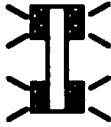

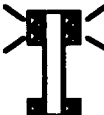
<u>TYPE</u>		<u>ADVANTAGES</u>
DUAL DEEP GROOVE		LOW DRAG LOW COST
DUAL DUPLEX PAIRS		HIGH CAPACITY LOW RUNOUT
DUAL ANGULAR CONTACT		LOW RUNOUT LOW DRAG LOW COST HIGH CAPACITY
DUPLEX PAIR/DEEP GROOVE		HIGH CAPACITY

Figure 6. Bearing Configuration Tradeoffs.

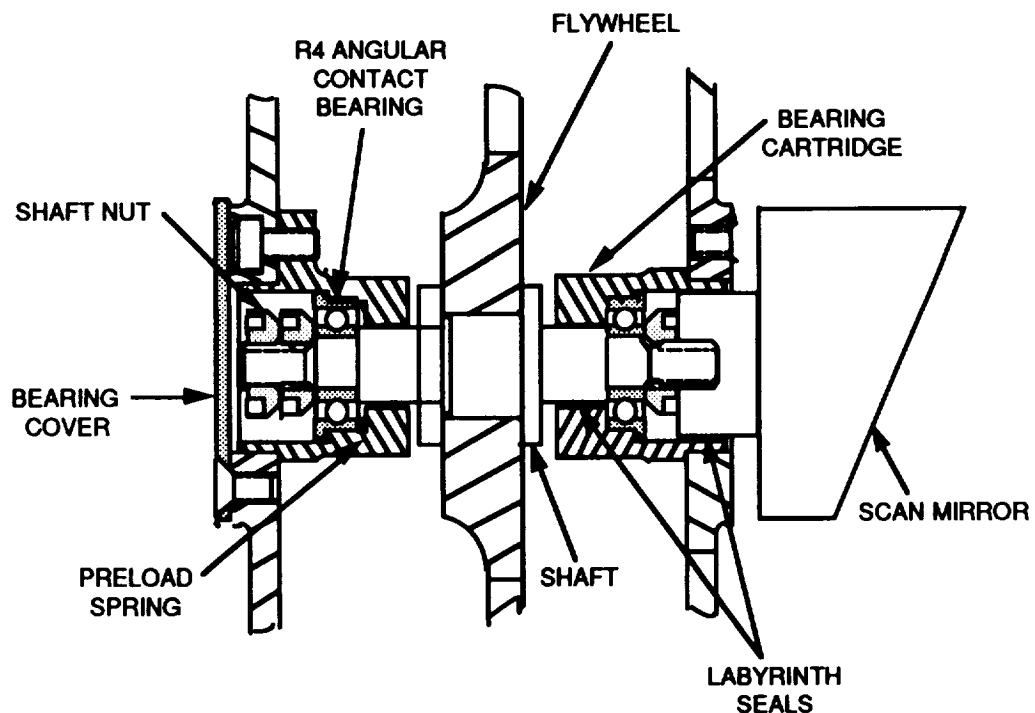


Figure 7. The final ball-bearing suspension system was designed to allow addition of a scan mirror with no modifications.

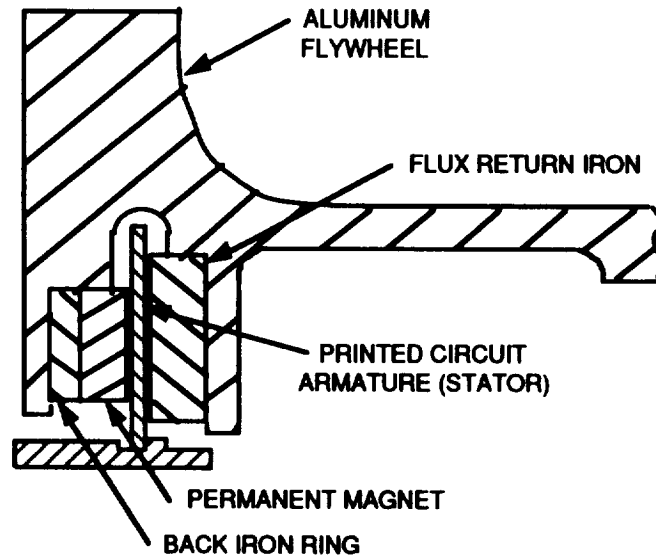


Figure 8. The Ironless Armature Brushless DC Motor is an optimum drive for momentum wheels due to its unique combination of high efficiency and high inertia/weight.

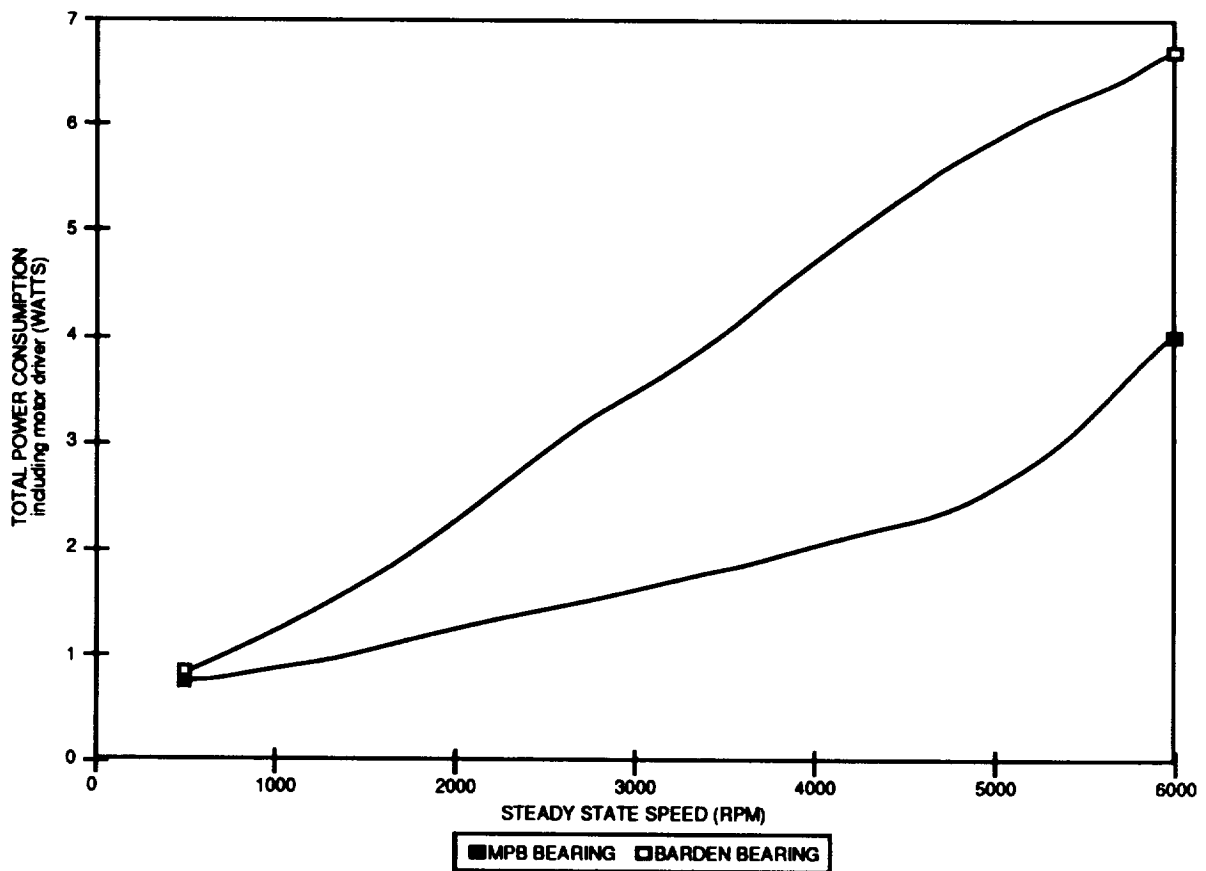


Figure 9. The total steady-state power consumption of the momentum wheel subassembly includes the motor driver and secondary power supplies.

Table 1. SCANWHEEL Baseline Design Specifications

Parameter	Minimum Requirement	Goal
MOMENTUM WHEEL SUBASSEMBLY		
Nominal Operating Speed	1000 rpm	±5000 rpm
Operating Life	1 year	3 to 5 years
Storage Life	5 years	5 years
Torque Capability	>0.02 N-m (2.8 oz-in)	Increasable
Torque Ripple	N/A	<0.002 N-m
Angular Momentum @ 1000 rpm	0.67 N-m-s (0.5 ft-lbf-sec)	Increasable
Power Consumption @ 1000 rpm	<1.0 W	<0.5 W
Weight	<2.5 Kg (5.5 lbm)	
Temperature Range	0°C to 50°C	-34°C to 71°C
Bus Voltage	6 V	6 V, 15 V or 28 V
SCANWHEEL ASSEMBLY		
Scan Cone Half Angle	45±1°	45° to 85° Variable
Scan Beam Width	1.5° (0°±0.75°)	
Blanking	90° Allowed	
Optical Passband	14-16 μ	14.3-15.6 μ
Optical Efficiency	65% Minimum	
Sun Rejection	No Damage	
Aperture	Restricted by XSAT Structural Opening	Ø1.25" Minimum
Position Sensor	Once Per Revolution Index Pulse	
Accuracy	±0.5°	±0.1°
*Field of Regard		

Table 2. Bearing Selection Comparison

Manufacturer	MPB	Barden
Part Number	CR4FM7LD	SFR4HX1
Material	52100 Steel w/TiC Coated Balls	440C Stainless Steel
Ball Size	3/32"	9/64"
Ball Compliment	9	8
Contact Angle	10.0°	12.7°
Axial Capacity	140 lbf	407 lbf
Radial Capacity	67 lbf	206 lbf
Dynamic Load Rating	172 lbf	520 lbf
Maximum PSD @ 365 Hz	0.028 g ² /Hz	0.26 g ² /Hz
Maximum PSD @ 90 Hz	0.28 g ² /Hz	2.4 g ² /Hz
Maximum Random rms acceleration	14.8 Grms	45.2 Grms
Maximum Steady-State acceleration	37.8 g's	116 g's

Table 3. Lubricant Property Comparison

	<u>Bray 815Z</u>	<u>Pennzane™ X2000</u>
Viscosity		
@100°C (ASTM D445)	45 cSt	14.7 cSt
@40°C (ASTM D445)	148 cSt	112.0 cSt
@-20°C (ASTM D2602)	1125 cSt	7092 cSt
@-40°C	11500 cSt	78608 cSt
Viscosity Index (ASTM D2270)	350	135
Flash Point (ASTM D92)	299°C	315°C
Point (ASTM D92)	330°C	326°C
Pour Point (ASTM D97)	-112°C	-57°C
Molecular Weight	7000 gm/mole	910 gm/mole
Density @ 20°C (ASTM D1298)	1.866 gm/ml	0.846 gm/ml
Total Weight Loss	0.8%	0.160%
Vacuum Condensable Material	0.05%	0.056%
Vapor Pressure 125°C	2 x 10 ⁻⁷ Torr	4 x 10 ⁻⁷ Torr
Vapor Pressure 20°C	8.7 x 10 ⁻¹² Torr	1 x 10 ⁻¹² Torr

Stepper Motor Instabilities in an Aerospace Application

Russell Kackley* and Sean McCully*

ABSTRACT

Stepper motors are frequently used in positioning mechanisms because they have several advantages over ordinary DC motors. However, there is frequently no feedback loop and the motor may exhibit instabilities under some conditions. A stepper motor in an aerospace positioning mechanism was investigated. During testing, the motor exhibited unstable behavior, such as backrunning and forward running. The instability was dependent on voltage pulse characteristics, temperature, positioning angle, step rate, and interaction between the two motors in the system. Both testing and analysis results verified the instability. A special-purpose FORTRAN code was written to simulate the system. This code was combined with another simpler code to show the performance of the system in the phase plane so that instability boundaries could be displayed along with the motor performance. The analysis was performed to verify that proposed modifications would produce stable performance before implementation in the hardware. Subsequent testing verified the analytic stability predictions.

Overview of Stepper Motor Characteristics and Operation

Stepper motors come in three basic types: permanent magnet (PM), variable reluctance (VR), and hybrid, which combines features of both the PM and VR types. The stepper motor under consideration for this paper is a hybrid stepping motor. In this configuration, the rotor consists of three components: an axially magnetized rotor and two pole pieces, one at either end of the rotor. Each pole piece is a toothed disk. Figure 1 illustrates this arrangement using only five teeth on the pole pieces. The motor under consideration has 50 teeth on the north and south pole pieces. The pole pieces are staggered by $1/2$ tooth pitch.

The stator of the motor is wound with wire to provide electromagnetic poles that interact with the rotors' permanent magnet poles. Stepper motors can be constructed with two, three, or more stator phases. The motor under consideration is a two-phase motor. This motor has four electromagnetic poles on each phase, for a total of eight stator poles. In addition, the rotor has 50 poles, for a total of 200 possible stable rotor positions. This results in a step angle of 1.8° .

The operation of a stepper motor is best explained with the aid of Figure 2. This figure shows the operation of a 90° two-phase stepper motor in which each

* Lockheed Missiles and Space Company, Inc., Sunnyvale, California

stator phase is sequentially energized, causing the rotor to step in a clockwise direction. The four-step sequence can be repeated to move the rotor through many revolutions. The motor can be made to run forwards or backwards simply by reversing the phase excitation sequence. When the rotor runs synchronously with the phase excitation, the motor is said to be maintaining step integrity. The operation of the 1.8° two-phase motor is identical, except that there are 200 steps for each revolution of the rotor instead of only four.

Stepper motors are frequently used in positioning mechanisms because they have several advantages over ordinary DC motors. Stepper motors have no brushes to wear out, are simple in both mechanical and electrical construction, and can often operate open loop without encoders or tachometers. However, each step applies an abrupt torque pulse to the motor and surrounding structure. This can cause structural modes to be excited in aerospace mechanisms where structures are lightweight with low damping and natural frequency characteristics. The motor may also exhibit instabilities under some conditions because there frequently is no feedback loop. Also, motors being used in vacuum environments may have problems dissipating the heat generated in the stator windings due to the absence of convection for heat dissipation. For this reason, many stepper motors are operated with a shaped rather than a square voltage pulse. This can aggravate instability problems if the peak voltage is enough to cause the rotor to overshoot the commanded position and the voltage is suddenly reduced before the rotor has a chance to dissipate the energy through damping or friction.

Stepper Motor Failure Modes

The desired behavior of a stepper motor is shown in Figure 3, in which the motor rotor is accurately following the commanded position. However, if there is insufficient damping or friction, or if the motor is stepped at a rate close to the motor's natural frequency, the motor can backrun (run opposite to commanded direction) at three times the commanded rate, as shown in Figure 4. Another failure mode occurs when there is insufficient damping or friction and the rotor overshoots the commanded position to the next stable equilibrium position, which is four steps ahead of the commanded position. This is called forward running and is shown in Figure 5.

Application Description

A Multiple Boom Assembly (MBA), shown in Figure 6, uses stepper motors to position the booms. The stepper motors are located at the shoulder and elbow pivots. Each motor is a two-phase, 1.8° stepper. Each motor phase has an identical primary and redundant winding to provide full electrical redundancy in the motor. The redundant windings are open-circuited when not in use so that no current flows through them. Also, the phase that is not being pulsed is open-circuited so that current is flowing in only one winding at a time. Stepper motors are used in this application for the reasons listed above, i.e., no brushes to

wear out and to eliminate the need for a feedback loop around the motor. Each stepper motor drives its respective boom through a harmonic drive coupled to a pinion gear. The combination of the motor, harmonic drive and pinion gear is called a Primary Drive Unit (PDU). Each PDU interfaces to a large bull gear on the boom. An optical encoder also interfaces with the bull gear to provide information on the boom angle. However, this information is not incorporated into a feedback loop to control the motors because the encoder resolution is only ± 11 motor steps. A standard H-bridge circuit is used to provide current to the motor windings. The motor step rates vary from 11 to 676 steps/sec. Figure 7 shows the pulse shape of the voltage applied to the windings. The pulse is stepped from a peak voltage to a holding voltage to minimize the i^2R heating of the motor windings, particularly at low step rates.

The Failure

If the rotor overshoots the commanded position by too much, it can gain or lose some integral multiple of four steps before settling down and running synchronously again. In addition, if the rotor oscillations are large enough when the next pulse occurs, the rotor can travel backwards to the next equilibrium position and become synchronized with the pulse timing such that the motor is running at three times the commanded rate and in the opposite of the commanded direction. Both forward and back running were exhibited in the motor used in the MBA. Although the PDU was tested at various subsystem levels to verify proper operation, and some motor instability problems were noted at PDU-level tests, it was thought at the time that these problems would disappear when the PDU was operated with the entire MBA. However, during a thermal-vacuum test, major instabilities occurred. The temperature range for the test was from 10 °F to 170 °F. The first failures occurred on the elbow motor at 169 steps/sec at 170 °F. The instability was observed both visually and in the encoder data. The outboard boom was observed to move erratically, gaining or losing steps at random and running at five times the commanded rate in the correct direction and three times the commanded rate in the wrong direction. This effect was also observed at room temperature at other step rates. However, the motor was stable when the temperature was 10 °F because the viscous damping in the system was high enough to eliminate any oscillations.

Problem Resolution

The instability was solved by making three modifications to the system. First, the duration of the maximum voltage was shortened to reduce the amount of electrical energy delivered to the motor. Second, the driving circuit was modified to short-circuit the quadrature winding to introduce additional electromagnetic damping. Finally, the minimum temperature was raised to 35 °F to make sure that adequate torque capability existed at cold temperature with the reduced input energy and additional damping. These solutions were chosen because they offered the best resolution to the problem with the least impact to cost and schedule. Because the problem was not identified until late in the

hardware development, major changes to the hardware were difficult to make. The following other solutions were proposed: (1) addition of mechanical or magnetic damping, (2) reducing the maximum temperature seen by the motor, (3) replacement with a different, more stable stepper motor, and (4) short-circuiting the redundant windings to introduce additional electromagnetic damping. The first three were considered very difficult to implement because of cost and schedule constraints. The fourth was rejected because it would have reduced the electrical redundancy in the motor. In addition, (4) would have added so much damping that excessive voltage would have been required to run the motor at cold temperature.

The selected solutions were verified by analysis before implementation in the hardware. The remainder of this paper discusses the analyses used to validate the selected solutions. Two analyses were undertaken to investigate the stability of the proposed solutions. The first modelled one motor and boom with Pro-MatlabTM and SimulabTM, two commercial servo-control simulation codes. The second analysis modelled the two-boom, two-motor system with a special-purpose FORTRAN code, called STEPPER. The model for one motor-boom assembly is shown in Figure 8. This basic model was used in both analyses, but the STEPPER code also modelled the dynamic coupling between the inner and outer booms. The motor-arm models included rotor inertia, damping, and friction; wave generator inertia, damping, and friction; harmonic drive friction, stiffness, and deadband; wire harness torque; and boom inertia.

An analysis technique described in reference 1 was found to be very useful in verifying the stability. In this technique, the motor rotor angular speed and angular error are used to construct a phase plane plot. In addition to the computed motor state, curves called separatrices are superimposed on the plot. Figure 9 shows an example of such a plot with a stable stepper motor. Superimposing the rotor dynamic behavior and the separatrices on the same phase plan provides a picture of the motor performance relative to the stability boundaries. Two important characteristics can be observed in the phase plane plots. First, if the rotor trajectory crosses the separatrix from left to right and stays on the right side of the separatrix, the motor is forward running (gaining steps). If the rotor trajectory crosses the separatrix from right to left, the motor is back running (losing steps), as shown in Figure 10.

The separatrices are calculated from a simplified motor model that neglects the relatively small effects of detent torque and the inductive time constant of the driving circuit. This approximation is described by the following differential equation:

$$J \frac{d^2\theta}{dt^2} + \left(b + \frac{K_T K_B \sin^2(A\theta)}{R_m} \right) \frac{d\theta}{dt} + \frac{K_T V_s \sin(A\theta)}{R_m} = -T_f \operatorname{sign} \left(\frac{d\theta}{dt} \right) \quad (1)$$

where:

J = rotor moment of inertia
 b = rotor viscous damping coefficient
 K_T = motor torque constant
 K_B = motor back emf constant
 A = number of pole pairs ($90^\circ/\text{step angle}$)
 R_m = motor winding resistance
 V_s = voltage applied to motor
 T_f = rotor coulomb friction
 θ = rotor angle

For any given $\left. \frac{d\theta}{dt} \right|_{t=0}$ and $\theta|_{t=0}$, the solution to (1) is called a trajectory,

which proceeds from the initial conditions to a point of zero velocity, called a singularity. The stability of each singularity depends on the slope of the torque-angle curve in the vicinity of the singularity. The slope is positive near a stable singularity (focal point) and negative near an unstable singularity. The focal points occur at 0, 4, 8, 12, ... steps relative to the commanded position and saddle points occur at 2, 6, 10, 14, ... steps. A good way to visualize the singularities is to consider a purely mechanical system, such as a pendulum. The focal points correspond to the pendulum at the bottom of its swing and the saddle points correspond to the pendulum at the top of its swing. Near the focal points, small torques will disturb the system, but it will always return to the focal point when the velocity decays to zero. On the other hand, near saddle points, even small disturbances will send the pendulum swinging around until it settles at a focal point.

There are an infinite number of trajectories in the phase plane because there are an infinite number of sets of initial conditions. The trajectories that pass through the saddle points are called separatrices. They divide the phase plane into regions with one focal point in each region. All trajectories within a region spiral into the focal point for the region.

In order to accurately model the MBA system, drive-system parameters had to be established. Except for the friction and damping parameters, most of the motor properties were well known. A test program was set up to measure the friction and damping parameters as accurately as possible because the motor stability was very sensitive to these values. Measurements were made at cold, room, and hot temperatures. Using the measured friction values, a set of twenty-one cases were run to try to simulate actual tested cases. The test hardware exhibited instability in five cases and stable behavior in 16 cases. The STEPPER code correctly predicted all five unstable cases but also predicted unstable behavior in seven of the 16 cases that should have been stable. This was taken

as evidence that STEPPER was conservative in predicting instabilities; i. e., that STEPPER would correctly predict all cases of instability, but might also predict instability when the actual hardware is stable.

For most aerospace mechanisms, a simulation is usually used to evaluate system performance under worst-case conditions. If the system still works when all parameters are stacked to the worst side of their tolerances, then we can be very confident that the mechanism will function as intended under real-world conditions. Unfortunately, this technique is dependent on finding a set of parameters to produce a worst case. This is very difficult when the parameters are inter-dependent. In the case of the stepper motor stability analysis, it was next to impossible because of the large number of interdependent parameters. In addition, the parametric technique depends on knowing that a parameter change had made the system more stable or less stable. This was impossible to determine. Therefore, it was decided that a Monte Carlo technique would be used. In this technique, a set of cases was run at the hot temperature, which was the worst case for stability. The input values were chosen at random from a uniform distribution of the input parameters over a range that was reasonable for each parameter. The input data was processed using a Microsoft EXCEL-based preprocessor to create hundreds of input cases in a short time with minimal data entry. The result was that four out of one hundred cases predicted instability. In all the failed cases, either four or eight steps were lost out of 200 commanded steps. The failed cases combined low friction, low damping, low holding voltage and high peak voltage. These parameters are the primary ones that would lead to motor instabilities. In addition, 100 cases were run to verify that adequate energy was available to overcome the increased viscous damping and to run the motor at 35 °F.

Simulab™ is a graphics-based analysis code that runs on a Macintosh. In this code, math models can be created in their block diagram form by simply picking the appropriate blocks and connecting them together in a click-and-drag fashion. Everything is done visually, including the debugging. After the model has been created and debugged, it can be "grouped" and "masked" to form its own new block. This is what has been done to form the library of components shown in Figure 11. This library provides a headstart for designers and analysts modelling more complicated systems. By picking and dragging from this library, some fairly complicated mechanisms can be created in a short time.

Four components from the Simulab™ library were used to analyze the two-phase stepper motor (Figure 12). The driving source for the stepper motor includes a maximum and minimum voltage step. The accuracy of this pulse depended on the integration step size that was chosen, so there was no way to control the pulse form as exactly as was done in STEPPER. The harmonic gear model contained a wave generator inertia with an input and output shaft stiffness and a cyclic torque term added to the driving torque. The load was modelled as

a single-degree-of-freedom, rigid-body inertia representing the shoulder boom with the elbow in a fixed position. The two-phase stepper motor model included in the library represents a case where the phase not being pulsed is short-circuited, allowing back emf and back emf damping to develop. To shut the back emf off in Simulab™, a logical switch was created that did not allow current to flow in the winding that was not being pulsed. This represented the motor as it existed during the development tests. Additional damping could be achieved through mutual inductance if the redundant coil was shorted in the phase being pulsed. This was modeled in Simulab™ with cross-coupling terms operating on the current in each phase of the motor.

Step responses of each motor are shown in Figure 13. These responses illustrate the difference in damping between the three different motor model cases. The motor with no electrical damping demonstrated a large overshoot from the commanded position with unacceptable ringing. Shorting the quadrature winding of the stepper motor added electrical back-emf damping to the response, reducing the overshoot and settling time. Still more electrical damping was introduced by shorting out the redundant windings in each phase. Because the primary and redundant windings share the same stator pole, shorting the redundant winding introduced a mutual inductance term which added to the back emf to create the response shown. It was decided that relying on the redundant coils for electrical damping would compromise the redundancy of the system, and cold-temperature torque margins would not be satisfied, so shorting the redundant coils was rejected as a solution option.

Modified System Test Results

Based on the successful analytic results, the hardware was modified and run through the test program. The hardware successfully passed all tests.

Lessons Learned

Several important lessons are evident from the failure and subsequent resolution of the MBA problem. First, stepper motors can exhibit instabilities and should be analyzed for them early in development. Second, stepper motor stability is very dependent on friction and damping, so it is important to know them as closely as possible and vary them in test and analysis to cover all possible conditions. Third, superimposing rotor dynamic behavior and separatrixes on the phase plane technique is a valuable tool for analyzing stepper motor stability. Finally, Simulab™ is a valuable tool for quickly constructing models of complex systems to analyze them before building and testing expensive hardware.

Reference

1. Taft, C. K., R. G. Gauthier, and T. J. Harned, *Stepping Motor Design and Analysis*, Twelfth Edition, University of New Hampshire, 1989.

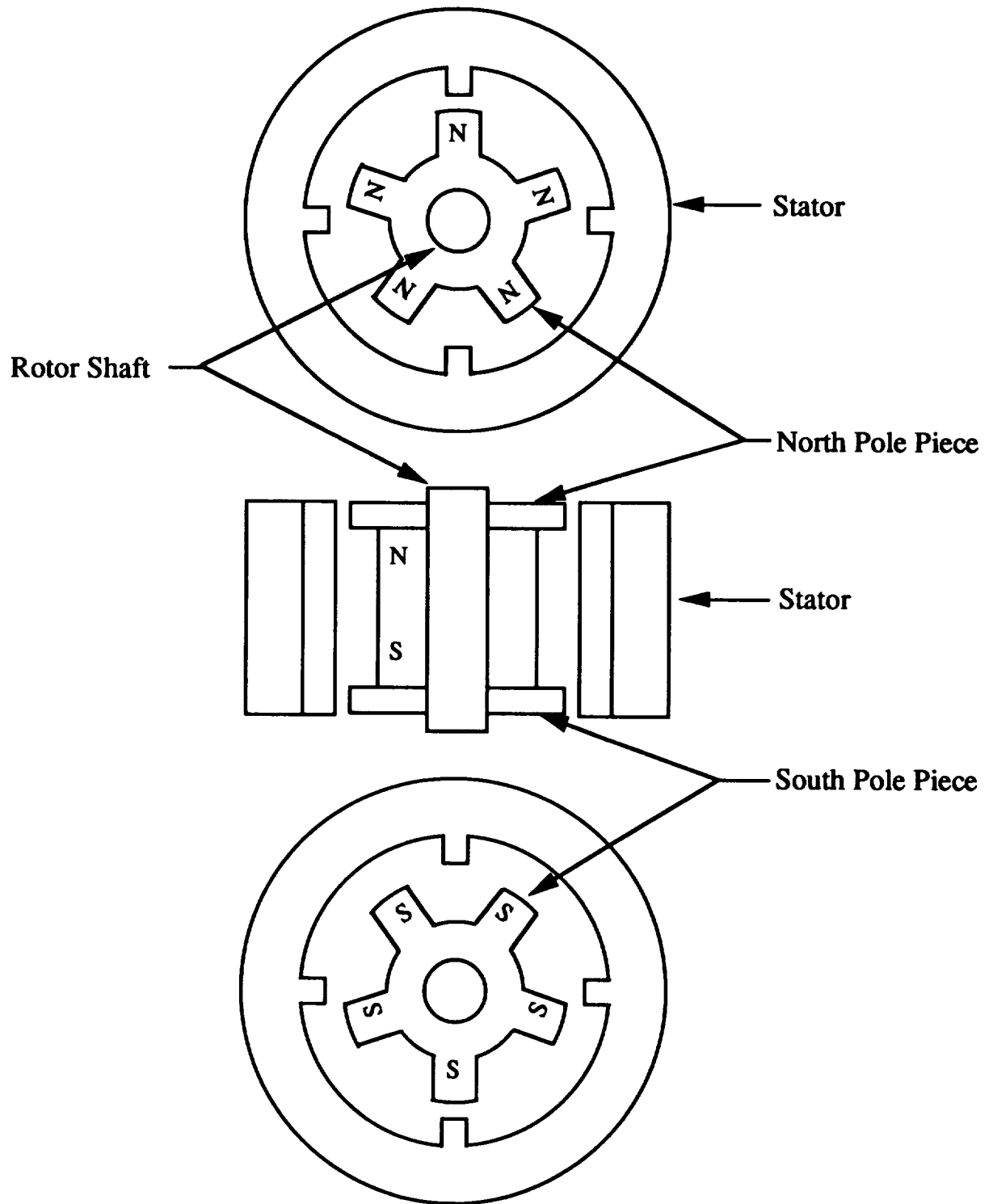


Figure 1
Motor with Five-Tooth Rotor

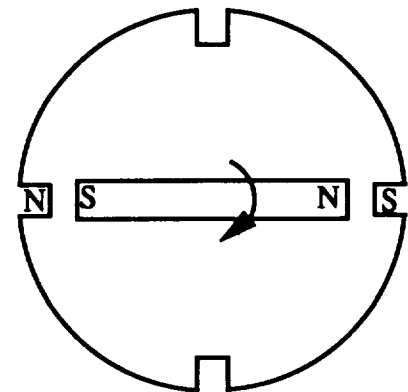
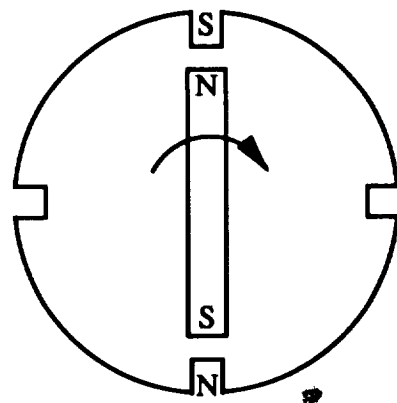
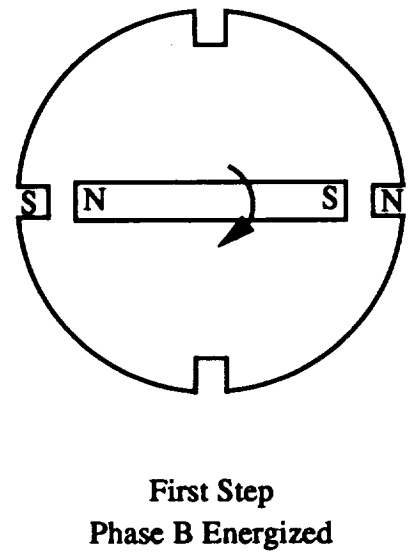
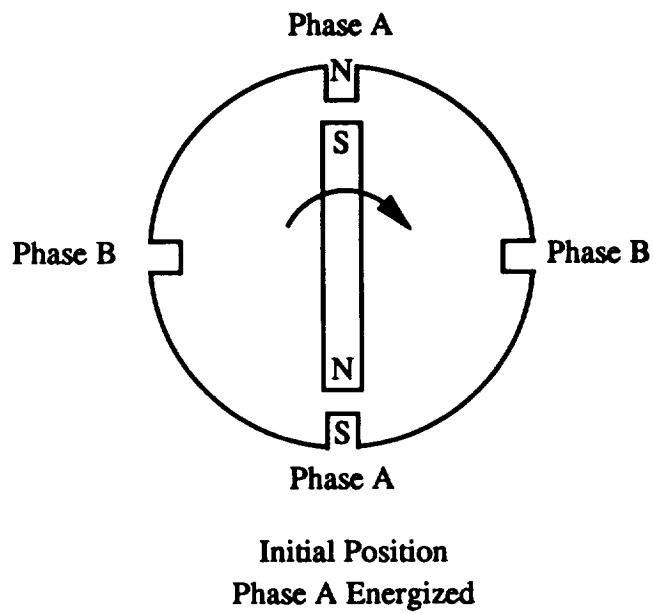
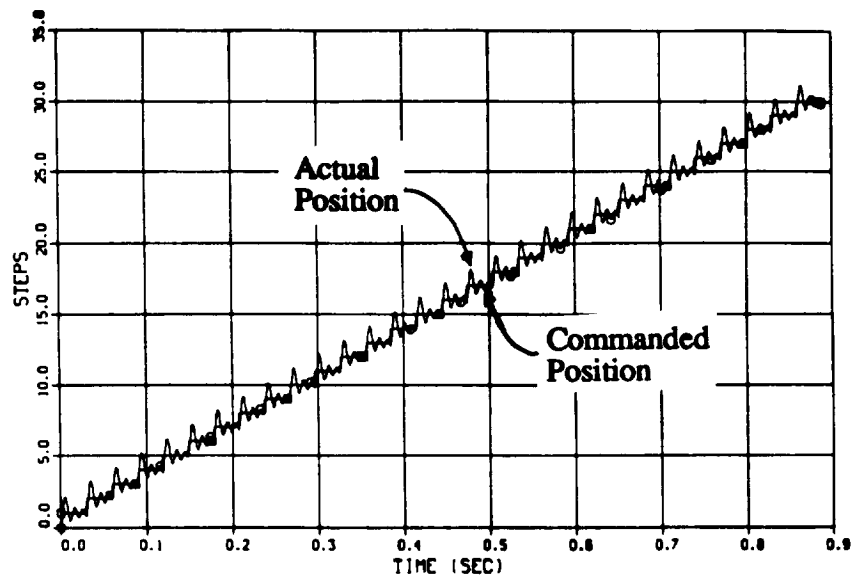
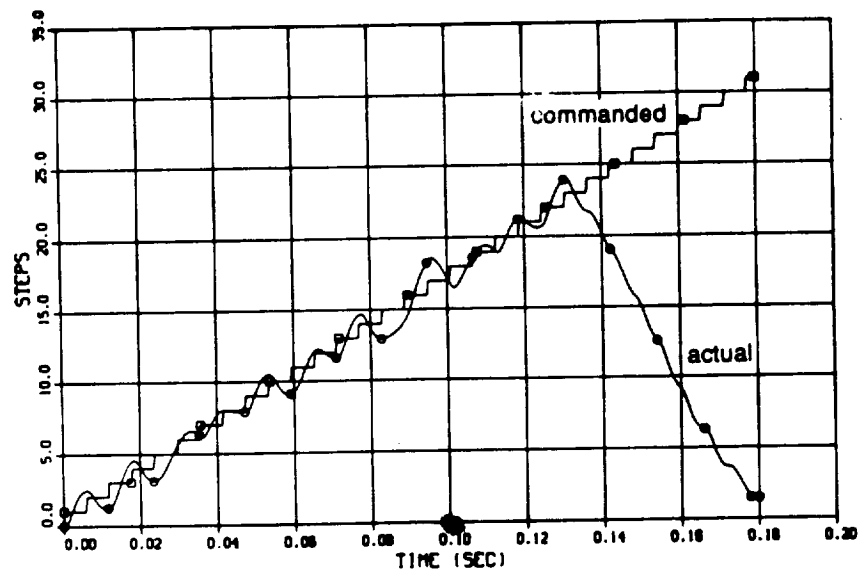


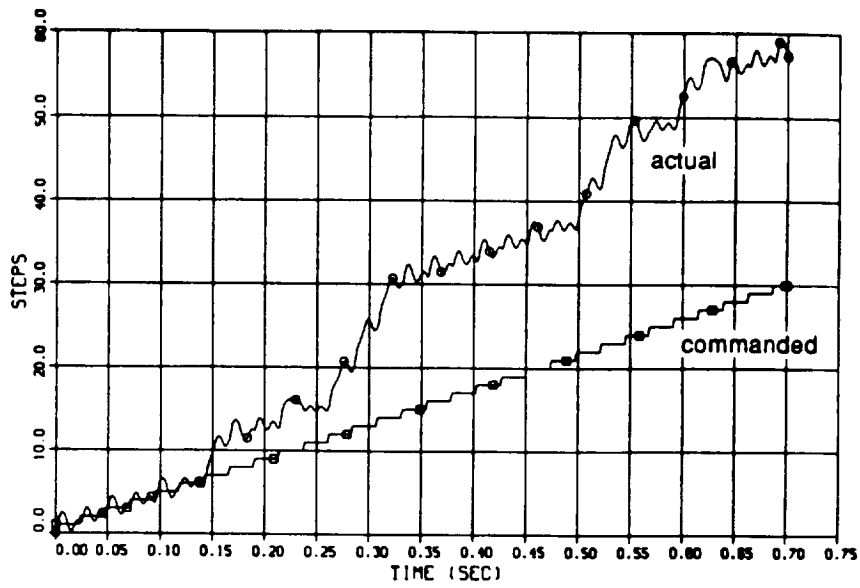
Figure 2
90° Stepper Motor



**Figure 3. Rotor Position vs Time
Rotor Following Command**



**Figure 4. Rotor Position vs Time
Rotor Running Opposite of Command Direction (Back
Running)**



**Figure 5. Rotor Position vs Time
Rotor Running Ahead of Command (Forward Running)**

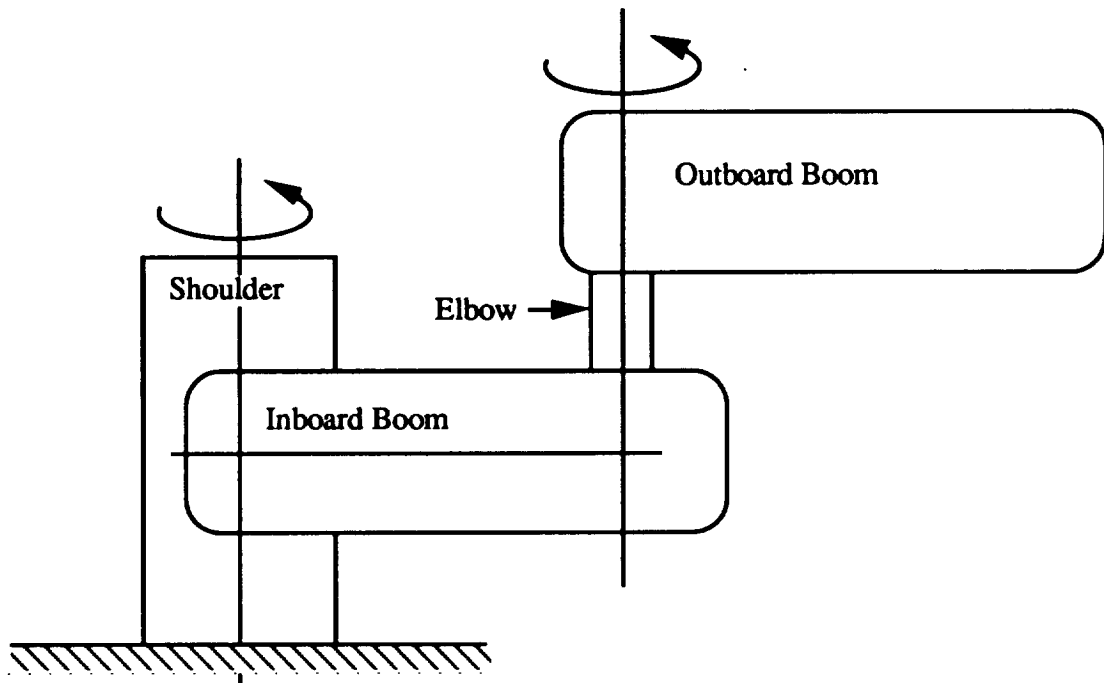


Figure 6. Multiple Boom Assembly

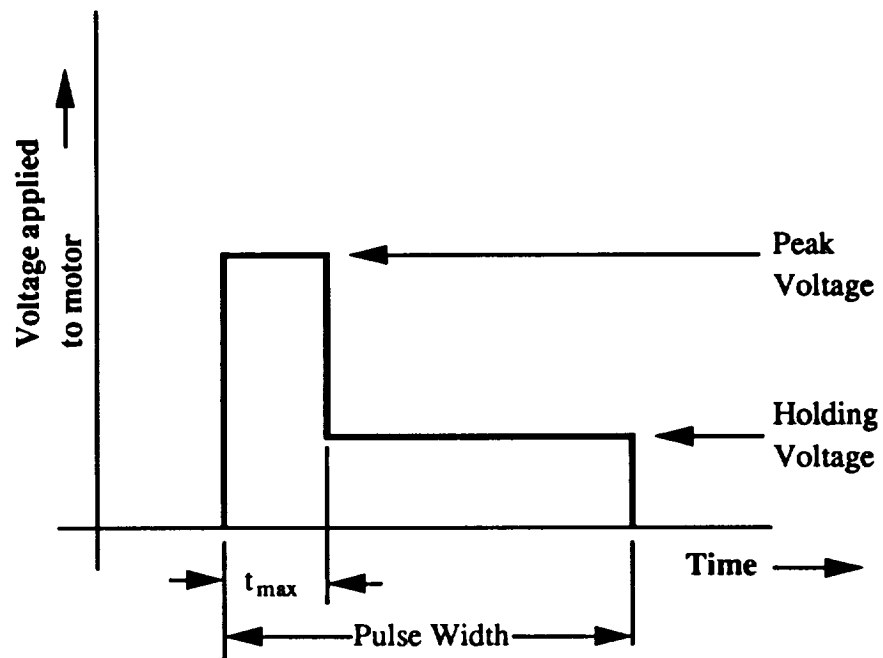


Figure 7
Motor Voltage Pulse Shape

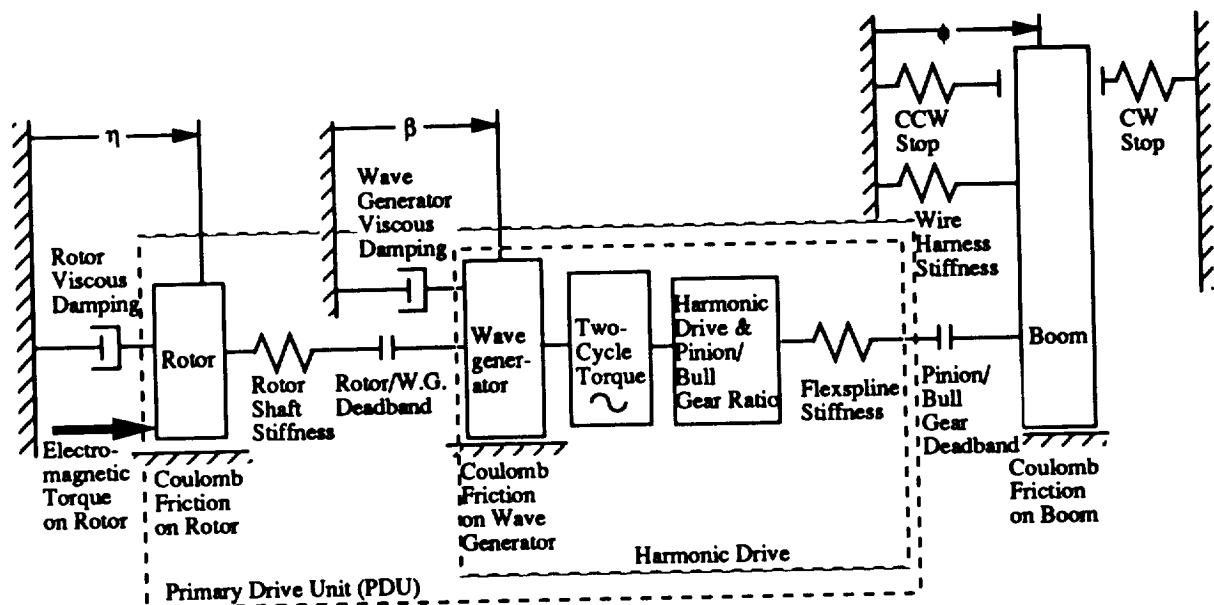


Figure 8
Schematic of One Boom

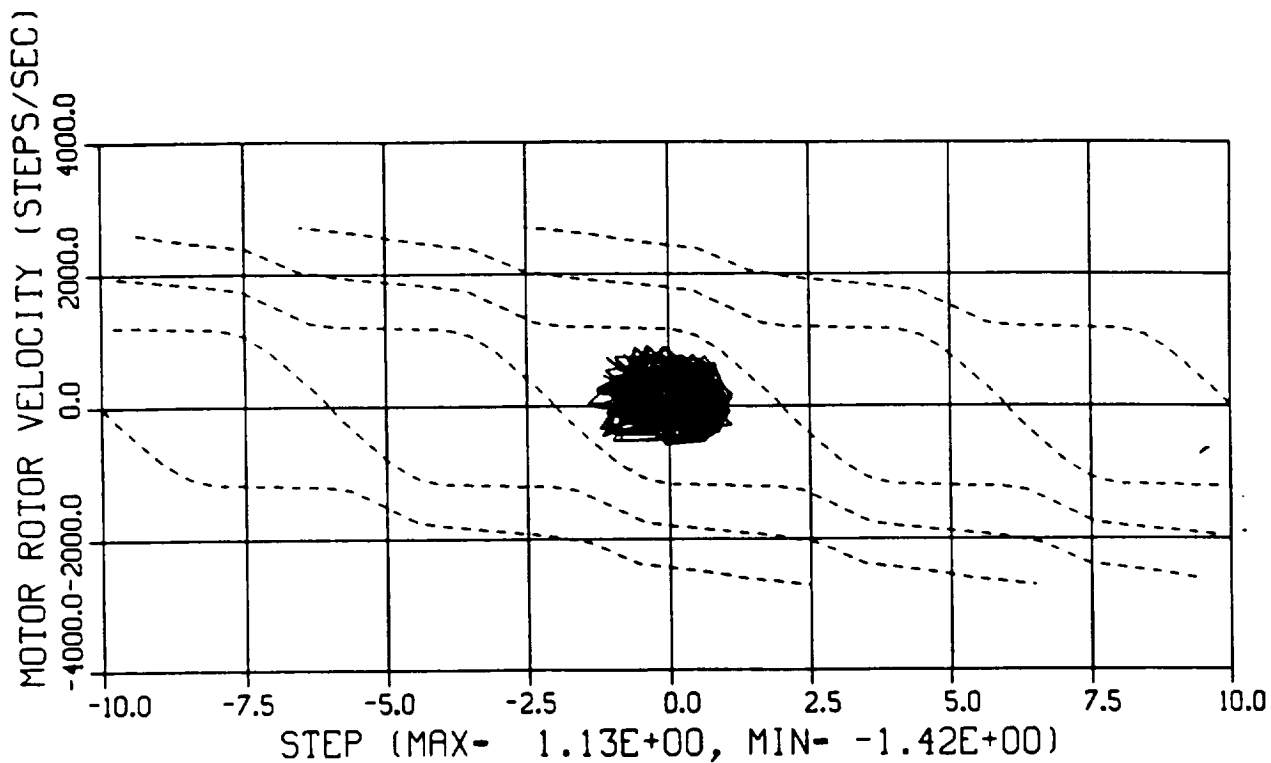


Figure 9. Phase Plane Plot

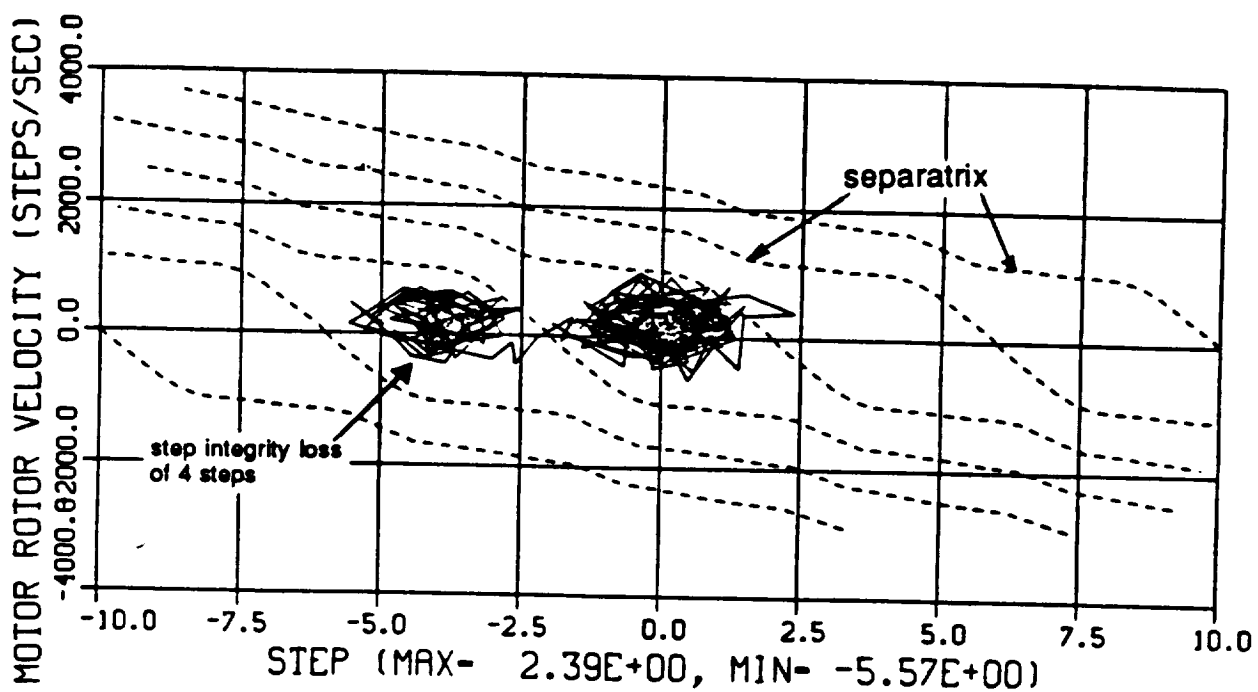
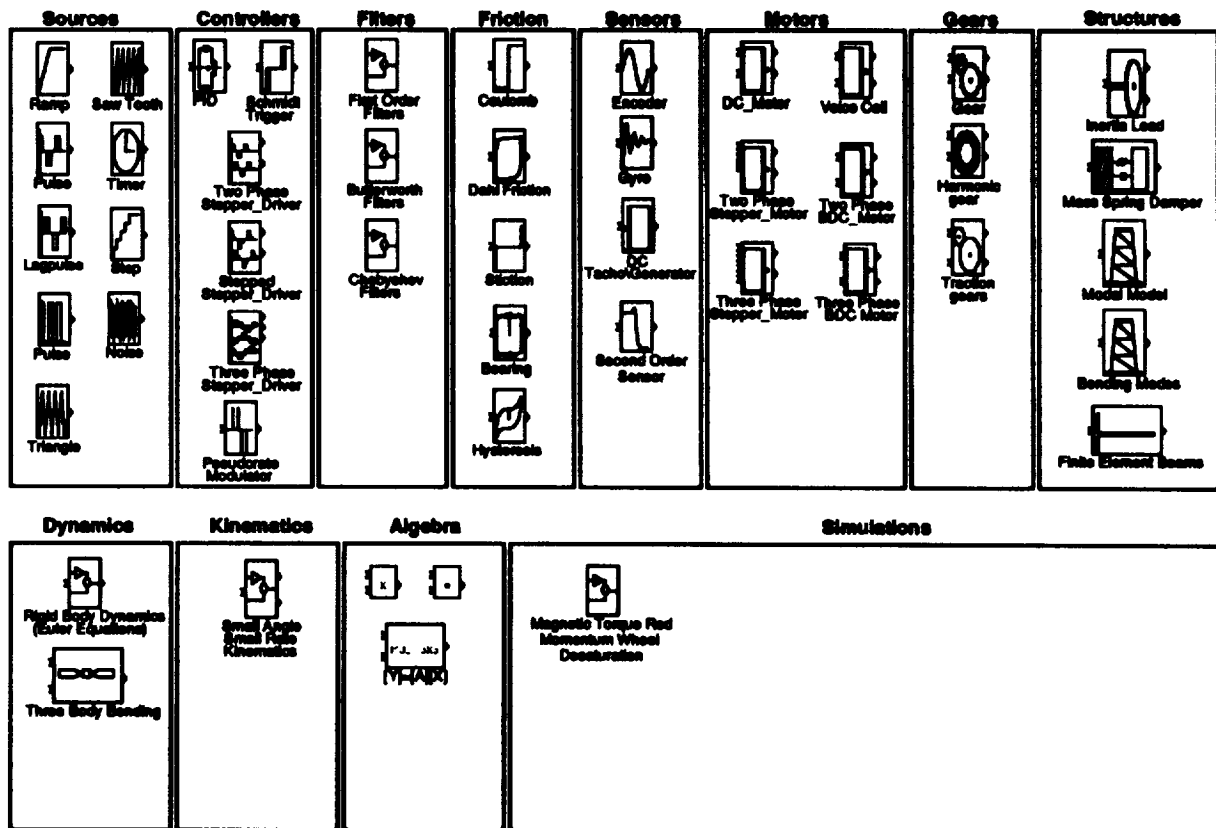


Figure 10. Phase Plane Plot Showing Loss of Steps



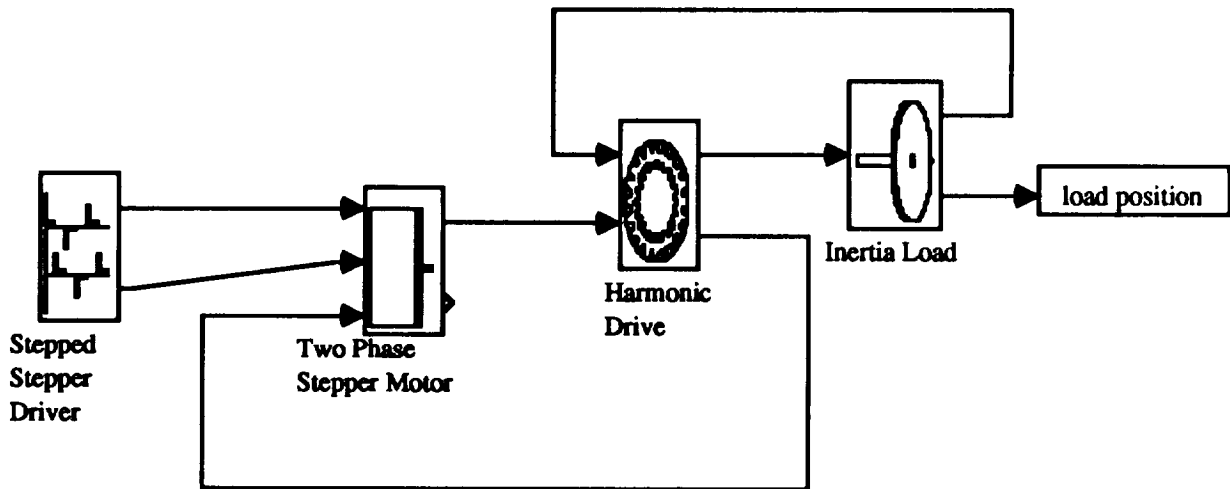


Figure 12. Simulab Model of Stepper Motor Analysis

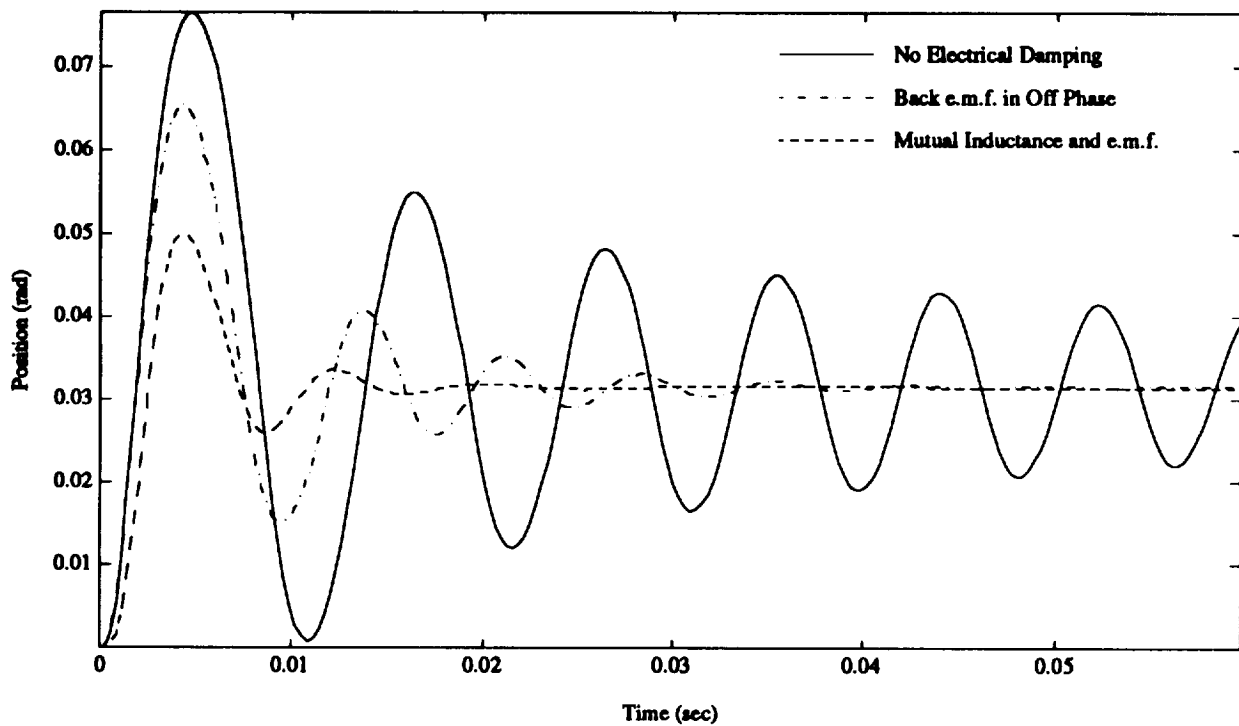


Figure 13. Motor Position Step Response

SOHO MAMA OPENABLE COVER/VACUUM SEAL MECHANISM

Mitchell T. Wiens*

ABSTRACT

This paper describes the requirements, design, and test results of an openable cover mechanism with a high-vacuum seal developed for the Multi-Anode Microchannel Array (MAMA) detectors, aboard the Solar and Heliospheric Observatory (SOHO) spacecraft. The mechanism, tested in summer/fall 1991, has completed 1000 test cycles in an inert atmosphere at room temperature and pressure. Measured mechanism performance included: vacuum seal less than 5×10^{-10} torr-litre/second, 103-degree (deg) angular range of travel, 20-minute (min) cycle time, and successful latching functions. An openable cover mechanism that provides a clean, high-vacuum seal is vital to the success of a MAMA detector operating over full wavelength coverage from 500 to 1600 angstroms.

INTRODUCTION

The SOHO spacecraft is a joint NASA and ESA mission to observe weak Extreme Ultraviolet emissions from the solar outer atmosphere against the strong visible-light background. The spacecraft will be placed in a halo orbit about the L1 Lagrange point where the gravitational fields from the Sun and Earth are equal, to perform accurate photometric measurements over a very wide range of intensities, to observe structures on very fine spatial scales, and to accurately determine very small wavelength shifts. Figure 1 (a) shows the MAMA detectors as mounted in the Ultraviolet Coronagraph Spectrometer (UVCS), an instrument aboard SOHO. Figure 1 (b) shows the optical system schematic for UVCS.

The scientific requirements dictate the contamination-sensitive detector array be sealed under vacuum with minimum particulate (MIL-STD-1246, Level 300) and molecular contamination [< 60 nanograms per square centimeter (ng/cm^2) non-volatile residue (NVR)] at a leak rate less than 1.5×10^{-8} torr-litre/second after initial vacuum processing at 225 deg Celsius (C). Operation in the wavelength range from 500 to 1600 angstroms requires unsealing the detector during operation for full wavelength coverage with an unrestricted field-of-view. Extensive ground-test operations and additional on-orbit operation dictated an operational life of 250 sealing/unsealing cycles. A magnesium fluoride (MgF_2) window is required for prelaunch aliveness testing and for alignment under sealed conditions. Package size could not exceed 80 millimeters (mm) x 85mm x 211mm due to the close spatial requirements of multiple detectors within the instruments. Operational temperature is +10 to +30 deg C. Mass could not exceed 2.7 kilograms (kg).

* Ball Corporation, Aerospace Systems Group,
Electro-Optics/Cryogenics Division, Boulder, Colorado

Early program trade studies were performed to identify potential ultra-clean high vacuum seals that could survive 225 deg C non-operational processing and perform reliably during 250 cycles of operation. The design uses structural materials selected for maintaining their strength properties at elevated temperatures and for close coefficient of thermal expansion (CTE) matches for dissimilar materials between -10 deg C and 225 deg C. Dissimilar metals were identified that could withstand high bearing loads in the design while operating unlubed (potential contamination source) and were tested to verify performance within requirements. Space-qualified dry lubrication was specified for mechanism bearing surfaces not located in detector critical path. Critical mechanism-drive functions were identified while extensive vendor searches were performed emphasizing small envelope requirements.

MECHANISM DESCRIPTION

Figure 2 shows an isometric exploded view of the MAMA openable cover/vacuum seal mechanism. A metal-to-metal belleville seal was selected to minimize contamination and to provide the best performance over the operational life. To optimize use of the restricted envelope, the cover mechanism employs a paraffin actuator, mounted with spherical bearings, to provide an off-axis linear retraction force against a rotary guide plate initially in the unsealed position above the paraffin actuator. The guide plate supports another plate on each side (reaction and seat plate as shown in Figures 2 and 3) with a triad of silicon nitride (SiN) balls separating each plate. Each triad is nested in ramped raceways machined into each plate (two raceways on an inner radius and one raceway on an outer radius about the pivot point) and is retained by a ball cage/separator. The inner seat is shrink fit into the seat plate and the belleville is fastened to the inner seat. A 6-mm-diameter MgF₂ window is mounted into the inner seat using indium solder. When in the unsealed position, the entire assembly is held together by a pair of pre-loaded tension springs and pivots about a needle bearing housed within the guide plate. Upon sealing, the actuator retracts, rotating the plates with belleville seals 75 deg into position above the detector array. At this point, the two non-actuating plates on either side of the guide plate each bump against a ball-bearing stop while the guide plate continues to rotate an additional 28 deg. During this final rotation, each triad of SiN bearing balls rolls unlubed up the ramps onto flats machined in each plate, wedging the non-actuating plates away from the guide plate and forcing the seat plate and belleville against its inner and outer seat and the reaction plate against a stationary backing plate, thus creating the vacuum seal. Unsealing is essentially the reverse of this motion, except a compression spring within the actuator provides extension force. Figure 4 provides a simplified picture of the mechanics of a single SiN ball.

BEARINGS AND LUBRICATION

The bearing and lubrication design approach addressed contamination concerns and high cycle life under high-seal loads. Wet lubrication was strictly prohibited because of its hydrocarbon levels. Dry lubrication was limited to the pivot bearing component supporting mechanism rotation.

Self-lube spherical bearings were selected to mount the paraffin actuator and to provide for linear to rotary motion transfer. SiN bearing balls allow unlubed operation of the cover mechanism above the detector array. Hybrid ball bearings (SiN balls/440C stainless-steel races), manufactured by Miniature Precision Bearing Corp., operate unlubed as mechanism stop bearings.

The pivot bearing design includes 21 individual 440C stainless-steel needle roller bearings, manufactured by Torrington Company, which were lubricated with an impinged, 1500-angstrom-thick coating of Molybdenum disulphide (MoS_2). A hardened bore within the 440C guide plate provides the outer bearing race. The mechanism pivots about a hardened stationary 440C shaft. Needle roller bearings are retained on either side of the guide plate by 304 stainless-steel thrust washers. The outer race, shaft, and thrust washers are lubricated with a 50,000-angstrom-thick coating of MoS_2 with polyimide binders. The pivot bearing design incorporates .015-mm radial clearance within the bearing to preclude moment loading due to the off-axis loading scheme.

The cover mechanism assembly as shown in Figure 3 consists of three 440C stainless-steel plates separated by two triads of Noralide NBD 100 SiN balls, AFBMA Grade 5, manufactured by Cerbec Ceramic Bearing Company. Mean Hertzian¹ compressive stresses on the bearing surfaces from the seal load and off-axis moment load were estimated to be 2.6 gigapascals² (GPa) (380 ksi). As discussed in New Departure Engineering Data³, the mean compressive contact-area stress that does not reduce fatigue life of a bearing is 3.45 GPa (500 ksi). The deformation and contact area for a ball in a race were measured by Whittemore and Petrenko⁴ and compared with the theoretical values.

This combination of dissimilar metals was chosen for its lowest wear coefficient measured from unlubed four-ball tests (a four-ball tester rotates one ball under load against three stationary balls) performed on several materials against 440C (the stationary material) to evaluate galling (adhesive wear) potential. Other unlubed materials tested against 440C were tungsten carbide (WC), 440C, and 52100 stainless steel. Results are shown in Table 1. The total torque that impedes the motion of a rolling element in contact with the raceway is a sum of the spin/slip and hysteresis loss components. The hysteresis contribution to torque is concerned with material fatigue, and among other factors, is due to the elasticity of the materials in contact. The spin/slip contribution will generate wear debris and for this reason, the torque component was isolated during the four-ball tests.

MATERIALS CHOICES

As previously mentioned, the cover mechanism plates are machined from 440C stainless steel, a common bearing quality material, and hardened to Rockwell 58C to avoid brinelling under high compressive loads. The ball/cage separators are machined from Vespel⁵ SP-1 (unfilled polyimide) to minimize particulate generation. Tension springs from Associated Spring are manufactured from 302 stainless steel.

VAT, Incorporated in Switzerland provides the manufacture and design of the belleville seal and conical seat surfaces. The seal design is based on VAT's off-the-shelf 40-mm commercial all-metal gate valve. The belleville seal is stainless steel with gold-over-silver plating to prevent oxidation of silver during bake-out. The seat material is a highly polished 316L stainless steel. It was selected for its low carbon content resulting in conical seat surfaces free of carbide inclusions.

The supporting structure including the backing plate and the detector mounting plate are manufactured from 6Al-4V titanium (Ti) to minimize weight and to maintain structural integrity after 225 deg C detector processing. The backing plate requires a high modulus-of-elasticity to minimize deflection under seal reactionary loads.

Free-machining stainless steel has been strictly prohibited because its high sulfur content would desensitize the detector.

MECHANISM COMPONENTS DESIGN, SELECTION, AND DEVELOPMENT

To specify the actuator requirements adequately and to design the cover mechanism ramp profiles, it was necessary to establish characteristics of the VAT vacuum seal, consisting of the belleville seal and its inner and outer conical seats. In particular, it was important to determine the load required to seat the belleville seal, establishing a vacuum-tight seal repeatedly, and the deflection of the belleville under this load. VAT had indicated the average load required was 50 kg per centimeter (cm) of outside seal circumference for their off-the-shelf commercial valve, equivalent to 630 kg for a 40-mm-diameter seal. Successful tests were performed across the operating temperature range on several seal assemblies to lower the required sealing load to 450 kg while reliably maintaining the required leak rate. This load reduction increased mechanism reliability through lower stresses and resulted in lower paraffin actuator output requirements. The belleville seal does not function as an ordinary belleville spring upon loading because it is constrained to rotate by the conical seat surfaces. This constraint makes the belleville extremely stiff, with a spring rate of 6 kg per micrometer (μm). Figure 5 shows a load/deflection curve produced from a composite of tests performed on several bellevilles.

During the design phase, several different ramp profiles for the ball raceways were studied in an effort to maximize mechanical advantage yet minimize Hertzian compressive stresses and actuator load. In addition, concerns about ball slippage, ball/raceway conformity and wear, and raceway uniformity were addressed. A computer program was developed to facilitate analysis of the large number of parameters and the non-linear behavior of some of the assembly components. The final optimized ramp profile was developed using a cosine function which maximized mechanical advantage at the end of the raceway (minimum slope) where the high sealing forces were generated while providing a uniform raceway with a .53 ball conformity.

The equations for the depth of each raceway are:

$$\begin{array}{lll} Y = A [1 - \cos(\pi\theta/B)] & 0 \leq \theta \leq B & \text{(ramp)} \\ Y = 2 A & \theta \geq B & \text{(flat)} \end{array}$$

where,

θ = angular ball travel relative to pivot (deg)

A, B = raceway parameters

The combined raceways between the guide plate and two non-actuating plates provide for a total of 3.8 mm of expansion to effect sealing. In addition, this travel allows the belleville to clear the seat surface during unsealing.

In the original mechanism design concept, the linear actuator consisted of a small stepper motor gearhead driving an acme screw to produce the required linear output. Motor lead time was incompatible with the program schedule. A electrically powered, paraffin-actuated, two-position, resettable-pin mechanism (actuator), produced by Starsys Research, promised to have a shorter lead time. In addition, it would be more reliable, less of a contamination source, would weigh less, and would cost less.

The 450-kg seal load requirement combined with the mechanical advantage provided by the cover mechanism and including margins levied an actuator output force capability as shown in Figures 6 (a) and (b). As can be seen from the two load profiles, most of the stroke (80%) requires low load. This stroke occurs over the 75 deg of motion mentioned earlier to position the cover mechanism above the detector array. A very high peak force is generated during the final 20% of stroke as the belleville seal is loaded. Load then drops off sharply as SiN balls roll onto flats. In addition, the actuator performs two other essential operations: latching and controlling cover mechanism backdrive upon unsealing.

The actuator is shown in Figure 7 (a) and (b). It employs a single, hermetically sealed paraffin actuator to provide a retraction (sealing) force and compression springs to provide an extension (unsealing) force. Two redundant 15-watt (W) heaters operating at 27 volts direct current (Vdc) induce expansion of the paraffin. When driven by the force of the thermally induced expansion of paraffin, a stroke-doubling shuttle causes the output shaft to retract, sealing the cover mechanism. The cover mechanism raceway flats allow overtravel of the actuator output ram, permitting latching of the binary latch⁶ housed within the actuator. Upon unsealing the cover mechanism, the paraffin actuator is heated to unlatch. After power is discontinued, compression springs within the actuator provide extension force against the shuttle to initially start cover mechanism unsealing. As the paraffin actuator cools, it provides an active damping force to control cover mechanism backdrive produced from the belleville seal as it unloads and drives the SiN balls down the ramped raceways. When the SiN balls have reached the end of the raceways (28-deg motion of guide plate), the cover mechanism continues to open the final 75 deg for unrestricted detector field-of-view. Miniature hermetically sealed switches from Honeywell, Inc. sense travel limits of the actuator output shaft and signal heater power on/off.

TEST SETUP

Figure 8 shows a schematic layout of the mechanism performance test setup. All mechanism performance tests to-date were completed in an inert (gaseous nitrogen) atmosphere at room temperature and pressure. Seal leak checks were performed in a helium (He) atmosphere with an Alcatel model ASM 51 leak detector. In addition to seal performance measurements, actuator cycle time and paraffin temperature were measured.

MEASURED PERFORMANCE

The main objective of the mechanism development tests was to demonstrate the mechanism/actuator concept's success in providing a high-vacuum seal after repeated cycling. Initial testing of the mechanism with a mechanical actuator provided evidence of the need for ball/cage separators to maintain the relative position of the SiN balls. The clearance designed in the pivot bearing to preclude moment loading caused a 'sagging' of the mechanism. The mechanism did not contact squarely as it expanded against the backing plate, causing the reaction plate to rock about two of the SiN balls and release of the third SiN ball. With the addition of ball/cage separators, the mechanism operated successfully and produced a high vacuum seal repeatedly. The first attempts at cycling with the paraffin actuator proved unsuccessful in controlling the backdrive created from the belleville seal during unsealing. The original actuator concept included two paraffin actuators (open and close) and a spring-loaded cam roller to control backdrive, shown in Figure 9. Phasing of the compression spring loading to the belleville seal unloading proved difficult. Attempts to modify the cam profile to match the backdrive profile more closely were unsuccessful. Extensive tests conducted to characterize the backdrive created when the belleville seal unloads during unsealing were crucial in revealing a control solution. Using a redesigned paraffin actuator to provide an active damping force upon cooling proved successful in controlling the backdrive. The spring-loaded cam roller and two- actuator design were replaced with the current design incorporating a single paraffin actuator with spring return and latch (described earlier). Ongoing tests have proven the mechanism's durability and reliability. Consistent vacuum seals less than 5×10^{-10} torr-liter/second have been achieved. The mechanism produces a mechanical advantage in excess of 16 to 1 (27-kg actuator input = 450-kg seal load). The mechanism has demonstrated full 103-deg angular range of travel and approximately 20-minute cycle time. The binary latch⁶ has performed flawlessly since incorporation into the design.

CONCLUSIONS

The openable cover/vacuum seal mechanism met all system performance requirements in an inert atmosphere at room temperature and pressure. Engineering development testing provided crucial information for effective design solutions. Additional thermal vacuum tests on the development unit are planned in January 1992 to ensure success within the operational environment. Vibration tests will follow. Integration of the mechanism with the MAMA detector in the Engineering Model Unit (EMU) is planned for early February 1992. This integration may prove to be the most difficult achievement due to the contamination-sensitive detector. Significant development of handling and assembly methods will occur to maintain detector integrity during integration.

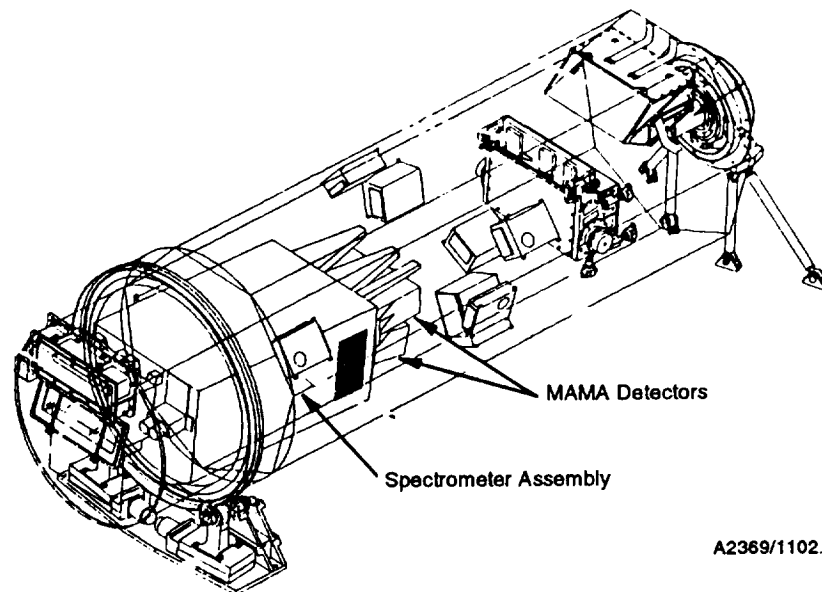
The SOHO MAMA mechanism development program success has established a baseline openable cover/vacuum seal mechanism design for a contamination-sensitive detector operating over full wavelength coverage at less than 1600 angstroms. The design incorporates minimal dynamic parts while providing a clean high vacuum seal, all within an extremely small mass and envelope budget. Test results have demonstrated the viability of the mechanism technologies that successfully meet leak rate requirements of 1.5×10^{-8} torr-liter/second or less over 250 operational cycles.

ACKNOWLEDGEMENTS

The author would like to acknowledge contributions made to the mechanism design, fabrication, test, and support activities: Dr. Gethyn Timothy of Stanford University and Principal Investigator for the MAMA detectors on SOHO; at Ball Aerospace Systems Group (BASG), Dick Maxwell, for his support and funding to write this paper; Rich Johnson for his conceptual design and resource throughout the design; Joe Girard for his structural analysis and resource throughout the design. Steve Daudt for system engineering direction and program support; Gary Kahn for his machining and craftsmanship with the hardware; Damon Phinney and Ed White for their technical support; Chris Dayton for his materials testing support; and, at Starsys Research, Daryl Maus and Scott Tibbitts for their timely actuator support.

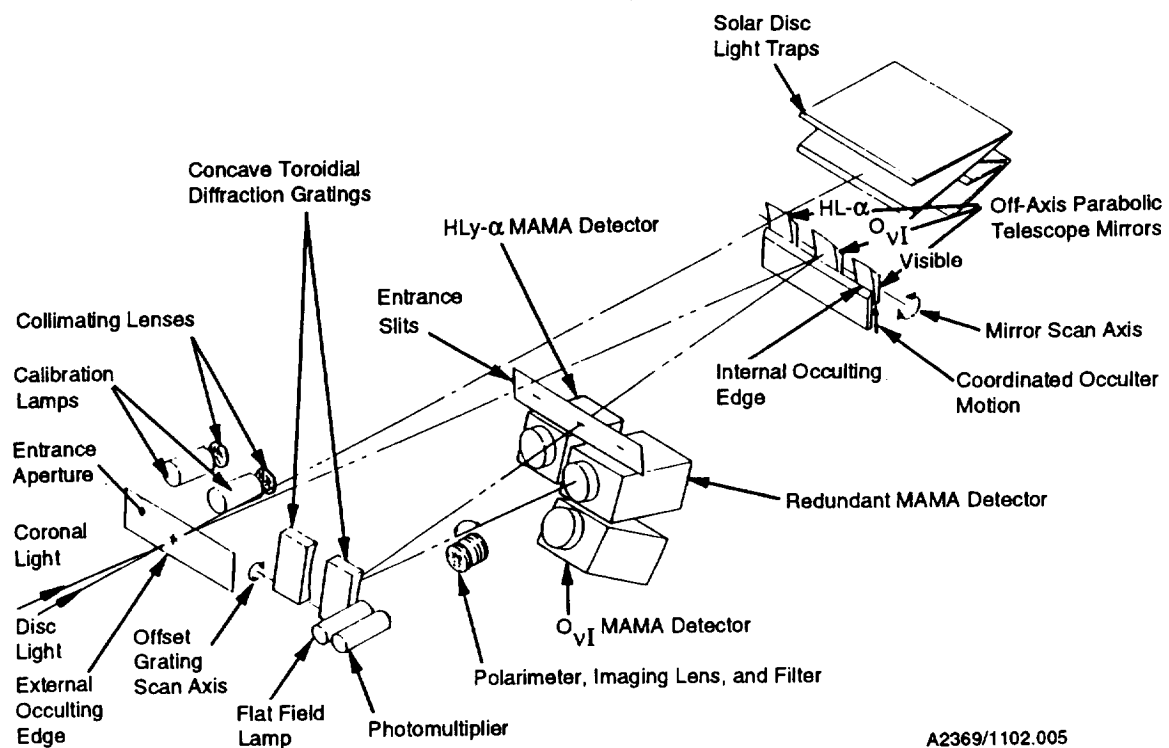
REFERENCES

1. Hertz, H. "Gesammelte Werke," vol. I, Leipzig, 1895.
2. Young, W. C. Roark's Formulas for Stress and Strain, 6th Edition, pgs 647-665.
3. Jones, A. B. New Departure Engineering Data, Analysis of Stresses and Deflections, pg 173, 1946.
4. Whittemore, H. L., and S. N. Petrenko. Friction and Carrying Capacity of Ball and Roller Bearings, Tech Paper Bur. Stand., No. 201, 1921.
5. Vespel is a trademark of the Du Pont Corporation.
6. Maus, D., and S. Tibbits. Resettable Binary Latch Mechanism for Use with Paraffin Linear Motors. Proc 25th Aerospace Mechanisms Symposium, 1991.



A2369/1102.004

Figure 1(a). Ultraviolet Coronagraph Spectrometer (UVCS)



A2369/1102.005

Figure 1(b). Optical System Schematic for UVCS

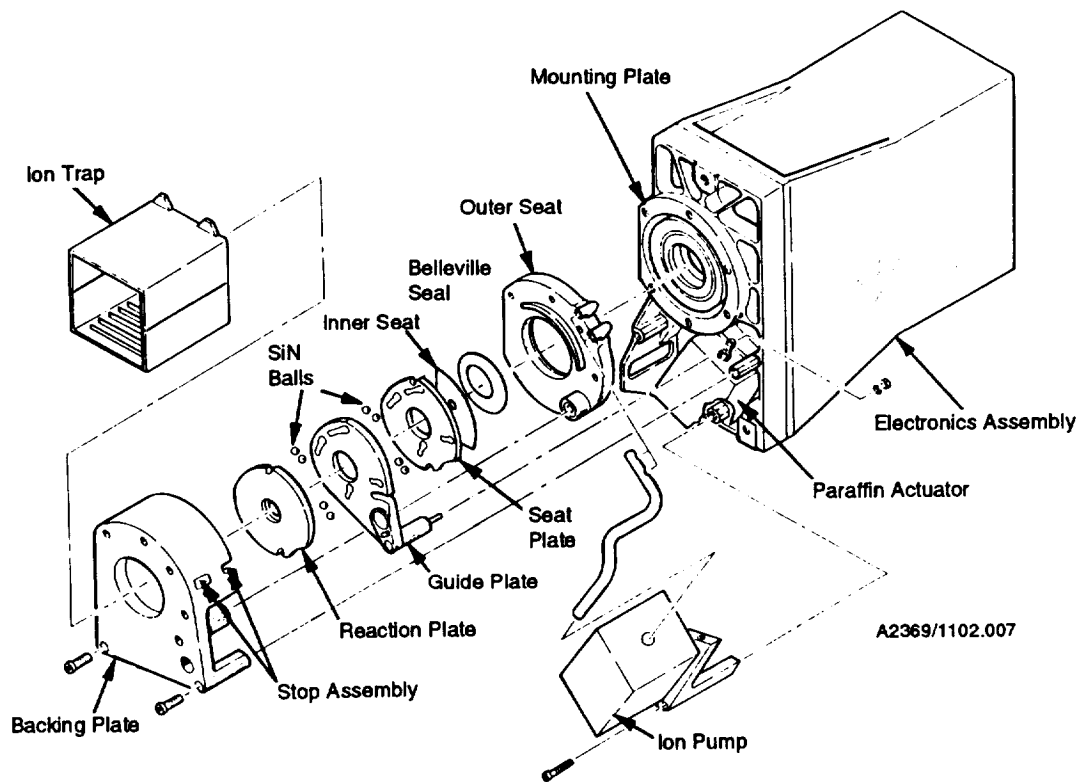


Figure 2. Isometric Exploded View of Openable Cover/Vacuum Seal Mechanism

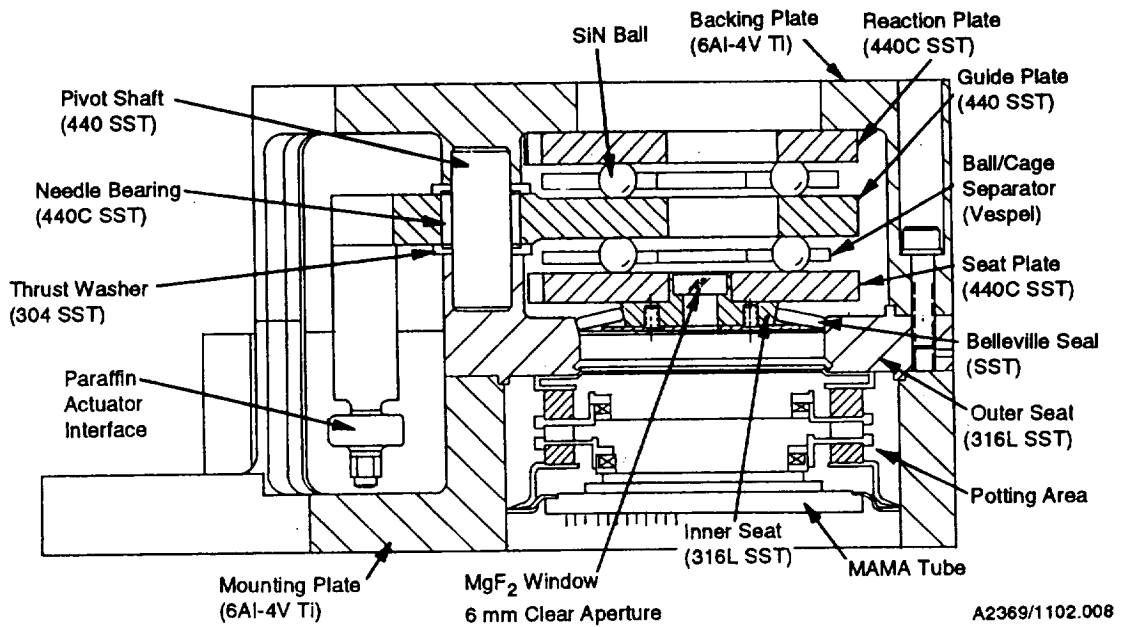


Figure 3. Cross-Section View of the Openable Cover/Vacuum Seal Mechanism

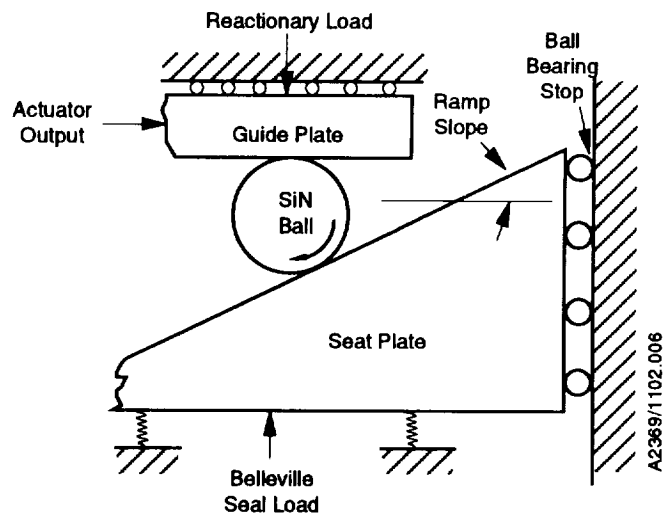


Figure 4. Silicone Nitride Ball Mechanics

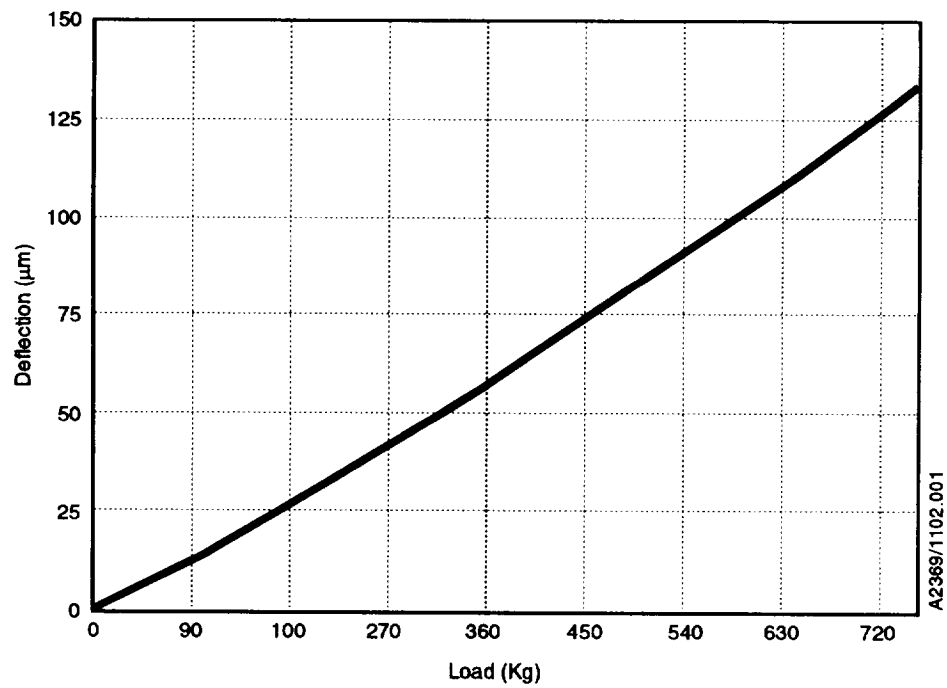


Figure 5. Belleville Seal Load/Deflection Curve

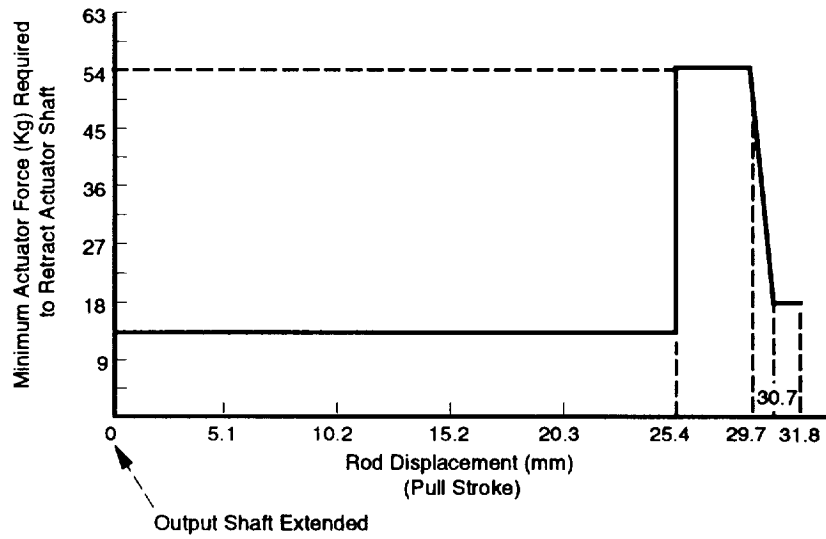


Figure 6(a). Actuator Retract Requirements

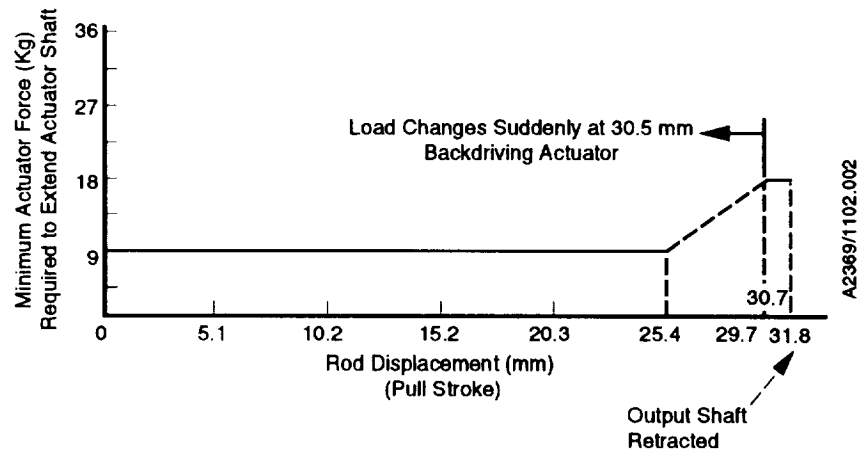


Figure 6(b). Actuator Extend Requirements

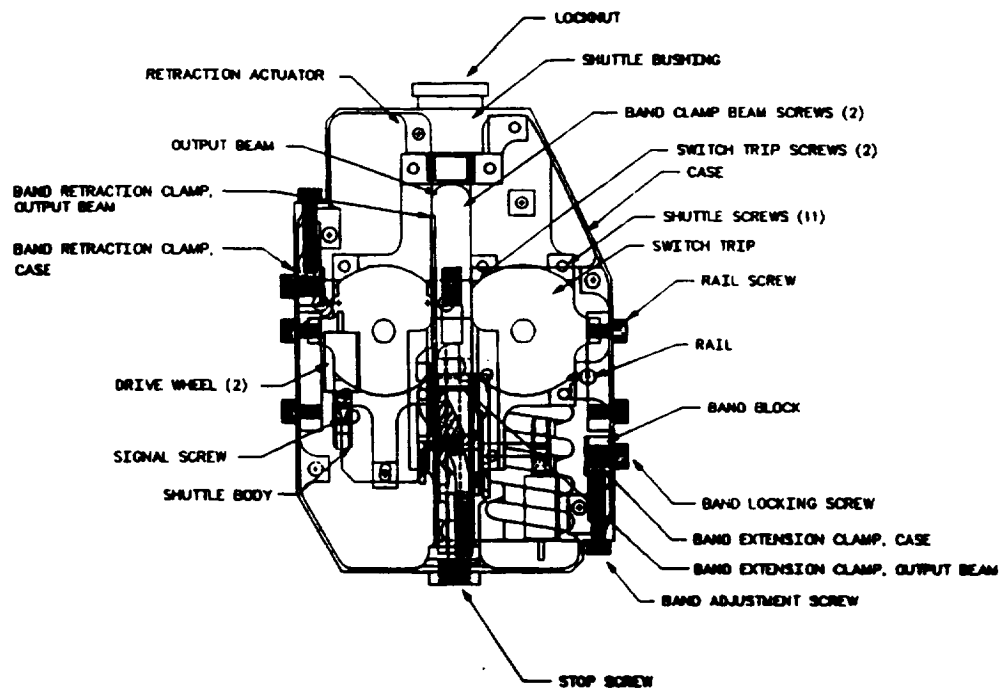


Figure 7 (a). Actuator Top View

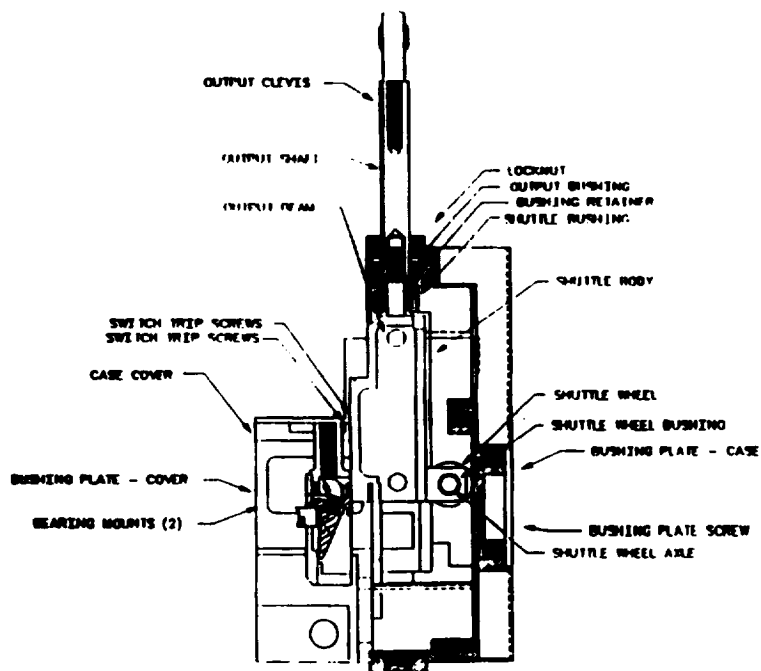


Figure 7(b). Actuator Side View

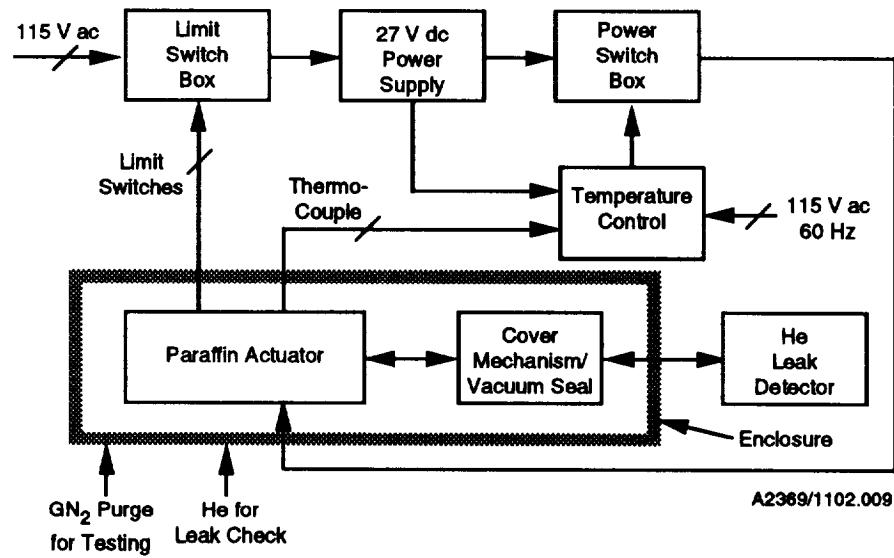


Figure 8. Schematic Layout of the Mechanism Performance Test Setup

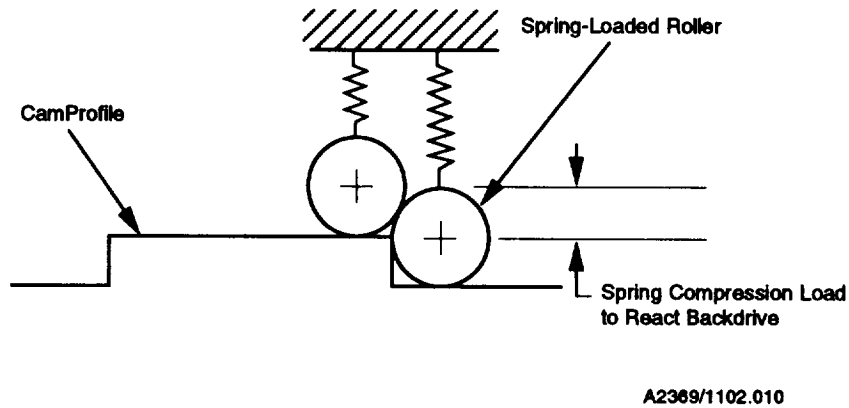


Figure 9. Actuator Spring-Loaded Cam Roller

Table 1. 4-Ball Test Data

ROTATING MATERIAL	STATIONARY MATERIAL	WEAR SCAR (mm)	(V) VOLUME WORN AWAY (mm ³)	(T) TRAVEL (mm)	(H) HARDNESS (Kg/mm ²)	(L) NORMAL LOAD PER CONTACT (Kg)	WEAR COEFFICIENT K=(VH)/(TL)	COMMENTS
440C		0.90 (width)	not measured	1210	894	20.4	—	Pitting
	440C	0.92	2.8×10^{-3}	10.4×10^3	894	20.4	1.2×10^{-5}	
52100		0.98 (width)	not measured	1252	888	20.4	—	Deep Grooves
	440C	0.97	3.6×10^{-3}	9823	894	20.4	1.6×10^{-5}	
WC		0.68 (width)	not measured	915	1565	20.4	—	WC Material Fatigue
	440C	0.75	1.24×10^{-3}	10.4×10^3	894	20.4	5.2×10^{-6}	
SiN		0.68 (width)	not measured	923	1759	20.4	—	Smoothest Surfaces
	440C	0.72	1.05×10^{-3}	10.4×10^3	894	20.4	4.4×10^{-6}	

A2369/1102.003

**ARM DEPLOY MECHANISMS TO HELP
CORRECT THE HUBBLE SPACE TELESCOPE'S VISION**

F. Kent Copeland*, Randall R. Whitaker*

ABSTRACT

As has been well publicized, the primary mirror of the Hubble Space Telescope was manufactured with an incorrect curvature which results in an aberrated output image. Ball Aerospace, under contract to Goddard Space Flight Center, is designing the Corrective Optics Space Telescope Axial Replacement (COSTAR) to provide correcting optics for the existing axial science instruments in the telescope. Integral to COSTAR are the arm deploy mechanisms which position and hold the corrective optic mirrors.

INTRODUCTION

There are four axial science instruments in the Hubble Space Telescope (HST). They are each about the size of a phone booth and are stacked together in a cruciform as shown in Figure 1. These instruments are designed to be removed and installed by astronauts performing a space walk. COSTAR will replace one of the existing axial science instruments, the High Speed Photometer, and provide corrective optics for the remaining three instruments. These are the Goddard High Resolution Spectrograph (GHRS), Faint Object Spectrometer (FOS), and the Faint Object Camera (FOC).

Once installed into the Hubble, a deployable optical bench (DOB) will extend 51 centimeters out from COSTAR's forward bulkhead (Figure 2). During and after DOB extension, four mechanisms within the bench will rotate mirrors mounted on beryllium arms out into the light paths of each of the other axial instruments. Thus, each instrument will "see" the mirror placed in front of its entrance aperture instead of the light directly from the telescope's secondary mirror. These COSTAR optics are precisely shaped to correct the aberrated light produced by the telescope. The mechanisms that rotate the mirror arms are the subject of this paper.

As initially designed, light entering the main barrel of the HST hits the primary mirror and reflects to the secondary mirror which in turn, reflects the light back through a hole in the middle of the primary mirror. Originally, this light would go directly into the entrance aperture of each axial

* Ball Aerospace Systems Group (BASG), Boulder, Colorado

science instrument (Figure 3a). With COSTAR in place, the light will strike a mirror designated M1. The light is reflected from M1 to mirror M2, which provides the actual correction to the light. The corrected light bundle is then reflected from M2 into the instrument (Figure 3b). There are five entrance apertures among the three axial science instruments. Each aperture requires a matched M1/M2 pair, so COSTAR carries ten total mirrors, five M1's and five M2's. Only two of the M1 mirrors are mounted on a deployable arm. The three others are mounted inside the DOB on tip/tilt mechanisms. All M2's are mounted on deploying arms.

Once the DOB is in place and the arm mechanisms have rotated the arms into position, tip and tilt actuators on each of the M1 mirrors are adjusted to optimize the system's alignment. After this is achieved, the mirrors, arms and deployable bench are left in place for normal telescope operations. Subsequently, the arm rotation mechanisms are operated only during a few specific viewing scenarios where the axial instruments want to see without COSTAR or when one of the axial instruments is replaced by a new second-generation instrument which will provide its own internal corrective optics. In these situations, the mirror arm will be rotated out of the way into its stow position.

MECHANICAL DESIGN OVERVIEW

The primary function of each of these mechanisms is to rotate an arm about 90 degrees and then with power off, hold it in position. This is deceptively simple. After accounting for envelope constraints, single failure tolerance, and other design drivers, the configuration becomes somewhat complex.

The basic mechanism configuration is shown in Figures 4 and 5. The arm rotates on a hinge shaft which is supported by bearings at each end. It is rotated by a stepper motor driving through a gearhead. The gearhead output drives a bevel gear on the hinge shaft. A compression spring is mounted to the arm and mechanism base and acts as an over-center toggle. That is, if the arm is between stow and top dead center, the spring tends to push the arm back toward stow. If the arm is past top dead center, the spring tends to rotate the arm in the direction of its deployed hard stop. There are several reasons for this arrangement. Because the arms are to be held in both stowed and deployed positions with no power to the motor, the spring alone will hold the arm firmly in place. The stepper may not drive the arm completely to the stop or else may slightly lift the arm off the stop if it is pulsing against it. The spring is sized to backdrive against the motor so that when motor power is off, the spring assures that the arm is against the stop. This provides highly repeatable arm positioning.

It is a COSTAR system requirement that if any single failure occurs, it must be possible to stow the arms. In the event that an arm deploy mechanism is unable to rotate the arm to stow, a contingency method is used to stow the arm: The COSTAR DOB is retracted back into the instrument enclosure. A four-bar "contingency stow linkage" strikes the COSTAR forward bulkhead and, as the bench moves, rotates the arm into its stowed position.

A potentiometer on the hinge shaft senses arm position. The motors are run open loop but in the event of a partial deployment, position telemetry information could help determine what corrective action to take.

The thermal environment surrounding the mechanisms is somewhat variable. Also, the mirrors need to be extremely accurately positioned. Therefore each arm has a bonded-on heater and temperature sensors to keep the arm temperature within ± 1.3 degrees centigrade. This limits thermally induced arm strain and mirror movements to acceptable levels.

An obvious design goal was to have as many common parts as possible among the mechanisms. As it turned out, due to significant differences in envelopes and other design drivers, the mechanism detail components differ substantially from one another. The actual deployment angle for each arm assembly is: 101 degrees for FOC M1, 79 degrees for FOC M2, 65 degrees for FOS M2, and 71 degrees for GHRS M2.

DESIGN REQUIREMENTS

1. Repeatable deployment position: ± 1 mm (.040 inch)
2. Repeatable deployment angle: ± 5 arc sec
3. Mechanism must remain stable in stowed or deployed position without power
4. Number of deployment cycles: 1000 minimum
5. Temperature range: survival: -50 to +50 Celsius
operating: -10 to +30 Celsius
6. Launch loads (ultimate): 5g constant, 50g momentary
7. Launch load acceleration vector direction: Unknown, design for worst case
8. Single-failure tolerant for a contingency stow
9. Dynamic relative motion clearance zone between DOB and enclosure: 1.27 mm (.050 inch)
10. Manufacturing and alignment tolerance zone with inner wall of DOB: 1.27 mm (.050 inch)
11. During and after deployment, required clearance zone with the HST and all other experiments: 12.7 mm (.50 inch) (Figures 6 and 7)
12. Clearance with ASI light ray aperture: 3 mm (.12 inch)

DETAILED MECHANISM DESCRIPTION

A stepper motor was chosen to rotate the arm for several reasons. The motor must run open loop. A stepper motor can place the arm close to its desired location with reasonable accuracy. Because the over-center spring is assisting arm rotation during the arm travel from top dead center to full deploy, the motor is required to act as a controlled brake to limit arm speed. No other type of motor would have worked as well.

The motor/gearhead must be able to drive against the force of the spring as well as the friction in the system. The spring must backdrive against friction and against the motor with power off, so the two had to be carefully designed to work together. As is typical in the design process, diametrically opposite needs had to be reconciled. While a motor with high-ratio gearing would easily rotate the arm, this high ratio would increase backdrive friction and necessitate a stronger spring. (There is no significant time constraint on arm actuation so speed reduction by increasing gear ratio was not a concern.) A stronger spring requires a stronger motor, which requires a stronger spring, which requires a stronger motor, and so on. To keep the gear ratio down, the motor itself should produce as much torque as possible. It should also have minimal intrinsic backdrive friction. Although a permanent magnet stepper motor has somewhat more torque output, a variable reluctance stepper was chosen because of its lower detent torque. Envelope size restrictions allowed a motor no larger than size 11; a 27-mm (1.062-inch) maximum outside diameter and 44.45-mm (1.75-inch) length including gearhead.

Backdrive friction/torque becomes especially significant when safety factors are used in the system design analyses. Our customer requested a safety factor of four to one on all loading. During analysis, care had to be taken to avoid putting margins on top of margins, which would have created unworkable design requirements.

The process used to size the spring and motor/gearhead was as follows:

1) The spring was sized to rotate the arm into the deployed position stop and overcome the friction of:

- a.) motor backdrive
- b.) gearhead backdrive
- c.) bevel gear backdrive
- d.) spring cartridge sliding motion
- e.) spring cartridge rotation pins
- f.) hinge bearings
- g.) contingency stow linkage pins

It also had to drive against spring force in the wire flex

leads which go over the hinge axis and provide electrical connection to the heaters and thermistors on each arm. These factors determined the force required from the spring with the arm at full deploy.

2) With mechanism geometry known, the amount the spring was compressed as the arm rotates from full deploy to top dead center was determined.

3) From these numbers, a commercial spring was selected. In choosing the actual spring, many factors were involved. Spring diameter and length were governed by envelope constraints within each mechanism. The amount of force in the spring increases as it is compressed when rotating from deploy to top dead center. The higher the spring rate, the greater this increase in force. As force goes up, the spring load and friction the motor must drive against also increase so a stronger motor would be required. If, however, the spring rate is too low, then to achieve a sufficient preload at deploy the spring has to be substantially compressed. As it is further compressed during arm rotation, the spring material yields or the spring bottoms out. The spring was carefully sized to have just the sufficient torque, but no more than necessary.

Sliding friction in the spring cartridge turned out to be a significant factor in overall system friction. One factor contributing to this sliding friction was cartridge "cocking" induced by the load from the spring not acting at the spring centerline. This is due to the ends of the springs shaped such that they apply load eccentric to the centerline. To help mitigate this, squared and ground ends on the spring were needed.

4) With the spring chosen, the required motor torque was then determined. It had to drive against the same loads as the spring cartridge and additionally, against the spring itself. Tolerances in the spring parameters also had to be accounted for.

The geometry of the system changes throughout the arm rotation range, consequently all the loading and friction had to be combined and calculated over the full arm travel to determine the maximum motor torque required. This analysis was performed for each mechanism to determine the worst-case motor torque required, since a common motor design would be used for all mechanisms.

Early in the design, simple analysis provided initial sizing values for the springs. Later calculations revealed that the early numbers were inadequate, largely because friction was ignored, and thus the actual spring cartridges

would have to be significantly increased in size. This caused problems with the ongoing mechanism designs.

To act as an overcenter toggle, either a compression or extension spring would work if the proper geometry were used. The choice was the subject of some debate during the early design process. While each has certain advantages, the compression spring was chosen for several reasons. The compression springs do not require tension hooks at the ends, which are subject to rotational wear and breakage. In the event of a spring break, the extension spring and end hooks could generate large pieces of broken wire which could jam the cartridge or cause other problems. If the spring breaks in a compression spring it may still function because it is contained within the cartridge. This might allow the two broken springs to act together end-to-end.

A cartridge was used to contain and mount the spring. It provides protection for the spring against foreign objects, especially during ground handling. It contains any pieces generated from a spring break. The cartridge allows simple attachment of the spring to the arm and base. It allows for easy preload adjustment of the compression spring by the insertion of spacers to control the amount of spring compression.

It was important that the arm/mirror assembly have a very low moment of inertia about the hinge axis because envelope restrictions on motor size limit its output torque. Beryllium was used for the arm because it has a high stiffness-to-weight ratio and a low coefficient of thermal expansion for stability. To further control thermal swings, a redundant heater and temperature sensor were bonded to the arm (Figure 4). The heater and sensor leads were incorporated into a single flexible circuit making the transition across the hinge axis flexible so it will not inhibit the deployment of the arm assembly.

The bevel gear set has a 2.77:1 gear ratio and is not directly attached to the hinge shaft. Instead, it rotates freely on the shaft and drives the arm assembly through a pin made of 6061-T6 aluminum (Figure 8). The pin acts as a shear pin in case the bevel gears or gearhead/motor jams and the arm is stowed by the contingency stow linkage. The material for the pin was chosen for its low and narrow range of shear strength 179,000-201,000 Mpa (26-30 ksi). The bevel gear material is custom 455 steel, which is appropriate for gears and shearing aluminum. The other half of the shear is one of the arm clamps, which is made out of 6AL-4V titanium. To minimize pin bending in a contingency stow operation, the pin is placed in double shear. The pin size is large enough to keep the arm assembly from rotating during a 50g launch load.

The arm is attached to the hinge shaft by a pair of clamps. One clamp acts as a shear, as previously described, while the other clamp holds the rotor portion of the potentiometer. The stator portion of the potentiometer is attached directly to the mechanism base. The potentiometer utilizes internal slip rings allowing current to be transmitted to the rotor, which eliminates the need to run wires from the rotor across the hinge axis. The potentiometer has a range of 120 degrees and an accuracy of ± 2 degrees.

The arm hinge shaft rotates on a set of ball bearings that have a 12.7mm (.50-inch) OD, 4.762mm (.1875-inch) ID and are 4.978mm (.1960-inch) wide with seven 1.59mm- (.21875-inch) diameter balls. On one end of the hinge shaft, the bearing has both inner and outer races restrained in the axial direction. The bearing at the opposite end of the shaft has only the inner race restrained in the axial direction while its outer race is held by the flexure described below. Controlling the mechanical fits among the housings, shaft, and bearings was critical in maintaining their accuracy and stiffness. To attain this, the fits of the outside diameter of the bearing to the base and the inside bearing diameter to the hinge shaft are .0025 (.0001-inch) clear to .0076mm (.0003-inch) interference. This produced an arm assembly stiffness (first-mode resonance) of 228Hz.

To achieve the desired bearing contact stress of 414,000 to 689,000 Mpa (60 to 100 ksi), a preload of 1.27-2.90 N (.29-1.33 pounds) was required. To maintain this preload over the full operational temperature range, a flexure was designed into the mechanism base. During mechanism assembly, the position of the bearing was measured and the bearing retainer shim was machined to provide the desired preload. The more the bearing retainer pushes on the bearing outer race, the more the bearing housing wants to move in the opposite direction causing the flexures to exert a load on the bearing.

To stow the arm if there is a failure in the motor or a jamming of the gear assembly, the DOB is retracted back into the enclosure. Due to multilayered insulation (MLI) protruding beyond the bulkheads, the arm assembly could not rely on contact from the bulkhead to force it back into the stowed position. Debris within the HST is unacceptable, therefore the arm cannot come in contact with the MLI. Accordingly, a four-bar linkage was designed to contact the bulkhead as the DOB retracts (Figure 9). This linkage rotates the arm from full deploy towards stow.

During a contingency stow operation, the linkage rotates the arm assembly within 5 degrees of its stowed position. If the over-center spring could not generate enough force to

complete the stowing operation, then a ramp on the snubber block which is on the arm would contact the bulkhead and complete the operation (Figure 10).

During launch, the mechanism experiences loads up to 50g's. The over-center spring does not exert enough force to compensate for this, accordingly, a snubber spring was incorporated into the design to carry part of the launch load. The snubber block on each arm contacts a preloaded and captured leaf spring when the DOB is retracted to its stowed position. The snubber spring is attached to a side panel of the enclosure and will absorb any dynamic movement during launch.

SUMMARY

The design of the arm deploy mechanisms was much more challenging than any of the engineering team members first anticipated. Restrictive envelope constraints were a major design driver. Initial analysis used to size some of the components ignored friction and the four-to-one safety factor our customer wanted. This hindered us later when more sophisticated analysis indicated our initial work was overly optimistic. While common sense dictated a maximum of commonality among the designs, practical considerations made each design more unique as configurations matured. These difficulties were overcome and four mechanisms which met all of the design requirements were developed and made to work. It was gratifying to work on a project which will be of major benefit to science.

ACKNOWLEDGEMENTS

The authors wish to thank our coworkers on the COSTAR design team. This design was truly a collaborative effort among several engineers and designers. They are Mike Greene, Rich Nyquist, Herb Morrison, and especially our lead engineer, Bob Renken, who provided valuable suggestions and insight throughout the project. We also appreciate the patience and careful grammatical criticism of our wives.

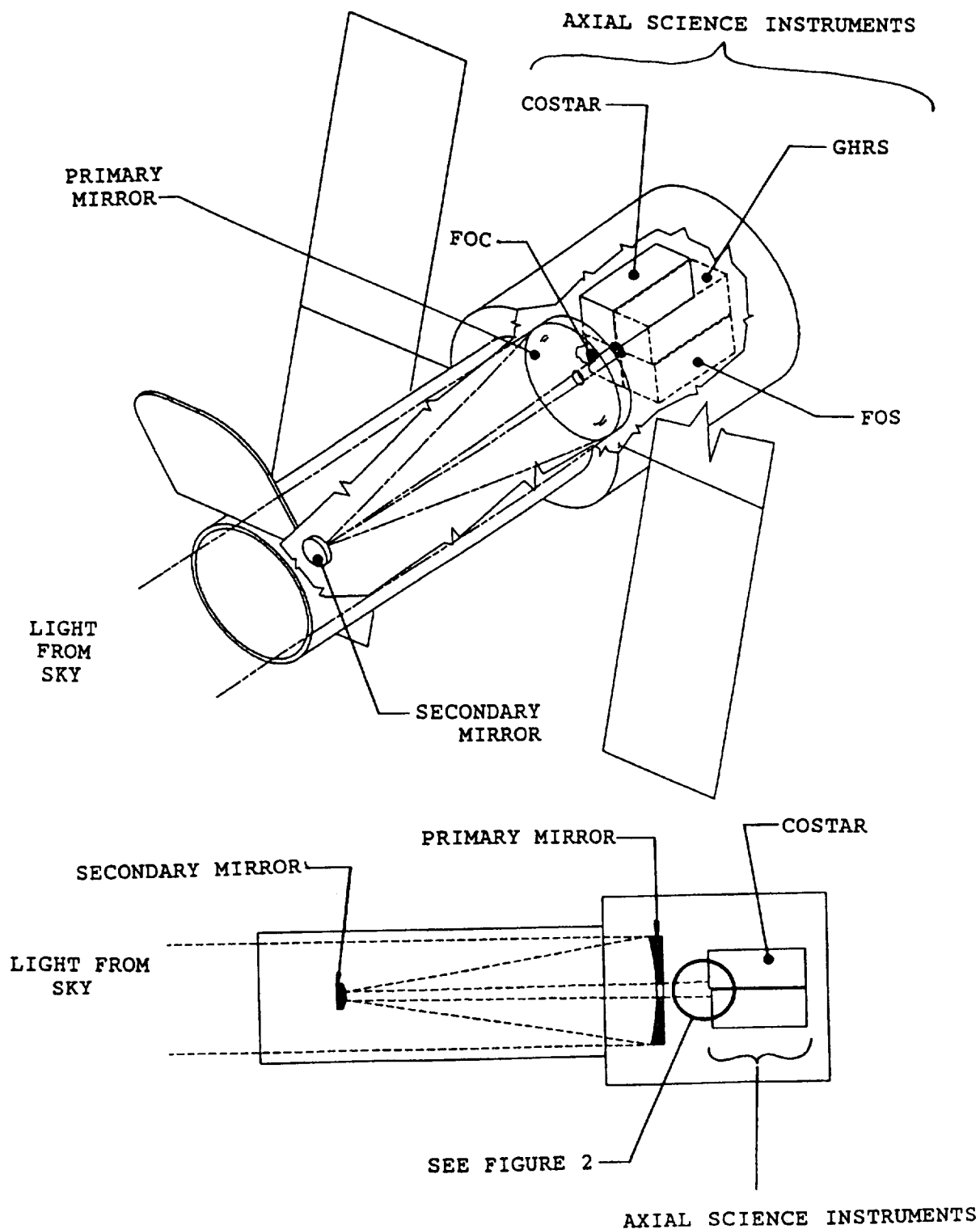


FIGURE 1. HUBBLE SPACE TELESCOPE (HST) CONFIGURATION AND LOCATION OF COSTAR.

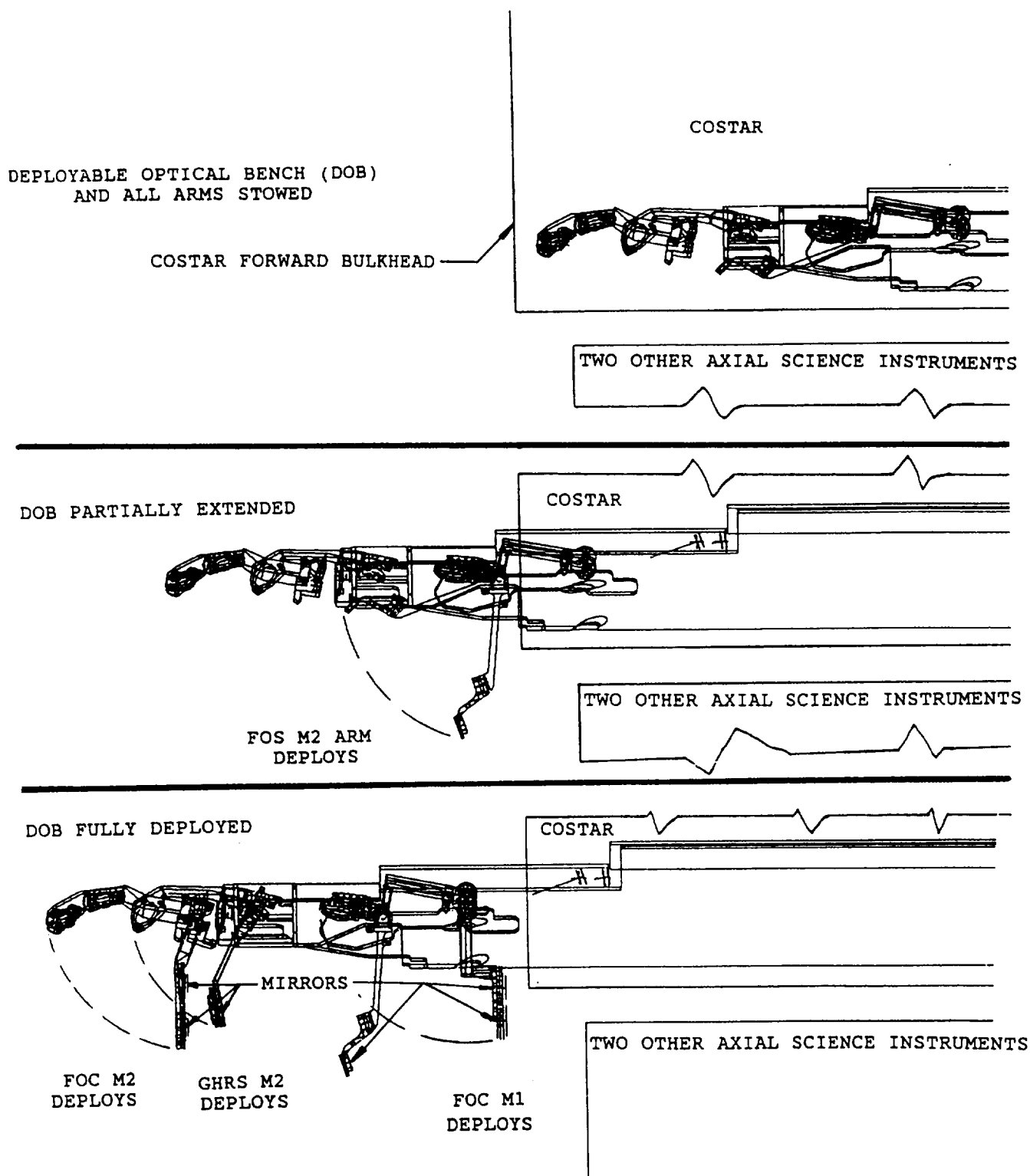


FIGURE 2. COSTAR DEPLOYABLE OPTICAL BENCH EXTENSION AND ARM DEPLOYMENT.

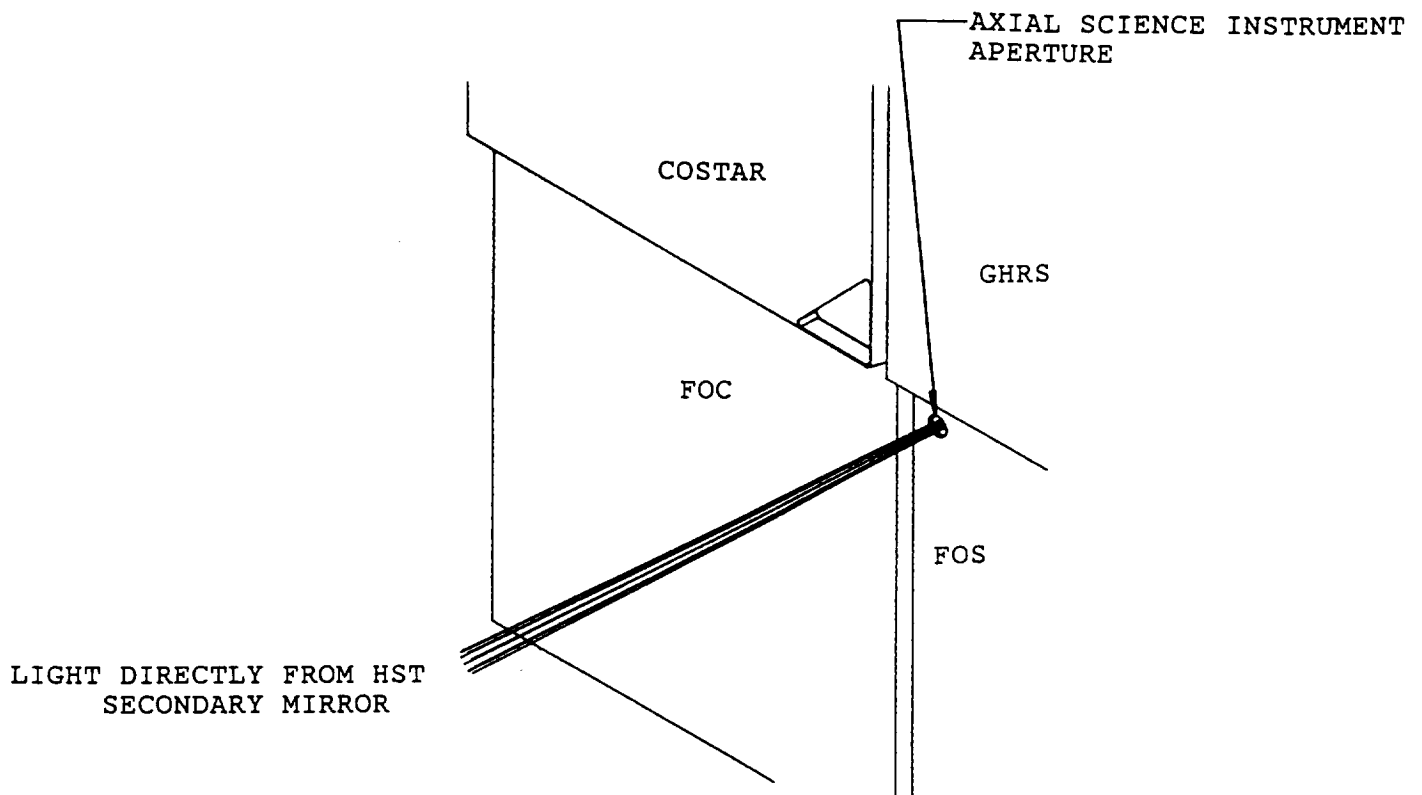


FIGURE 3A
AXIAL SCIENCE INSTRUMENTS WITHOUT COSTAR

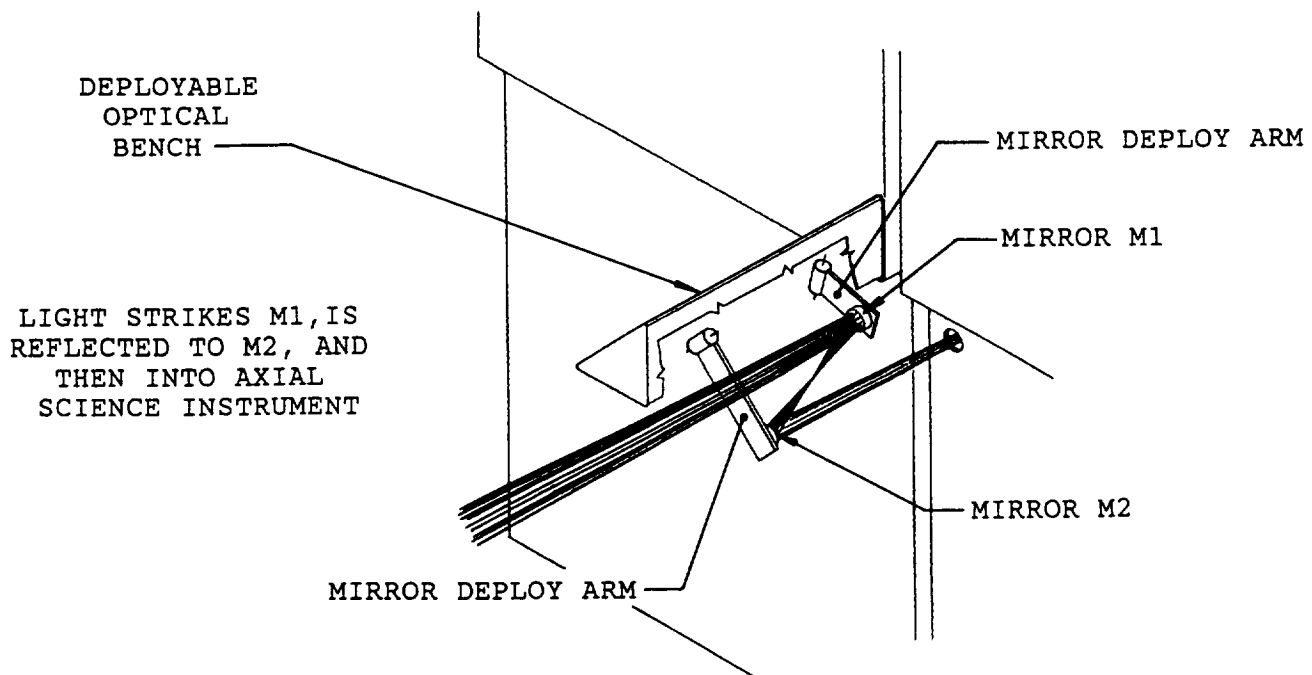


FIGURE 3B
AXIAL SCIENCE INSTRUMENTS WITH COSTAR

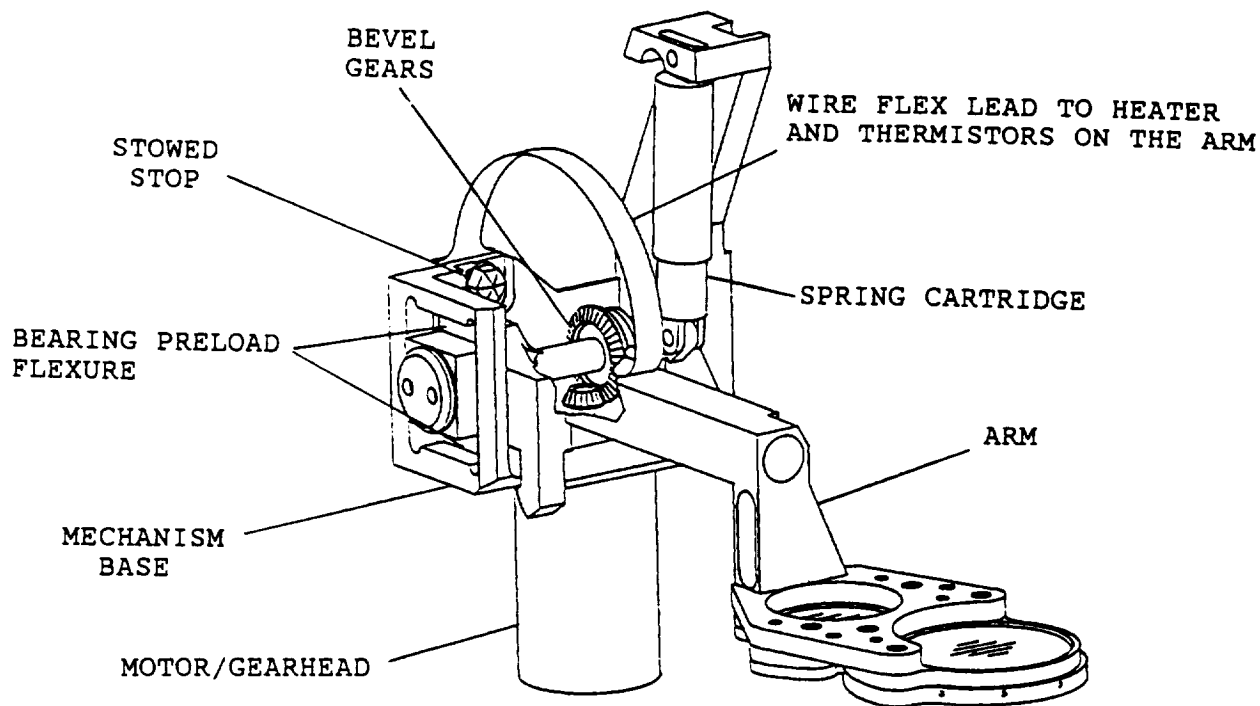


FIGURE 4

BASIC MECHANISM ISOMETRIC

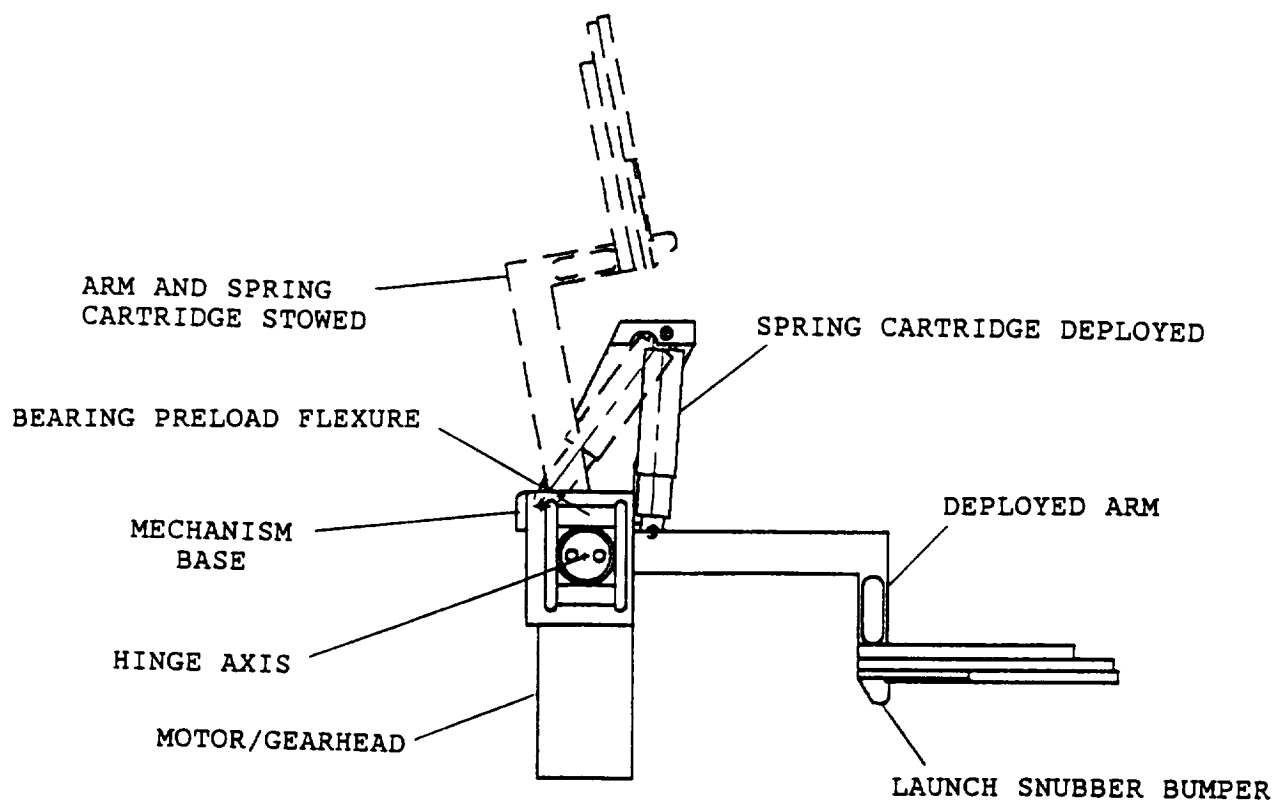


FIGURE 5. BASIC MECHANISM VIEW ALONG HINGE AXIS.

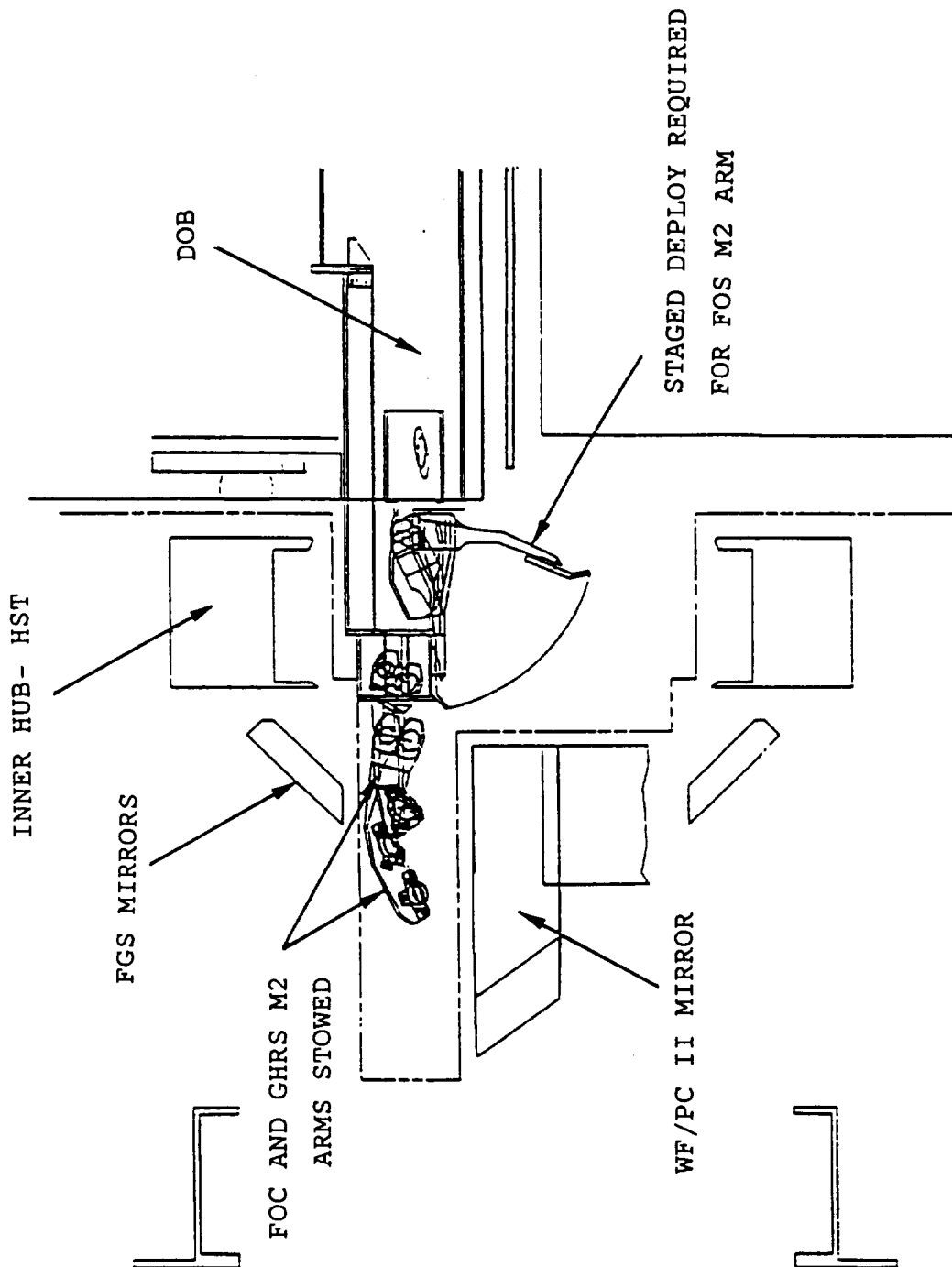


FIGURE 6
CROSS SECTION VIEW- HST

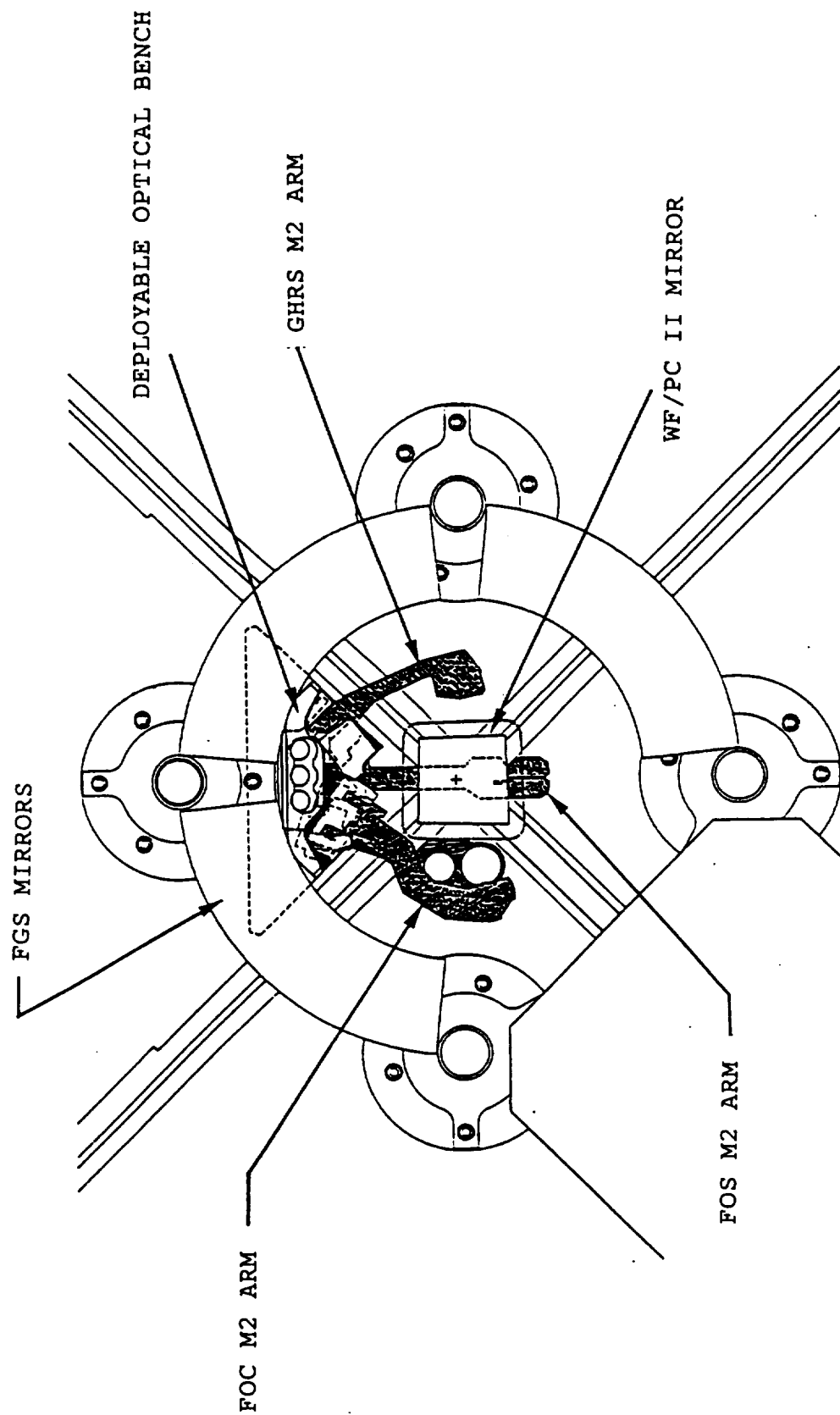


FIGURE 7
 VIEW LOOKING AFT

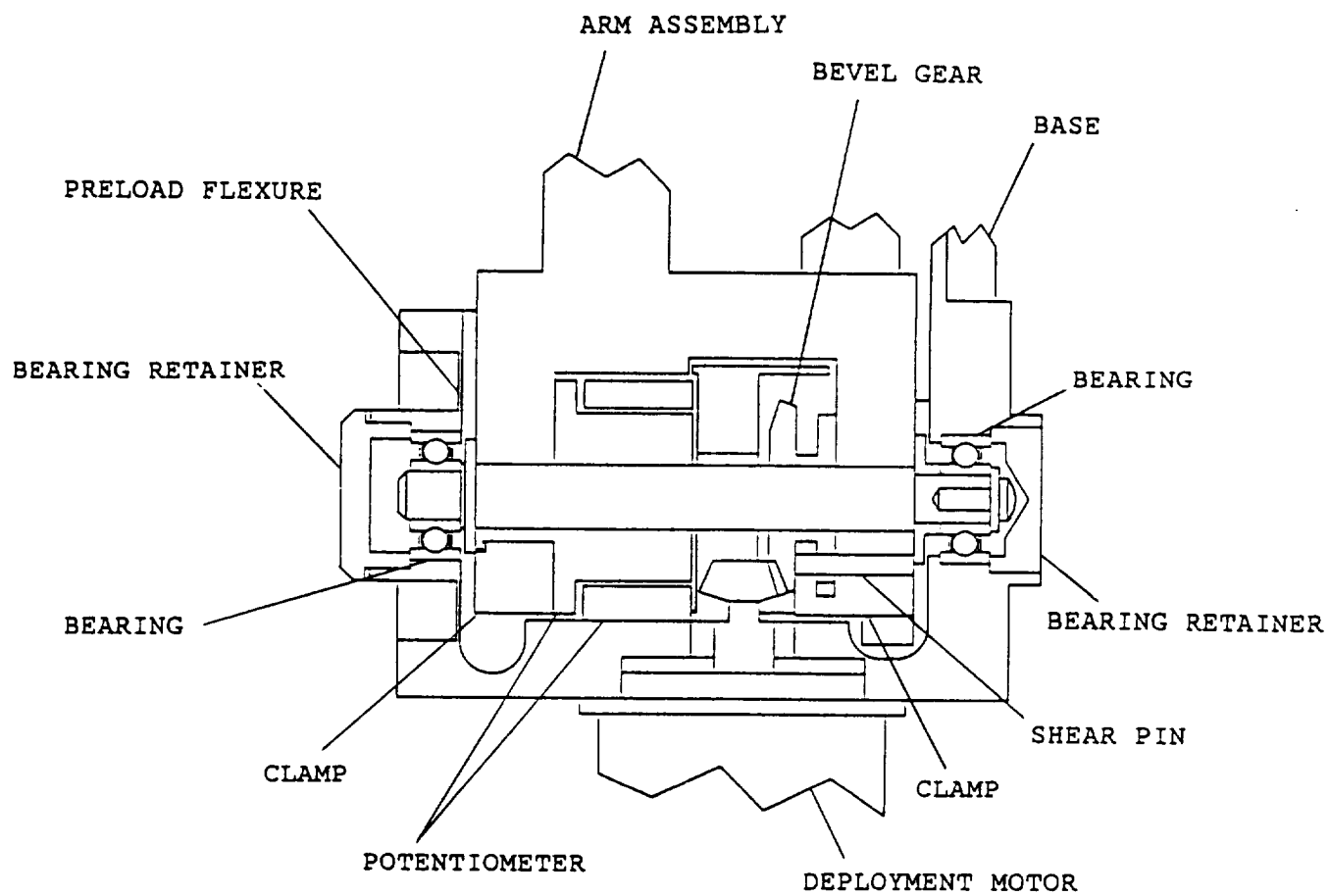


FIGURE 8
CROSS SECTION OF DEPLOYMENT MECHANISM

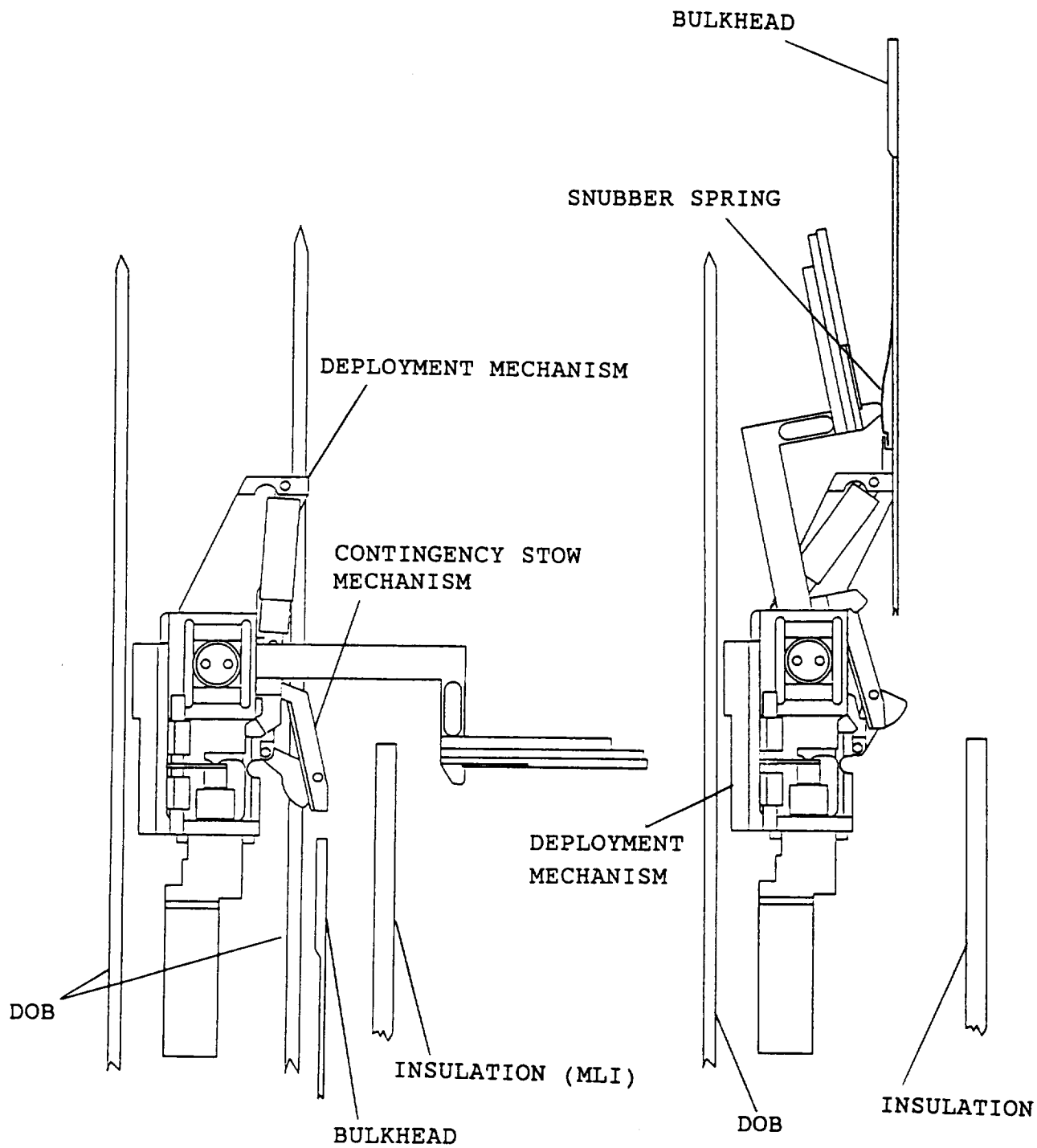


FIGURE 9
ARM ASSEMBLY- DEPLOYED

FIGURE 10
ARM ASSEMBLY- STOWED

DEVELOPMENT OF A RESETTABLE, FLEXIBLE APERTURE COVER

Scott Christiansen*

Abstract

A flexible aperture cover and latch were developed for the Thermal Ion Detection Experiment (TIDE). The latch utilized a high-output paraffin (HOP) linear motor to supply the force to operate the latch. The initial approach for the cover was to use a heat-treated, coiled strip of 0.05mm (.002-inch)-thick beryllium-copper as the cover. Development test results showed that one end of the cover developed a trajectory during release that threatened to impact against adjacent instruments. An alternative design utilizing constant force springs and a flexible, metallized Kapton cover was then tested. Results from development tests, microgravity tests, and lessons learned during the development of the aperture cover are discussed.

Introduction

This paper discusses the design and development of an aperture cover and latching mechanism. Several design and testing iterations were made before the final flight design was achieved. Setbacks and difficulties throughout this process yielded valuable lessons.

After final design of the Thermal Ion Detection Experiment (TIDE) was complete, it was determined that an aperture cover was required. TIDE is an instrument built by Southwest Research Institute (SwRI) for the Polar spacecraft mission. Fabrication of flight parts had already begun when Starsys Research Corporation (SRC) began the cover design. The unique design requirements coupled with the 11th-hour nature of the program presented a challenging development problem.

Design Requirements:

- Must be retrofitted to existing instrument design
- Large, complex aperture shape
- Seal aperture from particulates during ground handling through spacecraft shroud separation
- Resettable for repeated ground testing
- Extremely reliable (open aperture critical to instrument operation)
- Minimal weight (less than 295 grams)
- Extremely limited physical envelope due to the proximity of other instruments
- Minimal shock during opening of cover
- Non-magnetic materials and operation

*Starsys Research Corporation

Operating Requirements:

- Operating Temperatures from -30°C to 60°C
- Operating Pressure 1×10^{-5} torr or lower
- Spacecraft rotation of 6 rpm
- Launch vibration spectra: See Table 1

The shape and construction of the instrument demanded an unusual design. The basic shape of the instrument was a box with a rounded end (Figures 1 and 2 show drawings of the instrument). The rounded end was a cylindrical surface with a 17.8-cm (7-inch) radius. The aperture was a 6.4-cm (2.5-inch) wide tangential slot in this surface that allowed a 157.5-degree field-of-view for the instrument. The cover was required to protect against entry of particles into this aperture; a hermetic seal was not required. The type of seal required could be described as a "diffusion seal" which, prior to and during launch, could maintain dry nitrogen purge gas inside the instrument at a positive pressure. Escaping gas flow would be limited by the rate of diffusion past the cover-to-instrument seal.

Once on orbit, the latching mechanism would be energized, opening the latch and releasing the cover. The cover would then move clear of the aperture and stow itself in a position that was out of the field-of-view of the TIDE instrument and of any other adjacent instrument. The latching mechanism was to provide switch sensing to control power to the latch and to indicate successful cover release.

Initial Design and Development

The general approach in establishing a cover was to design a flexible, self-stowing cover that could be deployed around the end of the instrument over the aperture. Mechanical work required to stow the cover would be supplied by stored spring energy. The energy could be stored in the cover itself or in spring elements in a retrieval mechanism. The simplest approach would lie in storing the energy in the cover itself without having to rely on an additional mechanism. This was the basis for the initial design.

A coiled, flexible metal strip would have spring properties adequate to maintain a coiled shape even after being straightened and re-rolled many times. One end of this coiled strip would be solidly attached to the top of the instrument in line with the aperture. The free end of the cover would be unrolled over the aperture and held in place by the latching mechanism. Conformance of the cover to the instrument surface would be maintained by the tension created by the tendency of the strip to return to its coiled shape. Opening the latch would then release the free end of the cover, allowing it to uncover the aperture, roll up, and stow itself safely away from the field-of-view.

Cover

The cover needed to be flexible, strong, durable, and light. Beryllium copper sheet, 0.05mm (.002 inch) thick, was chosen as the cover material. The Be-Cu sheet could be processed to achieve the desired strength, toughness, and spring properties; the thin sheet was also flexible and relatively light. A strip 8.25cm (3.25 inch) wide X 81 cm (32 inch) long was cut from 0.05 mm Be-Cu sheet. The strip was then cold formed into a coil (approximately 1.5 cm in diameter) and age hardened to achieve the required strength and toughness to hold its shape.

Latch

The latch hardware was designed to mount inside a small unused space inside the instrument (see Figure 2). A latching arm extended through a panel to clamp on the free end of the Be-Cu cover in its deployed position. The release-latch design utilized a high-output paraffin (HOP) linear motor as the prime mover for release. The HOP linear motor was chosen because it best met the low shock, non-magnetic, and resettability requirements for the cover system. The latch was designed to maintain its closed position and retain the cover without requiring power until the HOP motor was energized to initiate release.

The latching mechanism was based on a slide and bell crank (see Figure 3). A compression spring maintained force against the slide to hold the latching arm in its closed position. When energized, the HOP motor pushed the slide, compressing the spring. The displacement of the slide caused the latching arm to rotate about its pivot point, swinging the latch open and releasing the cover. The latch design performed extremely well throughout development testing, and its configuration changed little throughout the development process. Figure 4 shows a photograph of the latch mechanism in its final flight condition.

Development Tests

The initial cover design apparently met all of the design requirements. It would fit well over the aperture and supply adequate sealing and it would be capable of being released and reset many times. The cover included no moving parts to cause reliability concerns. All materials were non-magnetic, and finally, the Be-Cu would be unaffected by the operating environment. Additional information about the behavior of the cover was required, however, to properly size the coil and establish the optimum heat treatment. The initial development tests were set up to characterize cover performance at room temperature and nominal conditions.

A mock-up of the instrument exterior and aperture was fabricated. Several cover coil configurations were fabricated to evaluate coil size and heat treatment. These covers were then tested to determine their performance characteristics in various orientations with respect to gravity.

Test results showed that the covers tended to "fly away" from the instrument in a large arc as the coil rolled itself up. The cover tended to travel approximately 25 cm (10 inches) above and 25 cm past the attachment point on the instrument before stowing was complete (see Figure 5). This behavior was unacceptable due to the proximity of other instruments. Analysis of slow-motion video records of the various cover configurations, as well as dynamic modeling of the system, indicated that the "fly away" tendency of the cover was an unavoidable characteristic of the freely self-coiling design.

A number of options for trying to control the trajectory of the coil were explored. Among them were:

- Addition of mass to alter the dynamic response of the cover.
- Addition of damping materials to make the motion of the cover "gentler."
- Additional hardware to "catch" and control the cover motion.

These approaches either slowed the motion without significantly changing the trajectory, or required awkward additional hardware which compromised the reliability of the simple self-stowing cover. The coiled beryllium-copper strip approach could not be an acceptable design without additional external restraining hardware.

Design Change

It was clear at this point in the development that trying to modify the self-rolling cover to work correctly was going to be very difficult, if not impossible. We were forced to decide between trying to force the original idea to work in some way or developing an alternative approach. Either task could be difficult and time consuming, but each had its attractive points. If we stayed with the original approach, we knew the problems, but had no solutions. If we were to change, we could come up with a new approach that seemed to be perfect, but we would not have discovered the problems.

Alternative Approach

The original approach of using a self-rolling cover contained a fundamental problem in its dynamic behavior. By definition, a free-flying cover would sweep out an area above the instrument equivalent to the size of the instrument. It became clear that an alternative approach would yield the highest probability of success. We then conducted a quick experiment to evaluate actively rolling up the cover material during the release and stowing phase. A small section of a household windowshade roller was obtained and fitted to our instrument test mock-up. A strip of 0.125mm (.005-inch)-thick Kapton, with a small tab on its end to engage the latch, was used for the cover. A single test of this cover configuration showed that it was the preferred solution. Creating a space-flight-worthy mechanism based on a windowshade roller was the next step.

Redesign

The new design approach presented a new set of problems. We now had chosen an approach that required active rolling of the cover in addition to changing the material of the cover. These new features complicated the mechanism and brought the emphasis of the development problem to another set of design characteristics:

- Since the retrieval of the cover material was accomplished with drive springs, reliability of these springs needed to be evaluated.
- In creating a roll-up device, additional mechanical components were introduced; these components needed to be addressed from a reliability viewpoint.
- All external surfaces of the instrument were required to be electrically conductive and grounded to the spacecraft frame. The change to Kapton required that additional measures be taken to establish electrical conductivity.
- Since the mechanism contained rotating components, features were required to ensure electrical conductivity across any rotating or sliding interfaces.

Mechanical Features

Mechanical features were incorporated into the design to address the reliability concerns. Neg'ator (a brand name of Ametek, Hunter Spring Products) springs were chosen for the drive springs. These are constant-torque springs formed from a coil of flat spring stock. As spring material is wound from the coil onto a larger coil (reversing the direction of bend), spring energy is stored. When released, the uncoiled material rolls back onto the original roll of material, supplying torque (see Figure 6). To create redundancy in the drive system, two independent drive springs were incorporated.

All rotating interfaces included redundant bushings. The bushings were fabricated from a molybdenum-disulfide filled polyimide (Envex 1115, Rogers Corp.) and sized so that both inside and outside surfaces were free to slide during rotation. If either surface were to seize or jam the other would still be free to allow rotation.

Additional reliability for the cover opening system was achieved by utilizing a specific physical property of the Kapton sheet. The sheet could be formed into a coil and then heat treated to retain its shape. This curled material would then tend to behave similarly to the Be-Cu material used previously, although the energy stored during unrolling the coil would be much less. The tendency for the Kapton to roll-up, however, was not strong enough to hinder the spring-driven mode of operation. The curl in the cover established that it could still roll itself up and stow itself out of view in the event of an unforeseen mechanical problem during release. Although this mode of release was not acceptable for the primary mode of operation, as an emergency back-up mode it was considered to be a desirable feature.

Electrical Features

Several electrical design features were incorporated into the new design. The Kapton used for the cover was an electrically non-conducting polymer. To satisfy the conductivity requirement, the Kapton needed to be coated with a conductive material. To satisfy additional requirements, the coating needed to have a low a/e ratio, be non-magnetic, and corrosion resistant. This combination limited the options for coating materials.

Vendors supplying metallized (sputtered) Kapton films for space applications generally apply the coatings to very thin sheet materials (usually from 0.0127 mm [.0005 inch] to 0.05 mm [.002 inch] thick) on one side only. Our application specified 0.127-mm (.005-inch)-thick Kapton coated on both sides. Most suppliers were not set up to coat material of this thickness, and set-up costs to do this on a custom basis were prohibitive. A supplier was found who had a small sputtering chamber and could complete a small coating run for us. The coating materials available through this vendor, however, were limited. Of those available to us chromium was chosen. It had suitable thermal and corrosion characteristics, and calculations showed that the resistance of a 1000-Å coating would meet our conductivity requirements.

Subsequent testing of the coated material indicated that the chromium coating was not acceptable. The more the Kapton was flexed during handling and testing, the higher the electrical resistance of the coated surface became, until it

eventually became essentially an open circuit. This condition did not meet the conductivity requirement and the causes of the problem were investigated. Initially, we suspected that our test methods were at fault, but no problems with the test equipment or method could be found. We then looked more closely at the coating. When high-magnification photographs (200X and 500X) were taken of the surface, a fine network of cracks was apparent (see Figure 7). The poor surface conductivity and the increase in resistance with continued handling are consistent with this cracking phenomenon. The cracking is a result of the inherent brittleness of pure chromium. The chromium did not have the ductility to handle the strains required to maintain a continuous coating when the flexible Kapton substrate was flexed. Cracking occurred and the effective conductivity of the thin coating was significantly degraded.

We then revisited the problem of trying to obtain non-standard coated film. When cost and schedule factors were considered, the most favorable approach was to find a standard product that could be used for our cover material. Our final solution was to use 0.05-mm (.002-inch) Kapton coated with pure copper. We had some previous experience with this material from our previous search. Evaluation test results showed that after heat treatment, the coating was durable, had good adherence, good conductivity, and was resistant to corrosion if kept clean.

Again, a design change raised new questions. The new choice of material was thinner than that used in our previous tests, and we needed to evaluate its strength and ability to hold its shape when covering the aperture. We conducted a series of test releases to verify that the material was strong enough and stiff enough for our requirements. The thin material was more difficult to handle, but proved adequately strong for this application. Conductivity measurements made after the test releases verified that the low resistance of the copper coating showed no change as a result of repeated flexing.

Grounding of the conductive cover to the spacecraft frame was also required. Since the cover was electrically isolated by the non-conductive bushings, an additional ground path needed to be devised. Brushes or sliding contacts were not desirable because of the particle generation risk, so a continuous non-sliding ground path was needed. A thin strip of Be-Cu was wound in a manner similar to a watch-spring and was attached at its inside end to the support shaft for the cover drive roll. This shaft was electrically grounded to the frame of the mechanism. The outside end of the grounding coil was attached to the inside of the cover drive roll. As the drive roll rotated back and forth the ground spring would wrap and unwrap around the shaft, maintaining conductivity throughout rotation. This ground spring assembly was completely enclosed to protect the coil and ensure against tangling.

Microgravity Testing

Throughout testing, gravity effects created difficulty by affecting the cover trajectory depending on the orientation of the test apparatus. Highly energetic releases such as the Be-Cu cover and the spring-driven Kapton cover were affected subtly, although characteristics of the trajectory could be related to gravity effects. It was also difficult to discern Coriolis effects when releasing under full gravity conditions. The back-up mode for the Kapton cover could not be tested at all because the low forces generated by the formed Kapton were not great enough to overcome gravity.

Near the end of the development phase of this project, SRC had the opportunity to access space on a KC-135 zero-g flight. This was a perfect opportunity to complete more detailed testing of the TIDE cover. There were several aspects of the cover's performance that we wished to characterize under microgravity conditions.

KC-135 Flight Preparation

In conducting microgravity tests, good preparation is vital for the experiment's success. Important aspects of preparing for a KC-135 flight include:

1. Experiment design
2. Personnel training
3. Physical Exams/Paperwork

Simplicity and ease of operation are the keys to success in designing an experiment for a KC-135 flight. The flight itself consists of a series of parabolas in which micro-gravity ("zero-g") and 2g conditions alternate for a total of 40 zero-g segments. The zero-g segments last about 20 to 25 seconds and the 2g segments last 30 to 40 seconds. The experiment must be designed to be able to gather meaningful data within the zero-g intervals. This is a relatively short period of time in which to conduct a segment of an experiment, especially when the disorienting conditions of the flight are considered. Valuable data could be lost or an entire experiment ruined if the operator was unable to perform adequately to complete the experiment. Simplifying and minimizing experimenter interaction with the test equipment is extremely important to experiment design.

The NASA KC-135 does not hold a current airworthiness certificate issued by the FAA. All personnel aboard the aircraft during flight are required to have completed Air Force physiological training for the aircraft. For this training, as well as for the flight, personnel must have passed an FAA Class III physical. Adequate time (up to several months could be required) to schedule the physical and the Air Force training prior to the KC-135 flight should be allowed.

Cover Testing

Our experiment utilized the instrument mock-up used during previous testing. The mock-up was modified to allow us to rotate the test set-up to simulate spacecraft rotation of 6 rpm. The experiment was divided into five segments:

1. Spring-driven stowing with no rotation.
2. Back-up mode stowing (self-curling) with no rotation.
3. Spring-driven stowing with controlled rotation of approximately 6 rpm.
4. Back-up mode stowing with controlled rotation of approximately 6 rpm.
5. Spring-driven mode with rapid uncontrolled rotation.

Tasks that were performed during the flight were limited to moving the test mock-up, resetting the cover, and releasing the cover using a remote manual actuator to open the latch. Test results in the form of photographs, VHS video, and high-speed video records (all supplied by the NASA KC-135 operation) were obtained.

Results

Spring-driven stowing:

- Repeatable, positive stowing in zero-g;
- Acceptable trajectory remaining close to instrument (the trajectory was the same as observed in ground releases; see Figure 5);
- Controlled rotation tests showed minor Coriolis effect;
- Positive stowing occurred in the rapid, uncontrolled rotation tests.

Back-up mode stowing:

- Inconsistent stowing behavior in stationary tests;
- Trajectory of coil was easily disturbed by minor perturbations in instrument motion;
- Coriolis effect in controlled rotation tests caused coil to "telescope" during stowing (Figure 9 shows this effect);
- All tests resulted in adequately stowed covers, even though final coil shapes and positions were inconsistent.

All releases performed aboard the KC-135 flight resulted in successful stowing of the cover. The spring-driven releases were positive and repeatable under all conditions. The back-up mode, although inconsistent, resulted in adequate stowing of the cover.

Lessons Learned

1. During design and development, difficulties and setbacks often occur. Sometimes a significant change in design philosophy is the best solution to a problem.
2. A single, rough test early in design can often provide information that is critical in making decisions concerning the direction of the design.
3. Common, everyday mechanisms can be used creatively to provide insights into more complex designs.
4. A low-force watch spring can provide an alternative to brushes and slip rings in providing electrical grounding for rotating mechanical members.
5. KC-135 zero-g testing offers a unique environment that can produce results that are extremely valuable in characterizing the performance of low-mass/low-force deployable mechanisms.
6. Keeping zero-g tests extremely easy to operate during the flight is vital to the success of the experiment. Experimenter interaction should be limited to pressing buttons and observation, if possible.

Conclusion

As verified by development testing, the final design met all the contract design requirements. Subsequent qualification testing verified that the final design met all the operating and environmental requirements, including thermal-vacuum and vibration requirements. The flight units have been fabricated and delivered for integration into the TIDE instrument. Launch for the Polar spacecraft is scheduled for 1994.

Table 1. TIDE Vibration Verification Test Requirements

Sine Burst

8 G lateral
15 G Axial (thrust)

Random Vibration

<u>Frequency</u>	<u>Acceleration Spectral Density</u>
20 Hz	0.0181 G ² /Hz
20 Hz - 100 Hz	+3dB/Octave
100 Hz - 300 Hz	0.09 G ² /Hz
300 Hz - 2000Hz	-3dB/Octave (0.016 G ² /Hz @ 2 kHz)

Overall level is 8.6 G RMS for 1-minute duration, each axis.

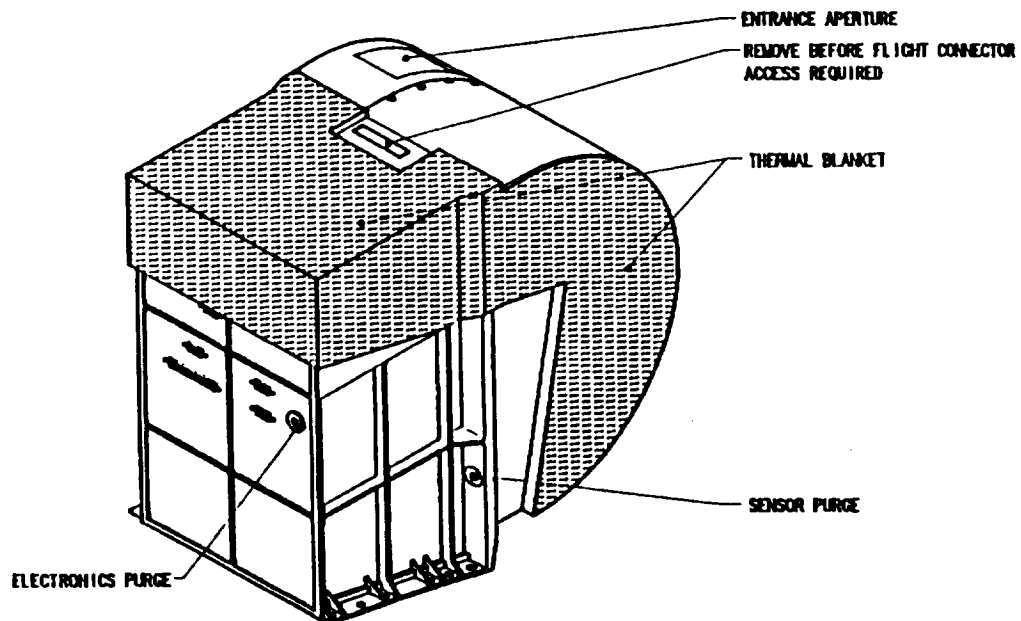


Figure 1. TIDE instrument prior to integration of cover and latch..

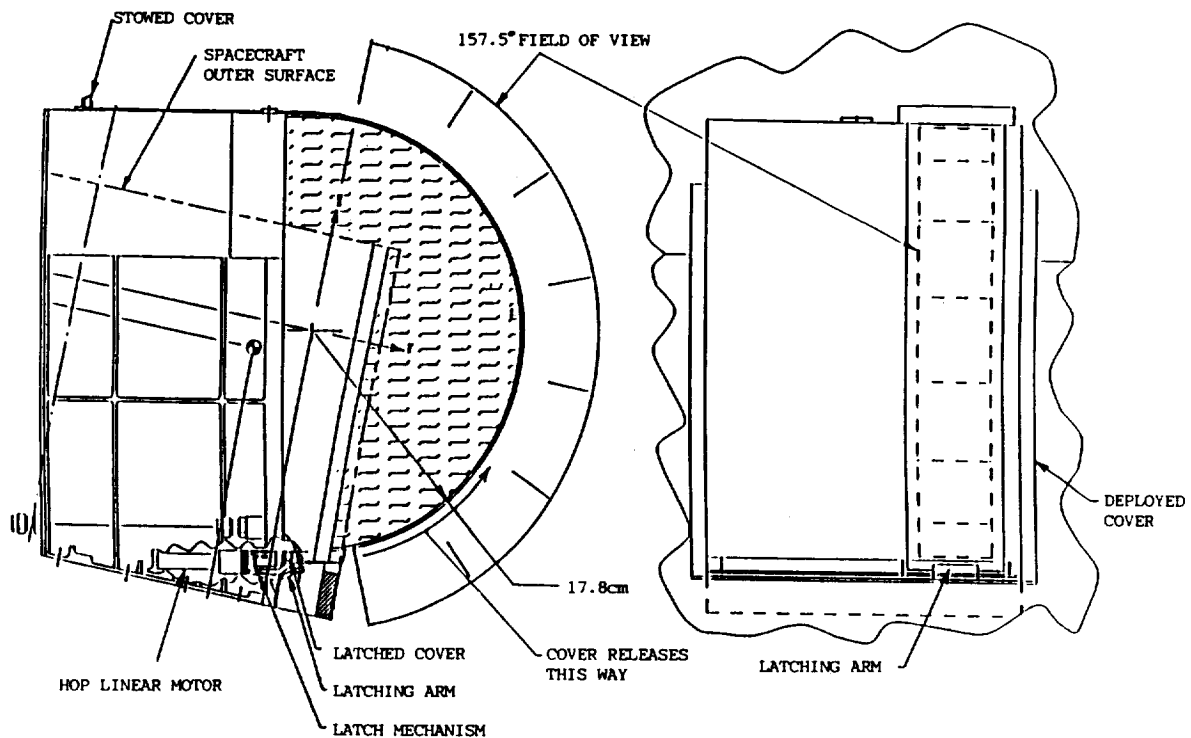


Figure 2. TIDE instrument showing locations of cover and latch

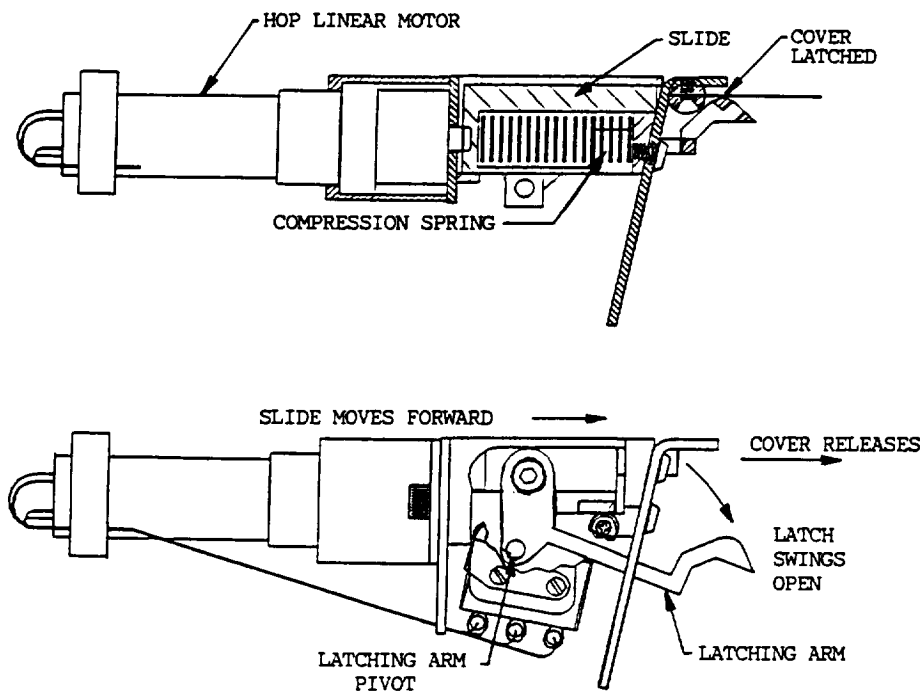


Figure 3. Latching mechanism; when the HOP motor is powered the latch opens.

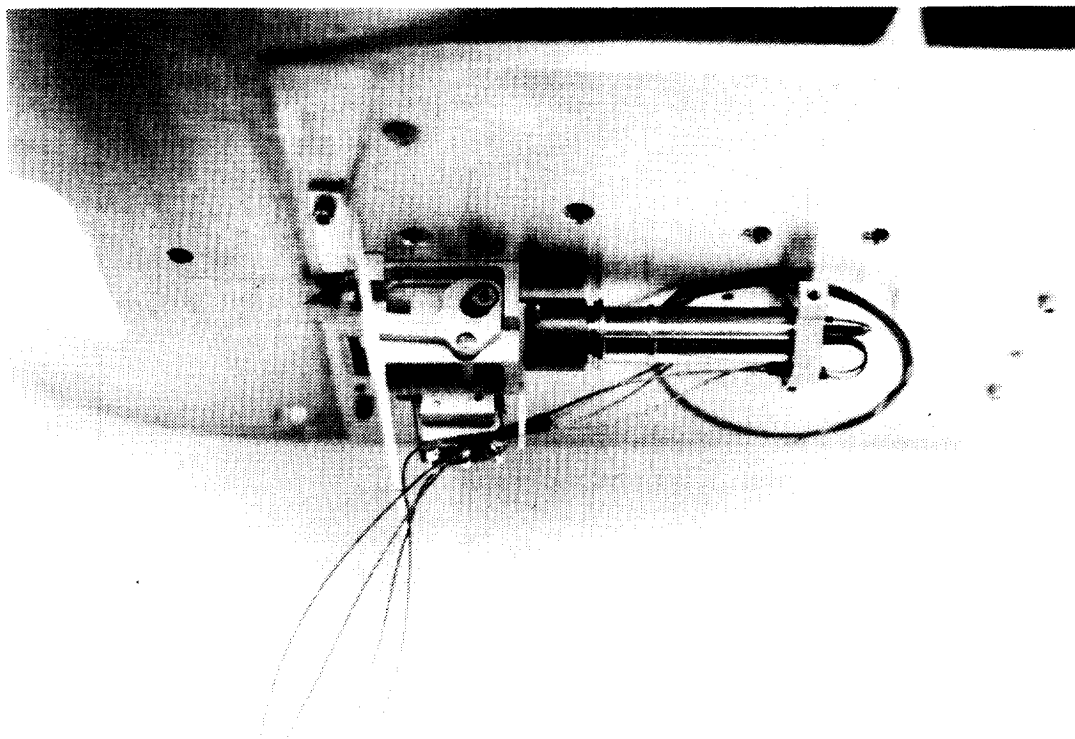


Figure 4. Latch mechanism flight design.

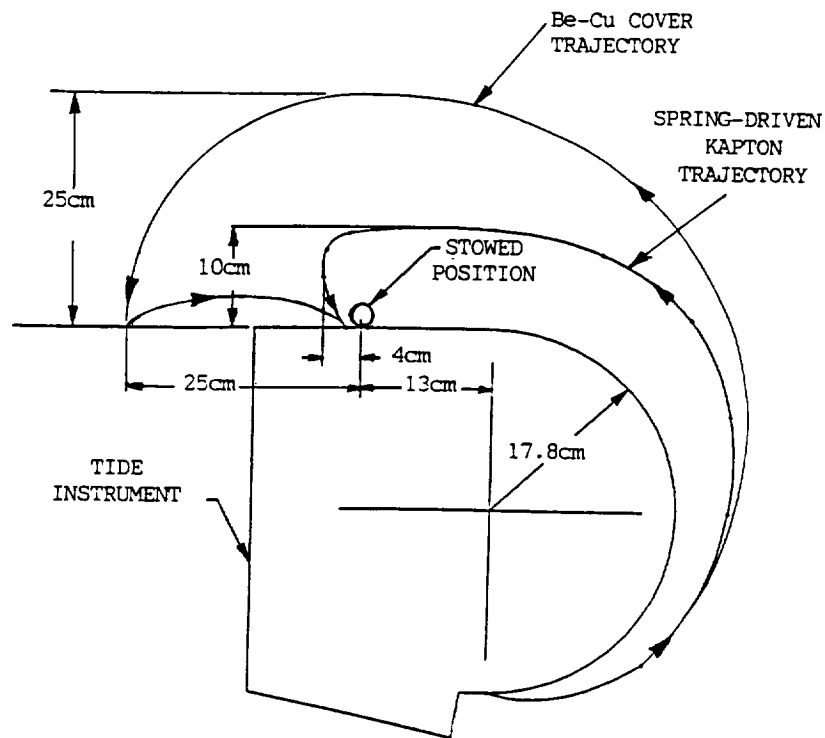


Figure 5. Schematic representation of development cover trajectories.

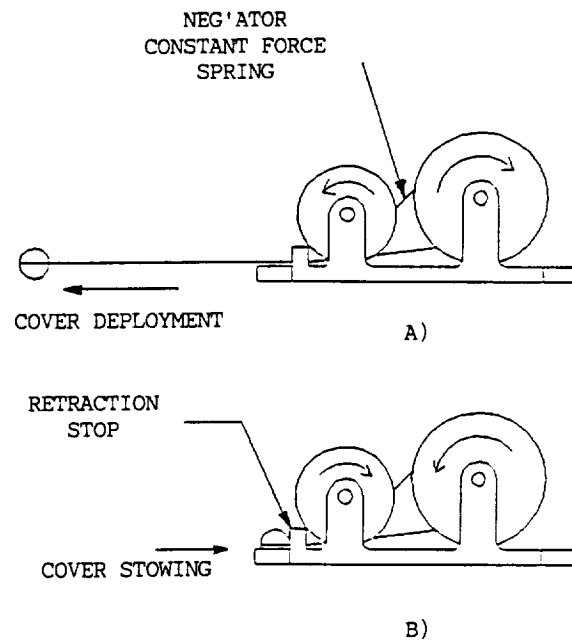


Figure 6. Constant force spring (Neg'ator) drive mechanism. A) On deployment the spring stores energy as it is wound backwards onto the larger wheel. B) The torque supplied by the spring retracts and stows the cover.

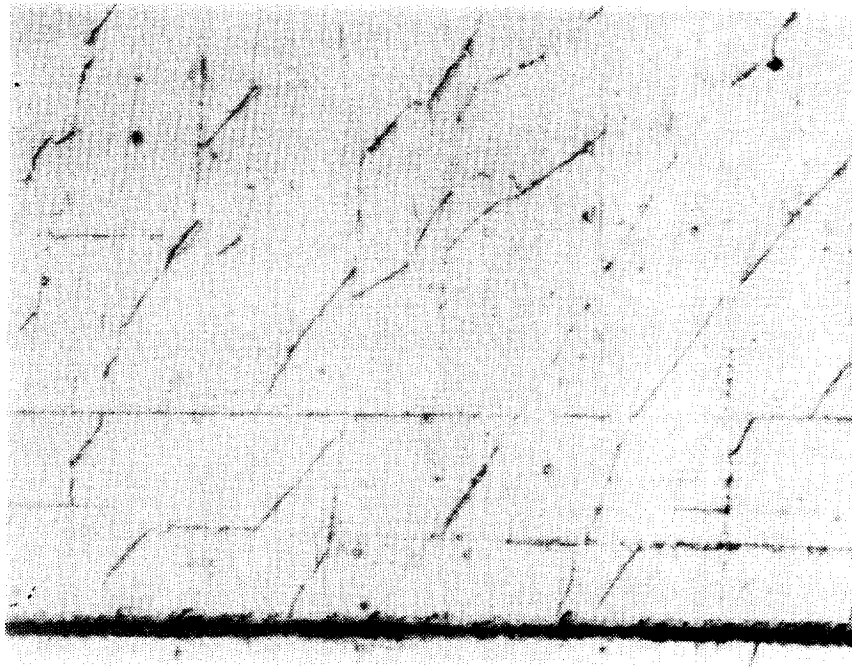


Figure 7. Fine network of cracks in chromium coating on 0.125mm Kapton (500X).

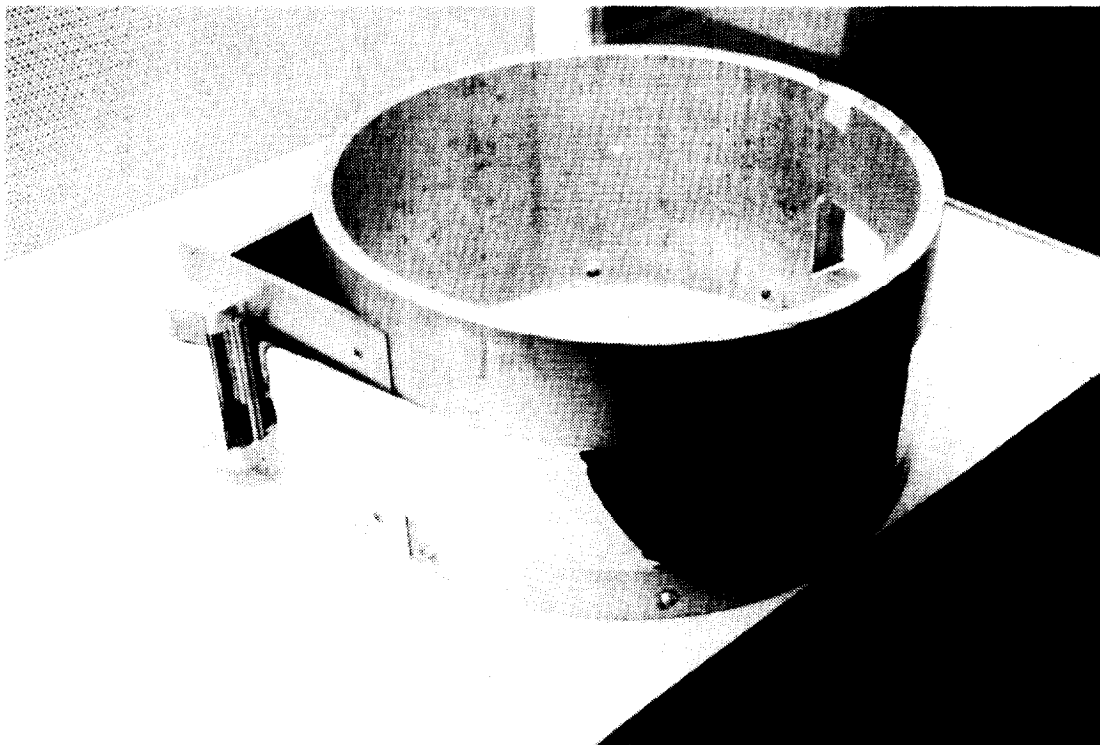


Figure 8. Flight design of cover and stowing mechanism mounted on test fixture.



Figure 9. KC-135 zero-g back-up mode stowing with controlled rotation. Twisting and telescoping due to Coriolis effect can be seen.

MILSTAR's FLEXIBLE-SUBSTRATE SOLAR ARRAY--LESSONS LEARNED

John Gibb*

ABSTRACT

MILSTAR's Flexible Substrate Solar Array (FSSA) is an evolutionary development of the lightweight, flexible substrate design pioneered at Lockheed during the seventies. Many of the features of the design are related to the Solar Array Flight Experiment (SAFE), flown on STS-41D in 1984. FSSA development has created a substantial technology base for future flexible substrate solar arrays such as the array for the Space Station Freedom. Lessons learned during the development of the FSSA can and should be applied to the Freedom array and other future flexible substrate designs.

INTRODUCTION

The FSSA is a large, lightweight, deployable solar array utilizing flexible substrate electrical panels, which are fan-folded when stowed (Fig. 1). When deployed, the array is 15.2 m long by 3.0 m wide (Fig. 2). Collectively, the solar cells, circuit paths, and Kapton® polyimide substrate is termed a blanket. The FSSA blanket has 69 active panels which contain solar cells, and an additional 7 spacer panels devoid of cells (inactive). Each panel is nominally 0.4 mm thick, and folded for stowage, the blanket stack is 2.5 cm thick.

The blanket stack is compressed between two foam and rubber lined honeycomb panels when stowed, to facilitate survival of the launch environment. Preload clamp and release action is produced by a multi-point preload/release mechanism. Upon preload release, the cover panel is rotated up and out of the blanket deployment path by two four-bar hinge mechanisms. Array deployment is then effected by a coilable-longeron Astro mast attached to the blanket by a spreader bar (upper tension bar). The mast pulls the panels out from the stowed stack as it extends. Orderly panel unfolding and alignment is assisted by three guidewires controlled by tensioning mechanisms. Near the end of the mast travel, the blanket is automatically tensioned by two mechanisms acting on a second spreader bar (lower tension bar).

DESIGN EVOLUTION

Initially, the design team studied a number of concepts for rigid and flexible substrate solar arrays. It became apparent that weight and volume requirements favored flexible-

*Lockheed Missiles & Space Company, Inc., Sunnyvale, California

substrate designs. The team was able to draw on LMSC's experience with the SAFE array as a model for the MILSTAR array. It should be

*Lockheed Missiles & Space Company, Inc., Sunnyvale, California noted that few of the MILSTAR array design team members had any direct experience working on the SAFE array. Primarily due to design requirement differences, but also due to this unfamiliarity, the FSSA did not start out as a replica of the SAFE design. Conceptually, both arrays fit approximately the same description, although most every mechanism has substantial differences in form and weight, if not function. The prime differences are in the ascent constraint structure, the preload/release mechanism, and the guidewire tensioning mechanism. The principal concern of the FSSA design team during the preliminary design phase was replicating a SAFE subsystem or mechanism with a lower weight. Although this tendency is natural in aerospace, it can narrow the design focus to the point that breakthroughs that eliminate, combine, or redefine functions are prevented.

Table 1 compares SAFE and FSSA specifications. The most obvious difference is size (SAFE is twice as long and one-third wider than FSSA), weight, (SAFE is 3.5 times heavier), and power (SAFE could have produced 3.1 times more power than FSSA if all panels were active). Thus, the FSSA is roughly one-third the size of SAFE. Improvements in photovoltaic cell technology are responsible for a 5.5% gain in power relative to area. Specific power-to-weight has improved 12%, reflecting not only better cells, but also the attention to detailed design to reduce weight for the FSSA.

Additional, critical differences apparent in Table 1 are the lack of a restow requirement for the FSSA, and the 10 year life requirement. The difference in deployed structural modes of the arrays is significantly affected by the 50% shorter coilable-longeron mast employed on the FSSA. However it is also influenced greatly by design differences reducing deployed tip mass. If all things were equal between the designs, the deployed modes of the array would increase in frequency by about 180% from the 50% reduction in length. Significantly, the FSSA has about 330% higher first-mode frequencies. During the development of the FSSA, the deployed array modal frequencies became a critical issue. Satellite Attitude Control System (ACS) simulations showed unacceptable structural response to control input, and redesign was required to raise the first bending modes about 10% in frequency.

As originally planned, MILSTAR was to use the STS with a Centaur upper stage to achieve High Earth Orbit (HEO). This was changed to the Titan IV (T-IV) with the Centaur after preliminary design of the FSSA was complete, as a consequence of the Challenger explosion. The effect of the change in ascent system on the array design turned out to be minimal, although structural analysis had to be repeated to verify margins. Generally, structural margins increased, although not enough to justify further paring of weight from the design. The peak dynamic loading on the blanket container system has been found to occur during Centaur engine shutdown, which is unaffected by STS or T-IV as the prime launch vehicle.

The heritage of several FSSA design features is apparent in Figure 3, depicting the SAFE array. It is more enlightening to discuss the differences between the two designs, and why they arose, than to describe the similarities. The FSSA blanket is smaller and substantially lighter than that of the SAFE (19% of SAFE's weight), thereby allowing the simplification of the containment structure from a deep-section strongback to 6.4-cm thick honeycomb cover and base panels. The deployable mast arrangement is similar, although the blanket container was relocated at the base of the mast with FSSA to reduce moment loading during ascent (the SAFE mast-to-blanket container configuration is driven by Shuttle cargo bay dimensions).

Activation of the SAFE blanket preload/release is dependent upon mast motion, whereas the FSSA designers made this function independent. The FSSA design team realized that a weight savings could be achieved by eliminating the heavy cam and linkage rod preload system used on SAFE, as well as lightening the relatively rigid cover structure. The FSSA preload system is distributed to eight points, facilitating the use of a lighter, less rigid cover. Actuation is performed by two separate pyrotechnic pinpullers. Each pinpuller releases preload at one mechanism directly, and at three additional slaved mechanisms via cables and bellcranks. Figure 1 shows the eight preload/release mechanism locations. Figure 4 shows a single preload/release mechanism. Preload is applied by tensioning the rod between the blanket container base and cover using the adjustment nut. A stack of Belleville washers in the load path reduces the spring rate of the combined mechanism and blanket container to accommodate differential thermal growth in the system. Originally, preload was set by measuring a gap between the inner and outer Belleville guides. This feature did not provide the measurement accuracy and repeatability desired, however.

Preload is released by allowing the tension rod assembly to rotate 135 degrees about its longitudinal axis. The upper portion of the rod is attached to a cam roller bearing, which rides on a helically cut ramp section attached to the blanket cover. The tip of the rod is held by a cover bracket hole, which locates the cam roller on the ramp until release, and acts as a bearing during rod rotation. Preload in the tension rod induces a torque to rotate the rod via the helical ramp. This torque is resisted by a bellcrank at the bottom of the rod assembly. The crank is held in place by either a pinpuller toggle on the master unit, or a cable connected to the master crank on the slave units. On each set of four preload/release mechanisms, two captured coil springs provide additional tension on the cables to rotate the cranks and tension rods, and to keep them in the released position.

The SAFE designers were required to restow the solar array blanket, and could not effectively use pyrotechnic actuation to do so. Therefore, they developed a scheme which used the first few centimeters of mast motion to drive a four-bar linkage and cam system to apply and remove preload. This system clamped the cover and base at four locations. Although it is relatively heavy compared to the FSSA system, it has the advantages of restow capability and a reduced number of command and telemetry signals required to deploy the solar array.

During deployment of the mast, the blanket is controlled by guidewires, which constrain the blanket panels to deploy in a circumscribed plane. The guidewires pay out under uniform tension, controlled by guidewire tensioning mechanisms. The initial design of this mechanism was similar to the SAFE mechanism, consisting of a cable reel retarded by three negator spring reels. This mechanism allowed restowing the blanket, as dictated by early requirements. In addition, to ensure the proper motion of the blanket panels during restow, rigid panel frames and biasing springs along the panel hinge lines were also employed. The restow requirement was eliminated after systems analysis proved that battery recharge was not required until final orbit placement of the satellite. This change allowed simplification of the blanket, since frames and hinge springs are required to discipline the blanket only during restow, not during deployment. The guidewire mechanism is also simplified, since it is no longer required to reel in the cable during restow. A second design was developed, which uses a friction clutch to regulate cable pay out (Fig. 5). This design reduces weight from about 1.4 to 0.3 kg per mechanism. It also has the advantages of fewer moving parts and bearing surfaces.

When the solar array blanket nears full deployment, it is tensioned to remain flat by stretching it between two spreader bars. The lower spreader bar attaches to two cables, each of which is controlled by a blanket tension mechanism (Fig. 6). This mechanism is essentially the same as that used on the SAFE, and is also similar to the preliminary design of the guidewire tensioning mechanism, except that its range of cable travel is 0.6 m. The cable reel is centrally located, and four negator springs act on a drum integral with the reel. As previously mentioned, the SAFE design used three negator springs. The fourth negator spring was added when analysis determined that the blanket would not be properly tensioned if one spring failed out of three, but would if one of four failed.

The cover rotation hinge mechanism is a relative latecomer to the FSSA design. Originally, the FSSA, like the SAFE, deployed its cover with the mast tip; the cover acted as the upper tension bar. During development of the satellite ACS, the predicted modal frequencies of the deployed FSSA were found to be unacceptably close to a resonance condition. A crash redesign program was initiated to boost the first mode frequencies of the deployed array by about 10% in bending. Although some structural stiffening was performed, the major focus of this effort was the reduction of the deployed tip mass by leaving the cover behind with the blanket container base. A lightweight composite upper tension bar replaces the cover to tension the blanket. The cover is now hinged to the base by two four-bar rotation mechanisms (Fig. 7), which deploy it up 2.5 cm, and then rotate it away from the blanket deployment path. At this point the mechanisms lock up to eliminate any cover freeplay motion. One single and one dual helical torsion spring provide actuation torque for each hinge mechanism. All pivot points have dual or redundant bearing surfaces, since the pivot pins are floated through all linkage and mounting holes. Monoball bearings are used to eliminate alignment sensitivity, which causes binding.

ANALYSIS

Per standard Lockheed practice, analysis of the solar array design was performed by the design team, backed up by structures, thermal, and dynamics specialists from a central pool, not co-located with the designers. Structural analysis for the most part was straightforward, and traditional methods were used. Unfortunately, the blanket container preload pressure distribution, which is not readily analyzed without using finite element methods, was never analyzed except by traditional methods, with many assumptions. This led to a lot of guesswork with regard to the static load capabilities of the blanket containment system, and also with regard to scenarios that may induce cell cracks.

Perhaps the most interesting analysis performed is a dynamic simulation of the blanket deployment using the Automatic Dynamic Analysis of Mechanical Systems (ADAMS) code. The ADAMS model was used to explore sensitivity of the blanket deployment to variations in guidewire tension, guidewire friction, flat conductor cable torques, hinge joint friction, spacecraft inertial rates, and mast deployment rates. Due to limitations in computer capability, reduced models of ten and twenty panels were created to evaluate scaling to the full blanket. Each panel was modeled as a rigid body connected by a single-degree-of-freedom revolute joint to its neighbor. To account for panel flexibility and cable bending forces, torques were applied at the hinge joints. The mast was modeled as a single rigid body pivoting at its base, again with suitable torques to account for stiffness. The model predicted that deployment would be well regulated under all conditions, even under high satellite spin rates. Scaling up to the full blanket was ascertained by comparing the ten-panel model results to the twenty-panel results. Besides the model predictions, extensive testing of the SAFE on STS-41D provides high confidence that the similar FSSA will deploy under all required conditions at 0-G.

TEST PROGRAM

As proof of concept, a mechanical development unit containing all mechanisms (except for the cover rotation hinges) was built near Critical Design Review. This development array contains a few panels using solar cells, but has glass cell simulators on all remaining panels. The development unit was tested in ambient conditions to simulate deployment in 0-G by a horizontal deployment fixture based on the SAFE ground test fixture (refs. 3 and 4). This fixture consists of a track supporting the mast from below, and a set of tracks suspending the blanket panels and tension bar(s) (or the cover) from above (Fig. 8). The mast is supported on carts traveling on the lower track, spaced at intervals of about 3 m. Low friction roller bearings minimize cart resistance to mast motion in the deployment direction, and Thompson linear bearings incorporated into each cart allow the mast a degree of freedom across the track. Each blanket panel is individually counterweighted. The counterweight and suspension system allows each blanket panel to move in the mast deployment direction, while following the motion of the panel CG as it moves inward toward the mast, to a final position along the inner hinge line. The blanket panels are necessarily suspended above their CG, midway between their hinge lines, and the deployed blanket is tensioned along a line that

coincides with the hinges closest to the mast (every other hinge). A small range of vertical motion is also accommodated by this blanket suspension system. The panel thickness is the most complicating factor to the blanket suspension system design. Because panel counterweights only 0.4 mm thick are impractical, and because it is desirable to use roller bearings on the track carriages suspending the panels, a stacked arrangement of carriage tracks and counterweights allows the test equipment to have reasonable thickness.

Several problems related to the horizontal deployment test equipment have occurred during testing, due to weaknesses in the original design. During one of the first development tests, the suspension wire supporting the 10-kg cover broke, causing a chain-reaction domino effect to propagate down the blanket. Several panels ended up on the floor of the test facility. After this incident, the cover support wire was increased in size and changed from single-strand music wire to braided cable to avoid a future mishap. However, the remaining suspension wires continue to plague the test fixture with fatigue-related breakage, and are now in the process of being converted to heavier gage braided cable as well. The main problem with the music wire cables occurs at their end fittings, which have small radius bends, inducing low-cycle fatigue failure. Revised end termination designs for the braided wire cable have ball end fittings, or relatively large-radius cable loops to eliminate these problems.

Ambient testing of the FSSA development unit proved that the basic design was sound. One of the most important test results was the discovery of panel-to-panel sticking, caused by assembly adhesive on the backside of the panels. Because of this, manufacturing and handling procedures were successfully revised to eliminate such problems on flight panels, by scrupulous attention to cleanliness during bonding operations.

Additional testing with the development hardware exposed it to the ascent acoustic environment, the release pyroshock environment, and ascent quasi-static loads. No anomalies occurred during the first two tests, proving that the foam and rubber insulation in the blanket container performed as intended. The quasi-static load testing of the blanket container did result in unexpected behavior, however. In order to properly load the stowed blanket in the preloaded container, the entire assembly was placed on a centrifuge, oriented such that the centrifuge arm was along the resultant load vector for the worst-case peak load condition. Before maximum load was reached, the blanket panels slipped relative to one another, and the cover also shifted (Figure 9). Experimentation found that the cover required lateral restraint, and preload was raised from an initial value of 9.3 kN to 13.4 kN to avoid slippage. Panel slippage while stowed and preloaded is a concern, since it can cause cell cracking. The centrifuge testing also found inadequacies in the preload setting/measurement method.

Several changes are incorporated into the flight FSSA units as a result of the development test program. The deployed mode requirement change easily caused the most modifications and additions to the design. The most significant changes include: cover rotation hinge mechanisms added; lightweight upper tension bar added; fourth negator

spring added to blanket tension mechanism; longeron lockup cams added to mast to avoid reliance on microswitches for deployment termination (deployment is shut off by a timer); blanket cover lateral restraint added; preload on blanket increased; strain gage load cells added to tension rods to measure preload in lieu of mechanical measurement. Several other minor changes have been made to some mechanisms, such as an improved coil spring containment cage on the preload/release mechanism cables, and modifications to the pinpuller toggles and bellcranks to eliminate impact damage caused by repeated ground test.

DESIGN ASSESSMENT

The principal improvements to flexible substrate solar-array design exhibited by the FSSA are:

1. Increased specific power-to-weight ratio by 12% relative to SAFE (5.5% due to cell technology improvements).
2. Increased first bending mode frequencies by 330% relative to SAFE (approximately 150% increase per given length).
3. Increased qualified life expectancy to 10 years from several weeks.

Many lessons have been learned during the design and testing of the FSSA. A summary of these includes:

DO's:

1. Establish written test requirements and a test plan as early as possible.
2. Devote sufficient resources to thoroughly prove 0-G deployment test equipment works, and that it is robustly designed with fail-safe features or high structural margins.
3. Minimize deployed mass at the deployed end of the array or mast (leave the cover at the base).
4. Create a finite-element model of blanket container preload distribution.
5. Perform development acoustic and shock testing as appropriate to establish minimum acceptable blanket preload to survive these environments.
6. Consider pretesting cell assemblies by uniformly preloading prior to incorporation in the blanket. This will eliminate or reduce cell cracking caused by cell assemblies with residual stresses.
7. Insist on high cleanliness standards during panel bonding, especially when the process involves cutting film adhesives, to avoid panel sticking.

8. Use electro-mechanical measurement of preload when it is critical. Ensure adequate strain reliefs are provided for connection wires.
9. Maximize spreader bar stiffness in the deployment plane, and perform analysis to ensure acceptably low deflection to avoid panel warping or wrinkling.
10. Be aware that MoS₂ coatings have a coefficient of friction dependent upon humidity. Variations are on an order of magnitude between ambient and vacuum conditions.

DON'T's:

1. Do not rely on preload and friction to hold a blanket stack in place during ascent; use a positive mechanical load path such as pins, skewers, or interlocking sections. A reduction in applied pressure from 9.7 kPa to 1.2 kPa (a factor of 8) should be possible if this is done.
2. Avoid overly complex electronic test consoles; if a simple power supply with polarity and on/off control suffices, use it.
3. Avoid using notch-sensitive materials as threaded fasteners (the original tension rod cam roller bearing screw was 440C CRES, and broke at the root of the first thread).
4. Do not apply MoS₂ coatings to both surfaces of a sliding/mating pair, or a higher coefficient of friction will result than if only one surface is coated (this occurred in the tension-rod Belleville washer stack).
5. Do not allow inexperienced engineers to design spacecraft mechanisms without sufficient supervision and design review (many details of the preload/release mechanism have required changes, due to the designer's lack of experience and insufficient review).

CONCLUSION

The flight FSSA has successfully been qualified in static load (centrifuge) and acoustic environmental testing. As this paper is written, qualification for pyroshock and thermal-vacuum conditions is forthcoming. Improvements to the reliability and ruggedness of the simulated 0-G blanket suspension system of the horizontal test equipment also are being made. Completion of the qualification program is anticipated by mid-1992.

ACKNOWLEDGEMENTS

I wish to especially thank Al Louie for his assistance and knowledge of the historical evolution of the FSSA design. Additionally, I greatly appreciate the valuable

technical details I have acquired from Terry Messersmith, George Welik, and Craig Wiesner. Finally, this paper would not have been possible without Marc Campell, Dale Lindberg, and Dave Putnam, who gave me the opportunity to do a little bit of designing (and a lot of testing) as part of the FSSA design team.

REFERENCES

1. D. E. Lindberg, "A 928-M² (10,000 ft²) Solar Array," Seventh AMS, NASA TM X-58106, p. 287, September 1972.
2. "Solar Cell Array Design Handbook," JPL SP 43-38, Vols. 1&2, October 1976.
3. D. T. Chung, L. E. Young, "Zero Gravity Testing of Flexible Solar Arrays," Fifteenth AMS, NASA CP-2181, p. 115, May 1981.
4. D. T. Chung, "Deployment/Retraction Ground Testing of a Large Flexible Solar Array," Sixteenth AMS, NASA CP-2221, p. 249, May 1982.
5. "Solar Array Flight Experiment Final Report," Contract NAS-9-31352, LMSC-F087173, April 1986.
6. Lockheed Missiles & Space Company, "Solar Arrays for Electrical Power in Space Fact Sheet," September 1990.

MECHANISMS OF THE SPACE ACTIVE VIBRATION ISOLATION (SAVI)

Frank Schmitt*

ABSTRACT

The Space Active Vibration Isolation (SAVI) is a concept for vibration isolation of one body from another with simultaneous precise control in 6 Degrees Of Freedom (DOF). SAVI achieves this using a combination of electromechanical linear actuators and magnetic actuators. A SAVI was built and tested to demonstrate these capabilities.

This paper describes the design, function, and performance of some SAVI mechanisms and associated test apparatus. Besides the linear actuators, the mechanisms of interest include a structure for simulating the body being pointed, another apparatus to simulate the body that is the vibration source, and mechanisms to off-load the weight of each of these two bodies from the experiment to approximate a zero-g condition.

INTRODUCTION

The success of an orbiting optical experiment, shown schematically in Figure 1, depends on the ability to accurately point a vibration-free optical bench assembly (forward body) at distant targets; the Honeywell SAVI system is directed toward accomplishing this goal. In Figure 1, the SAVI is shown between the optical bench and the rest of the spacecraft (aft body). The aft body for some spacecraft can be a source of considerable vibration.

The approach to meeting these pointing and isolation requirements employs magnetic suspension technology, which, due to its inherently noncontacting nature, is capable of superior isolation over a wide range of frequencies. A system of six magnetic actuators is backed by a system of six electromechanical linear actuators through a triangular structure called the Intermediate Gimbal Structure (IGS).

*Honeywell Inc., Satellite Systems Operation

The long stroke capability of the linear actuator allows a smaller, more efficient magnetic actuator to be designed. Both types of actuators are arranged in pairs at each of the three vertices of the IGS, as shown in Figures 2, 3, 4, and 5.

The chosen arrangement and orientation of the actuators allows 6 DOF and optimizes total SAVI weight and power within the required performance parameters. Table 1 summarizes the SAVI requirements and resultant actuator requirements.

The following paragraphs address design and performance of the actuators, the forward and aft bodies, and their gravity off-load mechanisms. The entire demonstration assembly is shown in Figures 5 and 6.

The SAVI and the associated test apparatus development began in 1986 with the building of a single-DOF demonstration unit and the conceptual design of the 6-DOF system. The 6-DOF test, described herein and shown in Figures 5 and 6, was set up and tested during 1989 and early 1990. Improvements and refined testing and characterization are underway and will continue over the next few years during a follow-on program.

OVERALL SYSTEM REQUIREMENTS, CONFIGURATION, AND SIZING

The basic requirements (shown in Table 1) for the system were -80-dB isolation of the forward body from the aft in 6 DOF between 1 and 2000 Hz, and retargeting the forward body $\pm 2^\circ$ in 1.5 s.

The upper attachment-point locations of the SAVI to the Forward-Body Truss (FBT) are a given requirement. Location of the magnetic actuators approximately above their corresponding linear actuator minimizes the moment load and excitation of the IGS.

The force and speed required for retargeting essentially determine the size of the actuators. Optimization of their alignment indicates that they should be aligned generally normal to a radial line from the center of rotation.

The design philosophy for all mechanical SAVI components required that they be capable of flight status with minimum changes.

In other words, the design is not to be dependent on processes, materials, or components that are not flight qualifiable.

LINEAR ACTUATOR

The following paragraphs describe the linear actuator; its cross-section is shown in Figures 7 and 8. The motor, nut, and screw sizes are determined by the load and speed requirements. Gearing was not used, eliminating the gear weight, the associated housing weight, and a source of backlash. By directly driving the screw, the motor was forced to be positioned directly behind the screw, which established the overall length. The nut, in turn, is attached to a hollow spline shaft that passes through a ball spline at the top of the actuator. A spherical bearing attached to the top of the spline shaft is the connection point to the IGS.

During normal operation, loads are transmitted through the spline shaft and nut to the screw shaft, which is supported by a duplex bearing pair mounted in the housing. The separable motor/resolver/tachometer package mounts to the housing directly behind the bearings.

The sleeve around the nut has axial stops at each end and is held in place by the overrun spring assembly. This preloaded spring is held between two plastic rings, which, in turn, are held between two flanges on the housing and two identically spaced flanges on the sleeve. In this way, a nut overrun in either direction compresses the spring and absorbs the energy of the nut, shaft, and motor/tachometer. The sliding of the plastic rings in the housing adds damping to this action.

A similar spring assembly is used between the actuator housing and the lower gimbal mount. This spring limits the axial forces on the actuator that might occur in an anomalous test situation. An overload in either direction compresses the spring and slides the end rings, thereby limiting forces and absorbing energy.

The overload spring housing has two trunnions that fit into pairs of preloaded bearings in the gimbal; the gimbal trunnions, in turn, mount to the aft body through two pairs of preload bearings. The joints at all interfaces through which the load passes have either clamped, interference, or tight-sliding fits to minimize axial play. Axial play anywhere represents a dead band to the control system. Similarly, a preloaded ball spline is used to prevent the roller nut from rotating, which would produce axial play.

Selection of the nut/screw was driven by the need for high load capacity, zero axial play (i.e., preloadable), high stiffness, and efficiency. The efficiency requirement narrowed the candidates to ball and roller screws; the high stiffness and high load capacity led to the selection of roller screws over ball screws.

The spline shaft is driven by the roller nut and guided by the ball spline. A row of recirculating balls contacts the spline shaft on each side of its three ribs and is preloaded against the ribs. Low friction and the ability to preload and bear radial loads were the main features that lead to the selection of a ball-type spline. Since the spline shaft telescopes over the screw, the screw is protected from external damage, debris, and lubricant loss. Rubbing seals are used to contain the ball-spline lubricant. The spline shaft is bored to accommodate the screw and sized to fit the bushing, which supports the upper end of the screw during rotation and translation in the bore.

A brushless DC motor was chosen to drive the linear actuator. Its characteristics for the peak-power points, half and full speed, are shown in Table 2. Figure 7 shows the motor together with its resolver. The tachometer, with its optical commutator, is mounted in the same housing with the motor, which is separable from the linear actuator for independent fabrication and test.

The gimbal ring shown in Figure 8 was designed to have a large section modulus to achieve the required overall axial actuator stiffness without being excessively heavy. A channel cross-section and mounting flats for the trunnions were machined in the ring. A box cross-section was then formed by welding a strip of flat stock over the channel.

A calculation of the axial stiffnesses of the linear actuator components was made, which showed the need to improve the nut and gimbal stiffness to achieve the overall linear actuator stiffness required for system performance. Workable levels for these stiffnesses were attained but comfortable margins over system requirements were never achieved.

Initial sizing for the linear actuator was performed using the two peak-power points, full- and half-speed retarget, which do not include all dynamic effects. Once the motor size, inertia, screw leads, friction, etc., were determined, these characteristics were entered in the overall system dynamic simulation for a final check and adjustment. Motor

hub inertia and the lead of the screw also required adjustments at this point. The final total weight of the actuator with the gimbal was 90 kg (198 lb).

The end attachments of the linear actuator are a 2 DOF (gimbal) on the bottom and a 3 DOF (spherical bearing) on the top. Because there can be a component of rotation about the linear actuator, one end must have a rotational DOF. A third DOF at the other end would allow the actuator to rotate about its axis without restraint; consequently, it is not used.

MAGNETIC ACTUATOR

A single magnetic actuator is shown in the cutaway portion of Figure 4. This is one of six magnetic actuators that are aligned with the linear actuators. Each magnetic actuator consists of two horseshoe electromagnets, one on each side of a flat-plate armature. The core is laminated, and each leg of the magnet has a coil. The two electromagnets are mounted in stator supports that bolt to the IGS platforms. The armatures attach to the forward body through the armature supports. Stops are provided to limit travel in all three directions when the system is not powered. During operation, there is no contact in any part of the magnetic actuator. Table 3 gives the important actuator parameters.

GRAVITY OFF-LOAD DEVICE

Because all of the actuators are sized for on-orbit operations (i.e., dynamic loading, not gravity forces), the entire weight of the forward-body assembly was supported by a spring mechanism. This mechanism is shown in Figures 9 and 10 and consists of an arm mounted on a hinge, which is acted on by a vertical and a horizontal set of springs. The forward-body assembly is hung vertically from the arm. When the arm is horizontal, the forward-body assembly weight is exactly balanced by the preload of the vertical springs. When the arm is displaced from horizontal, the preloaded horizontal springs apply a moment to the arm that is in a direction to increase the displacement (i.e., its effect on the arm is like a negative spring). By choosing correct spring rates, spring preloads, and spring attachment locations, this negative spring rate can be made to nearly balance the positive spring

rate of the vertical spring. The net result is a mechanism that counteracts the forward body's weight over a range of vertical displacements.

In addition to low stiffness, low friction and low hysteresis are necessary for good performance. This was accomplished by using flexible-element bearings at all pivot points, rather than sliding- or rolling-type bearings. The stiffness introduced by the flexible elements combines with the other springs and is balanced along with them so that the net stiffness can remain near zero.

Commercial flexural pivots were used at the arm's fulcrum and at the suspension spring attachment points. The ends of the compensation spring assemblies were attached to the arm and to the base structure with a short length of cable to provide low-friction flexibility.

Due to the inherent nonlinearities in the geometry of this approach, exact cancellation of the suspension and compensation spring's stiffnesses is not possible. Table 4 shows the calculated characteristics and the net errors for the design used. It was desired to keep the force error below 4.5 N (1 lb) at 13 mm (~0.5 in.) displacement of the forward body. The as-built effective stiffness was estimated to be <0.113 N/m (<1 lb/in.) at full deflection; the system performed satisfactorily using this setup. During dynamic test conditions, a bounce of the compensation spring at 2 Hz developed. A redesign of the compensation spring assembly is being considered to decouple this mode.

The forward body assembly was hung from the spring mechanism by a rod that attached to the forward body through a 2-DOF gimbal. The gimbal axes were placed through the forward body's mass center. Commercial flexural pivots were also used in the gimbal to avoid friction and hysteresis.

AFT-BODY ASSEMBLY

As a simulator of the aft body, this assembly sums the vibration from the six shakers to create a 6-DOF vibration, and serves as a mount for all six linear actuators. There is a closed-loop control system around the shakers that moves the shaker heads in response to forces on them so as to simulate the dynamic movement of the real aft body. The aft

body structure, configured as a "Y", is a weldment of aluminum tubes with platforms on the end of each leg, as seen in Figure 11.

Each shaker is attached to the aft body by a strut having a spherical bearing at each end to avoid lateral loadings on the shaker. The aft body is suspended from a tripod by a compression spring in the aft body to prevent the weight of the aft body and the SAVI from bearing on the shakers.

FORWARD-BODY TRUSS

The primary function of the FBT is to hold the primary and secondary mirrors in correct relationship to each other and to the optics in the aft body. The FBT is shown in Figures 6, 7, and 12; its characteristics are shown in Table 5.

The lower structure of the FBT was built of identical struts joined at the hubs. This configuration was chosen to minimize the number of struts, to provide three attachment points on hubs for each of the seven mirror segments, and to provide attachment surfaces at each of the three corners below the truss to interface with the SAVI.

Weights attached to the top surface of the lower truss structure simulate a primary mirror; weights clamped to the legs at the top of the FBT simulate a secondary mirror. Primary mirror weight is about 2000 kg (4440 lb), while the secondary mirror weight is 140 kg (309 lb); the entire FBT assembly weighs 3000 kg (6600 lb).

The entire FBT was suspended by a rod from the FBT suspension overhead, which attaches to the center primary mirror plate through the 2-DOF gimbal, as shown in Figure 12.

For the FBT to be controllable by the SAVI, its first flexible body mode had to be placed between 7 and 10 Hz. This is the most significant requirement (outside of the geometry) in the design of the FBT and necessitated several analyses and design iterations.

The three tripod legs, shown in Figures 6 and 7, were the main masses involved in the first mode. To raise their frequency to 8 Hz, it was necessary to increase their diameter from 127 to 178 mm (5 to 7 in.) and to provide moment restraints at the end attachments. At the top, struts were added horizontally and diagonally between the legs; at

the bottom, diagonal struts were added to attach the leg more rigidly to the top and bottom layers of the truss.

It was desired to keep the FBT representative of a flyable structure that is light and space erectable. Graphite-epoxy tubing was used throughout with aluminum end fittings. This also allowed the coefficient of thermal expansion of the structure to be near zero. The end fittings of the 1-M struts in the lower truss were of a type designed and tested for ease of assembly by astronauts. They proved to have an undesirable amount of nonlinearity for controllability and are being replaced.

RESULTS

The SAVI performance as an isolator was established to be better than -50 dB, this being the limit of the test equipment's ability to measure. The measurable part of the isolation data was somewhat below the 80-dB goal but followed the predicted characteristics for frequency. The following component problems contributed to a reduction in performance.

The linear actuator performed well with the exception of its low overall end-to-end stiffness, and its stiction and drag being high with respect to the models. The stiffness will improve if the overload and overrun springs are removed; these are required for protection during testing only. Another linear actuator design has been generated since the SAVI design, which eliminates the gimbal and other significant compliance sources.

Stiction and drag probably result from the spherical bearings, which were built snug to give the linear actuator virtually zero end-play. For both of these problems, it was possible to adjust the control loops to compensate for these anomalies.

The FBT gravity off-load gimbal set was overloaded by an impact just before the start of testing, breaking the flexural pivots. The largest commercially available size had been used but the safety factor was small. The gimbal set had been designed with stops, which caught the FBT after the flexure failure. Solid rods that allowed rolling and possibly some sliding contact were used in place of pivots so that testing could continue.

The aft body/shaker control system proved to be unstable, so the shakers were operated open loop. Damping or tuning of the aft body will be investigated.

CONCLUSIONS

During the course of testing, the SAVI performed its required functions. Retargeting was generally good; however, the desired levels of isolation were not reached. Several contributing factors were identified. Time did not permit detailed investigations of or solutions to these problems; this will take place during the follow-on program.

The usefulness of the SAVI and the rest of the test equipment as a test bed was established. The follow-on program will use the majority of the test equipment and the SAVI itself as-is to pave the way for a flight program.

REFERENCES

B.J. Hamilton, and D.R. Carter, "Laboratory Demonstration of SAVI Magnetic Suspension Technology," storyboard presentation, 14th Annual AAS Control Conference, February 26, 1991.

ACKNOWLEDGEMENTS

The work described herein was performed by Honeywell Inc., Satellite Systems Operation (SSO), Glendale, Arizona, and funded by Phillips Laboratory, Kirtland Air Force Base, New Mexico.

The author would like to acknowledge the contributions of Paul Ashley, Honeywell SSO, to the linear actuator design, and of Project Engineer Brian Hamilton, also of Honeywell SSO, to the mechanical design concepts.

TABLE 1. SAVI REQUIREMENTS

	Demonstration System Requirements
Isolation	6 DOF, -80 dB, 1 to 2000 Hz
Retarget Torque	27,000 N-m <ul style="list-style-type: none"> • Magnetic actuator force – 3200 N (720 lb) • Linear actuator force – 4000 N (900 lb)
Articulation	± 2 degrees <ul style="list-style-type: none"> • Linear actuator extension – ± 0.11 m (4.5 in.) • Linear actuator rate – 0.25 m/s (9.85 in./s)
Suspended mass	3000 kg (6600 lb)
Disturbance spectrum	Swept sine (with full spectrum instrumentation)

TABLE 2. LINEAR ACTUATOR - MOTOR, RESOLVER, AND TACHOMETER CHARACTERISTICS

Parameter	Design Value	
Speed	0 to ± 3200 rpm	
Motor (8-Pole, 2-Phase):	<u>At 1600 rpm</u>	<u>At 3200 rpm</u>
– Torque	5.3 N-m (750 oz-in.)	3.5 N-m (465 oz-in.)
– Shaft Power	888 W	1100 W
– Power Loss	80 W	90 W
– Efficiency	91%	92%
– Torque Ripple	<4%	—
– Drag Torque	<0.30 N-m (<40 oz-in.)	—
Assembly Weight (with resolver and tachometer)	<11.8 kg (<26 lb)	—

TABLE 3. MAGNETIC ACTUATOR DESIGN DESCRIPTION

Parameter	Description	
Type	Lightweight Horseshoe with Flux Feedback	
Force Capability	± 3200 N	
Motion Range	± 2.5 mm	
Magnetic Gap (Go)	4.5 mm	
Excitation	< 80 V pk	
(worst case)	< 20 A pk	
Power (Max Gap and Force)	740 W	
Mass		
Each Stator	14.6 kg	(32.12 lb)
Armature	9.7 kg	(21.3 lb)
Total	38.9 kg	(85.5 lb)

Stator Core Material: Vanadium Permendur

Armature Material: Vanadium Permendur

TABLE 4. SUSPENSION AND COMPENSATION SPRINGS SELECTION

Compound Spring/Single Pivot			
Suspension spring parameters:			
Stiffness		=	152,000 N/m (870 lb/in.)
Length		=	1.1 N/m (45 in.)
Preload		=	29,000 N (6600 lb)
Compensation spring parameters:			
Stiffness		=	44,000 N/m (193 lb/in.)
Length		=	3.4 m (135 in.)
Preload		=	12,900 N (2,900 lb)
Link Lengths:			
Suspension spring to pivot		=	254 mm (10 in.)
Compensation spring to pivot		=	1,142 mm (45 in.)
Load point to pivot		=	254 mm (10 in.)
Disp mm (in.)	Net Load N (lb)	Average Stiffness N/m (lb/in.)	Local Stiffness N/m (lb/in.)
13 (0.5)	29,355.0 (6599.6)	140 (0.8)	613 (3.5)
10 (0.4)	29,355.9 (6599.8)	88 (0.5)	403 (2.3)
7 (0.3)	29,356.4 (6599.9)	35 (0.2)	228 (1.3)
5 (0.2)	29,356.8 (6600.0)	0 (-0.0)	105 (0.6)
2.5 (0.1)	29,356.8 (6600.0)	-35 (-0.2)	17 (0.1)
0 (0.0)	29,356.8 (6600.0)	0 (0.0)	0 (0.0)
-2.5 (-0.1)	29,356.8 (6600.0)	-35 (-0.2)	-35 (-0.2)
-5 (-0.2)	29,356.8 (6600.0)	0 (-0.0)	17 (0.1)
-7 (-0.3)	29,357.2 (6600.1)	-35 (0.2)	105 (0.6)
-10 (-0.4)	29,357.7 (6600.2)	88 (0.5)	228 (1.3)
-13 (-0.5)	29,358.6 (6600.4)	140 (0.8)	421 (2.4)

TABLE 5. FORWARD BODY TRUSS CHARACTERISTICS

Description	Parameter
Overall height	8.1 m (26.7 ft)
Weight	864 kg (1900 lb)
Lower truss (primary mirror end)	
Struts	
Number required	267
Length	1 m
Tube diameter	50 mm (1.956 in.)
Tube wall thickness	2 mm (0.086 in.)
Tube material	Graphite/epoxy 80 deg wind angle
Attachments	Slide/twist latch fittings
Tripod legs	
Length	8.71 m (28.6 ft)
Diameter	177 mm (7.0 in.)
Wall thickness	4.8 mm (0.188 in.)
Attachments	End plugs and clamp-on collars (both ends)
Corner to corner	
At base	6.2 m (20.4 ft)
At top	1.2 m (4 ft)
Upper truss (secondary mirror end)	
Struts	9
Size	50 mm
Attachment	Bolt ended struts

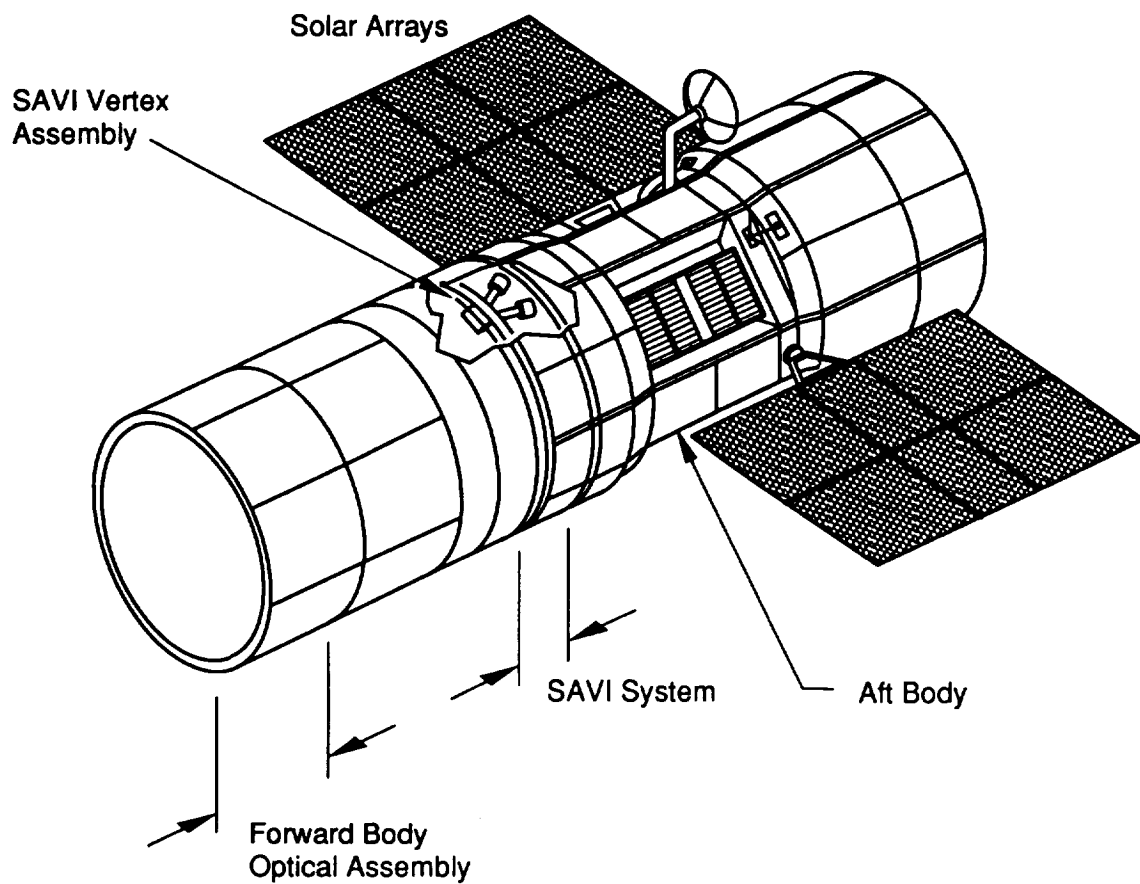


Figure 1. Satellite with SAVI Mounted Optical Assembly

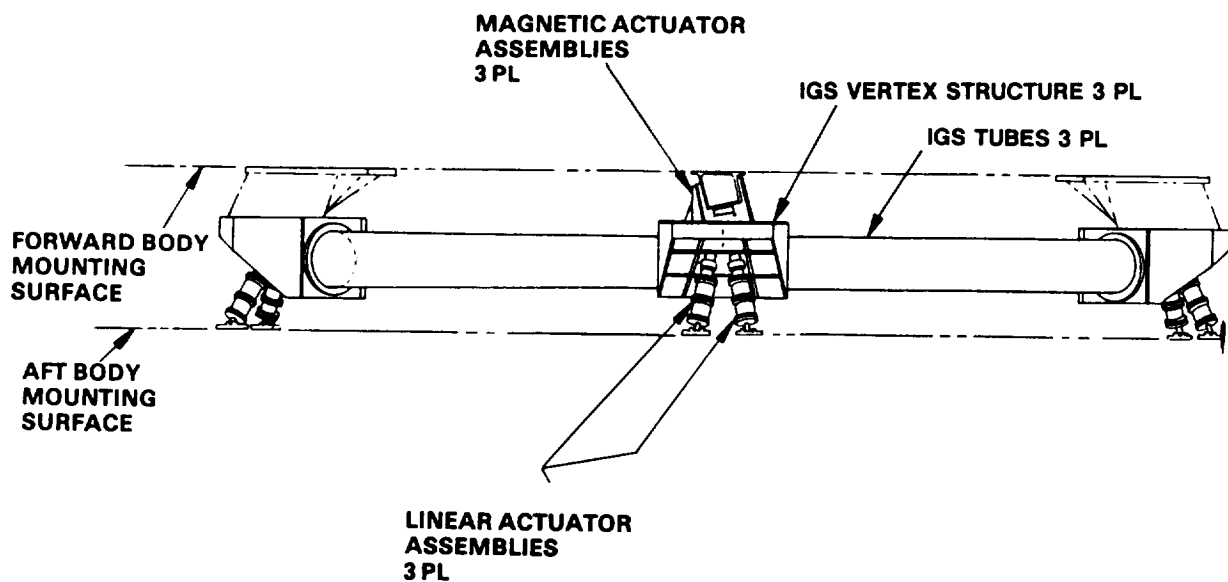


Figure 2. SAVI (Edge View)

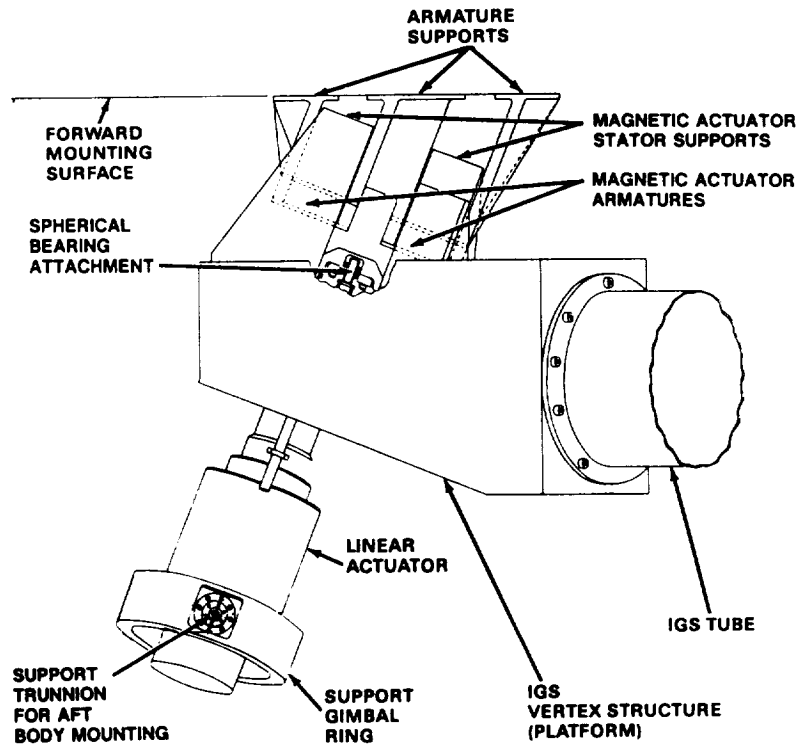


Figure 3. Vertex Assembly Tangential View

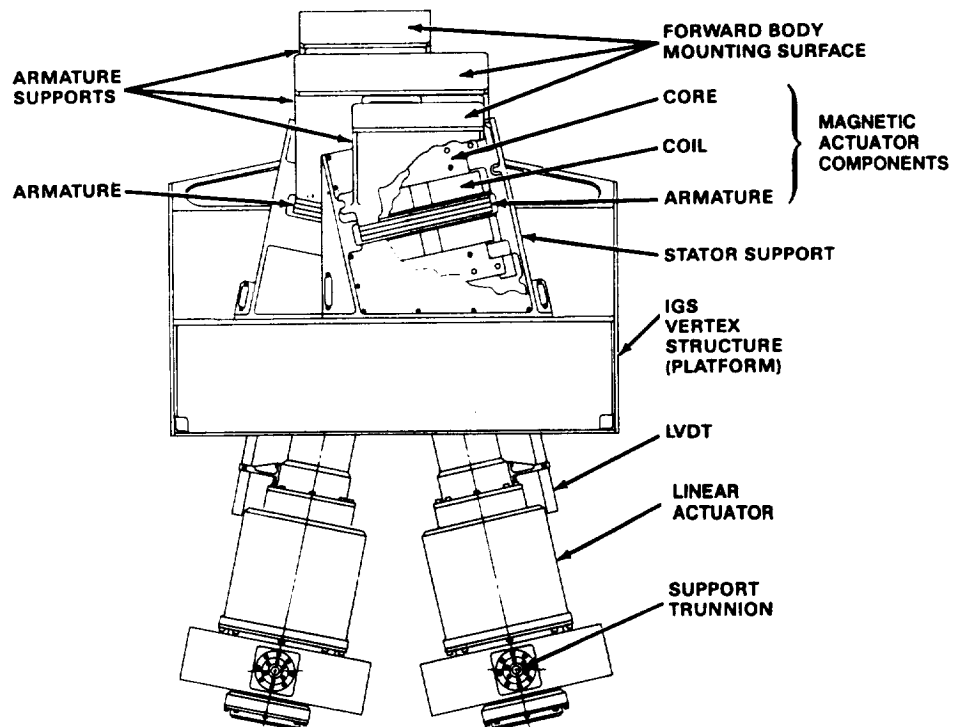


Figure 4. Radial View Vertex Assembly

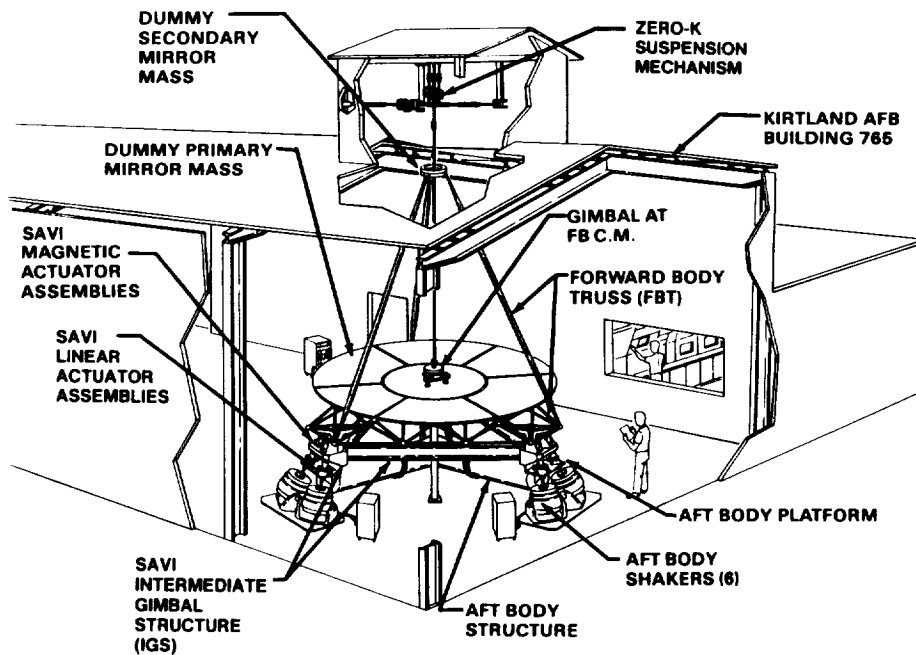


Figure 5. SAVI Demonstration Assembly

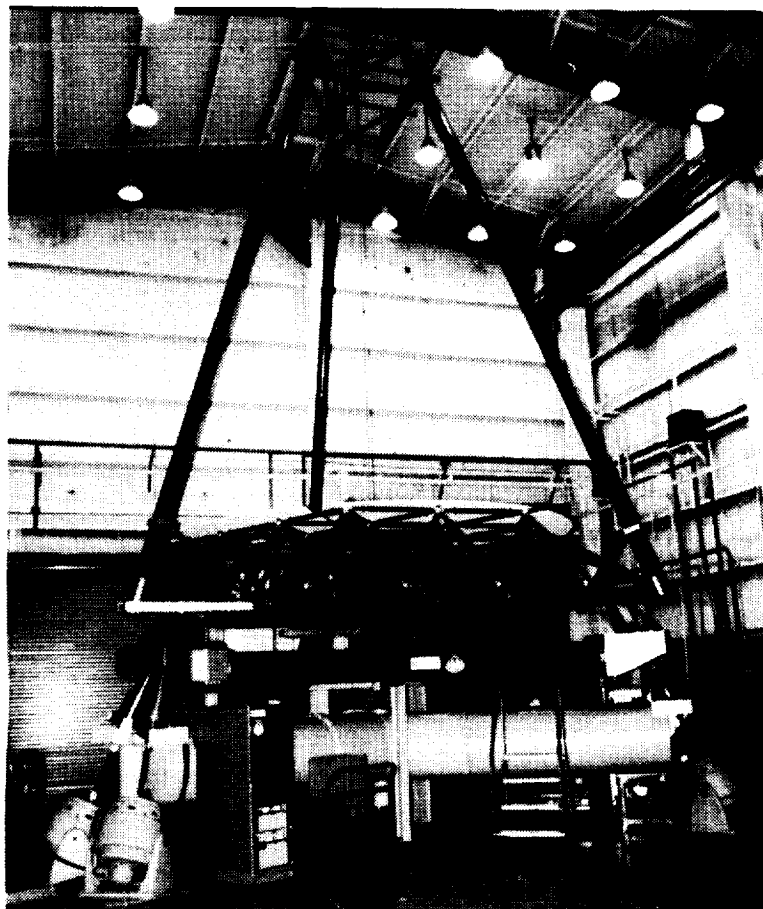


Figure 6. SAVI Prototype Demonstration Setup

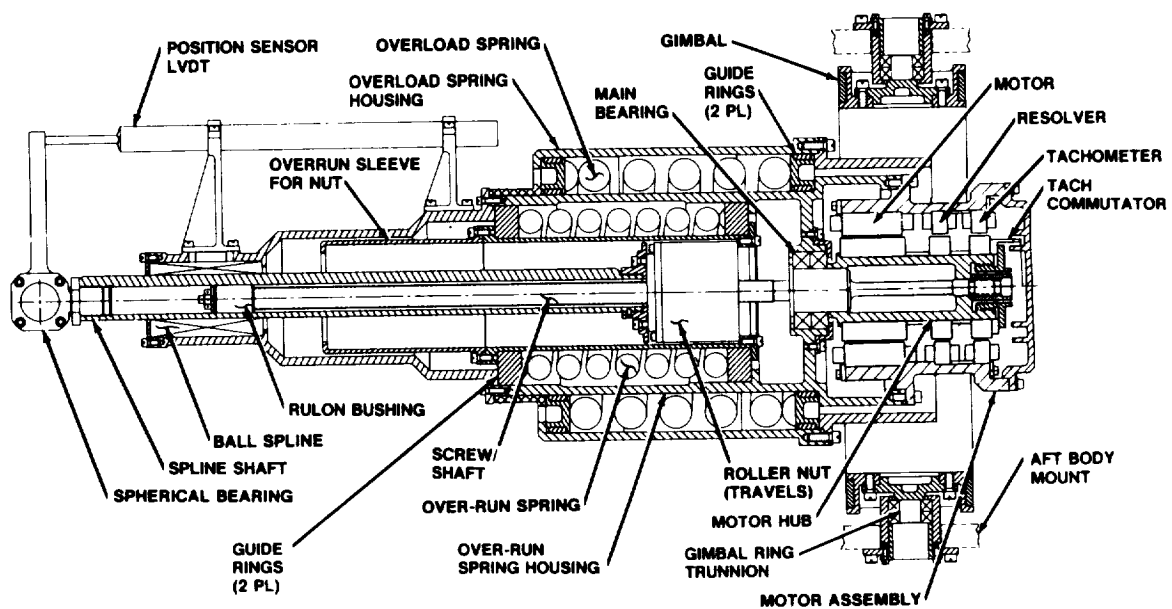


Figure 7. Linear Actuator Assembly - Cross-section

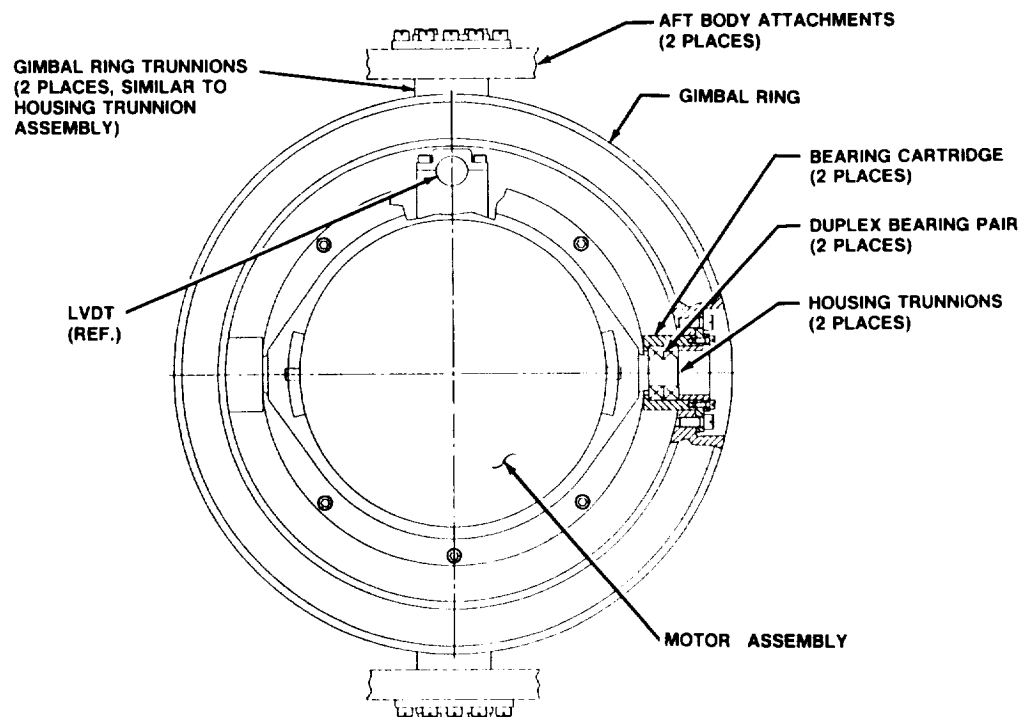


Figure 8. Linear Actuator Assembly - Motor End View

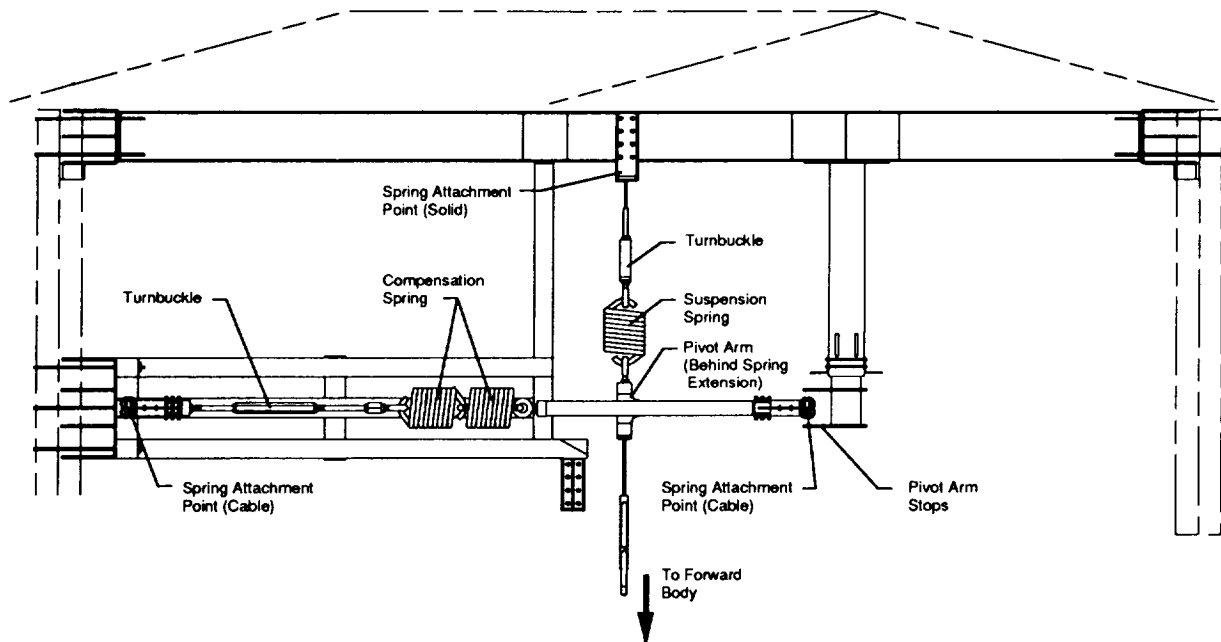


Figure 9. Compound Spring

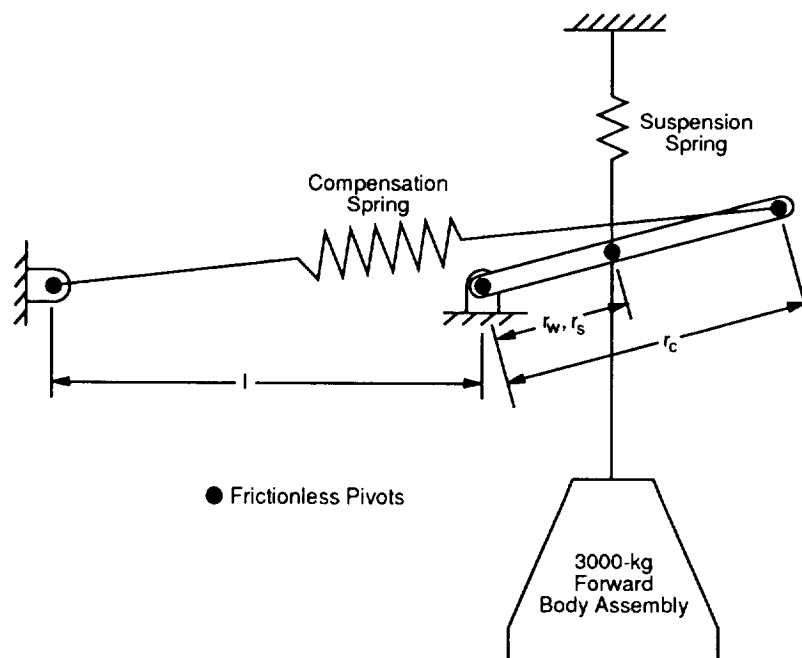


Figure 10. Compound Spring Schematic

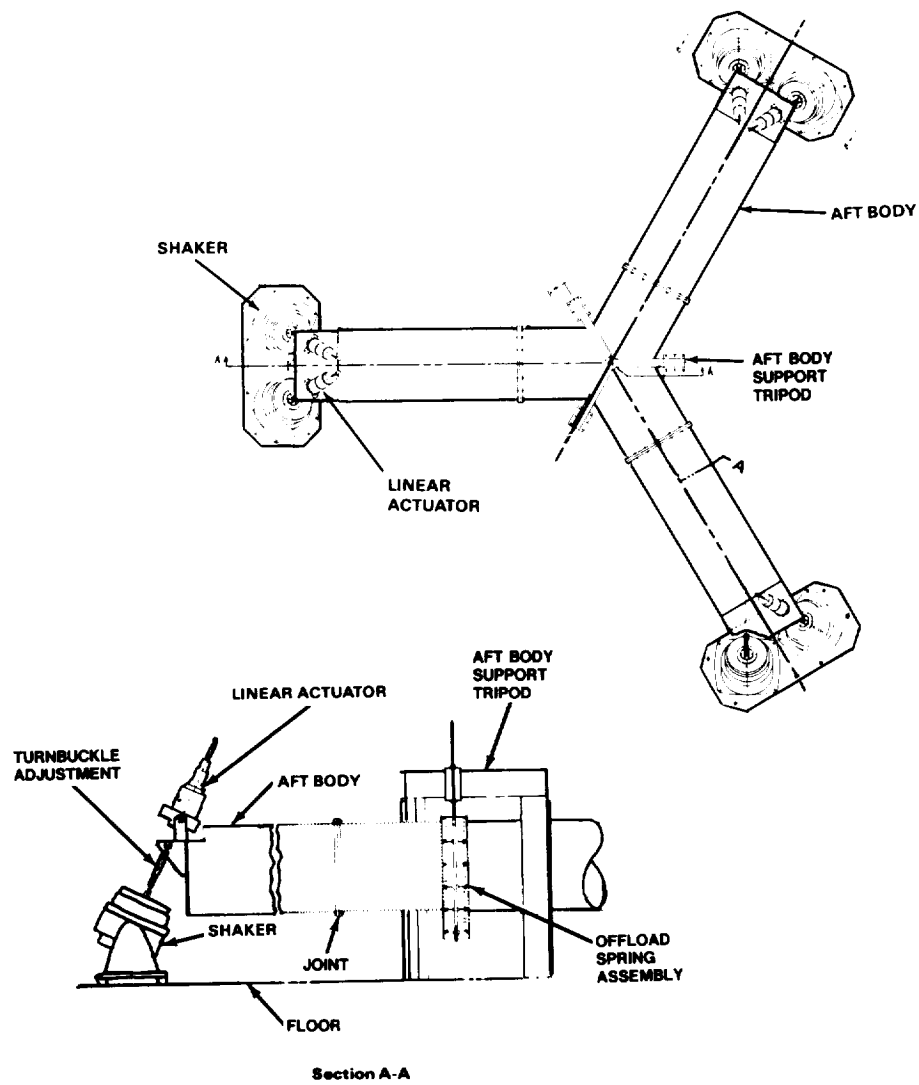


Figure 11. Aft Body

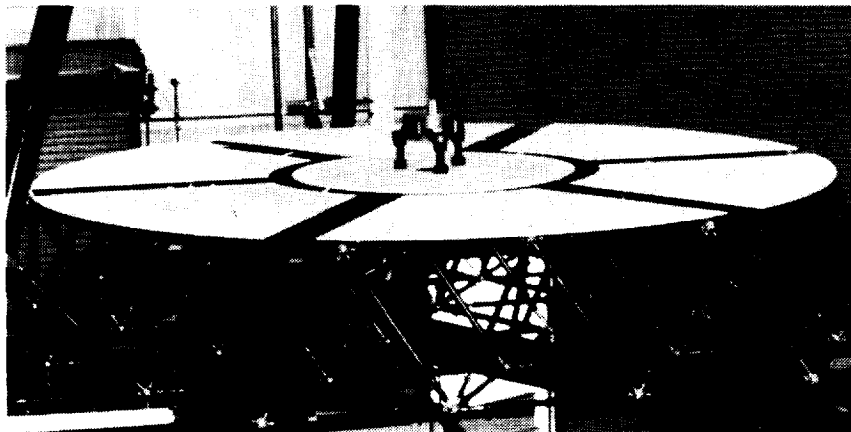


Figure 12. Forward-body Truss Structure

A 23.2:1 Ratio, 300-Watt, 26 N-m Output Torque, Planetary Roller-Gear Robotic Transmission: Design and Evaluation

Wyatt S. Newman*, William J. Anderson†, William Shipitalo‡ and Douglas Rohn‡

Abstract

This paper describes the design philosophy and measurements performed on a new roller-gear transmission prototype for a robotic manipulator. The design incorporates smooth rollers in a planetary configuration integrated with conventional toothed gears. The rollers were designed to handle low torque with low backlash and friction while the complementary gears support higher torques and prevent accumulated creep or slip of the rollers. The introduction of gears with finite numbers of teeth to function in parallel with the rollers imposes severe limits on available designs. Solutions for two-planet row designs are discussed. A two-planet row, four-planet design was conceived, fabricated and tested. Detailed calculations of cluster geometry, gear stresses and gear geometry are given. Measurement data reported here include transmission linearity, static and dynamic friction, inertia, backlash, stiffness, and forward and reverse efficiency. Initial test results are reported describing performance of the transmission in a servomechanism with torque feedback.

I Introduction

Robotic manipulator systems have been proposed for an increasing variety of tasks in space. Like all servomechanism systems, robotic arm actuators require high-performance mechanical power transmissions. Requirements include: high efficiency, linearity, low backlash, low torque ripple and low friction. In [22, 7, 10, 11], experiments in improving the transmission performance of harmonic drives, by far the most common robot transmission, are described. Harmonic drives, however, introduce appreciable compliance, cogging and friction. In [19, 9, 5], the conventional gearing of the Puma manipulator (particularly the base joint) is investigated under feedback. Traditional gearing also suffers from friction and cogging, though, and, while stiffer than harmonic drives, can exhibit the additional problem of backlash. To avoid the problems inherent in mechanical transmissions, some designers have recommended eliminating transmissions altogether

*Assoc. Professor, EEAP Dept, Case Western Reserve University, Cleveland, OH

†NASTEC, Inc, Cleveland, OH

‡Research Engineer, NASA Lewis Research Center, Cleveland, OH

by using direct torque coupling to motor shafts [6, 20, 21, 8, 17]. Resulting designs, though, require exceptionally massive motors and produce low-output torques.

This paper describes the design and evaluation of a new transmission applicable to high-performance robot joints. The drive incorporates a planetary arrangement of smooth rollers that produce torque amplification through rolling contact, backed up by conventional gearing for higher torque capacity. As a result, the drive is unusually smooth, backlash-free, and back-drivable. With these virtues, such a transmission could improve the precision and smoothness of a robot joint. We present details of the transmission design and open-loop transmission measurements. In addition, preliminary closed-loop torque control performance measurements are given. Our measurements indicate that use of roller-gear transmissions could contribute to significantly improved robot performance.

II Transmission Design

In this section, we present the design philosophy and engineering data for the fabrication of roller-gear drives, both generally and in detail for the 23.2:1 robot joint drive.

II.A Roller-/Gear Design Background

An interesting though little-known class of transmissions utilizes traction as the means to transfer torque. Early speed-changing mechanisms, dating back to Leonardo da Vinci, used smooth wheels of unequal size in frictional contact to produce smooth output motion. Traction drives are currently used in a variety of paper and film handling applications, such as copier machines and computer plotting devices. They are also widely used in mechanisms which require a continuously variable transmission ratio. Examples of traction-type linear actuators are ubiquitous, ranging from the wheel/rail contact of locomotives to capstan-drive tape recorders and phonograph turntables.

Limitations of planetary gear systems led to the development of new types of drives. Conventional planetary gear systems use only a single row of planet gears, have limited speed ratios, and the number of load-sharing planets that can be used is inversely related to the speed ratio. As an example, a four-planet drive has a maximum ratio of 6.8 before the planets interfere. A solution to the speed ratio and planet number limitations of single-row planetary systems was devised by A. L. Nasvytis [16]. Nasvytis replaced the single row of equal diameter planets with two or more rows of stepped or dual diameter planets. He devised traction drives which employ pure rollers, and roller-gear drives which employ combinations of rollers and gears. Both concepts extended the range of possible speed ratios to 150 to 1 in a single stage.

The maximum tangential force that can be transmitted through a roller contact is a function of the normal load and the available traction coefficient which, in turn, depends on the materials and lubrication mode. These factors limit drive torque so, in applications where space is at a premium and the torque to be transmitted exceeds the capability of a pure roller drive, alternative designs are required. Roller-gear drives offer

such an alternative. Roller-gear drives incorporate spur gears in parallel with smooth rollers; the result is high stiffness, zero backlash and low torque ripple provided by rollers, with the higher load capacity of conventional gearing. The incorporation of gears imposes design constraints, however. In a pure roller drive, numerous roller configurations can usually be found that produce a given speed ratio. Gears have finite numbers of teeth, and the choice of tooth sizes is limited by available cutters, so choices of roller configurations (which must be matched to the gears) are limited.

In a roller-gear arrangement the rollers provide positioning for the gears, allow the use of multiple planet rows, remove backlash from the torque path, attenuate gear cogging and torque ripple, and support the radial component of gear tooth forces.

Virtues of traction drives relative to competing power transmissions include 1) zero backlash; 2) high torsional stiffness; 3) low breakaway torque; 4) low torque ripple; 5) low velocity ripple; and 6) low noise. An excellent review of the state of the art of traction drives and modern applications is given in [12]; engineering design data can be found in [14, 13]. Two examples of roller-gear drives designed for helicopter transmissions and rotary actuator applications are given in [3, 4].

While traction drives are not new, their use in servomechanisms is rare [15]. The virtues of traction drives, however, should be ideal for robot joint applications. Under contract to NASA Lewis Research Center, two new roller-gear transmissions, appropriately sized for robot joints, were designed and tested [1, 2]. One transmission, with a ratio 29:1 and rated output torque of 820 N m , is appropriate for a robot base joint, and the second transmission, at $R=23.2:1$ and load rating of 26 N m , is appropriate for an elbow or remotized wrist actuator. In this paper, we focus on this latter, smaller drive. For more extensive detail on the design and test data, the reader is referred to [1, 2].

II.B Cluster Geometry

Figure 1 shows the angular relationships of the rollers and gears in a two-planet row roller-gear drive. Let N_r be the number of teeth on each gear, the subscript r denoting the roller designation (a , x_1 , y_1 , x_2 , y_2 or c). Let n be the number of planet gears per row. Then, the geometric relationships that must be satisfied are:

$$\theta = 360/(2n) \quad (1)$$

$$(y_1 + x_2)/\sin(\theta) = (a + x_1)/\sin(\gamma) \quad (2)$$

$$(y_1 + x_2)/\sin(\theta) = Z/\sin(90 + \alpha) \quad (3)$$

$$\alpha + \gamma + \theta = 90 \text{ deg} \quad (4)$$

It can be shown that:

$$Z = (a + x_1)\cos(\theta) + \sqrt{(y_1 + x_2)^2 - (a + x_1)^2 \sin^2(\theta)} \quad (5)$$

The arc of contact between the y_1 and two adjacent x_2 gears is $(180 - 2\alpha)$. This arc must contain an integral number of teeth for assembly. Actually, the arc may contain an

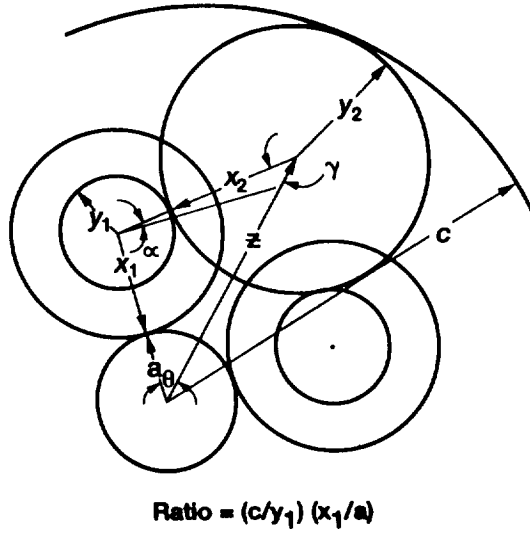


Figure 1: Angular relationships of rollers and gears in a two planet row roller-gear drive

integral number of fractional teeth where the fraction is $1/n$. Fractional tooth designs will, however, require indexing of gears, and then pinning to their rollers, at assembly. For straightforward assembly an integral number of teeth in the arc is much preferable. Then $N_{y1}(180 - 2\alpha)/360$ should be an integral number. Then:

$$N_{y1} = 360K_1/(180 - 2\alpha) \quad (6)$$

where K_1 and N_{y1} are integral numbers.

The arc of contact between the x_2 and two adjacent y_1 gears is 2γ . Similarly, then, $2\gamma N_{x2}/360$ should be an integral number. Then:

$$N_{x2} = 180K_2/\gamma \quad (7)$$

where K_2 and N_{x2} are integral numbers. Further, N_a and N_c must both be divisible by n :

$$N_a/n = K_3 \quad (8)$$

$$N_c/n = K_4 \quad (9)$$

where K_3 and K_4 are integral numbers. Equations 1 through 9 must be satisfied simultaneously to obtain a valid solution for two row roller-gear drives with n planet roller-gears per row. Finally, the numbers of teeth on each meshing gear pair must be in the ratio of their radii:

$$N_a/N_{x1} = a/x_1 \quad (10)$$

$$N_{y1}/N_{x2} = y_1/x_2 \quad (11)$$

$$N_c/N_{x2} = c/y_2 \quad (12)$$

As a final practical design constraint gear pitches should be limited to standard pitches for which cutters are available. This means that in many cases the cutting pitch diameter and the operating pitch diameter will not be quite the same. This implies a lower limit on tooth size or fineness of diametral pitch (as does the torque to be transmitted, of course) because the smaller the tooth the more serious are tooth mismatches. Radii x_2 and y_2 should be as nearly coincident as possible for efficient operation.

Geometries satisfying equations 1 through 9 for two row drives having four, five, six and eight planets per row have been worked out and are given in [1]. A typical design procedure is to first determine a value for a and the diametral pitch of the sun gear that will safely transmit the torque, using standard gear design procedures. Values of y_1 , x_2 , and c are then determined from the geometry of the selected solution appropriate for the number of planets in the design. The drive ratio will be:

$$R = (N_c/N_{y1})(N_{x1}/N_a) \quad (13)$$

The drive size will evolve from the value of c . The design procedure is an iterative one, since drive ratio, torque, and size are key design parameters.

II.C Gears

The four planet solution chosen from [1] was $\alpha = 6.000$ deg and $\gamma = 39.000$ deg. This led to the gear geometries shown on Table 1.

GEAR	a	x_1	y_1	x_2	y_2	c	units
Number of Teeth	24	51	15	60	60	164	dimensionless
Diametral Pitch	43		38		38		teeth/in
Pitch Dia.	0.5581	1.1860	0.3947	1.5789	1.5789	4.3158	in
Pressure angle	20	20	20	20	20	20	deg
Operating center distance	0.870		0.9775		1.3749		in
Contact ratio	1.66		1.66		1.30		dimensionless
Backlash at operating ctr	0.0005/0.0015		0.0007/0.0017		0.001/0.0025		in/in
Operating Pitch Dia.	0.5568	1.1832	0.3910	1.5640	1.5864	4.3361	in
Width	0.25	0.25	0.375	0.343	0.343	0.375	in
Tangential force, F_T	8.89 (39.6)		13.45 (59.85)		26.52 (118)		lbf (N)
Bending stress	4.37 (0.03)		4.87 (0.033)		7.65 (0.053)		ksi (GPa)
Max compressive stress	55.4 (0.38)		6.4 (0.044)		3.18 (0.022)		ksi (GPa)
Material	LaSalle ETD 150 Steel, Rc 32 min.						

Table 1: Four-Planet, 26 N-m, Roller-Gear Transmission Design Data.

Complete gear calculations are given in [2]. The extent of the design constraint can be gauged by examining the second row planet gear, designated as x_2 , in meshing with y_1 , and as y_2 in meshing with c . The cutting pitch diameter of the gear is 1.5789 in.; its operating pitch diameters are 1.5640 in. with y_1 and 1.5864 in. with c . This mismatch in meshing conditions requires careful treatment of tooth design. For this drive, $R = (164/15)(51/24) = 23.23$.

In contrast to the gear constraints imposed by fixed tooth numbers, no such constraint exists with roller designs. The second row planet roller (x_2, y_2 , Table 2) is a dual diameter roller which exactly accommodates the required kinematics.

ROLLER	a	x_1	y_1	x_2	y_2	c	units
Nominal Dia.	0.5568 (14.14)	1.1832 (30.05)	0.3910 (9.93)	1.5642 (39.73)	1.5870 (40.31)	4.3351 (110.6)	in (mm)
Width	0.125 (3.18)		0.130 (3.30)		0.125 (3.18)		in (mm)
Load ¹	29 (129)		158 (703)		243 (1081)		lbf (N)
Max compressive stress	75.6 (0.52)		201 (1.38)		82 (0.57)		ksi (GPa)
Hertzian deformation	3.1×10^{-5} (7.87×10^{-4})		1.32×10^{-4} (3.35×10^{-3})		2.5×10^{-4} (6.35×10^{-3})		in (mm)
Radial bending deflection	-	-	-	-	-	5.5×10^{-4} 1.39×10^{-2}	in mm
Material	M-50 Steel (AMS-6490), Rc 60-62						

Table 2: Four-Planet, 26 N-m, Roller-Gear Transmission Design Data

II.D Rollers

The rollers react the radial forces in the gear tooth contacts so that the gears transmit purely tangential forces and remove backlash by transmitting torque when gear backlash or tooth spacing errors are being taken up. The rollers thus contribute to smoother torque transfer by helping to reduce gear cogging and by making the drive backlash-free.

Roller preloading required to react radial forces in the gears is significantly lower than that required to transmit any appreciable fraction of the drive torque. If standard tooth form gears with a 20 deg pressure angle are used,

$$F_R/F_T = \tan(20 \text{ deg}) \quad (14)$$

$$F_R = 0.364 F_T \quad (15)$$

F_N , the preload normal force between the rollers, must exceed F_R to enable the rollers to react F_R without losing contact.

The torque transmitted by a roller-gear pair will be proportional to F_T . The torque that the rollers can transmit will be the product of F_N and μ , the traction coefficient.

$$(F_T)_{\text{roller}} = \mu F_N \quad (16)$$

A number of iterative calculations of roller torque fraction, normal load and Hertzian contact were made to determine a feasible level of torque that could be carried through the rollers without extending roller widths much beyond 0.125 inches. A torque fraction of 0.20 was settled upon as reasonable. A traction coefficient of 0.06 was assumed for

¹Loads, stresses, deformations and deflections are for 20% torque transfer through the rollers at an assumed traction coefficient of 0.06

traction oil or traction grease lubrication. Rollers were configured as straight cylinders with line contact except for the ring roller, which was crowned for ease of assembly.

Table 2 lists roller geometry data together with loads and deformations for 20% torque transfer through the rollers. Each roller is sized so that its deformed diameter matches that of the gear with which it acts in parallel. The ring rollers are sized so that the roller cluster is compressively loaded when they are assembled over the second-row planet rollers.

II.E Design Features

Figure 2 shows a cross section of the drive, and Figure 3 is a photo of the assembled roller-gear cluster, taken from the output side. Input is to the sun roller-gear with torque transfer through the four first-row planet roller-gears to the four second-row planet roller-gears to the ring roller-gear and thence to the output. Each gear has a dual set of rollers acting in parallel with it. Only the second row planet roller gears are located on bearings. The sun and first-planet roller-gears float and are located by roller-gear action. Splash lubrication is provided by charging the drive with approximately 1 oz. (28 g) of traction fluid.

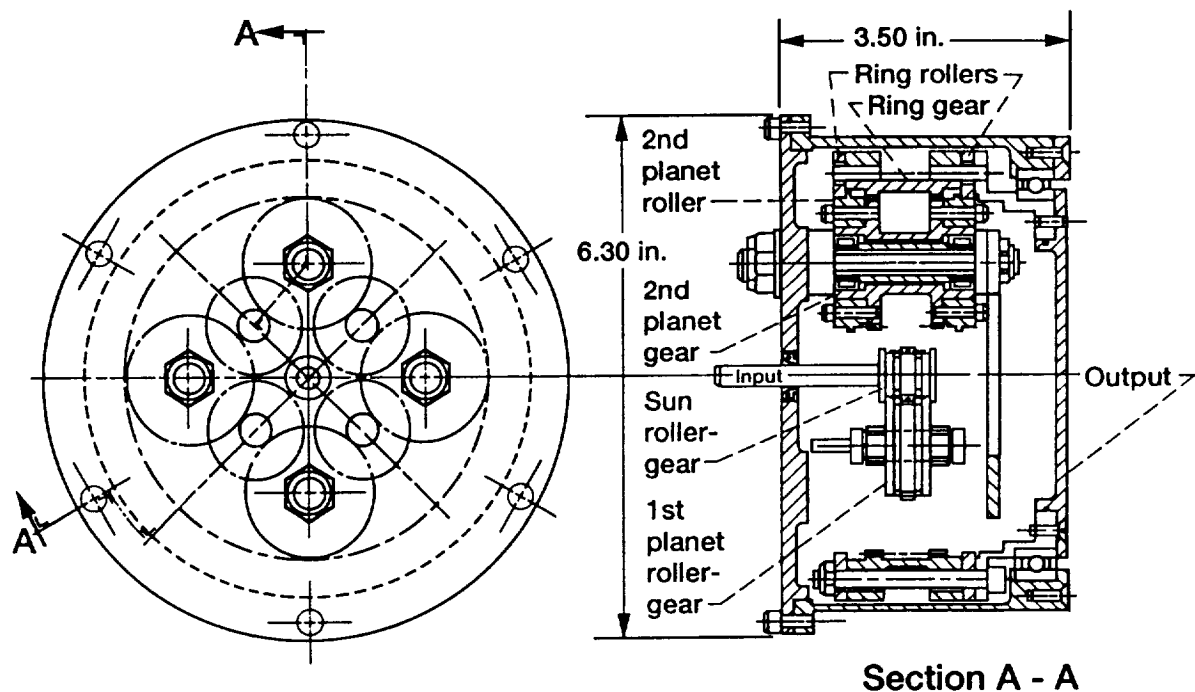


Figure 2: Roller Configuration and Cross Section.



Figure 3: Roller-gear cluster assembly viewed from output side

III Test Data

Measurement data reported here includes transmission linearity, static and dynamic friction, inertia, backlash, stiffness, and forward and reverse efficiency. Initial test results are reported, describing performance of the transmission in a servomechanism with torque feedback.

The experimental procedure, setup, data and analysis are presented for each of the listed measurements. Transmission linearity is measured to within 0.001 degree. Friction is measured using reactionless rotating torque transducers, and is reported as a function of input speed, with the transmission operating both as a speed reducer and as a speed increaser. Inertia is determined through sinusoidal excitation experiments. Backlash was immeasurable, but less than 0.001 degree with respect to the output angle. Stiffness measurements indicate that the transmission behaves as a "stiffening spring," with stiffness increasing with load. Efficiency measurements taken were unusually complete, including driving the transmission as a controlled velocity source and as a controlled torque source, both as a speed reducer and as a speed increaser.

III.A Linearity

Torque ripple is introduced by transmissions through an equivalent variable transmission ratio. For geared drives, the average transmission ratio is fixed by the relative numbers of gear teeth. While this transmission ratio must be a predictable constant, over the

course of a cycle the apparent transmission ratio can vary about this mean due to machining and assembly imperfections. Such variations introduce cyclic accelerations of the transmission input and output, producing an apparent "torque ripple." In fact, the effect is a position ripple, and the resulting torque ripple depends on the dynamics of the transmission as well as the dynamics of the loads attached to both of the transmission ports. Thus, position ripple should be minimized, or, equivalently, transmission linearity should be maximized to minimize resulting torque disturbances. Transmission linearity measurements are reported here.

To measure transmission linearity and backlash, high-resolution optical incremental encoders were coupled to the input and output shafts of each of the transmissions. Corresponding input vs output rotations were recorded.

The shaft sensors used were BEI series 143 optical incremental encoders, which provided 360,000 counts per revolution. Each transmission was tested with an encoder at the input and at the output. A computer program was written to sample the encoder angles and compute a ratio of input to output position increments for each 1 degree (1000 counts) of output (low-speed) rotation. The transmission input was rotated slowly by hand during sampling in one direction, thus avoiding effects of backlash, mechanical dynamics, and sampling rate limitations. The experimental procedure was evaluated using an "ideal" transmission with unity ratio, i.e. a solid shaft. The measured ratio proved to be unity within 0.1%, corresponding to plus or minus one encoder count, indicating an experimental accuracy of 0.1%.

A plot of measured input vs output angle over a full revolution of the transmission output appears perfectly linear, and is thus not shown. Numerical evaluation of the data shows that deviations from perfect linearity peaked at about 1%, though a more representative variation is 0.3%. The same variations apply to the transmission ratio, which was 23.23 on average, but varied incrementally by as much as 1% in the worst case. To observe the small deviations from linear, the slope of input vs output, or the *incremental transmission ratio*, was computed over each one degree of output and plotted vs output angle in Figure 4.

III.B Friction

In addition to low backlash and high linearity, another potential advantage of roller-gear drives is low friction. Drive torques were measured operating both as an unloaded speed reducer and as an unloaded speed increaser.

For all friction measurements, shaft torques were measured using Himmelstein model MCRT 2402T non-contact rotating torque transducers with rated 0.1% linearity. Two meters were used: a 50 in-lb range meter and a 350 in-lb range meter. Himmelstein strain-gauge amplifiers were used to produce analog torque signals. The two meters were calibrated relative to each other in a process which included calibration of the analog-to-digital converters and the strain-gauge amplifiers as well as the torque meters.

For each datapoint of the friction measurements, the input was driven by a dc servomotor with proportional plus integral velocity control. For a complete dataset, the

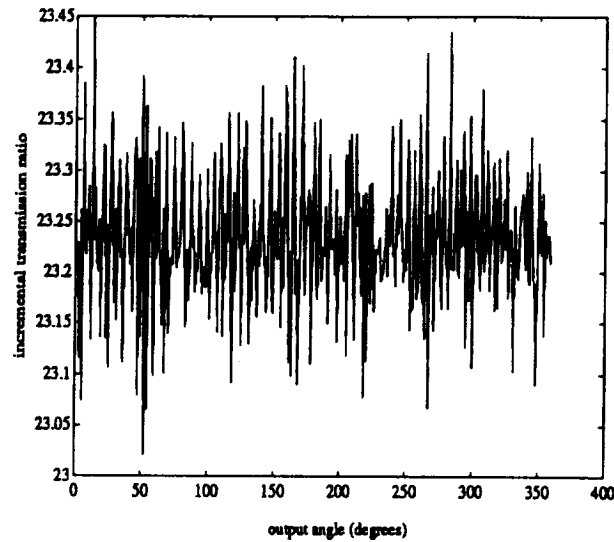


Figure 4: Incremental Transmission Ratio.

motor was commanded to successive velocities in increments of 20 rad/sec from 0 to 180 rad/sec, then back down in increments of -20 rad/sec, through zero to -180 rad/sec, then in increments of 20 rad/sec back to 0. At each new speed, the data was permitted to settle for 10 seconds, then data was sampled continuously over 15 seconds and averaged. In these measurements, the strain-gauge amplifier low-pass filter frequency was set to 1Hz. Filtered analog data was sampled by 12-bit analog-to-digital converters at a rate of 1 kHz, and averaged over 15,000 samples for each datapoint. Resulting datapoints are highlighted, and connecting lines illustrate the history of data collection.

Friction test data of the transmission is shown in Figure 5 and Figure 6 as a reducer and increaser, respectively. The data shows a significant Coulomb friction and a lesser viscous (speed-dependent) friction. Slopes of the friction curve about the origin should not be interpreted as an apparent saturating viscous effect. The slopes here are merely a graphical consequence of connecting discrete datapoints. In fact, the Coulomb friction effect extends down to zero velocity. The reducer friction and increaser friction are roughly the same ratio as the speed ratio, though not precisely so. Friction/speed hysteresis (friction depending on history of velocity excitation) is noticeable. The speed hysteresis may be due to variations in internal loading due to inertial transients when changing between successive steady-state velocities.

III.C Inertia

To measure the transmission's inertia, its low-speed shaft was coupled to a dc servomotor through a 50 in-lbf reactionless torquemeter. The servomotor was controlled with acceleration feedforward and proportional-plus-derivative feedback to produce a smooth sinusoidal motion with an amplitude of 1.0 radians at a frequency of 2.5Hz. Over each

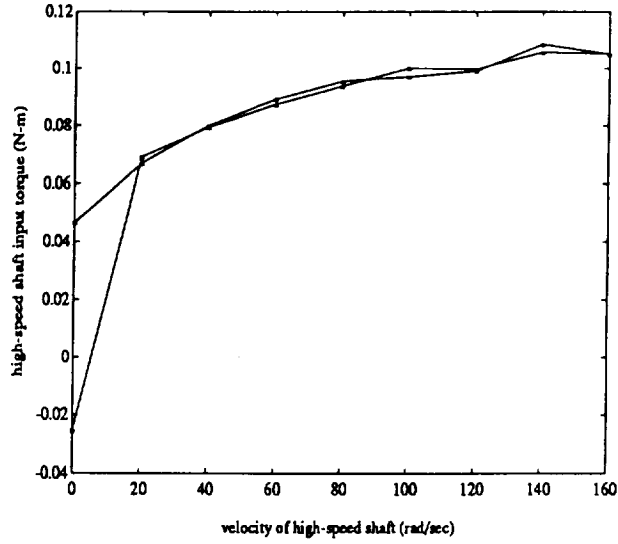


Figure 5: Unloaded Input Friction as a Speed Reducer.

sinusoid, the torque meter and the drive angle were sampled at 1kHz. One hundred of these sinusoids were sampled synchronously and averaged together to reduce noise.

The torque meter was low-pass filtered in analog at 100Hz before sampling. To correct the measurements for inertia of the couplings and the inertia of the torque meter itself, the same data acquisition routine was run on the system with the transmission removed. Inertia of the measurement system was found to be less than 2% of the transmission's output inertia.

The measured data was curve-fit to pure sinusoids, resulting in a torque signal of 4.4 N-m amplitude, 2.5Hz, leading the position signal by 140 degrees. If the torque signal were due entirely to inertial effects, then it would have led the position signal by 180 degrees. The actual phase shift implies that the inertial effect has a magnitude of 3.35 N-m, while an apparent viscous effect has a magnitude of 2.85 N-m in-phase with the velocity. The chosen excitation produced an angular acceleration of 247 rad/sec^2 . Thus, the inertial torque of 3.35N-m implies an apparent transmission output inertia of $0.0135 \text{ Kg} - m^2$.

III.D Backlash

An unusual feature of roller-gear drives is that, ideally, they exhibit no backlash. Since the rollers always maintain rolling contact, there should be no deadzone between input and output angles.

Backlash measurements used the same experimental setup as the transmission ratio tests. High-resolution encoders were coupled to both the input and the output of each transmission. The input shaft was rotated by hand forward, reverse, forward, and reverse again through an angle corresponding to 0.5 degree of output rotation. The

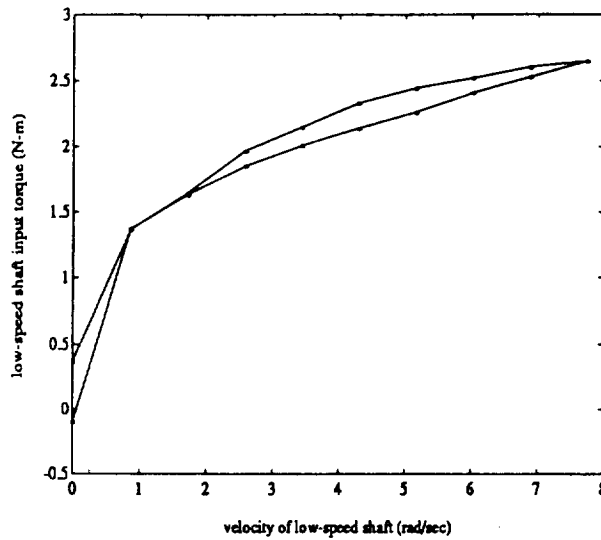


Figure 6: Unloaded Input Friction as a Speed Increaser.

encoders were sampled at a high rate, and input and output angles were recorded for each 0.050 degree of output rotation. Using the prescribed cyclic input, backlash in the transmissions would appear as a hysteresis in the input vs output angle plots. The measured datapoints retraced themselves almost identically (and, thus, the straight-line dataplot is not shown). Any possible hysteresis was smaller than the measurement accuracy of 0.001 degree of output angle. Thus, while “zero” backlash has not been proven, backlash was at least unobservable to within 0.001 degree of output angle.

III.E Stiffness

To measure the input stiffness of the transmission, the high-torque shaft was held stationary (secured to ground) while the input was torqued through the 50 in-lbf reactionless torque meter. Torques were applied manually, held steady by observing the torque-meter output. The input torque and twist angle were sampled in the steady state (static torque balance) at 1kHz over 15 seconds, and the mean values were recorded. Eleven datapoints were recorded using input torque values of 0, 0.5 and 1.0 N-m, imposed alternately. Stiffness of the measuring system was found to be 10 times higher than the input stiffness of the transmission, thus validating the test.

The transmission input behaved as a nonlinear, stiffening spring. An average stiffness up to 50% of maximum rated torque was approximately 30 N-m/rad. A representative (incremental) input stiffness for loadings from 50% to 100% of the rated torque was 40 N-m/rad.

III.F Efficiency

Power transfer efficiency was measured in four regimes: 1) controlled velocity source on the high-speed shaft, controlled torque source on the low-speed shaft, power flow from high speed to low speed (conventional measurement, speed-reducer operation); 2) controlled velocity source on the low-speed shaft, controlled torque source on the high-speed shaft, power flow from low speed to high speed (speed-increaser operation); 3) controlled velocity source on the high-speed shaft, controlled torque source on the low-speed shaft, power flow from high speed to low speed (torque increaser operation); and 4) controlled velocity source on the high-speed shaft, torque source on the low-speed shaft, power flow from low speed to high speed (torque reducer operation). Efficiencies were measured up to the rated torque, though only up to 60% of the rated speed due to equipment limitations. Measurements cases (3) and (4) were consistent with cases (1) and (2), and are thus not reported here.

To measure efficiencies, two transmissions were coupled together at their high-torque shafts through a rotating, 350 in-lb range torque meter. The high-speed shafts of each transmission were driven by dc servomotors. The transmission under test was coupled to its drive motor through a rotating, 50 in-lb range torque meter. All devices were coupled using Thomas miniature flexible disc couplings, which provide relatively high torsional stiffness along the shaft axis and compliance along all five remaining degrees of freedom.

For measurement cases (1) and (2), the high-speed shaft of the transmission under test was controlled to run at specified speeds from -180 to 180 rad/sec. As in the friction experiments, each datapoint was obtained by controlling the drive speed through a proportional-plus-integral speed controller, waiting 10 seconds for settling after each new speed command, and sampling torque and speed data for 15 seconds during steady-state conditions. Both torque meters were low-pass filtered in analog at 1Hz and digitally sampled at 1kHz to obtain a 15,000-point average for each datapoint.

To produce a desired load torque, the second transmission and servomotor were controlled in a proportional-plus-integral torque feedback loop, based on the measured output torque of the transmission under test. The controlled torque source achieved accurate steady-state torque loads at all input speeds.

Each dataset was obtained at a fixed "output" (low-speed) torque while the "input" (high-speed) velocity was incremented through a range of values. As in the friction experiments, the data was collected starting from rest, incrementing in steps of 20 rad/sec up to 180 rad/sec, then retracing the positive-velocity measurements in speed decrements of 20 rad/sec, then continuing through zero down to -180 rad/sec, and finally retracing the negative velocity measurements in increments of 20 rad/sec back to rest. Individual datapoints are highlighted, showing repeatability and/or hysteresis in the measurements.

Load torques were held constant in each dataset at six values in equal increments from 0 to 25 N-m. Note that a positive "output load" in combination with a negative "input velocity" corresponds to power flow in the "reverse" direction. That is, at negative velocities the torque source at the low-speed shaft acts as a power source, and the velocity controller at the high-speed side acts as a controlled brake which sinks power. In this

regime, the transmission may be thought of as acting as a speed increaser rather than a speed reducer. This type of measurement is somewhat unusual, since transmissions are seldom measured with active torque sources. Additional measurements, cases (3) and (4), were performed to validate the procedure.

Efficiency data for velocity control of the high-speed shaft is shown in Figure 7. This plot includes 222 datapoints, each of which consists of a 15,000-sample average under steady-state conditions. Each datapoint is marked, and lines are drawn between successive samples, illustrating the history of the data collection and possible hysteresis. The efficiency plot does not include the zero-velocity datapoints, as efficiency is undefined at zero speed. The efficiency is computed as the ratio of power extracted from the transmission to the power delivered to the transmission. For positive velocities, the efficiency is the low-speed power over the high-speed power, while for negative velocities the efficiency is the high-speed power over the low-speed power. The slope of the efficiency curves through zero velocity is a graphical consequence of connecting successive datapoints, and it should not be interpreted as a valid efficiency derivative near zero velocity.

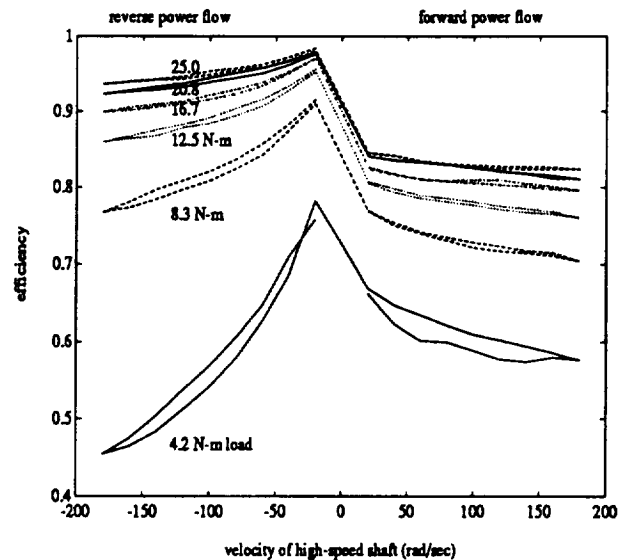


Figure 7: Efficiency: High-Speed Velocity Source and Low-Speed Torque Source.

An unusual result of the measurements was that the “back-driven” operation modes of torque reducer and speed increaser resulted in higher efficiencies than the normal “forward” operation modes (speed reducer, torque increaser). Peak efficiency was 98.5%, occurring at low speed, maximum torque, with power flow in the “reverse” direction (from low-speed shaft to high-speed shaft). To confirm that this phenomenon was not an artifact of the measurement process, speed and torque sources were reversed (measurement cases (3) and (4)), and the same effect was observed. Power transfer was more efficient when power flowed from the low-speed port to the high-speed port, and efficiency was highest at the highest torque loads and the lowest speeds.

III.G Performance as a Servomechanism

High stiffness, zero backlash, low friction and high linearity (equivalently, low torque ripple) are all desirable properties of mechanisms to be used in feedback systems. An “acid test” of a servomechanism applicable to robot joints is a measure of the mechanism’s performance within a torque-feedback loop. The transmission was tested in this mode, which, for a single degree of freedom, is equivalent to an active tension-control device.

Two dc servomotors were used: one as the drive input, and another as a controllable load. The load was connected to the transmission output through a reactionless torque meter, and the measured torque was fed back to the transmission drive motor to regulate the load torque. The active load, simulating an independent energetic environment interaction, was driven independently as a controlled velocity source.

The external (environment) velocity was initially controlled to 1 rad/sec, then increased smoothly but rapidly to 3 rad/sec. The transmission was controlled separately to produce a 1.13 $N\,m$ output torque. The velocity imposition and the torque response of the torque-controlled transmission is shown in Fig 8. The torque response includes an inevitable rapid torque rise due to transmission inertial effects, but stabilizes quickly to the desired torque at the conclusion of the imposed acceleration transient. The response shows that the transmission can exert a desired velocity-independent torque under closed-loop control with seemingly negligible frictional influence. In separate tests, the transmission was evaluated within a force-control loop under conditions of impact with a rigid obstruction. The transmission exhibited good responsiveness while maintaining contact stability. Such behavior is essential for designing robots with programmable compliance or high-bandwidth force reflection, and the performance reported here is unusually good for mechanical drives. Further detail on the use of this drive within feedback loops can be found in [18].

IV Summary and Conclusion

A 23.2:1 ratio, 300-watt, 26Nm output torque, two-planet row, four-planet roller-gear transmission is briefly reviewed. Detail calculations of cluster geometry, gear stresses, and gear geometry are given. Measurement data reported include transmission linearity, static and dynamic friction, inertia, backlash, stiffness, and forward and reverse efficiency. Initial tests of the transmission in a torque feedback loop are reported.

The new drive was found to have high linearity, relatively low friction, high stiffness and negligible backlash. Efficiency peaked at 98.5% under conditions of maximum torque, minimum speed, operating as a speed increaser. Virtues of the drive should be particularly valuable when used within servo feedback loops. The drive was evaluated as an actively controlled torque source, a particularly demanding application of importance to high-performance robots, and it performed unusually well. Based on measured performance, this drive should find valuable applications in servomechanisms.

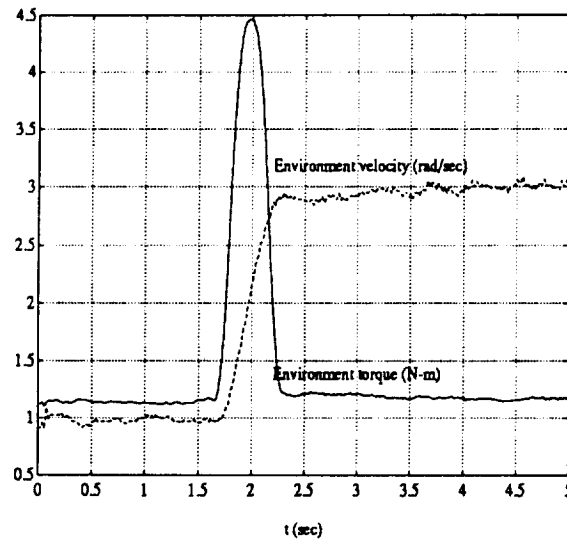


Figure 8: Operation of the Transmission in Closed-Loop Tension Control.

References

- [1] William J. Anderson. Roller-gear drives for robotic manipulators. Final Report for NASA Lewis Research Center, Contract NAS 3-25282, Aug 1988.
- [2] William J. Anderson and W. Shipitalo. Roller-gear drives for robotic manipulators: Design, fabrication and test., Final Report for NASA Lewis Research Center, Contract NAS 3-25803, Sept. 1991.
- [3] Anon. Endurance test of an-1 roller gear drive, US AAVLABS Technical Report 65-31 (TRW Engineering Report 6371), U.S. Army Aviation Material Laboratories, Fort Eustis, VA, Contract DA 44-177-AMC-30 (T), Aug 1965.
- [4] Anon. High torque cmg rotary actuator, Report to NASA Goddard Space Flight Center by General Electric Co, Aircraft Equipment Division, Binghamton, NY, Contract No. NAS 5-20298, June 1972.
- [5] Brian Armstrong. Friction: Experimental determination, modelling and compensation, In *Proceedings of International Conference on Robotics and Automation*, pages 1422-1427, IEEE, 1988.
- [6] H. Asada, K. Youcef-Toumi, and R. Ramirez, Design of the m.i.t. direct-drive arm, In *International Symposium on Design and Synthesis*, Tokyo, Japan, July 1984. Japan Society of Precision Engineering.
- [7] J. D. Chapel and R. Su, Attaining impedance control objectives using h-infinity design methods, In *Proceedings of the IEEE International Conference on Robotics and Automation*, pages 1482-1487, Sacramento, CA, April 1991. IEEE.
- [8] R. Curran and G. Mayer, The architecture of adeptone direct-drive robot, In *Proceedings of the American Control Conference*, pages 716-721, Boston, MA, July 19-21, 1985.
- [9] P. Elosegui, R. W. Daniel, and P. M. Sharkey, Joint servoing for robust manipulator force control, In *Proceedings of the IEEE International Conference on Robotics and Automation*, pages 246-251, Cincinnati, OH, May 1990. IEEE.

- [10] M. H. Hashimoto, Yoshihide Kiyosawa, Hideki Hirabayashi, and Richard P. Paul, A joint torque sensing technique for robots with harmonic drives, In *Proceedings of the IEEE International Conference on Robotics and Automation*, pages 1034-1039, Sacramento, CA, April 1991. IEEE.
- [11] Minoru Hashimoto, Robot motion control based on joint torque sensing, In *Proceedings of the IEEE International Conference on Robotics and Automation*, pages 256-261, Scottsdale, AZ, May 1989. IEEE.
- [12] F. W. Heilich and E.E. Shube, *Traction Drives: Selection and Application*, Marcel Dekker, NY, NY, 1983.
- [13] S. H. Loewenthal, D. A. Rohn, and N. E. Anderson, Advances in traction drive technology, *SAE Transactions*, 92, 1983. section 3.
- [14] S. H. Loewenthal and E.V. Zaretsky, *Mechanical Design and Systems Handbook*, chapter Section 34, Traction Drives, McGraw Hill, New York, 1985.
- [15] Stuart H. Loewenthal, Douglas A. Rohn, and Bruce M. Steinetz, Application of traction drives as servo mechanisms, In *Proceedings, 19th Aerospace Mechanisms Symposium*, pages CP-2371, Ames Research Ctr, Moffet Field, CA, May 1-3, 1985.
- [16] A. L. Nasvytis, Multiroller planetary friction drives, SAE paper 660763, Oct 1966.
- [17] Wyatt S. Newman and Jay J. Patel, Experiments in torque control of the adeptone robot, In *Proceedings of the IEEE International Conference on Robotics and Automation*, pages 1867-1872, Sacramento, CA, April, 1991. IEEE.
- [18] Wyatt S. Newman, Yuandao Zhang, William J. Anderson, and William Shipitalo, Experimental evaluation of a new traction-drive robotic transmission, Technical Report TR-91-156, Center for Automation and Intelligent Systems Research, Case Western Reserve University, Cleveland, Ohio, Sept. 1991.
- [19] Lawrence Pfeffer, Oussama Khatib, and John Hake, Joint torque sensory feedback in the control of a puma manipulator, *IEEE Journal of Robotics and Automation*, 5(4):418-425, Aug 1989.
- [20] D. Schmitz, P. K. Khosla, and T. Kanade, Development of cmu direct-drive arm ii, In *Proceedings of the 15th International Symposium on Industrial Robotics*, Tokyo, Japan, September 11-13, 1985.
- [21] R. Welburn, Ultra high torque motor system for direct drive robotics, In *Robots 8 Conference Proceedings*, pages 19.63-19.71, 1984.
- [22] Chi Haur Wu and Richard P. C. Paul, Manipulator compliance based on joint torque servo, In *IEEE Conference on Decision and Control*, pages 88-94, Albuquerque, New Mexico, December 1980. Also in *Int J. Rob Res*, Vol 4, No 3, Fall 1985.

Space Station *Freedom* Common Berthing Mechanism

Erik Illi*

ABSTRACT

The Common Berthing Mechanism (CBM) is a generic device used to join the pressurized elements of the Space Station *Freedom* (SSF) utilizing the Space Shuttle Orbiter Remote Manipulator System (SRMS) or the Space Station Remote Manipulator System (SSRMS). The two berthing halves, the active and the passive, maintain a pressurized atmosphere to allow astronaut passage, as well as to provide a structural linkage between elements. The generic design of the CBM allows any Passive Berthing Mechanism to berth with any Active Berthing Mechanism, permitting a variety of pressurized module pattern to be built.

INTRODUCTION

The Space Station *Freedom* (Figure 1) is composed of three main sections--the solar arrays which provide power to the station, the truss which supports and connects all Space Station hardware, and the pressurized elements which provide a hospitable environment for the astronauts to live in and work in.

The mass and volume restrictions imposed by the Space Shuttle Orbiter requires the pressurized elements of the Space Station to be segmented into interconnecting elements. The design scheme of the pressurized elements divided them into two types--the common modules and the nodes (Figure 2). The common module, long and cylindrical in shape, is the module type used to house life support, habitation, and laboratory equipment. The common module has a CBM at each of the two axial ports of the module. The node, shorter than the common module, is used to connect the common modules into an efficient pattern. For this, the nodes are equipped with a CBM at each of their six ports--two on the axial ends and four around the radius, 90 degrees apart. The primary design requirements for a mechanism to join these modules on-orbit are as follows:

- Join the pressurized modules;
- Provide pressurized passage for astronauts and utilities;
- Withstand launch, pressure, and on-orbit loads;
- Meet Shuttle payload volume and weight requirements when connected to the pressurized elements;

* The Boeing Company, Huntsville, AL

- Meet maximum atmospheric leak-rate requirements;
- Survive the low-Earth orbit environment for the 30-year life of the Space Station with the necessary factors of safety.

It was desired and baselined to berth the pressurized modules (bringing the elements together by means of a third party--i.e., robotic arm) rather than to dock them (bringing together without a third party).

Berthing structural/mechanical components perform four necessary functions:

- align berthing halves in proper orientation
- capture and berth the two elements
- maintain a structural connection
- maintain pressurized atmosphere between elements.

Among the preliminary concepts was an androgynous berthing mechanism which, as its name implies, allows any berthing mechanism to mate with any other berthing mechanism. It was determined that an androgynous mechanism would require unnecessary complexity, weight, development time, and expense when compared to a male/female-type configuration. As of mid-November, 1991, the current design consists of elastomeric seals, capture latches, alignment guides, powered bolts, and shear tie assemblies mounted on two structural rings. These assemblies are divided into two CBM halves--the Active Berthing Mechanism (ABM) and the Passive Berthing Mechanism (PBM) (Figures 3 and 4). All active, power-consuming components are located on the ABM to eliminate the requirement for power to be supplied to both modules during berthing operations. The following is a description of each component and the reason for its usage in the CBM.

ACTIVE BERTHING MECHANISM

Structural Ring

The purpose of the structural ring (Figure 3) of the Active Berthing Mechanism is fourfold--to maintain a pressurized passageway between elements, to provide a seal surface when mated to the Passive Berthing Mechanism, to provide structural support and a load path between pressurized elements, and to provide a mounting interface for berthing hardware.

The structural ring of the Active Berthing Mechanism is a machined forging of 2219-T852 aluminum having an outside diameter of approximately 2.0 meters (80 inches) and inside diameter of approximately 1.8 meters (71 inches) with a depth of .19 meter (7.5 inches). The ring is attached to the pressurized element by 64 bolts and sealed by a weld to ensure pressure integrity. The ring supports the Alignment Guides, Powered Bolts, Capture Latches, and Differential Pressure Transducers.

The structural ring was originally designed to carry just the launch, pressure, and on-orbit loads, but was later strengthened to support the deflection loads created by the pressurization of the radial port on the nodes (Figure 2). The ring design accommodates the mounting of berthing hardware, such as the capture latch while not extending into the Orbiter Payload Bay envelope on the Node radial port. The original ring diameter was increased from 1.68 meters (66 inches) to permit the routing of utility connections internal to the CBM.

Alignment Guide Assembly

The Alignment Guide Assembly (Figures 5 and 6) ensures proper orientation of the two berthing halves for successful component mating. The alignment guide blade on the ABM slides between two alignment guide blades on the PBM to properly orient the berthing halves (Figure 7). The Alignment Guide Assembly is made of anodized 2219-T87 aluminum with a low-friction surface coating. The guides are designed to withstand impact loads which may occur due to SRMS runaway conditions.

A 1989 study of alignment mechanisms included both external and internal alignment guides, a telescoping berthing arm, conical guides, and a mortar-and-pestle guide (similar to a probe and drogue). The internal alignment guide arrangement was chosen because it was located internal to the berthing ring and it has performed well in preliminary testing. Tests conducted at the Neutral Buoyancy Facility at Marshall Space Flight Center evaluating the accessibility and maintainability of external berthing mechanism components revealed that EVA maintenance was difficult, if not impossible, thus, driving the CBM design to internal components. In addition, internal alignment guides could be launched deployed, reducing Extra-Vehicular Activity (EVA) time needed for berthing.

The alignment guide concept dates back to the Apollo-Soyuz program where a set of very large plate petals were used to align the docking system. Fortunately, the SRMS coupled with an adequate camera/target system is capable of more accurate positioning thus, reducing the necessary size of the alignment guides, saving much weight and volume as denoted in the design.

Capture Latch Assembly

The Capture Latch Assembly (Figures 8 and 9) is composed of four identical mechanisms which extend, capture, bring the berthing flanges together, and maintain position for the Powered Bolts to engage. The capture envelope of the capture latch compensates for misalignments between berthing flanges due to SRMS and visual errors without jeopardizing the capture sequence. Only three latches are necessary for capture, therefore allowing one failure without hindering berthing operations. The capture latch, which is fastened to the active berthing ring, is composed of a four-bar linkage driven by a motor, with an internal clutch, which is controlled internal to the pressurized element. The latch has been designed to provide sufficient force to backdrive the SRMS (overcoming the inertial of the SRMS drive motors) in limp mode . The linkages are made of 7050 or 7075 aluminum while the other components are mostly 15-5 stainless steel.

Several proposals were made for a device to bring the two berthing flanges together. The three most favorable are a capture clamp (a pincer-like device which grapples a trunnion), a gear-driven capture latch and a linkage-driven capture latch. Although the capture clamp did not need alignment guides and was similar to devices presently used in the aerospace industry, the linkage-driven capture latch was chosen based on its superior reliability and larger capture envelope. It also provides a more controlled capture (the capture latch maintains contact with the passive flange while the capture clamp allowed the trunnion on the passive flange to bounce around) and is lighter, including the alignment guides.

Powered Bolt Assembly

The Powered Bolt Assembly (Figure 10) creates the structural tie and provides the necessary compressive force to the elastomeric seal to ensure pressure integrity. The bolts preload the joint to at least 42,275 newtons (9500 pounds) per bolt after bringing the berthing flanges into metal-to-metal contact. The bolt's guide threads move the bolt into the nut allowing them to engage without any applied load. Then, the guide threads disengage allowing the bolt to compress the flanges together (Figure 11). The 5/8-inch-diameter bolt with .625-18 UNJF rolled thread is made of Inconel 718 (AMS 5664) and coated with a dry film lubricant to help prevent galling during the nearly 400 engage/disengage cycles required. The bolt ends are tapered to help align and engage them with the Powered Bolt Nut (discussed in the PBM section). The housing is made of high-strength Nitronic 60 (UNS S21800) while the drive train is made of Custom 455 (S45500 H950). The Powered Bolt Actuator can provide up to 101.7 newton-meters (900 inch-pounds) torque to drive the bolt to the required preload. The required torque was originally only 19.78 newton-meters (175 inch-pounds), but it was found through analysis that the radial port on the Space Station Nodes, when pressurized, will deflect the berthing flange. The additional torque was necessary to overcome the flange deflections to bring the flanges into metal-to-metal contact before preloading the bolted connection.

A V-clamp was also evaluated for providing the structural connection between the berthing flanges. The V-clamp consisted of a formed metal band which tightened via drive bolts oriented tangentially around the outside of the flanges. The main reason the V-clamp was not chosen was its lack of redundancy; if one of the drive bolts failed, the clamp failed. The Powered Bolt Assembly was designed so that one of the bolts could fail without jeopardizing structural integrity. In addition, the Powered Bolt was chosen because it did not require EVA to maintain (all components are located internal to the CBM), whereas the V-clamp had most of its components external to the berthing flange. Furthermore, the V-clamp had difficulty in creating a predictable uniform clamping force.

Differential Pressure Transducers

Due to the criticality of maintaining pressure within the berthing vestibule area, differential pressure transducers along with a monitoring system are necessary to periodically check the seal performance (Figure 12). In each ABM, two differential pressure

transducers are connected to a firmware controller that alerts the crew should the seals fail prematurely.

Pressure transducers were chosen over other methods mainly because they do not require extensive crew time to check the seals. The suitability of Pressure Decay, Flow Meter, and Trace Gas Analysis techniques were assessed in addition to Differential Pressure Transducers. The Pressure Decay and Flow Meter methods base their operation on a pressurized vessel of known volume. It is impractical to check each seal independently by monitoring the pressure in or the flow rate out of the vessel when connected to a leak check port. Since each seal must be checked on a regular basis, it is obvious that Pressure Decay and Flow Meter Methods would require a great deal of crew time as well as equipment. The Trace Gas Analysis technique involves introducing an inert gas into the pressurized volume and detecting leaks outside of the seal using a probe to check for the inert gas.. The necessary EVA to probe outside each seal location is not practical from both cost and EVA time standpoints.

Shear Tie Assembly

The purpose of the Shear Tie Assembly is to remove the high torsional shear load on the Powered Bolts created by the Orbiter docking to one of the cantilevered modules on the Space Station. The shear tie is made of 6061 aluminum and is, obviously, manufactured to tighter tolerances than the bolt. The tighter tolerances will inadvertently make the shear ties act as alignment guides of sorts.

Other shear-carrying devices were evaluated including an eccentric-shaped deployed pin, a pair of pins with mating slots, and a device similar to the current design, but using interlocking teeth instead of the single protrusion. The shear tie was chosen over these because it was simple, did not depend on flanges being in flat contact, was more easily aligned, and was less likely to damage the berthing flanges.

PASSIVE BERTHING MECHANISM

Structural Ring

The structural ring (Figure 4) of the Passive Berthing Mechanism, which is machined from a 2219 aluminum forging, has the same outside diameter of approximately 2.0 meters (80 inches) and inside diameter of 1.8 meters (71 inches) as the ABM structural ring, but is nearly twice as deep at .343 meter (13.5 inches). In order to meet clearance requirements, the additional depth of the structural ring is necessary to make up for the depth of the Active Berthing Mechanism, which is constrained by the Orbiter Payload Bay envelope, when mounted to a Node radial port. The structural ring is attached to the pressurized element by 64 bolts and sealed with a weld to maintain pressure within the berthing vestibule. The ring supports the Capture Latch Fittings, Powered Bolt Nuts, Alignment Guides, Shear Tie, and retains the berthing seals.

Originally, some of the passive berthing mechanisms on the Space Station were to include flexible bellows with actuators. Their purpose was to compensate for manufacturing and pressurization tolerance build-up around a module loop to allow it to be closed. After much investigation and testing, it was found that such a bellows system could not reliably be produced to meet all the requirements necessary to ensure mission success. Currently, the plan is to use a single compliance element to close a module loop if such a configuration is desired. The single compliance element will have fewer restrictions on it (e.g. weight, operational envelopes) allowing for a reliable mechanism to be produced using current technology without impacting the CBM design for the earlier module flights.

Capture Latch Fitting

The Capture Latch Fitting (Figure 8 and 9) provides the hook on the PBM to receive the Capture Arm. The fitting, made of 7075 aluminum, is bolted on the passive ring in four places. The reason for the use of the capture latch assembly is explained in the Active Berthing Mechanism section.

Alignment Guides

The eight Alignment Guides on the PBM (Figure 6), meshing with the four on the ABM, ensure proper orientation of the berthing halves relative to each other allowing the Powered Bolts to engage. Originally, all alignment guides were to be identical, but in an effort to save weight, the blades on the passive side were changed, retaining only the necessary surfaces. The design of the two alignment guides on the PBM are identical; they are simply mirror images. Again, the reasoning behind the use of these alignment guides is explained in the Active Berthing Mechanism section.

Powered Bolt Nuts

The Powered Bolt Nut (Figures 10 and 11) is designed to float to compensate for manufacturing, pressure and temperature distortions so the Powered Bolt can still engage with misalignments between the mating berthing flanges. The nut is made of Nitronic 60 (UNS S21800) and sits on a spherical washer to accommodate the floating movements. A spring is mounted behind the nut to allow it to move backward in case the first thread was not grabbed. It should be noted that only a minimal temperature gradient can be tolerated between the berthing flanges during berthing operations because of the Class 3 thread requirement.

Berthing Mechanism to Berthing Mechanism Seals

The current configuration uses a set of Gask-O-Seals¹ (Figure 14) with three seal beads to provide two-fault tolerance across the gap between the berthing flanges. The Gask-O-Seal consists of a retainer plate with machined grooves into which an elastomer is molded to create the seal element. O-ring seals were considered, but were not chosen because they were not easily maintainable. The Gask-O-Seal is maintainable because it comes in sections, allowing much easier handling during cumbersome EVA. Metal seals were also considered, but were not selected due to the high seating forces inherent in this type of seal. More importantly, the metal seals could not accommodate pressure distortions (particularly those oval in nature) between the berthing flanges.

CONCLUSION

Currently, development testing is being performed on the aforementioned hardware at both the component and system levels to refine the design. The tests have been formulated to cover a broad range of design scenarios which require confirmation and/or validation of current design approaches and analysis techniques, as well as to test attainability of imposed manufacturing complexities. The planned development tests will:

- Provide data on the ability of mechanisms to withstand static and vibrational launch loads;
- Demonstrate reliable mechanism performance in a thermal vacuum environment;
- Test the Berthing Mechanism Actuator and Control System performance;
- Evaluate the integrated performance of the Alignment Guides, Capture Latch and Powered Bolts;
- Evaluate the effects of capture and berthing dynamics on the seals and seal surface;
- Evaluate the ability of a fully berthed assembly to withstand proof and ultimate pressurization of the vestibule; and
- Evaluate the effects caused by on-orbit loads resulting from Logistics Module berthing, station reboost and Orbiter docking.

It is believed that the current configuration will meet all program requirements with minor modifications and will be ready for flight in May 1997 when Node 2 is launched.

ACKNOWLEDGEMENTS

The author wishes to thank Harry Warden* for much of the CBM history, Bob Foster* and David Smith* for their inputs, and Don Dickey* for his graphics support. In addition, the author thanks the National Aeronautical and Space Administration (NASA) and the Boeing Company for permitting publication of this paper.

* The Boeing Company, Huntsville, AL

¹Parker Seals Group, Lexington, KY

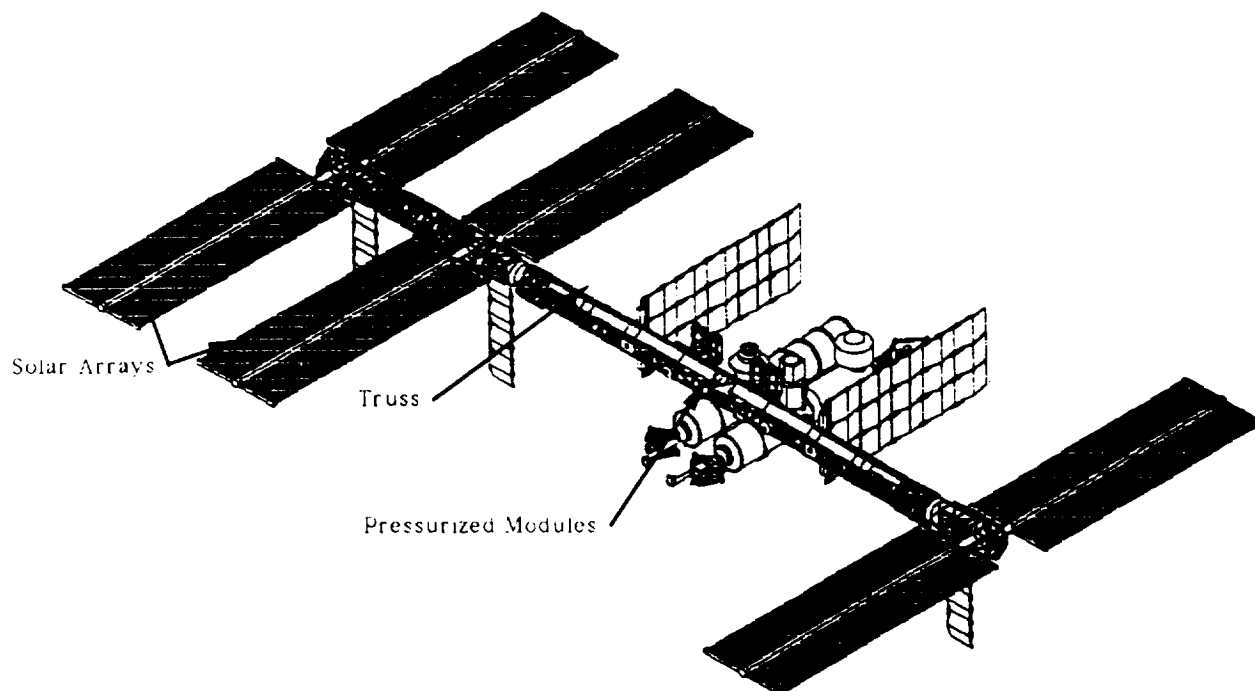


Figure 1--Space Station Freedom

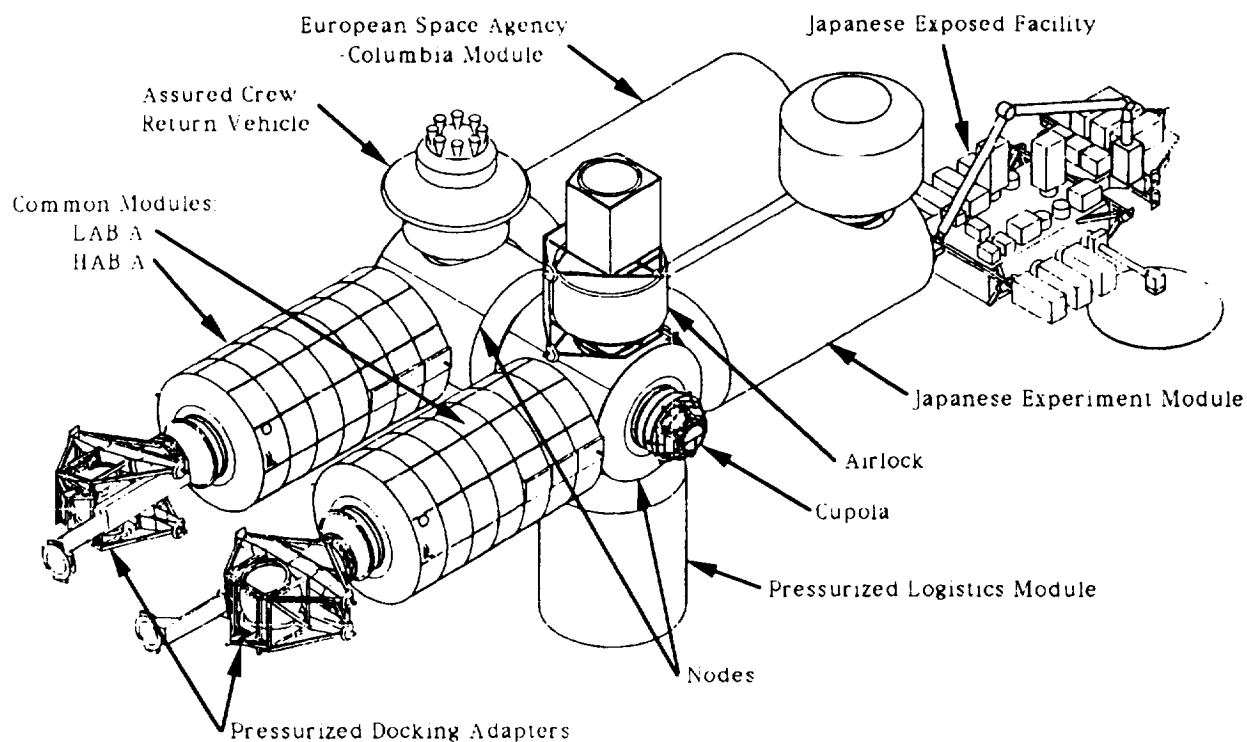


Figure 2--Space Station Freedom Pressurized Module Pattern

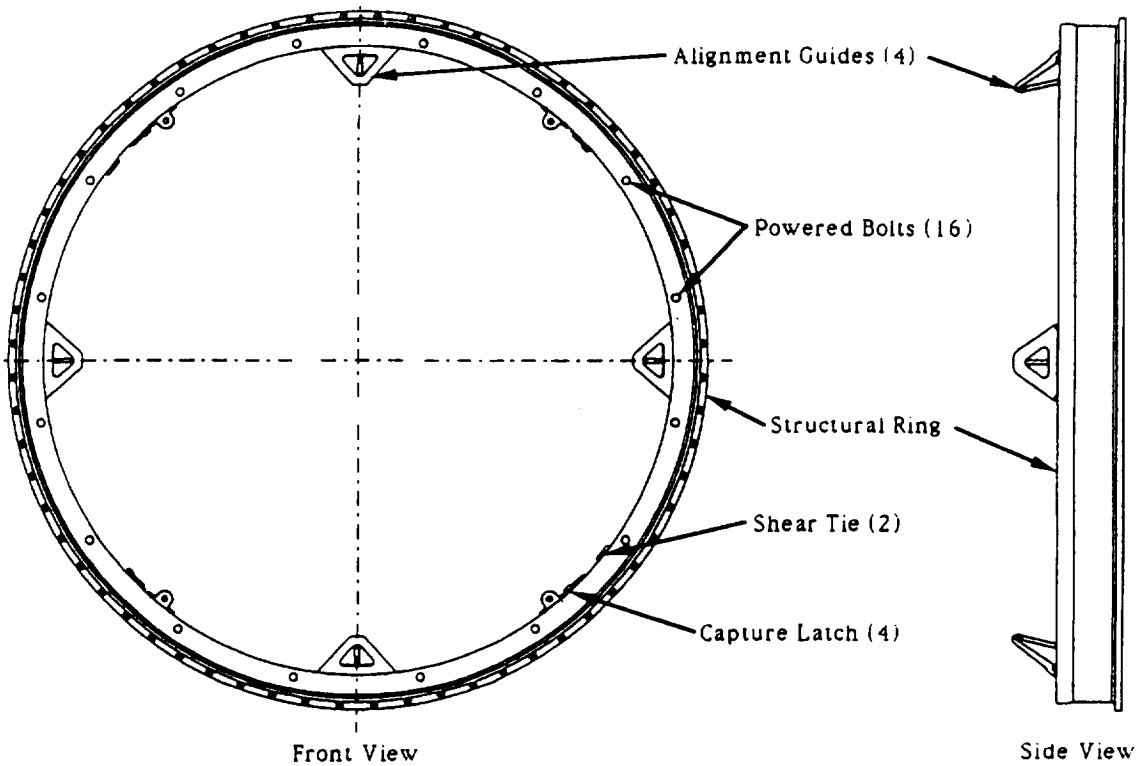


Figure 3--Active Berthing Mechanism

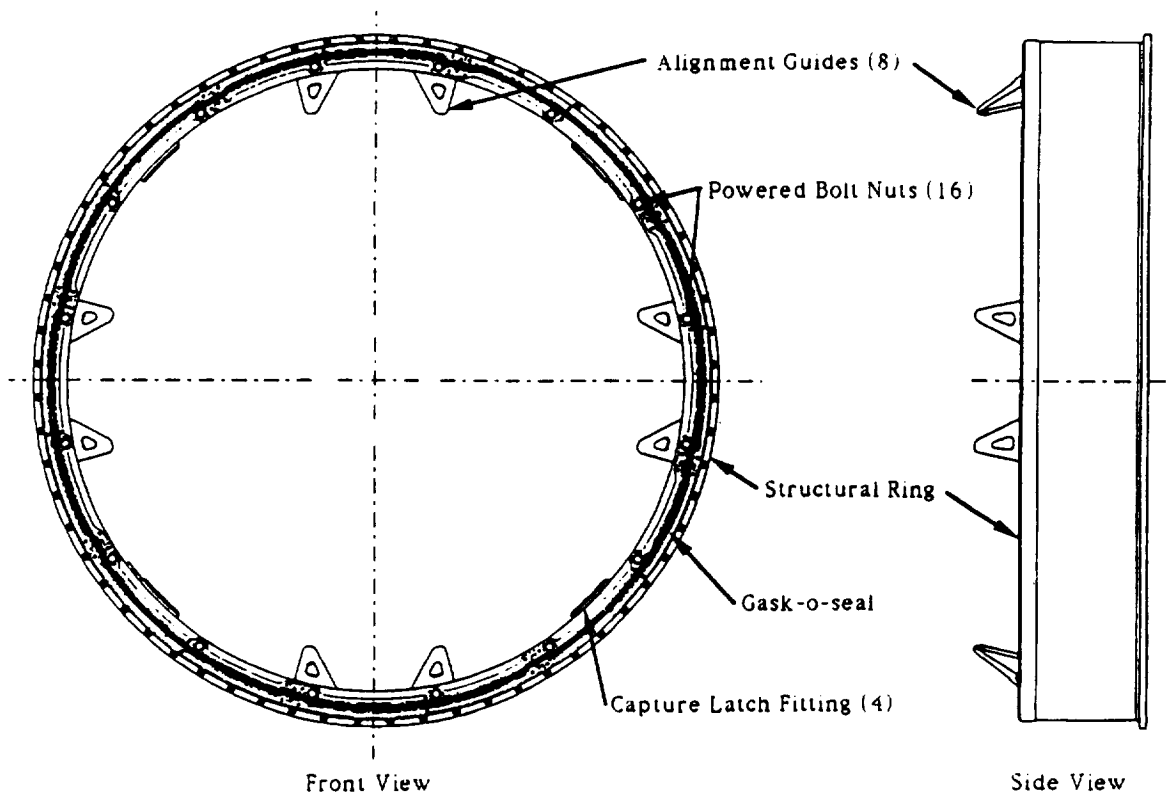


Figure 4--Passive Berthing Mechanism

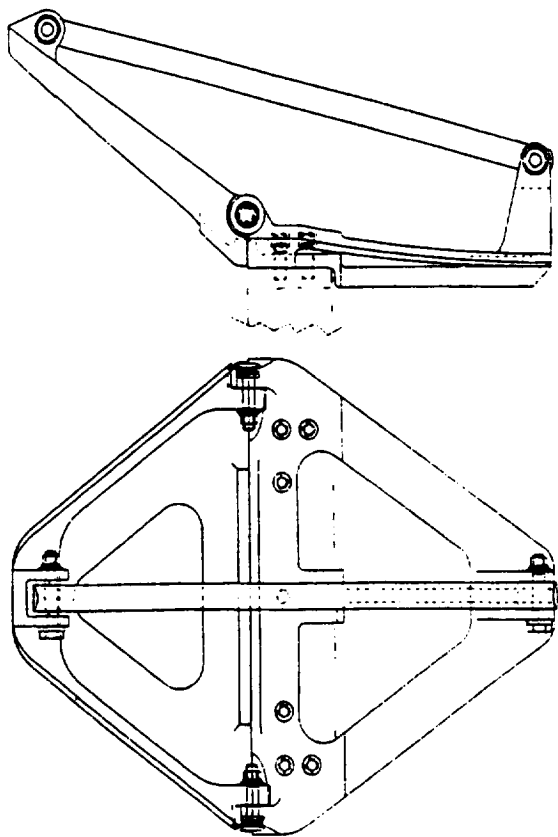


Figure 5--Active Berthing Mechanism Alignment Guide

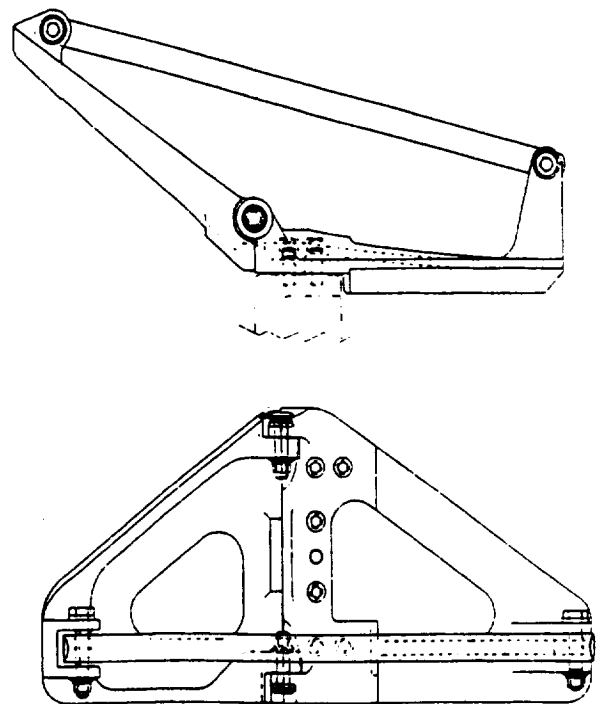


Figure 6--Passive Berthing Mechanism Alignment Guide

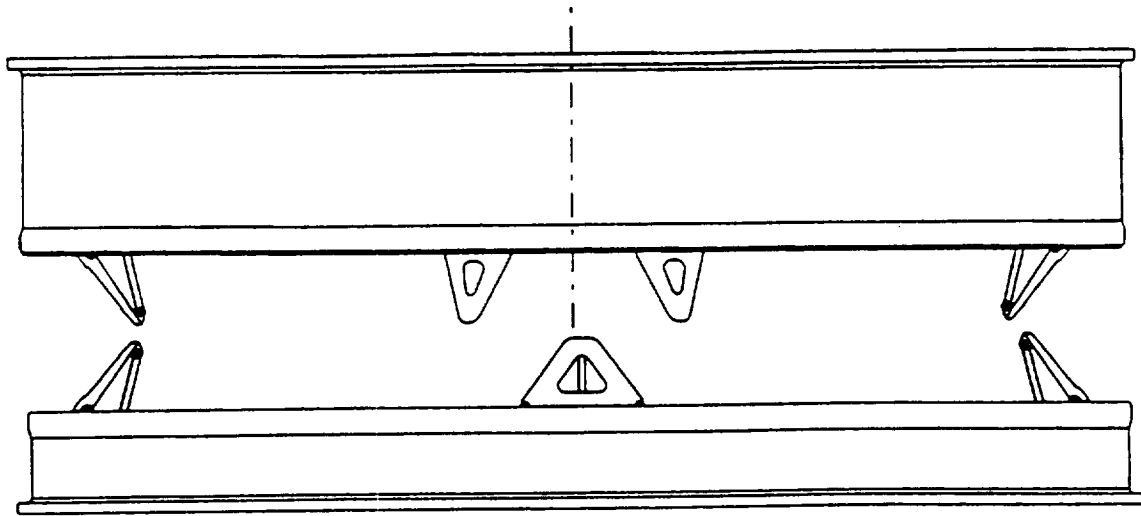


Figure 7--CBM Connectivity

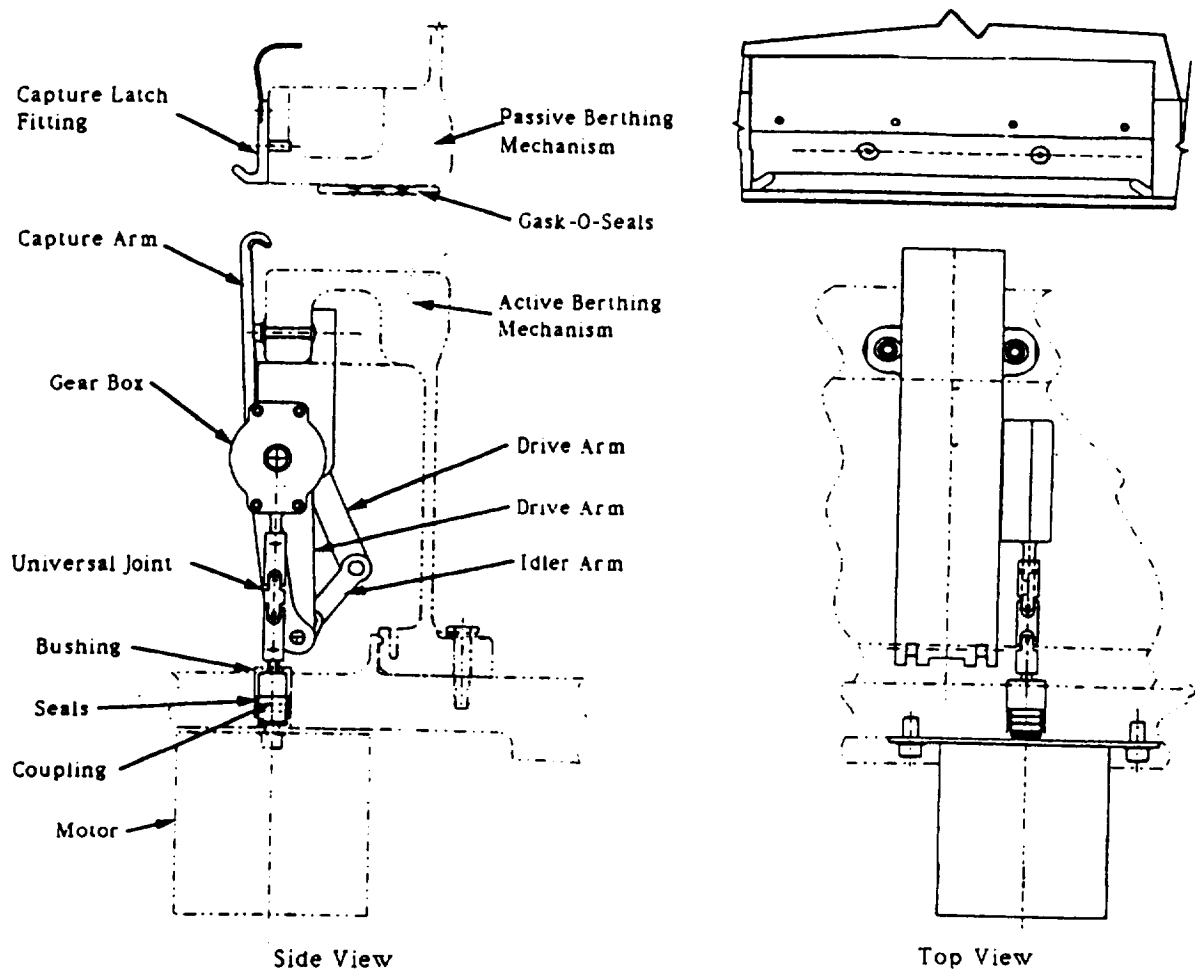


Figure 8--Capture Latch Assembly

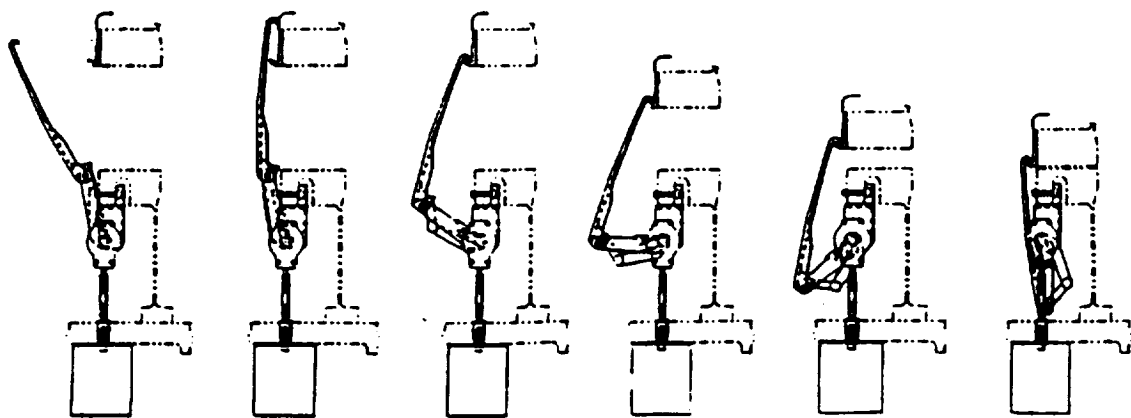


Figure 9--Capture Latch Motion

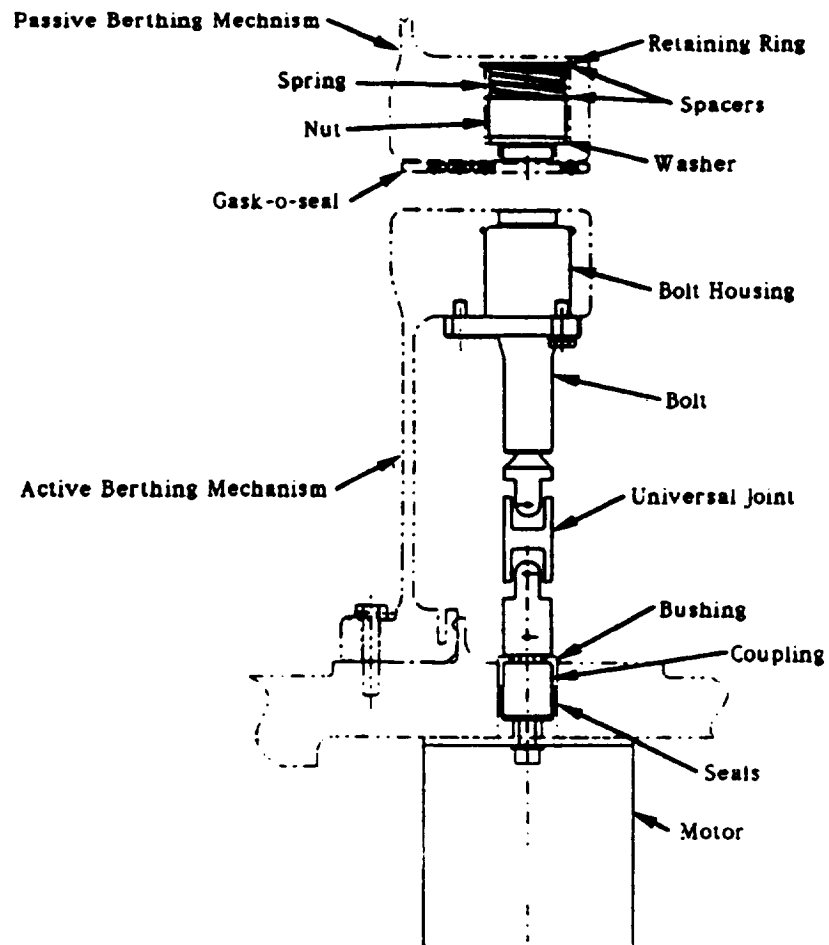


Figure 10--Powered Bolt

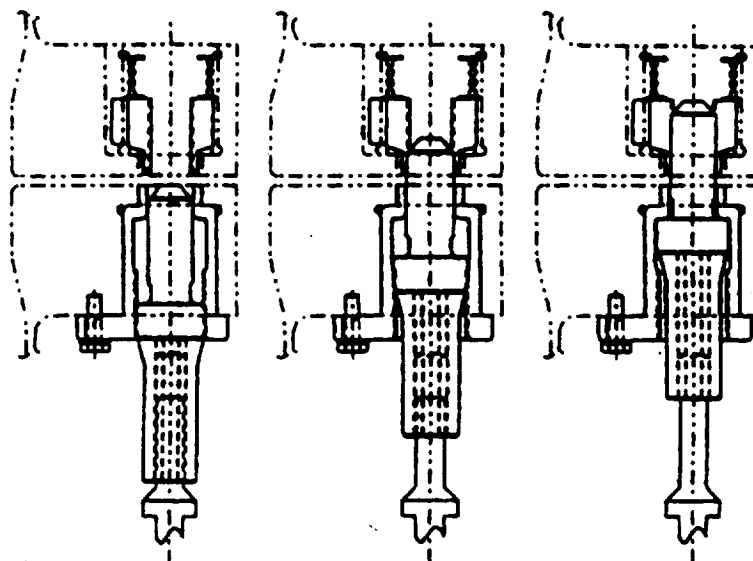


Figure 11--Powered Bolt Motion
(Note: Seal not shown for clarity)

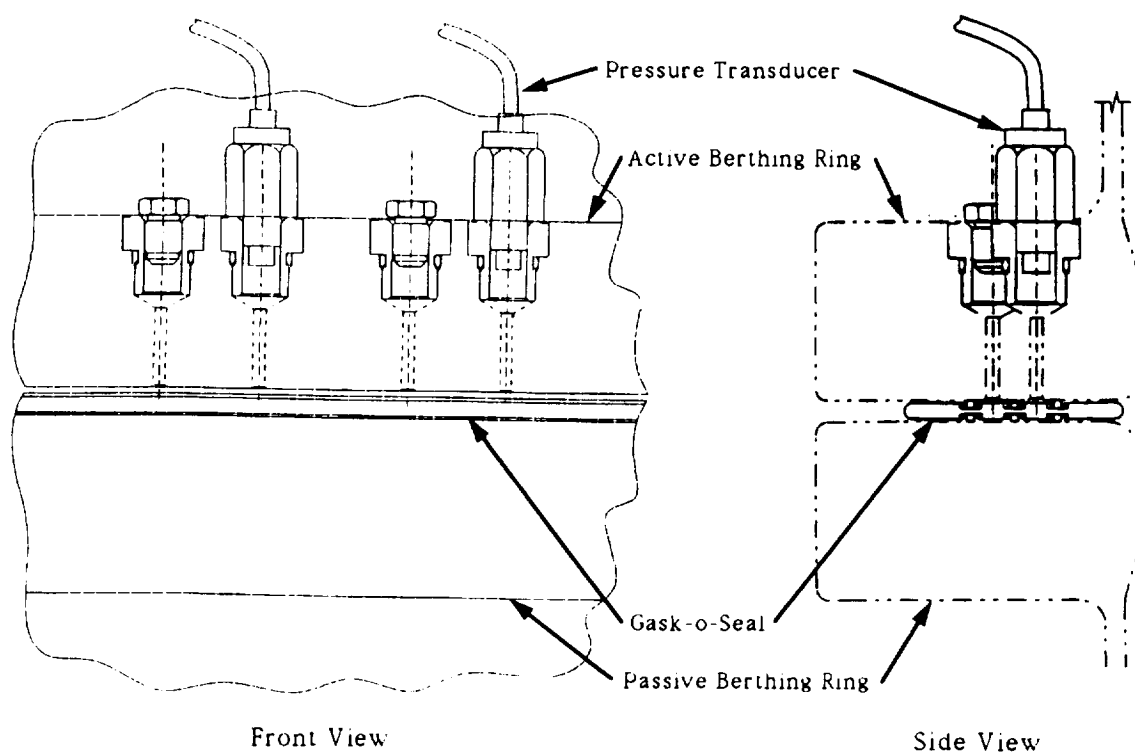


Figure 12--Differential Pressure Transducer

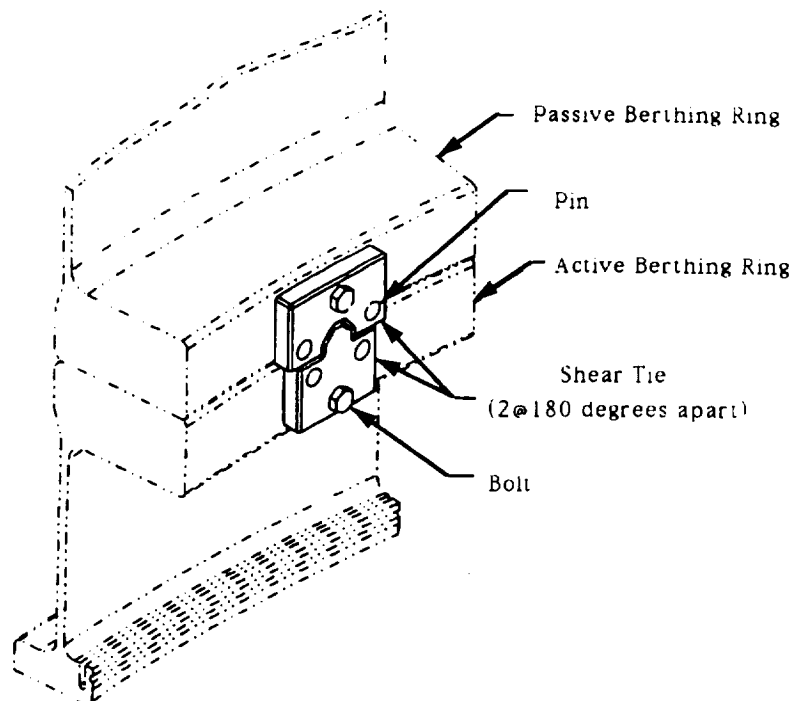


Figure 13--Shear Tie

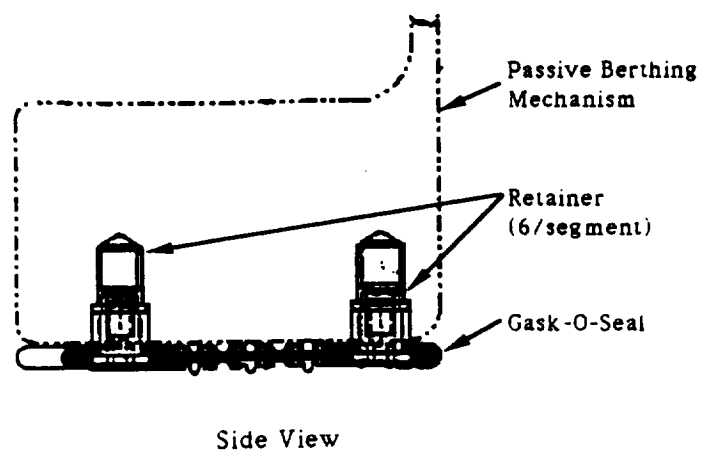
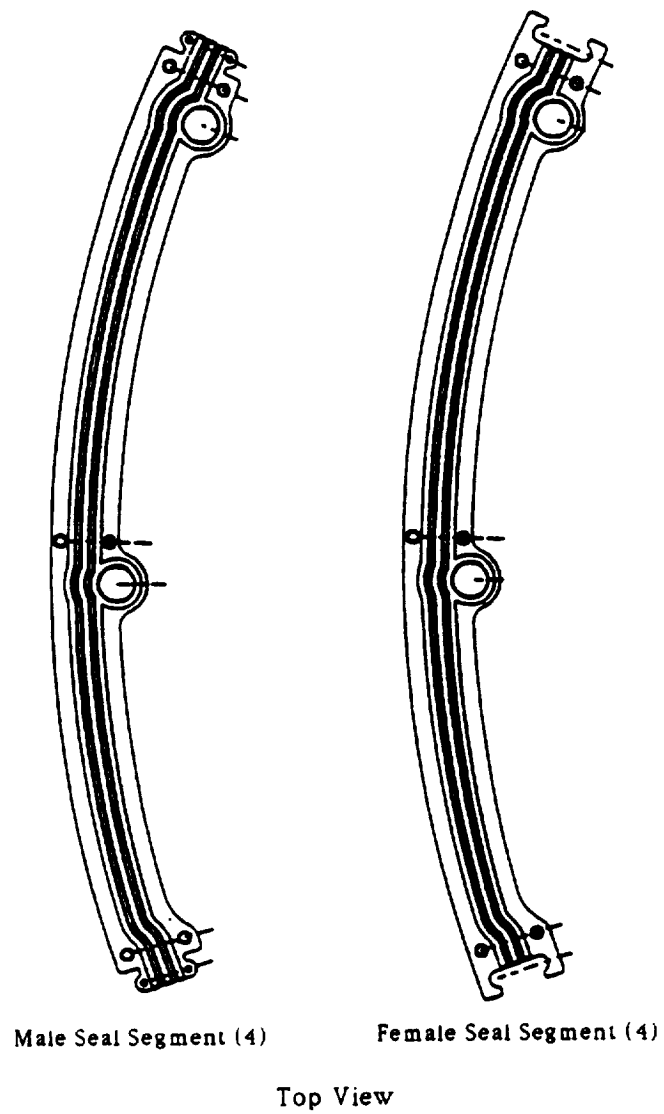


Figure 14--Gask-O-Seal

EDITOR'S NOTE: This paper was received as the proceedings went to press; it has not been edited for publication.

A MULTIPURPOSE MODEL OF
HERMES-COLUMBUS DOCKING MECHANISM

J.J. González-Vallejo *, W. Fehse **, and A. Tobias **

ABSTRACT

One of the foreseen missions of the *HERMES Spacevehicle* is the servicing to *COLUMBUS Free Flying Laboratory (MTFF)*. Docking between the two spacecraft is a critical operation in which the *Docking Mechanism (DM)* has a major role.

In order to analyse and assess robustness of initially selected concepts and to identify suitable implementation solutions, through the investigation of main parameters involved in the docking functions, a multipurpose model of DM was developed and tested. This paper describes main design features as well as the process of calibration and testing.

INTRODUCTION

Docking and Berthing Systems for unpressurised and pressurised connections between spacecraft have been investigated in Europe since beginning of eighties. Initial technology investigations, based on docking systems for the unmanned vehicles (see figure 1), paved the way for the current HERMES and COLUMBUS projects that require docking systems with pressurised passages.

HERMES main mission is the servicing of the MTFF, however, visits to the *Space Station Freedom (SSF)* and *MIR Orbital Complex* are also design missions of the HERMES (See figure 2). To perform external and internal servicing operations of the MTFF the HERMES has to be provided with a Docking System which characteristics will be driven by such mission. When HERMES visits the SSF it has to be provided with a Docking/Berthing System compatible with the SSF *Common Berthing Mechanism (CBM)*.

A DM is required to perform various functions leading to the joining of two manned or man-tended spacecraft in order to provide a safe pressurised passageway between the two vehicles for crew and goods transfer. The phase B configuration of DM for HERMES-MTFF is shown in figure 4.

In the frame of the ESA's *Rendezvous and Docking Pre-Development Programme (RVD-PDP)* technology investigations on docking systems and dynamics are currently being performed. Some objectives of the programme

* SENER, Ingeniería y Sistemas. Bilbao, Spain.

** ESA - European Space Technology Centre. Noordwijk, The Netherlands.

are to assess robustness of the concepts initially selected and to identify suitable implementation solutions through the investigation of main parameters driving DM's characteristics.

Validation of the existing simulation tools (Docking Dynamics Facilities and Simulation Programmes) has also been an additional objective of the programme. This has been performed by cross comparison of the results during testing at Docking Dynamics Facilities with those obtained by software simulations.

For these purposes a *Docking Mechanism Model (DMM)* able to be reconfigured to provide various functional schemes was developed.

OBJECTIVES AND MAIN REQUIREMENTS

Functions of a DM can be classified in two main groups: those related with docking dynamics (relative positioning and reception, capture, centring, residual energy dissipation,...) and those needed to establish a structural and functional joint of the two spacecraft (latching, passage pressurisation, utility connection,...).

Objectives of the programme in this area were mainly linked with those parameters related with the docking dynamics process that are the drivers of the DM characteristics. These parameters are:

- Approach conditions due to the mating process: direct docking in case of HERMES-MTFF or berthing to the SSF CBM by means of SSRMS. (Table 1).
- Mass properties of the vehicles to be mated.
- Capture strategies: "capture before contact strategy".
- Dynamics: induced forces and moments during mating operations, rebounds, attenuation, etc.
- Configuration of the DM and characteristics of its elements.
- Performance of the DM Front-End elements: Guiding petals, attenuation system, capture latches.

Consequently the main issues to be investigated concerning Docking System functions were defined as follow:

- Guidance: Guiding petal concept. Sensitivity of the docking process to parameters like: petal location (internal or external with respect to the docking ring), number of guiding elements, shape of petals (guiding angles), etc.

- Attenuation: Stiffness and damping characteristics of the attenuation system to cope with the energy dissipation needs due to contact conditions, so that induced loads as well as attenuation strokes and tranquillisation times can be within adequate values.
- Capture: Capture latch system concept and performances. Sensitivity of the docking process number and location of capture latches, capture velocity, capture strategy, etc, had to be investigated.

First step consisted in the definition of the requirements to be considered in the design, development and testing of the DMM. These were derived from the objectives of the programme and interface constraints, and they can be summarised as follows:

- a) The above described issues to be investigated imposed the requirement of a modular design of the DMM able to provide different functional configurations. This modular design shall be provided by:
 - A set of guiding petals that shall be able to provide different shapes and that can be mounted in different positions, either internally or externally, to configure guiding assemblies of 3 or 4 petals.
 - Capture latches and corresponding control electronics that shall be provided with tuning capability of the operating velocities and capture ranges. Capture latches shall also be compatible with different mounting locations and configurations.
 - An attenuation system in which the main parameters (stiffness and damping parameters) can be tuned in a wide range.
 - Main bodies of the DMM that shall provide supporting structure to the required configurations and be compatible with the former set of elements.
- b) Due to interface limitations derived from the *Docking Dynamics Test Facility (DDTF)* (CNES/Matra), where the DDM had to be mounted, model dimensions and masses were limited. Envelope limitations lead to a scaled down model: 1400 mm docking ring diameter (1700 mm total envelope including external petals). Masses were limited to 250 kg on the static part and 75 kg on the moving part of the DDTF.
- c) The objective of a cross verification of the DDTF results with respect to those obtained by software simulations imposed the necessity of good knowledge of the characteristics of the DMM, so that, a high representative mathematical model could be implemented in the analysis and simulation programmes.

This necessity imposes two kind of additional requirements:

- Actual characteristics of the DMM and its elements shall be determined by testing, and mathematical models representative of their behaviour shall be established.
- As a goal DDM elements shall be designed in such a way that different functions to be performed by different elements shall be decoupled. For instance, being stiffness a parameter to be investigated, docking dynamics should be only governed by the attenuation system stiffness (to be tuned) and the stiffness of other elements should be higher enough to be decoupled from the attenuation system one and to be characterised as rigid bodies in the mathematical models.

MODEL DESCRIPTION

The DMM is a mechanism which characteristics can be tuned in accordance to the required investigation and it is able to be reconfigured as to provide various functional schemes. In figure 5 two configurations can be seen: guiding petals and capture latches externally located with four units of each set and both sets internally located with also four units of each. Other combinations are possible: 3 or 4 external petals with 3 or 4 internal petals, etc.

As in the HERMES-MTFF DM baseline, the DMM consists of two halves: one active and one passive. The active one (chaser) simulates the part mounted on the HERMES, being the passive one (target) the one that would be mounted on the MTFF.

The *DMM passive half* is mounted on the moving part of the DDTF and it is composed of two type of elements: docking ring and guiding petal set.

The DMM active half, which is mounted on the fixed part of the DDTF, consists of the following assemblies: support flange, docking ring, guiding petals, capture latch assembly and attenuation system.

The support flange of the active half is the structural interface with the DDTF fixed part, being supported on three points to six force detector rods. It is a circular ring with a pi-section made in 6061-T6 Aluminium Alloy. This item provides a rigid support to the attenuation system. Tests were carried out to verify that the stiffness of this element was high enough with respect to the attenuation system. The stiffness when loaded in central point between supports were:

- Longitudinal load: $2.8E+6$ N/m
- Radial load: $2.1E+8$ N/m

The docking rings are in both chaser and target. Each ring is supported at three point at 120 deg apart: the target ring supported by

the DDTF actuators (target ring) and the chaser by all six dampers of the attenuation system on three points. These rings were designed to provide attachment points to petals, attenuation system and capture latches in all possible configurations.

Due to the mass restrictions and stiffness requirements together with the limitations in dimensions, and in order to optimise the stiffness/mass rate, the rings were made in a closed section (215 x 50 mm) that was initially machined to incorporate internal stiffeners and then welded to close the ring section. The material selected was 6061-T6 Aluminium Alloy as for the support flange. Tests were performed to verify structural behaviour: the minimum stiffness of 2.78×10^6 N/m was found when the ring is longitudinally loaded in the centre of two support points.

Guiding petals are mounted on docking rings of both passive and active parts of the DMM. Its dimensions are defined by the DDTF simulation capabilities in terms of velocities and misalignments. As the guiding element of a petal is the edge each petal was divided in two *semi-petals*, each one consists of the petal blade and its support bracket. With this petal configuration different kind of petals for different DMM configurations can be achieved.

Docking dynamics sensitivity with respect to the petal characteristics is another point of study: low values of petal inclinations (w.r.t. docking axis) allow better self-alignment during mating but increase first contact distance between docking rings implying higher capture ranges. For this purpose each petal can be oriented to provide inclinations of 30/45 deg with respect to the docking axis and 30/45 deg (when externally located) or 20/35 deg (when internally located) with respect to the docking plane radius.

Petals were made from 7075-T6 Aluminium Alloy. In order to reduce the friction coefficient the petal edges were polished and treated with *Molikote 321R*. A dynamic friction coefficient of 0.09 was obtained.

Stiffness of each semi-petal (blade and bracket) was also measured in three directions (radial, tangential longitudinal). A minimum value of 2.4×10^6 N/m was found.

The attenuation system consists of a set of specially designed viscous fluid damped coil spring dampers. Eight dampers were built and those six with a better behaviour were selected for implementation in the DMM. Figure 6 shows the attenuation system on which the chaser docking ring is mounted.

Each damper can be mounted in different positions, with different inclinations, so that different relationships between axial, bending (pitch, yaw), shear and torsional stiffness of the attenuation system can be implemented.

Besides stiffness and damping rates of each single damper can be tuned. Any damping rate in a range from 10,000 Ns/m to 220,000 Ns/m can be

achieved for each damper (See figure 11). By cancelling coils of the spring stiffness can be adjusted to $1.6E+4$ N/m, $4.0E+4$ N/m, $7.5E+4$ N/m and $14.0E+4$ N/m.

Main components of each damper are: regulation valve, spring, metallic bellow, linear regulation rod, pipe to expansion chamber and linear displacement sensors. These components are shown in figure 7.

Energy dissipation is produced by the flow of the oil through the regulation valve. Several design solutions of the valve were considered, having the finally selected one an excellent behaviour providing a linear damping law as demonstrated during test campaign.

After evaluation of different design solutions for dampers a solution based on *metallic bellows* was selected. This solution drastically reduce the problems of frictions with respect to conventional solutions like piston based, then a more accurate mathematical model could be obtained.

By means of a *linear regulation rod* the length of each damper can be adjusted for new configuration (damping strokes, etc) study or to recover the radial motion of the docking ring due to 1-g effect (docking axis is in horizontal position in the DDTF).

Linear sensors were implemented in the dampers in order to know the relative position of the damping ring with respect to the fixed part.

Determination of an accurate mathematical model was one of the most challenging issues during the development of the attenuation system. In figure 8 a schematic model of the damper is shown with identification of the parameters governing the behaviour of the damper. The process that was established for this purpose followed the logic diagram that is displayed in figure 9. A test campaign and subsequent analyses led to the definition of the damper mathematical model. The correctness of such approach was confirmed by the comparison between the actual results and the theoretical ones, as shown in the sample of figure 10.

The capture latch assembly consists of a set capture latches and its driving electronics. Sets of three or four elements can be mounted to DMM.

For capture operation capture latches have to move sequentially through the following positions: stowing point, ready-to-capture point, capture position, and latching position. upon detection of capture conditions latches are actuated and move fast to the capture position in which they close the escape trajectory of the target ring.

For the purpose of the RVD-PDP investigations, latches are driven by stepper motors. As instrumentation, microswitches are used for the latch open and close position as well as to open the latches (operation abort) in case of capture out of safe operational range, other positions (capture and ready-to-capture are detected/defined by counting of commanded motor steps. Detection of capture conditions is entrusted to the computer of the motion simulation facility (DDTF). Each latch has its driving electronics

which can be independently tuned (frequency output for latch velocity regulation). In order to analyse capture strategies, latch motor can be driven at different velocities during each capture operation.

Latch concept is based on a four bars linkage type of mechanism with an overcentred position in the latching point. Geometry of the elements has been study to provide, for the same motor speed, fast motion from ready-to-capture point to capture point and slow from this point to latching position. Some levers and their mounting positions can be changed to provide different capture ranges.

Capture latches can mounted either on the docking ring or fixed to the support flange. The last location is needed when retraction of the attenuation ring is an additional function of the capture latches.

DOCKING DYNAMICS TESTING AND SIMULATIONS

DMM was installed on the DDTF and several docking conditions were simulated. In parallel the same test campaign has been simulated by means of the "*SENER Dynamics Analysis Programme*" (*SENDAP*). *SENDAP* environment consists of a suit of programmes designed to model the dynamics of multi-system, multi-body flexible or rigid structures with active control elements.

Figure 14 shows plots obtained with both methods. Actual results obtained from motion simulation facility (DDTF) and theoretical ones obtained with simulation programme (*SENDAP*) present a good correlation.

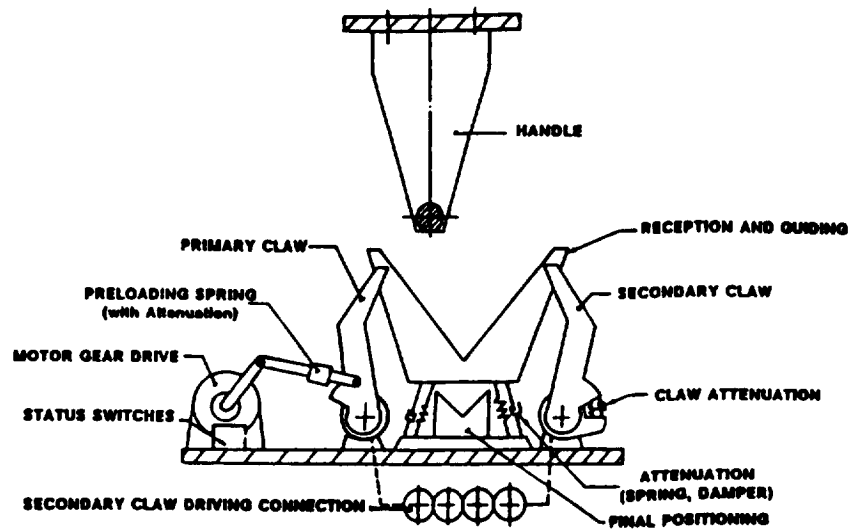
CONCLUSIONS

The DMM is a multipurpose mechanism that due to its versatility can be used as proof-of-concept system for different docking mechanisms and operational logics, as well as for the investigation of aspects like effects of failures, design loads, etc.

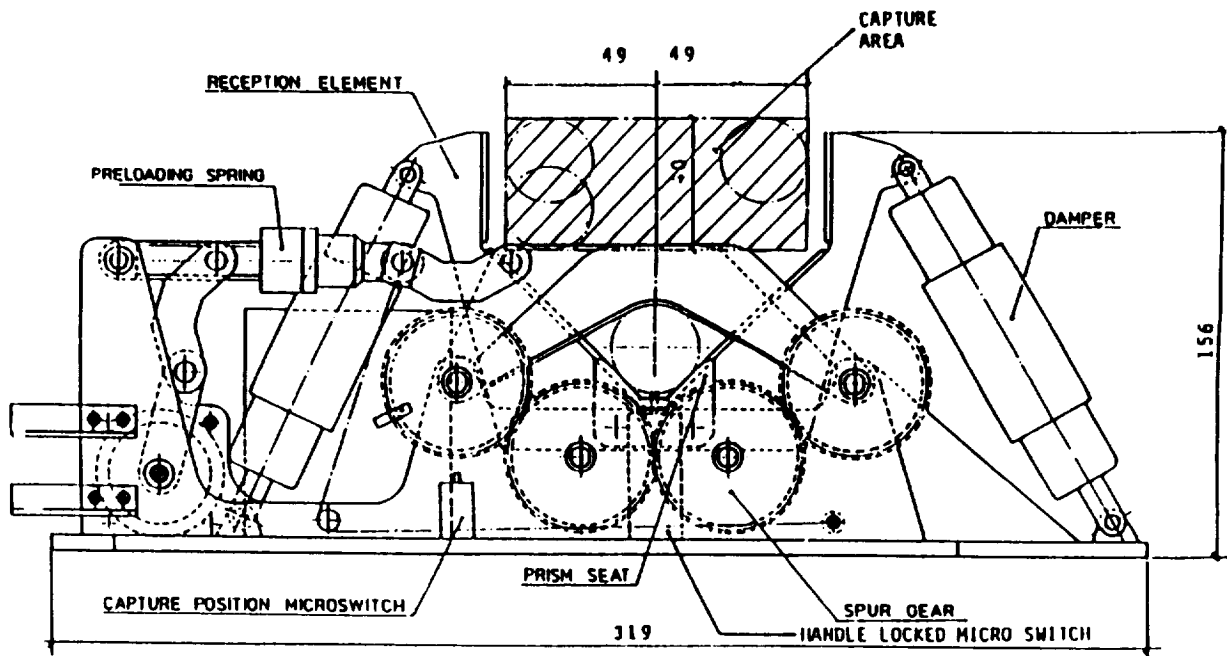
Results of the tests and simulations have confirmed correctness of the RVD-PDP philosophy, the selection and definition of requirements, design, fabrication and assembly of the DMM as well as the logic of the testing and its performance in order to obtain the actual characteristics and the calibration of the DMM and its components.

ACKNOWLEDGEMENT

The authors wish to express their appreciation to their numerous colleagues in ESA, MATRA and SENER for the contribution to the work reported in this paper.



Generic Latch Design



Latching Mechanism Design

Figure 1. Docking System for Unmanned Spacecraft. Latching Mechanism.

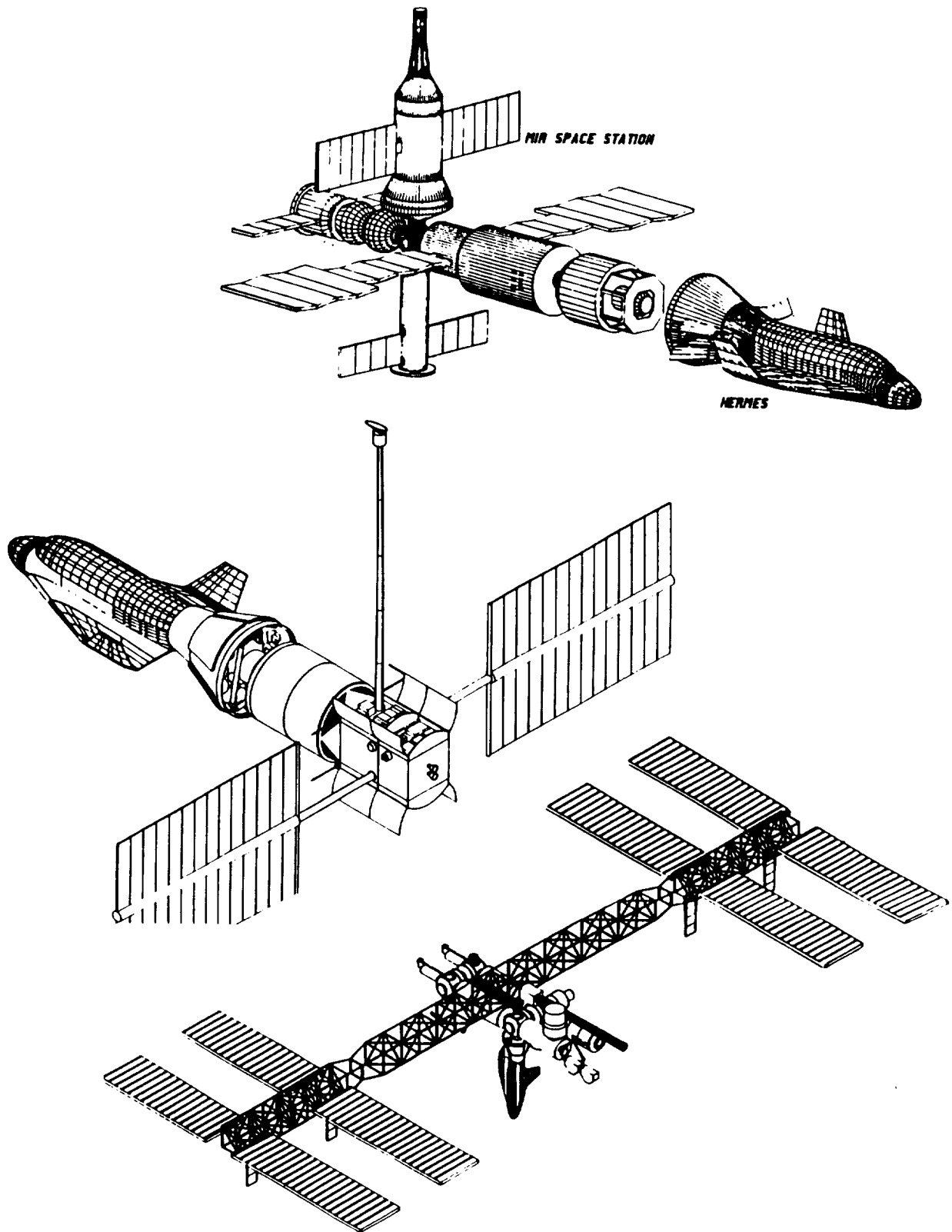


Figure 2. HERMES: Docking and Berthing Scenarios.

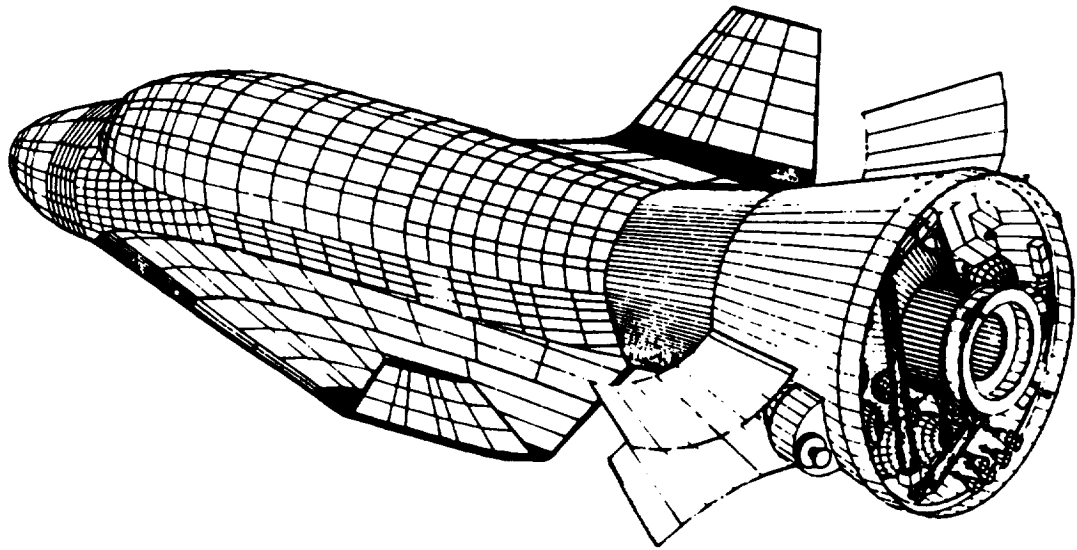


Figure 3. HERMES Spacevehicle with Docking Mechanism.

Table 1. Approach conditions.

CONTACT CONDITIONS	MIR APAS	FREEDOM BERTING	HERMES DOCKING
AXIAL VELOCITY V_x (m/s)	0.05-015	0.048	0.03
LATERAL VELOCITY V_z (m/s)	0.25 V_x	0.046	0.02
LAT. MISALIGNMENT (m)	0.2	0.077	0.05
ANGULAR RATE ($^\circ$ /s) ROLL	0.4	0.52	0.2
($^\circ$ /s) YAW/PITCH	0.4	0.2	0.2
ANGULAR ERROR (deg) ROLL	4	1.5	1.5
(deg) YAW/PITCH	4	1.5	1.5

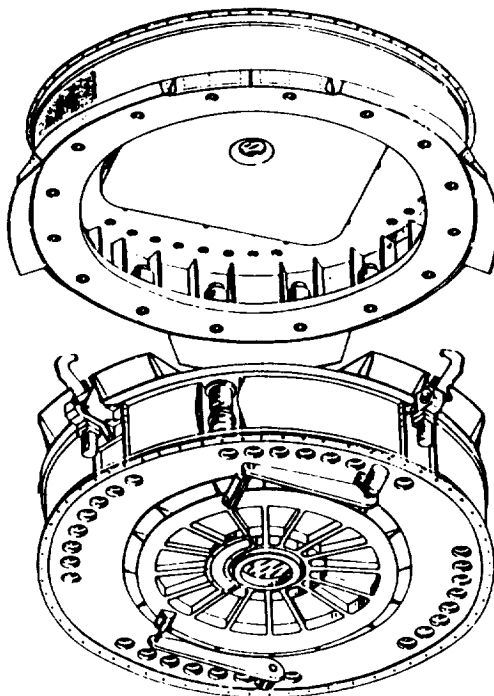


Figure 4. HERMES-MTFF DM.
(Phase B configuration).

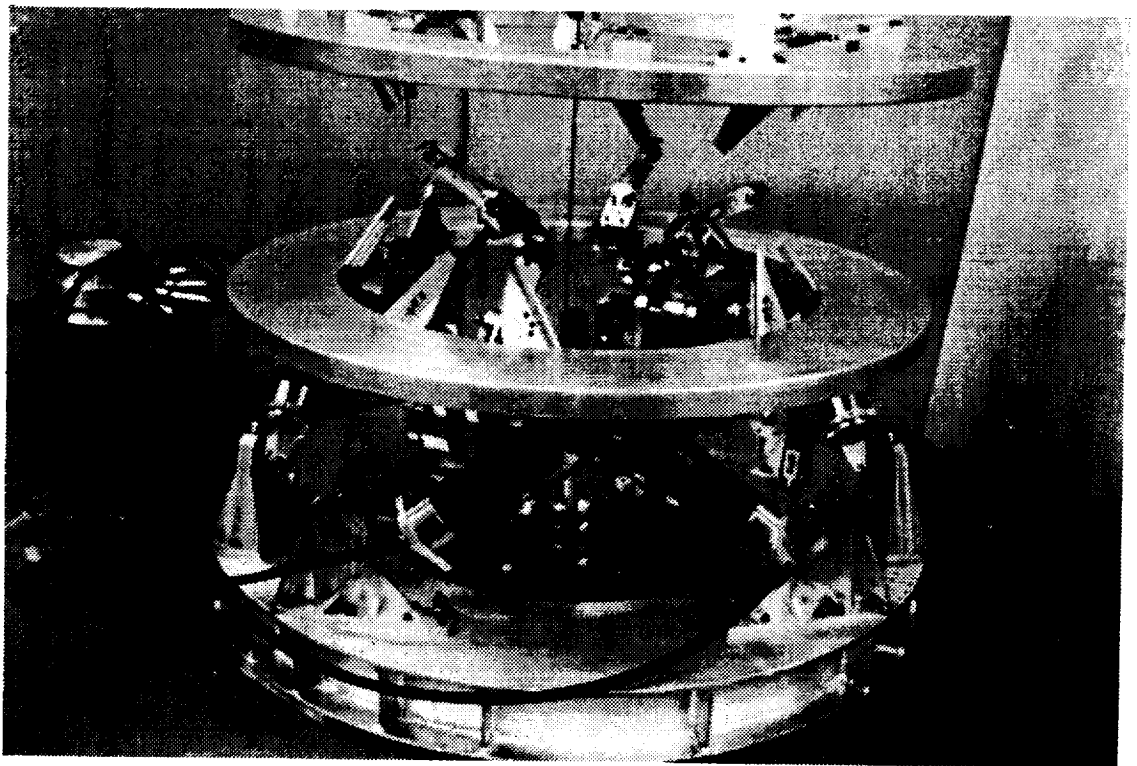
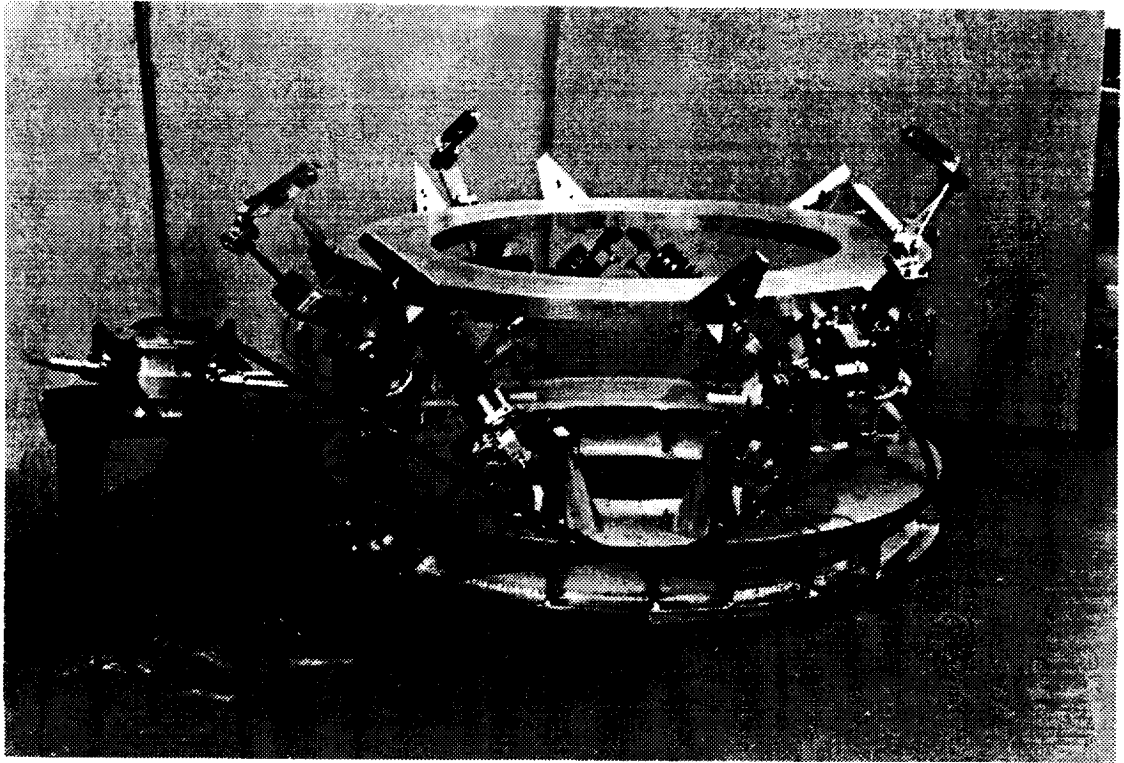


Figure 5. DMM: External (top) and Internal (bottom) configurations.

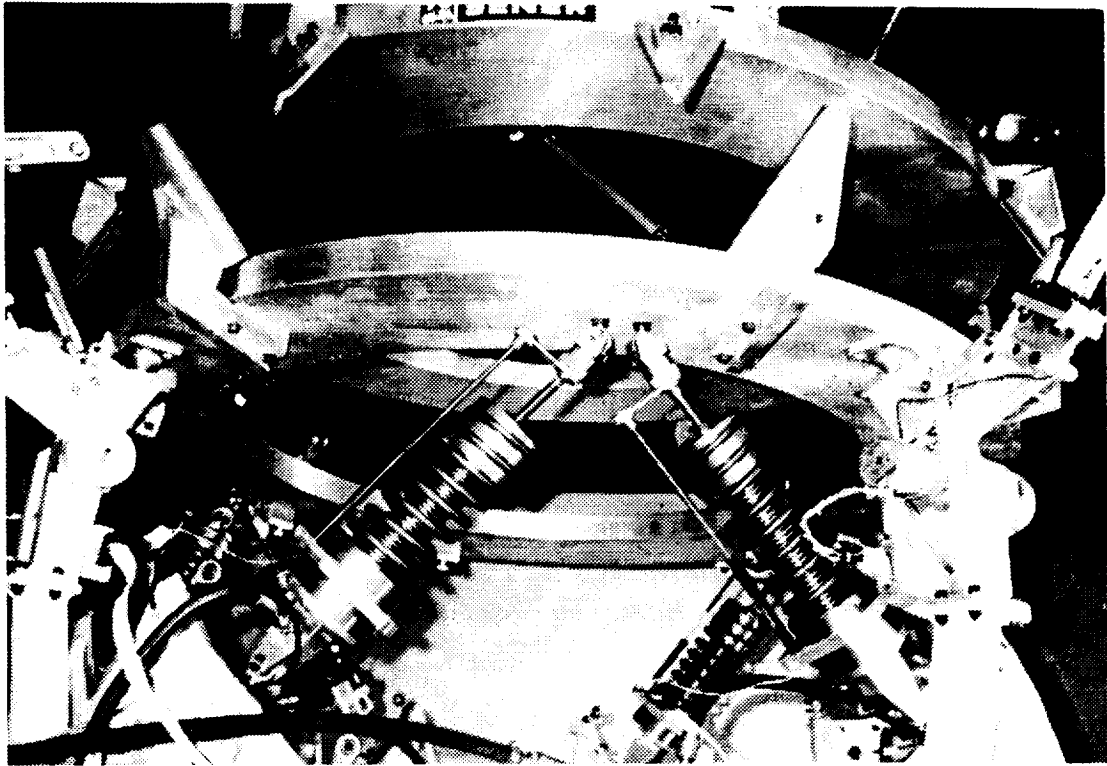


Figure 6. DMM: Target (top) in front of the chaser (bottom).

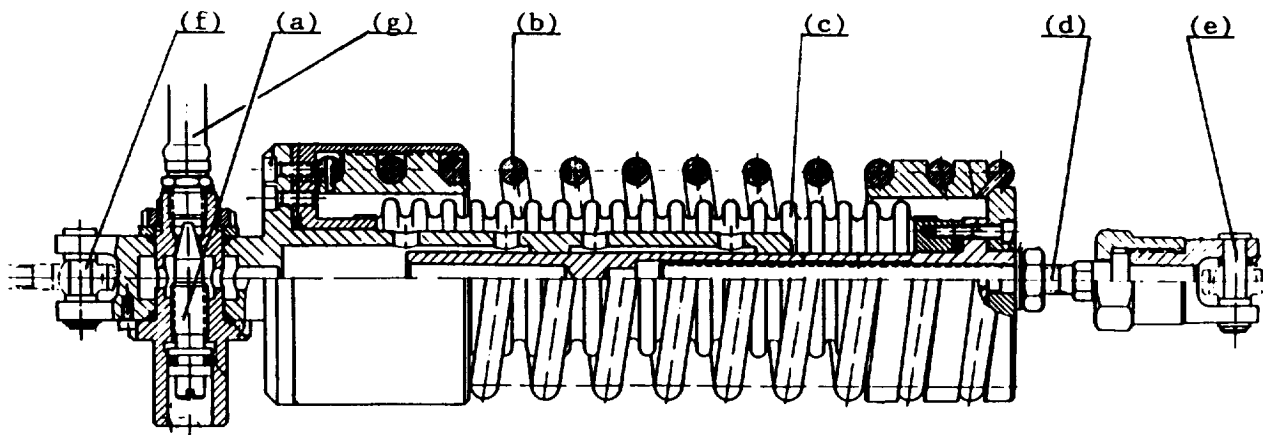


Figure 7. Damper main components: (a) regulation valve, (b) spring, (c) metallic bellow, (d) linear regulation rod, (e) docking ring support, (f) support flange bracket joint, (g) pipe.

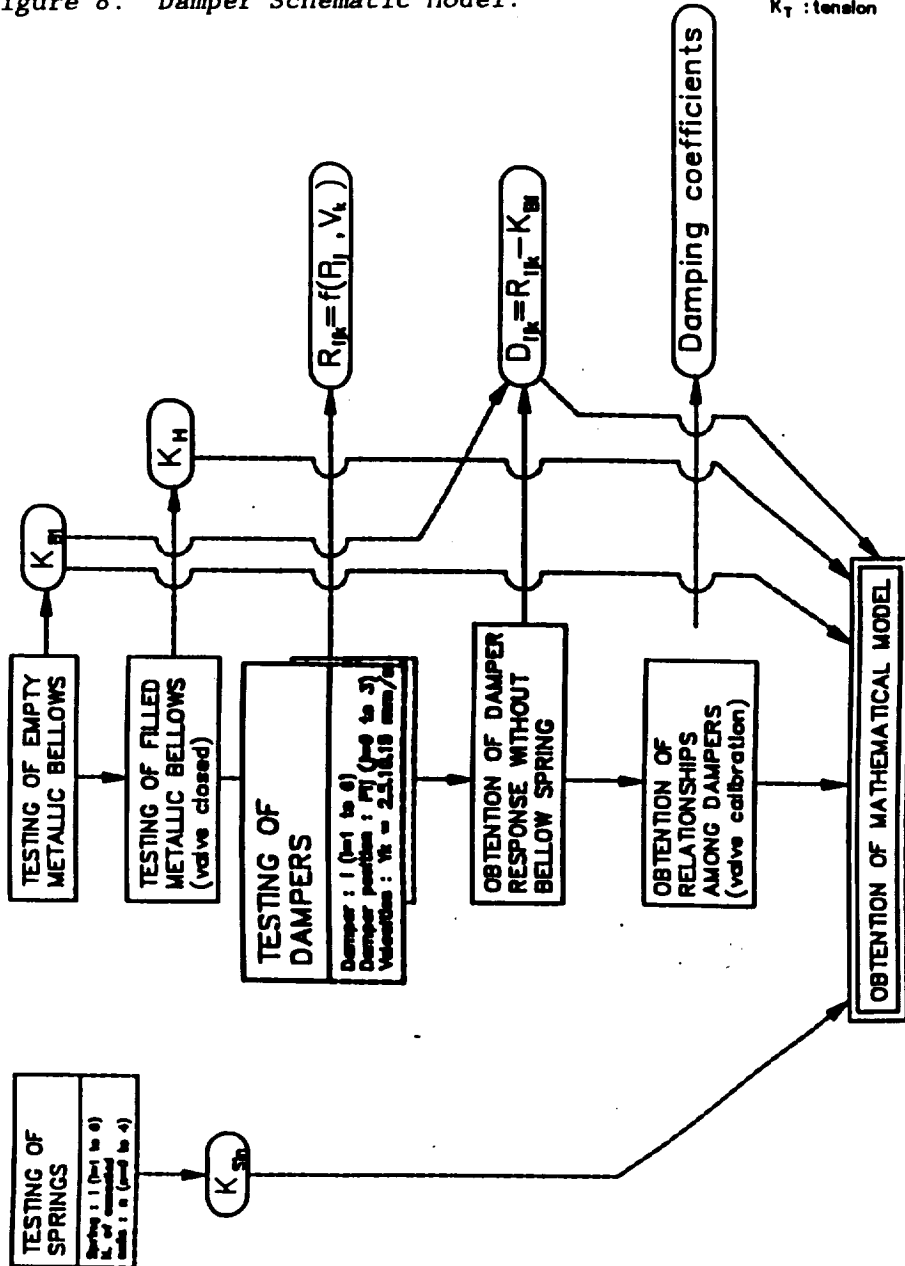
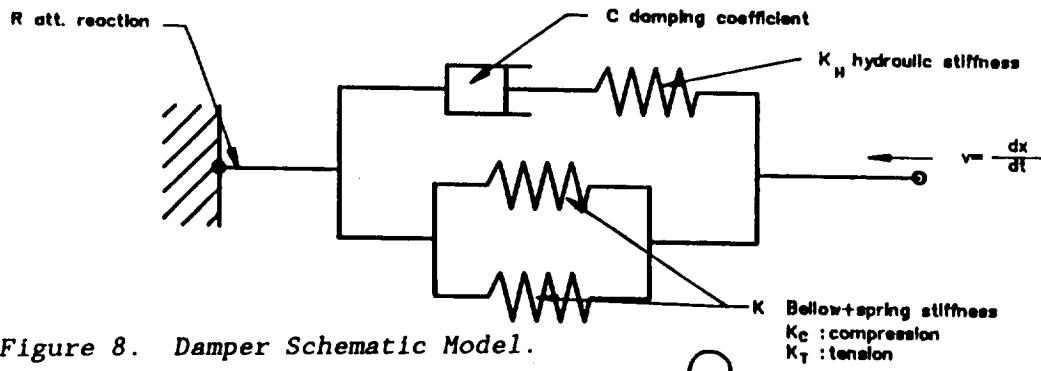


Figure 9. Damper. Testing Logic Diagram for Math. Model Definition.

DAMPER 8. V=5 mm/s. POSITION 3.

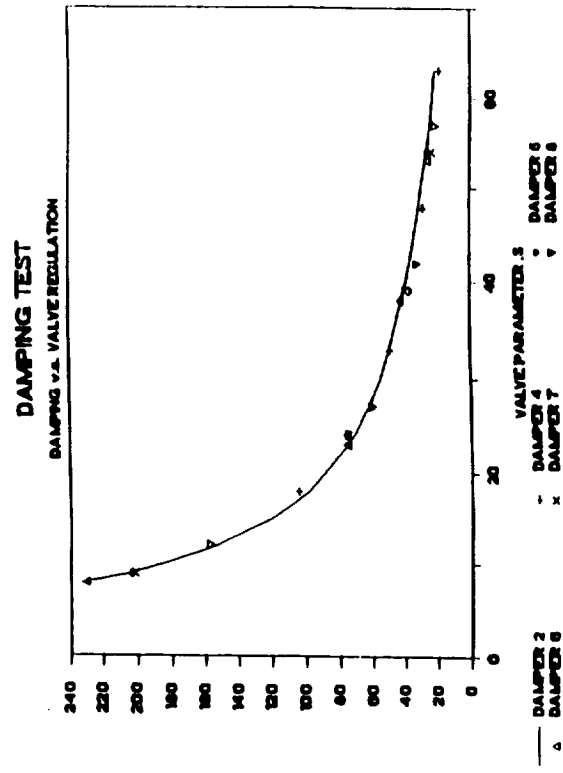
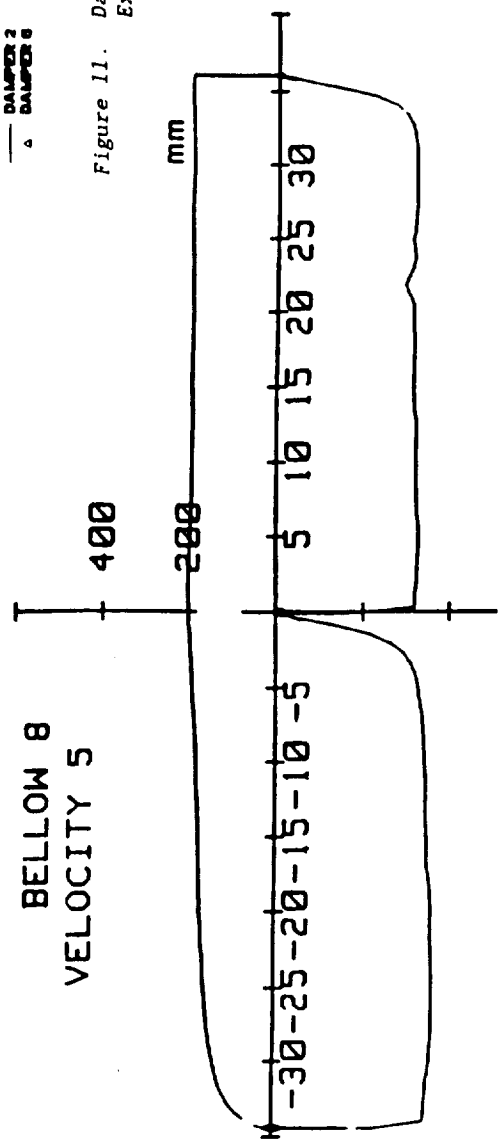
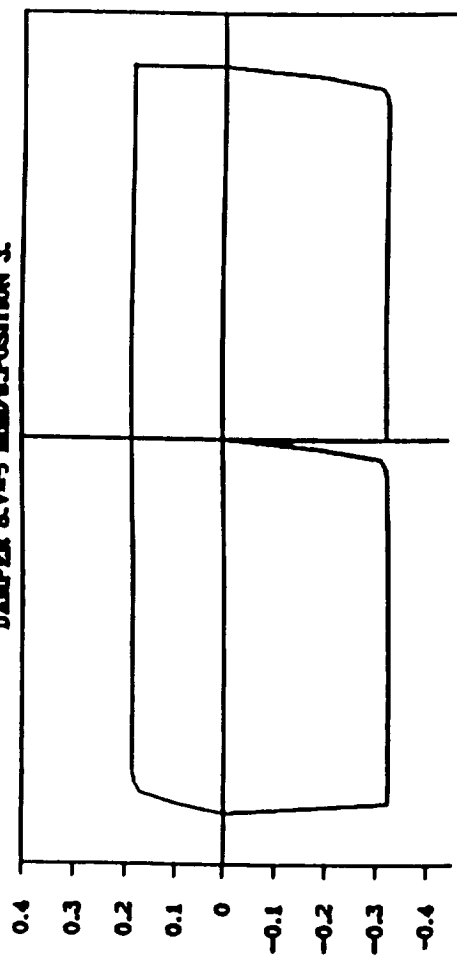


Figure 11. Damper Calibration: Damping Rate VS Valve Position. Experimental Results. (Damping rate in N*s/mm).

Figure 10. Damper. Analytical VS Experimental Results.

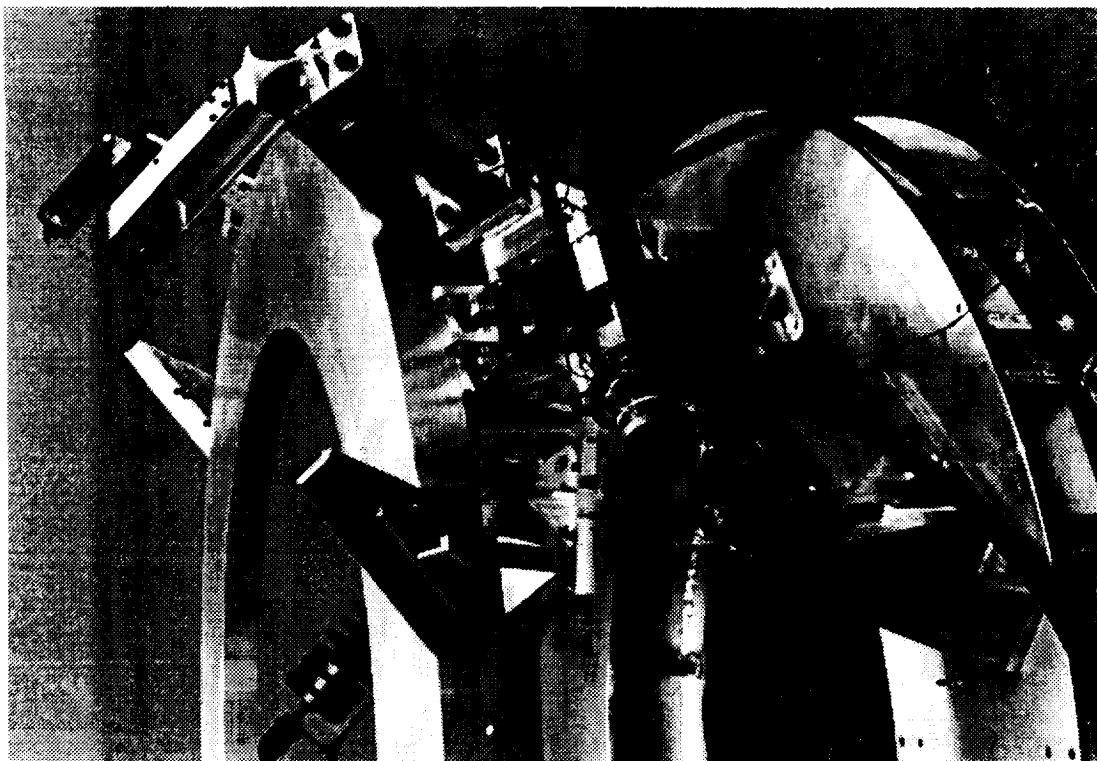


Figure 13. Capture Latch on the DMH mounted
between two semi-petals.



Figure 12. Capture Latch.

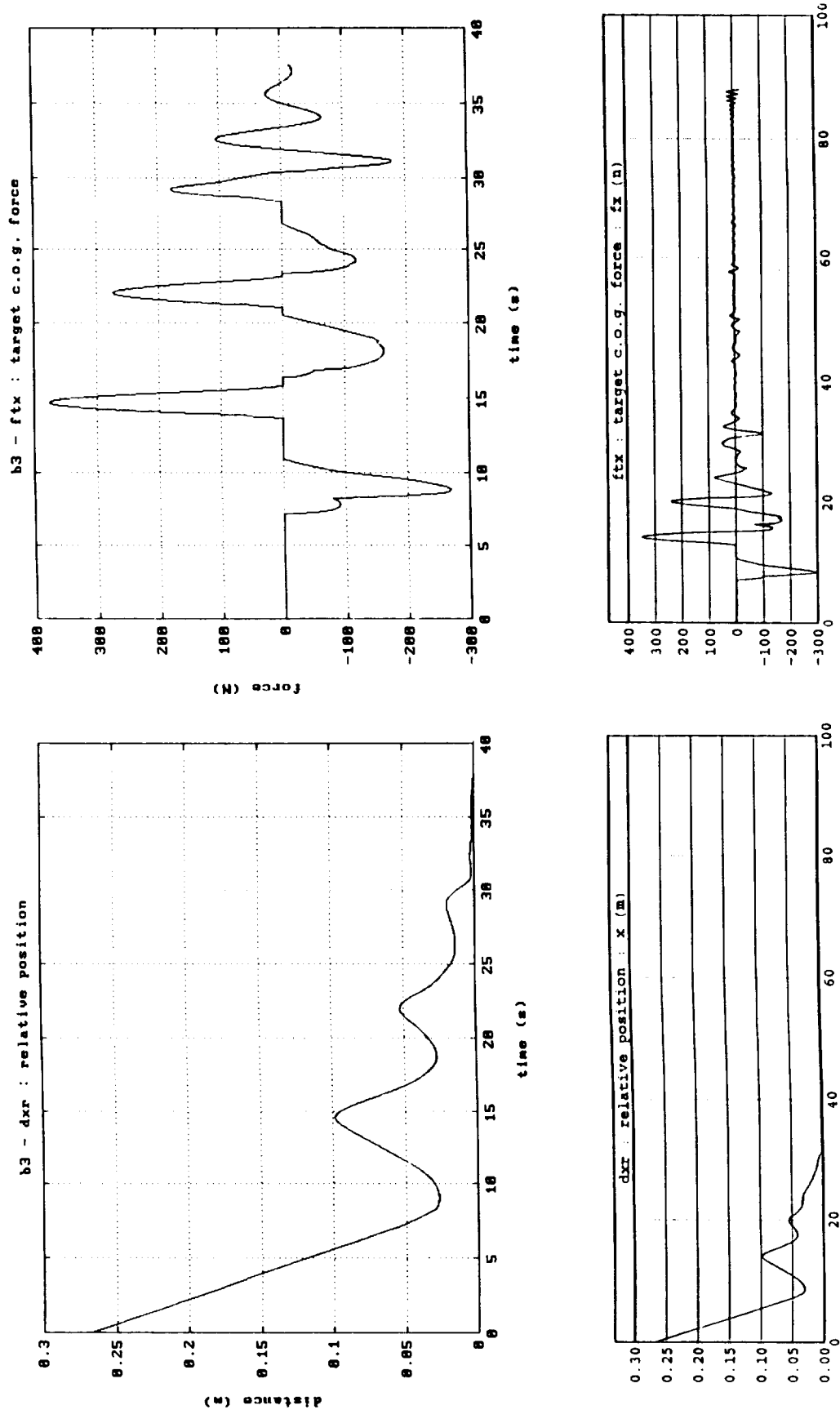


Figure 14. Theoretical results (SENDAP simulations) (top) VS actual results (DDTF simulations) (bottom).

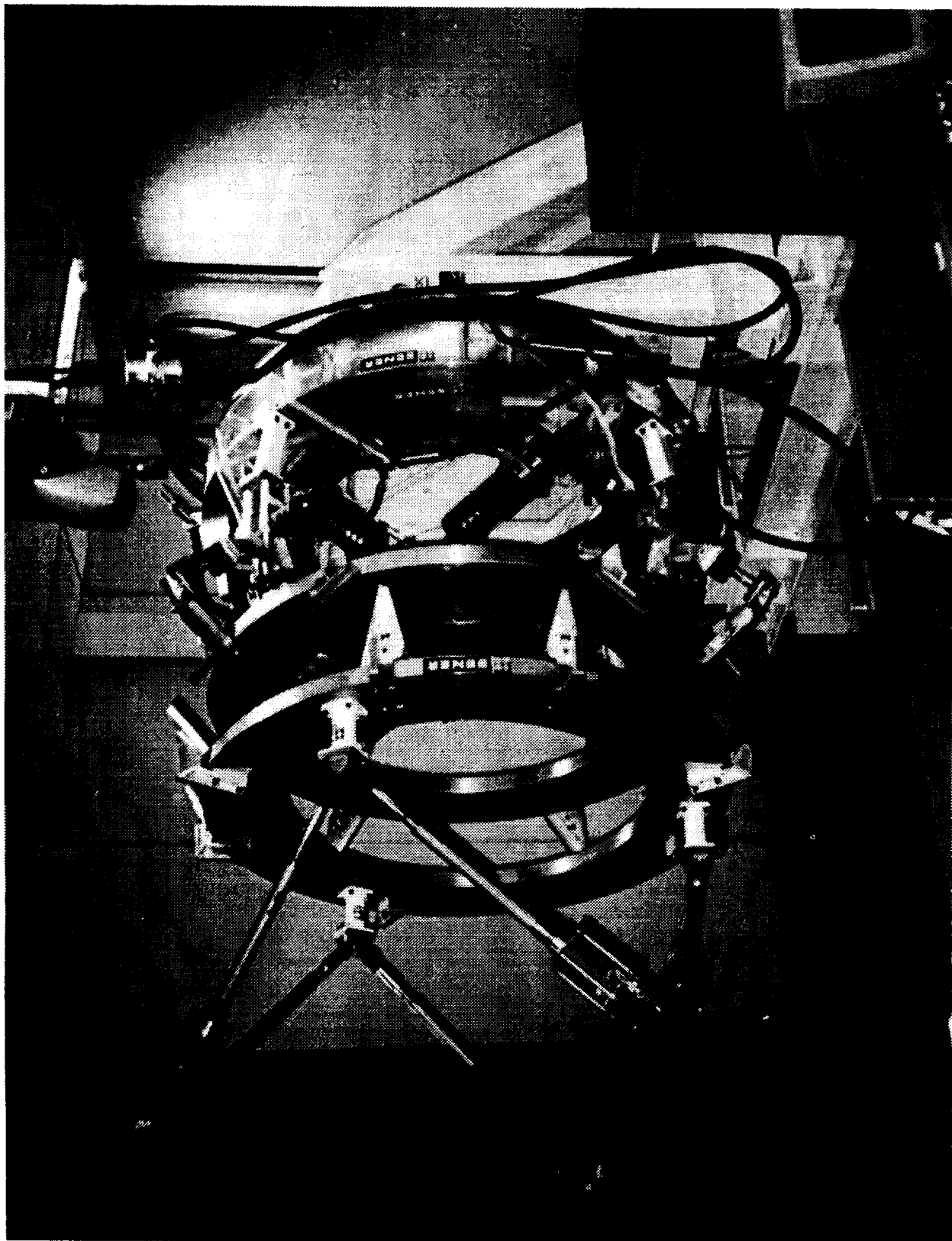


Figure 15. The Docking Mechanism Model on the DDTF.

DESIGN, DEVELOPMENT, AND FABRICATION OF EXTRAVEHICULAR
ACTIVITY TOOLS FOR THE TRANSFER ORBIT STAGE

L.M. Albritton*, J.W. Redmon*, T.R. Tyler*

ABSTRACT

Seven extravehicular activity (EVA) tools and a Tool Carrier have been designed and developed by MSFC in order to provide a two-fault tolerant system for the transfer orbit stage (TOS) shuttle mission. The TOS is an upper stage booster for delivering payloads to orbits higher than the shuttle can achieve. Payloads are required not to endanger the shuttle even after two failures have occurred. The Airborne Support Equipment (ASE), used in restraining and deploying TOS, does not meet this criteria. The seven EVA tools designed will provide the required redundancy with no impact to the TOS hardware.

INTRODUCTION AND BACKGROUND

The TOS system is a shuttle-carried upper stage booster. The TOS system is shown in Figure 1 and consists of the solid rocket motor and the Airborne Support Equipment (ASE) which is the hardware for carrying and deploying the booster from the shuttle bay. To launch TOS, a latch is opened, allowing the forward cradle of the ASE to be rotated open 102 degrees. Then the TOS solid rocket motor is tilted 45 degrees. This allows the TOS booster and the attached satellite to be launched over the top of the shuttle forward bulkhead. Figure 2 shows these operations but as they would be done to restow the TOS satellite. All operations for deploying the TOS booster are accomplished by redundant electromechanical actuators.

In order to be carried as a shuttle payload, a two fault tolerant system is required. This means that the system can tolerate two failures and still not endanger the shuttle. After the TOS hardware had been developed and built, it was realized that the system was not two fault tolerant. The system power was not redundant and a failure of two actuators could prevent the closing of the shuttle doors.

Once the problem was identified, NASA personnel determined that an EVA scenario could be used to provide the extra fault tolerance. This scenario utilized several existing EVA tools but also required the development of new and unique tools. The design of these unique tools was driven

* NASA/Marshall Space Flight Center, Huntsville, AL

by the following:

- 1) The TOS hardware was already built and any changes to the existing hardware would be very expensive. Therefore, the tools were required to operate without modifying the existing TOS hardware.
- 2) The tools were not to be flown in place but installed on -orbit when required. The TOS hardware was already qualified, and adding any new hardware would require requalification. One tool was an exception to this.
- 3) Many requirements were derived and very few load requirements were available. Often, the load requirements that did exist changed significantly after proper analysis and testing became available. Many of the tools were significantly overdesigned because of this and the possibility of future requirement changes.
- 4) The schedule was short in order to meet the required launch date.

TOS EVA TOOLS

Seven EVA tools were designed to support the TOS mission. These tools essentially replaced the main actuators with a manual override. The primary tasks to be accomplished were to disengage the existing electromechanical actuators by pulling their pins, de-tilt the TOS motor and satellite, close the forward cradle of the ASE and relatch the system. Figure 3 shows where the EVA tools would interface the TOS hardware.

Dust Cap Removal Tool: Before pulling the actuator pins, a dust cap must be removed in order to allow access. Figure 4 shows the dust cap removal tool. It operates much the same as a common oil filter wrench does by clamping around the circumference of the cap. However, the tool also provides a rotating tether point and utilizes a flight manifested 1/2-inch-box end wrench.

Pin Puller and Drive Socket: The pin that disengages the actuators and allows free movement of the ASE components is pulled by the EVA Pin Puller shown in Figure 5. The tool is required to retract the pin against a 1200-lb load caused by a 5600-lb side load on the pin. The EVA Pin Puller is composed of a series of threads, two right-handed and one left-handed, and is operated through two hexagonal interfaces. A flight-manifested 3/8 drive ratchet and 7/16 hex socket are required for operation. Also, a 1 1/2 hex socket, not previously available for EVA use, was developed for operation of the EVA Pin Puller. It is outfitted with a special tethering device.

Tilt Bracket: The tilt bracket is shown in Figure 6. This bracket is permanently mounted on the rear skirt of the ASE. It is used as an attachment point for applying a load to de-tilt the TOS motor and satellite. The EVA winch and the

Payload Retention Device (PRD) exist in the EVA tool inventory and are used to apply the de-tilt load. The rear of the tilt bracket has a hinged bracket which is prevented from rotating during launch with quick release pins. The EVA winch is attached to this bracket and is used to control the motion of the de-tilt.

Rotation Device: The Rotation Device, shown in Figure 7, is used to close the forward ASE cradle from full open to within the capture range of the Tension Device. The Rotation Device consists of two brackets that clamp to the upper and lower halves of the ASE and an ACME screw device which provides the method of power transmission.

Tension Actuator and Trunnion Link: The Tension Actuator and Trunnion Link, shown in Figure 8, are used to fully close the forward ASE. Small pads, located on the forward ASE, are compressed around the circumference of the spacecraft and require the Tension Actuator to apply approximately 3800 lbs. Once the pads are compressed and the forward ASE is fully closed, an over-center latch can then be engaged allowing the removal of the Tension Actuator. The Trunnion Link is attached to the Tension Actuator and provides a load path to the bottom cradle trunnion.

A cross section of the Tension Actuator is shown in Figure 9. An input torque is applied by a standard EVA power tool into a 10-to-1 ratio worm gear arrangement. The worm gear rotates a shaft which is supported by a quadraplex set of angular contact ball bearings. The end of the shaft is threaded with ACME threads which transforms the rotational motion to a linear motion. The internal ACME threads are tapped into the end of a spline. This spline acts as an inner race for a linear spline bearing with recirculating balls. The bearing allows the spline to translate in and out but not to rotate. The Trunnion Link is attached by a 3/4-inch quick release pin and only is loaded by a linear force with no torque. This device weighs approximately 60 pounds and can provide a much larger load than the 3800-lb load requirement. This device is overdesigned due to the changing and often uncertain load requirements for the task. The actual load capability is dependent on the friction which will not be known for certain until after testing. However, it is estimated to be approximately 9000 lbs.

Latch Arm Wrench: The Latch Arm Wrench, shown in Figure 10, is used to close the latch which secures the forward ASE. Consisting of a 6-inch octagonal socket and a 3/4 drive ratchet with a 60-inch moment arm, this tool will deliver the 300 ft-lbs of torque required to compress the latch members through the over-center position.

Tool Carrier: Those tools which are too large to be stowed in the middeck lockers are secured during launch and reentry by the TOS EVA Tool Carrier, shown in Figure 11. The four items stowed by the carrier are the Latch Arm Wrench ratchet, the Rotation Device ACME screw device, the Tension Actuator, and the Trunnion Link. The carrier consists of a plate with various brackets designed to cradle the tools and latches (Figure 12) which hold the tools in place. Although each is configured differently, the seven latches are each over-center, spring loaded, and secured with two ball lock pins. One latch per tool is designed to push the tool slightly as the latch is opened. The carrier latches are required to be easy to operate, to still operate after two failures, and to keep the tools secure during the random vibrations of launch and reentry without damaging the tools.

TESTING

In order to validate designs, the tools are required to pass a stringent test program. For each tool, a qualification unit, flight units and flight spares are being built. Mock-ups were also made to support the neutral buoyancy test.

Neutral Buoyancy Test: The neutral buoyancy test simulated a weightless environment and provided a means to test the ergonomic aspects and EVA acceptability of the tools. A full scale payload bay with an ASE mock-up aided in acquiring data on EVA work-sites and tool translations. The test apparatus is shown in Figure 13. Two series of tests were conducted. The first test occurred in October 1990 and evaluated the preliminary concepts for the tools. A second test occurred in August 1991 and evaluated mature designs and also investigated tool translation and foot restraint positions. Two astronauts participated in the tests.

Load Test: The load test ensures that the tools are able to withstand the required loads during the entire mission. All flight and flight back-up tools are required to be subjected to a load 1.2 times the design load. The qualification tools are to be subjected to a load 1.4 times the design load. After inspection, the qualification tools will be loaded to the point of failure. This failure loading is greater than is normally required for flight hardware but will be done to provide some estimate of the tools' capability. This information would be useful if load requirements changed after the tools were qualified.

Thermal Test: The thermal test will subject the tools to temperature ranges exceeding those which will be experienced on orbit. This test will occur at the Johnson Space Center (JSC) in a manned thermal chamber. Loads at 1.0 times the limit loads will be applied to the Tension Actuator

and the Rotation Device screw. Qualification, flight, and flight-spare tools will be subjected to a hot and a cold cycle. The tools will be functionally tested at each extreme. The tool temperature for the cold cycle is below -130 degrees Fahrenheit and the hot cycle is above 185 degrees Fahrenheit.

Vibration Testing: The tools which are carried into orbit in the payload bay require vibration testing. This testing simulates the launch and landing environment and requires the tools to be stowed in their launch configuration on the tool carrier. The tools carried in the middeck locker will not be vibrated. This test will ensure that the tools will still be functional after the severe launch environment.

Offgassing Test: The tools stored in the middeck locker in the habitable areas will undergo an offgassing test to verify that no harmful substances are present.

SUMMARY

Seven EVA tools and their stowage device were designed and developed at MSFC to support the TOS mission. Stringent testing will ensure proper operation of the tools if their use is required on orbit.

This task was initially to be a very informal project with a very short schedule. As the program progressed, however, the importance of the tools determined that the tools were to meet the Class B requirements for space flight hardware. Because of the high visibility of the project and the very short schedule, the program became very success oriented. There was no time to develop engineering models to verify designs. The tools had to be designed right the first time.

In order to minimize mistakes and expedite the development, manufacturing and testing, a management concept called Total Quality Management (TQM) was utilized. The main emphasis of TQM is to involve the appropriate disciplines from the very beginning of the project. This project required involvement from all of the following organizations:

- Design
- Project Office
- Stress
- Materials
- Quality
- Safety
- Manufacturing
- Procurement
- Astronauts Office
- Crew Systems
- Payload Integration

Overall, the tool designs have been well received, with good comments from the Astronaut Office.

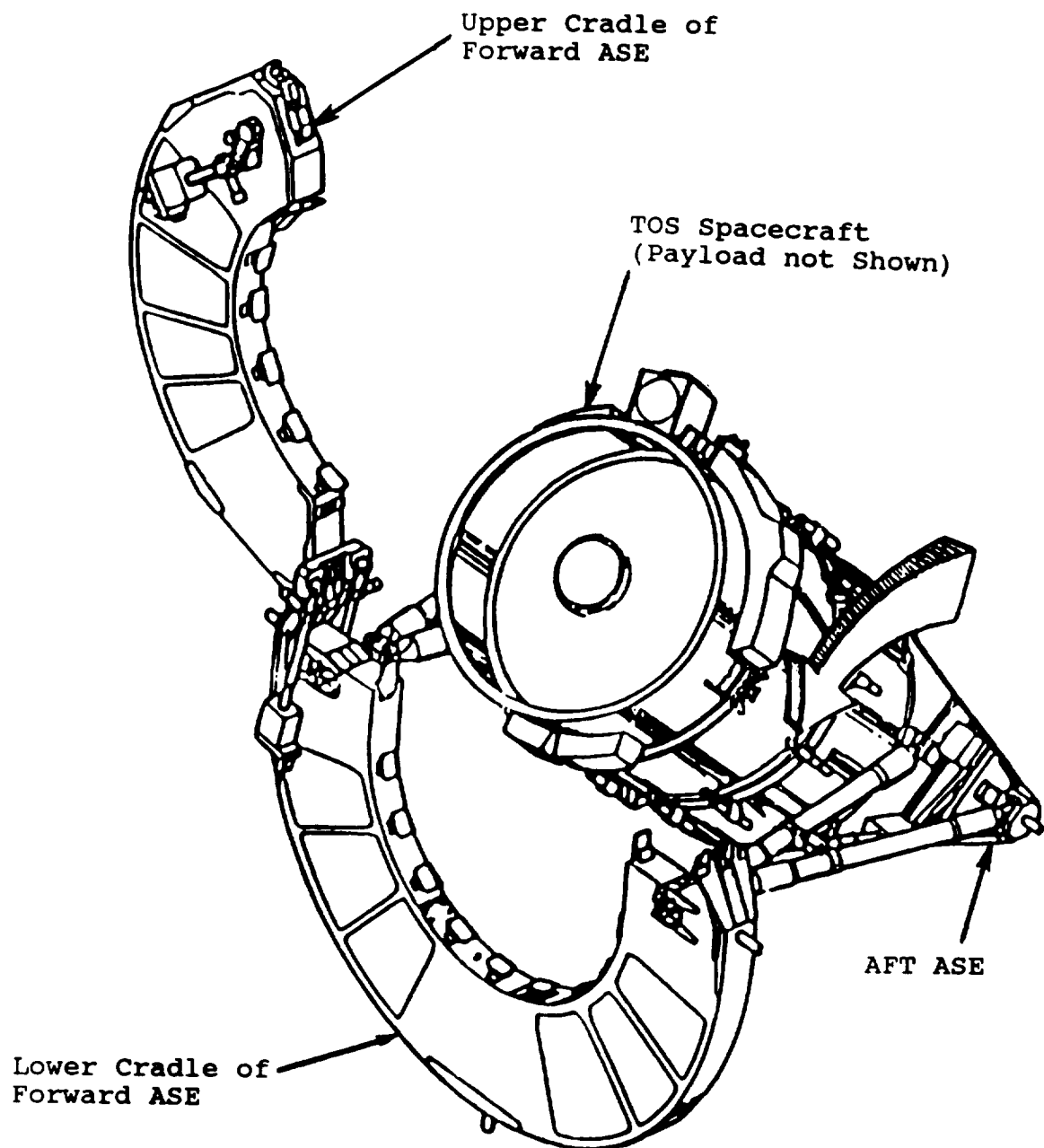


Figure 1: TOS Hardware.

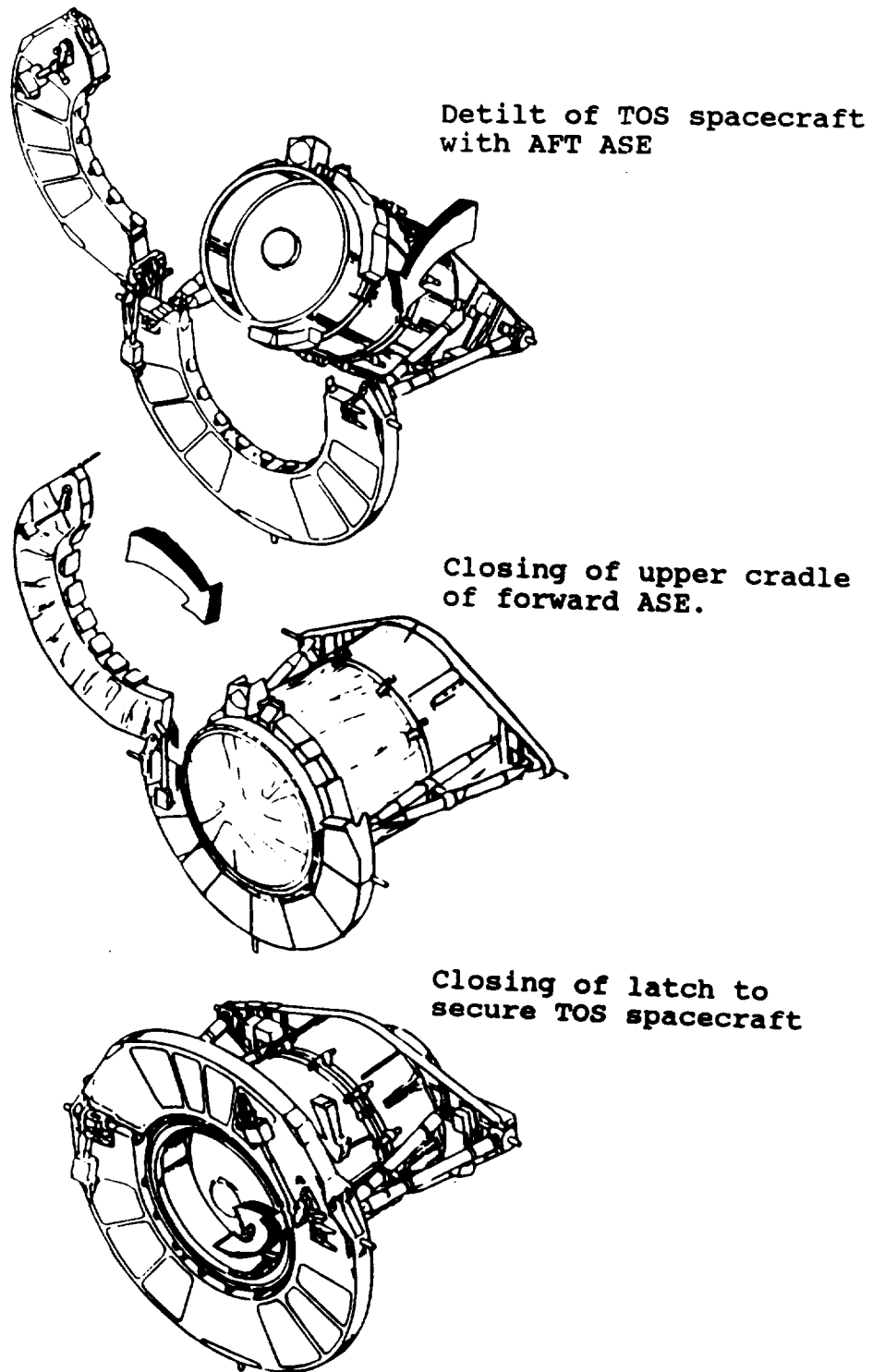


Figure 2: Operations for Stowing TOS Spacecraft.

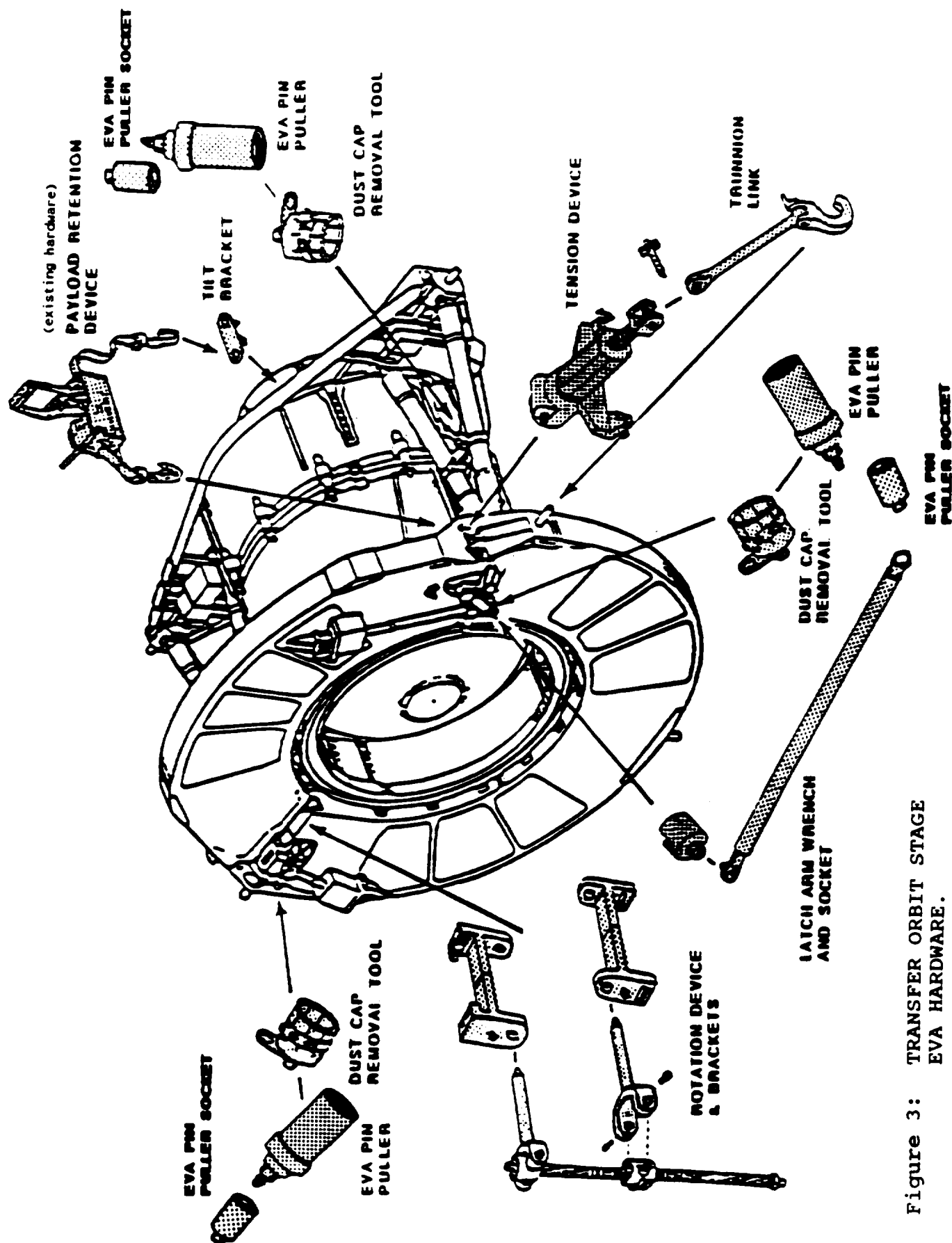


Figure 3: TRANSFER ORBIT STAGE
EVA HARDWARE.

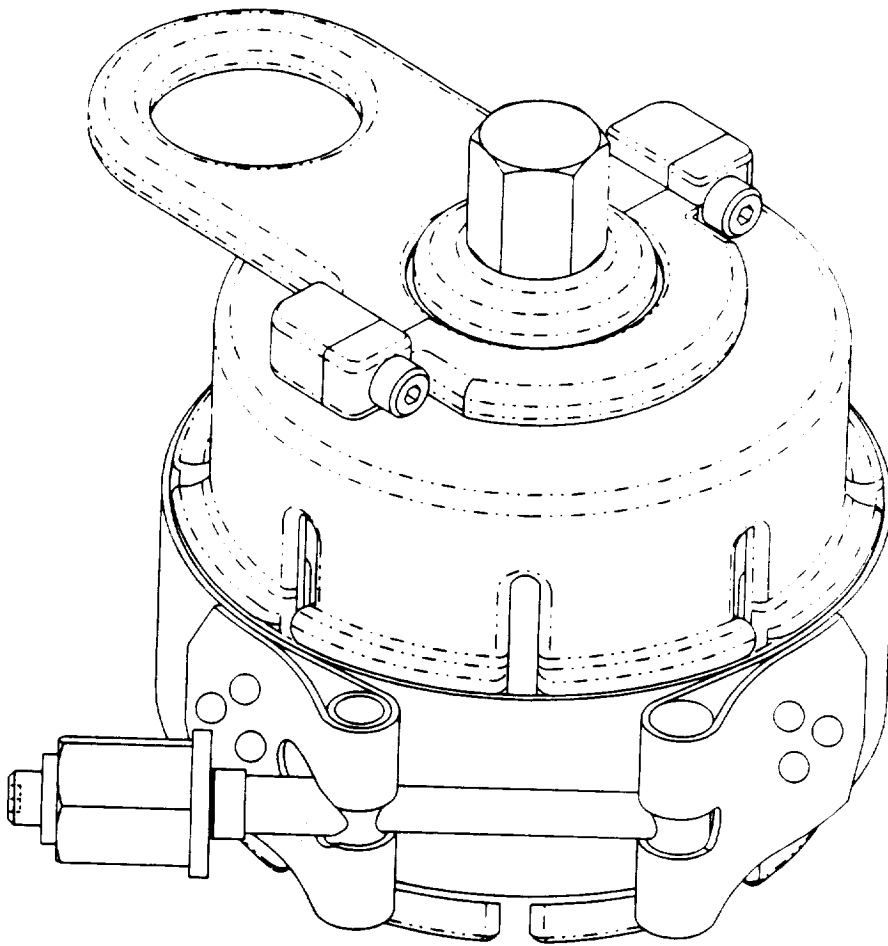


Figure 4: Dust Cap Removal Tool.

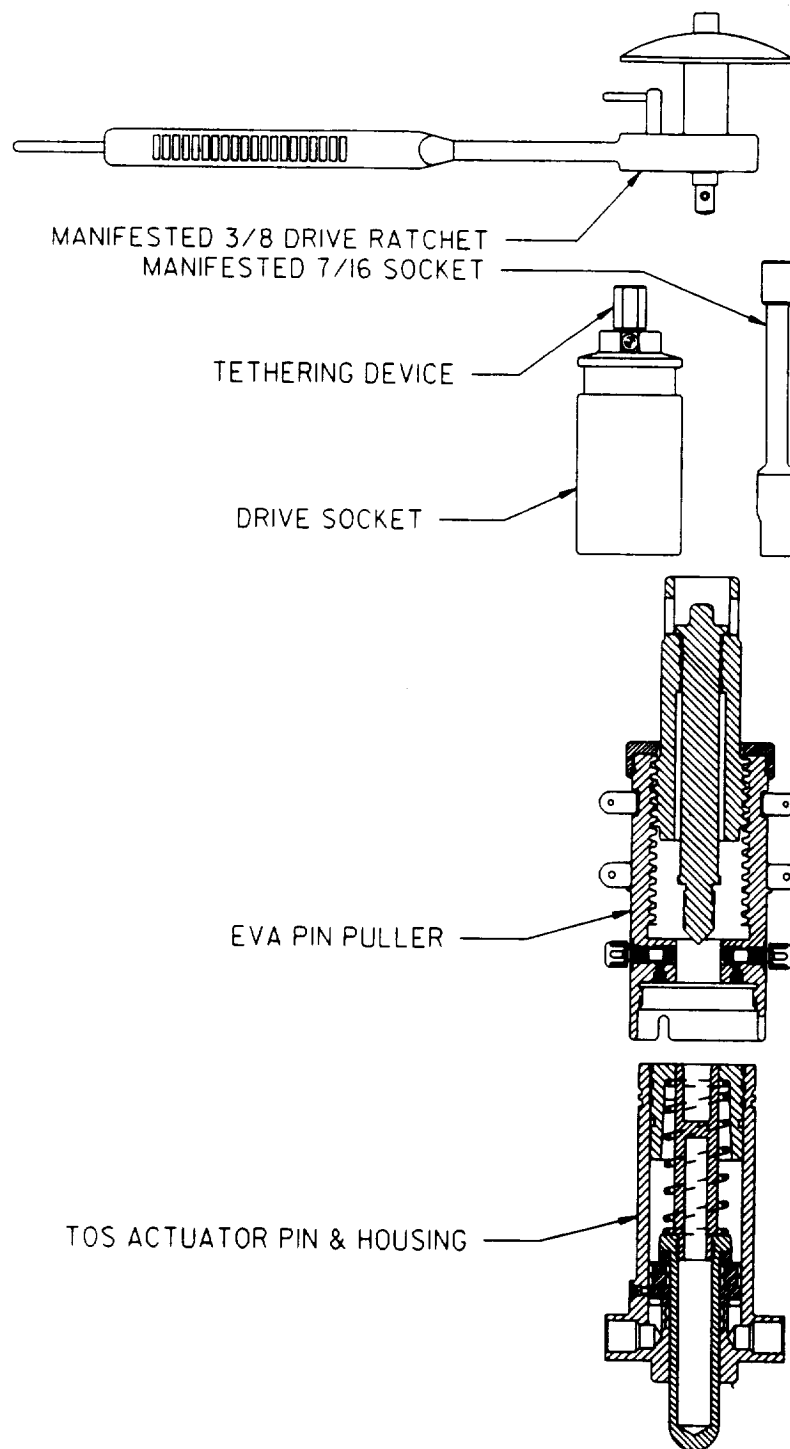


Figure 5: Pin Puller.

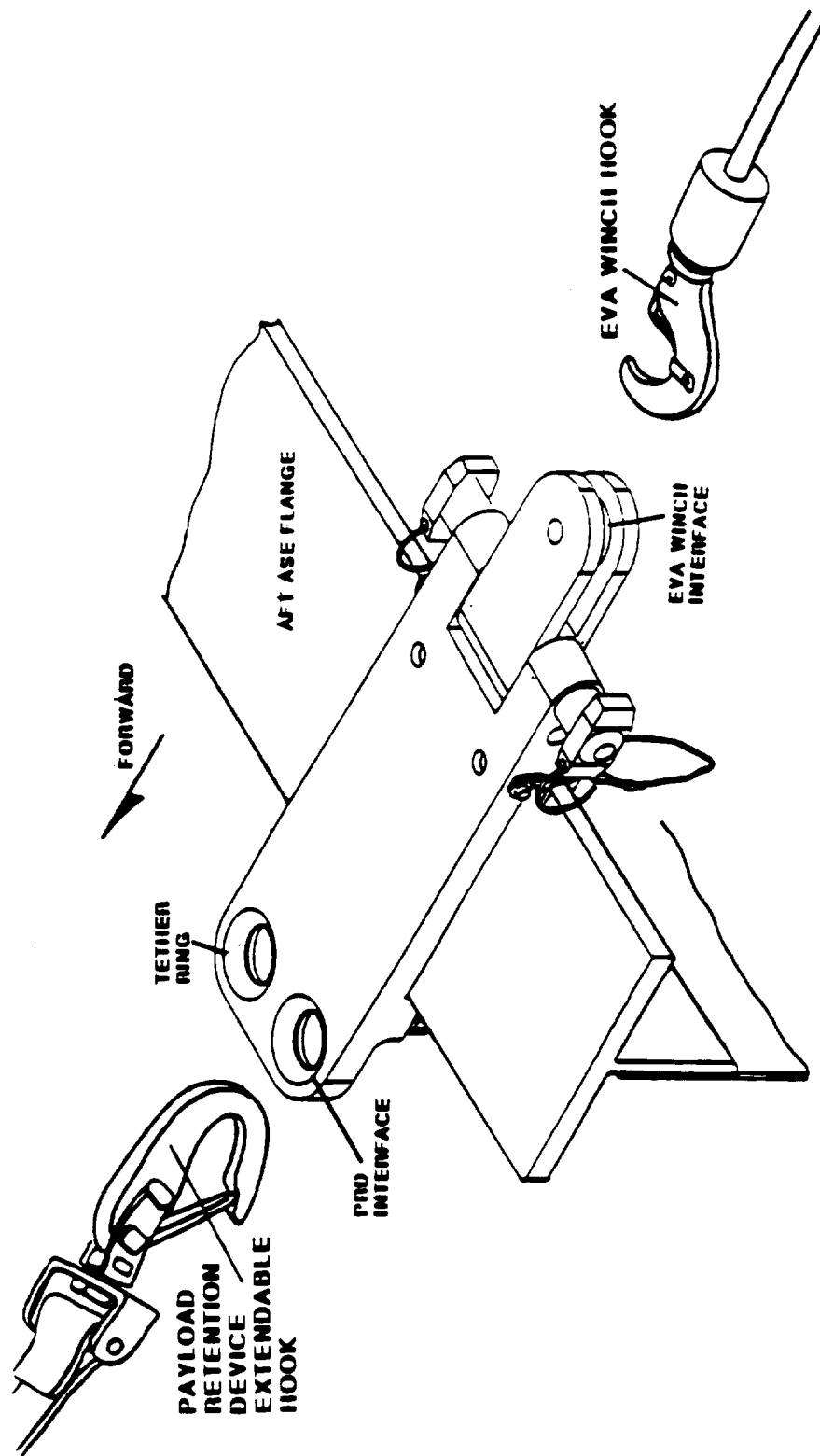


Figure 6: Tilt Bracket.

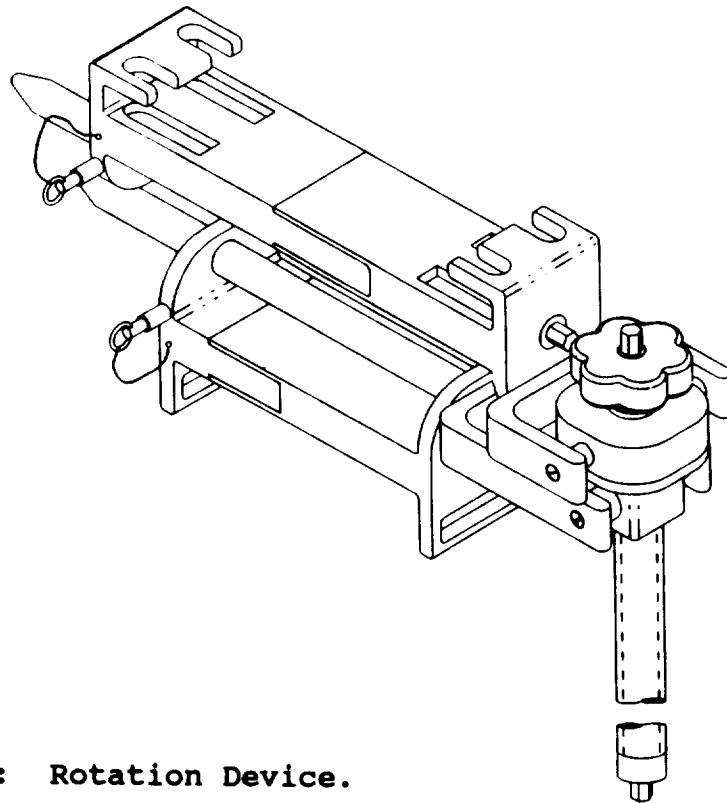


Figure 7: Rotation Device.

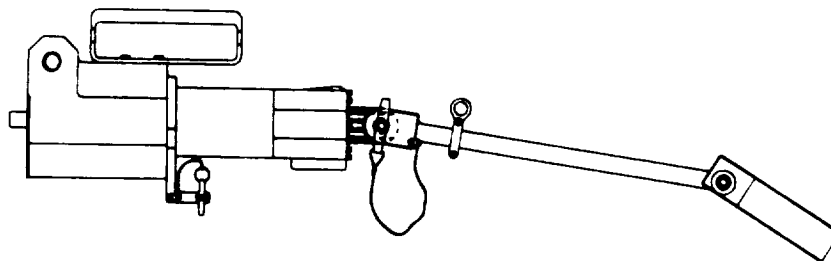


Figure 8: Tension Actuator and Trunnion Link.

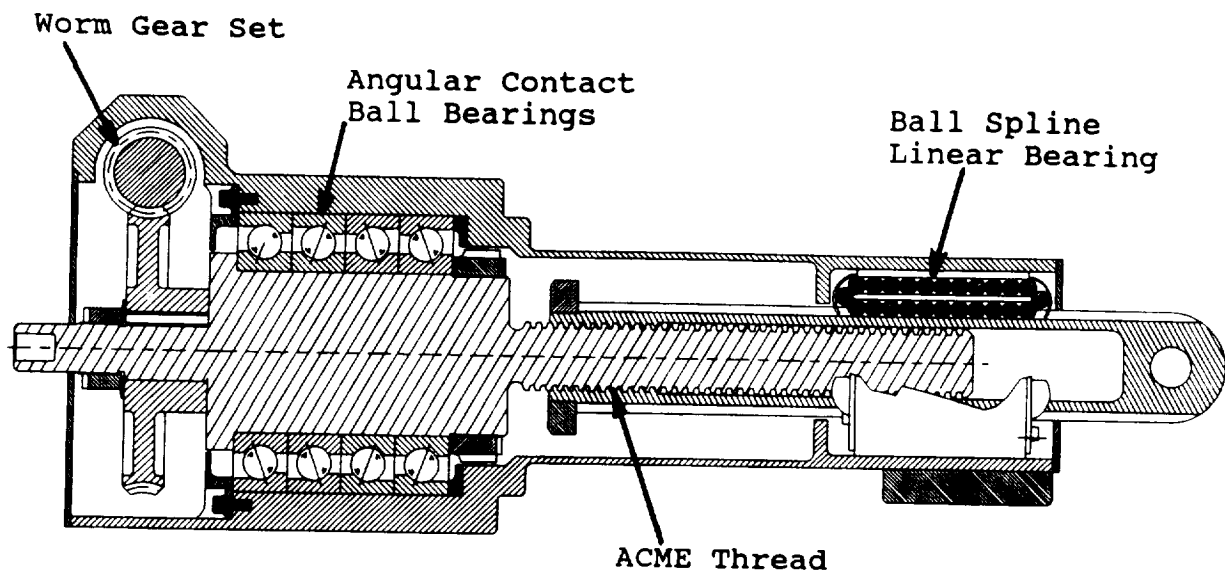


Figure 9: Tension Actuator Cross Section.

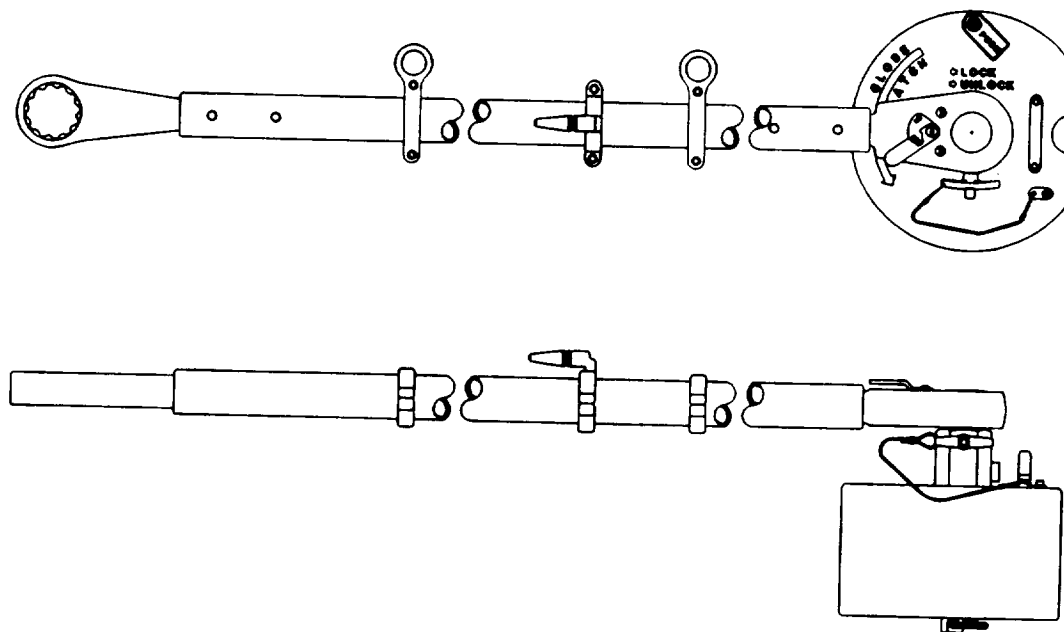


Figure 10: Latch Arm Wrench and Socket.

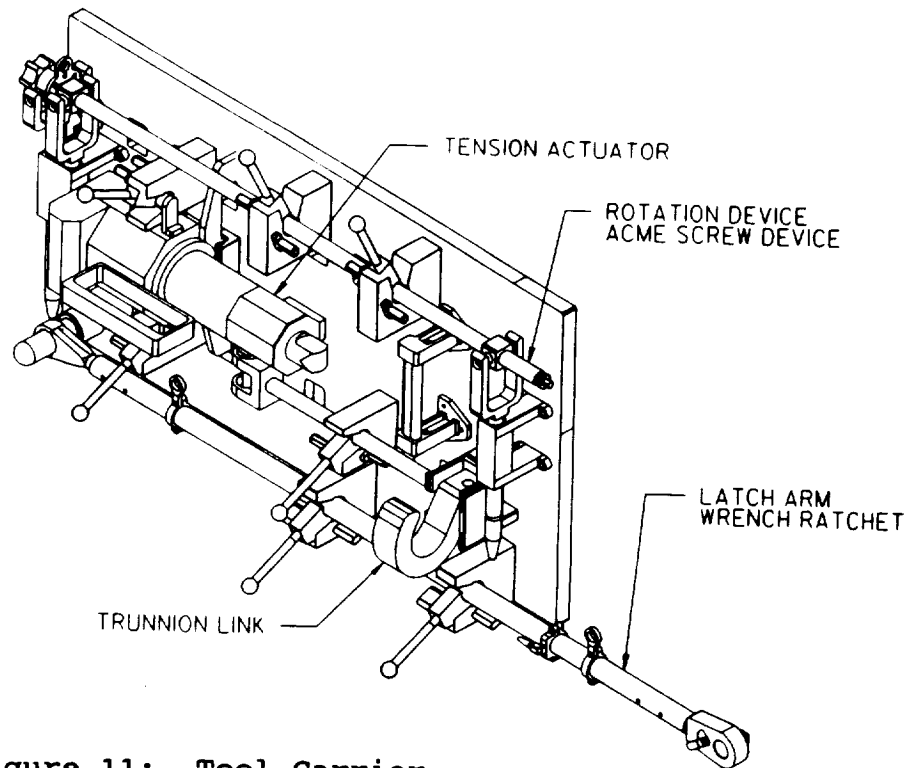


Figure 11: Tool Carrier.

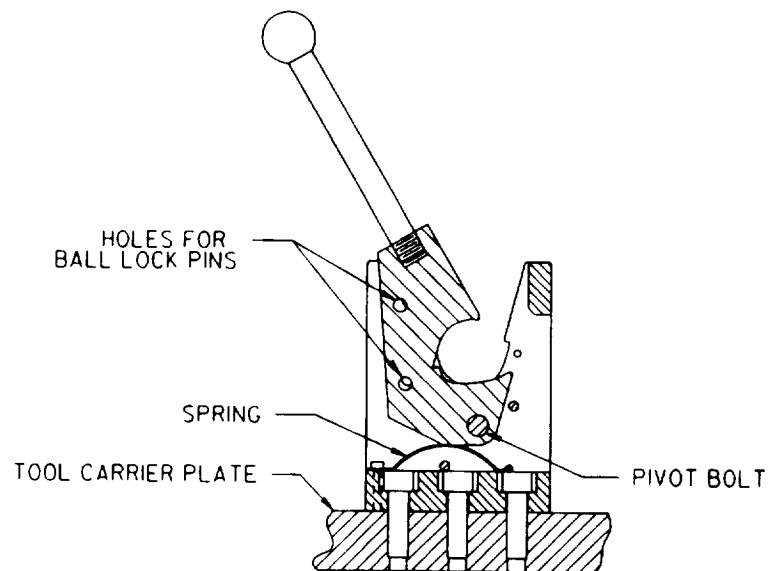


Figure 12: Tool Carrier Latch.

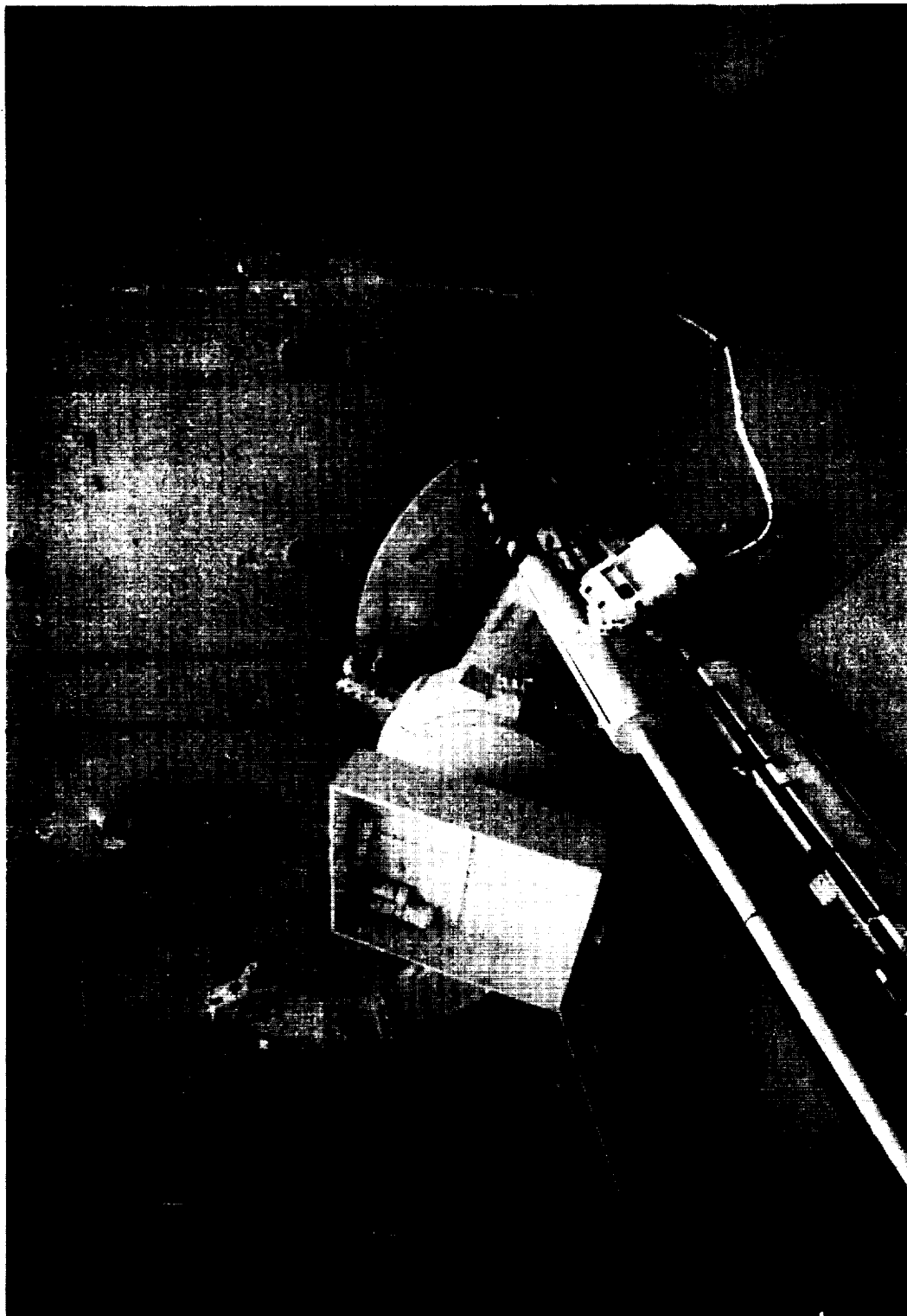


Figure 13: Neutral Buoyancy Test Hardware.

DEVELOPMENT OF A PRECISION, SIX-AXIS LABORATORY DYNAMOMETER

P. J. Champagne,* S. A. Cordova,* M. S. Jacoby,* and K. R. Lorell*

ABSTRACT

This paper describes the design, fabrication, test, and operation of a unique six-axis force/torque dynamometer developed at the Lockheed Palo Alto Research Laboratory. The specimen table used to hold components under test is supported in a full six-axis kinematic mount. Support struts fabricated from high-strength steel with special integral two-axis flexures link the specimen table to the load cell transducers. Realtime force/torque coordinate transform, rms calculation and data averaging, and color six-axis display with controllable scaling are provided by a specially programmed desktop computer. The extensive structural analysis and design optimization required to obtain a stiff, well-damped, lightweight structure is described in detail. Geometric optimization of the kinematic mount and fabrication details of the struts are also described.

INTRODUCTION

Miniaturized linear-drive Stirling cycle cryocoolers designed with noncontacting parts are ideal for long-life cryogenic cooling on board a wide range of spacecraft. They consume little power, have an almost indefinite operational life, and require no expensive ground handling equipment or procedures. A major problem in using these cryocoolers with sensitive focal plane instruments is the vibration induced by the reciprocating motion of internal motor/suspension components in both the compressor and expander. The development of a Stirling cryocooler system optimized for minimal residual vibration has been a major goal at the Lockheed Palo Alto Research Laboratory.

Instrumentation capable of measuring a wide spectrum of vibration sources associated with Stirling cryocooler operation had to be developed as part of this program. Requirements for this vibration measurement system included the ability to measure six degrees of freedom simultaneously, resolution to better than 0.004 N (0.001 lb) with a dynamic range of at least 10^4 , continuous monitoring and display of root mean square (rms) forces and torques, structural stiffness so that vibration modes in excess of 300 Hz could be measured, and a load-carrying capacity sized to hold a complete cryocooler (approximately 7 kg). In addition, the measurement device had to have substantial seismic isolation from the laboratory environment so that millipound-level forces would not be overwhelmed by background noise.

Description of Stirling Cryocoolers

A split-cycle Stirling cryocooler consists of three main components: a compressor which provides a pressure pulse to the helium working fluid, a regenerator/cold finger in which heat is exchanged between the actual device being cooled and the cooler working fluid, and an electronic control system which provides the drive signals to the compressor and regenerator. Figure 1, a cutaway drawing of the refrigerator mechanical components, shows the linear drive motors used to power the compressor and regenerator, as well as details of the cold finger and transfer tube which connect the two units. The schematic of a refrigerator system in Figure 2 shows all three components connected.

* Lockheed Palo Alto Research Laboratory

The Problem of Vibration

The compressor and expander operate using reciprocating motions of their internal components: the piston in the case of the compressor and the stack of gauze screens inside the cold finger in the case of the expander. Inertial forces generated by the motion of these masses can be as large as 60–70 N in the compressor and about an order of magnitude lower in the expander.

Cancellation of induced vibration requires that the sum of the inertial forces generated by the motion of the reciprocating masses in the compressor and expander be as close to zero as possible. In typical cryocooler systems currently under development at Lockheed, the inertial forces are cancelled by using dual mechanisms mounted so that the motions of their moving components oppose each other. Compressors are mounted back-to-back; expanders are either mounted back-to-back (in a dual refrigerator system), or a single expander has an integrally mounted active balancer. The motions of the moving components are precisely controlled using a custom electronic control system developed at Lockheed to minimize induced vibration (Ref. 1).

Need for a Dynamometer

The residual vibration levels achieved using Lockheed's electronic cryocooler control system combined with the mechanical arrangement described above are extremely small. Typical levels for back-to-back compressors operating with a 4-mm stroke are below 0.02 N at the drive frequency (usually about 50 Hz). Harmonics of the drive frequency, often as high as 1.5 kHz, may still have small amounts of energy, and thus are important to observe and measure. In addition, as part of the baseline measurement for a force cancellation control system, it is important to know the uncompensated forces being generated by a single compressor or expander. These forces may be as high as 60 or 70 N.

The electronic force cancellation techniques only apply to the axial forces generated by the cryocooler. Lateral forces and torques are also of interest, especially since the only means of controlling them is through the careful balancing and alignment of the two opposing coolers. Should two compressors, for example, be either noncoaxial or noncoaligned, the resulting forces and torques could easily exceed the residual achieved for the actively controlled axial forces.

In order to effectively measure the performance of the active force cancellation system as well as ascertain how well the system has been aligned and balanced, some type of realtime multiaxis force measuring system must be used. This system must have sufficient dynamic range to measure both the compensated and uncompensated force levels, and must have an unimpaired frequency response sufficient to observe harmonics out to at least 300 Hz, and, ideally, as high as 1.5 kHz. The instrument developed for this purpose is a precision six-axis dynamometer utilizing special mechanical and electronic hardware, as well as software custom-developed to measure and display the forces and torques generated by cryocoolers.

REQUIREMENTS

Approach

The two common approaches to characterizing the vibration forces produced by oscillating machinery are indirect, using accelerometers, and direct, with force transducers.

The *indirect approach* is to measure the accelerations that are a result of internally generated forces. This is done with accelerometers and requires that the specimen be suspended without mechanical restraints. The unrestrained suspension is usually approximated by mounting the specimen on soft springs and providing generous service loops for the connecting cables. This approach requires minimal fixturing and excels in higher frequency measurements where all structures appear relatively flexible. However, it is indirect, and requires the mathematical transformation

$$F = M * A$$

to convert the measured acceleration values to the desired force values. This transformation depends not only on the accuracy of the acceleration value, but also the mass—which is another measured value. In addition, the correct mass value to measure is obscured by the fact that in complex machinery, portions of the total mass are in relative motion during operation.

The *direct approach*, called a dynamometer, directly measures the reaction forces produced. This approach uses load cells and requires a rigid suspension of the specimen. Since in reality, no structure or force measuring transducer is perfectly rigid, this approach is limited to measuring relatively lower frequencies. It has the advantage, however, of measuring the desired value directly and is not dependent on a theoretical transformation or the measurement of any other variable.

For the purposes of accurately characterizing cryocoolers, the direct, dynamometer approach was deemed best. This is due to the relatively low operating frequency of the reciprocating mechanisms, the requirement for connecting cables and pipes, and the ambiguity in the determination of the exact effective mass.

Design Goals

The basis of a dynamometer, simply put, is to rigidly suspend the specimen from an immovable mass base and then measure the forces induced in the connecting structure during operation. Even minute motions of either the specimen or the base invalidate the measurement since some of the vibrational energy will be absorbed by the acceleration of the masses instead of being transmitted by the structure. Of course, in the real world no mass is truly immovable, and no structure is truly rigid. The design goal of the dynamometer is to approximate this ideal closely enough for the desired measurements to be valid.

In order to obtain true simultaneous/independent six-axis measurements, six separate single-axis transducers are used. Each transducer has to be incorporated in such a way that it is subjected to a unique and purely axial load. This requires a true kinematic (statically determinate) structure. Transverse and torsional loads on the transducer would corrupt the measurements by producing unpredictable results, since single-axis transducers are calibrated to pure axial loads.

These requirements led to the basis of the dynamometer design. This design features a test specimen mounted on a platform or table, which is suspended from a large mass via six struts resting on six load cells.

SYSTEM DESCRIPTION

Mechanics

Architecture. Once the determination was made to develop a six-strut dynamometer, the next step was to determine the architecture of the structure. The objective was to achieve the highest possible structural rigidity.

Several configurations of six-strut geometries were considered. Conventional orthogonal, radial, and tangential geometries (see Figure 3) have been used in similar systems, such as the cryocooler dynamometer built by JPL (Ref. 2). Each of these has its advantages and all are capable of full six-axis measurements. However, experience has shown that system structural rigidity with no natural vibration modes below 600 Hz is difficult to achieve. This is because most structural components, while relatively stiff in axial loading, are weaker in bending. The conventional structures studied support the specimen table above the base on three primary vertical struts, with the remaining three struts oriented horizontally in various arrangements. This results in the need for some kind of vertical structure on which to anchor the horizontal struts. The horizontal loading of this vertical structure results in bending loads—and bending loads compromise the rigidity of the system.

To overcome this problem, a new approach was sought. The unique hexapod architecture of the Lockheed dynamometer is the result of this search. The hexapod architecture (Figure 4) supports a triangular specimen table at three points. Each support point has a set of struts at matching angles to the base and approximately perpendicular to each other. Each strut terminates in an axial transducer at its base. The hardware design resulting from this architecture is shown in Figure 5.

While this hexapod design uses the same six struts as in convention designs, it has them oriented in an axisymmetric arrangement in which each strut is a straight load path from the specimen table directly to the seismic mass base. With this configuration, there is no vertical structure and therefore none of the inherent bending and flexibility associated with it.

Although not as readily obvious as the conventional geometries, the hexapod configuration is a true stable kinematic structure in which there are no indeterminate load paths. Therefore, the outputs of the six load cells represent six independent degrees of freedom. As a by-product of this fact, there are no adjustments necessary during assembly (other than the inherent minor pivoting of the strut joints) to allow for tolerance variations in the components.

Because the hexapod struts are not in a conventional arrangement, they do not directly read forces and torques in a conventional (orthogonal or polar) coordinate system. Vibration force and torque requirements and specifications are usually stated with reference to an orthogonal coordinate system. Some means of coordinate transformation is necessary in order for the hexapod-based measurements to be readily understood. The solution chosen is to perform this transformation electronically on the transducer signals before they are viewed or analyzed. The analog electronics designed into the system are capable of transforming the load cell outputs, in real time, into the conventional orthogonal force and torque vectors. In this way, a superior mechanical design is obtained while maintaining simplicity in the available output data.

Seismic Mass. The base on which the hexapod is mounted must be stable and have a mass large enough that any reaction to the vibrational forces of the test specimen is negligible. Granite was chosen as the material for this base because of its density, inherent stability, and freedom from magnetic interactions, as well as its availability and relatively low cost. The size of the granite block was set to obtain an effective weight of approximately 1400 kg (3000 lb) and yet be able to fit through standard door openings. The proportions are close enough to square that flexibility of the block itself is not an issue.

The block is supported on pneumatic mounts to isolate it from ambient vibrations transmitted through the floor. The mounting system has a very low natural frequency (approximately 1 Hz) and thus effectively eliminates the introduction of background noise into the measurements. The suspension system has been included as an integral part of a wheeled cart which allows for ease of installation and relocation.

Transducer. The selection of the single-axis transducers was driven by the requirement for high sensitivity and high rigidity. Strain-gage-type transducers in the high-sensitivity ranges were found to require relatively large amounts of axial motion and were quickly eliminated as viable choices. Piezo-electric transducers are quite rigid, even in the high-sensitivity ranges, and were the obvious choice. The fact that they are based on a capacitive effect, and thus not capable of true static measurements, was not a problem, since frequencies below 1 Hz were not of interest.

Because load cells in the highest sensitivity range are susceptible to damage from shock overloads, an alternative support structure was included in the design. This structure can support the specimen table independent of the load cells and thus protect them from such excessive loads as might occur during installation and setup of large test specimens. To use this feature, the specimen table is unbolted from the three strut yokes and lowered onto the three hard stop brackets shown in Figure 6. Alignment holes and removeable pins are provided at each yoke for ease of reassembly when testing is to begin.

Strut. Besides elevating the specimen table to a height which can accommodate the intended specimen at its approximate center of mass, the purpose of the struts is to transmit pure axial loads to the single-axis transducers. The struts must be perfectly rigid and yet function as if connected by a frictionless ball joint at each end. Such struts may exist in theory, but in reality, only functional approximations can be achieved. In this case, a specialized form flexure-ended struts was devised.

The joints at the end of the struts turned out to be one of the most critical areas of the entire design. The joint must be free to rotate, as would a ball-joint connection, at the same time it cannot have any of the friction or play associated with typical hardware. It also cannot possess any of the minor irregularities of an antifriction bearing (such as sleeve or ball bearings). Fortunately, in a rigid dynamometer application, the range of actual rotation required of the joint is extremely small. This leads to the selection of a flexure-type joint. Flexures are inherently free of irregularities of motion and, because of the small motions required, can be designed to be flexible enough to limit the amount of moment transmitted by the strut.

The flexures implemented in the Lockheed dynamometer are a specialized form of integral, cross-linked, single-axis bending elements. Each end of each strut rod is relieved by a narrow slit from both sides until only a small neck-downed portion of the rod remains. This is done at two closely spaced locations such that the bending elements are mutually perpendicular and close to the strut ends (see Figure 7). Each bending element acts as a flex point in

a single axis. The combination of both elements approximates the two-axis motions of a universal or ball joint. The fact that the bending element is an integral part of the strut rod eliminates the need for extra parts and connections.

The technique used to form the flexure area has been devised to give maximum axial stiffness while maintaining close control over flexural stiffness and material stresses. The very short bending element allows the flexures to be located close to the strut ends and limits the inherent reduction in axial stiffness to a small area. In addition, the geometry of the relief is carefully selected to act as an integral stop to limit motions of the flexure so that the yield strength of the material is never exceeded (see Figure 8).

Specimen Table. The goal of the specimen table design is to connect the specimen to the struts with minimum flexibility. The table was shaped to accommodate the mounting of a typical cryocooler component. It has a large hole in the center to allow location of the specimen at the apex of the struts and to provide easy access from both top and bottom for connecting cables. The table structure is analogous to a triangular bridge between three support points. In order to achieve the performance goals of the dynamometer, the material and design of the table were selected to optimize stiffness and reduce weight. This was accomplished through the use of extensive computer modeling and resulted in a one-piece design, deeply pocketed to form the intricate triangulated rib structure shown in Figure 9.

Electronics

The electronics for the dynamometer are shown schematically in Figure 10. The six load cells are connected to charge amplifiers whose outputs are then fed to both the analog electronics and the analog-to-digital converters in the PC. The electronics have a dual function. First, they enable the direct measurement of the load cell outputs and provide an analog coordinate transform so that high-bandwidth force/torque measurements may be made using monitor points on the front panel. Second, the electronics provide an interface for the PC used to compute and display the forces and torques. In addition, the PC has, as part of its software, a realtime coordinate transform algorithm, so it could be used independently to determine the six forces and torques. However, because of limitations inherent in the PC's ability to sample analog signals and rapidly compute the coordinate transformation, do the correct scaling, and generate the display, the bandwidth of the PC data is limited to below 300 Hz, and therefore the software transform is generally not used.

Software

Analog voltages from the six load cells are converted to digital signals for processing and display as force and moment values. A flexible data processing scheme is implemented via a CRT display and user interface.

The load cells at each of the six legs of the dynamometer produce output voltages which are proportional to the loads measured. These signals are digitized through an analog-to-digital converter built into the computer. Since each load cell has its own scale factor (volts output per Newton input), the input signals must be normalized before further computation. The normalization may be done by using an analog circuit or by enabling the normalization option in the software. Once this is done, the numbers exist as an input vector of forces in the dynamometer coordinate frame, and must be transformed into a vector of forces and torques in an orthogonal frame whose origin is located along the axis of symmetry of the unit(s) being tested. The transformation requires a matrix multiplication of the 6×6 coordinate transform matrix by the 6×1 input vector of forces. The result is the desired 6×1

output vector containing the forces and torques. Processing continues with a digitally implemented notch filter used to minimize structural resonance in the dynamometer. The rms of the data is calculated, and a running data average is performed with a user-specifiable number of data points to average. The rms and data averaging computations provide a smoothed output signal appropriate for display. Data processing options are independent of each other and may be performed in any combination.

The timer chip on the analog-to-digital converter board is used to implement the timing scheme of the software. Since the bandwidth of the computed data is a direct function of how fast these functions can be executed, it is critical that the computer be able to at least sample the data and perform the rms computation at approximately 1 kHz. At this sample rate, the effective bandwidth of the data is between 300 and 500 Hz. In order to accommodate the relatively slow computational speed of the 80386DX microprocessor, the data is taken in a lump, with 20 ms allocated for this task. The actual time required for this task is determined in the software after the user decides on a desired sample frequency. Twenty ms is more than enough time to accomplish the data acquisition. Note that raw data could be displayed real time using the 80386DX. However, the 6×6 matrix multiplication for the coordinate transformation is the main contributor to the speed limitation of the data processing portion of the software. Thus, the data processing is done independently of the data acquisition. For example, 250 data points are currently being acquired at a 1-kHz sample rate and stored in the computer's far memory. The software starts processing the stored data 20 ms after it first began the data acquisition. Data processing occurs at whatever speed the 80386DX can accommodate. The processed data is then displayed on the screen at two different rates.

Figure 11 is a black-and-white version of the color display screen. The force and moment values are displayed on their respective orthogonal coordinate axes at a speed which is microprocessor limited. The tabulated force and moment data is displayed at a slower rate of 1 Hz to enable the user to easily read the constantly changing values. When 100 ms has elapsed from the initial start of data acquisition, another chunk of data is acquired at the user-specified sample frequency. Raw data, which is constantly being stored in the computer's far memory, is dumped to a file on user command. Data storage is the only program mode that inhibits the display of the data. All other switches between program modes are done without affecting the validity of the incoming data or the constantly updated display.

STRUCTURAL OPTIMIZATION

The dynamometer is intended to measure cryocooler residual vibration levels not only at its operating frequency, but also through the higher harmonic frequencies. In order to measure these harmonics with confidence, vibrations in the dynamometer itself must interfere as little as possible with the residual vibrations generated by the specimen cryocooler. This means that the lowest vibration mode of the dynamometer should occur at the highest possible frequency. This is accomplished by optimizing support strut geometry, maximizing the bending and torsional stiffnesses of the specimen table while minimizing the specimen table weight, and maximizing the axial stiffness of the support struts.

Geometry

Structural design analysis started with the overall dynamometer geometry. To help determine the optimal design, Lockheed's DEWAR design code (Ref. 3) was utilized. DEWAR is an existing software program originally developed for the analysis of stored cryogen-type coolers. It performs automated thermal optimization of cryogenic support

systems that use discrete supports with *pinned ends* and have specific structural performance goals, such as frequency, clearance, support system material allowables, etc. These structures typically use axisymmetric shell structures in conjunction with stiffening rings to hold large amounts of cryogenic fluids or solids, which provide the required cooling to instruments or optics. These large shell structures are, in turn, supported within a vacuum shell by struts or straps. The structural analyzer within the DEWAR code uses analytical descriptions of shell behavior and simplified numerical procedures describing ring-shell interactions to determine the structural performance of a given design. Thermal optimization is achieved by changing various structural design parameters, such as support thicknesses and winding angles (in the case of struts constructed of composite materials), strut attachment points on the dewar and vacuum shell, etc., until minimum thermal conductance of the overall support system is obtained.

For the dynamometer, thermal conductance of the support system is not a design consideration. However, by fixing the strut thickness (and strut *unit* axial stiffness) in conjunction with a specified minimum frequency, DEWAR can be forced to optimize support system geometry parameters only.

The lowest natural frequency of the dynamometer will occur during testing of the largest supported mass and/or configuration mass moments of inertia. For purposes of this analysis the supported mass includes struts, specimen table and associated bracketry, and the specimen itself. Accordingly, estimates of mass properties corresponding to the testing of a cryocooler compressor pair (approximately 7 kg) oriented vertically with respect to the granite base support were used.

After using DEWAR to experiment with various geometry variables, the optimal ascension angle of the struts, γ , was determined to be 35° . Accounting for clearance and assembly constraints, the final azimuthal angle θ is 90° . At the specimen table, this combination of geometric parameters places the center of the strut pairs at the center of mass of the supported specimen (see Figure 12), eliminating the component of force associated with moments about the horizontal axes.

Once the geometry was optimized, it was left to optimize the stiffness of the various components of the structure. This was accomplished through the use of finite-element modeling.

Finite-Element Model

In order to maximize the bending and torsional stiffnesses of the specimen table, a detailed finite-element model of the entire dynamometer hexapod structure was constructed, including a specimen mass equivalent to a cryocooler compressor pair. In the physical case, the struts are rigidly attached to the specimen table yokes and to stainless-steel fixtures at the granite base. Since the struts contain integral flexures designed to reduce the bending stiffness of the struts, they were approximated in the model as simple bars with an axial stiffness (EA) of 4.45×10^6 N and pinned ends. The specimen table yokes are ribbed to reduce weight and to provide access to the strut attachment fasteners. For simplicity, these were approximated in the model as solid structures of reduced density. This approximation in the model leads to predicted system frequencies slightly higher than those measured due to the neglect of the softer bending stiffnesses associated with the ribbed structure.

The compressors were modeled as cylindrical solids having the correct mass and moments of inertia and were attached to the specimen table through extremely thick shell

elements. These approximations may artificially stiffen the specimen table somewhat. As a consequence of these approximations, the model overpredicts system frequencies. However, the intent of the model is to assess the impact of detailed design and material alternatives on the bending and torsional stiffnesses of the specimen table. Therefore, it is the *difference* in predicted system frequencies between design alternatives that is important in the specimen table optimization.

The finite-element model is shown in Figure 13. Examples of the modes of vibration that were predicted are shown in Figure 13a-d. Lockheed's DIAL finite-element analysis package was used, and was run on a Digital Equipment Corporation DEC 5000/200 workstation. The finite elements chosen had quadratic displacement functions; 8-node shell, 3-node bar, and 20-node solid elements were used. The model contained 240 shell elements, 6 bar elements, and 60 solid elements, for a total of 4503 degrees-of-freedom.

Specimen Table and Strut Yokes. Material and thickness alternatives for the specimen table and yokes were assessed by computing the primary natural frequencies of the whole system. Candidate materials for the specimen table were stainless steel and magnesium. Both materials have approximately the same ratio of elastic modulus to density ($E/\rho = 10^8$), but magnesium has a lower density; therefore a magnesium specimen table would result in a smaller system mass. Magnesium is commonly used in vibration testing fixtures for its low mass and excellent bulk damping characteristics. These considerations led to the selection of magnesium for the specimen table.

Table 1 describes some of the parameter optimization iterations that were performed during the design process. The initial conditions assumed that all components were magnesium and that all ribs were 8 mm thick. Through this optimization process, the predicted first-mode frequency was raised over 70 Hz.

Struts. Since the dynamometer derives its ability to measure and resolve the vibration forces generated by the cryocoolers through static determinacy, the struts must be pinned, or simply supported, at the strut ends. The integral flexures used to approximate this condition act to greatly reduce the overall bending stiffness of the struts. However, the strut, including the flexures, must provide a high axial stiffness to maximize system frequencies while still providing the minimum bending stiffness to approximate the end conditions required for static determinacy. The flexure design must achieve a compromise between these two competing requirements.

With respect to overall axial stiffness, the struts behave as several springs in series. The total axial stiffness of the struts is maximized by increasing the strut diameter to the maximum extent possible, by reducing the overall strut length, and by maximizing the thickness of the integral flexures. The overall stiffness of the strut is driven by the "softest" axial spring within the strut, which in this case is the flexure. However, increasing the thickness of the flexures will increase their bending stiffness and therefore undermine the static determinacy of the system. Dynamometer assembly and disassembly requirements set the minimum angular rotation which the flexures must withstand without yielding the strut material. The actual design of the flexures and struts was accomplished through the use of beam theory for an element subject to a bending moment (in this case, the bending moment resulting from the required angular displacement).

The overall axial stiffness of the strut was then computed by first computing the extensional stiffness of each strut component (flexures and shaft), EA_i/L_i , and then summing these component stiffnesses according to the springs-in-series model. However, it was con-

sidered that the axial stiffness of the strut would be overestimated by this approach. Due to the extreme difference in the cross-sectional area between shaft and flexure, not all of the shaft area will contribute stiffness in the regions adjacent to the flexures. To test this hypothesis, a simplified finite-element model of a generic strut with two flexures was constructed. This model, with its boundary conditions, is shown in Figure 14. The axial stiffness of this strut was first calculated with the springs-in-series approach. Using this approach, the predicted total axial stiffness is 7.8×10^5 N/mm. The finite-element model predicts an axial stiffness of 5.1×10^5 N/mm, thus confirming the hypothesis that the simplified springs-in-series model is not adequate in this case. The apparent explanation is that not all of the cross-sectional area acts to resist axial forces in the regions adjacent to flexures. To confirm this, the axial stiffness of the generic strut was recalculated assuming that only an area equal to the profile area of a flexure was acting in the shaft between the two flexures. This assumption, used in a springs-in-series model, yielded a total axial stiffness of 3.9×10^5 N/mm, in substantial agreement with the axial stiffness predicted by the finite-element model.

The goal of the dynamometer strut, designed using the original springs-in-series model, was to provide an axial stiffness of 1.7×10^5 N/mm. It is clear from the above discussion that the actual axial stiffness of the struts is less than the design goal. This explains, in large part, the frequency difference between the predicted modes and the observed structural resonances.

EXPERIMENTAL RESULTS

Calibration

To ensure the accuracy of the dynamometer measurements, calibration of the output was required. This was done to verify the coordinate transformation as well as the operation of the load cells.

Since piezoelectric transducers are not capable of true static measurements, the straightforward method of using dead weights for calibration was not applicable. At the same time, the dynamic response to the *addition* of weights made data acquisition difficult. However, it was possible to use the *removal* of weight for this purpose. In this method, an accurately measured weight was placed on the specimen table and the output from the load cells was allowed to decay over time. After this reading returned to the null point, the weight was suddenly, but carefully removed from the table. The display computer was set to monitor the output and capture the peak reading.

Due to the axisymmetry of the hexapod structure, a single weight will load all six transducers. All transducers and all elements of the transformation electronics are used to convert this load into a single Z-axis force. Therefore, it was possible to verify the operation of the transducers and the design and operation of the transformation electronics by observing the results of this one calibrated weight. Since the absolute accuracy of this verification test is limited, the factory calibration factors for each individual load cell were assumed to be accurate and were entered into the computer unchanged.

Measurements of Cryocooler Vibrations

The Lockheed six-axis dynamometer was used for the first time to make measurements as part of the Advanced Infrared Sounder (AIRS) cryocooler development program (Ref. 4). One of the goals of this development program was to make accurate performance measurements of the Lockheed vibration cancellation system. The dynamometer was expected to achieve these high-accuracy results.

Two back-to-back compressors driven by the Lockheed electronic control system were mounted on the dynamometer. Dynamometer outputs were observed on both the PC screen and using a Hewlett-Packard 3562A dynamic signal analyzer connected to the analog-transformed monitor points. A photograph of the two compressors mounted on the dynamometer can be seen in Figure 15. Also seen in the figure is the computer display generated by the dynamometer PC. Figure 16 is an output from the dynamic signal analyzer. This spectrum is remarkable in that it shows dynamometer data out to 1.562 kHz. In addition, the resolution of the dynamometer output is below 0.01 N. This indicates not only how sensitive the instrument is, but also how well the seismic isolation system works.

An important element in Figure 16 is the dynamometer resonance which occurs just below 400 Hz. Initially, these resonances interacted with the electronic control system and limited its performance because the control system gain had to be reduced substantially in order not to become unstable. However, with the addition of a simple passive damper used to absorb the energy of this extremely high Q mode, the dynamometer structural dynamics were no longer interactive with the control system and the gains could be increased to extremely high levels with no adverse effects.

REFERENCES

- 1 Aubrun, J-N., R. R. Clappier, K. R. Lorell, and T. C. Nast: A High Performance Force Cancellation Control System for Linear-Drive Split-Cycle Stirling Cryocoolers, *Proceedings of the Cryogenic Engineering Conference*, NASA Marshall Space Flight Center, Huntsville, AL, June, 1991.
- 2 Larson, C., A. Mauritz, D. Moore: *Development and Application of a Sensitive Six Axis Dynamometer*, JPL D-6611, NASA/Jet Propulsion Laboratory, October 23, 1989.
- 3 Bushnell, D.: Improved Optimum Design of Dewar Supports, *Computers and Structures*, Vol. 29, No. 1, 1988.
- 4 Nast, T. C., R. R. Clappier, D. O. Murray, and B. Hocking: *Final Report for the AIRS Cooler Development Program*, LMSC-P000132, Lockheed Missiles and Space Company, Inc., November 18, 1991.

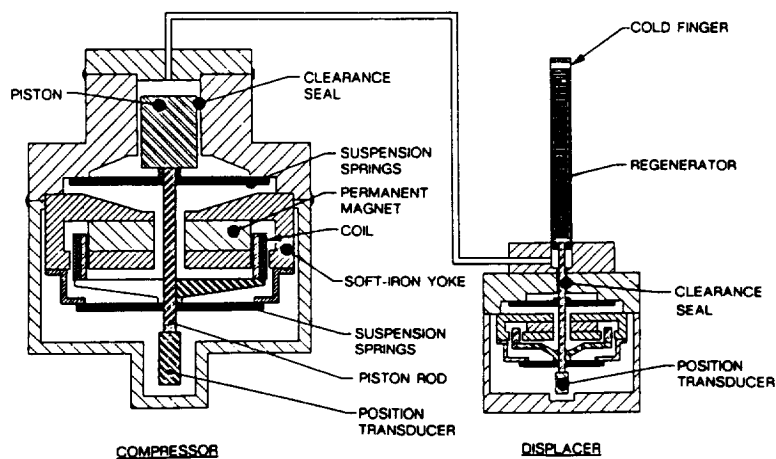


Figure 1 Split Stirling Cooler Schematic

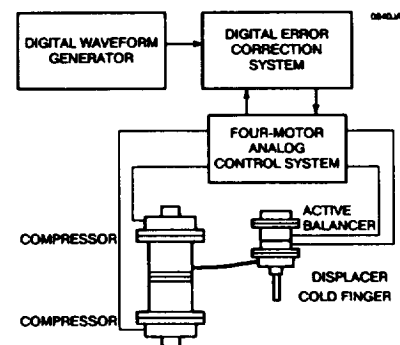
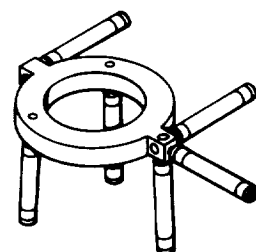
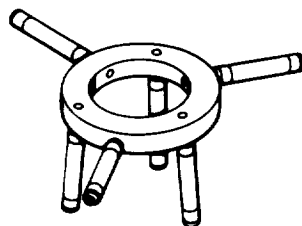


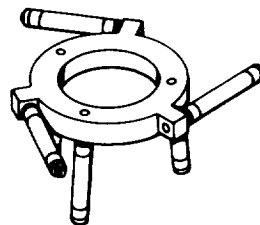
Figure 2 Cryocooler System Block Diagram



ORTHOGONAL CONFIGURATION



RADIAL CONFIGURATION



TANGENTIAL CONFIGURATION

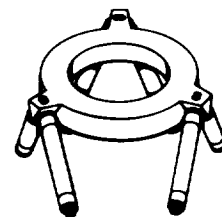


Figure 4 Hexapod Geometry

Figure 3 Conventional Geometries: Orthogonal, Radial, and Tangential

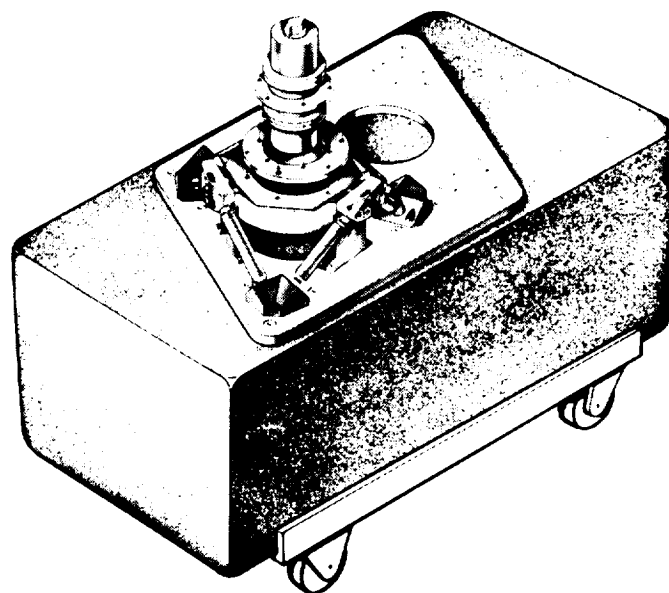


Figure 5 Lockheed Six-Axis Dynamometer

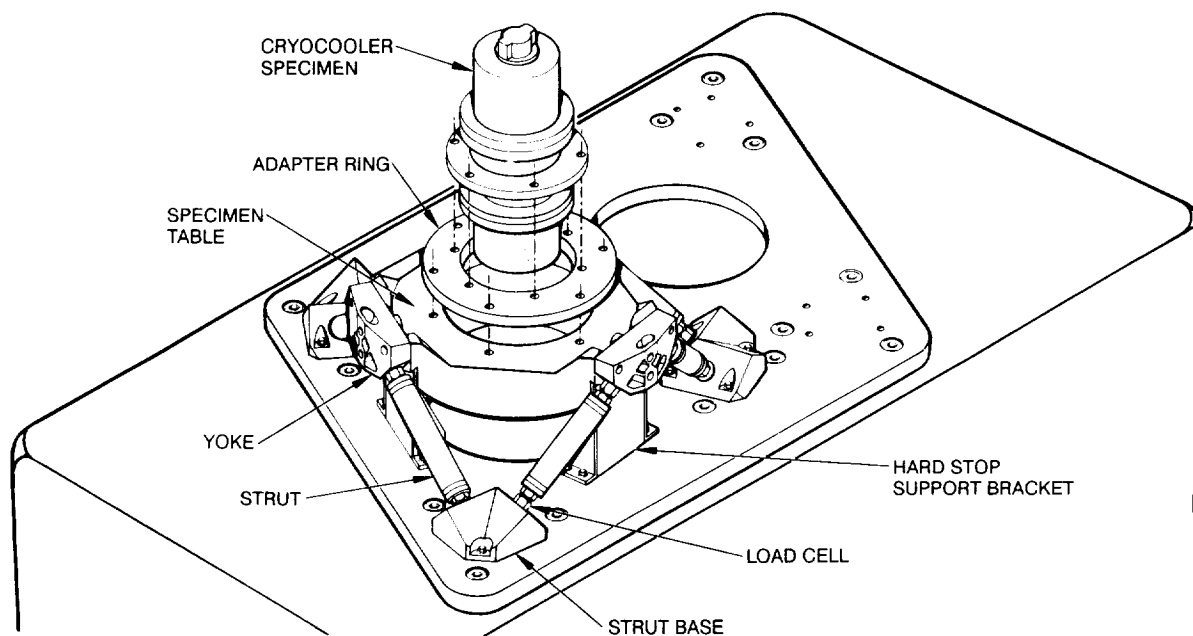


Figure 6 Dynamometer Components

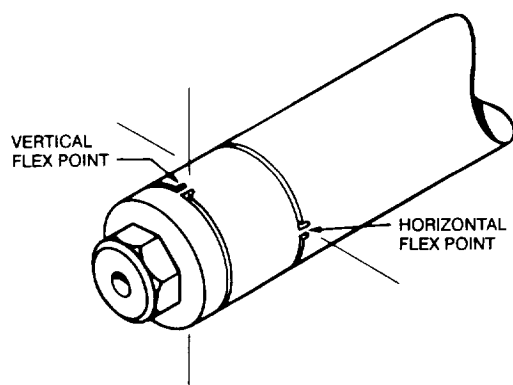


Figure 7 Strut Design With Integral Crossed Flexures

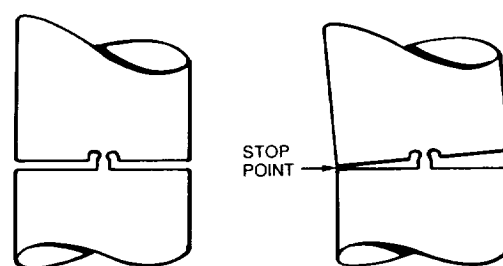


Figure 8 Flexure Design With Integral Stops

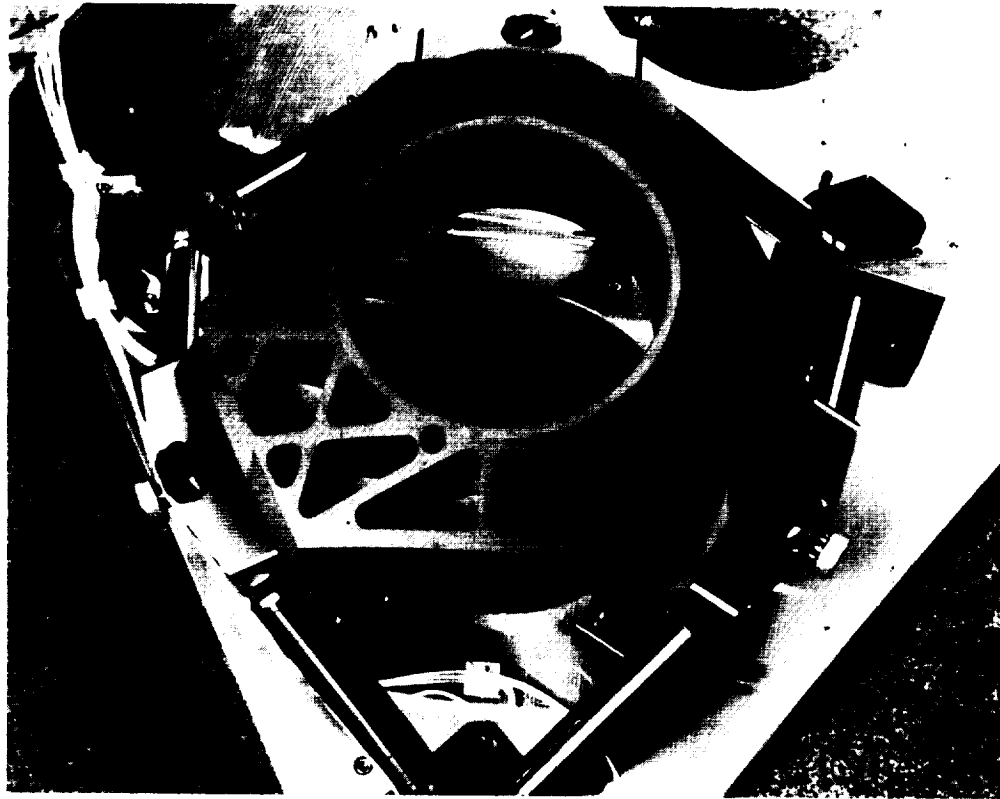


Figure 9 Specimen Table Rib Structure

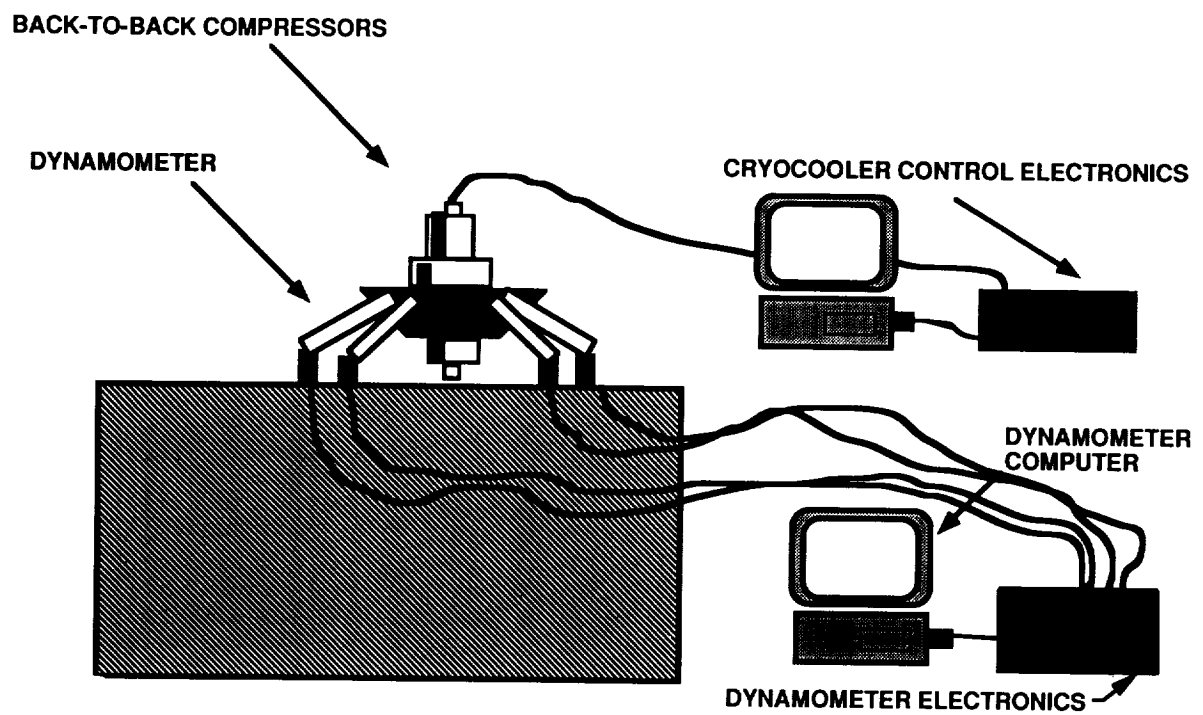


Figure 10 Dynamometer Test Setup

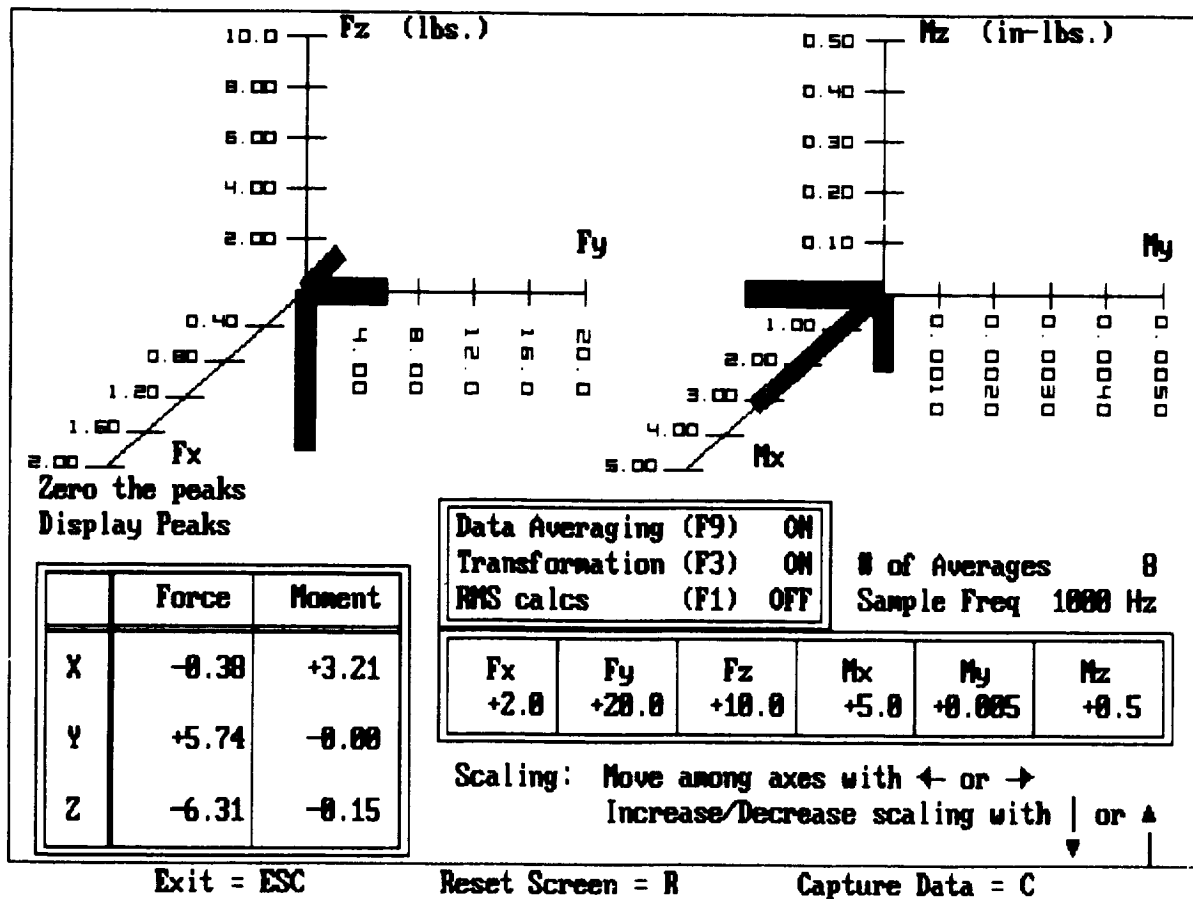


Figure 11 Display Screen Graphics

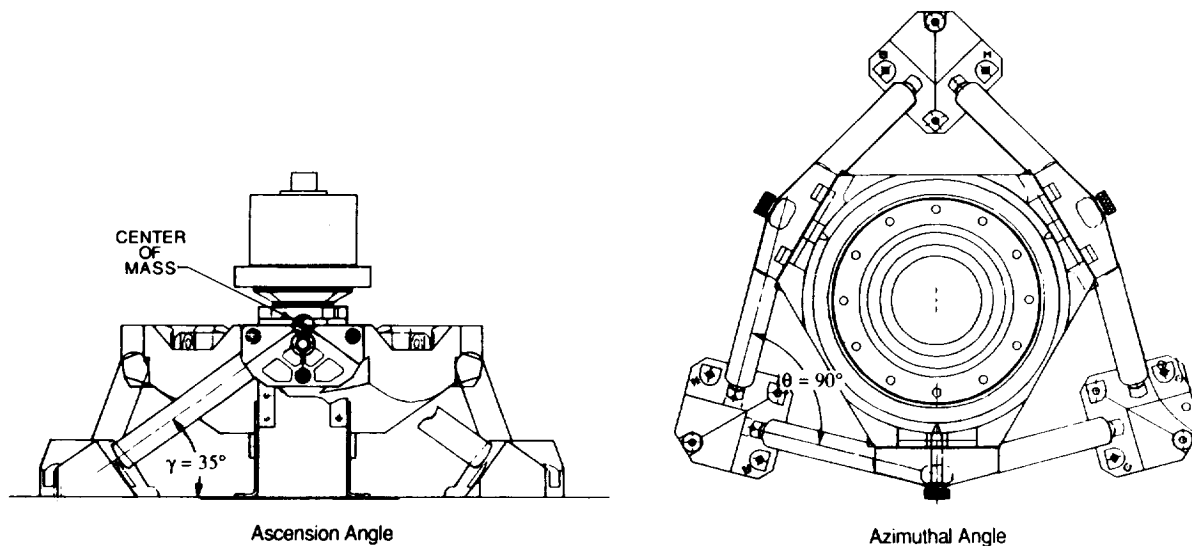
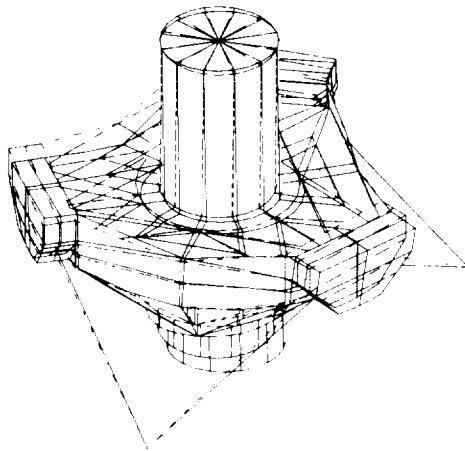
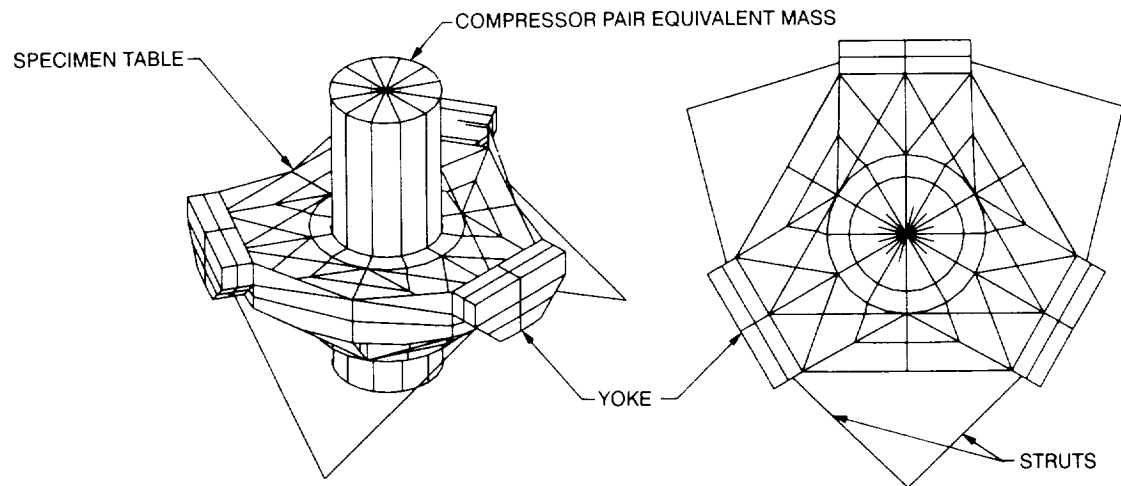
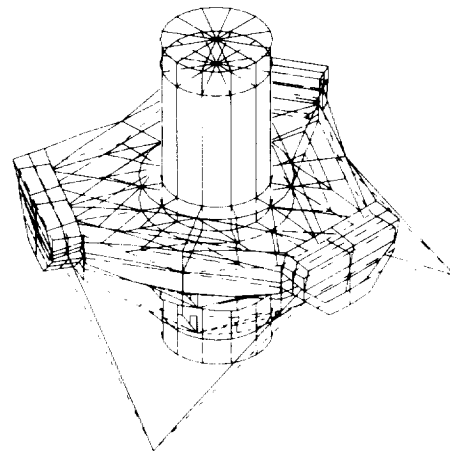


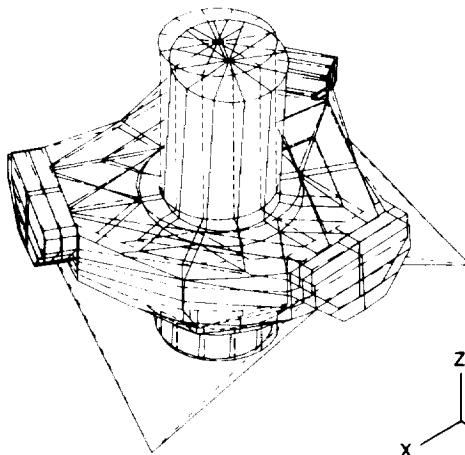
Figure 12 Optimized Hexapod Geometry



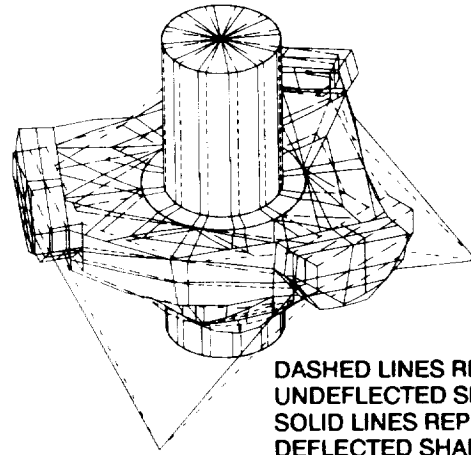
a. Example of Lateral Vibration Mode



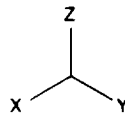
b. Example of Axial Vibration Mode



c. Example of Pitching Vibration Mode



d. Example of Rolling Vibration Mode



DASHED LINES REPRESENT UNDEFLECTED SHAPE
SOLID LINES REPRESENT DEFLECTED SHAPE

Figure 13 Finite Element Model of Hexapod

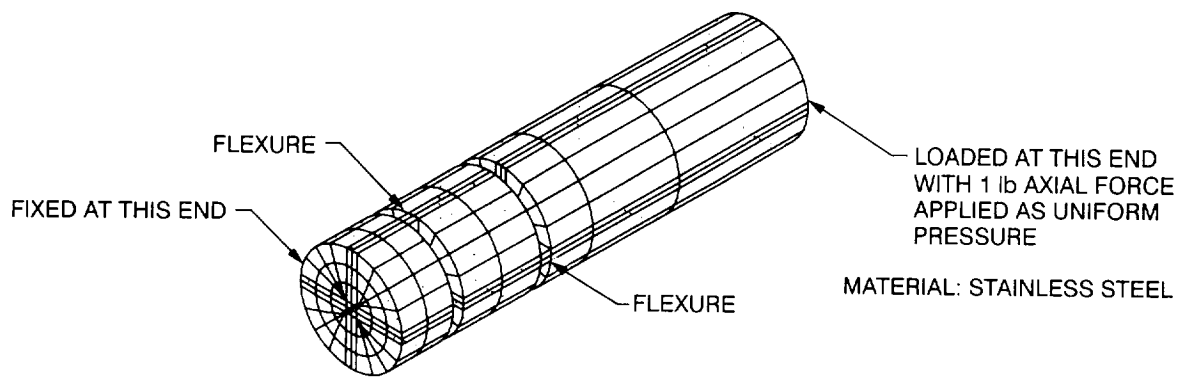


Figure 14 Finite Element Model of Generic Strut



Figure 15 Dynamometer Testing of a Cryocooler

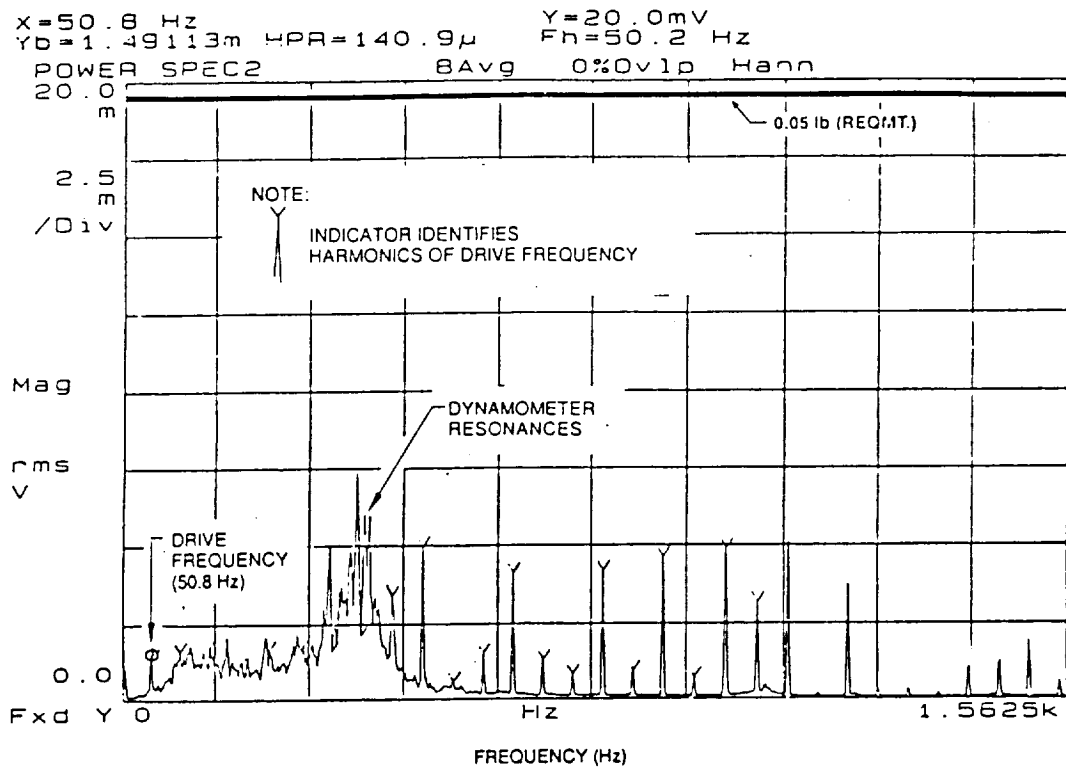


Figure 16 Frequency Spectrum of Cryocooler Vibrations

Table 1 DEVELOPMENT OF A PRECISION SIX-AXIS DYNAMOMETER

Case	Design Parameter	Calculated First Mode Frequency (Hz)	Selected?
1	Optimize specimen table top plate thickness		
2	$t = 6 \text{ mm}$ (initial condition)	504.9	No
3	$t = 8 \text{ mm}$	516.9	No
	$t = 10 \text{ mm}$	526.2	Yes
4	Optimize specimen table outer web thicknesses		
	t (short side) = 8 mm	529.0	No
	t (long side) = 6 mm		
5	t (short side) = 8 mm (initial condition)	530.5	No
	t (long side) = 8 mm (initial condition)		
6	t (short side) = 12.5 mm	530.9	Yes
	t (long side) = 8 mm		
7	Reduce specimen table spoke rib thickness from 8 mm to 6 mm, all ribs	531.5	Yes
8	Change material for strut yokes to stainless steel	553.4	Yes
9	Reoptimize specimen table top plate thickness by increasing to 12.5 mm	576.7	Yes

MECHANICAL DESIGN OF A ROTARY BALANCE SYSTEM
FOR NASA-LANGLEY'S VERTICAL SPIN TUNNEL

J. W. ALLRED & V. J. FLECK

ABSTRACT:

A new, lightweight Rotary Balance System is presently being fabricated and installed as part of a major upgrade to the existing 20-Foot Vertical Spin Tunnel (Figure 1) located at NASA's Langley Research Center. This upgrade, to improve model testing productivity of the only free-spinning vertical wind tunnel in the Western Hemisphere, includes a modern fan/drive and tunnel control system, an updated video recording system, and the new rotary balance system. The rotary balance is a mechanical apparatus which enables the measurement of aerodynamic force and moment data under spinning conditions (100 rpm). This data is used in spin analysis and is vital to the implementation of large amplitude maneuvering simulations required for all new high performance aircraft. The present system is over 40 years old and is worn beyond acceptable tolerances, as well as being susceptible to frequent breakdowns. It has serious limitations in model weight, position adjustment and spin-rate capabilities. The new rotary balance system described in this report will permit greater test efficiency and improved data accuracy. Rotary Balance testing with the model enclosed in a tare bag can also be performed to obtain resulting model forces from the spinning operation. The rotary balance system will be stored against the tunnel sidewall during free-flight model testing.

UPDATED CAPABILITIES:

High-performance aircraft development has increased the requirements for highly classified testing of a model in both free-spinning and rotary-balance operations. The 20-Foot Vertical Spin Tunnel is presently experiencing heavy usage by DOD agencies and the air frame contractors. The new upgraded system will permit greater test efficiency with an increase in the model weight limit to 25 pounds from the present limit of 15 pounds. Table 1 gives the other improved capabilities of the new system. The reduced deflections and rotations at the model center of gravity, which greatly increase testing accuracies at various model pitch, sideslip and roll angles, are also listed in Table 1.

New improved position adjustments will enhance model testing with up to 90-degree pitch angles, plus or minus 45-degree sideslip angles, and plus or minus 90-degree roll angles. Model spin-rate capability will increase from 90 rpm to 100 rpm. The new mechanisms include cables, electrical motors, actuators, linkages, and bearing surfaces to position the model in the desired position for testing. Motors and clamping actuators are located to minimize the forces and moments, which add

significantly to the model deflection at the maximum spin rate. A unique clamping/braking design utilizes the applied force from the actuator to hold the roll position during testing. The reaction force from the actuator prevents translation of the model support vertical arm during testing. The rotary balance system can also be stored against the tunnel sidewall to provide unrestricted free-flight model testing.

DESIGN APPROACH:

Several design iterations have been performed since the initial concept was presented in the Preliminary Engineering Report (PER), which was completed in September 1988. The initial design did not meet the current research requirements, which were not defined in sufficient detail in the PER. This design (Figures 2, 3, and 4) resulted in a larger tunnel air-flow blockage than the two percent which was acceptable for aerodynamic testing. Also the concept could not withstand the 100-rpm rotational speed without large deflections and rotations of the model's center of gravity. An inhouse multidisciplined design team was formed in the Facilities Engineering Division to define the essential research requirements, redesign the Rotary Balance System and evaluate the existing tunnel support structure.

The inhouse design and analysis incorporated a concept to reduce the weights and moment arms of the pitch and sideslip drive motors and brakes. The location of these components drove the large deflections and rotations at the model's center of gravity. Many mechanisms in the inhouse design were used to locate weights near the upper support of the vertical arm. The final concept and member sizes were obtained by using beam elements in a finite element model. Model weight, aerodynamic model forces and centrifugal loads were used in this analysis to optimize the components.

DESIGN CRITERIA:

Major design guidelines and criteria used in this design are given in the Wind Tunnel Model Systems Criteria, which is NASA Langley Handbook LHB 1710.15. This handbook defines the allowable stress levels for models and rotating equipment, such as the Rotary Balance System. Safety considerations are also identified, such as the prevention of fasteners becoming loose during operation or during dynamic loadings.

MECHANISMS:

The Rotary Balance System (Figure 5) is sidewall-mounted in the test section of the 20-Foot Vertical Spin Tunnel such that the model is positioned in the center of the vertical upward air flow. This mount consists of a hinge connection (Figure 6) at the

tunnel structure, which provides a rigid anchor for the 2000-pound Rotary Balance System. The hinge connection also permits the system to be rotated to the stored position during free-spin testing. Electric boat winches are used to pull the system to the stored position and to pull it into the center of the test section for the start of the Rotary Balance operation.

The 5.5-horsepower spin-drive motor is located behind the tunnel sidewall near the hinged connection and rotates with the 3.1-meter (10-foot) boom as it is moved into the center of the test section from the stored position. A gearbox speed reducer is also mounted on the pivoted structure. This speed reducer is used to obtain the 100 rpm maximum required speed for the system from the 1750-rpm motor. A flexible coupling is used between the gear reducer output shaft and the 3.1-meter-long drive shaft. A shear pin is also incorporated at this connection to prevent system damage in instances when large accelerations and decelerations may occur due to motor or speed reducer failures. Flexible couplings are also used on the opposite end (Figure 7) of the drive shaft to compensate for drive-shaft deflection and misalignments. The vertical hollow center shaft provides space for the 175 electrical leads used for power supply, motor control, and for data acquisition from the test model mounted on the end of the sting. This center rotating shaft extends to the slip ring assembly at the top and to the horizontal arm located beneath the support boom. Bearings are used to minimize rotational loads as the forces are taken out at the 90-degree gear assembly. The bevel gear assembly is housed in an oil bath to reduce frictional loads and wearing of the gear components. All parts below the gear and bearing assembly rotate about the tunnel center line.

The horizontal arm assembly (Figure 8) is a unique design which incorporates and supports many operations with a minimum amount of frontal flow blockage area. Major components of this assembly are the translational drive frameless motor, torque multiplier, cable drive with pulleys, counterweight, and vertical arm support on the opposite side of the vertical rotation shaft. The counterweight and vertical arm subassemblies consist of brakes or clamps driven by linear actuators which apply forces to the horizontal arm. One unique feature of this design is the horizontal movement of the vertical arm and counterweight by use of a single motor and cable system. Since the cable is attached to the near side of the vertical arm and to the far side of the counterweight, both subassemblies move inward simultaneously when the motor turns counterclockwise as viewed from the top. Both units move outward when the motor turns clockwise. This operation maintains a balance of weight and moment about the vertical center-line spin shaft. Additional weights can be added at final checkout after assembly.

Another feature of this lightweight design is the frameless and compact motors which are mounted on the counterweight end of the horizontal arm. This reduces the amount of lead required for

the counterweight. The half-horsepower motor has a torque multiplier between the motor and the pulley to increase the torque which is applied to the cable drive system. The torque multiplier has a ratio of eighty nine (89) to one, which provides sufficient translational speed to meet the required velocity of two inches per second. The unit also has a one arc minute maximum backlash, which provides the required repeatability. The pretensioned cables are oversized in stiffness such that the frictional forces produce insignificant stretch.

These cables are not required to hold the counterweight and the vertical arm subassemblies in place while the horizontal arm is rotating at 100 rpm. This is accomplished by a unique brake design which is used to force the serrated brake pads into matching serrations machined in the main beams of the horizontal arm. The counterweight subassembly (Figures 9 and 10) consists of an electrical linear actuator which is fixed at the clevis or rod end. The trunion support of the actuator will move vertically when the actuator rod is forced out of the housing. This trunion reaction forces the actuator upward and thereby forces the brake arms inward. The mechanical advantage applies a 5000-pound force between the brake pads and the horizontal arm.

The vertical arm (Figure 11) has a similar operation to clamp this subassembly during rotation of the horizontal arm about the tunnel center-line. However, this reaction force applies a frictional torque to a conical surface which is part of the roll operation. This surface must be clamped after the model is rotated into the tunnel center line after the sideslip operation of the model. This compact assembly is unique in that it prevents translational movement of the vertical arm and prevents rotation of the vertical arm. The plus or minus 90-degree rotation of the vertical arm assembly is obtained by a similar frameless motor and torque multiplier as used in the cable drive system mounted on the horizontal arm. Shock absorbers are used at each end of the horizontal arm to prevent the vertical arm and counter weight subassemblies from impacting the ends of the horizontal arm end structure.

Sideslip of the model is moved through the plus or minus 45-degree angle by use of a similar motor and torque multiplier used in the other two drive systems. However, there are two connecting arms (Figure 12) between the output shaft and the model sting/support center-line located 60 inches below the horizontal arm. A brake assembly is also used to hold the sideslip position during operation. The electrical linear actuator applies a clamping force on the arch, which is attached to the torque multiplier output shaft.

Pitching of the model is accomplished by the use of another electrical linear actuator and by a sliding assembly located on the shaft of the sting support. These linkages rotate the sting at the pitch point while allowing the sideslip operation to occur at the same time by use of the housing around the center shaft.

The actuators contain acme screw threads on the rod assemblies and therefore will hold the forces with power required from the actuator motors. They become self-locking, therefore pitch operation does not require a brake or clamp to hold the model at the correct pitch angle for testing.

RESULTS:

The design and analysis of the complete assembly required many iterations and optimizations of all components. The main features of the design which enabled minimization of deflections and rotations to values less than the research requirements are as follows:

1. Locating as much weight as possible near the horizontal arm.
2. Using lighter and higher strength materials to account for weight reduction and centrifugal forces.
3. Using lightweight frameless motors and compact torque multipliers.
4. Using applied actuator forces and reaction forces to reduce the number of actuators,
5. Using one motor to horizontally translate the vertical arm and the counterweight subassemblies.
6. Designing low-friction moving surfaces for minimum horsepower requirements.
7. Providing compact design with minimum cross-sectional area to reduce air-flow blockage.

SUMMARY:

The fabrication and shop testing of the complete Rotary Balance System is presently underway with tunnel installation to start in April 1992. This unique design of many subassemblies provides simplicity in the application of properly located off-the-shelf components. This new improved Rotary Balance System provides significant enhancement over the existing system by providing greater test efficiency and improved data accuracy. Deflection requirements for the maximum model weight at the maximum rotating speed of 100 rpm were met.

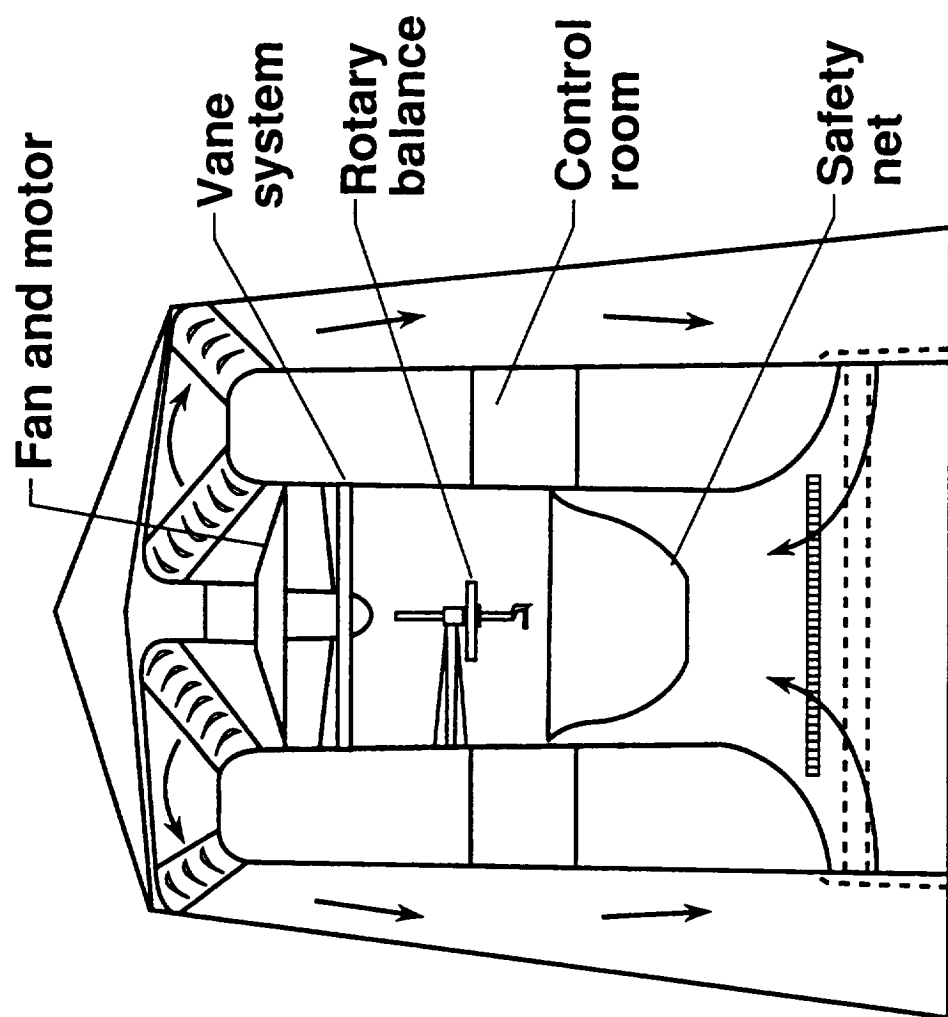


Figure 1. Elevation view of vertical spin tunnel.

TABLE 1 - ROTARY BALANCE REQUIREMENTS (past and future)					
	Existing rig	PER req't	Original design	Final design	Comments
Model weight (lbs.)	15	25	15	25	Meets PER
Spin rate (RPM's)	±90	±100	±100	±100	Meets PER
Side slip (deg.)	±20	±45	±30	±45	Meets PER
Spin radius (in.)	0-27	±20	0-38.5	0-46	Increase PER
Lateral deflection	Large	±1/4	~	~	Per req't deleted
Angular deflection	Unknown	~	±1°	±1°	Req't added
Slip rings	40 total	80+	80+	80+	Meets PER
Blockage	<2%	~	<2%	<2%	Req't added
Winches	Manual	Electric	Electric	Electric	Meets PER
Aft sting	No	Yes	~	Yes	Meets PER
Retractable	No	Yes	No	Yes	Req't deleted

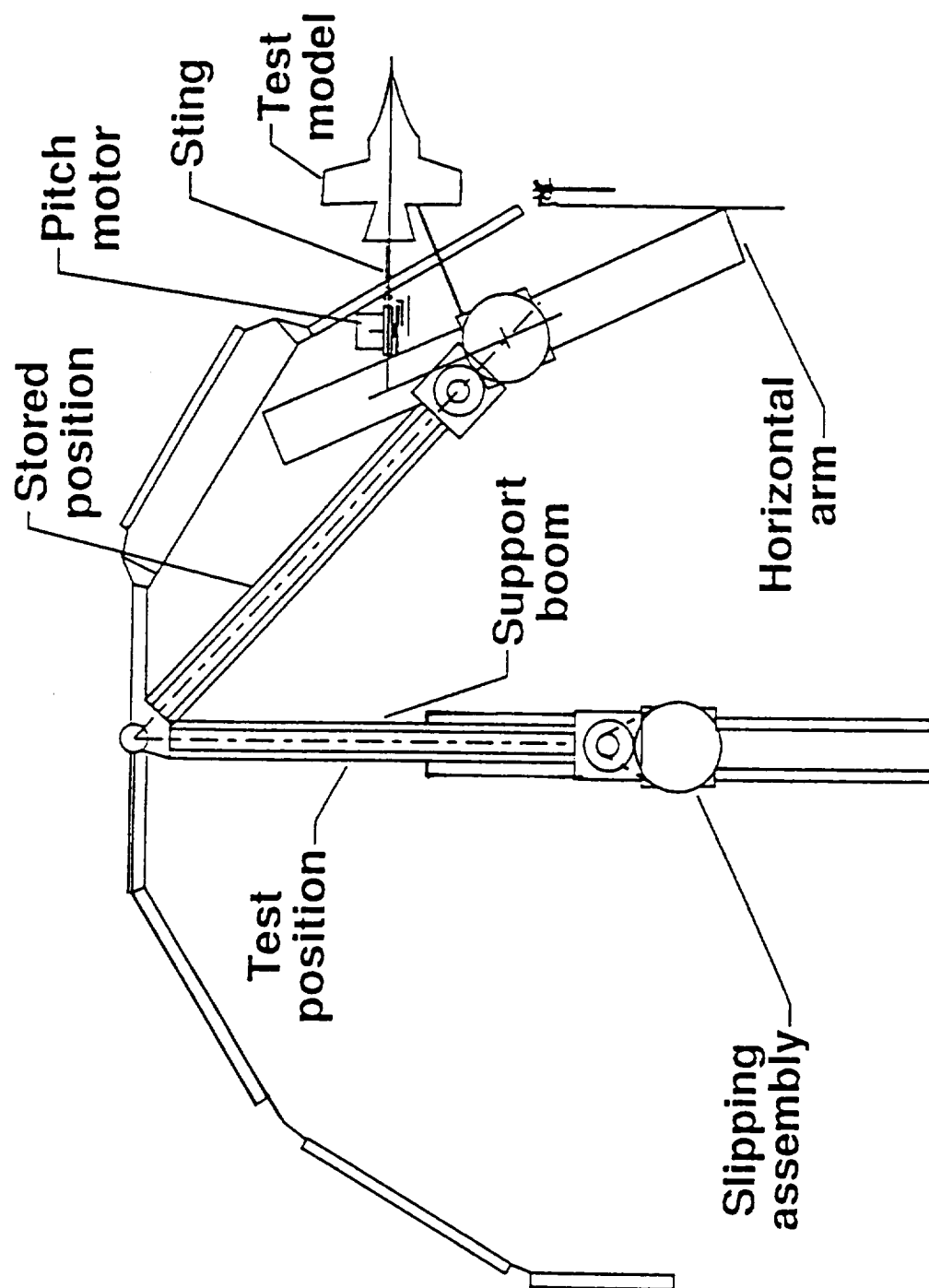


Figure 2. Plan view of A/E design.

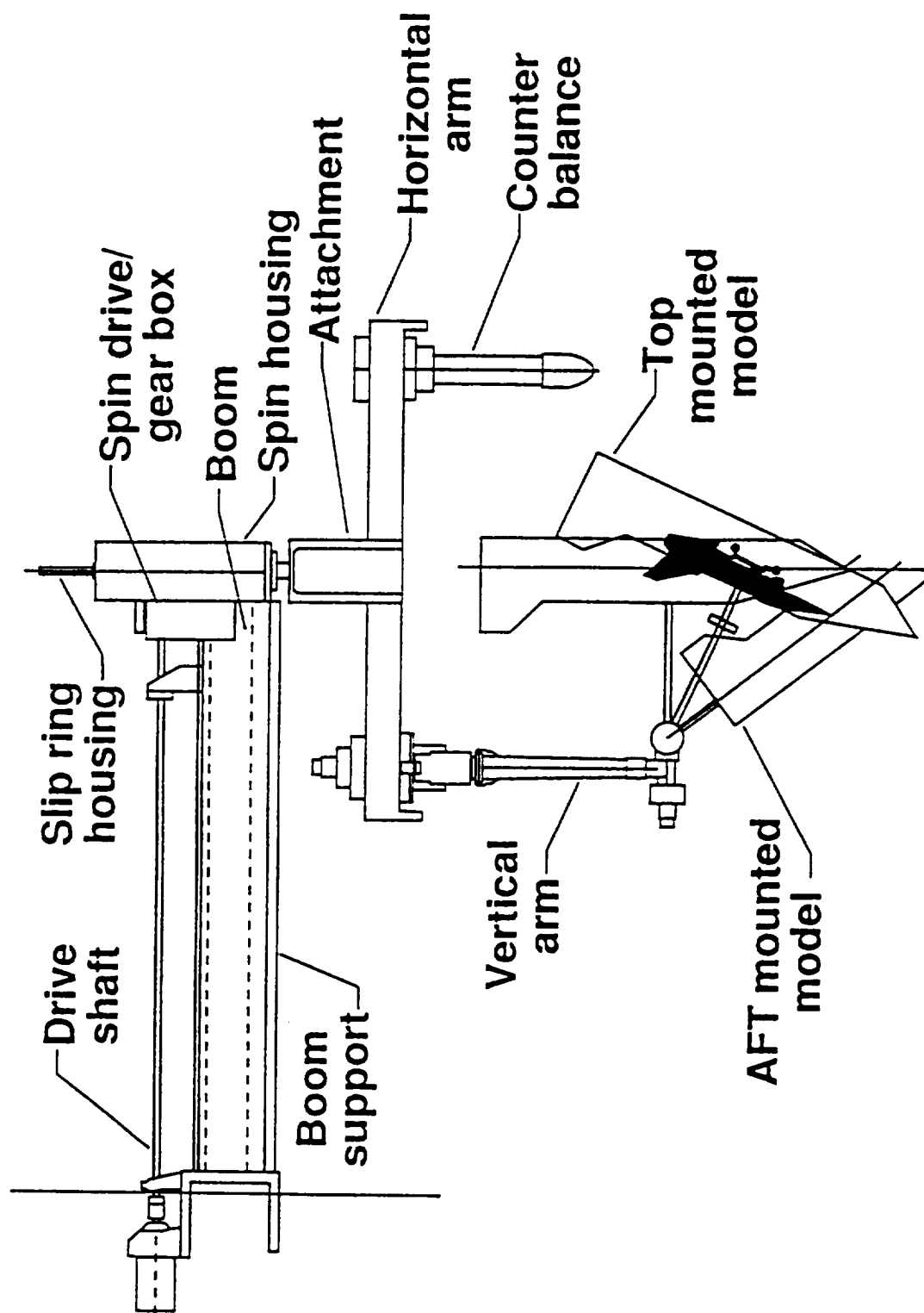


Figure 3. Elevation view of A/E design.

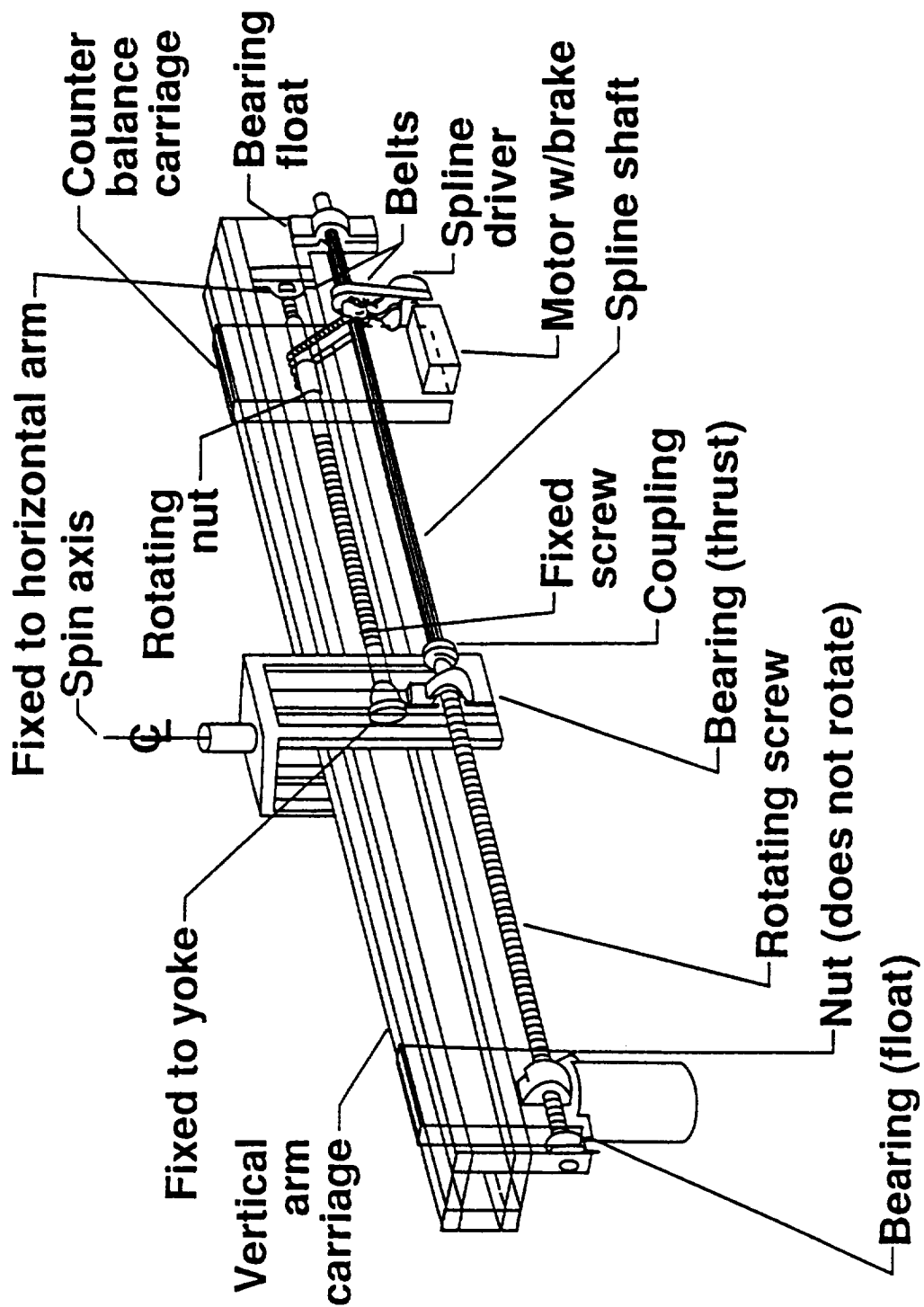


Figure 4. Vertical arm/counterweight drive.

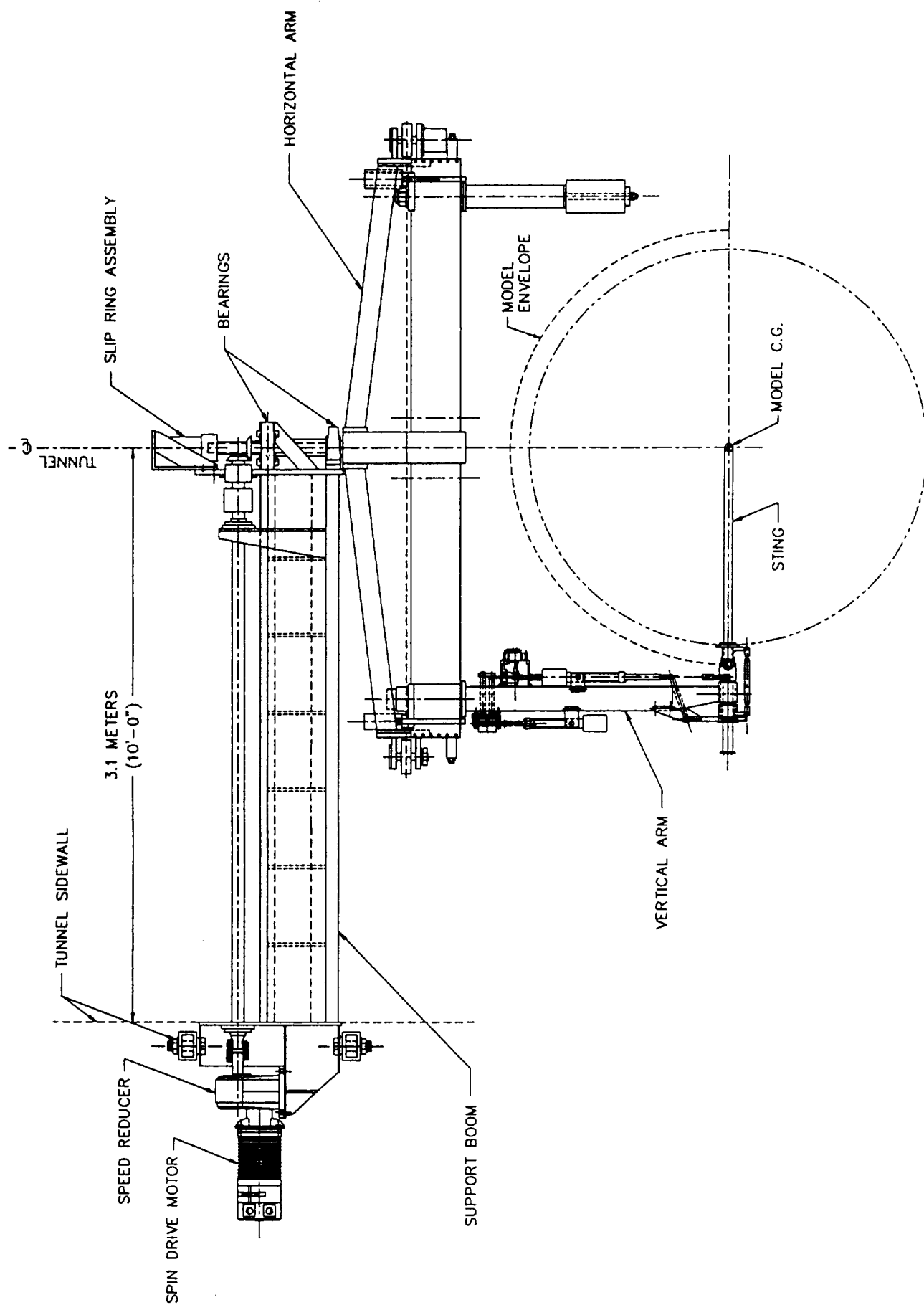


Figure 5. Elevation view of in-house design.

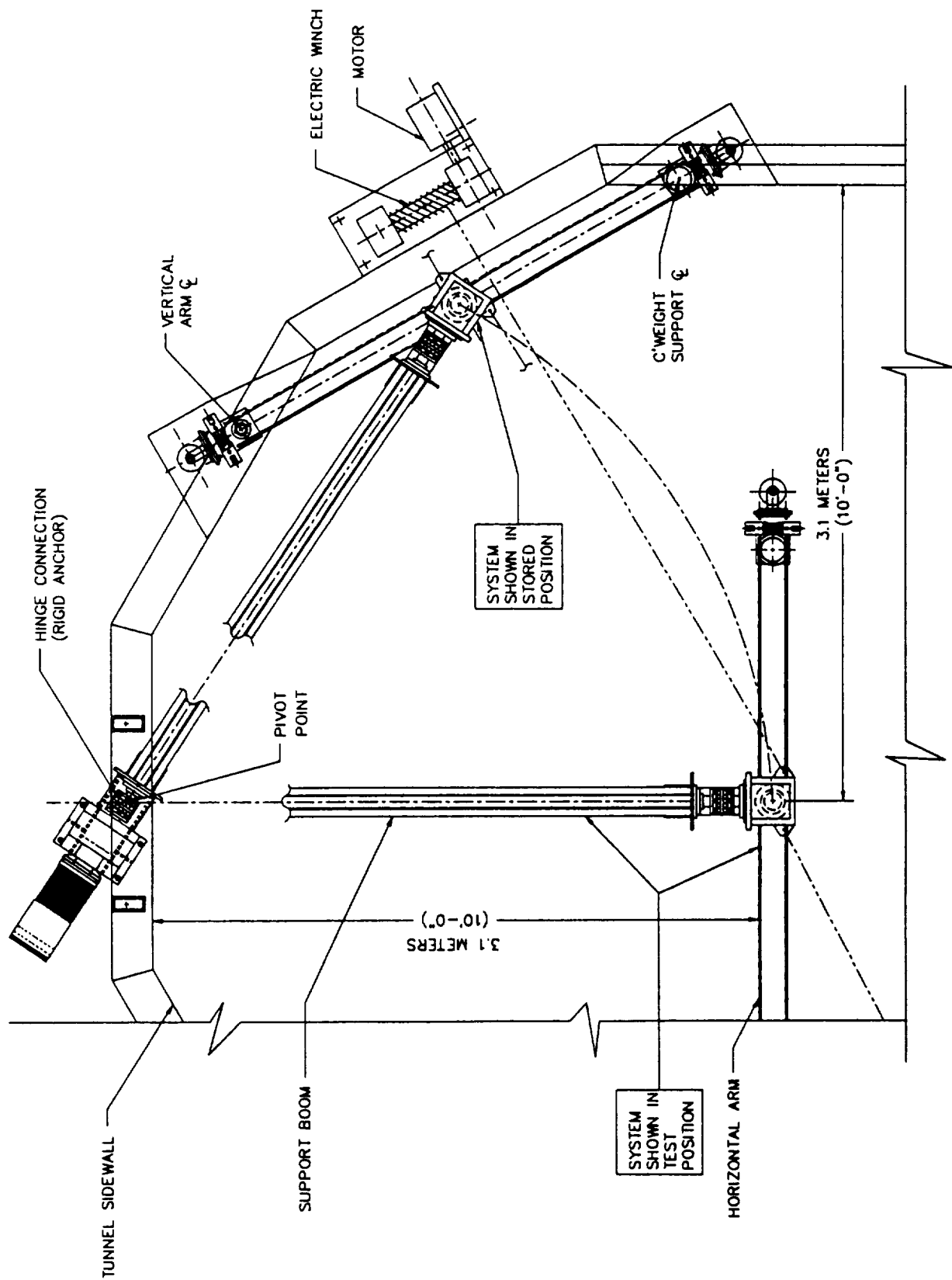
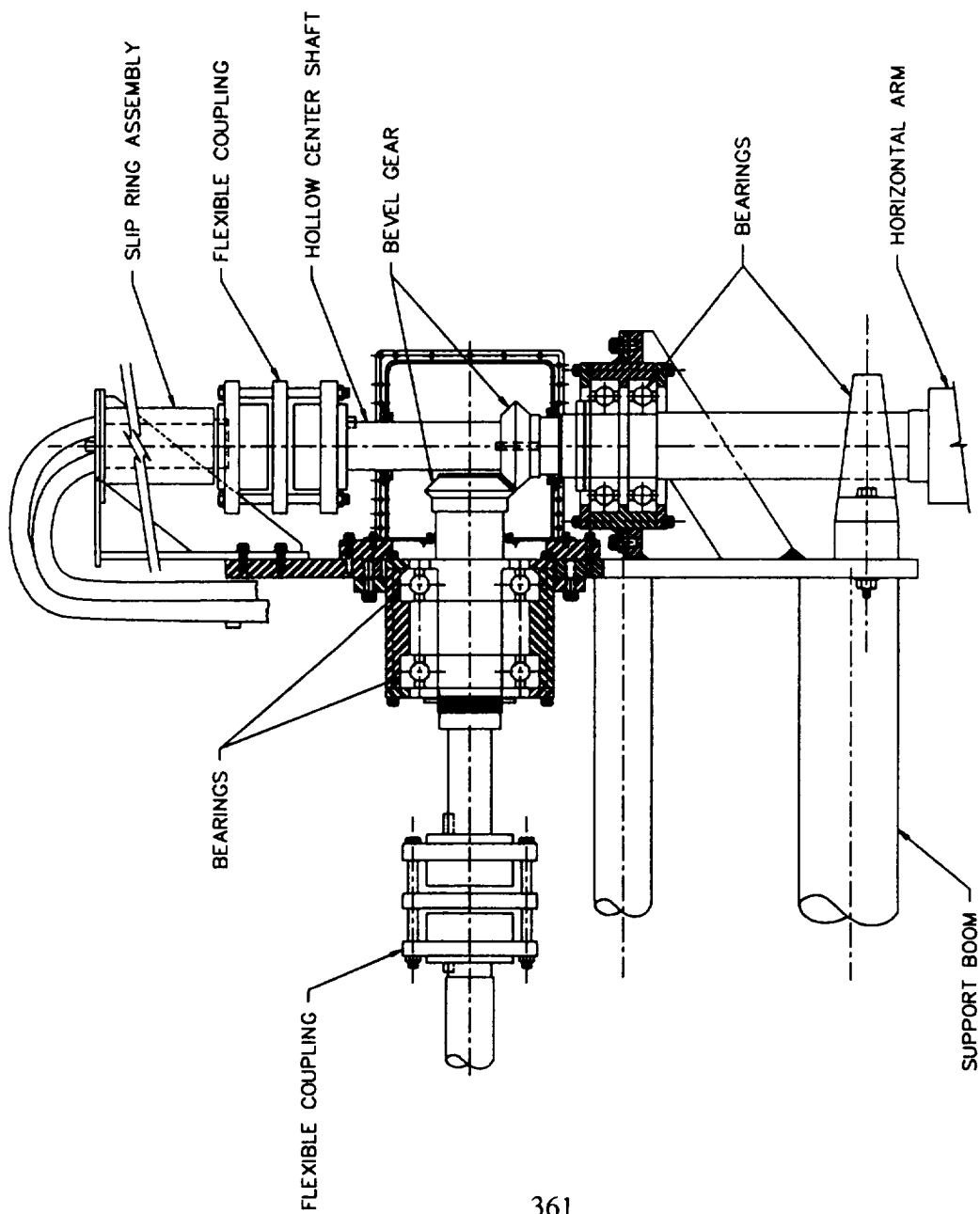


Figure 6. Plan view of in-house design.



END VIEW

SIDE VIEW

Figure 7. Center shaft details.

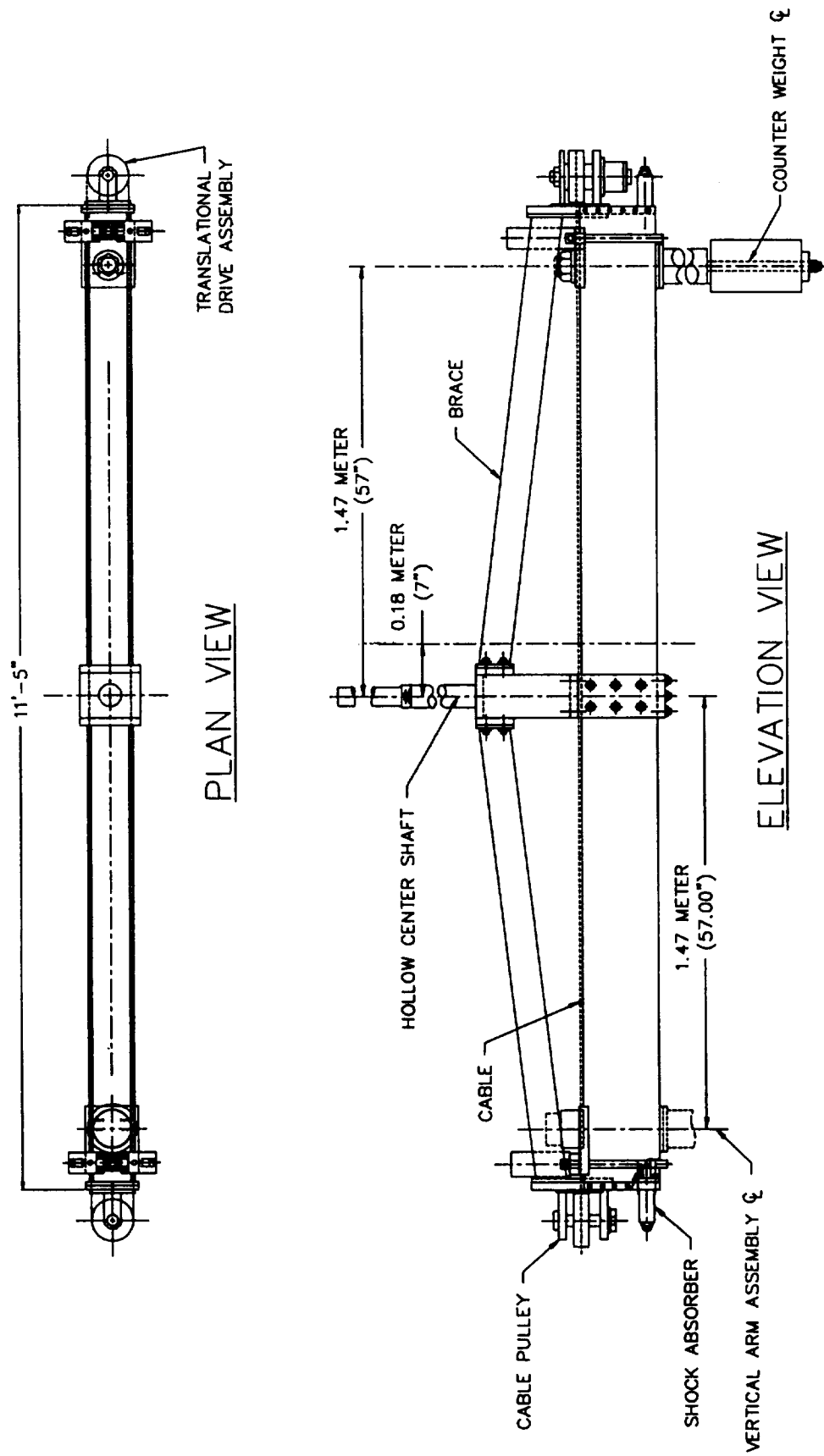


Figure 8. Horizontal arm assembly.

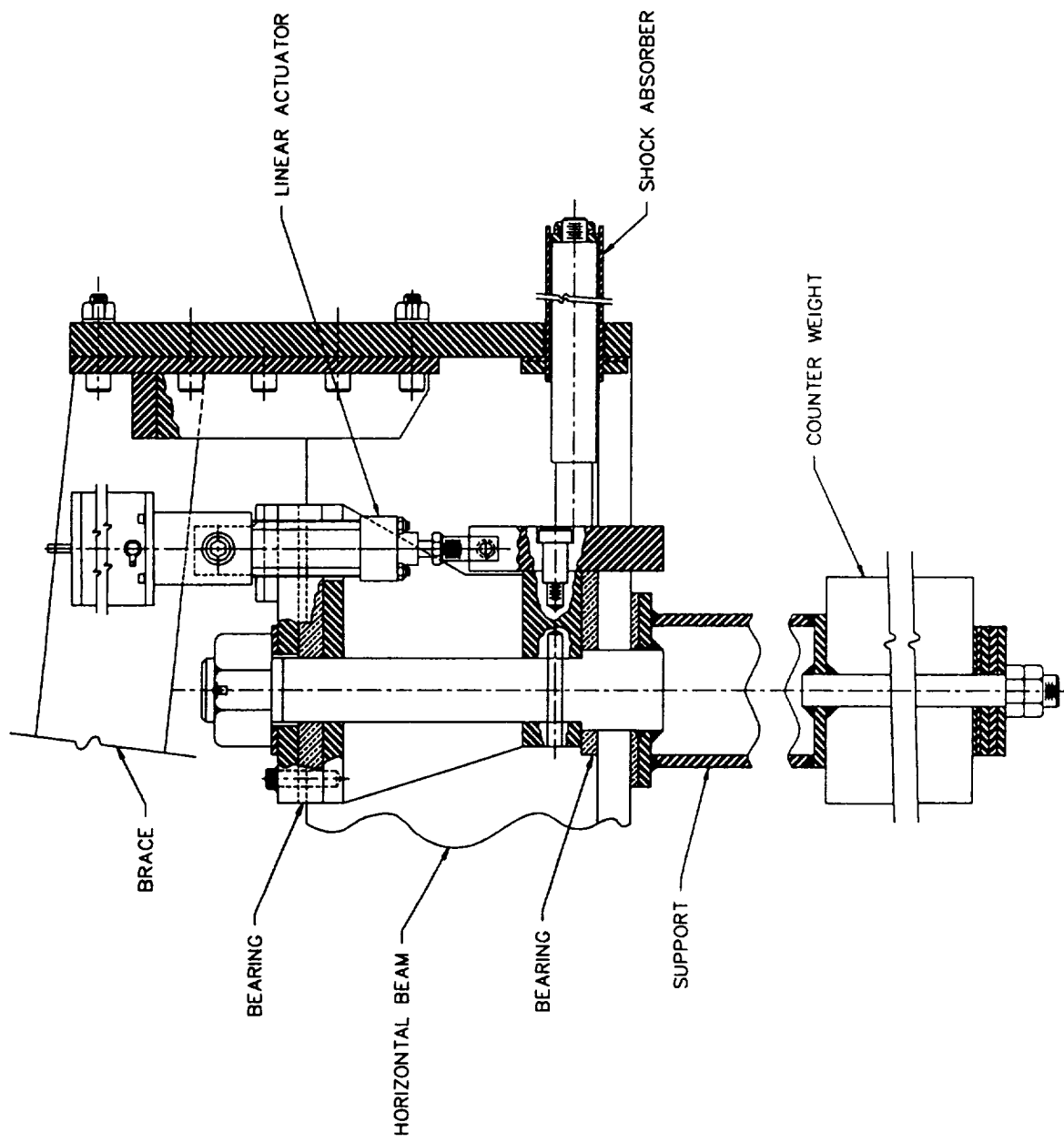


Figure 9. Horizontal arm with counterweight details.

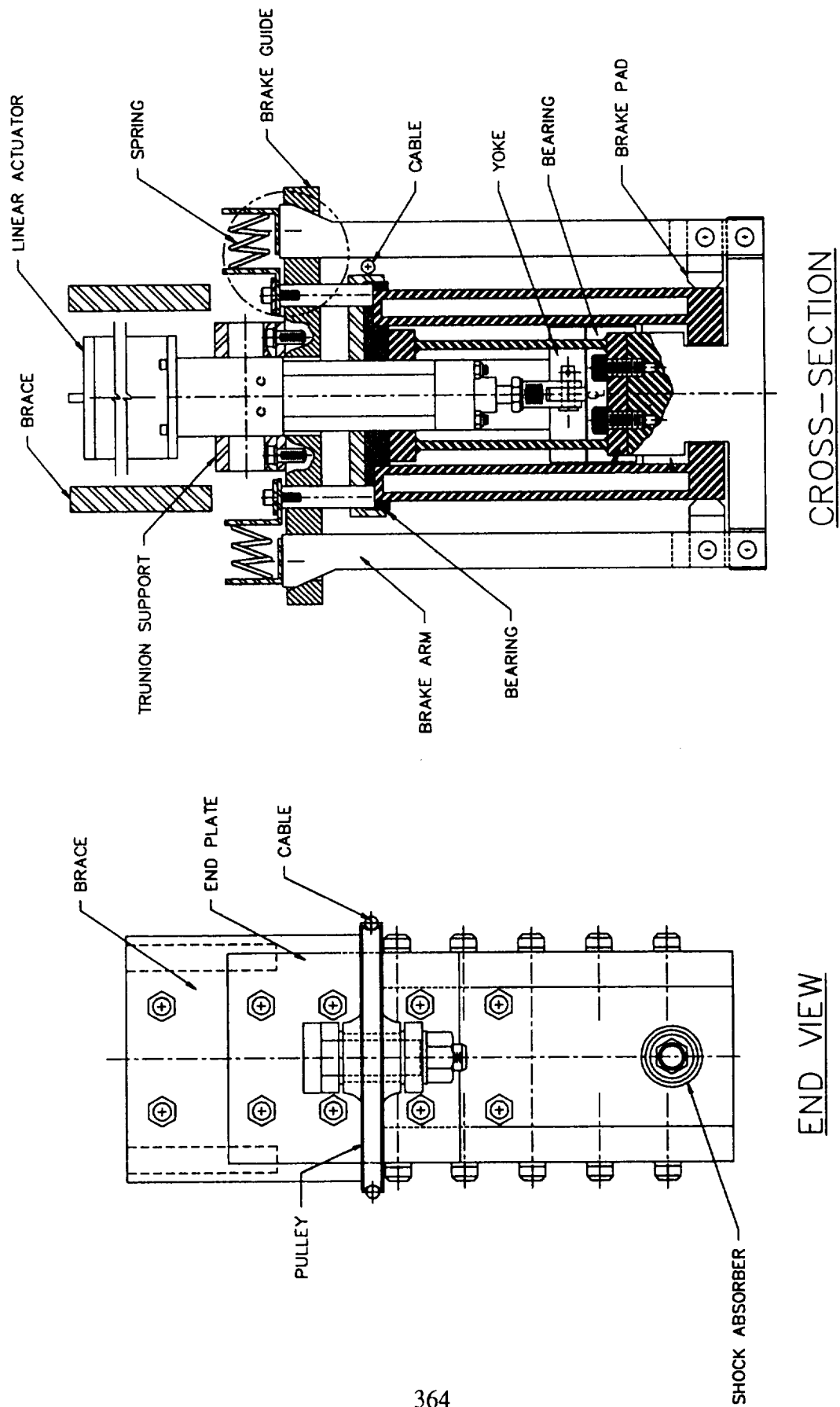


Figure 10. End view and brake cross-section.

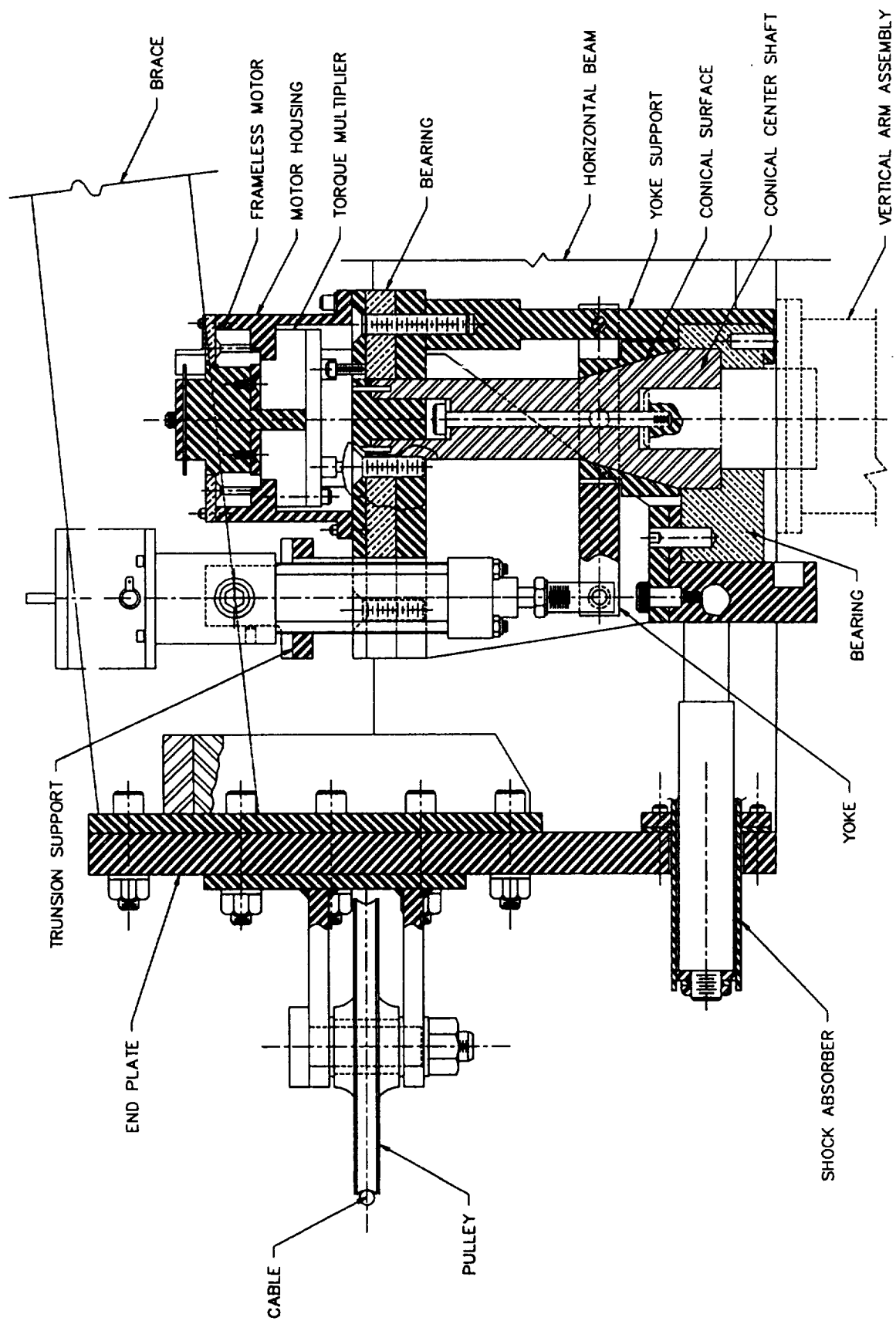


Figure 11. Vertical arm roll and brake details.

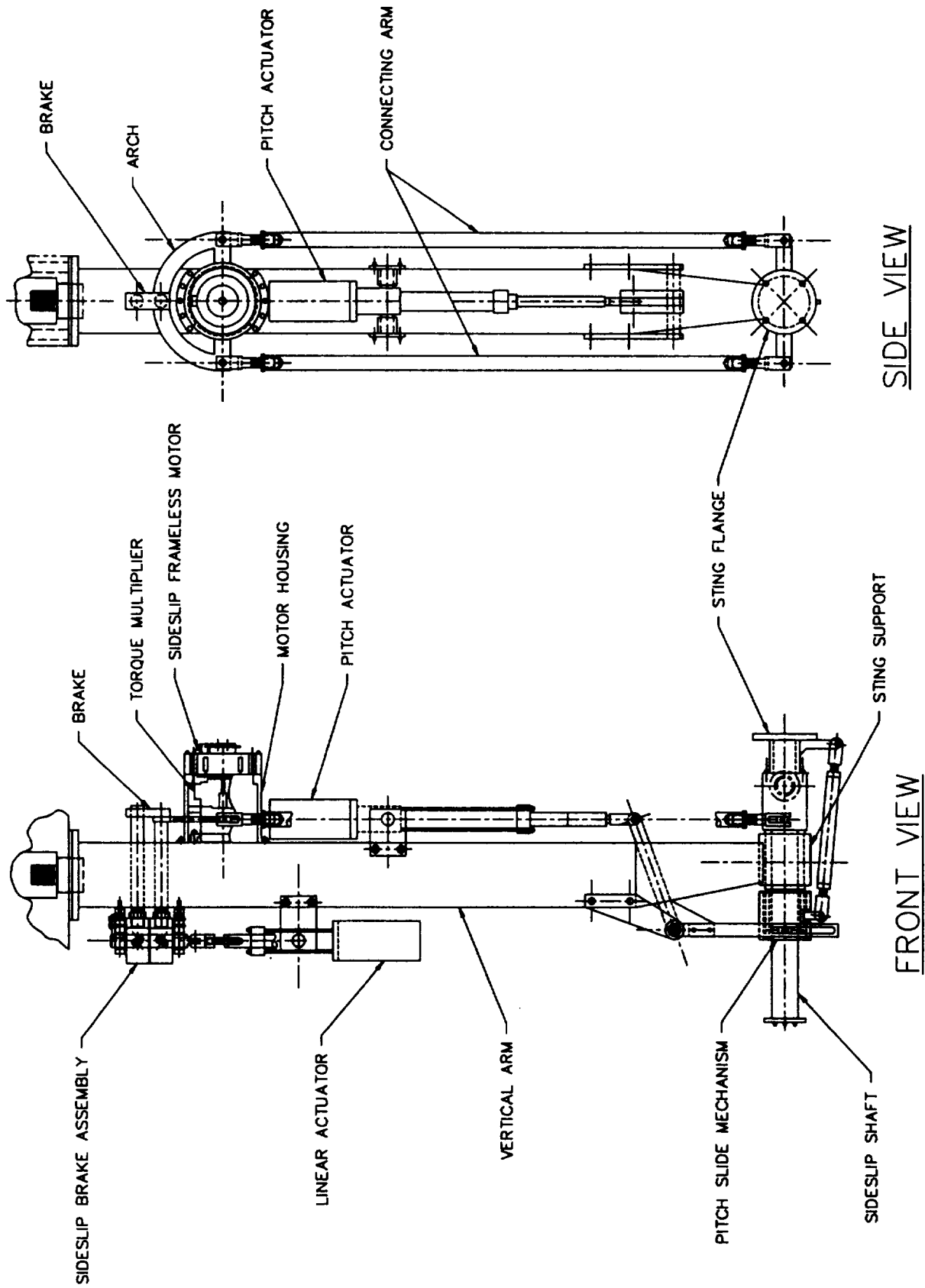


Figure 12. Vertical arm assembly.

12-FOOT PRESSURE WIND TUNNEL RESTORATION PROJECT
MODEL SUPPORT SYSTEMS

GLEN E. SASAKI, NASA AMES RESEARCH CENTER

ABSTRACT

The 12-Foot Pressure Wind Tunnel at Ames Research Center, is a variable-density, low-turbulence wind tunnel that operates at subsonic speeds, and up to 6 atmospheres total pressure. The restoration of this facility is of critical importance to the future of the United States aerospace industry. As part of this project, several state-of-the-art model support systems are furnished to provide an optimal balance between aerodynamic and operational efficiency parameters. Two model support systems, the Rear Strut Model Support, and the High Angle of Attack Model Support are discussed. This paper covers design parameters, constraints, development, description, and component selection.

INTRODUCTION

The design and fabrication of modern model support systems is an increasingly complex problem due to the higher performance requirements and the variety of specialized research for modern aircraft development. Also, the need for productivity in terms of manpower is more critical today than it has been in the past. It is the goal of the 12 Foot Pressure Wind Tunnel (PWT) Restoration Project to retain the tunnel's outstanding aerodynamic characteristics, while modernizing the tunnel's operation and equipment.

One of the most notable new features of the 12-Foot PWT is the ability to isolate the test section from the tunnel circuit during pressurized operation (figure 1). To accomplish this, the test section is enclosed in a 13-meter (42-ft) diameter spherical plenum. This plenum, which is part of the tunnel pressure shell, can be isolated from the tunnel with mechanical hatches, similar to an airlock in a submarine. This allows access to the test section without the time-consuming and energy-wasteful depressurization of the entire tunnel. This unique feature will reduce access time to the test section, and improve overall operational efficiency. The plenum, however, has greatly restricted the space in which the model supports must fit. The integration of the model supports with the Test Section Isolation (TSI) system, and within the plenum, was a significant challenge.

DESIGN PARAMETERS

In initiating this work, several design parameters were identified as being critical to the final product:

AERODYNAMIC BLOCKAGE

The total amount, as well as the location of this blockage is critical to both tunnel performance and test results. Total blockage affects the drive power required and may limit the maximum obtainable tunnel speed. This is highly critical for model support elements which are permanently installed in the test section. Also, blockage too close to a model requires complicated mathematical correction of the test data to provide "free stream" results.

LOAD CAPACITY

The load capacity will limit the size and types of tests that can be performed. For permanent support elements, it would be undesirable to limit the versatility of the tunnel by having insufficient load capacities. However, load capacity affects the size, and therefore the blockage of the support.

STIFFNESS

Adequate stiffness of the system is important for both structural dynamics (resonance) as well as rigidly maintaining the model orientation while obtaining aerodynamic data. Again, stiffness translates to size, and therefore, blockage.

Secondary design parameters affecting the details of the system design are:

ACCURACY

It is essential for the aerodynamicist to know precisely the spacial orientation of the model for any data point in order to properly draw conclusions. In order to accomplish this, the researchers compensate for the slightest deflection of the mounting hardware. It is not easy, however, to correct for backlash in a mechanical system since it is difficult to determine when it occurs. Therefore, the design must eliminate--or minimize--backlash and its effects. The angular positioning accuracy goal for all model supports is .01 degree. In order to achieve this accuracy, all axes are monitored by the state-of-the-art control system with special precision transducers.

MODEL INSTALLATION PRODUCTIVITY

A major project goal is to improve overall tunnel operational productivity. This includes reducing the amount of time to install and remove models. To accomplish this, models will be built-up and functionally checked out prior to installation in the tunnel. Model support preparation in the test section should be minimized. Therefore, the majority of the model support equipment permanently resides inside the test section or plenum. Model mounting interfaces also allow quick installation with minimal alignment required.

RELIABILITY AND MAINTAINABILITY

Very important to maximizing tunnel efficiency is reduction of downtime for repair and maintenance. All bearings requiring routine lubrication should have accessible lubrication ports. Critical seals should be easily replaced. Critical items subject to wear should be both easy to inspect and replace.

DESIGN CONSTRAINTS

TEST SECTION ISOLATION (TSI) SYSTEM

The plenum size, and the rotating test section severely constrained the physical size of the model supports.

TEST SECTION GEOMETRY

The cylindrical test section with 120-cm (4-ft) flats on the walls, ceiling and floor, was retained from the original tunnel design. This made the provisions for certain modes of model articulation difficult to incorporate. Also, provision for safe and efficient model installation was difficult with the relatively narrow test section floor.

INTEGRATION OF MODEL SYSTEMS

The integration of all the model supports in the space within the plenum as well as with the TSI structure was a complicated process, especially with the large mechanisms required to support the high loads and large motion ranges.

CONCEPT DEVELOPMENT

The original tunnel had model supports that provided the basic functions of most of the new designs. It was determined that the original systems could not be easily modified for use in the new tunnel or meet new performance requirements for future research. Many iterations were necessary to develop the current model support designs. Most valuable during this concept development phase were "Peer Reviews," in which non-project personnel from varying backgrounds were invited to review drawings and procurement specifications, and to freely ask questions and offer suggestions. Tunnel operational personnel and mechanics offered unique insight based on past tunnel performance and testing.

SYSTEM DESCRIPTIONS

REAR STRUT MODEL SUPPORT (RSS)

The Rear Strut Model Support (figures 2 and 3) provides +30 to -20 degrees of pitch, ± 122 cm (± 48 in) of vertical travel (heave), and with a removable mechanism, provides ± 180 degrees of roll. This system is designed to support 44,400 N (10,000 lbs) of model lift load centered at a distance 340 cm (11 feet) from the pitch mechanism pivot.

HEAVE DRIVE

The primary structure is a 762-cm (25-ft) tall strut which is driven vertically by a rollerscrew drive assembly and guided by cam followers. The rollerscrew is driven at both top and bottom to minimize screw shaft wind-up. The drive consists of two DC brushless motors which are electronically synchronized to share torque. The motors are integrated with cycloidal drive speed reducers which output to the rollerscrew shaft. The rollerscrew nut is mounted to the strut and provides the vertical translation as the screw rotates. The nut and the two screw-shaft end bearings allow for shaft bending due to strut deflection, and the lower bearing is released axially to accommodate shaft elongation due to temperature differentials or loading.

PITCH SYSTEM

The pitch assembly consists of what is essentially a four-bar linkage arrangement. The linkage is driven through a bellcrank, by a 360,000 N (80,000 lb) capacity electromechanical linear actuator assembly mounted at the top of the strut. This actuator uses a rollerscrew connected to a harmonic-drive speed reducer and driven by a DC brushless motor.

STRUT BALANCE SYSTEM

A pair of pneumatic cylinders serve to provide partial support of the strut assembly dead weight, thereby improving the heave drive positioning accuracy. These cylinders are connected to a large volume air tank which provides essentially a constant pressure to the cylinders ($\pm 10\%$). This makes the balance system totally "passive" since air pumps are not required during operation. Each end of the cylinders require an independent air storage tank (one high and one low pressure). The two tanks are necessary because it is not possible to maintain a constant balance load with a single tank and one side vented to the plenum, since the tunnel pressure varies significantly (up to 6 atmospheres).

ROLL MECHANISM

The roll drive mechanism is attached to the pitch output mounting interface. The requirement of a 5-cm (2-in)-diameter hole through the center of the mechanism for model instrumentation and balance wires, called for a unique drive arrangement. All bending loads are supported by the outer housing while the rotary and axial loads pass through the core. The roll is actuated by use of a hollow core "pancake" brushless DC motor and a harmonic drive speed reducer. The harmonic drive is uniquely suited for this application because of its hollow core. This design is actually closely modeled after a design developed for the original tunnel. The new design however, incorporates some load and control system improvements.

One concern currently being studied is the EMI (electromagnetic interference) affect of running low-voltage instrumentation wiring near the power cables and through the center of the DC brushless motor. Depending upon the outcome of testing, plans are to provide an outer cable path for sensitive instrumentation or power cables.

HIGH ANGLE-OF-ATTACK MODEL SUPPORT (HAA)

The High Angle-of-Attack Model Support (figures 4 and 5) provides pitch angles from -15 to $+95$ degrees, yaw angle range of ± 180 , and roll of ± 180 degrees. The system is designed for a lift load of $\pm 27,000$ N ($\pm 6,000$ lbs), with the future capability to support up to $\pm 58,000$ N ($\pm 13,000$ lbs) of lift.

The HAA design is actually an integration with two other model support systems, the "Bipod" (figure 6a), mounted on a vertically translating platform for landing studies, the "Turntable," which provides yaw rotation for the Bipod, HAA, as well as "Semi-span" models (figure 6b), which are models split down the plane of symmetry.

PITCH SYSTEM

A single strut is attached to the carriage and penetrates the floor through a special seal mechanism. The strut can be defined for the specific test (size, angle, sting attachment, etc.). The strut designed as part of the Project also provides model roll.

The pitch axis drive consists of a "carriage" assembly which is guided by cam followers on two 70-degree-arc rails. Pitch actuation is provided by two electric motors driving pinions through speed reducers. The pinions engage geared racks which are integral with the pitch guide rails.

TURNTABLE YAW

The pitch drive system is mounted to a 560-cm (18-ft)-diameter, electrically driven, geared bearing which provides the yaw rotation. This bearing, referred to as a slewing ring bearing, is similar to those used for large jib crane pivots. The drive consists of a pinion driven by a harmonic-drive speed reducer and DC brushless motor.

ROLL MECHANISM

Mounted to the pitch carriage is a removable strut assembly which supports the test model. The strut assembly furnished by the Project has an integral roll drive and separates into two sections, providing a means for pitching the model through the design range in two steps. The roll is powered by a DC brushless motor coupled by a chain drive to the model interface, through a harmonic-drive speed reducer.

COMPONENT SELECTION

DRIVE MOTOR SELECTION

Early in the design process, it was decided that electromechanical mechanisms would be used instead of hydraulic cylinders and motors. The decision was based primarily upon the concern over the periodic maintenance required to replace hydraulic cylinder and motor seals, and the common leaks that occur in the hydraulic systems. Mechanically, hydraulics can be as efficient and possibly more cost efficient than the electromechanical systems, but past poor experiences with hydraulic systems made it unattractive.

DC brushless motors were selected because of their compactness and good past performance in similar applications. All actuated systems use the same type of motor in order to make the control system interface designs simpler. An exception to this was the RSS Roll Mechanism, which required a special frameless "pancake" motor.

TORQUE MULTIPLIERS

There are a number of torque multipliers/speed reducers available. The most common high-gear-ratio industrial speed reducers are multiple-stage spur gearboxes or worm drives. These tend to have unacceptable or undefined amounts of backlash, as well as low efficiencies. Less common are harmonic and cycloidal drives. These devices have high efficiencies, little or no backlash, and with their use in industrial robotics, have become more cost effective. These speed reducers have been incorporated into most of the new 12-Foot PWT model support designs.

ROLLERSCREWS

To generate linear motion from the electric motor rotary motion requires some sort of screw device. Commonly used devices are acme thread and ball screws. The acme screw has unacceptable low efficiencies and high friction. Ball screws in the sizes required, had larger nuts than a rollerscrew with the same capacity.

CONCLUSIONS

The close integration of the various model support systems within the test section and plenum area is a key feature of the 12-Foot PWT model support designs. Use of the Turntable yaw system for HAA, Bipod, and Semi-span tests, for instance, reduces the need for separate pieces of costly equipment. Also, the permanent installation of the majority of the hardware greatly reduces the operations involved in preparation and installation of different tests.

Another feature of these systems is that most of the airstream support components are removable while the larger equipment outside the airstream are permanent. This allows the researcher to provide test-specific components to meet specific needs such as lower blockage or higher load capacity than those provided by the 12-Foot PWT Restoration Project.

It is hoped that this "integrated" approach to model support systems can be adapted and improved upon in future tunnel designs.

As of the writing of this paper, detailed "shop" drawings of the model support systems are being completed, and the fabrication of some components has begun. Fabrication of the remaining systems is planned to start in early 1992, with installation in mid 1993.

ACKNOWLEDGEMENTS

The concepts for the model supports systems were a joint effort of DSMA International, Inc., Ontario, Canada, and NASA ARC. DSMA was responsible for the engineering of the final designs. The author would like to thank Willbur Vallotton, Donald Kassner, and Thomas Koizumi of NASA ARC, for their efforts in the concept development, and Paul Townson, DSMA Model Support Systems Lead Engineer, for many long hours making the concepts actually work.

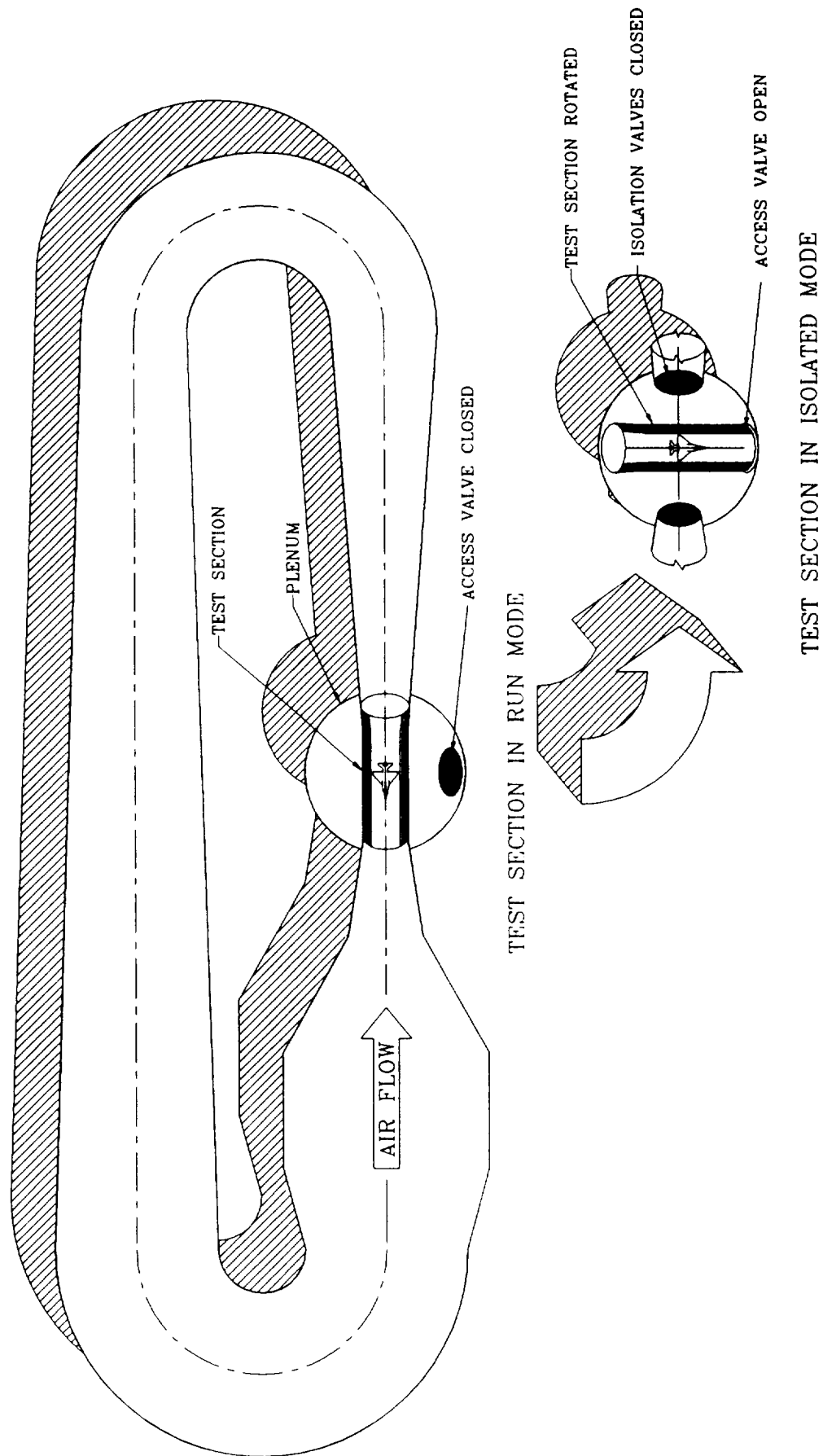


Figure 1. 12 FT PWT TSI System

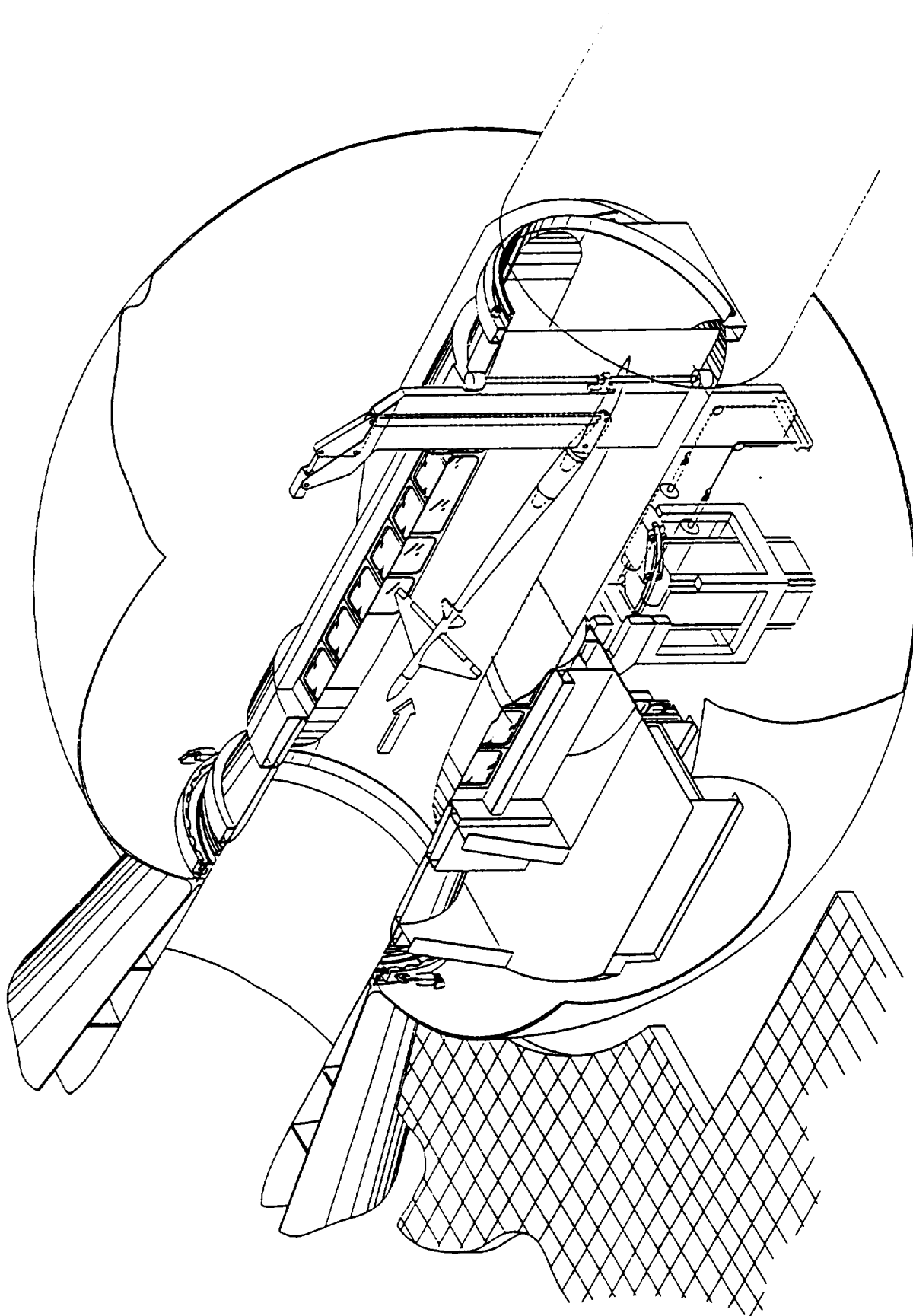


Figure 2. RSS Model Support System Installation

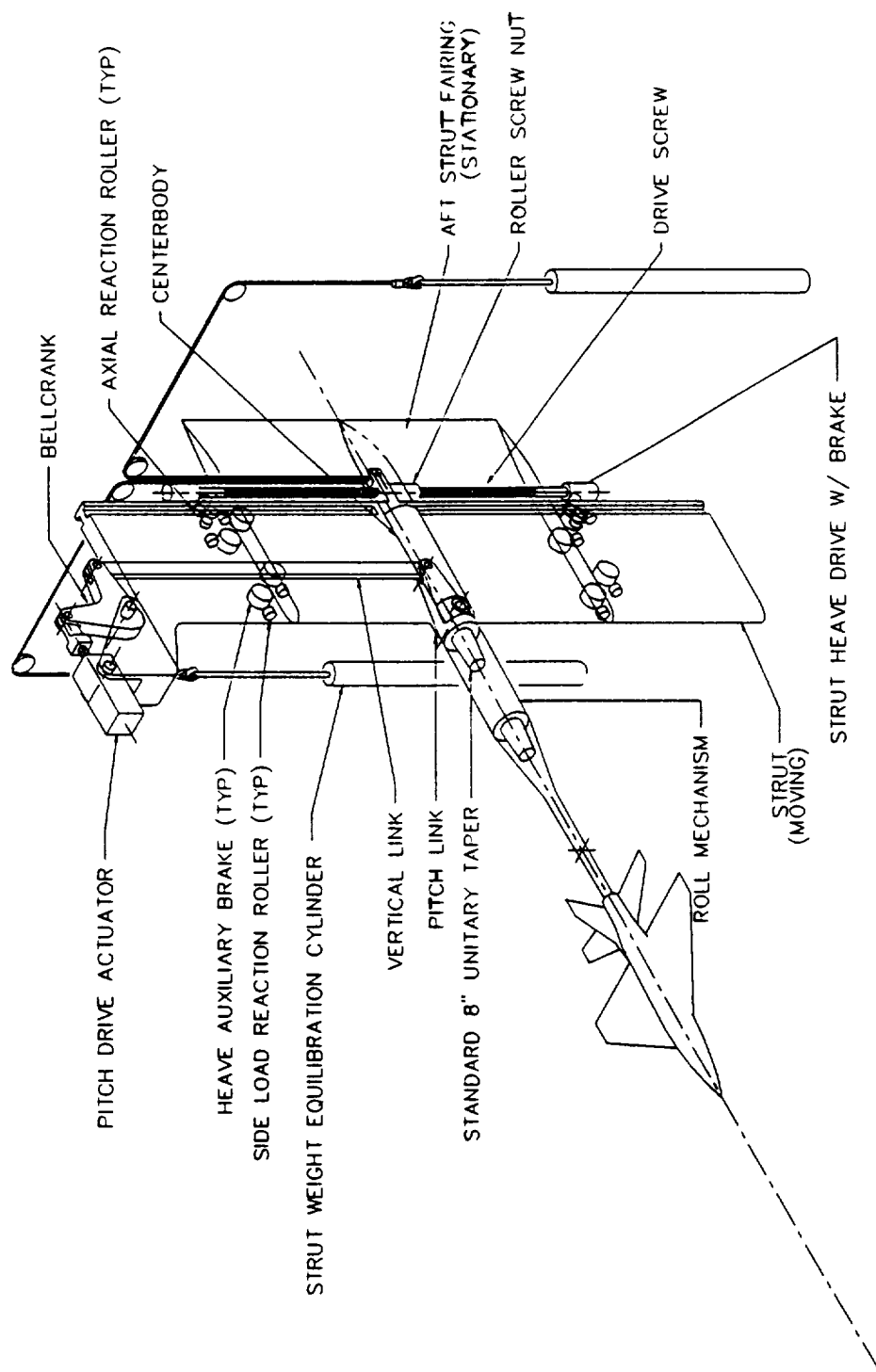


Figure 3. RSS Model 1 Support System Details

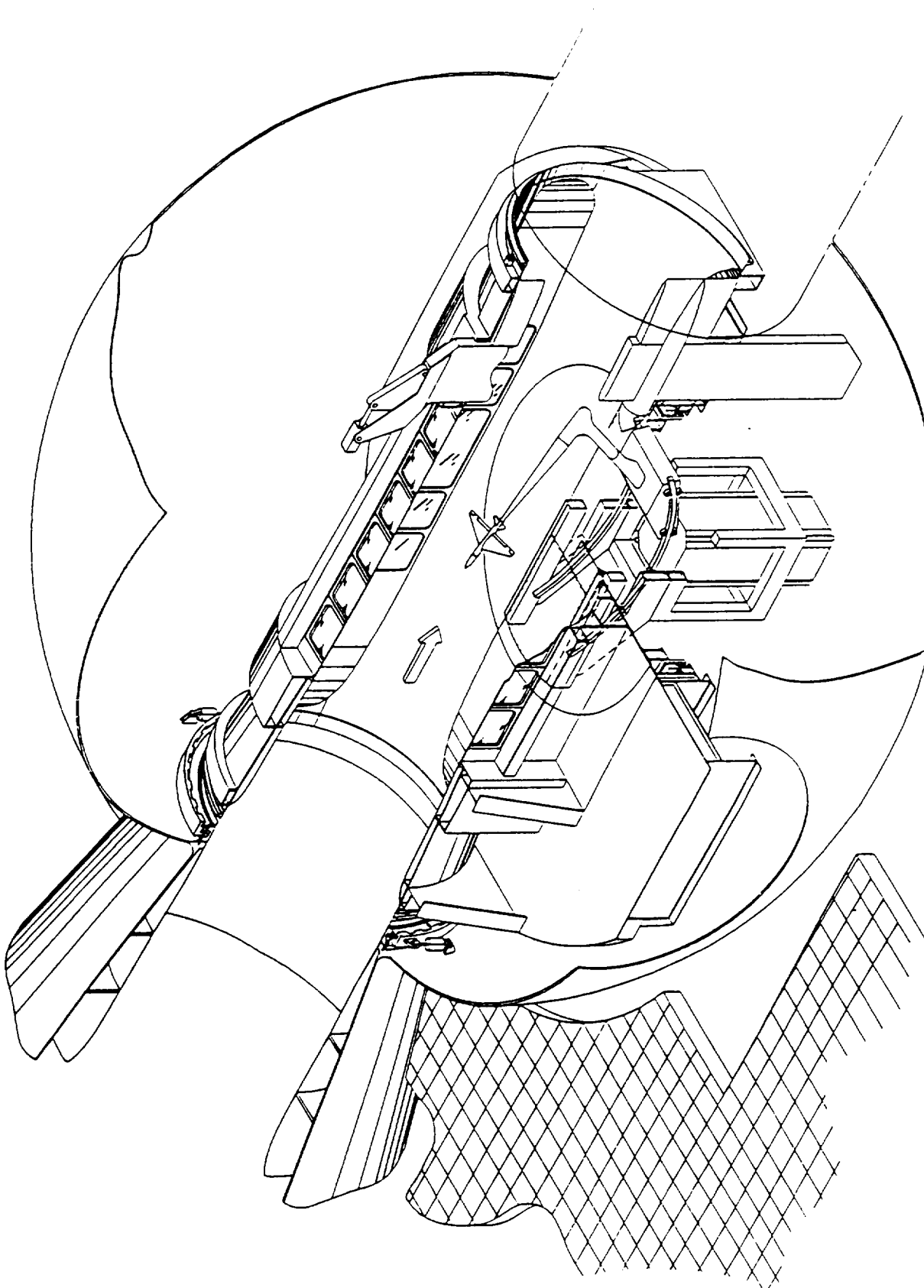


Figure 4. HAA Model Support System Installation

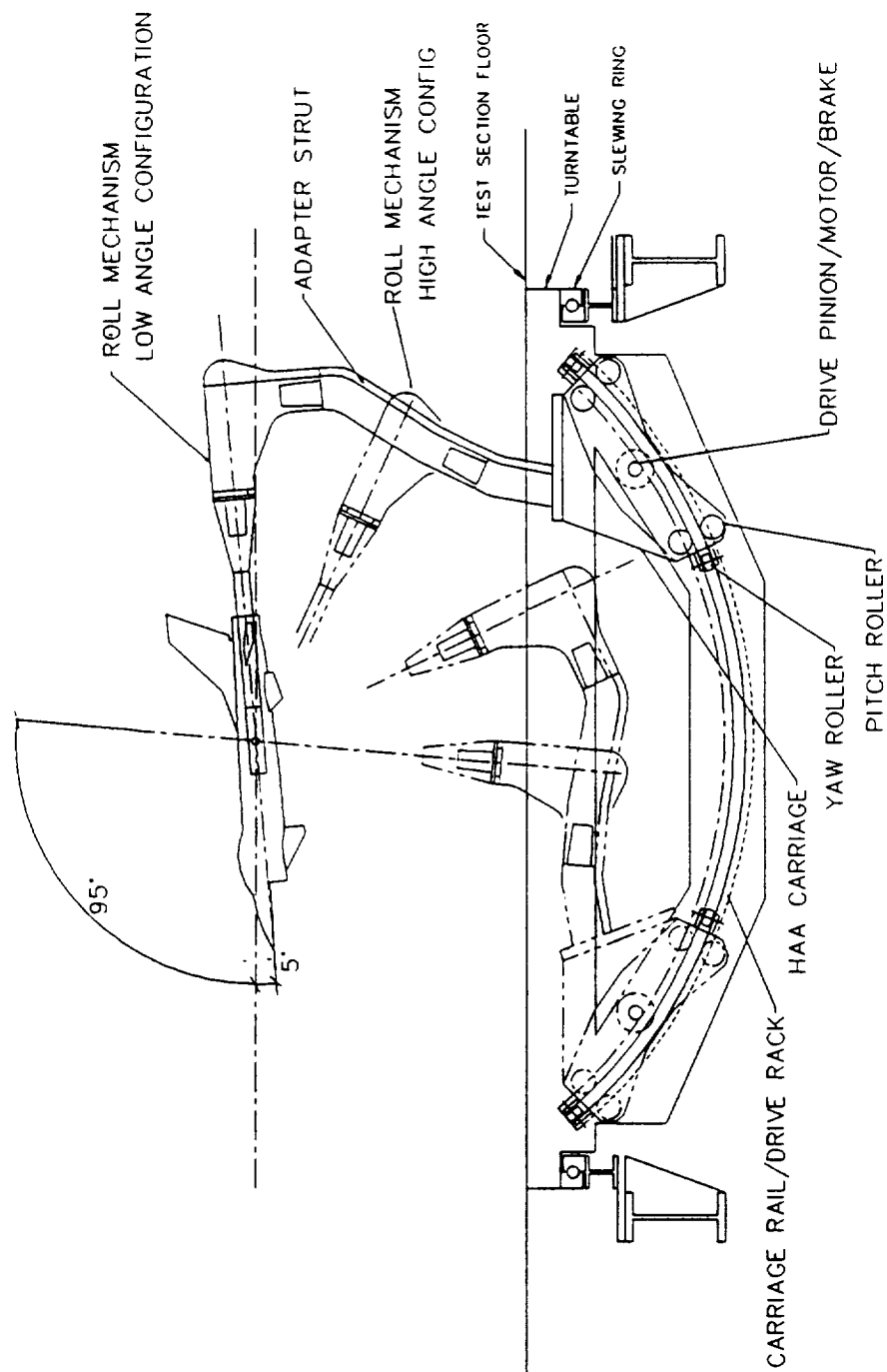


Figure 5. HAA Model Support System Details

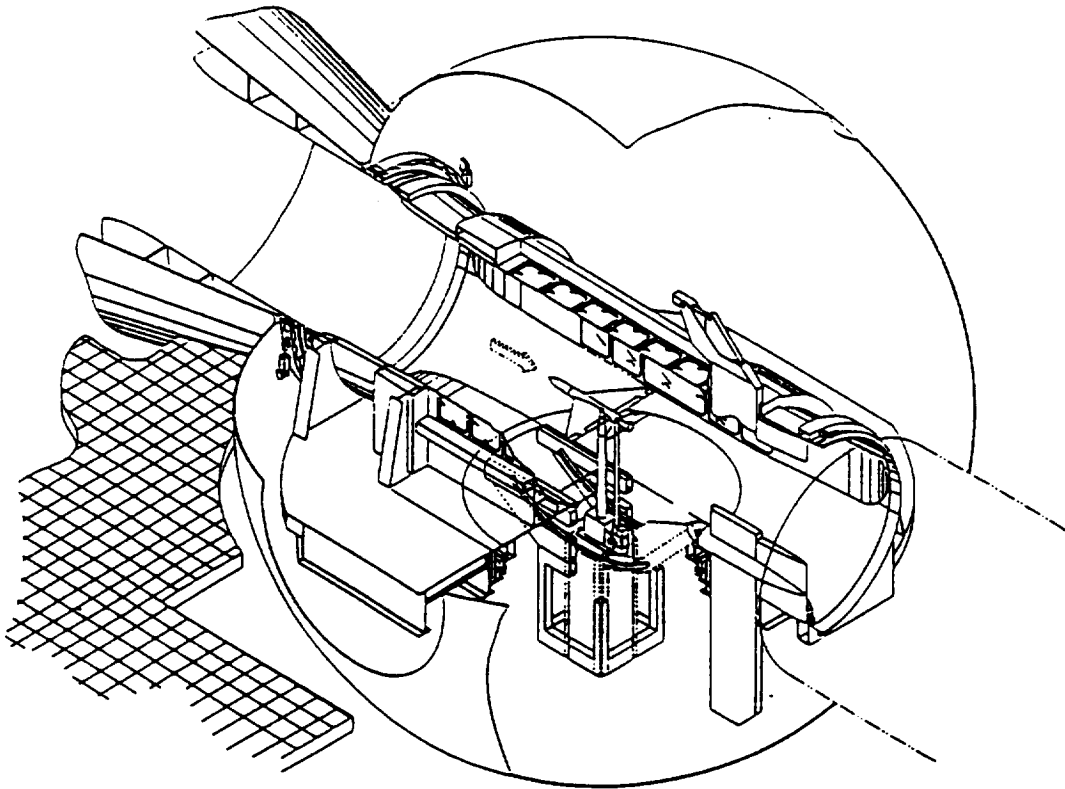


Figure 6a. Bipod Model Support Installation

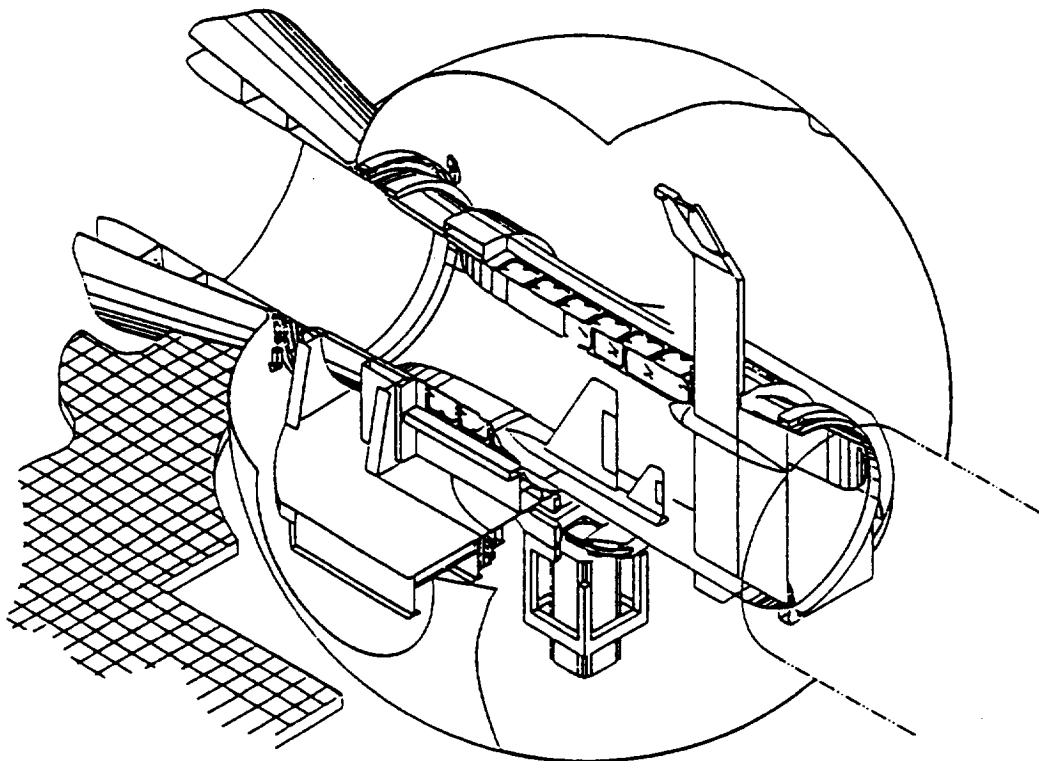


Figure 6b. Semi-Span Model Installation

REPORT DOCUMENTATION PAGE			Form Approved OMB No. 0704-0188	
<small>Public reporting burden for this collection of information is estimated to average 1 hour per response, including the time for reviewing instructions, searching existing data sources, gathering and maintaining the data needed, and completing and reviewing the collection of information. Send comments regarding this burden estimate or any other aspect of this collection of information, including suggestions for reducing this burden, to Washington Headquarters Services, Directorate for Information Operations and Reports, 1215 Jefferson Davis Highway, Suite 1204, Arlington, VA 22202-4302, and to the Office of Management and Budget, Paperwork Reduction Project (0704-0188), Washington, DC 20503.</small>				
1. AGENCY USE ONLY (Leave blank)	2. REPORT DATE May 1992	3. REPORT TYPE AND DATES COVERED Conference Publication		
4. TITLE AND SUBTITLE 26th Aerospace Mechanisms Symposium		5. FUNDING NUMBERS		
6. AUTHOR(S)				
7. PERFORMING ORGANIZATION NAME(S) AND ADDRESS(ES) NASA-Goddard Space Flight Center Greenbelt, Maryland 20771		8. PERFORMING ORGANIZATION REPORT NUMBER 92B00052		
9. SPONSORING/MONITORING AGENCY NAME(S) AND ADDRESS(ES) National Aeronautics and Space Administration Washington, D.C. 20546-0001		10. SPONSORING/MONITORING AGENCY REPORT NUMBER NASA CP-3147		
11. SUPPLEMENTARY NOTES California Institute of Technology, Pasadena, CA 91109. Lockheed Missiles and Space Company, Inc., Sunnyvale, CA 94088.				
12a. DISTRIBUTION/AVAILABILITY STATEMENT Unclassified - Unlimited Subject Category 39		12b. DISTRIBUTION CODE		
13. ABSTRACT (Maximum 200 words) The proceedings of the 26th Aerospace Mechanisms Symposium, which was held at the Goddard Space Flight Center, Greenbelt, Maryland, on May 13, 14, and 15, 1992, are reported. Technological areas covered include actuators, aerospace mechanism applications for ground-support equipment, lubricants, latches, connectors, and other mechanisms for large space structures.				
14. SUBJECT TERMS Circuitry, Piezoelectrics, Robotics, Hand Controller, Telescoping, End-Effector, Satellite Attitude Control, Bearings, Tribology, Friction Brakes		15. NUMBER OF PAGES 396		
		16. PRICE CODE A17		
17. SECURITY CLASSIFICATION OF REPORT Unclassified	18. SECURITY CLASSIFICATION OF THIS PAGE Unclassified	19. SECURITY CLASSIFICATION OF ABSTRACT Unclassified	20. LIMITATION OF AB- STRACT	